

University of Nevada, Reno

**Response of Lead Rubber Bearings in a Hybrid Isolation System During  
a Large Scale Shaking Experiment of an Isolated Building**

A dissertation submitted in partial fulfillment of the  
requirements for the degree of Doctor of Philosophy in  
Civil Engineering

by

Camila Berton Coria

Dr. Keri L. Ryan – Dissertation Advisor

December 2015

**Copyright by Camila Berton Coria 2015**

**All Rights Reserved**



University of Nevada, Reno

THE GRADUATE SCHOOL

We recommend that the dissertation  
Prepared under our supervision by

**CAMILA BERTON CORIA**

entitled

**RESPONSE OF LEAD RUBBER BEARINGS IN A HYBRID  
ISOLATION SYSTEM DURING A LARGE SCALE SHAKING  
EXPERIMENT OF AN ISOLATED BUILDING**

be accepted in partial fulfillment of the  
requirements for the degree of

**DOCTOR OF PHILOSOPHY**

Keri L. Ryan, Ph.D., Advisor

Ian G. Buckle, Ph.D., Committee Member

David H. Sanders, Ph.D., Committee Member

Ramin Motamed, Ph.D., Committee Member

Eric L. Wang, Ph.D., Graduate School Representative

David W. Zeh, Ph.D., Dean, Graduate School

December, 2015

## Abstract

Response of Lead Rubber Bearings in a Hybrid Isolation System During a Large Scale  
Shaking Experiment of an Isolated Building

By

Camila Berton Coria

Keri L. Ryan, Advisor

Seismic isolation systems have been proven to provide superior performance and meet continued functionality performance objectives for many facilities around the world, and are thus being considered for the future generation of nuclear power plants in the United States. Experimental simulation of a hybrid lead-rubber isolation system for a 5-story steel moment frame was performed at Hyogo Earthquake Engineering Research Center (E-Defense) of the National Institute for Earth Science and Disaster Prevention in Japan. The isolation system was developed for the seismicity of a potential nuclear site in Central and Eastern United States (CEUS) site. The isolation system was tested to displacements representing beyond design basis ground motions at the CEUS site and design basis ground motions for a Western United States. Forces in the lead-rubber (LR) bearings were measured by an assembly of load cells. The design of the isolation system was constrained by the experimental setup. The light axial loads on the system necessitated the use of a hybrid system of elastomeric bearings and rolling bearings, known as cross linear (CL) bearings. The CL bearings provided support beneath some of the columns without contributing to the system base shear, so that the target displacement

at the desired isolation period could be met. Additionally, the CL bearings provided substantial resistance against the tensile demands generated by overturning as a result of the light axial loads.

The following behaviors, many of which have been observed before, were observed in the response of LR bearings during this test program: (1) pinching near the center of the measured bearing hysteresis loop, attributed to the small size of the lead plug; (2) loss of characteristic strength over the duration of an excitation, associated with heating of the lead plug; (3) no loss of shear resistance at large displacements due to the stabilizing influence of the CL bearings; and (4) transfer of axial forces from LR bearings to CL bearings at large displacements, referred to as the load transfer effect, causing the LR bearings to sustain tension that was not induced by overturning. The load transfer effect, occurs due to the rigidity of the frame system connecting the bearings, the discrepancy in stiffness between the CL and LR bearings in the vertical direction, and the effective decrease in stiffness of the LR bearings at large horizontal displacements.

A numerical simulation model that represents current numerical approaches for design was developed for the isolation system and the structure. The lead-rubber bearings were modeled with a bilinear force-displacement relation with uncoupled behavior in the horizontal and vertical directions, referred as the uncoupled bearing model. Due to the amplitude dependence of the bearing response, the parameters of the uncoupled model were calibrated independently for each simulation to assess the experimental LR bearing response. Although the uncoupled bearing model could produce base shear and bearings displacements that closely matched the experimental response, the peak bearing

responses (base shear and horizontal displacements) were not captured by the uncoupled bearing model. The revised bounding analysis methodology was investigated to determine if the peak bearings responses could be reliably bounded with this approach. The bounding analysis was not 100% reliable to bound the observed experimentally peak horizontal displacement and peak base shear of the LR bearings due to spectral variation of the excitations. However, the new bounding analysis procedure that considers the responses of both upper bound and lower bound to bound both peak displacements and peak forces, was found to be an improvement over current design practices.

The uncoupled bearing model could not predict the load transfer effect that was observed during the experiment. Thus, a multi-spring LR bearing model with coupled behavior in the horizontal and vertical directions that could predict the load transfer effect was developed and validated. The numerically predicted horizontal responses obtained from the multi-spring bearing model and uncoupled bearing model were nearly identical.

Significant portions of this dissertation were taken from a report (Ryan et al. 2013a) prepared for the sponsor one year following the test. The author of this dissertation worked collaboratively on that report with other authors. All data from the experiments is permanently archived and publicly accessible in the NEES Project Warehouse (Ryan et al. 2013b, 2013c, 2013d).

*To my husband, son and mother:*

*Manuel Coria, Caleb Manuel Berton Coria and Elizabeth Cristina Cascarelli*

## ACKNOWLEDGMENT

I am now writing these words in this dissertation because God has blessed me beyond measures by giving me the opportunity to work with my exceptional-supportive advisor, Dr. Keri L. Ryan, for family and friends that were fundamental for my success.

Dr. Ryan, your kindness, friendship, continuous guidance and support in my studies and in my personal life made everything possible and worthwhile. I am greatly honored that you entrusted me to work on this project with you. I definitely have the best advisor! I also want to extend my gratitude to my committee members: Dr. Ian Buckle, David Sander, Ramin Motamed and Eric Wang for your support. I am extremely grateful for the sponsors of this project: the U.S. Nuclear Regulatory Commission through Contract NRC-HQ-11-C-04-0067; the National Science Foundation (NSF) Network for Earthquake Engineering Simulation (NEES) through NSF Grants CMMI-1113275 and CMMI-0721399; Japan's National Research Institute for Earth Science and Disaster Prevention (NIED); Dynamic Isolation Systems; and Aseismic Devices Company. I want to specially thank Amarnath Kasalanati for his kind and knowledgeable advices during this project.

Throughout my studies I had many friends that contributed directly or indirectly to my success. Nhan Dao, your work in this project was inspiring and fundamental, thank you from the bottom of my heart for all your support. I also want to thank Hamed Shotorbani, Jean Guzman, Chunli Wei, Manuel Diaz, Yolanda Baez, Marcos Sanches, Richard Wosnik, and Dr. Kirk Hagen for their support throughout my educational career. The



spiritual support given by Patricia and Ruben Parra, the Muniz family, Juliana Feitosa, Daniela Carvalho, and Denise Gori was extremely important, thank you! Other friends, you are not named here but I am very thankful for your help and encouragement.

Words are not sufficient to express how blessed I am to have you, Manuel Coria, as my husband. You are my rock. Thank you for supporting me physically, mentally and spiritually so I could follow my dream. None of this would have been possible without you being by my side. I love you. My dear mom, only you and I know what a blessing you are in my life. Thank you for taking care of my precious son while I finished this project. My dear son, as little as you are thank you for understand that mommy needed to work, I love you with all my heart. My dear sister, brother, and sister-in-law thank you for your emotional and spiritual support. Paulo and Dalva Barreto, thank you for opening the doors for me to come to USA to study. I will forever remember that you were all there to lift me up and pray for me when I was weak. From the bottom of my heart, thank you!

## TABLE OF CONTENTS

<b>Acknowledgment .....</b>	<b>v</b>
<b>Tabel of Contents .....</b>	<b>vii</b>
<b>List of Figures.....</b>	<b>xii</b>
<b>List of Tables .....</b>	<b>xxvi</b>
<b>Nomenclatures.....</b>	<b>xxviii</b>
<b>Chapter 1: Introduction .....</b>	<b>1</b>
1.1 Background of Seismic Isolation and its Consideration for Safety Related Nuclear Facilities .....	1
1.2 State of Knowledge and Motivation for Full Scale Testing.....	5
1.3 Testing of a Hybrid Isolation System at E-Defense .....	10
1.4 Research Objectives .....	13
1.5 Dissertation Organization.....	14
<b>Chapter 2: Design and Configuration of the 5-story Steel Moment Frame Testbed Structure .....</b>	<b>16</b>
2.1 Description of Testbed Structure.....	16
2.1.1 Basic Dimensions.....	16
2.1.2 Design Spectra and Design Criteria .....	18
2.1.3 Framing System .....	19
2.1.4 Slabs .....	22
2.1.5 Material Properties.....	23
2.2 Non-Structural Components and Contents.....	24
2.3 Weights.....	25
2.4 System Identification.....	27
2.5 Condition of the Testbed Prior to Testing.....	29
<b>3. Design of the Isolation System .....</b>	<b>30</b>
3.1 Target Response of a Nuclear Site .....	30
3.2 Isolation System Design.....	33
3.2.1 Estimated Displacement Demands .....	33

3.2.2	Configuration of Lead-Rubber Bearings .....	36
3.2.3	Selection of the Bearing Dimensions.....	40
3.2.4	Selection of the Lead Plug Dimensions .....	42
3.2.5	Cross Linear Bearings.....	44
3.2.6	Summary of Design Properties .....	48
3.3	Selection and Scaling of Ground Motions .....	50
3.3.1	Imposed Limitations for Safety .....	52
3.3.2	Vogtle and Diablo Canyon Motions .....	53
3.3.3	Remainder of the Test Program .....	60
<b>Chapter 4: Experimental Program .....</b>		<b>63</b>
4.1	Design of Connection Assembly .....	63
4.2	Instrumentation.....	68
4.2.1	Load Cells .....	69
4.2.2	Displacement Transducers .....	69
4.2.3	Accelerometers .....	72
4.3	Installation of the Specimen on the Earthquake Simulator .....	74
4.4	Test Schedule .....	79
4.5	Table Motions .....	85
4.6	Derived Responses .....	92
4.6.1	Horizontal Displacement of the Isolation System .....	92
4.6.2	Isolator Forces.....	95
4.6.3	Horizontal Acceleration and Story Drifts .....	97
<b>Chapter 5: Summary of Experimental Simulation Results for the Hybrid LR Isolated Building .....</b>		<b>99</b>
5.1	Isolator Displacements .....	99
5.2	Torsional Response .....	105
5.3	System Base Shear .....	109
5.4	Axial Forces in LR Bearings.....	113
5.5	Isolation System Re-Centering.....	119
5.6	Floor Accelerations in the Testbed Building.....	123

5.7	Story Drifts in Testbed Building .....	127
5.8	Summary of Observations.....	129
<b>Chapter 6: Technical Response of Hybrid LR Isolation System.....</b>		<b>130</b>
6.1	Bolt Slip in LR Bearings .....	130
6.2	Transfer of Load Between Bearings.....	139
6.3	Repeatability of Isolation System Response after Many Tests .....	157
6.4	Summary of Observations.....	171
<b>Chapter 7: Numerical Simulation Model of Testbed Structure .....</b>		<b>173</b>
7.1	Modeling Beams and Columns .....	175
7.2	Modeling Panel Zones.....	178
7.3	Modeling Gravity Load and Mass.....	181
7.4	Modeling Damping .....	183
7.5	Adjusting Vertical Reaction.....	187
<b>Chapter 8: Model for Isolation Bearings and Bearing Characterization.....</b>		<b>191</b>
8.1	Lead-Rubber Bearings .....	191
8.1.1	Horizontal Direction Modeling Assumptions .....	192
8.1.2	Vertical Direction Modeling Assumptions .....	193
8.2	Cross Linear Bearing.....	195
8.2.1	Horizontal Direction Modeling Assumptions.....	196
8.2.2	Vertical Direction.....	197
8.3	Composite Vertical Properties of the Isolation System .....	198
8.4	Characterization of Lead-Rubber Bearings.....	199
8.4.1	Characterization by Dynamic Isolation Systems .....	201
8.4.2	Characterization Based on Experimental Data .....	204
8.4.3	Trilinear Characterization .....	215
8.4.4	Final Bearing Parameter Selection for Numerical Simulation .....	220
8.5	Comparison of Experimental and Numerical Simulation Considering Characterized Bearing Properties .....	221
8.5.1	Isolator Response .....	222
8.5.2	Structural Response .....	235

<b>Chapter 9: Estimating Peak Isolation System Demands Through Bounding Analysis</b>	<b>243</b>
9.1 Introduction.....	243
9.2 Determining $\lambda_{rest}$ from Prototype Test Data.....	247
9.3 Comparison of Numerical and Experimental Data Considering Bounding Values .....	251
9.4 Bound Analysis.....	262
<b>Chapter 10: Model of Multiple Spring Lead-rubber bearing .....</b>	<b>274</b>
10.1 Construction of the MS-LRB Model .....	279
10.1.1 Vertical Direction.....	282
10.1.2 Horizontal Direction .....	286
10.2 Validating a Single MS2 Bearing Model.....	289
10.2.1 Validation of Horizontal Behavior.....	290
10.2.2 Validation of Vertical Behavior.....	295
10.2.3 Validation of Horizontal-Vertical Coupling .....	299
10.3 Validating the MS-LRB in a Simplified Single-Story Model .....	303
10.3.1 Validation of Horizontal Behavior.....	304
10.3.2 Validation of Horizontal Behavior.....	306
10.4 Summary of Observations.....	312
<b>Chapter 11: Comparison of Experimental and Three Numerical LR Bearings Responses .....</b>	<b>314</b>
11.1 Test Specimen Model Combined with Three LR Bearing Models .....	316
11.1.1 Sine 100% (Y) - 1 .....	316
11.1.2 Diablo 95% (XY).....	323
11.1.3 Vogtle 100% .....	331
11.1.4 Rinaldi 88% (XY).....	340
11.1.5 Calibration of Vertical Springs Stiffness in the MS2 and MS4 Bearing Models.....	347
11.1.6 Structural Response .....	350
11.2 Alternative Construction of the MS-LRB model.....	356
11.3 Summary of Observations.....	357
<b>Chapter 12: Conclusions .....</b>	<b>359</b>

12.1	Characteristics of Lead-Rubber Bearing Response .....	360
12.2	Hybrid Lead-Rubber (LR) and Cross-Linear (CL) Bearing System .....	361
12.3	Predictability of the System Response .....	362
12.3	Development and Response of a Multi-Spring Bearing Model .....	364
<b>References .....</b>		<b>366</b>
<b>Appendix A .....</b>		<b>377</b>
<b>Appendix B .....</b>		<b>398</b>
<b>Appendix C .....</b>		<b>407</b>
<b>Appendix D .....</b>		<b>416</b>
<b>Appendix E .....</b>		<b>436</b>
<b>Appendix F .....</b>		<b>461</b>

## LIST OF FIGURES

Figure 2-1:	The 5-story steel moment frame specimen.....	17
Figure 2-2:	Basic dimensions of the specimen: (a) typical plan view from floors 2 to 5, and (b) elevation view.....	18
Figure 2-3:	Design spectrum for Japanese Level II and Level III earthquakes .....	20
Figure 2-4:	Beam, beam to column connection and slab.....	20
Figure 2-5:	Column base: (a) view from top (b) view from bottom, (c) rendering of stiffeners.....	21
Figure 2-6:	Horizontal braces at base level. ....	22
Figure 2-7:	Hospital room.....	24
Figure 2-8:	Office room.....	25
Figure 2-9:	Location of steel weights at roof.....	26
Figure 2-10:	Transfer function during white noise excitation in fixed-base configuration: (a) x-direction and (b) y-direction.....	28
Figure 2-11:	Cracks in concrete slab and rust on steel member .....	29
Figure 3-1:	5% damped URS for the DBE at the Vogtle site (Source: Huang et al. 2009) .....	32
Figure 3-2:	5% damped response spectra for the 30 sets of spectrum compatible maximum-minimum motions: (a) maximum component, (b) minimum component and (c) vertical component. (Source: Huang et al. 2009) .....	32
Figure 3-3:	Idealized bilinear force-displacement relationship for LR bearings, determined by post-yield stiffness $K_d$ (stiffness of rubber), characteristic strength $Q_d$ (strength of lead plug) and initial stiffness $K_l$ or yield displacement $D_y$ . An effective or secant stiffness $K_{eff}$ is determined as the peak-to-peak stiffness based on maximum force $F_{max}$ and displacement $D_{max}$ . ....	34
Figure 3-4:	Displacement demand representing (a) median response to maximum-minimum motions and (b) 90% percentile response to 150% maximum-minimum motions for Vogtle site. ....	35
Figure 3-5:	Drawing of testbed base plan with column labels (N = North, E = East, S = South, W = West, C = Center). ....	37
Figure 3-6:	Illustration of a connection assembly with triaxial load cells to measure bearing forces.....	38
Figure 3-7:	(a) Configuration Option 1 with LR bearings beneath 4 corner columns, (b) Configuration Option 2 with LR bearings (circles) beneath 4 edge	

	columns and low friction bearings (squares) beneath remaining columns. The supported weights (in units of kN) at the isolators based on tributary loads are also indicated. ....	39
Figure 3-8:	Proposed design options for LR bearings .....	41
Figure 3-9:	Axial force capacity of proposed LR bearings versus lateral displacement .....	41
Figure 3-10:	Photo of installed CL bearing illustrating orthogonal LM guides assemblies on top and bottom. ....	45
Figure 3-11:	Total base shear ( $V_b$ ) and overturning forces ( $F_{OT}$ ) acting on an elevation view of the testbed building. ....	47
Figure 3-12:	(a) Final plan drawing of the hybrid LR isolation system, (b) photo of LR bearing, and (c) photo of CL bearing. ....	49
Figure 3-14:	Calculated displacement histories of the isolation system in x and y-directions for 6 Vogtle motions by SDOF analysis .....	55
Figure 3-15:	Predicted displacement trace of each isolator for the OpenSees building model subjected to 150% Vogtle #13 .....	57
Figure 3-16:	Predicted displacement trace of each isolator for the OpenSees building model subjected to 150% Vogtle #13, with input ground excitation components rotated by 11.25 degrees. ....	59
Figure 3-17:	Predicted displacement trace of each isolator for the OpenSees building model subjected to 100% Diablo Canyon #15. ....	60
Figure 4-1:	Load cell connection assemblies used for: (a) East bearing and (b) North, South and West bearings. ....	65
Figure 4-2:	Connection assembly .....	66
Figure 4-3:	Load cell drawings with bolt patterns and elevation views: (a) Type A and (b) Type B .....	67
Figure 4-4:	Connection of Type A and Type B load cells to top and bottom connection plates .....	67
Figure 4-5:	Magnitude of low-pass Butterworth Filter transfer function .....	69
Figure 4-6:	Load cell channels for the hybrid LR isolation configuration .....	70
Figure 4-7:	Layout of displacement transducers at base. ....	71
Figure 4-8:	Instrumentation for measuring story drift .....	71
Figure 4-9:	Layout of displacement transducers to measure story drift in 2 <sup>nd</sup> to 5 <sup>th</sup> stories .....	72
Figure 4-10:	Accelerometers at the top connection plates to estimate inertia forces ....	73
Figure 4-11:	Layout of accelerometers at the 5 <sup>th</sup> floor .....	74
Figure 4-12:	Connection assembly .....	75
Figure 4-13:	Connection assemblies on the simulator platform .....	76



Figure 4-14:	Installing the LR bearings to the connecting assemblies and the CL bearings to the simulator platform .....	76
Figure 4-15:	Lowering the testbed building over the isolation system.....	77
Figure 4-16:	Bolt holes for connecting the testbed structure to the isolation system....	77
Figure 4-17:	Drilling and tapping holes at the bottom of the specimen .....	78
Figure 4-18:	Acceleration history of target and realized RRS88 motion in the hybrid LR isolation configuration test.....	89
Figure 4-19:	Ratio of realized to target motion 5% damped spectral accelerations – hybrid LR isolation configuration.....	90
Figure 4-20:	Ratio of realized to target motion 5% damped spectral accelerations – fixed-base configuration .....	91
Figure 4-21:	Configurations for solving displacement of the isolation system. (a) original configuration, (b) displaced configuration .....	95
Figure 4-22:	Free body diagram illustrating derivation of isolator reaction.....	96
Figure 4-23:	Diagram illustrating the computation of drift at the geometric center.....	98
Figure 5-1:	Peak vector sum displacement recorded in any LR bearing for each earthquake simulation .....	102
Figure 5-2:	Maximum isolator (LR bearing) displacement (a) for each ground excitation relative to DB and EDB levels, (b) versus intensity for Vogtle motions.....	103
Figure 5-3:	X-direction, y-direction and overall peak (vector sum) displacement of each LR bearing for each earthquake simulation.....	103
Figure 5-4:	Displacement trace (x vs y-direction displacement) of the East LRB for (a) WSM80, (b) DIA95(XY), (c) VOG100 and (d) VOG175.....	104
Figure 5-5:	Peak rotation angle of the base for each earthquake simulation.....	106
Figure 5-6:	Displacement trace of each isolator during the Vogtle 175% simulation	107
Figure 5-7:	Computed torsion amplification factor for several motions. ....	109
Figure 5-8:	Base shear coefficient for all simulations: total, x and y-directions .....	111
Figure 5-9:	Base shear coefficient for each simulation alongside the design backbone curve.....	113
Figure 5-10:	Peak compressive force in any LR bearing for each earthquake simulation .....	117
Figure 5-11:	Peak tensile force in any LR bearing for each earthquake simulation. (A tensile force of zero indicates that tension was not observed).....	117
Figure 5-12:	Peak axial forces in each LR bearing for each simulation: (a) Peak compression force, (b) normalized peak compression force, (c) peak tension force, and (d) normalized peak tension force. ....	118

Figure 5-13:	Axial force in the LR bearing at the peak horizontal displacement, and maximum and minimal compressive axial force for each input motion compared to the critical load.....	119
Figure 5-14:	X-direction, y-direction, and total (vector sum) displacement recorded in each LR bearing at the end of every earthquake simulation.....	121
Figure 5-15:	Permanent displacement of around 11 mm on the East bearing due to sliding of the bottom steel plate.....	122
Figure 5-16:	Permanent displacement at the location of each LR bearing at the end of one simulation compared to the beginning of the next.....	123
Figure 5-17:	Peak acceleration profile for all simulations in both horizontal directions. . .....	126
Figure 5-18:	Peak floor acceleration profiles for increasing intensity of Vogtle input excitation (75% - 175%)......	126
Figure 5-19:	Peak absolute and normalized acceleration profile comparing XY and 3D excitations for Diablo (95% and 80% respectively) and Rinaldi (88%).	127
Figure 5-20:	Peak story drift throughout the height of the building for all excitations in x and y directions.....	128
Figure 6-1:	Movement of (a) East LR bearing relative to (b) top and (c) bottom plates. .....	132
Figure 6-2:	Horizontal force history of the East bearing (LRB-E) in the x- and y-directions for a subset of the trials.....	133
Figure 6-3:	X and y-direction hysteresis loops (horizontal force vs. displacement) of the East bearing (LRB-E) during Vogtle 125% and Vogtle 150%.....	136
Figure 6-4:	Horizontal ( $F_x$ and $F_y$ ) and vertical ( $F_z$ ) force history of all four LR bearings during Vogtle 150%.....	137
Figure 6-5:	Propagation of bolt slip through the height of the structure in x-direction during Vogtle 150%; unfiltered horizontal force in LRB-E and 1 <sup>st</sup> – 6 <sup>th</sup> floor acceleration in SE column.....	138
Figure 6-6:	Resultant action on LR bearings as a result of CL bearings and base diaphragm constraint.....	139
Figure 6-7:	History of average horizontal displacement (x, y and vector sum), and axial force in individual LR bearings and summed over all LR bearings for Sine Wave (XY).....	141
Figure 6-8:	History of average horizontal displacement (x, y and vector sum), and axial force in individual LR bearings and summed over all LR bearings for Diablo 95% (XY).....	142
Figure 6-9:	History of average horizontal displacement (x, y and vector sum), and axial force in individual LR bearings and summed over all LR bearings for Rinaldi 88% (XY).....	143

Figure 6-10:	History of axial force in individual LR bearings and summed over all LR bearings for Rinaldi 88%. .....	147
Figure 6-11:	History of axial force in individual LR bearings and summed over all LR bearings comparing Rinaldi 88% – dashed line – and Rinaldi 88% (XY) – solid line. A low pass filter with a cutoff frequency of 2 Hz was applied to the total axial force for Rinaldi 88% and is superimposed over the total, shown as a red dashed line.....	148
Figure 6-12:	History of average vector sum displacement at building center, axial force in individual LR bearings and axial force summed over all LR bearings comparing Diablo 95% – dashed line – and Diablo 80% (XY) – solid line. A low pass filter with a cutoff frequency of 2 Hz was applied to the total axial force for Diablo 80% and is superimposed over the total, shown as a red dashed line. ....	149
Figure 6-13:	History of average vector sum displacement at building center, axial force in individual LR bearings and axial force summed over all LR bearings for Vogtle 175%. A low pass filter with a cutoff frequency of 2 Hz was applied to the total axial force and is superimposed over the total, shown as a red dashed line. ....	150
Figure 6-14:	Relative change in the total (summation over all LR bearings) compressive force .....	152
Figure 6-15:	Sample feedback acceleration at the center of the earthquake simulator (averaged over several accelerometers) in the x and y-directions compared for the first and second Sine 100% (Y) and Vogtle 75% simulations. ...	158
Figure 6-16:	5% damped response spectra for the feedback acceleration at the center of the earthquake simulator (averaged over several accelerometers) in the x, y and z-directions compared for the first and second Sine 100% (Y) and Vogtle 75% simulations.....	159
Figure 6-17:	Y-direction force vs. displacement (hysteresis loops) for the 1 <sup>st</sup> and 2 <sup>nd</sup> simulation of Sine 100%(Y). ....	162
Figure 6-18:	Y-direction displacement and force histories for the 1 <sup>st</sup> and 2 <sup>nd</sup> simulation of Sine 100% (Y). ....	163
Figure 6-19:	X-direction force vs. displacement (hysteresis loops) for the 1 <sup>st</sup> and 2 <sup>nd</sup> simulation of Vogtle 75%. ....	165
Figure 6-20:	Y-direction force vs. displacement (hysteresis loops) for the 1 <sup>st</sup> and 2 <sup>nd</sup> simulation of Vogtle 75%. ....	166
Figure 6-21:	X-direction displacement and force histories for the 1 <sup>st</sup> and 2 <sup>nd</sup> simulation of Vogtle 75%. ....	167
Figure 6-22:	Y-direction displacement and force histories for the 1 <sup>st</sup> and 2 <sup>nd</sup> simulation of Vogtle 75%. ....	168

Figure 6-23:	X vs. y-direction displacement (displacement trace) for the 1 <sup>st</sup> and 2 <sup>nd</sup> simulation of Vogtle 75%.....	169
Figure 6-24:	Y-direction force vs. displacement (hysteresis loops) identified by cycle for the 1 <sup>st</sup> and 2 <sup>nd</sup> simulation of Sine 100% (Y).....	170
Figure 6-25:	X-direction force vs. displacement (hysteresis loops) for the 1 <sup>st</sup> and 2 <sup>nd</sup> cycles of Vogtle 175%.....	171
Figure 7-1:	(a) Photo and (b) OpenSees model of the testbed building without isolators .....	174
Figure 7-2:	Primary beam, beam-to-column connection, and slab.....	174
Figure 7-3:	Behavior of a representative composite fiber section beam with and without axial restraint: (a) fiber section geometry and (b) force-displacement relationship.....	177
Figure 7-4:	Composite section behavior: (a) moment-curvature relationship of the section, (b) component 1 of resultant section modeled by steel material model, and (c) component 2 of resultant section modeled by hysteresis model.....	178
Figure 7-5:	Panel zone model for beam to column connection. (a) beam to column connection, (b) numerical model of panel zone.....	179
Figure 7-6:	Gusset plate and its finite element model: (a) gusset plate, (b) Von-Mises stress due to gravity load.....	181
Figure 7-7:	Rayleigh damping model for the fixed-base and hybrid LR isolated building model .....	185
Figure 7-8:	Additional damper for adjusting the damping coefficient of the 2 <sup>nd</sup> mode in the X direction.....	187
Figure 8-1:	Horizontal force-displacement of LR bearing for numerical simulation	193
Figure 8-2:	Vertical force-deformation of LR bearing for numerical simulation: (a) elastic-no tension, (b) elastic, and (c) combined.....	194
Figure 8-3:	Horizontal force-displacement of CL bearing for numerical simulation	196
Figure 8-4:	Vertical force-deformation of CL bearing for numerical simulation: (a) elastic-no tension, (b) elastic, and (c) combined.....	198
Figure 8-5:	Comparison of fitted hysteresis loop and parameters to test data.....	202
Figure 8-6:	Hysteresis loop of Test A and D for one of the isolation pairs.....	203
Figure 8-7:	Projection of displacement trace to main axis for Vogtle 100% .....	205
Figure 8-8:	Selection of cycle for characterization for Vogtle 100% .....	206
Figure 8-9:	Hysteresis loop of peak cycle for the projected-direction for East bearing for Vogtle 100%.....	208
Figure 8-10:	Numerical and experimental hysteresis loop using (a),(c) isolator design parameters and (b),(d) characterized parameters. ....	212

Figure 8-11:	Y-direction hysteresis and force history of test data of the East bearing compared to (a)-(b) characterization model, and (c)-(d) design model for Sine 100%(Y)-1. ....	213
Figure 8-12:	X and y-direction displacement history of experimental data compared to (a) characterized model and (b) design model for Vogtle 175%, East bearing.....	215
Figure 8-13:	Force vs. displacement loop for the East LRB in Sine 100% (Y)-1 .....	216
Figure 8-14:	Conceptual force vs. displacement of lead plug for monotonic loading (courtesy of Dynamic Isolation Systems) .....	217
Figure 8-15:	Comparison of numerical and experimental simulation force versus displacement of the East bearing for SIN100(Y)-1 and VOG100 using (a), (c) a trilinear hysteretic model and (b), (d) a bilinear hysteretic model. ....	219
Figure 8-16:	Comparison of numerical simulation with 100% and 85% characterized values of $Q_d$ to the experimental data for Vogtle 100%; displacement history and hysteresis loop in the y-direction for the East bearing. ....	221
Figure 8-17:	Comparison of numerical and experimental simulation for El Centro 130%; displacement trace and displacement histories (x and y) in each LR bearing, labeled by position (E, S, N, W). Numerical simulation uses the characterized model with 85% of the characterized value for $Q_d$ . ....	226
Figure 8-18:	Comparison of numerical and experimental simulation for El Centro 130%; bearing force vs. displacement or hysteresis loops (x and y) in each LR bearing, labeled by position (E, S, N, W). Numerical simulation uses the characterized model with 85% of the characterized value for $Q_d$ . ...	227
Figure 8-19:	Comparison of numerical and experimental simulation for Vogtle 100%; displacement trace and displacement histories (x and y) in each LR bearing, labeled by position (E, S, N, W). Numerical simulation uses the characterized model with 85% of the characterized value for $Q_d$ .....	228
Figure 8-20:	Comparison of numerical and experimental simulation for Vogtle 100%; displacement trace and displacement histories (x and y) in each LR bearing, labeled by position (E, S, N, W). Numerical simulation uses the characterized model with 85% of the characterized value for $Q_d$ . ....	229
Figure 8-21:	Comparison of numerical and experimental simulation for Vogtle 175%; displacement trace and displacement histories (x and y) in each LR bearing, labeled by position (E, S, N, W). Numerical simulation uses the characterized model with 85% of the characterized value for $Q_d$ . ....	230
Figure 8-22:	Comparison of numerical and experimental simulation for Vogtle 175%; displacement trace and displacement histories (x and y) in each LR bearing, labeled by position (E, S, N, W). Numerical simulation uses the characterized model with 85% of the characterized value for $Q_d$ .....	231

- Figure 8-23: Comparison of numerical and experimental simulation for Diablo 95%; displacement trace and displacement histories (x and y) in each LR bearing, labeled by position (E, S, N, W). Numerical simulation uses the characterized model with 85% of the characterized value for  $Q_d$ . ..... 232
- Figure 8-24: Comparison of numerical and experimental simulation for Diablo 95%; displacement trace and displacement histories (x and y) in each LR bearing, labeled by position (E, S, N, W). Numerical simulation uses the characterized model with 85% of the characterized value for  $Q_d$ . ..... 233
- Figure 8-25: Comparison of numerical and experimental simulation for Vogtle 175%; history of base rotation angle. Analysis uses the characterized model with 85% of the characterized value for  $Q_d$ . ..... 234
- Figure 8-26: Comparison of numerical and experimental simulation for El Centro 130%; x and y-direction roof acceleration histories, peak acceleration profiles, 2nd story drift histories, and peak drift profiles. Numerical simulation uses the characterized model with 85% of the characterized value for  $Q_d$ . ..... 236
- Figure 8-27: Comparison of numerical and experimental simulation for Vogtle 100%; x and y-direction roof acceleration histories, peak acceleration profiles, 2nd story drift histories, and peak drift profiles. Numerical simulation uses the characterized model with 85% of the characterized value for  $Q_d$ . ..... 237
- Figure 8-28: Comparison of numerical and experimental simulation for Vogtle 175%; x and y-direction roof acceleration histories, peak acceleration profiles, 2nd story drift histories, and peak drift profiles. Numerical simulation uses the characterized model with 85% of the characterized value for  $Q_d$ . ..... 238
- Figure 9-1: (a) variation in the normalized  $\lambda_{test}^{K_d}$  and  $\lambda_{test}^{Q_d}$  observed during the manufacturer prototype test, (b) force-displacement loop of prototype test for 300 mm (Trial ID A) and 500 mm (Trial ID B)..... 249
- Figure 9-2: Normalized displacement and total base shear plotted against experimental peak displacement for all ground motions with exception of WMS80, VOG75-2, SIN100-2 for all methods using UB parameters and design values. .... 256
- Figure 9-3: Normalized displacement and total base shear plotted against experimental peak displacement for all ground motions with exception of WMS80, VOG75-2, SIN100-2 for all methods using LB parameters and design values. .... 257
- Figure 9-4: Comparison of normalized displacement and base shear plotted against experimental peak displacement for Method 3 Bin1, Bin 2 and Bin Combined using UB parameters. .... 258

Figure 9-5:	Comparison of normalized displacement and total base shear plotted against experimental peak displacement for Method 3 Bin1, Bin 2 and Bin Combined using LB parameters.....	259
Figure 9-6:	Comparison of the median determined from regression analysis for all methods using UB and LB parameters. ....	261
Figure 9-7:	(a) Peak isolator force and (b) peak isolator displacement obtained experimentally, and from Design, Method1-UB, and Method1-LB of selected ground motions. ....	262
Figure 9-8:	Idealized force-displacement loop for Design, Method 1-UB, and Method 1-LB compared with prototype loop for a peak displacement of (a) 300 mm and (b) 500 mm.....	263
Figure 9-9:	Idealized force-displacement loop considering the Design, Method1-UB and Method1-LB bearing parameters for a design peak displacement of 500 mm. ....	265
Figure 9-10:	Comparison of the Design, Method 1-UB and Method 1-LB smoothed hysteresis loops with the response of DIA95(XY) in the projected direction. ....	266
Figure 9-11:	Comparison of experimental force-displacement loop with Design, Method1-UB and Method1-LB in the projected, x- and y-directions for DIA95(XY).....	269
Figure 9-12:	Comparison of experimental force-displacement loop with Design, Method1-UB and Method1-LB in the projected directions for VOG175. ....	270
Figure 9-13:	Comparison of experimental force-displacement loop with Design, Method1-UB and Method1-LB in the projected directions for SIN100(Y)-1.....	270
Figure 9-14:	Comparison of experimental force-displacement loop with Design, Method1-UB and Method1-LB in the projected directions for ELC130.....	271
Figure 9-15:	5% damped displacement spectrum for VOG175, DIA95(XY), SIN100(Y)-1, and ELC130.....	272
Figure 10-1:	Multi-spring mechanical model (Yamamoto et al 2009; Kikuchi et al. 2010).....	277
Figure 10-2:	Mechanistic model for elastomeric bearing (Han et al. 2014).....	278
Figure 10-3:	(a) undeformed multiple spring model, (b) multiple spring model under vertical and horizontal deformations. ....	281
Figure 10-4:	(a-b) MS2 with shear springs in two directions (X and Y), (c-d) MS4 with shear springs in four directions (X, Y and $\pm 45^\circ$ from x-axis).....	282
Figure 10-5:	(a) Axial load transfer elements, (b) elements in shear layer .....	283
Figure 10-6:	Force-displacement relationship for vertical springs.....	284

Figure 10-7: Horizontal force-displacement of LR bearing: (a) rubber, (b) lead plug, (c) combined.....	286
Figure 10-8: Forces generated in a (a) single vs (b) double truss configuration subjected to a horizontal displacement in the x-direction.....	288
Figure 10-9: Single bearing system for validation of MS2 .....	290
Figure 10-10: Force-displacement relationship for the truss, plastic spring, and composite due to a controlled cyclic displacement history analysis in the y-direction of the MS2 model. ....	292
Figure 10-11: Force-displacement relationship for the truss, plastic spring, and composite from subjecting (a) the MS2 model and (b) the MS4 model to the y-component of SIN100(Y)-1 simultaneously in the x- and y-direction. ..	293
Figure 10-12: Truss and plastic spring force trace from subjecting the MS2 model to the y-component of SIN100(Y)-1 simultaneously in the x- and y-direction. ....	294
Figure 10-13: Yield surface of MS2 model. ....	294
Figure 10-14: Force-displacement relationship of MS2 model in the vertical direction for the center and edge vertical springs. ....	296
Figure 10-15: Vertical vs horizontal bearing displacement using low rigidity for the MS2 rigid shear beam. ....	298
Figure 10-16: Vertical vs horizontal bearing displacement using high rigidity for the MS2 rigid shear beams. ....	299
Figure 10-17: Force-displacement relationship of (a) MS2 and (b) MS4 models with varying axial force as a function of $P_{cr}$ . ....	301
Figure 10-18: Theoretical vs numerical influence of the axial load on the horizontal stiffness for the (a) MS2 and (b) MS4 model. ....	302
Figure 10-19: OpenSees model of a simplified single-story structure with MS2 and CL isolators. ....	304
Figure 10-20: Force-displacement relationship for the truss, plastic spring, and composite in the East bearing due to a controlled cyclic displacement history of the SSS Model in the y-direction. ....	305
Figure 10-21: Force-displacement loops for each LR bearing in the SSS model due to a controlled cyclic displacement history in the y-direction. ....	306
Figure 10-22: Theoretical vs numerical vertical bearing displacement due to a controlled cyclic displacement history.....	308
Figure 10-23: Displacement and vertical force history of each LR bearing due to a horizontal displacement in the y-direction of the SSS model.....	311
Figure 10-24: Load transfer in the SSS model due to a horizontal displacement. ....	312
Figure 11-1: (a) Elastic-perfectly plastic, (b) elastic, (c) bilinear force-displacement relationship in the vertical direction. ....	316



Figure 11-2: Comparison of experimental and numerical simulation for Sine 100%; displacement history in each LR bearing, labeled by position (E, S, N, W). Numerical simulation of uncoupled, MS2, and MS4 LR bearing models. ....	318
Figure 11-3: Comparison of experimental and numerical simulation for Sine 100%; displacement trace in each LR bearing, labeled by position (E, S, N, W). Numerical simulation of uncoupled, MS2, and MS4 LR bearing models. ....	319
Figure 11-4: Comparison of experimental and numerical simulation for Sine 100%; horizontal force history (x and y) in each LR bearing, labeled by position (E, S, N, W). Numerical simulation of uncoupled, MS2, and MS4 LR bearing models. ....	320
Figure 11-5: Comparison of experimental and numerical simulation for Sine 100%; force-displacement loop in y-direction in each LR bearing, labeled by position (E, S, N, W). Numerical simulation of uncoupled, MS2, and MS4 LR bearing models. ....	321
Figure 11-6: Comparison of experimental and numerical simulation for Sine 100%; vertical force history in each LR bearing, labeled by position (E, S, N, W). Numerical simulation of uncoupled, MS2, and MS4 LR bearing models. ....	322
Figure 11-7: Comparison of experimental and numerical simulation for Diablo 95% (XY); displacement history in each LR bearing, labeled by position (E, S, N, W). Numerical simulation of uncoupled, MS2, and MS4 LR bearing models. ....	325
Figure 11-8: Comparison of experimental and numerical simulation for Diablo 95% (XY); displacement trace in each LR bearing, labeled by position (E, S, N, W). Numerical simulation of uncoupled, MS2, and MS4 LR bearing models. ....	326
Figure 11-9: Comparison of experimental and numerical simulation for Diablo 95% (XY); horizontal force history (x and y) in each LR bearing, labeled by position (E, S, N, W). Numerical simulation of uncoupled, MS2, and MS4 LR bearing models. ....	327
Figure 11-10: Comparison of experimental and numerical simulation for Diablo 95% (XY); force-displacement loop in x-direction in each LR bearing, labeled by position (E, S, N, W). Numerical simulation of uncoupled, MS2, and MS4 LR bearing models. ....	328
Figure 11-11: Comparison of experimental and numerical simulation for Diablo 95% (XY); force-displacement loop in y-direction in each LR bearing, labeled	

	by position (E, S, N, W). Numerical simulation of uncoupled, MS2, and MS4 LR bearing models. ....	329
Figure 11-12:	Comparison of experimental and numerical simulation for Diablo 95% (XY); vertical force history in each LR bearing, labeled by position (E, S, N, W). Numerical simulation of uncoupled, MS2, and MS4 LR bearing models. ....	330
Figure 11-13:	Comparison of experimental and numerical simulation for Vogtle 100%; displacement history in each LR bearing, labeled by position (E, S, N, W). Numerical simulation of uncoupled, MS2, and MS4 LR bearing models. ....	333
Figure 11-14:	Comparison of experimental and numerical simulation for Vogtle 100%; displacement trace in each LR bearing, labeled by position (E, S, N, W). Numerical simulation of uncoupled, MS2, and MS4 LR bearing models. ....	334
Figure 11-15:	Comparison of experimental and numerical simulation for Vogtle 100%; horizontal force history (x and y) in each LR bearing, labeled by position (E, S, N, W). Numerical simulation of uncoupled, MS2, and MS4 LR bearing models. ....	335
Figure 11-16:	Comparison of experimental and numerical simulation for Vogtle 100%; force-displacement loop in x-direction in each LR bearing, labeled by position (E, S, N, W). Numerical simulation of uncoupled, MS2, and MS4 LR bearing models. ....	336
Figure 11-17:	Comparison of experimental and numerical simulation for Vogtle 100%; force-displacement loop in y-direction in each LR bearing, labeled by position (E, S, N, W). Numerical simulation of uncoupled, MS2, and MS4 LR bearing models. ....	337
Figure 11-18:	Comparison of experimental and numerical simulation for Vogtle 100%; vertical force history in each LR bearing, labeled by position (E, S, N, W). Numerical simulation of uncoupled, MS2, and MS4 LR bearing models. ....	338
Figure 11-19:	Comparison of experimental and numerical simulation for Vogtle 100%; vertical force history in each LR bearing, labeled by position (E, S, N, W). Numerical simulation of uncoupled, MS2, and MS4 LR bearing models. A low pass filter with a cutoff frequency of 2 Hz was applied to the vertical force. ....	339
Figure 11-20:	Comparison of experimental and numerical simulation for Rinaldi 88% (XY); displacement history in each LR bearing, labeled by position (E, S, N, W). Numerical simulation of uncoupled, MS2, and MS4 LR bearing models. ....	341

Figure 11-21: Comparison of experimental and numerical simulation for Rinaldi 88% (XY); displacement trace in each LR bearing, labeled by position (E, S, N, W). Numerical simulation of uncoupled, MS2, and MS4 LR bearing models. ....	342
Figure 11-22: Comparison of experimental and numerical simulation for Rinaldi 88% (XY); horizontal force history (x and y) in each LR bearing, labeled by position (E, S, N, W). Numerical simulation of uncoupled, MS2, and MS4 LR bearing models. ....	343
Figure 11-23: Comparison of experimental and numerical simulation for Rinaldi 88% (XY); force-displacement loop in x-direction in each LR bearing, labeled by position (E, S, N, W). Numerical simulation of uncoupled, MS2, and MS4 LR bearing models. ....	344
Figure 11-24: Comparison of experimental and numerical simulation for Rinaldi 88% (XY); force-displacement loop in y-direction in each LR bearing, labeled by position (E, S, N, W). Numerical simulation of uncoupled, MS2, and MS4 LR bearing models. ....	345
Figure 11-25: Comparison of experimental and numerical simulation for Rinaldi 88% (XY); vertical force history in each LR bearing, labeled by position (E, S, N, W). Numerical simulation of uncoupled, MS2, and MS4 LR bearing models. ....	346
Figure 11-26: Calibration of vertical spring stiffness in the MS2 bearing model for Diablo 95% (XY). ....	348
Figure 11-27: Calibration of vertical spring stiffness in the MS2 bearing model for Sine 100% (Y). ....	349
Figure 11-28: Calibration of vertical spring stiffness in the MS2 bearing model for Rinaldi 88% (XY). ....	350
Figure 11-26: Comparison of experimental and numerical simulation for Diablo 95% (XY); x-direction roof acceleration histories, peak acceleration profiles, 2 <sup>nd</sup> story drift histories, and peak drift profiles. Numerical simulation of uncoupled, MS2, and MS4 LR bearing models. ....	352
Figure 11-27: Comparison of experimental and numerical simulation for Diablo 95% (XY); y-direction roof acceleration histories, peak acceleration profiles, 2 <sup>nd</sup> story drift histories, and peak drift profiles. Numerical simulation of uncoupled, MS2, and MS4 LR bearing models. ....	353
Figure 11-28: Comparison of experimental and numerical simulation for Vogtle 100%; x-direction roof acceleration histories, peak acceleration profiles, 2 <sup>nd</sup> story drift histories, and peak drift profiles. Numerical simulation of uncoupled, MS2, and MS4 LR bearing models. ....	354

Figure 11-29: Comparison of experimental and numerical simulation for Vogtle 100%; y-direction roof acceleration histories, peak acceleration profiles, 2<sup>nd</sup> story drift histories, and peak drift profiles. Numerical simulation of uncoupled, MS2, and MS4 LR bearing models..... 355

## LIST OF TABLES

Table 2-1: Yield and Ultimate Strength of Steel from Coupon Tests (Source: Kasai et al. 2010) .....	23
Table 2-2: Estimated Weight of the Specimen by Component and Floor Level (unit: <b>kN</b> ) .....	27
Table 2-3: Experimentally Determined Natural Periods and Damping Ratios of the Fixed-base Building .....	28
Table 3-1: Required Diameter of the Lead Plug .....	43
Table 3-2: Ratio of Lead Plug Diameter to Bearing Diameter ( $D_{LP}/D$ ) .....	44
Table 3-3: Lead Rubber Bearing Properties .....	50
Table 3-4: Cross Linear Bearing Properties.....	50
Table 3-5: Predicted x, y and Vector Peak Displacement in the Different Isolator for the Building Model Subjected to 150% Vogtle #13 Record, with Rotated Horizontal Components of Input Motion.....	58
Table 3-6: Common Earthquake Records Considered for Three Test Configurations.....	62
Table 4-1: Properties of Load Cells .....	66
Table 4-2: Vertical Load on Each Bearing After Installation.....	79
Table 4-3: Simulation Schedule for the TP Isolation Configuration .....	82
Table 4-4: Simulation Schedule for the Hybrid LR Isolation Configuration .....	83
Table 4-5: Simulation Schedule for the Fixed-base Building.....	84
Table 4-6: Peak Acceleration of Target and Realized Motions for the TP Isolation Configuration .....	87
Table 4-7: Peak Acceleration of Target and Realized Motions for Hybrid LR Isolation and Fixed-base Configurations .....	88
Table 5-1: List of Ground Motion (GM) Simulations by Number, Name, Abbreviation and the Directions Considered. ....	104
Table 5-2: Peak Base Shear for all Simulations: Total, X and Y Directions.....	110
Table 5-3: Peak Base Shear Coefficient for all Simulations: Total, X and Y Directions. ....	111
Table 7-1: Weight and Eccentricity (Distance from Geometric Center to Center of Mass) of Numerical Simulation Model .....	183
Table 7-2: Experimentally Determined Natural Periods and Damping Ratios of the Fixed-base Building .....	185
Table 8-1: Compression Shear Test Schedule .....	201
Table 8-2: Recorded and Fitted Parameters for Test A .....	204

Table 8-3: Characterized Isolator Parameters for all Tests in the Sequence .....	204
Table 8-4: Characterized Bearing Parameters for Each Earthquake Simulation .....	210
Table 9-1: Default Maximum and Minimum $\lambda$ -factors for $K_d$ and $Q_d$ (ASCE7-16) .....	245
Table 9-2: Average Characterized Isolator Parameters for $D_{max} = 300$ mm and 500 mm .....	248
Table 9-3: Bounding Cases Considered for the Numerical Simulation.....	254

## NOMENCLATURES

<b>Symbol</b>	<b>Definition</b>
$A_b$	Crass-sectional area of the bearing
$a_{cX}$	Horizontal acceleration of the compound including top connecting plate and bottom half of the isolator
$a_{cZ}$	Vertical acceleration of the compound including top connecting plate and bottom half of the isolator
$a_{xC}$	Acceleration at the geometric center of the floor in x-direction
$a_{xSE}$	X component of the horizontal acceleration at the South-East corner
$a_{yC}$	Acceleration at the geometric center of the floor in y-direction
$a_{ySE}$	Y component of the horizontal acceleration at the South-East corner
$b$	Plate width
$b_{cf}$	Flange width of column
$B_L$	Damping coefficient
$c$	Damping coefficient of additional damper
$c_{nm}$	Constant dependent on nth mode shape
$c_s$	Side cover rubber thickness
$d$	Given horizontal displacement of the bearing
$D$	Overall diameter
$D_D$	Design displacement
$\delta_h$	Horizontal displacement
$D_{iso}$	Isolator displacement
$D_{LP}$	Diameter of the lead plug
$D_M$	Bearing displacement at the center of rigidity
$D_{max}$	Maximum isolator displacement
$D_{min}$	Minimum isolator displacement
$D_p$	Lead diameter
$D_{peak}$	Absolute peak displacement for selected cycle
$\Delta R_i$	Additional reaction
$D_{TM}$	Maximum displacement
$\delta_v$	Vertical displacement
$DX_{A'}$	Displacement component at the center bearing in X direction
$\delta_{xC}$	Story drift in the x-direction at the geometric center

$\delta_{xSE}$	Story drift in the x-direction at the South-East corner
$D_y$	Yield displacement
$D_{y,rub}$	Yield displacement of rubber
$DY_{A'}$	Displacement component at the center bearing in Y direction
$E$	Elastic modulus
$EDC$	Energy dissipated per cycle
$EDC_{bilin}$	Energy dissipated per cycle for a bilinear force-displacement loop
$EDC_{test}$	Energy dissipated per cycle for experimental data
$e_u$	Rubber's elongation-at-break
$f$	Frequency
$F$	Shear force
$F_{1x}$	X-component of the axial force of truss 1 (x-direction)
$F_2$	Axial force on truss 2 (x-direction)
$F_{2x}$	X-component of the axial force of truss 2 (x-direction)
$F_{2y}$	Y-component of the axial force of truss 2 (x-direction)
$F_3$	Axial force on truss 3 (y-direction)
$F_{3y}$	Y-component of the axial force of truss 3 (y-direction)
$F_4$	Axial force on truss 4 (y-direction)
$F_{4y}$	Y-component of the axial force of truss 4 (y-direction)
$F_{CLB}$	Axial force on CL bearings
$F_{max}$	Maximum force
$F_{min}$	Minimum force
$F_{OT}$	Overtopping force
$F_{peak}$	Absolute peak force for selected cycle
$F_y$	Yield force
$G$	Shear modulus
$g$	Gravitational acceleration
$\gamma$	Calibration factor
$h$	Plate height
$I$	Moment of inertia
$k$	Horizontal stiffness
$K_I$	Initial stiffness of bearing
$K_{I\_char}$	Characterized initial stiffness
$K_{I\_lead}$	Initial stiffness of lead
$K_{I\_rub}$	Initial stiffness of rubber



$K_{1s}$	Initial stiffness of the CL bearing
$K_b$	Horizontal stiffness of low-damping natural rubber
$K_{bo}$	Reduced horizontal stiffness of the LR bearing
$K_d$	Post-yield stiffness of bearing
$K_{d,char}$	Characterized post-yield stiffness
$K_{d,des}$	Design post-yield stiffness
$K_{d,fit}$	Fitted post-yield stiffness
$K_{d,max}$	Maximum post-yield stiffness for bounding analysis
$K_{d,min}$	Minimum post-yield stiffness for bounding analysis
$K_{eff}$	Effective or secant stiffness
$K_H$	Kinematic hardening modulus
$K_{L1}$	First stiffness of the lead-plug for trilinear model (Figure 7-14)
$K_{L2}$	Second stiffness of the lead-plug for trilinear model (Figure 7-14)
$K_{L3}$	Third stiffness of the lead-plug for trilinear model (Figure 7-14)
$K_{LC}$	Vertical stiffness of load cell
$K_{plate}$	Plate bending stiffness
$K_t$	Tension vertical stiffness for LR bearing
$K_{total}$	Total vertical stiffness
$k_{truss}$	Equivalent elastic stiffness of axial element
$K_v$	Compressive vertical stiffness for LR bearing
$K_{vc}$	Compressive vertical stiffness for CL bearing
$K_{vj}$	Vertical stiffness on vertical spring j
$K_{vr}$	Reduced vertical stiffness of LR bearing
$K_{vt}$	Tension vertical stiffness for CL bearing
$L$	Length of element
$L_A$	Distance between a and A' measured by the displacement transducer
$\lambda_{ae}$	Uncertainty factor for bounding analysis - aging and environmental effects
$L_{clear}$	Clear length between adjacent load cells
$\lambda_{max}$	Maximum property modification factor
$\lambda_{min}$	Minimum property modification factor
$\lambda_{sec}$	Uncertainty factor for bounding analysis - manufacturing uncertainty
$\lambda_{test}$	Uncertainty factor for bounding analysis - prototype test
$m_{nm}^*$	Modal mass of the nth mode

$m_c$	Mass of the compound including top connecting plate and bottom half of the isolator
$M_{yF}$	Yield strength of spring representing bending of the flanges
$M_{yp}$	Yield strength of spring representing shear behavior of panel zone
$N$	Number of rubber layers
$N_{LR}$	Number of lead-rubber bearings
$P$	Axial load
$P$	Vertical force
$P_{allow}$	Allowable axial load at a lateral displacement of zero
$P_{cr}$	Reduced buckling load
$P_{crit}$	Critical axial load
$P_{cro}$	Nominal critical buckling load
$Q_d$	Characteristic yield strength of bearing or system
$Q_{d,char}$	Characterized characteristic strength
$Q_{d,des}$	Design characteristic strength
$Q_{d,fit}$	Fitted characteristic strength
$Q_{d,lead}$	Characteristic strength of lead
$Q_{d,max}$	Maximum characteristic strength for bounding analysis
$Q_{d,min}$	Minimum characteristic strength for bounding analysis
$Q_{d,rub}$	Characteristic strength of rubber
$Q_{LR}$	Total characteristic strength of lead rubber bearings
$Q_{roll}$	Total characteristic strength of rolling bearing
$R$	Radius of curvature of friction pendulum bearing
$R_{cX}$	Dynamic reaction component in x-direction at the load cell level
$R_{cZ}$	Dynamic reaction component in z-direction at the load cell level
$R_{i,test}$	Reaction at bearing I at the beginning of a test simulation
$R_X$	Dynamic reaction component in x-direction at the isolator level
$R_Z$	Dynamic reaction component in z-direction at the isolator level
$R_{Z,init}$	Initial static vertical reaction
$S_F$	Initial stiffness of spring representing bending of the flanges
$S_p$	Initial stiffness of spring representing shear behavior of panel zone
$T$	Period
$t_{bp}$	Bottom mounting plate thickness
$t_{cf}$	Flange thickness of column

$T_d$	Post-yield period of bearing or system
$T_{eff}$	Effective period of bearing or system
$t_{ip}$	Internal plate thickness
$T_r$	Total thickness of rubber
$t_r$	Layer thickness
$t_s$	Shim thickness
$t_{tp}$	Top mounting plate thickness
$v$	Equivalent uniform load on the beam element
$V_b$	Total base shear in the isolator system
$V_i$	Shear force at the $i^{\text{th}}$ node
$V_j$	Shear force at the $j^{\text{th}}$ node
$V_p$	Volume of panel zone web
$W$	Estimated weight on each CL bearing
$W_i$	Tributary weight supported by the $i^{\text{th}}$ isolator
$W_{LRBs}$	Total weight carried by the LR bearings
$W_T$	Total static weight of the building
$W_{T,LRB}$	Total static weight on LR bearings
$W_{total}$	Total weight of the structure
$x$	Length of the gusset plate
$X_a$	X- coordinate of node a
$X_{A'}$	X-coordinate of displaced node A'
$y$	Width of the gusset plate
$Y_a$	Y-coordinate of node a
$Y_{A'}$	Y-coordinate of displaced node A'
$\zeta$	Viscous damping ratio
$\zeta_n$	Additional damping ratio
$\beta$	Equivalent damping ratio
$\Delta x$	Displacement of center bearing in x-direction computed by data processing
$\Delta y$	Displacement of center bearing in y-direction computed by data processing
$\mu$	Coefficient of friction of a sliding or rolling bearing
$\sigma_u$	Ultimate strength
$\sigma_y$	Yield strength
$\sigma_{y,LP}$	Dynamic yield strength of the lead plug

$\phi$	Rotation of center bearing computed by data processing
$\phi_{pn}$	Horizontal displacement at base in the nth mode shape
$\phi_{qn}$	Horizontal displacement at roof in the nth mode shape
$\omega_n$	Angular frequency of the nth mode
$\omega_{z,rigid}$	Vertical frequency of a "rigid body"

## **CHAPTER 1: INTRODUCTION**

### **1.1 Background of Seismic Isolation and its Consideration for Safety Related Nuclear Facilities**

Seismic base isolation is a technology used to protect structures from the damaging effects of earthquake ground motion by decoupling the structure from the foundation through the incorporation of a flexible interface between the two. Flexible isolation devices are incorporated to shift or elongate the natural period of the structure in the horizontal direction away from the typical dominant energy of the earthquake, thereby significantly reducing the accelerations, inertial forces, and subsequently base shear demands on the structure. Increased displacements are accommodated in the isolation system, while structural deformations are substantially reduced such that the structural system practically moves “rigidly” above the isolators.

Seismic isolation has been shown to successfully protect the structural system and content of numerous structures in prior earthquakes. Most recently, many isolated buildings were shaken in the 2011 Tohoku Earthquake and Tsunami, with isolator displacement demands ranging from 20 to 40 cm (Nishiyama et al. 2011). Seismic isolated structures around the world now number in the several thousands, and seismic isolation systems have been incorporated into the design of nuclear power plants in France and South Africa (Malushte and Whittaker 2005). As a result, seismic isolation is being considered for the future generation of nuclear power plants in the United States.

The structures, systems, and components of nuclear power plants are required to be designed for natural phenomena (such as earthquakes) without loss of capability to perform their safety functions (10 CFR 50, 2011). Seismic isolation is most effective for stiff, short period structures. Safety related nuclear structures fit this description since their horizontal period is on the order of 0.1 to 0.25 sec. If designed to remain elastic under strong ground motions, a short period structure attracts high acceleration demands that are transmitted to any internal equipment. If, on the other hand, a short period structure is designed to yield, it can experience large ductility demands relative to a longer period structure with a comparable strength reduction factor (e.g. Chopra 2012). Fortunately, the flexibility of the isolation system shifts the natural period of the building to significantly reduce both force demands to the structural system and acceleration demands to internal equipment. Thus, seismic isolation could be considered for safety related nuclear facilities if the overall system is analyzable and the response is predictable.

Two major classes of isolation devices have been used in the United States: elastomeric bearings and friction pendulum bearings. Elastomeric bearings are composed of alternating layers of natural, or synthetic, rubber bonded to intermediate steel shim plates. A rubber cover is provided to protect the internal rubber layers and steel plates from environmental degradation and corrosion. Elastomeric bearings can be categorized as: (1) low-damping natural or synthetic rubber and (2) high-damping rubber. Low-damping natural rubber material exhibits nearly linear shear stress-strain behavior up to approximately 150% shear strain, wherein the horizontal stiffness  $K_b$  is calculated as:

$$K_b = \frac{GA_b}{T_r} \quad (1.1)$$

where  $G$  is the shear modulus,  $A_b$  is the cross-sectional area of the bearing, and  $T_r$  is the total thickness of rubber. A typical range of  $G$  for seismic applications is 0.4-0.9 MPa (60-130 psi). The equivalent damping ratio,  $\beta$ , for low-damping natural rubber ranges between 2% and 3% at 100% shear strain. To limit displacements across the isolation interface, external supplemental damping devices or alternative isolation devices are typically used in parallel with low-damping natural rubber bearings. A higher level of damping can be achieved through the addition of fillers to the rubber; however, recently such devices are rarely used in the United States.

Another type of elastomeric bearing is the lead rubber bearing. From a construction perspective, lead-rubber bearings differ from low-damping natural rubber bearings only by the addition of a lead-plug that is press-fit into a central hole in the bearing. The lead-plug deforms plastically under shear deformation, enhancing the energy dissipation capabilities compared to the low-damping natural rubber bearing. The horizontal force-deformation relationship of a lead-rubber bearing is characterized using bilinear behavior with an effective, or secant stiffness ( $K_{eff}$ ) calculated as:

$$K_{eff} = \frac{Q_d}{d} + K_d \quad (1.2)$$

where  $Q_d$  is the bearing characteristic strength, which is controlled by the yield strength of the lead in shear and the area of the lead-plug;  $K_d$  is the post-yield stiffness and  $d$  is a given horizontal displacement of the bearing. The vertical stiffness of all types of elastomeric bearings (low damping rubber, high damping rubber, and lead rubber) is

typically thousands of times larger than the horizontal stiffness so that isolation systems composed of elastomeric bearings provide isolation only from the horizontal components of ground shaking.

The Friction Pendulum™ (FP) bearing, developed by Earthquake Protection Systems, Inc. is a sliding bearing that supports the weight of the structure on a bearing that rests on a sliding interface. A single FP bearing consists of a single sliding interface, while a Triple Pendulum™ (TP) bearing consists of multiple sliding interfaces. The sliding interface is designed with a low coefficient of friction, which limits the resistance to horizontal forces. The single FP bearing consists of a base-plate, an articulated slider and a spherical concave dish. Under horizontal motion, the spherical concave dish displaces horizontally relative to the articulated slider and base-plate. Friction between the two surfaces provides frictional resistance and energy dissipation, whereas the radius of curvature of the spherical concave dish provides a restoring force. The shear force-horizontal deformation behavior of FP bearings is characterized using a bilinear relationship. The horizontal strength, or zero-displacement force-intercept,  $Q_d$ , is controlled by the bearing material and the weight  $W$  carried by the isolators, according to:

$$Q_d = \mu W \quad (1.3)$$

where  $\mu$  is the sliding coefficient of friction of the bearing interface. The sliding coefficient of friction can range between 0.03 and 0.2. The post-yield stiffness of the FP bearing is controlled by weight acting on the isolator and the radius of curvature,  $R$ , of the spherical concave dish. The TP bearing consists of four spherical sliding surfaces and three independent pendulum mechanisms. The internal pendulum mechanism with two



concave plates and a rigid slider determines the response during low intensity shaking. The outer stainless steel concave surfaces, when designed with different curvatures and friction coefficients, provide two independent pendulum mechanisms that determine the response during medium to high intensity shaking. Both the single FP and the TP bearings provide no resistance to tensile forces and thus are free to uplift. In certain situations uplift in the bearings could occur, e.g. bearings on the perimeter of slender structures or those located under braced frames. For these situations resistance to uplift is considered desirable.

## **1.2 State of Knowledge and Motivation for Full Scale Testing**

The following briefly summarizes the research and development that has led to the modern seismic isolation systems used today. Early proof of concept earthquake simulator or “shake table” tests are discussed, as well as later tests that examined system level technical concerns. Then, numerical simulation capabilities for elastomeric isolation bearings that have been developed mostly in conjunction with device level testing are reviewed. Finally, the need for full scale earthquake simulator testing of isolated structures is addressed.

Initial development and proof-of-concept earthquake simulator testing was carried out in the United States on elastomeric and friction pendulum isolators in the 1980’s and 1990’s (e.g., Kelly et al. 1980a, 1980b; Kelly and Hodder 1981; Zayas et al. 1987; Mokha et al. 1988, 1990; Kelly and Chalhoub 1990; Constantinou et al. 1990; Al-Hussaini et al. 1994). In Japan, research and development was also carried out at construction

companies that built several demonstration buildings to be tested by earthquakes (Kelly 1988).

Earthquake simulator testing eventually progressed beyond basic validation to examine performance of the overall isolation system under challenging loading conditions, and elastomeric bearings have been tested to various limit states under dynamic loading. For example, a series of uplift experiments were performed on slender structures isolated with elastomeric bearings (Griffith et al. 1988a, 1988b), and researchers have developed and tested several uplift restraint devices suitable for elastomeric isolation systems (e.g. Griffith et al. 1990; Kasalanati and Constantinou 2005). Uplift restraint in elastomeric bearings is often provided through limited engagement of the elastomers in tension by providing a fully bolted connection detail for the elastomeric bearing. One project designed a series of experiments to drive an isolated structure out to its ultimate capacity, including large isolator displacement demands and structural yielding (Clark et al. 1997). The experiment showed that design strategies can be adopted to ensure that the isolation system is not the weak link, and that isolators can withstand significant tension due to structure overturning. At least two studies performed earthquake simulator tests where the intensity of the excitation was increased until the bearings ruptured (Sato et al. 2002; Takaoka et al. 2011). A more detailed review of the history of earthquake simulator or “shake table” testing of isolated building structures was provided in Warn and Ryan (2012).

Recently, much progress has been made in understanding and modeling the macro-mechanical behavior of natural rubber and lead-rubber bearings. Bidirectionally coupled

bilinear or Bouc-Wen models are frequently used by commercial software to represent the hysteretic behavior of lead-rubber bearings. These models are incapable of representing the amplitude dependence of the hysteretic properties and the lateral-axial interaction of the response, which may or may not be significant. In lead-rubber bearings, theoretical models have been developed to account for the decrease in characteristic strength of the lead plug with repeated cycling due to viscous heating of the lead plug (Kalpakidis and Constantinou 2009a, 2009b). In addition to the heating effect of the lead plug, Constantinou et al. (2007) also evaluated the effects of history of loading, aging, and environmental conditions (such as extreme temperature variation) on the behavior of elastomeric isolation hardware. Since the exact state of the bearing at the time of a seismic event is unknown, probable maximum and minimum values of  $K_d$  and  $Q_d$  were suggested by Constantinou et al. (1999). The lower and upper bound values of  $K_d$  and  $Q_d$  are determined with the use of system property modification factors, which are multipliers to the nominal design parameters to account for variation in isolation system properties (Constantinou et al., 2007). In general, the upper bound properties are used to estimate the base shear demands, while the lower bound properties are used to estimate the displacement demands.

Bounding values have been implemented by the American Association of State Highway and Transportation Officials (AASHTO) design guidelines (AASHTO, 1999) and a more rigorous bounding analysis will be implemented in the new edition of the American Society of Civil Engineers ASCE 7 guidelines for the analysis and design of new buildings (ASCE, 2016) and ASCE 41 for the rehabilitation of existing buildings (ASCE,

2017) with seismic isolation systems. In the ASCE 7 implementation, the upper and lower bound properties are to be applied separately to the numerical model and the largest value of each response parameter determined by the upper and lower bound analyses is to be used for design (ASCE, 2016).

The influence of axial load on the horizontal force-deformation behavior of elastomeric bearings leads to complexity that can affect the analyzability of the overall system; however much recent research has been completed to evaluate the critical load capacity and post-buckling behavior of the bearings. The overlapping area approximation was developed to estimate the reduction in critical load capacity with increasing displacement (Buckle and Liu 1994). Several studies have experimentally evaluated stability and post-buckling behavior of elastomeric bearings (Buckle et al. 2002; Warn and Whittaker 2006; Weisman and Warn 2012; Sanchez et al. 2012). They all concluded that the overlapping area approximation is conservative, and improvements have been proposed. Experimental studies also evaluated the reduction in vertical stiffness at large horizontal displacements (Warn and Whittaker 2007).

A simple two-spring model that includes the influence of vertical load on the horizontal response was developed by Koh and Kelly (1987) for linear material behavior and extended by Ryan et al. (2005) for nonlinear material behavior. Another extension of the two-spring model considered large displacement/rotation theory to predict the stable post-critical behavior that has been observed in test data (Nagarajaiah and Ferrell 1999). The Koh-Kelly linear model was also modified by Iizuka (2000) to introduce finite deformation and nonlinear springs to predict the large-deformation behavior such as

hardening, load deterioration and buckling phenomena of lead rubber bearings. A more recent variation to the Koh-Kelly model was developed by Kumar et al. (2014), where the effect of the axial load on the horizontal behavior is considered indirectly by selecting mechanical properties in the horizontal and vertical directions that are dependent on each other. More advanced distributed spring models accounting for these second-order effects have been developed that are also capable of exhibiting zero or negative tangential horizontal stiffness (Yamamoto et al. 2009, Kikuchi et al. 2010). However, these models rely on experimentally calibrated parameters. Therefore, Han et al. (2014) proposed a variation of Yamamoto and Kikuchi bearings models that does not rely on experimentally calibrated parameters, making it more practical for design purposes.

Most of the aforementioned studies (especially earthquake simulator tests) involved reduced scale structural models and reduced scale isolation bearings. Despite the wealth of data on reduced-scale systems, the following knowledge gaps specific to the response of the isolation system still need to be addressed.

- Dynamic test data of full-scale elastomeric bearings is not available for a system earthquake simulator test. A full scale system test is necessary to verify that the complex phenomena observed in reduced-scale bearings under realistic earthquake loading (e.g. velocity effects, temperature effects, horizontal and vertical interaction) are scalable to much larger devices. Earthquake simulator tests of a full scale building isolated with high damping rubber bearings and natural rubber bearings with dampers were performed (Sato et al. 2011), but bearing force data was not recorded as part of that particular program.

- Earthquake simulator testing of isolated building models under combined horizontal and vertical loading is somewhat limited. Full scale testing should be performed that emphasizes realistic three-dimensional input and strong vertical input recorded in near-fault ground motions.

### **1.3 Testing of a Hybrid Isolation System at E-Defense**

An opportunity was seized to test a full scale building with base isolation at the Hyogo Earthquake Engineering Research Center of Miki, Japan, also known as E-Defense, that houses the only single earthquake simulator capable of reproducing three-dimensional earthquake excitation to test full scale structures (<http://www.bosai.go.jp/hyogo/ehyogo/>).

The developed test program made use of an existing 5-story steel moment frame building structure that had been tested at E-Defense in early 2009 as part of a program on value-added buildings (Kasai et al. 2010). The test plans evolved testing structural and non-structural contents of a moment frame building in the fixed-base configuration as well as the isolated configuration. The test program was developed prioritizing the testing of TP bearings as they were the initial focus of the research. However, the incremental cost of testing an additional isolation system incorporating lead-rubber bearings that could be designed for representative nuclear seismicity was low. Thus, shortly before the planned start of testing, the project team, with product and in-kind support from Dynamic Isolation Systems, Inc., proceeded with the design and manufacture of an additional isolation system using lead rubber (LR) bearings to be tested at E-Defense. The payload

project was able to utilize support assemblies incorporating triaxial load cells to measure the shear and axial forces in the lead-rubber bearings.

The main objective for the payload project, which differs from the objectives of this dissertation, was to evaluate the performance of the elastomeric isolation system designed for a safety related nuclear structure in *beyond design basis* earthquake (DBE) shaking. Ground motions were developed for a representative central and eastern United States soil site. The test program was developed considering the performance objectives of ASCE 43-05 (ASCE 2008), that the isolation system has less than 1% probability of unacceptable performance for 100% DBE shaking and less than 10% probability of unacceptable performance for 150% DBE shaking. For acceptable performance, individual isolators are expected to (1) sustain no damage during DBE shaking; (2) sustain gravity and earthquake induced axial loads at 90<sup>th</sup> percentile lateral displacements consistent with 150% DBE shaking; and (3) have 1% or less probability of impacting the surrounding structure for 100% DBE shaking and 10% for 150% DBE shaking. The third objective was not directly assessed in the test program, but relates to the predictability of the isolation system.

The moment-frame structure was light, which precluded the use of only elastomeric bearings to simultaneously provide sufficient period elongation and meet the displacement demands at a representative United States nuclear site. This led to the pairing of LR bearings with near frictionless tension-capable Cross Linear (CL) bearings manufactured by THK, referred to as the hybrid LR isolation system. The low friction of the CL bearings added negligible horizontal stiffness to the isolation system, which

allowed the total base shear to be resisted solely by the LR bearings, which was desired. As LR bearings are displaced horizontally, their vertical stiffness decreases, which can lead to buckling of the bearings at large horizontal displacement. In the hybrid LR isolation system, the CL bearings were expected to provide overall stability to the isolation system at large horizontal displacements. Moreover, the CL bearings provided tensile resistance to overturning loads, which was considered desirable in light of the preliminary calculations of overturning demands. Furthermore, LR and CL bearings have been used together in over 100 projects in Japan. Thus, the hybrid system was found to be a reasonable solution for the test.

A possible disadvantage of the hybrid LR isolation system is that as the bearings displace, axial loads can transfer between the LR and CL bearings. The load transfer between these devices, referred as the load transfer effect, occurs due to the rigidity of the frame system connecting the bearings, the discrepancy in stiffness between the CL and LR bearings in the vertical direction, and the effective decrease in stiffness of the LR bearings at large horizontal displacements. Axial force demands on the bearings can vary greatly due to load transfer effects. Thus, prediction of the axial force demand on the bearings is essential for design and to protect the devices from excessive tension or compression forces. Load transfer was observed during the test program and caused LR bearings to sustain tension during some of the simulations. To the knowledge of the author, the load transfer effects have not been reported by other authors prior to the E-Defense test.



## 1.4 Research Objectives

The main objectives of this dissertation are:

- (1) Analyze the response of the LR bearings during the E-Defense test, as it was one of the first known full-scale experiment that incorporated LR bearings and CL bearings, and one of the first system level full-scale validations of seismic isolation.
- (2) Develop a numerical model that represents current numerical approaches used by registered design professionals to investigate and predict the lateral displacement and the horizontal and vertical force of the LR bearings. The load transfer effect is not predicted by this simplified numerical model.
- (3) Determine whether the bounding analysis methodology can reliably bound the displacement and force response of the LR bearings. This objective is motivated by the fact that current simplified numerical models do not always predict peak force and displacement demands of the LR bearings.
- (4) Develop a numerical model that can predict load transfer effects to evaluate peak tensile and compressive axial force demands in LR bearings. A secondary objective to the development of this model was to make the mechanics and implementation transparent and easily modifiable by other users, and hence provide registered design professionals with a way to check for load transfer effect in the design when pertinent.

The extensive data obtained from the E-Defense test is used to investigate the bound analysis methodology and to validate the numerical models.

## 1.5 Dissertation Organization

This dissertation is organized as follows. Chapter 2 describes the 5-story steel moment frame building, for which the hybrid LR isolation system was designed, as well as the nonstructural components and building content that were monitored during the tests. Chapter 2 is mainly an excerpt from Dao and Ryan (2015) with some pertinent modifications and is included in this dissertation for completeness. The design of the hybrid LR isolation system, including the iterative thought process through which the final selections were derived, is described in Chapter 3. This chapter also explains the consideration for selection and scaling of ground motions during the 2 days of testing on the hybrid LR isolation system. Chapter 4 summarizes the test program, including the assembly and connection of isolators and building to the earthquake simulator, instrumentation to measure structural and bearing responses, shaking test schedule, amplitude of realized table motions relative to the targets, and algorithms to generate derived data. For completeness, the shaking test schedule includes the test days for the TP configuration and the fixed-base configuration, although the test results for these systems are discussed only briefly in this dissertation. A statistical summary of the test results for the hybrid LR building configuration is given in Chapter 5, where peak values of key response quantities are identified for every simulation. Chapter 6 examines the technical response and unique aspects of the hybrid LR isolation system.

The latter part of the dissertation furthers the understanding of the test data through development, validation and synthesis of a robust numerical simulation model of the hybrid LR isolation system and building. Chapter 7 describes the numerical model of the

superstructure. In Chapter 8, the modeling assumptions for the LR bearings and CL bearings are presented, and the parameters of the model are calibrated to the bearing test data. Furthermore, the numerically predicted responses of the LR bearings with calibrated bearing properties and the superstructure are compared to the test data for four representative excitations at the end of Chapter 8. Chapter 9 examines the bounding analysis methodology. A new implementation of a numerical LR bearing model that can predict load transfer between the LR bearings and CL bearings is developed and validated in Chapter 10. The numerically predicted responses of two configurations of the new LR bearing presented in Chapter 10 and the superstructure are compared to the test data in Chapter 11. Chapter 12 summarizes the major findings from this dissertation.

## **CHAPTER 2: DESIGN AND CONFIGURATION OF THE 5-STORY STEEL MOMENT FRAME TESTBED STRUCTURE**

### **2.1 Description of Testbed Structure**

The testbed structure used in this experiment program was designed by Hyogo Earthquake Engineering Research Center in 2008 and used in a test in March 2009 (Kasai et al., 2010). The author of this dissertation was not involved in its design. Hereafter is description of the testbed structure to enable later interpretation of results. The complete structural drawings of the building with hybrid LR isolation system are given in Appendix A.

#### **2.1.1 Basic Dimensions**

The testbed specimen was a five-story steel moment frame building with rectangular plan (Figure 2-1). The building was 10 x 12 m (32.8 x 39.4 ft) in plan and approximately 16 m (52.5 ft) in height, with 2 bays in each direction. The bay widths in the long direction – 12 m or 39.4 ft – were 7 m (23 ft) and 5 m (16.4 ft) to promote torsion, which is typical of asymmetric structures. Figure 2-2 shows the basic dimensions of the building and the assumed coordinate system for presentation of results, where the Z-axis is the vertical axis. The previous researchers chose to simulate a 5-story steel specimen because it is on the high side of the typical building stock in Japan and without added damping, would be

susceptible to more significant demands than comparable taller buildings (Kasai et al. 2010).



**Figure 2-1: The 5-story steel moment frame specimen**

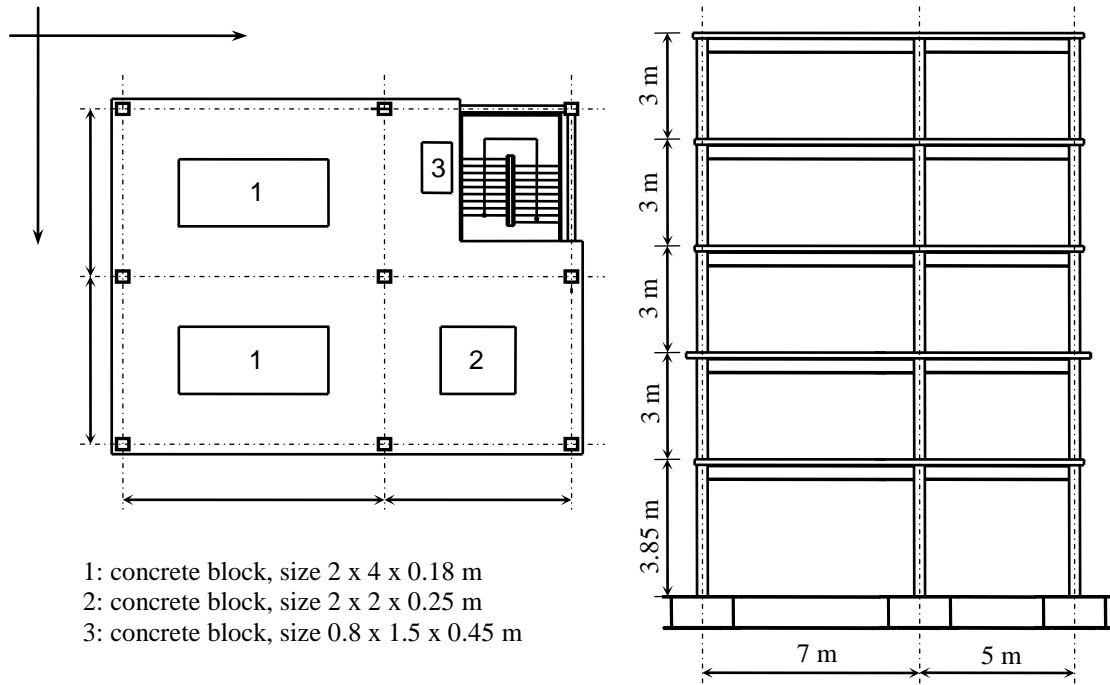


**Figure 2-2: Basic dimensions of the specimen: (a) typical plan view from floors 2 to 5, and (b) elevation view.**

### 2.1.2 Design Spectra and Design Criteria

The design of the lateral system was based on Japanese Level II and Level III earthquake design spectra (Figure 2-3). Because the testbed was designed to be a “value-added” building (Kasai et al. 2008), whose structural components and non-structural components are protected for major earthquakes, the story drift angle of the frame was limited to 0.005 rad for a Level II earthquake, whereas the drift angle limit for conventional frames would be 0.01 rad. The structure was also required to remain elastic for a drift angle up to 0.01 rad (Kasai et al. 2008).

### 2.1.3 Framing System

The lateral system was designed and detailed according to Japanese code and construction practice. The framing system was a three dimensional steel moment frame where the columns were engaged in flexure about both their principal axes. The columns were made of 350 mm x 350 mm (13.8 in x 13.8 in) hollow box sections with thickness varying from story to story. The beams were either rolled or built-up I-sections. The primary beams, which were connected to the columns, consisted of a small-section segment at the middle and two large-section segments at the ends (Figure 2-4). These 3 segments were all 400 mm (15.7 in) height and bolted together at the approximate inflection points determined from gravity loading. Connections between columns and beams were all fully restrained moment connections, with both flanges and web of the beam welded to the column. Generally, the flanges of the primary beams were haunched at their ends to form plastic hinges away from the columns and improve the beam-to-column connection. Continuity plates were also provided to protect the panel zones (Figure 2-4).

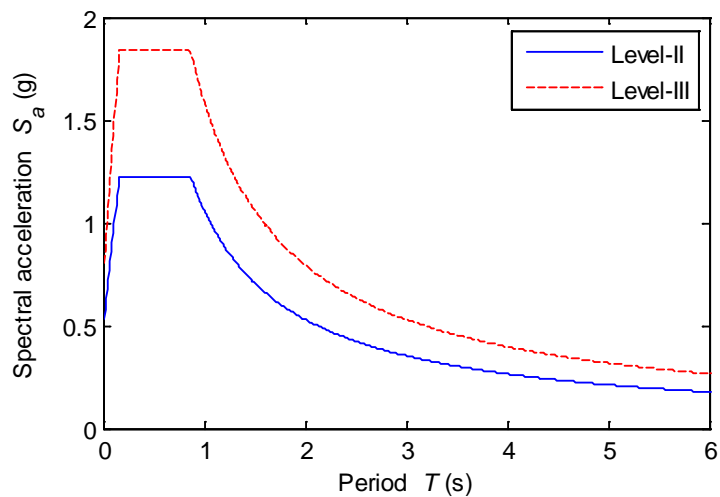


**Figure 2-3: Design spectrum for Japanese Level II and Level III earthquakes**

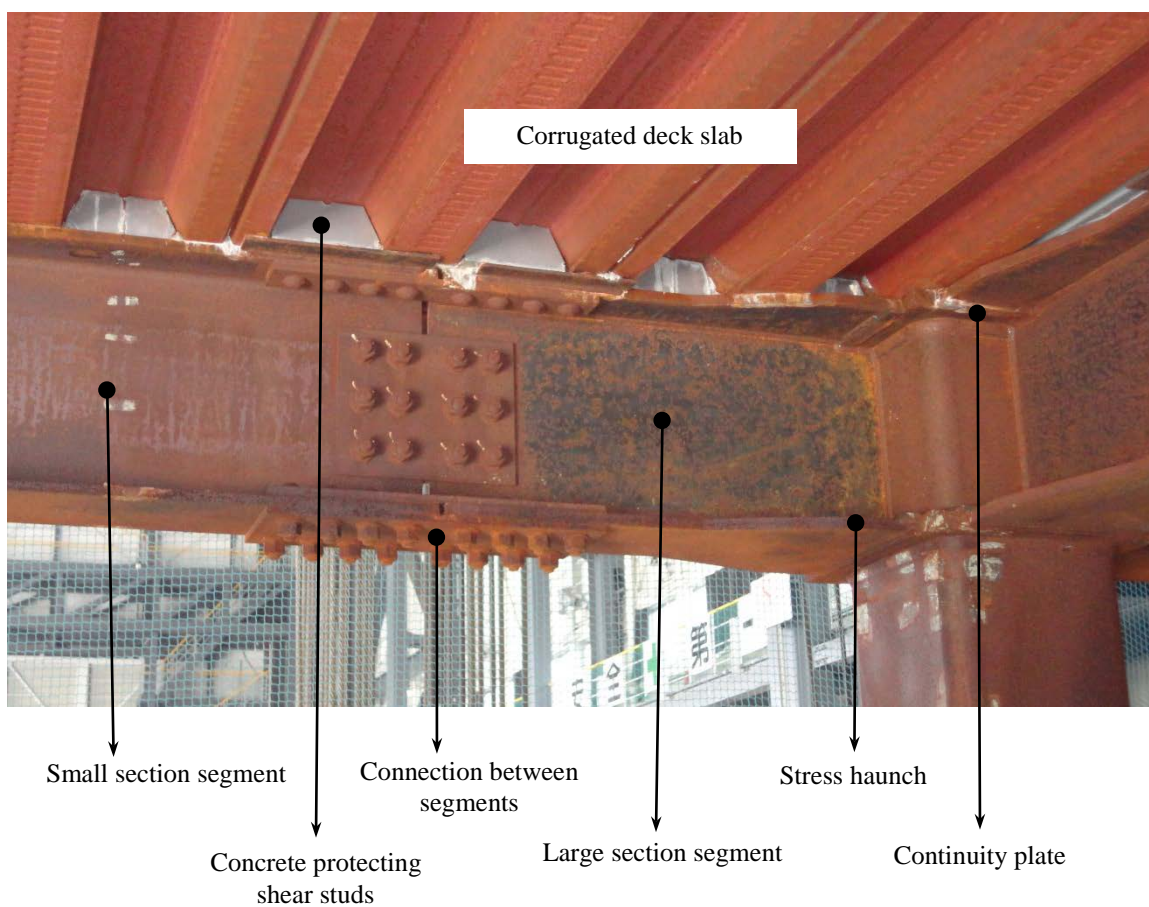


**Figure 2-4: Beam, beam to column connection and slab**



To connect the testbed to the shaking table and provide the stiffness required to “fix” the testbed at its base, column bases and grade girders were designed with special details. The column bases were detailed as steel boxes with dimension of 2.5 m x 2.5 m x 0.9 m (8.2 ft x 8.2 ft x 3 ft) (Figure 2-5). Vertical stiffeners were installed inside the boxes. The grade girders were bolted to the column bases and were the same height as the column bases (0.9 m or 3 ft). The foundation framing was braced in its plane as shown in Figure 2-6.

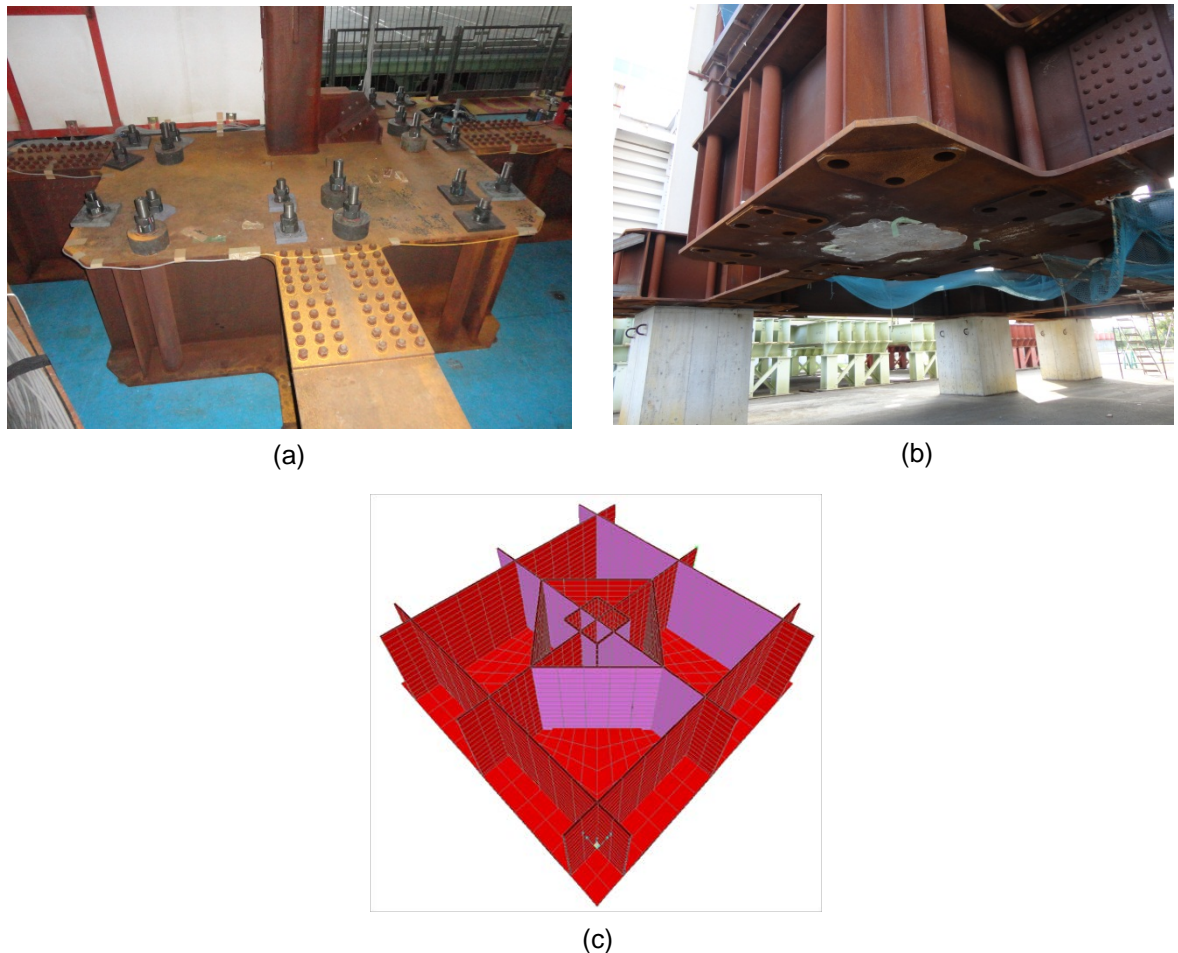


**Figure 2-5: Column base: (a) view from top (b) view from bottom, (c) rendering of stiffeners**

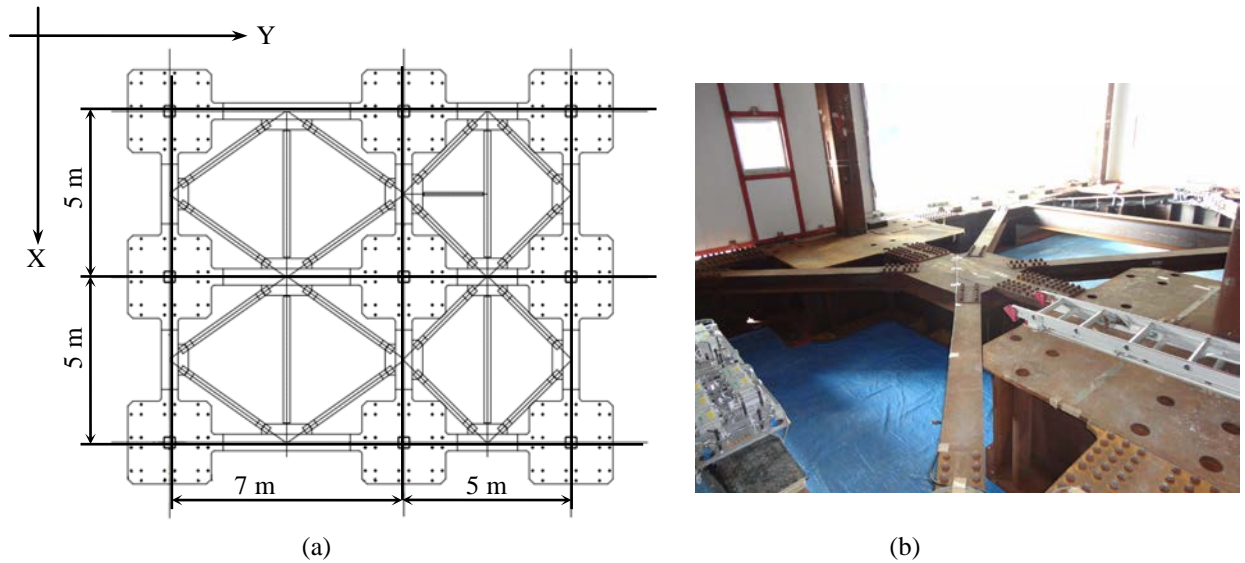


**Figure 2-6: Horizontal braces at base level.**

#### 2.1.4 Slabs

The composite floor slabs were formed from 75 mm (3 in) high corrugated (ribbed) steel decking and 80 mm (3.1 in) thick normal weight concrete cast over the ribs of the deck. The corrugated steel deck (Figure 2-4) was 1.2 mm (0.05 in) thick and oriented parallel to the Y-direction. Typical reinforcement in the floor slabs was a single layer of  $\phi 10$  mm @ 150 mm ( $\phi 0.4$  in @ 5.9 in) rebar in both directions placed at the slab mid-thickness.

The roof slabs were 150 mm (5.9 in) normal weight concrete slabs cast on a 1.2 mm (0.05 in) flat steel deck. Reinforcement for the roof slab included layers of  $\phi 13$  mm @ 200 mm ( $\phi 0.5$  in @ 7.9 in) rebar in each direction at the top and bottom of the slab. The roof slab was nearly twice as thick as the floor slabs as it was designed to carry roof mounted equipment (e.g., air conditioning system, water tanks) and a penthouse.

Shear studs connected the concrete slabs to the primary beams to provide a fully composite connection (Figure 2-4).

### 2.1.5 Material Properties

The specified yield strengths of steel were 295 MPa (42.8 ksi) and 325 MPa (47.1 ksi) for the columns and beams, respectively. The expected ultimate tensile strengths were 400 MPa (58 ksi) for columns and 490 MPa (71 ksi) for beams. Coupon tests showed that yield and ultimate strengths of the steel varied from member to member and the average ratio of measured to nominal strength was 1.2 (Kasai et al. 2010). Table 2-1 presents the range of observed yield strength  $\sigma_y$  and ultimate strength  $\sigma_u$  of steel used for the beams and columns.

**Table 2-1: Yield and Ultimate Strength of Steel from Coupon Tests (Source: Kasai et al. 2010)**

<b>Member</b>	<b><math>\sigma_y</math>(MPa)</b>	<b><math>\sigma_u</math>(MPa)</b>
Columns	346 – 398	430 – 470
Beams	331 – 422	510 – 557

The compressive strength of the normal weight concrete used in the slabs was 21 MPa (3 ksi); the measured compressive strength of standard samples was 24 MPa (3.5 ksi). The concrete slabs were reinforced by SD295A grade rebar. The nominal yield stress for the rebar was 295 MPa (42.8 ksi); measured rebar strengths were unavailable.

## 2.2 Non-Structural Components and Contents

Nonstructural components, including an integrated system of interior walls, suspended ceilings, and sprinkler piping were installed in the 4<sup>th</sup> and 5<sup>th</sup> stories, where the floor acceleration was expected to be maximized. The overview of the nonstructural component response in both isolated and fixed-base building configurations is discussed in Soroushian et al. (2012) and is out of the scope of this dissertation.

To investigate the response of non-anchored contents in the isolated and fixed-base buildings for different earthquake excitation, furnishings representing a hospital room on the 4<sup>th</sup> floor (Figure 2-7) and an office room on the 5<sup>th</sup> floor (Figure 2-8) were installed in specially designed enclosed areas. Both rooms were 2 m x 4 m (6.6 ft x 13.1 ft) in plan and were constructed on top of the concrete mass blocks already present on the floors (Figure 2-2(a)). Contents in the hospital room included a wheeled patient bed, a dresser containing medical equipment, a medical cart, a storage cart, IV poles, a mobile lamp, medical bottles and boxes. Many of these items were wheeled. The office room was furnished with desks, chairs, computer system, bookcases and a photocopy machine.



Figure 2-7: Hospital room



**Figure 2-8: Office room**

### **2.3 Weights**

In addition to the weight of structural components, nonstructural components and contents, additional mass in the form of concrete and steel blocks were installed to simulate permanent live load. Concrete weights, whose typical size and position on the floors are shown in Figure 2-2(a), were built as a permanent part of structure on floors 2 to 5, while steel blocks were tied to the roof as shown in Figure 2-9. The categorized weights of the testbed components are listed in Table 2-2. This information was used to design the isolation system, model the structure and compute inertia forces from recorded accelerations.

In the 2009 experimental program that first used the testbed building (Kasai et al. 2010), steel blocks were distributed uniformly to the roof level to represent additional weight of equipment such as an air conditioning unit, water tank, or even a small penthouse. Each block included either 7 or 8 steel plates of size 2.1 m x 4.3 m x 0.025 m (6.9 ft x 14.1 ft x 0.08 ft). The roof slab was specifically designed to accommodate the additional weight,

which summed to 820 kN (184 kips). For this experimental program, the weight at the roof was altered from that used in 2009 experiments to introduce additional mass eccentricity and increase torsional response; specifically, about one third of the steel plates were removed on the West side of the building (Figure 2-9). The altered weight of the steel plates for this experimental program was 535 kN (120 kips). The intent of the added weight as designed for the original experiments was to simulate equipment weight in a typical building lacking a basement (Kasai 2011). However, this supplementary weight far exceeds the concentrated weight introduced by a typical single piece of roof mounted equipment, such as a chiller (about 80 kN or 18 kips), and thus might be considered atypical or even unrealistic. The issue is noteworthy because the supplementary weight influenced the seismic response of the building, which is discussed throughout the dissertation.

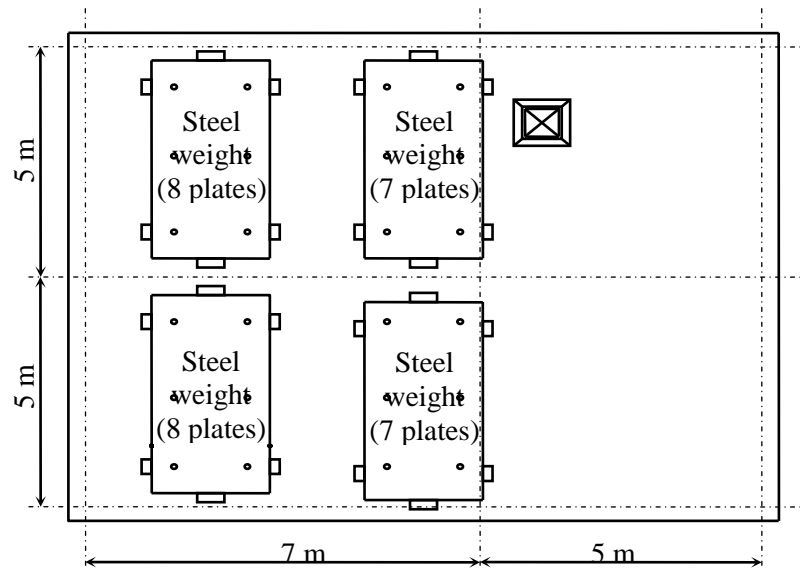


**Figure 2-9: Location of steel weights at roof**

The estimated total weight of the testbed, about 5122 kN (1151 kips), was well below the maximum capacity of the E-Defense earthquake simulator, which is 12000 kN (2700 kips) (Tagawa and Kajiwara 2007). The actual weight of the specimen measured during testing was 5220 kN (1174 kips) as reported in Section 4.3.

**Table 2-2: Estimated Weight of the Specimen by Component and Floor Level (unit: kN)**

Floor	Structural	Conc. Weight	Steel weight	Non-structural	Total
Roof	599	0	535	19.4	1153
5F	478	258	0	35.5	771
4F	497	268	0	16.2	781
3F	528	213	0	41.2	782
2F	527	176	0	89.6	792
Base	794 <sup>(*)</sup>	0	0	48.4	842
Sum w/ base	3422	914	535	250	5122
Sum w/o base	2628	914	535	202	4279

(\*) Before the test, the weight of structural component at base was estimated at 256 kN. This low value did not account the weight of column bases. The total weight of the specimen corresponding to this value was 4585 kN.

## 2.4 System Identification

The experimental response of the fixed base building to white noise excitations was analyzed (Sasaki et al., 2012) to find the periods and damping ratios of natural modes of the structure. Figure 2-10 shows examples of transfer functions determined from the white noise excitation on the fixed-based building conducted prior to the primary earthquake excitation. The period and damping ratio corresponding to the fundamental response modes were evaluated by curve fitting theoretical transfer functions to the

measured transfer functions using a least square algorithm. Table 2-3 summarizes the periods and damping ratios of first 3 modes in both directions determined from this process. Rocking of the earthquake simulator has been observed to affect the natural frequencies and mode shapes (Kasai et al., 2011; Sasaki et al., 2012); however, the effect of rocking was ignored in the modes presented in Table 2-3. The tested moment frame building has a natural period in the range of 0.65 to 0.70 seconds.

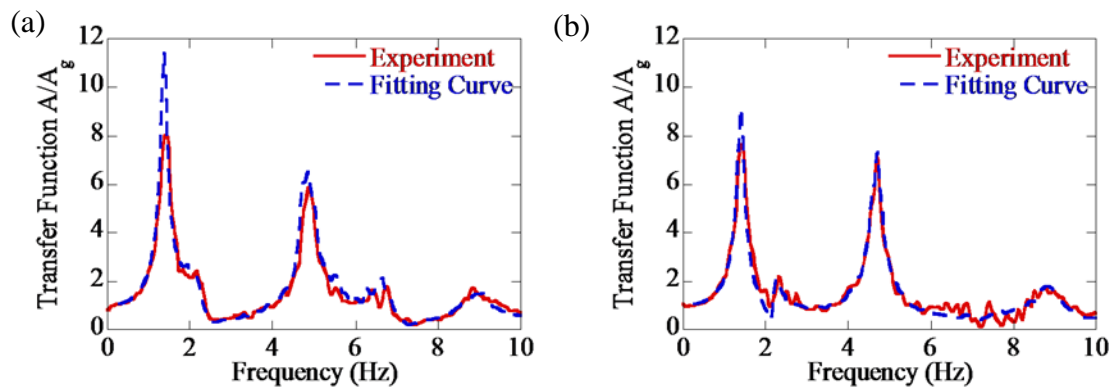


**Figure 2-10: Transfer function during white noise excitation in fixed-base configuration: (a) x-direction and (b) y-direction**

**Table 2-3: Experimentally Determined Natural Periods and Damping Ratios of the Fixed-base Building**

	White noise X		White noise Y		White noise 3D	
	Period (s)	Damping ratio (%)	Period (s)	Damping ratio (%)	Period (s)	Damping ratio (%)
Mode 1 X	0.65	3.3	n/a	n/a	0.68	4.1
Mode 2 X	0.20	1.6	n/a	n/a	0.21	2.0
Mode 3 X	0.11	3.3	n/a	n/a	0.11	3.7
Mode 1 Y	n/a	n/a	0.68	2.5	0.69	3.5
Mode 2 Y	n/a	n/a	0.21	1.7	0.21	1.9
Mode 3 Y	n/a	n/a	0.11	2.6	0.11	3.6



## 2.5 Condition of the Testbed Prior to Testing

The testbed was built in 2008 and tested first in March 2009 equipped with several types of damping devices (Kasai et al. 2010). The testbed was stored outdoors and unprotected between April 2009 and July 2011.

Several cracks in concrete slabs formed during the March 2009 test (Kasai et al. 2010). Examples of these cracks are shown in Figure 2-11. Steel beams and columns had not been painted and some corrosion was present in August 2011 (Figure 2-11). The effects of this damage were not quantified but suspect they are insignificant.



**Figure 2-11: Cracks in concrete slab and rust on steel member**

### 3. DESIGN OF THE ISOLATION SYSTEM

#### 3.1 Target Response of a Nuclear Site

A main objective of the test program was to demonstrate the stable response of an isolation system subjected to *beyond design basis* shaking at a representative nuclear site. Extensive prior work was performed by Huang *et al.* (2009) to characterize the site specific response spectra and displacement demands of representative isolation systems for three potential United States nuclear sites: North Anna, Vogtle and Diablo Canyon. North Anna represents a Central and Eastern United States (CEUS) rock site, Vogtle represents a CEUS soil site, and Diablo Canyon represents a Western United States (WUS) rock site. During an initial consultation, the external Advisory Board recommended designing an isolation system suitable for one of the three sites. The options were quickly narrowed down to focus on the Vogtle site while eliminating the other two sites from consideration. Even in beyond design basis shaking, the displacement demands for the North Anna site were too small to fully realize the shaking potential of both present isolation hardware and the E-Defense earthquake simulator facility in Japan. On the other hand, the displacement demands for the Diablo Canyon site were quite large, making it extremely difficult to size the lead-rubber bearings to provide sufficient flexibility, displacement capacity, and stability for the lightweight structure. Because of these difficulties, it is recognized that isolation of a safety related nuclear

facility may be more likely to come to fruition on a CEUS site; thus, the Vogtle site was deemed a more appropriate selection.

The development of site specific response spectra and spectrum matched motions for the Vogtle site, as utilized in this study, was described in detail in Huang et al. (2009) and is hereby summarized. Spectra representing the design basis earthquake (DBE) were developed by Southern Nuclear Operating Company. The uniform risk spectrum (URS) was developed by a combination of probabilistic seismic hazard analysis (PSHA), site response analysis, and conversion of the uniform hazard spectrum (UHS) to a URS. The seismic hazard was de-aggregated for a mean annual frequency of exceedance (MAFE) of  $10^{-4}$  and  $10^{-5}$ . Spectral shapes were developed for both high and low frequency spectral ranges using the attenuation relationship of McGuire et al. (2001) for Central and Eastern United States. Site response analysis was conducted to determine the amplification of rock motion to the free field surface. Site class factors and resulting spectra for the high and low frequency sets were merged into one, which led to the site specific UHS. The UHS was converted to a URS according to the procedure of ASCE 43-05 (ASCE 2008). These site specific spectra for horizontal and vertical response are shown in Figure 3-1.

Thirty spectrum matched motions were developed using seed ground motions selected based on the controlling magnitude  $M_w$  and distance  $r$  pair ( $M_w = 7.2$  and  $r = 130$  km) for the low frequency spectral range. Each set of ground motions included two horizontal components and a vertical component. These seed motions were spectrally matched to the Vogtle site specific URS for the DBE to get 30 spectrum compatible motions. These

motions were then amplitude scaled to develop maximum-minimum spectrum compatible motions. The maximum and minimum components consider the effects of directionality, wherein the minimum demand occurs at an orientation perpendicular to the maximum demand. The 5% damped response spectra for the 30 sets of developed maximum-minimum motions for the Vogtle site (Huang et al. 2009) are shown in Figure 3-2.

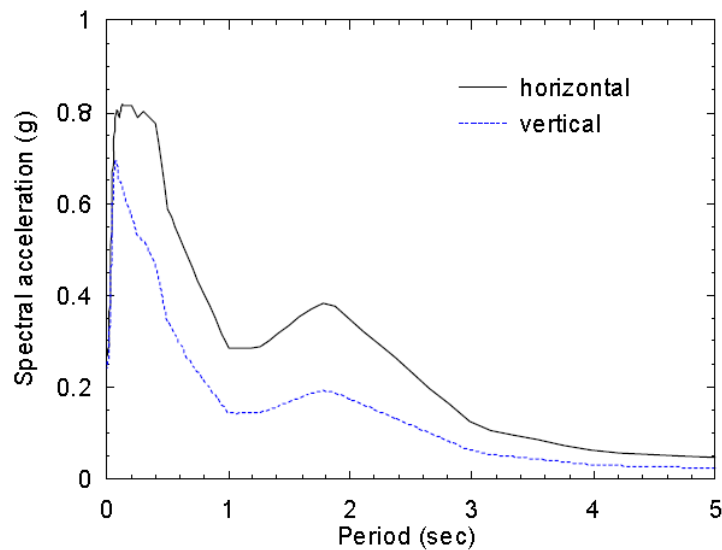


**Figure 3-1: 5% damped URS for the DBE at the Vogtle site (Source: Huang et al. 2009)**

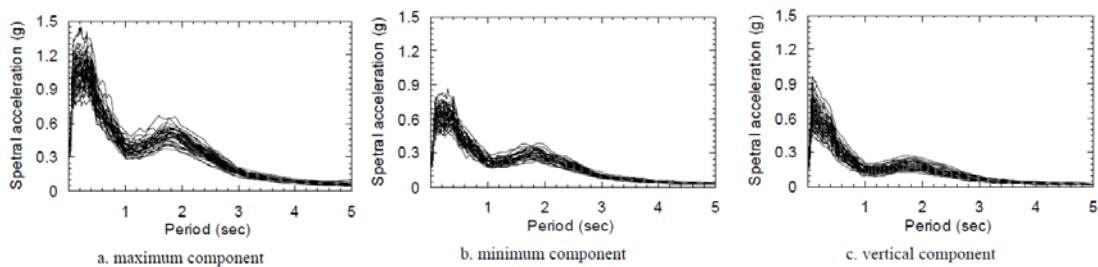


**Figure 3-2: 5% damped response spectra for the 30 sets of spectrum compatible maximum-minimum motions: (a) maximum component, (b) minimum component and (c) vertical component. (Source: Huang et al. 2009)**

## 3.2 Isolation System Design

The design properties of the LR bearings to be used in the test program were selected with the following considerations in mind. First, as mentioned above, the isolation system was to be tested under beyond design basis ground motions. Thus, the general procedure utilized was to scale the record(s) for the Vogtle site (Huang et al. 2009) to an intensity level corresponding to beyond design basis, estimate the displacement demands in the isolation system, and size the isolators accordingly. Second, the configuration and force demands in the isolators were to be selected such that connection assemblies designed for the complementary tests on the TP bearings could also be used to measure the shear and axial forces in the LR bearings. Third, safety requirements were imposed by the facility to protect the equipment.

### 3.2.1 Estimated Displacement Demands

To obtain an approximate estimate of the isolator demands, the isolated building was modeled as a simple spring-mass system (rigid structure supported by a flexible isolator driven by bidirectional pairs of ground motions), consistent with the assumptions in Huang et al. (2009). The spring, or isolator, was modeled with a bi-directionally coupled bilinear force-displacement relationship (Figure 3-3) characterized by the post-yield stiffness  $K_d$  (corresponding to the period  $T_d$ ), and the yield strength normalized by the weight ( $Q_d/W$ ). The post-yield stiffness is generally associated with the horizontal stiffness of the rubber while the yield strength is associated with the shear strength of the lead plug. Additional 2% viscous damping was assigned to the isolator model in each

horizontal direction based on the post-yield stiffness of the isolator (Huang et al. 2009). The weight of the building was estimated to be 4540 kN (1020 kips) for design.

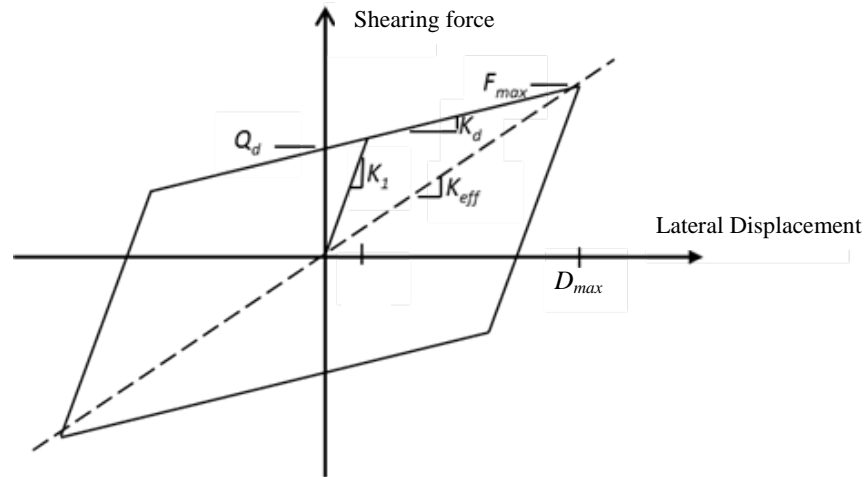


**Figure 3-3: Idealized bilinear force-displacement relationship for LR bearings, determined by post-yield stiffness  $K_d$  (stiffness of rubber), characteristic strength  $Q_d$  (strength of lead plug) and initial stiffness  $K_1$  or yield displacement  $D_y$ . An effective or secant stiffness  $K_{eff}$  is determined as the peak-to-peak stiffness based on maximum force  $F_{max}$  and displacement  $D_{max}$ .**

A subset of the parameters considered by Huang et al. (2009) was used as a starting point for this project, namely  $T_d = 2$  and 3 sec, and  $Q_d/W = 0.06$  and 0.09. The systems with  $Q_d/W = 0.06$  and 0.09 are hereafter referred to as Q6 and Q9. Other values of  $T_d$ , between 2 and 3 sec, were considered. The isolation period was desired to be greater than 2 sec to maximize the isolation effect and go beyond the soil-column related peak in the Vogtle spectrum just below 2 sec. A challenge with this testbed was to provide both the flexibility and the displacement capacity required at  $T_d = 3$  sec due to the relatively low weight of the building. Figure 3-4(a) shows the median displacement demands of the maximum-minimum motions (Figure 3-2) predicted for a Q6 and Q9 system at different

periods, determined by statistical analysis of the responses of the single degree-of-freedom (SDOF) system; the values at 2 and 3 sec are identical to those in Huang et al. (2009). Reducing the period for the Q6 system below 3 sec did not reduce the displacement demand, which is likely related to the local maximum in the response spectrum near 2 sec. The peak displacement demand of the Q6 nonlinear system occurred between periods of 2.4 and 2.6 sec. For the Q9 system, the displacement demand decreased monotonically as the period was reduced below 3 sec. Figure 3-4(b) shows the 90% percentile displacement demand of the maximum-minimum motions scaled to 150% – representative of beyond DBE shaking – for a Q6 and Q9 system. For this case, reducing the period below 3 sec caused the 90<sup>th</sup> percentile displacements to increase for both Q6 and Q9 systems. Based on these observations, a target period of 3 sec was selected for initial design and both Q6 and Q9 systems were considered.

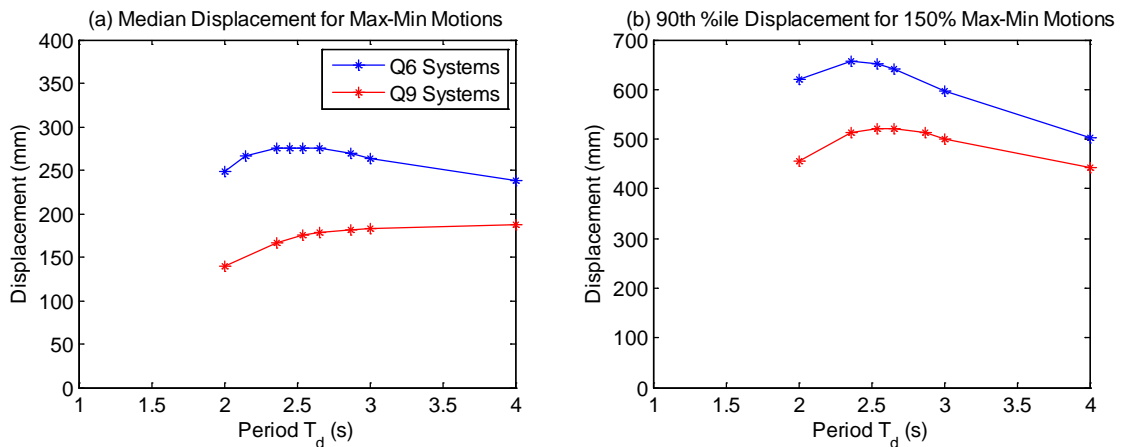


**Figure 3-4: Displacement demand representing (a) median response to maximum-minimum motions and (b) 90% percentile response to 150% maximum-minimum motions for Vogtle site.**

### 3.2.2 Configuration of Lead-Rubber Bearings

As mentioned previously, the testbed was a 2 bay frame in each direction with 9 columns. The configuration of columns at the base labeled by direction coordinates is shown in Figure 3-5. Forces in LR bearings could potentially be obtained by bolting the bearings to connection assemblies. The connection assemblies, which were designed for the TP isolation system (Dao and Ryan, 2015), consisted of 7 to 9 load cells sandwiched between two steel plates (e.g. Figure 3-6). Further details of the connection assemblies are provided in Chapter 4.

The target design parameters of the system could only be achieved with a small number of LR bearings. Thus, a design using four LR bearings was proposed. Given that LR bearings would not be placed beneath every column, two alternatives were considered. In Configuration Option 1, LR bearings were to be placed at the four corner columns (SE, SW, NE and NW) with no isolators beneath the remaining 5 columns (Figure 3-7(a)). In Configuration Option 2 (Figure 3-7(b)), LR bearings were to be placed beneath the four edge columns (S, E, W and N), and complementary low friction bearings were to be placed beneath the remaining 5 columns, comprising a hybrid isolation system as introduced in Chapter 1. (Note that the selected CL bearings were one of several types of low friction bearings that could have been used for this purpose.) The weight supported by each isolator based on tributary load calculation is indicated for each configuration option. Configuration Option 1 was preferred since the LR bearings were to carry the total weight of the building, leading to a good test of the isolator stability, which was



related to the test objectives. Configuration Option 1 was ultimately eliminated because the base diaphragm was not believed to be sufficiently stiff to suppress bouncing of the unsupported columns, and the expected loads on individual isolators exceeded the capacities of the designed connection assemblies (Figure 3-6).

Thus, Configuration Option 2 was selected. The LR bearings were located at the edge columns in Configuration Option 2 (Figure 3-7(b)) where they were expected to carry larger axial forces, which was desirable for a better test of the stability of the bearings at large displacements. A drawback to this arrangement was that it decreased the torsional resistance of the isolation system from Configuration Option 1.

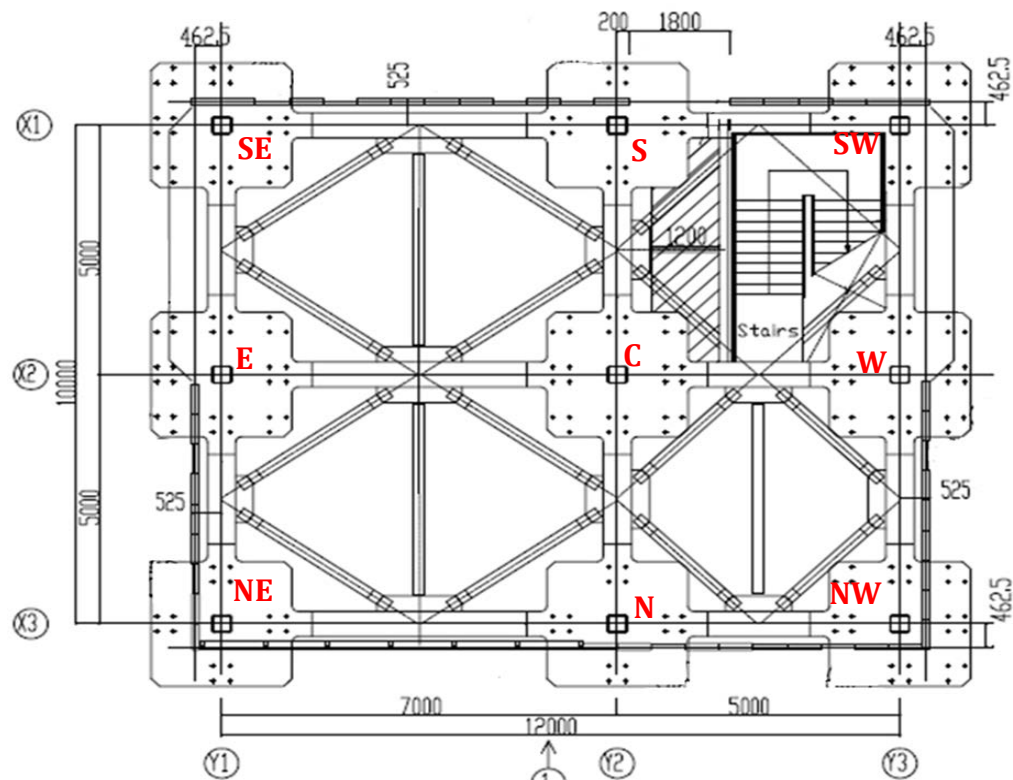


**Figure 3-5:** Drawing of testbed base plan with column labels (N = North, E = East, S = South, W = West, C = Center).

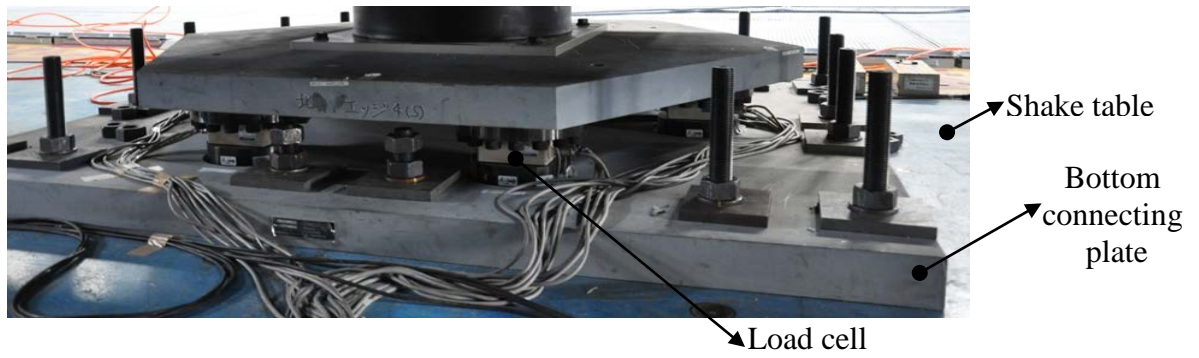
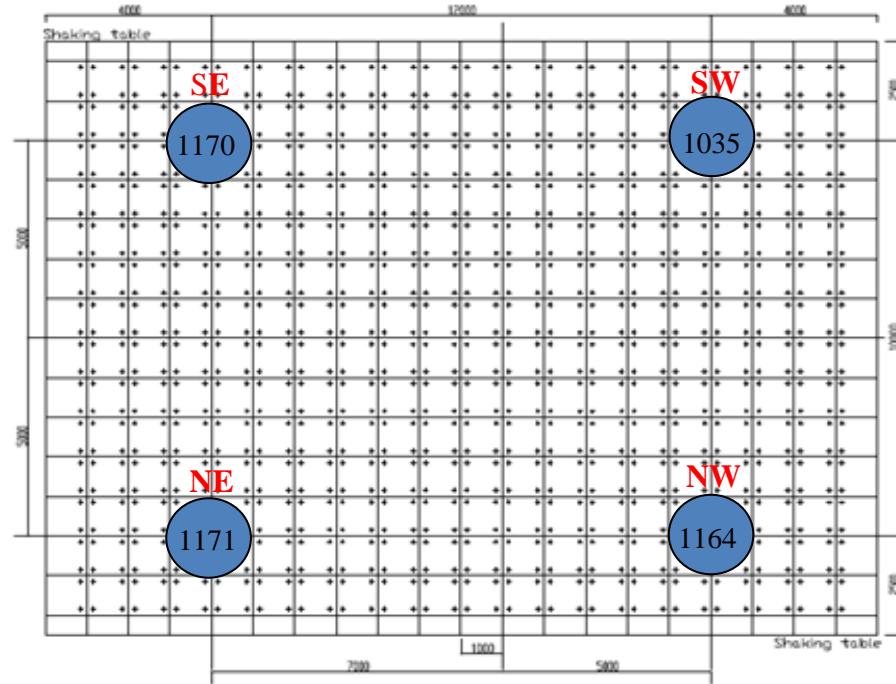
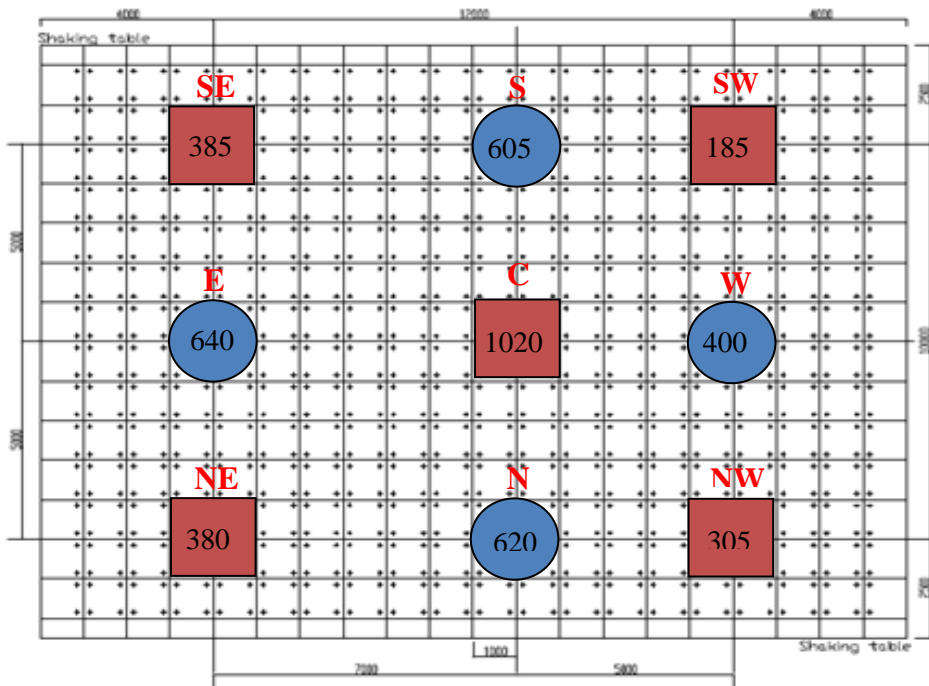


**Figure 3-6:** Illustration of a connection assembly with triaxial load cells to measure bearing forces.



(a)



(b)

**Figure 3-7: (a) Configuration Option 1 with LR bearings beneath 4 corner columns, (b) Configuration Option 2 with LR bearings (circles) beneath 4 edge columns and low friction bearings (squares) beneath remaining columns. The supported weights (in units of kN) at the isolators based on tributary loads are also indicated.**

### 3.2.3 Selection of the Bearing Dimensions

Based on the target period  $T_d = 3$  sec and a displacement demand of 600 mm (23.6 in) for a Q6 system and 500 mm (20 in) for a Q9 system (Figure 3-4(b)), three alternative isolators were proposed by Dynamic Isolation Systems, who provided the bearings for this project. The parameters for each alternative are shown in Figure 3-8, where  $D$  is the overall diameter,  $N$  is the number of rubber layers,  $P_{allow}$  is the allowable axial load at a lateral displacement of zero, and  $D_{max}$  is the maximum displacement capacity of the bearing at the anticipated axial load demand. All options assumed 6 mm (0.236 in) thick rubber layers and a shear modulus  $G = 0.41$  MPa (0.06 ksi). The post-yield stiffness  $K_d$  was calculated from

$$K_d = \frac{GA_b}{T_r} \quad (3.1)$$

where  $A_b$  is the area of the bearing, and  $T_r$  is the total thickness of rubber.  $P_{allow}$  was computed as the maximum axial load of the bearing in the undeformed configuration divided by a factor of 3, which is standard industry practice in the United States to provide a high margin of safety under gravity loads. Figure 3-9 illustrates the theoretical axial load capacity (computed as a minimum of buckling, elastomer limit or stress limit) for each proposed bearing design as a function of lateral isolator displacement (Constantinou et al. 2007). The peak axial load demand was estimated for the trial calculations as the peak dead weight supported by any isolator (based on tributary area) increased by a factor of 1/3 for overturning: 850 kN (191 kip). For the trial design the

displacement capacity was estimated as the displacement at an axial load of 850 kN (191 kip) on the axial force-lateral displacement curve (Figure 3-9).

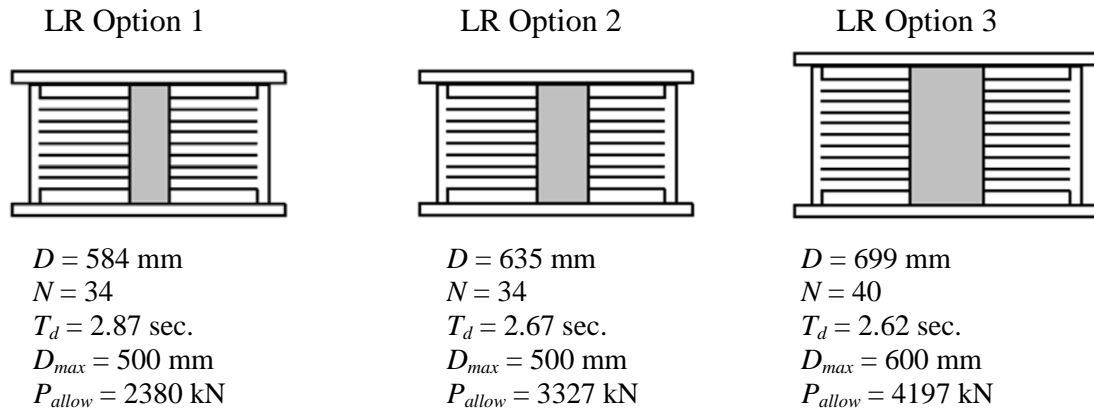


**Figure 3-8: Proposed design options for LR bearings**

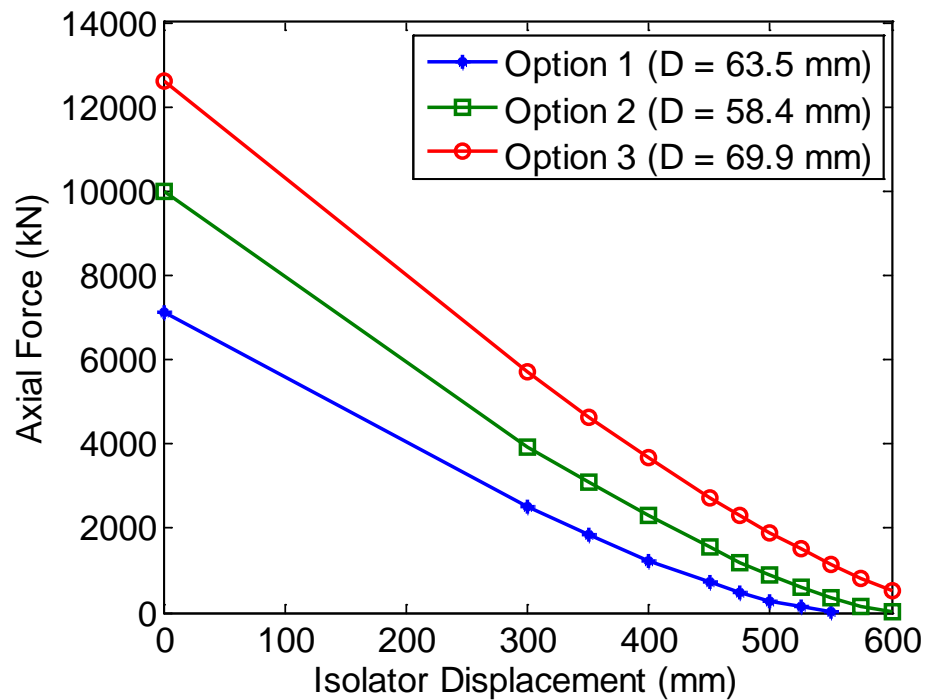


**Figure 3-9: Axial force capacity of proposed LR bearings versus lateral displacement**

LR Option 1 was the most flexible of the three ( $T_d = 2.87$  sec) and it nearly met the target period, but its displacement capacity was limited. The target displacement could only be achieved for Q9. LR Options 2 and 3 provided nearly the same effective period, but LR Option 3 had a substantially higher displacement capacity, which was achieved by increasing the diameter and height of the bearing. LR Option 3 was preferred to LR Option 2.

### 3.2.4 Selection of the Lead Plug Dimensions

Initially, lead plugs were sized for Q6, Q9 and an intermediate option Q7.5 ( $Q_d/W = 0.075$ ), where contributions to the zero-displacement force intercept were to be made by low friction bearings with a friction coefficient  $\mu = 0.06$  and the lead plugs in the LR bearings. Recall that LR bearings were to be installed under the edge columns (columns S, E, W and N in Figure 3-7(b)) and low friction bearings were to be installed under the remaining 5 columns. The low friction bearings alone would have provided a yield force of approximately 120 kN (27 kips) based on the tributary weight and a coefficient of sliding or rolling friction of 0.06. The lead plugs were sized to provide the remainder, based on the following equation:

$$\begin{aligned} Q_{LR} &= \left( \frac{Q_d}{W} \right) W - Q_{roll} \\ &= N_{LR} \sigma_{y,LP} (\pi/4) D_{LP}^2 \end{aligned} \quad (3.2)$$

where  $Q_{LR}$  and  $Q_{roll}$  are the characteristic strength of the LR bearings and low friction bearings, respectively.  $N_{LR}$  is the number of LR bearings (4),  $\sigma_{y,LP}$  is the dynamic yield strength of the lead plug and  $D_{LP}$  is the diameter of the lead plug. For this calculation,  $\sigma_{y,LP}$  was taken as 7.94 MPa (1.15 ksi), which is the value recommended by Dynamic Isolation Systems for their products. Table 3-1 lists the required diameter of the lead plug for Q6, Q7.5 and Q9, tabulated from Equation (3.2). The required diameter of the lead plug increased by about 33% (from 77 mm (3.0 in) to 106 mm (4.2 in)) from a Q6 to a Q9 design.

**Table 3-1: Required Diameter of the Lead Plug**

Label	Yield strength $\sigma_{y,LP}$ in MPa (ksi)	Strength required Q in kN (kip)	Strength required per bearing in kN (kip)	Area lead plug in mm <sup>2</sup> (in <sup>2</sup> )	Diameter lead plug $D_{LP}$ in mm (in)
Q6	7.94 (1.15)	146.8 (33)	36.7 (8.25)	4620 (7.2)	77 (3.0)
Q7.5	7.94 (1.15)	213.5 (48)	53.4 (12.00)	6720 (10.4)	93 (3.6)
Q9	7.94 (1.15)	280.2 (63)	70.0 (15.75)	8850 (13.7)	106 (4.2)

If the diameter of the lead plug is small, then the hysteresis may be pinched as seen in later figures. Importantly, if the plug is too small, little energy dissipation is achieved. If the diameter of the lead plug is too great, then the isolator may not provide sufficient confinement of the core during repeated cycling. The rule of thumb, based on years of experimentation and analysis is that the ratio of the diameter of the lead plug to the bonded diameter of the bearing is between 1/6 and 1/3. Table 3-2 presents the ratio of  $D_{LP}/D$  for the different combinations of bearing and lead plug sizes. For most combinations, the ratio did not meet the minimum of 1/6. The diameter ratios were lowest

for LR Option 3, which provided the largest displacement capacity. Based on Table 3-2, the combination of LR Option 3 and Q9 almost met the minimum diameter ratio requirement, but the displacement demand would be lower for a Q9 design, such that the provided capacity of the bearing would not be fully utilized in the test. Thus, an alternative low friction bearing was considered, as described in the next section.

**Table 3-2: Ratio of Lead Plug Diameter to Bearing Diameter ( $D_{LP}/D$ )**

	Q6 ( $D_{LP} = 76.7$ mm)	Q7.5 ( $D_{LP} = 9.25$ mm)	Q9 ( $D_{LP} = 106.2$ mm)
LR Option 1 ( $D = 584$ mm)	0.13	0.16	0.18
LR Option 2 ( $D = 635$ mm)	0.12	0.15	0.17
LR Option 3 ( $D = 699$ mm)	0.11	0.13	0.15

### 3.2.5 Cross Linear Bearings

The cross-linear (CL) bearing manufactured by THK allows nearly resistance-free linear motion. The LM Guide technology allows free rolling motion of a weight supporting part on a rail, where the part and the rail are internally separated by recirculating ball bearings. The CL bearing uses two orthogonally mounted LM Guide assemblies (Figure 3-10). The CL bearing can be combined with traditional isolation devices to support the weight of the building without increasing the total base shear of the isolation system. The coefficient of friction of the rolling system varies from 0.48-0.62%, leading to a negligible contribution to the base shear for a reasonable value of the supported weight.



Making use of the CL bearings means that  $Q_{roll}$  in Equation (3.2) can be taken to zero; thus allowing the lead plugs to provide the yield strength in entirety. Opting for a Q6 design, the required diameter of the lead plug was 101.6 mm (4.0 in), which provided the estimated total yield strength of 267 kN (60 kip) or 66.75 kN (15 kip) per bearing.



**Figure 3-10: Photo of installed CL bearing illustrating orthogonal LM guides assemblies on top and bottom.**

Besides its low friction rolling capability, the CL bearing provides significant resistance to tensile forces. A more careful evaluation of overturning on the hybrid isolation system suggested that the LR bearings alone would be unable to resist the tensile demands. The tensile force demands in the system at a displacement of 600 mm (23.6 in) were estimated as follows. First, the total base shear  $V_b$  in the isolation system was estimated as:

$$\begin{aligned}
 V_b &= N_{LR}(Q_d + K_d D_{\max}) \\
 &= 4(66.75 \text{ kN} + 0.65 \text{ kN/mm} \cdot 600 \text{ mm}) \\
 &= 1827 \text{ kN (411 kip)}
 \end{aligned}
 \tag{3.3}$$

The post-yield stiffness  $K_d$  and strength  $Q_d$  assumed LR Option 3 with a lead plug diameter  $D_{LP} = 101.6 \text{ mm (4 in)}$ . The base shear was assumed to act at 9 m, which is about half the height of the building (Figure 3-11). The overturning moment generated by the base shear was balanced by an overturning force  $F_{OT}$  times the shortest base dimension of the building (10 m). Thus,  $F_{OT}$  was calculated as 9/10 of the base shear  $V_b$  ( $F_{OT} = 1644 \text{ kN or 370 kip}$ ). The overturning demand was assumed to be carried by tension on the more lightly loaded South side of the building (Figure 3-7(b)). The total tension  $T$  carried by the three isolators (SE, S and SW) was computed as:

$$\begin{aligned}
 T &= F_{OT} - \sum_i W_i \\
 &= 1644 \text{ kN} - (385 + 605 + 185) \text{ kN} \\
 &= 469 \text{ kN (105 kip)}
 \end{aligned}
 \tag{3.4}$$

where  $W_i$  is the tributary weight supported by the  $i^{\text{th}}$  isolator, summed over the SE, S and SW isolators. Without CL bearings, the 469 kN (105 kip) of tension would be carried by a single LR bearing. Since CL bearings were utilized, the CL bearings were expected to carry the overturning induced tension and each CL would be subjected to about 235 kN (53 kip) tension. In reality, the tensile demands may not be equally balanced by the CL bearings, since the SW bearing carries significantly less weight than the SE bearing according to tributary area (Figure 3-7(b)).

Equation (3.4) suggested that peak compressive force on a given side of the building could increase by a factor of 2 or more due to overturning. The initial estimate of axial force demand (850 kN or 191 kip) used to estimate the displacement capacity of the LR bearings would then be unconservative. However, the CL bearings were much stiffer in compression than the LR bearings, and the vertical movements of LR and CL bearings were coupled together by the rigidity of the base diaphragm. This base diaphragm constraint was expected to prevent individual LR bearings from shortening or buckling, thus enhancing the overall stability of the isolation system such that the projected axial force limits would not be relevant. The interaction and load transfer between LR bearings and CL bearings is a unique aspect of this isolation system, which is evaluated extensively later in this dissertation. The suitability of the tested hybrid system for nuclear facilities is also evaluated based on a synthesis of the experimental data.

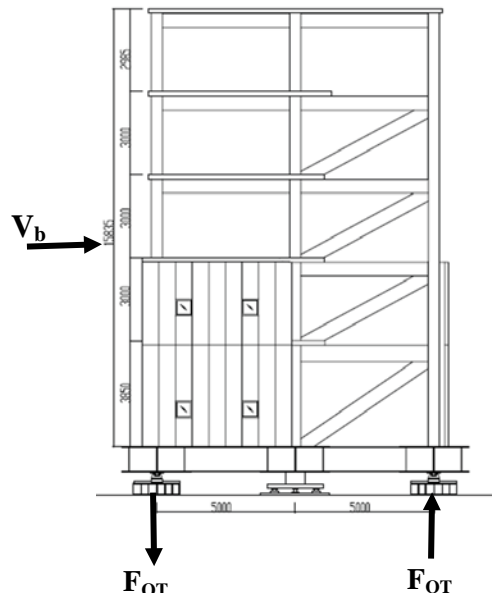


**Figure 3-11:** Total base shear ( $V_b$ ) and overturning forces ( $F_{OT}$ ) acting on an elevation view of the testbed building.

### 3.2.6 Summary of Design Properties

The final hybrid LR isolation system design included four LR bearings and five CL bearings. The configuration of the bearings (LR bearings at edge columns and CL bearings at center and corner columns) is shown in Figure 3-12, along with photographs of the devices taken prior to installation. LR Option 3 was used for the LR ( $D = 699$  mm or 27.5 in, 40 rubber layers, post yield stiffness  $K_d = 0.65$  kN/mm or 3.71 kip/in and  $T_d = 2.6$  sec) and the lead plug was sized for Q6 ( $D_{LP} = 101.6$  mm or 4 in). The estimated displacement capacity of the LR bearings based on a stability limit was 600 mm (23.6 in). The CL bearings were designed with a displacement capacity of 600 mm (23.6 in) imposed by a low force capacity stopper at the end of travel in each perpendicular direction that was not intended to be reached.

The dimensions and target stiffness and strength parameters of the LR bearings are listed in Table 3-3. All parameters were provided by the manufacturers. Several of the parameters are modeling parameters recommended for a bilinear representation of the force-deformation relation, as shown in Figure 3-3. The bearings were tested by Dynamic Isolation Systems prior to shipment to E-Defense. Force-deformation characterization was generated for cycles of amplitude 300 mm (11.8 in), 500 mm (19.7 in) and 650 mm (25.6 in) at different axial loads. Pseudo-static tests were performed and dynamic material properties were not provided. The results of this characterization are reported in Chapter 7.

The main properties of the CL bearings are listed in Table 3-4. The vertical stiffness of the CL bearings in compression and tension was provided by Aseismic Devices Co. Design drawings and specification sheets for both LR and CL bearings provided by the manufacturers are included in Appendix B.

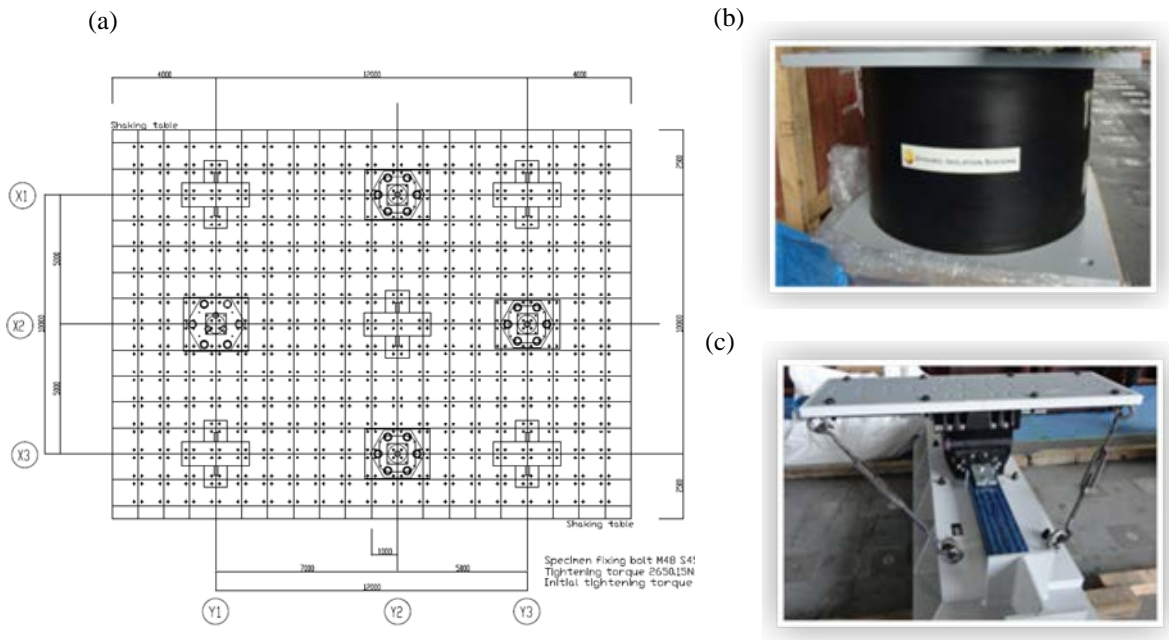


**Figure 3-12: (a) Final plan drawing of the hybrid LR isolation system, (b) photo of LR bearing, and (c) photo of CL bearing**

**Table 3-3: Lead Rubber Bearing Properties**

<b>Bearing Dimensions</b>		
Overall Diameter, $D$	=	6985 mm (27.5 in)
Number of Rubber Layers, $N$	=	40
Lead Diameter, $D_p$	=	101.6 mm (4.0 in)
Shim Thickness, $t_s$	=	3 mm (0.1196 in)
Layer Thickness, $t_r$	=	6 mm (0.236 in)
Side Cover Rubber Thickness, $c_s$	=	12.7 mm (0.5 in)
Top Mounting Plate Thickness, $t_{tp}$	=	25.4 mm (1in)
Bottom Mounting Plate Thickness, $t_{bp}$	=	25.4 mm (1in)
Internal Plate Thickness, $t_{ip}$	=	25.4 mm (1in)
<b>Isolator Properties</b>		
Effective Period, $T_{eff}$	=	2.27 sec
Post Yield Period, $T_d$	=	2.62 sec
Design Displacement, $D_D$	=	300 mm
Maximum Displacement, $D_{TM}$	=	600 mm
Post-Yield Stiffness, $K_d$	=	0.65 kN/mm (3.7 kip/in)
Initial Stiffness, $K_I$	=	6.5 kN/mm (37 kip/in)
Characteristic Strength, $Q_d$	=	65.7 kN (14.8 kip)
Yield Force, $F_y$	=	73 kN (16.4 kip)
Yield Displacement $D_y$	=	11.28 mm (0.44 in)
Compressive Vertical Stiffness, $K_v$	=	1500 kN/mm (8566 kip/in)
Tension Vertical Stiffness, $K_t$	=	30 kN/mm (171 kip/in)
Shear Modulus, $G$	=	0.414 MPa (0.06 ksi)
Rubber Ultimate Strain (at-break), $e_u$	=	5.5

**Table 3-4: Cross Linear Bearing Properties**

<b>Isolator Properties</b>		
Coefficient of Friction, $\mu$	=	0.48%-0.62%
Yield Displacement, $D_y$	=	0.1 mm
Compressive Vertical Stiffness, $K_{vc}$	=	3471 kN/mm (19821 kip/in)
Tension Vertical Stiffness, $K_{vt}$	=	245 kN/mm (1399 kip/in)

### 3.3 Selection and Scaling of Ground Motions

The test program for the hybrid LR isolation system was developed based on the recommendations and interests of several different parties, including the research sponsor, the Advisory Board members, the manufacturers, the project team and Japanese collaborators. Two days of testing were planned for the hybrid LR isolation system

configuration, where 7 independent trials (in extreme cases 8) could be executed each day.

Demonstrating the stable performance of elastomeric isolation systems in design or beyond design basis earthquakes is an important step to enable the use of base isolation for safety related nuclear structures. The seismic hazard at the Vogtle site is well known to the nuclear engineering community, and thus a record representing the seismic hazard at the Vogtle site was prioritized for the test program. A Vogtle record was sought from among the set of 30 maximum-minimum spectrum compatible ground motion pairs developed by Huang et al. (2009) that would produce a peak LR bearing displacement demand of about 600 mm (23.6 in) when scaled to 150%, in accordance with the beyond design basis target. Extensive pre-test analysis was conducted to identify the best Vogtle record for this purpose. While the isolation system was designed specifically for beyond design basis motions at the Vogtle site, its capabilities also permitted the system to be subjected to a Diablo Canyon record, representative of a WUS rock site, scaled to about 100%. The Diablo Canyon record was selected from a set of 30 maximum-minimum spectrum compatible ground motion pairs developed by Huang et al. (2009) using a procedure similar to the one described for the Vogtle site. The sponsor requested that the maximum displacement demands on the LR bearings be imposed in as few trials as possible so that the bearings were in their virgin state. The performance of bearings made from natural rubber has generally been found to be stable after repeated cyclic testing, although the hysteresis of LR bearings can be affected by heating of the lead plug and strain hardening induced by cumulative travel effects (Constantinou et al. 2007). An

additional objective evolved from these considerations, which was to repeat one of the early trials at the end of the test program to evaluate the consistency of the LR bearing response.

Once the sponsor objectives had been met, other objectives could be entertained. For example, the project team aimed to identify a service level, design level, and maximum considered earthquake (MCE) level motion to be replicated on all three building configurations (TP isolation system, hybrid LR isolation system, and fixed base). The Japanese collaborators aimed to identify a strong Japanese motion that could be replicated on all three building configurations. Dynamic Isolation Systems requested a sine wave characterization test to be repeated at the beginning and the end of the test program.

The test facility imposed additional constraints on the test program based on safety considerations, which are described next.

### **3.3.1 Imposed Limitations for Safety**

The following limitations related to target demands and test sequence were imposed.

1. The target displacement demand of the LR bearings was limited to 550 mm (21.6 in). In initial discussions, Japanese collaborators imposed a displacement limit equal to the design displacement of 300 mm (11.8 in), which was comparable to displacements permitted in previous tests at E-Defense. A compromise was reached after a) it was demonstrated that shear rupture was not expected before displacements of 800-900 mm (31.5-35.4 in), b) it was demonstrated that the CL



bearings would stabilize the entire isolation system, and c) Dynamic Isolation Systems agreed to in-house characterization tests of the LR bearings to displacements of 650 mm (25.6 in) prior to shipment of the bearings to Japan.

2. The target displacement demand of the CL bearings was limited to about 400 mm (15.7 in) in each of the x and y perpendicular directions, which is a factor of safety of about 1.5 relative to the displacement limit of the CL bearings. This agreement was reached after Aseismic Devices Co. agreed to add a safety stop at the end of travel in each direction. The safety stop was not intended to stop the momentum of the building if a high impact collision of the rolling system with the safety stop were to occur.
3. The largest displacement was to be approached over a series of 3 or 4 incremented trials that gradually increased the intensity of the earthquake shaking. This incremental approach was intended to validate the numerical simulation and allow adjustment to the intensity of the largest imposed record as necessary. This constraint conflicted with the objective to impose the largest intensity record early in the test sequence, but could not be avoided.

### **3.3.2 Vogtle and Diablo Canyon Motions**

Substantial effort was expended to identify the best Vogtle record and best Diablo Canyon record for the testing program. Six Vogtle records were considered; these records were identified by evaluating the peak bidirectional displacement demand of the SDOF system to all 30 pairs of Vogtle records scaled by 150%, and selecting those that predicted a peak displacement closest to 550 mm (21.6 in). Displacement traces (x vs y-

direction displacement) and displacement histories for the 6 records that were considered are shown in Figure 3-13 and 3-14. Preference was given to the records that included multiple cycles of large displacement (Figure 3-14), and followed a partially circular trace rather than a linear trace in a given direction (Figure 3-13). Vogtle #13 and Vogtle #9 were considered to meet these criteria better than the other records.

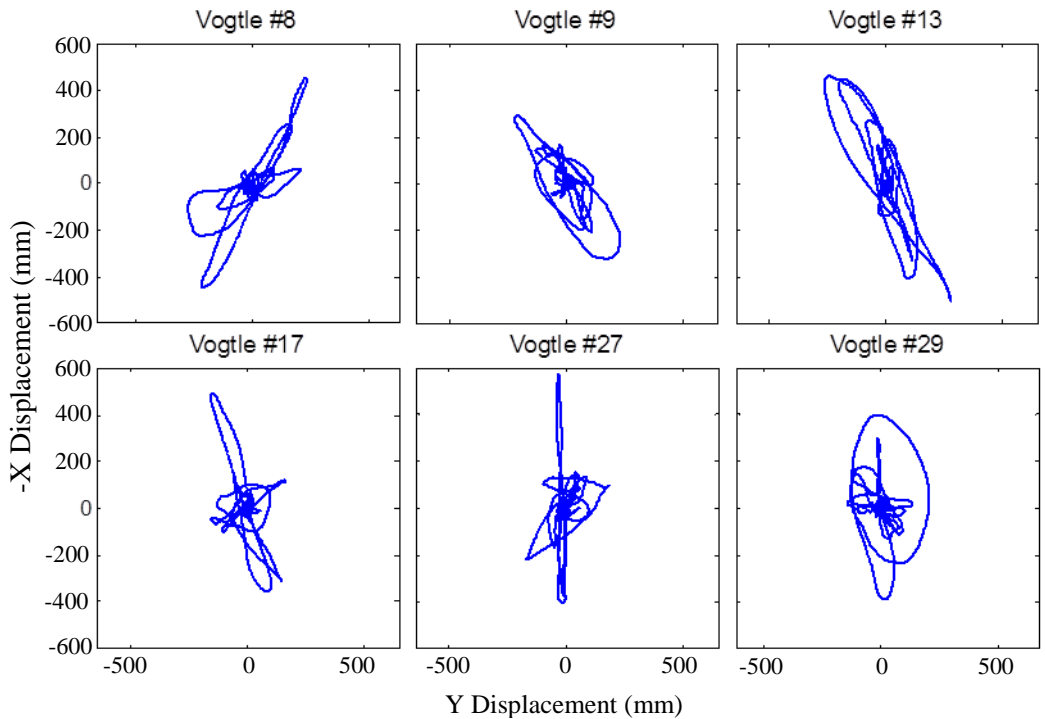


**Figure 3-13: Calculated displacement trace of the isolation system for 6 Vogtle motions by SDOF analysis**

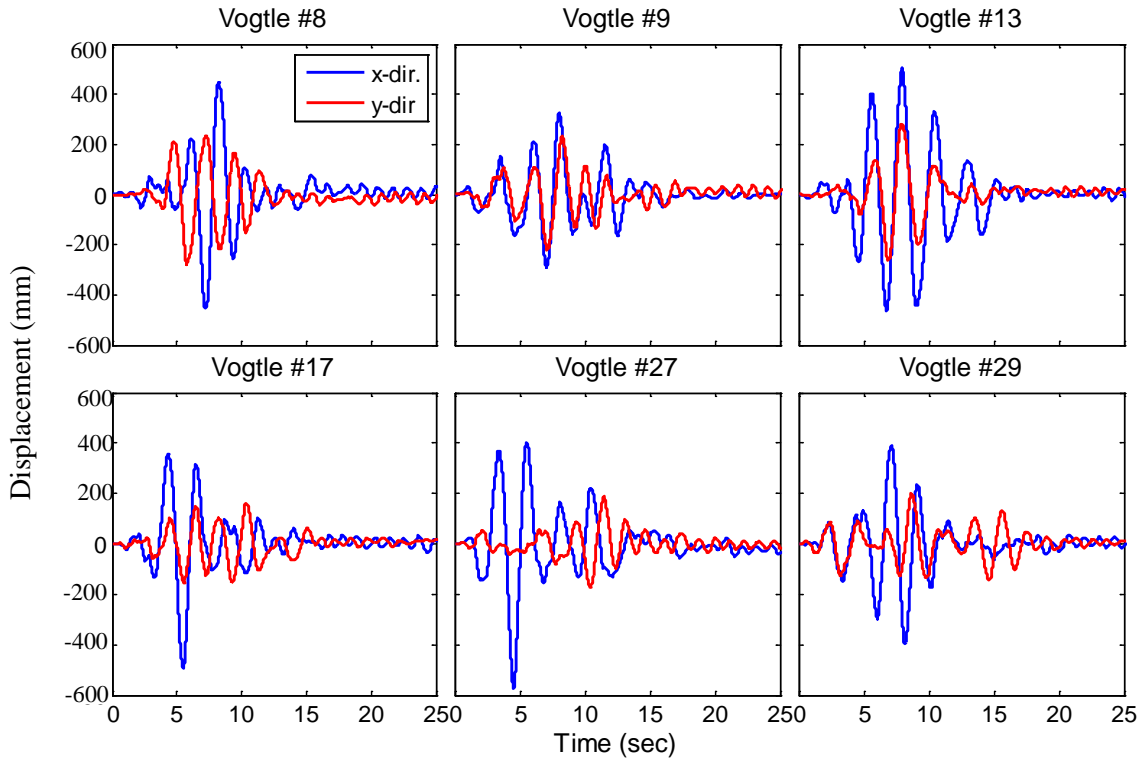


**Figure 3-14: Calculated displacement histories of the isolation system in x and y directions for 6 Vogtle motions by SDOF analysis**

Next, the records were applied to the isolated building model that was developed in OpenSees (described in Chapter 8) to obtain a more accurate assessment of the displacement and force demands. In general, the peak displacement demands of the isolators in the building model were somewhat larger than in the SDOF model. Upon examining the data, two sources of discrepancy were identified. First, the building model did not contain viscous damping alongside the isolation system. Displacements in the SDOF model were re-evaluated after removing this damping (2% of critical calibrated to the isolator post-yield stiffness), and they increased substantially, which indicated that the response was sensitive to the seemingly small additional damping. Although some

viscous energy dissipation may be present, the damping was removed from the SDOF model to err on the side of conservatism.

Second, substantial rotational demands at the base level were predicted by the analysis of the building model, which caused amplification of the displacement on one side or corner of the building compared to the other. To illustrate this, the displacement traces of each bearing are presented in Figure 3-15. Due to the rotation, the peak displacement in one bearing was predicted to be 540 mm (21.3 in), while the peak displacement predicted in the opposite corner was only 460 mm (18.1 in). The project team was skeptical about the significant amount of torsion predicted by the analysis, and experimented with the modeling assumptions to develop confidence in the prediction and possibly identify a cause. Several alternative assumptions were considered, including bearing placement at the corners rather than on the edges, and accounting for the rotational stiffness of both the LR and CL bearings. None of the modifications significantly altered the amplitude of the rotational demands, and the experimental data later validated the torsion predicted by numerical simulation (see Chapters 5 and 9). The rotational demands observed in the isolation system resulted from limitations on the number and placement of LR bearings for the testbed structure. In a large building or safety related nuclear structure with hundreds of isolators, isolation system asymmetries and rotational demands could be eliminated or minimized by strategic placement of bearings with and without lead plugs.

With the exception of Vogtle #13, the peak displacements predicted by the building model exceeded those predicted by the SDOF model without viscous damping. Thus,

Vogtle #13 was selected since the displacement predicted by the building model was closest to that predicted by SDOF model for the desired scale factor of 150%.

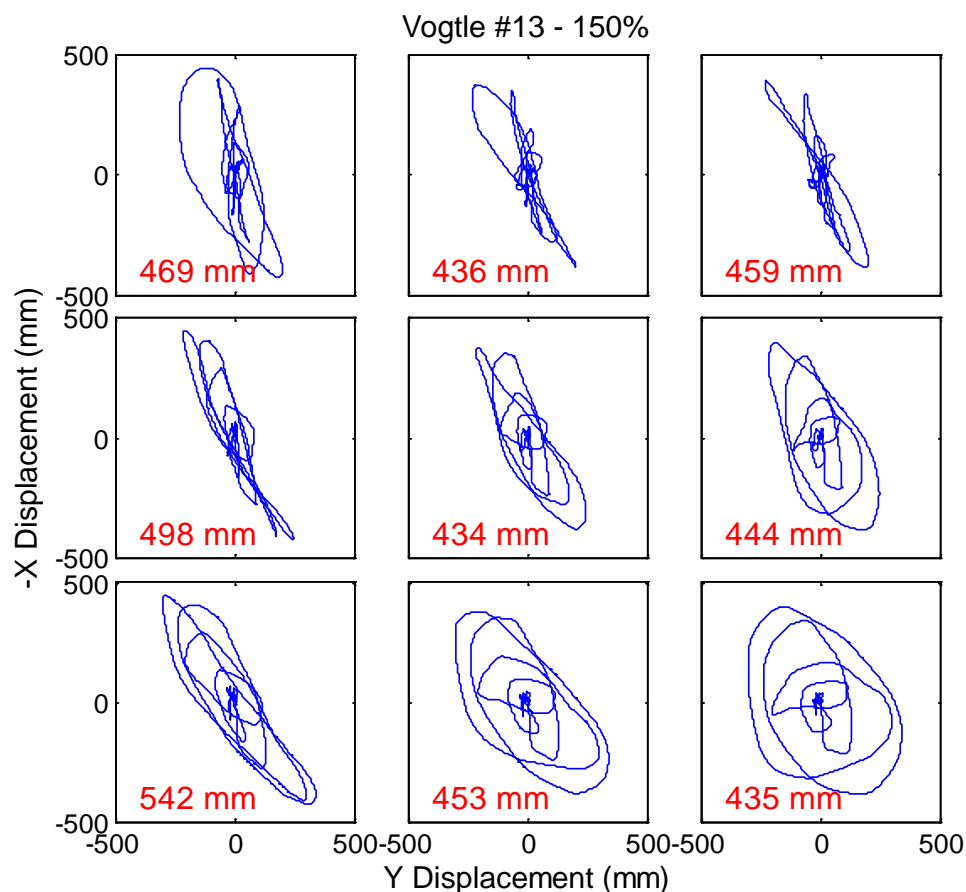


**Figure 3-15: Predicted displacement trace of each isolator for the OpenSees building model subjected to 150% Vogtle #13**

While the LR bearings could be subjected to displacements of up to 550 mm (21.7 in), the CL bearings were not permitted to exceed displacements of 400 mm (15.7 in) in the x and y-directions. Thus, the components of the input ground motion were rotate such that the peak displacement demand occurred at approximately 45 degrees, which would simultaneously minimize the demands in x and y-directions and maximize the vector

displacement. To determine the rotation of the input motion, the building model was analyzed to the Vogtle #13 input excitation rotated at increments of 11.25 deg. Thus, rotated inputs at 0, 11.25, 22.5, 37.75, and 45 deg were considered. Based on this analysis (summarized in Table 3-5), a rotation angle of 11.25 degrees was selected. The anticipated peak displacement demand in any LR bearing for Vogtle #13 rotated by 11.25 degrees and scaled to 150% was 490 mm (19 in), while the peak displacement in any CL bearing in the x or y direction was 400 mm (16 in). Adjustments to the scale factors were made on the day of testing, and the actual peak scale factor applied was 175%. The complete final schedule of simulations actually conducted is summarized in Chapter 4.

**Table 3-5: Predicted x, y and Vector Peak Displacement in the Different Isolator for the Building Model Subjected to 150% Vogtle #13 Record, with Rotated Horizontal Components of Input Motion**

<b>Bearing</b>	<b>Rotation Angle (degrees)</b>	<b>X - Peak Displacement (mm)</b>	<b>Y - Peak Displacement (mm)</b>	<b>Vector Peak Displacement (mm)</b>
<b>Lead Rubber</b>	0	337	450	498
	11.25	390	399	494
	22.5	437	332	491
	37.75	474	274	503
	45	499	208	508
<b>Cross Linear</b>	0	337	451	542
	11.25	390	399	546
	22.5	437	331	543
	37.75	474	274	534
	45	499	208	521

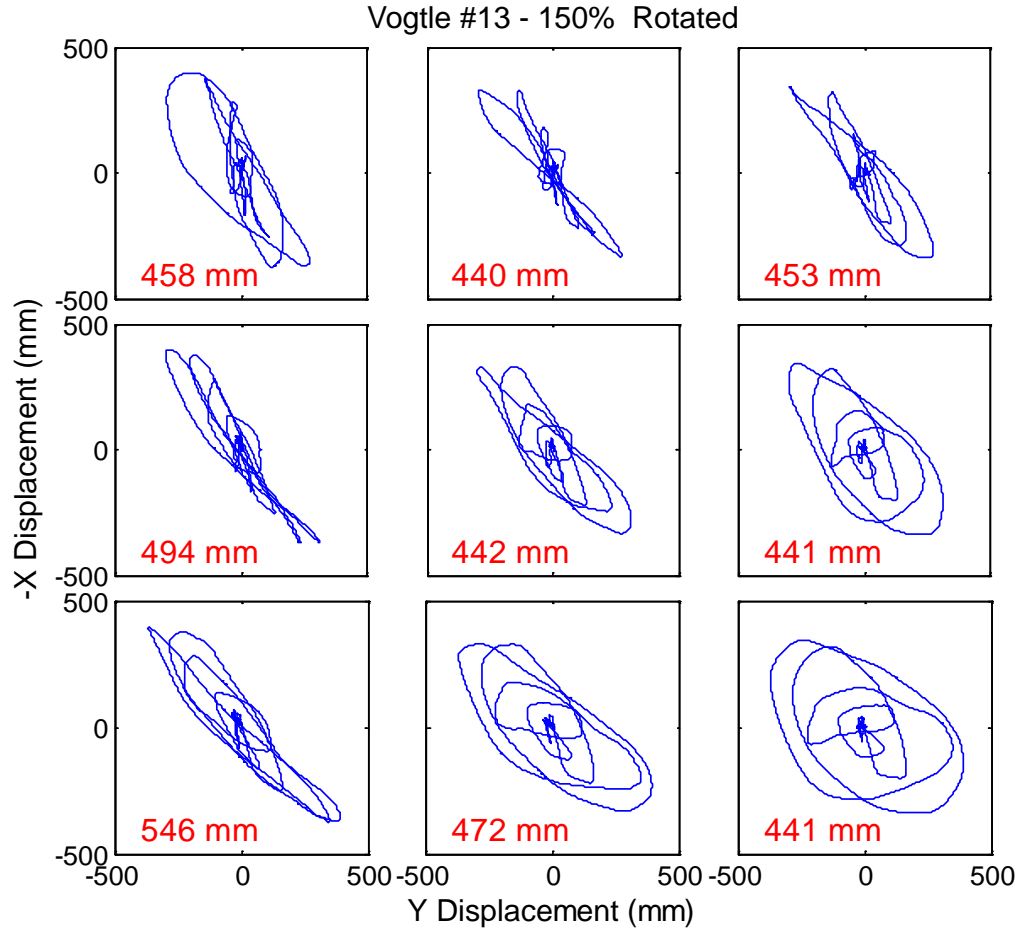


**Figure 3-16: Predicted displacement trace of each isolator for the OpenSees building model subjected to 150% Vogtle #13, with input ground excitation components rotated by 11.25 degrees.**

A similar process was used to select the input motion to represent the design ground shaking at the Diablo Canyon site, with a target scale factor of 100%. The Diablo Canyon #15 record was selected for the test program. The predicted displacement trace of the isolators for Diablo Canyon #15 scaled to 100% is shown in Figure 3-17. Rotation was not required for this input motion since the vector displacement was approximately maximized without rotation. The actual scale factor applied to Diablo Canyon #15 during testing was 95%.

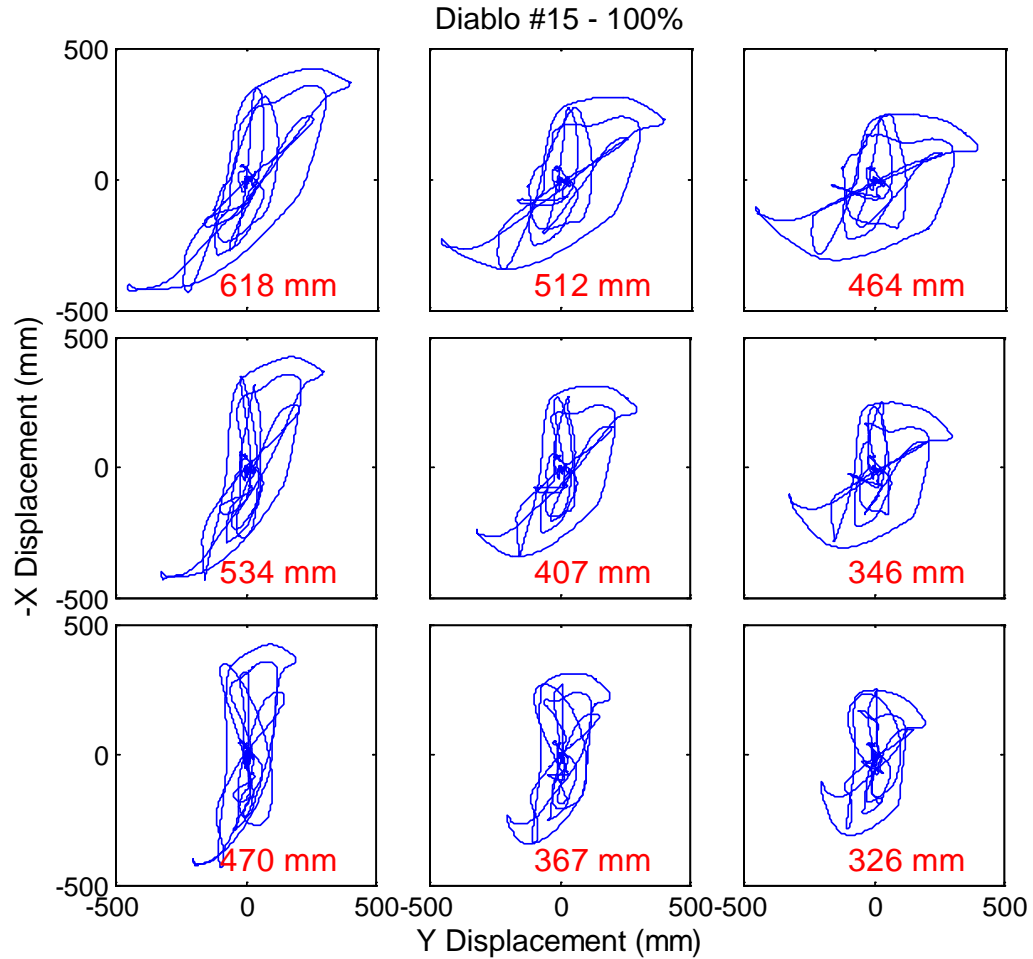


**Figure 3-17: Predicted displacement trace of each isolator for the OpenSees building model subjected to 100% Diablo Canyon #15.**

### 3.3.3 Remainder of the Test Program

As mentioned previously, the objectives of the sponsor were prioritized in the planning of the test program. These objectives were to simulate the response of LR bearings to motions representing the seismicity at a potential nuclear site, and impose design basis and extended design basis demands on the system. Once these objectives had been satisfied, objectives of other interested parties could be entertained.



For comparative purposes, the project team (United States and Japan collaborators) proposed to include in the test program 3 ground motions, one each representing a service level, design level and MCE as defined by the United States building code (ASCE 2010), that would be commonly applied to each of the three building configurations. The assumed seismic hazard associated with these events is presented in Dao and Ryan (2015). In addition, Japan side collaborators requested that a large motion recorded during a Japan earthquake be commonly applied to each of the three building configurations. The preliminary selections are shown in Table 3-6.

During the testing of the TP isolation configuration, which was chronologically first in the sequence, the response of the building was particularly affected by the strong vertical excitation of the 1994 Northridge recorded at Rinaldi Receiving Station. This excitation was not part of the planned test program for the hybrid LR isolation or fixed-base configurations. However, late modifications to the planned test program were accommodated to repeat this excitation as a 3D excitation and an XY excitation (omitting the vertical component) in each building configuration to better comprehend the response of isolated and non-isolated buildings to strong vertical excitation.

In the end, not all objectives were met due to safety considerations (see Table 3-6) and compromises were made. The imposed safety limits were numerically predicted isolator displacements  $\leq 550$  mm for the hybrid LR isolation system and numerically predicted structural drift limits  $\leq 1.2\%$  for all configurations. A suitable MCE level earthquake that met the safety limitations for the hybrid LR isolated and fixed-base configurations could not be identified, and the MCE comparison was removed from the test program. The

selected design event (El Centro) was never applied to the fixed-base configuration, and the selected Japan motion (Iwanuma) as well as Rinaldi were applied to the fixed-base building at reduced scale factors in the horizontal direction.

**Table 3-6: Common Earthquake Records Considered for Three Test Configurations**

Objective	Earthquake Record	Scale Factor	Simulation Considered Safe?		
			TP Config.	Hybrid LR Config.	Fixed-Base Config.
Service Earthquake	1987 Superstition Hills, Westmorland Sta. (3D)	80%	Yes	Yes	Yes
Design Earthquake	1940 Imperial Valley, El Centro Sta. (3D)	130%	Yes	Yes	Safety questions
MCE Earthquake	1994 Northridge, Sylmar OR 1995 Kobe, Takatori (3D)	100%	Yes	No, safety imposed displacement limit	No, safety imposed story drift limit
Japan Earthquake	2011 Tohoku Earthquake, Iwanuma (XY)	100%	Yes	Yes	No, Scaled to 70%
XY vs 3D Input Comparison	1994 Northridge, Rinaldi Rec. Sta. (XY)	88%	Yes	Yes	No, Scaled to 35%
XY vs 3D Input Comparison	1994 Northridge, Rinaldi Rec. Sta. (3D)	88%	Yes	Yes	No, Scaled to 35% (88% in vertical)

## **CHAPTER 4: EXPERIMENTAL PROGRAM**

Development of the experimental program for the three test configurations (TPB, hybrid, fixed base) was a collaborative effort between a large team of investigators in U.S. and Japan. Many aspects of the experimental setup were applicable to all three systems, and thus not developed directly by the author for the exclusive purposes of this dissertation. As such, some of the information in this chapter is an excerpt from Dao and Ryan (2015) and presented here for completeness.

### **4.1 Design of Connection Assembly**

A plan was developed and executed for securely connecting the isolation devices (both LR bearings and CL bearings) to the structure and to the earthquake simulator. As described in Chapter 3, the connection design for the hybrid LR isolation system made use of connection assemblies, each consisting of a layer of load cells sandwiched between a square or rectangular base plate and a hexagonal shaped top plate, that were designed for the TP isolation configuration. Details of the assembly design calculations and supporting finite element analysis were described in Dao and Ryan (2015). The assemblies were used at the N, S, E and W column locations to measure the forces in the LR bearings.

The connection assemblies were not used at CL bearing locations, for several reasons. First, the axial force demands on the CL bearings were expected to be high since the CL

bearings would carry all overturning induced axial forces. Second, Aseismic Design Corporation, the provider of the CL bearings, calculated that the supporting plates of the connection assembly were too flexible to prevent rotation (bending) of the bearings about the horizontal axes, and thus ensure their proper function. Although very small, the contribution of the CL bearings to the total base shear could not be measured.

Three distinctly configured load cell connection assemblies had been devised for the TP isolation configuration tests according to expected tributary weight carried by the bearings at different plan locations: one for the center column, one for the edge columns, and one for the corner columns. For the hybrid LR isolation system, the edge connection assembly were used for three of the four bearings. However, the center connection assembly was substituted at the East edge location, because erratic measurements were observed in the assembly used at that location in the prior TP configuration tests.

The plan drawings of the two connection assemblies utilized for the hybrid LR configuration are shown in Figure 4-1, and a photograph of a constructed assembly is shown in Figure 4-2. The center column assembly placed 3 Type A load cells on a circle 350 mm (13.8 in) from the center of both plates and 6 Type B load cells on a circle 900 mm (35.4 in) from the center of both plates, both with equal angular spacing. The edge column assemblies placed 1 Type A load cell at the center of both plates, and 6 Type B load cells on a circle 750 mm (29.5 in) from the center of both plates with equal angular spacing. The Type A and Type B load cells differed in their capacities as listed in Table 4-1. Drawings of the load cells are shown in Figure 4-3, which indicate the bolt pattern for the top and bottom rings and the elevation. The connection plates were produced by

milling a steel plate with thickness = 102 mm (4 in) down to 95 mm (3.7 in), which leveled the surface. Because the two types of load cells differed in height, the thickness of each bottom connection plate was milled down to 91 mm (3.6 in) at Type A locations and 76 mm (3.0 in) at Type B locations (see Figure 4-4). The load cells were installed upside down between the top and bottom connection plates. The complete set of drawings for connection the load cell assemblies, LR bearings and testbed building to the simulator platform are given in Appendix C.

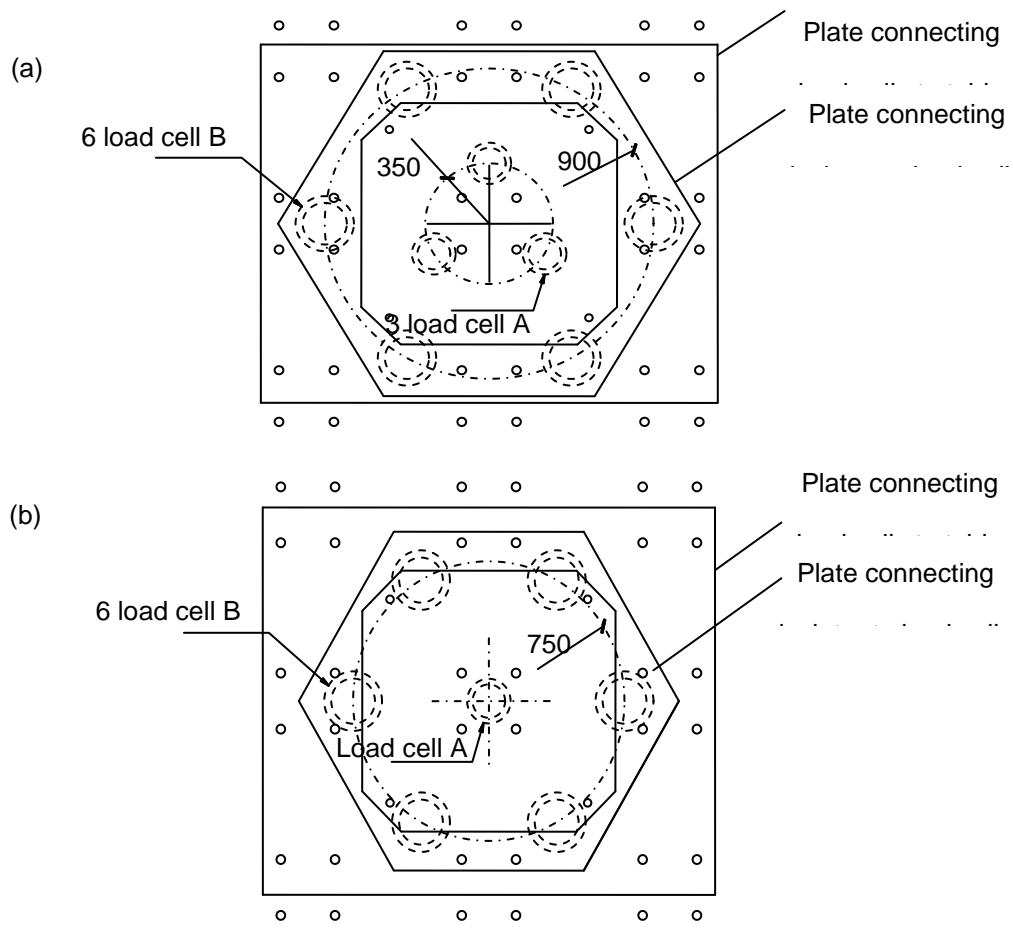


**Figure 4-1: Load cell connection assemblies used for: (a) East bearing and (b) North, South and West bearings.**

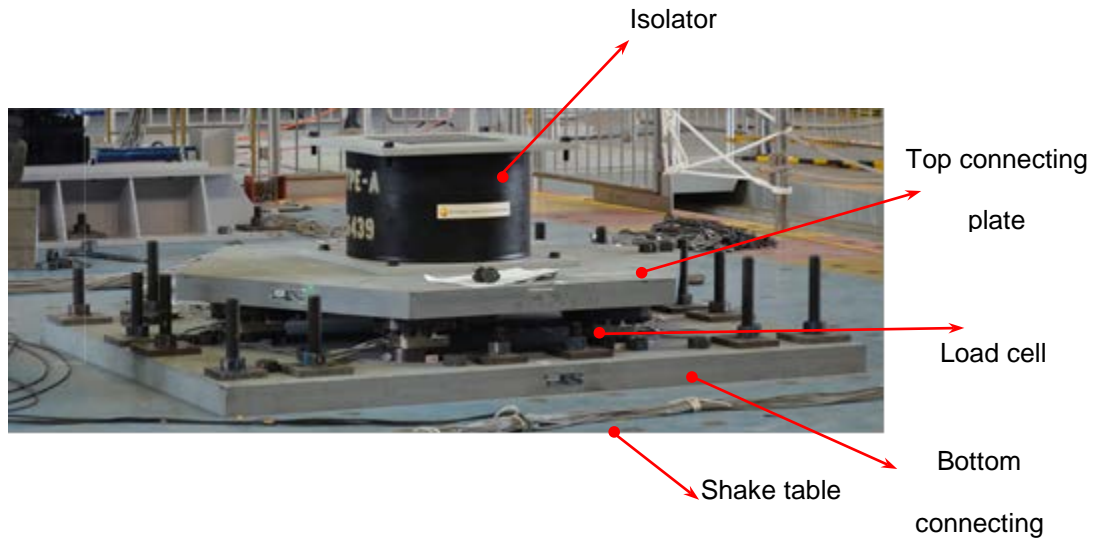


**Figure 4-2: Connection assembly**

**Table 4-1: Properties of Load Cells**

Type	Number (units)	Height (mm)	Vertical capacity (kN)	Horizontal capacity (kN)	Vertical stiffness (kN/mm)	Horizontal stiffness (kN/mm)
A	44	180	400	250	8500	2400
B	32	195	700	400	14000	3500

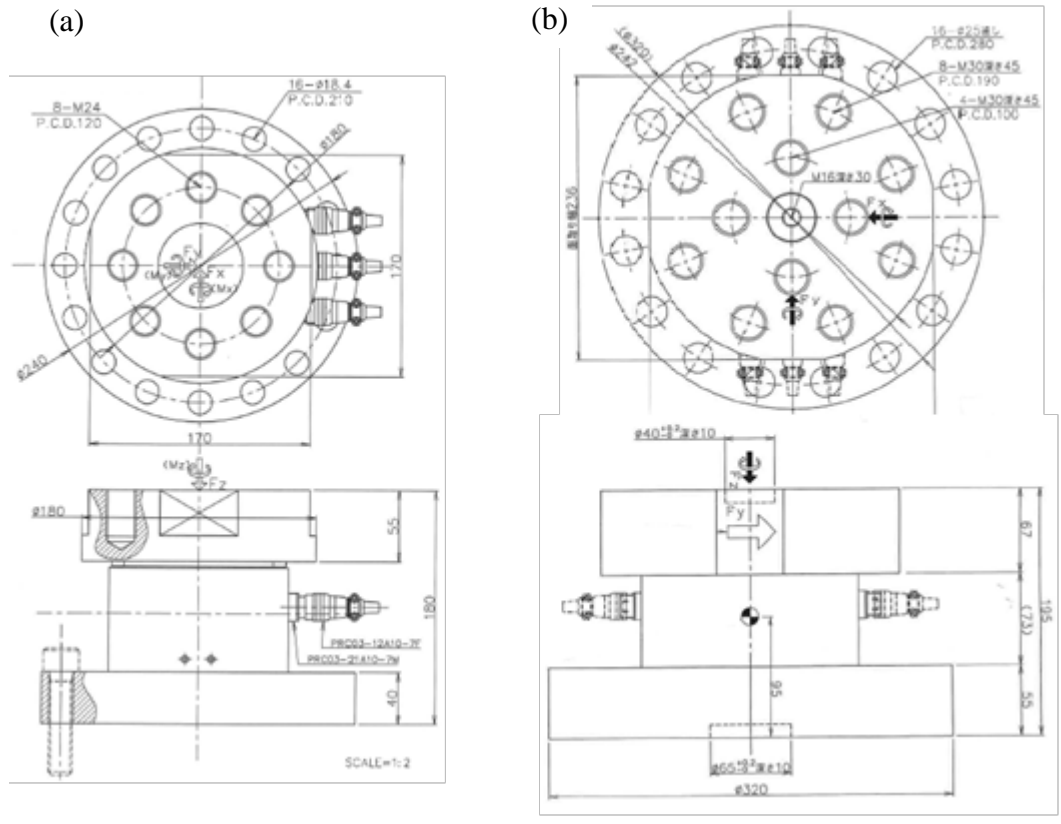


Figure 4-3: Load cell drawings with bolt patterns and elevation views: (a) Type A and (b) Type B

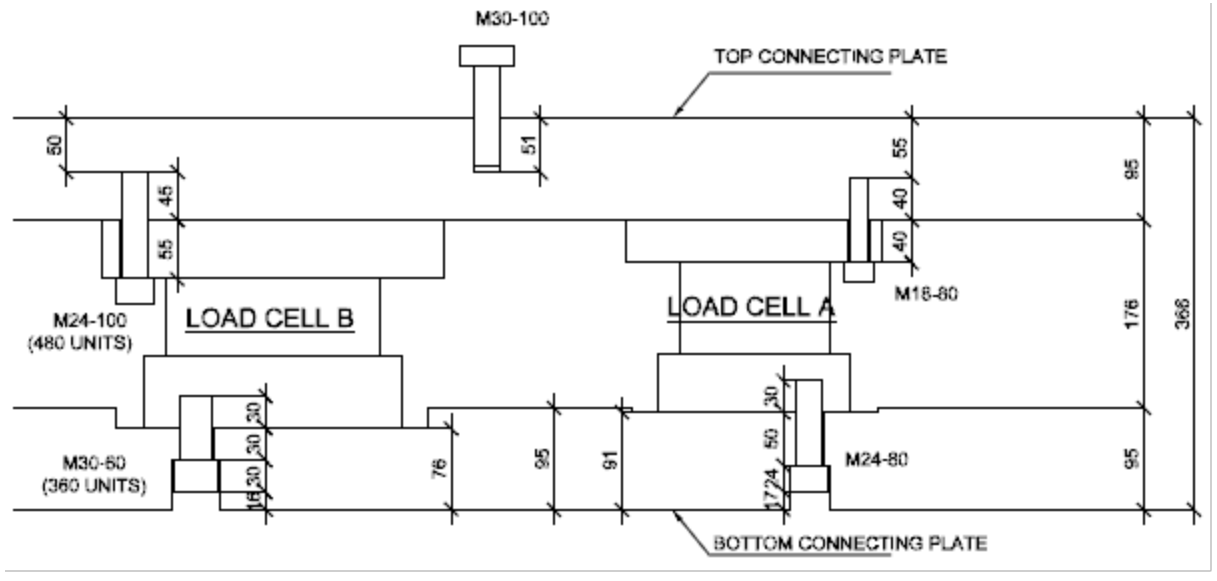


Figure 4-4: Connection of Type A and Type B load cells to top and bottom connection plates

## 4.2 Instrumentation

Approximately 470 channels were used for measuring the responses of structural and nonstructural components in the building with the hybrid LR isolation system. The sampling frequency of all channels was 1000 Hz. The results included in this dissertation were based on measurements from the following three types of sensors:

- Sensors for measuring force: load cells (90 channels)
- Sensors for measuring displacement: displacement transducers (26 channels)
- Sensors for measuring acceleration: accelerometers (100 channels)

The following describes the details of each sensor type.

Unless otherwise mentioned, all recorded data of the structural responses presented in the dissertation was filtered using a Low-Pass Butterworth filter with a cut off frequency of 50 Hz. The filter shape as a function of normalized frequency is shown in Figure 4-5. The low pass filter “filtered out” or eliminated the high frequency components of the signal while preserving lower frequency components, including the dominant isolation frequency. The shape of the Butterworth filter provides a smooth transition from filtered to preserved frequencies. The cutoff frequency of 50 Hz was selected to eliminate noise that would not affect structural or equipment response and performance.



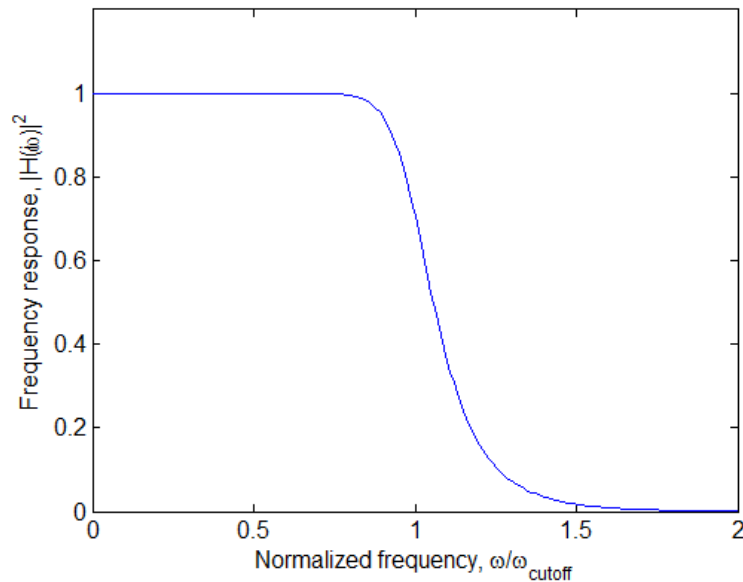


**Figure 4-5: Magnitude of low-pass Butterworth Filter transfer function**

#### 4.2.1 Load Cells

Triaxial load cells were used to measure the forces in the LR bearings in all three directions. Figure 4-6 illustrates the load cell channels for each of the North, South, East and West bearings. The East bearing used a configuration of 9 load cells while the other bearings used only 7 load cells.

#### 4.2.2 Displacement Transducers

Displacement transducers were used to measure the displacement of the isolation system and story drift. Figure 4-7 shows the layout of displacement transducers (wire pots) at base level for measuring the displacement of the isolation system. Three wire pots each were installed at the column bases at the North side and East side to measure the displacement in the x and y-directions, respectively. Three transducers were required to

uniquely determine the translation and rotation of the isolation system and three additional channels were included for redundancy.

Laser-based transducers were used to measure story drift. Each sensor was attached to a vertical instrumentation frame and its reflecting plate was attached to the floor above as shown in Figure 4-8. A pair of transducers measured the relative displacement between the two floors in each direction at 2 locations (Figure 4-9). Assuming a rigid floor diaphragm, 3 unique displacement transducers were needed for determining relative displacement between the adjacent floors. An additional displacement transducer was added in each story for redundancy. The layout of the 4 displacement transducers in the 2<sup>nd</sup> to 5<sup>th</sup> story is shown Figure 4-9. In the 1st story, the 4 displacement transducers were installed at the SE and NW columns.

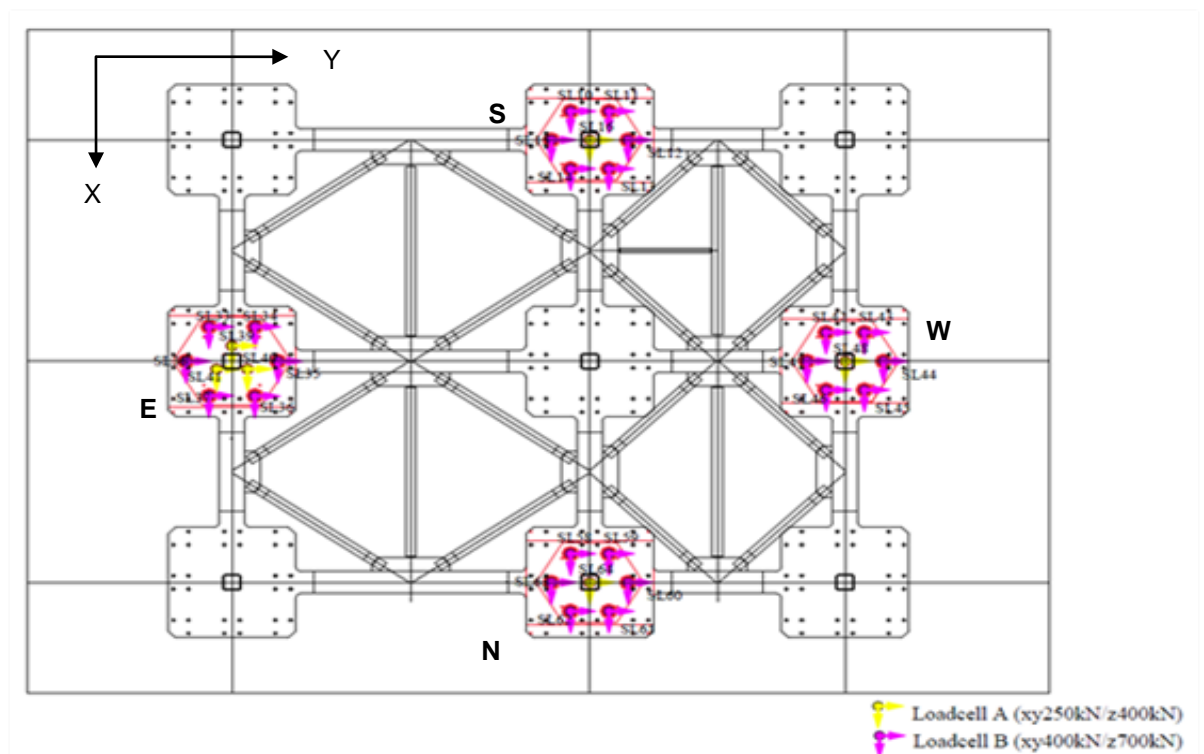


**Figure 4-6: Load cell channels for the hybrid LR isolation configuration**

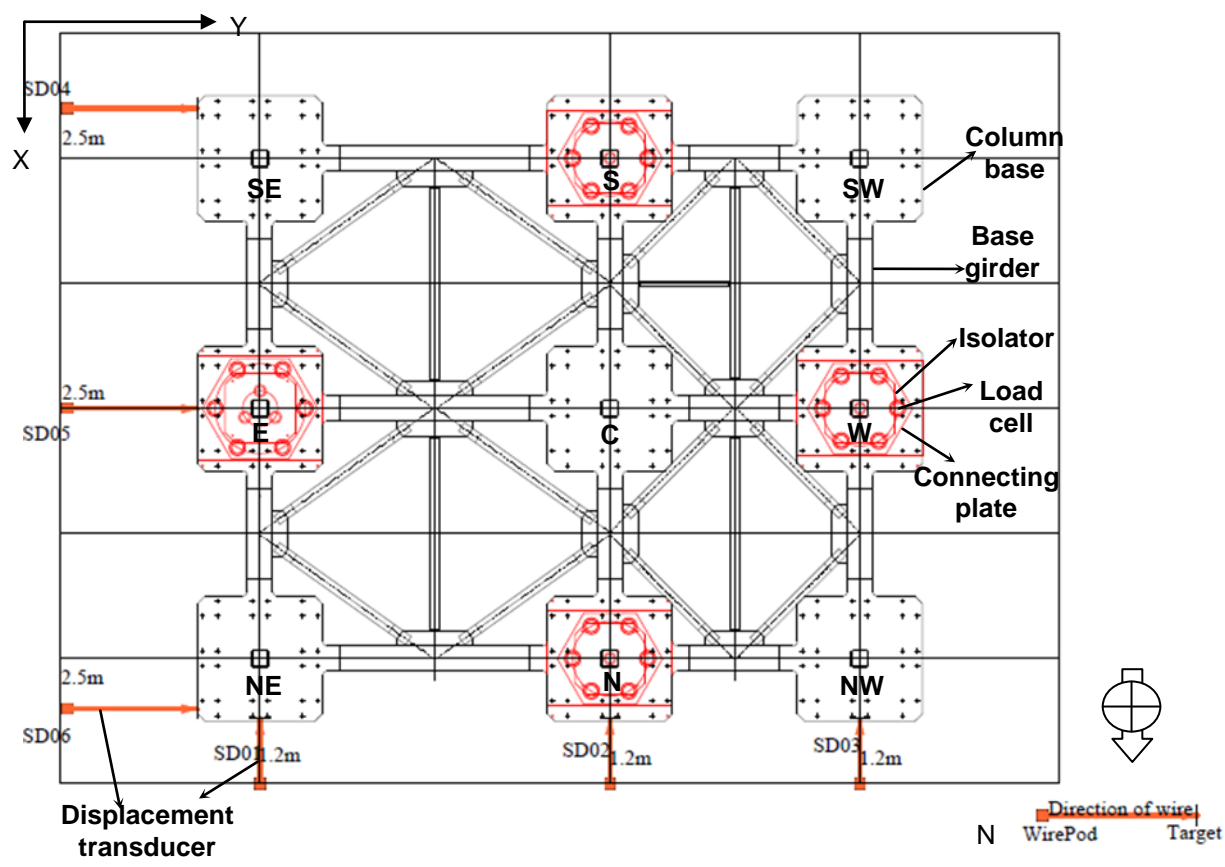
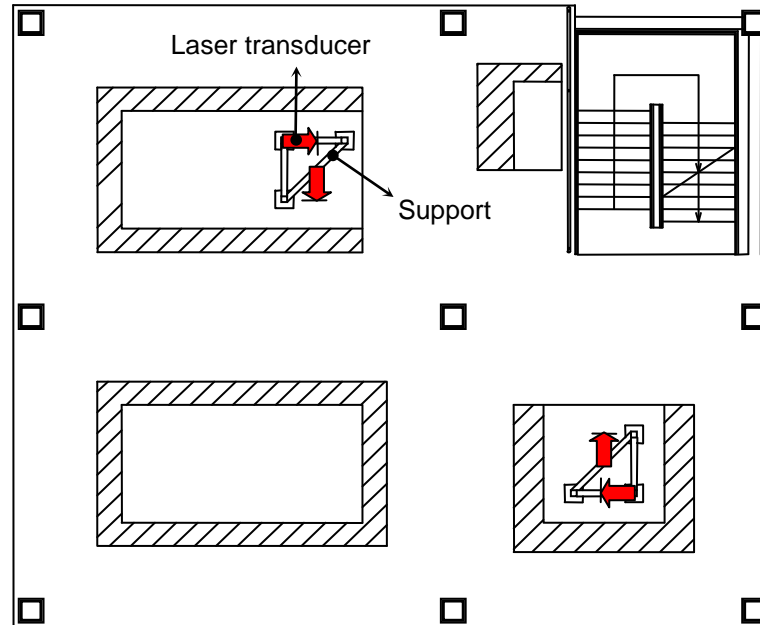


Figure 4-7: Layout of displacement transducers at base



Figure 4-8: Instrumentation for measuring story drift



**Figure 4-9:** Layout of displacement transducers to measure story drift in 2<sup>nd</sup> to 5<sup>th</sup> stories

### 4.2.3 Accelerometers

Three triaxial accelerometers were installed to measure the 3 components of acceleration at the 4 corners of the earthquake simulator platform. Accelerations at the center of the platform were also measured by permanent sensors integrated into the simulator control system. The measured acceleration at the center of the table included all 6 six components (3 translational components and 3 rotational components) of motion.

Two uniaxial accelerometers were also installed on the top plates of the connection assemblies (Section 4.1) to measure the horizontal acceleration of the plates (Figure 4-10). The recorded acceleration is used to derive the bearing forces. The load cells described in Section 4.2.1 did not measure the isolator force but rather the force just beneath the top connection plate. These forces differed by the inertia force associated

with the top connection plate and the bottom half of the isolator. Since the total mass separating these two locations was large (about 4 tons) depending on location and the expected acceleration was also large (approximately equal to the input acceleration, about 1 g), the inertia force, which was significant compared to the isolator force, was accounted for.

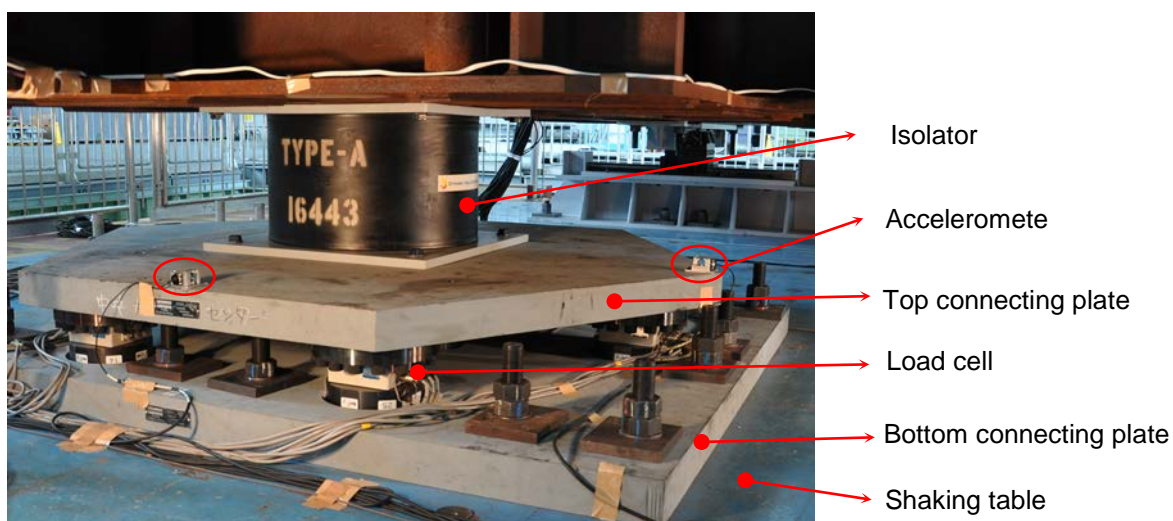


**Figure 4-10: Accelerometers at the top connection plates to estimate inertia forces**

Floor accelerations (2 horizontal and vertical components) were measured using 3 triaxial accelerometers installed at the SE, NE and NW corners of every floor. These triaxial accelerometers were attached to the column face just above the floor slab. Vertical accelerations at other locations on the floor slab were also recorded. Figure 4-11 shows the layout of accelerometers on the 5<sup>th</sup> floor, which was a typical layout for all floors. The vertical accelerometers were attached to the bottoms of the slabs.

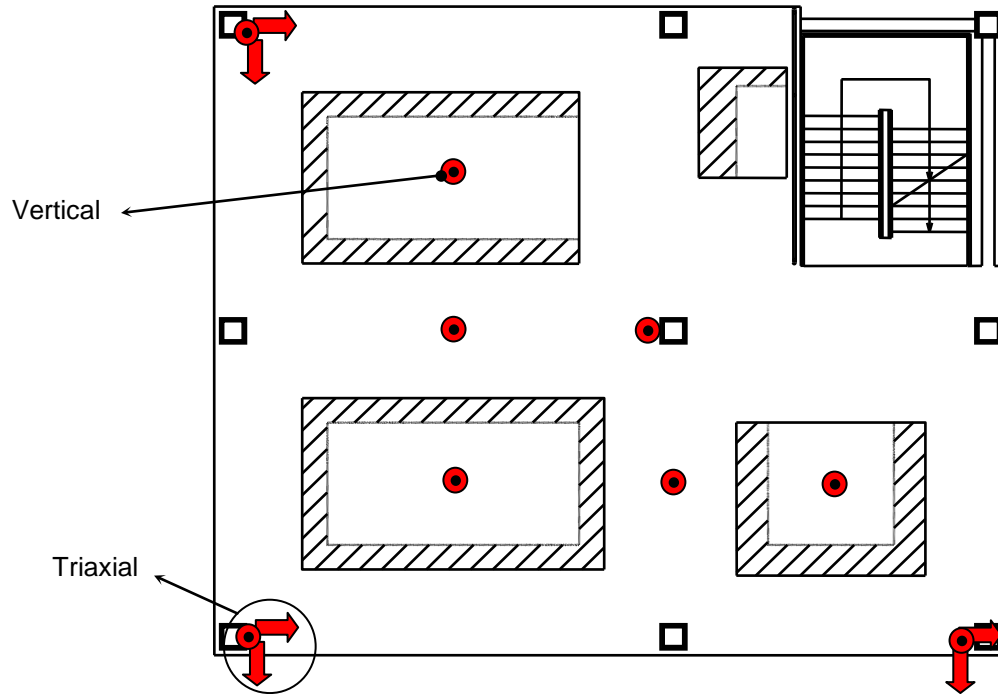


**Figure 4-11: Layout of accelerometers at the 5<sup>th</sup> floor**

### 4.3 Installation of the Specimen on the Earthquake Simulator

The connection assemblies were put together using the following process. Holes were drilled and tapped in the steel connection plates as needed. The load cells were first bolted to the top hexagonal shaped plate of the connection assembly (Figure 4-2). The bottom plate was then added to the assembly (Figure 4-12). The connection assemblies were then turned over and bolted to the earthquake simulator platform using 48 mm (1.9 in) diameter threaded rods (see Figure 4-13). The installation of the testbed building with the hybrid LR isolation system, immediately followed testing and removal of the TP isolation system. After removal of the TP bearings and rearrangement of the connection assemblies, the LR bearings were bolted to the connection assemblies while CL bearings were bolted directly to the simulator platform (Figure 4-14). The building was then

transported across the laboratory using two 400-ton-cranes and lowered over the isolation system (Figure 4-15).

The testbed building was connected to the isolation system through bolt holes in the column bases that had been drilled and tapped from below (Figure 4-16). Drilling and tapping these holes in the overhead position was a laborious and expensive process (Figure 4-17). As such, measures were taken to limit the number and size of connecting bolts. Four M24 bolts were used to connect each LR bearing to the structure above and the connecting plates below. These bolts were attached through 30 mm (1.2 in) oversized holes in the top connecting plates and 33 mm (1.3 in) oversized holes in the bottom connecting plate. The oversized holes were used to help align the testbed building with the isolators.



**Figure 4-12: Connection assembly**



**Figure 4-13: Connection assemblies on the simulator platform**



**Figure 4-14: Installing the LR bearings to the connecting assemblies and the CL bearings to the simulator platform**





**Figure 4-15: Lowering the testbed building over the isolation system**

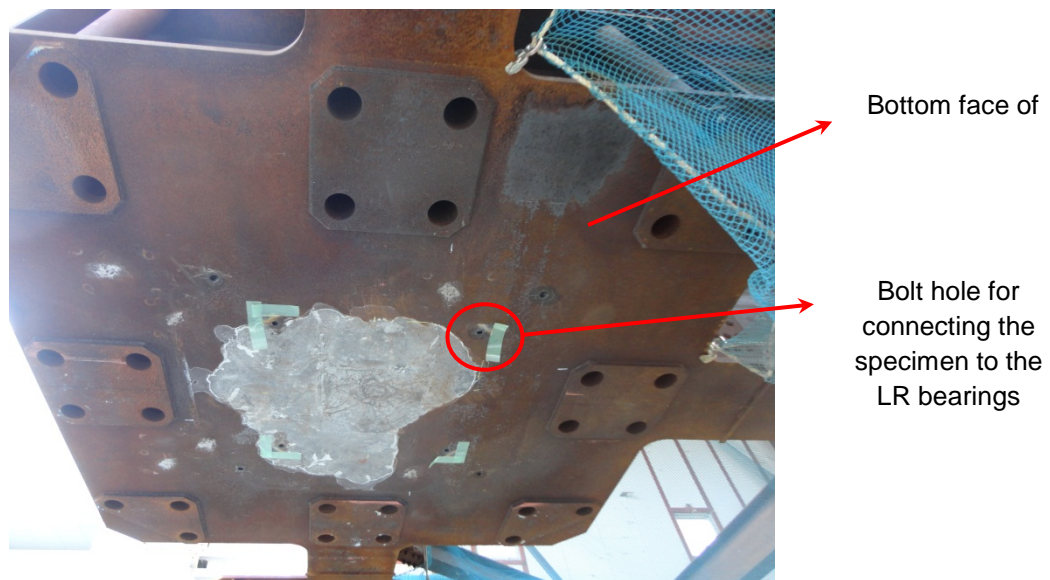


**Figure 4-16: Bolt holes for connecting the testbed structure to the isolation system**



**Figure 4-17: Drilling and tapping holes at the bottom of the specimen**

The measured weight of the building (excluding the isolators) was 5220 kN (1173 kip). This weight was determined during the testing of the TP isolation configuration, as described in Dao and Ryan (2015), since static forces were measured in every bearing. The measured weight of the testbed was about 17% greater than the 4540 kN (1020 kips) anticipated in the design (Section 3.2). The change in weight affected the realized stiffness and strength of the isolation system. However, since the properties of the LR bearings are highly amplitude dependent (see Section 8.4), the influence of this change in supported weight was not explored in detail.

The static vertical load on an isolator is expected to be proportional to the mass of the tributary area. This condition could have been obtained if the testbed had been erected directly on the isolation system (similar to the expected construction process). However, the testbed had been built and stored outside for more than 2 years before testing so that its base was warped and the distribution of vertical load on all isolators deviated from the calculated values. Table 4-2 shows the measured vertical load on each LR bearing after

the building was bolted to the isolation system and the expected vertical load on the isolators based on the pre-test simulation model. The expected vertical load on each isolator was scaled by 1.17 compared to the values reported earlier (Figure 3-7) to adjust for the actual weight (=5220 kN or 1174 kips) of the testbed. The table shows that most of the LR bearings were carrying less gravity load than expected based on tributary area. The static load in the West bearing was very small at 235 kN (53 kip). Steel shims were installed to achieve a distribution of gravity load similar to that assumed for design, with limited success.

**Table 4-2: Vertical Load on Each Bearing After Installation**

Bearing	E	S	N	W	Percent of Total
Actual load (kN)	435	755	490	235	37%
Expected load (kN) <sup>(*)</sup>	749	708	725	468	51%
Difference (%)	-41.9	6.6	-32.4	-49.9	

<sup>(\*)</sup> The expected load was linearly scaled such that the total vertical load matches the measured load

#### 4.4 Test Schedule

The test schedule included 3 days of shaking (21 simulations) for the TP isolation configuration, 2 days of shaking (15 simulations) for the hybrid LR configuration, and 1 day of shaking (5 simulations along with white noise and sine sweep) for the fixed-base configuration. Dao and Ryan (2015) discussed the selection of the ground motions for the TP configuration, while Chapter 3 described the selection of ground motions for the

hybrid LR configuration. Since only a minimal number of simulations could be included for the fixed-base configuration, motions were selected that would allow a broad comparison between the three different configurations, and to provide insight into the influence of vertical excitation (Ryan et al., 2013a).

Although the majority of the inputs were 3D, some of the earthquake motions were applied as horizontal (XY) only, which enables a study of the effect of vertical excitation. Other reasons for not including the vertical component of excitation for some simulations included: 1) lack of access to the vertical record, 2) the capacity of the earthquake simulator limited the application of all 3 components at full scale, and 3) test-day decisions to limit damage to nonstructural components.

For the isolation configurations, the floors containing nonstructural components and contents were inspected only at the end of the test day, with one exception. On the first test day (TP isolation configuration), nonstructural components and contents were inspected after Rinaldi 88%, which generated some unexpected ceiling damage and disruption to contents. The shaking of the fixed-base building, completed in 1 day, included 5 earthquake excitations. For the fixed-base configuration only, nonstructural components were inspected and partially repaired after every simulation, thus 3D white noise excitation preceded and followed every earthquake simulation for system identification before and after the repairs. Unidirectional white noise excitations were also applied at the beginning and end of the day. Damage to nonstructural components and content disruption was observed in all system configurations under large intensity vertical excitation, and the damage was similar in all configurations. The nature of the

damage is not discussed in this dissertation. Further information about the response of the nonstructural components is provided in Soroushian et al. (2012).

For completeness, the simulation schedule for all three building configurations is listed in Tables 4-3 to 4-5. In Tables 4-3 and 4-4, the shaded simulations are 3D excitations and the rest are XY simulations. Color coded groups of simulations represent the same input at different scale factors; for instance, red = the Vogtle suite of motions in Table 4-4. In the shaking schedule for the fixed-base building (Table 4-5), the earthquake simulations are shaded and the motion in red use the same input with different scale factors. The scale factor represents the percentage of the original recorded motion or simulation that was applied in each direction. The nomenclature introduced in Table 4-4 (simulation abbreviation) is used throughout the dissertation to refer to different simulations in the hybrid LR system. The abbreviation consists of the first three letters of the station name with the scale factor. If the input excitation is not 3D, then “(XY)” is added for bidirectional horizontal input and “(Y)” is added for unidirectional input in the y-direction. If the simulation is repeated with the same input, the repetitions are labeled “-1” and “-2”. Thus, “SIN100(Y)-1” reflects the first repetition of a sine wave input scaled to 100% and the input is unidirectional in the y-direction; “VOG150” reflects the Vogtle record scaled to 150% and the input is 3D.

**Table 4-3: Simulation Schedule for the TP Isolation Configuration**

Date dd/mm/yy)	Time	Duration (sec)	Simulation abbreviation	Motion	Scale factor			Damage inspectic
					X	Y	Z	
17/08/11	12:01	41	SIN65(X)	Sine-wave	0.65	0	0	
	12:40	41	SIN100(X)	Sine-wave	1.00	0	0	
	13:42	41	WSM80	Superstition Hills, Westmorland,	0.80	0.80	0.80	
	14:30	41	ELC130	Imperial Valley, El Centro	1.30	1.30	1.30	
	15:20	20	RRS88	Northridge, Rinaldi Rec. Sta.	0.88	0.88	0.88	Yes
	17:16	41	SYL100	Northridge, Sylmar	1.00	1.00	1.00	
	17:49	41	TAB50	Tabas, Tabas Sta.	0.50	0.50	0.50	Yes
18/08/11	11:36	41	LGP70	Loma Prieta Los Gatos Pres. Ctr.	0.70	0.70	0.70	
	12:26	82	TCU50(XY)	ChiChi, TCU065	0.50	0.50	0	
	13:56	82	TCU70(XY)	ChiChi, TCU065	0.70	0.70	0	
	14:32	196	IWA100(XY)	Tohoku, Iwanuma	1.00	1.00	0	
	15:46	327	SAN100(XY)	Sannomaru	1.00	1.00	0	
	16:35	41	TAK100	Kobe, JMA Takatori	1.00	1.00	1.00	
	17:05	41	KJM100	Kobe, Kobe JMA	1.00	1.00	1.00	Yes
19/08/11	11:30	21	RRS88(XY)	Northridge, Rinaldi Rec. Sta.	0.88	0.88	0	
	12:17	82	TCU80(XY)	ChiChi, TCU065	0.80	0.80	0	
	13:08	41	TAB80	Tabas, Tabas Sta.	0.80	0.80	0.80	
	14:02	41	TAB90(XY)	Tabas, Tabas Sta.	0.90	0.90	0	
	14:51	41	TAB100(XY)	Tabas, Tabas Sta.	1.00	1.00	0	
	15:28	82	SCT100(XY)	Michoacan, SCT	1.00	1.00	0	
	16:19	41	TAK115	Kobe, JMA Takatori	1.15	1.15	1.00	Yes

**Table 4-4: Simulation Schedule for the Hybrid LR Isolation Configuration**

Date (dd/mm/yy)	Time	Duration (sec)	Simulation abbreviation	Motion	Scale factor			Damage inspection
					X	Y	Z	
25/08/11	11:20	41	WSM80	Superstition Hills, Westmorland	0.80	0.80	0.80	
	12:22	21	SIN100(Y)-1	Sine-wave	0	1.00	0	
	13:06	41	VOG75-1	Vogtle #13	0.75	0.75	0.75	
	13:56	41	VOG100	Vogtle #13	1.00	1.00	1.00	
	14:34	41	VOG125	Vogtle #13	1.25	1.25	1.25	
	15:15	41	VOG150	Vogtle #13	1.50	1.50	1.50	
	16:18	41	VOG175	Vogtle #13	1.75	1.75	1.75	
	16:53	41	DIA80	Diablo #15	0.80	0.80	0.80	Yes
26/08/11	12:03	41	DIA95(XY)	Diablo #15	0.95	0.95	0	
	12:49	41	ELC130	Imperial Valley, El Centro	1.30	1.30	1.30	
	13:45	196	IWA100(XY)	Tohoku, Iwanuma	1.00	1.00	0	
	14:38	21	RRS88(XY)	Northridge Rinaldi Rec. Sta.	0.88	0.88	0	
	15:21	21	RRS88	Northridge Rinaldi Rec. Sta.	0.88	0.88	0.88	
	16:15	41	VOG75-2	Vogtle #13	0.75	0.75	0.75	
	16:59	21	SIN100(Y)-2	Sine-wave	0	1.00	0	Yes

**Table 4-5: Simulation Schedule for the Fixed-base Building**

Date dd/mm/yy)	Time	Duration (sec)	Simulation abbreviation	Motion	Scale factor			Damage inspection
					X	Y	Z	
31/08/11	10:20	40	WHT100(X)-1	White noise	1.00	0	0	
	10:30	40	WHT100(Y)-1	White noise	0	1.00	1.00	
	10:39	40	WHT100(Z)-1	White noise	1.00	1.00	1.00	
	10:51	41	WSM80	Superstition Hills, Westmorland	0.80	0.80	0.80	
	11:03	40	WHT100-1	White noise	1.00	1.00	1.00	Yes
	12:07	40	WHT100-2	White noise	1.00	1.00	1.00	
	12:19	21	RRS35(XY)	Northridge, Rinaldi Rec. Sta.	0.35	0.35	0	
	12:28	40	WHT100-3	White noise	1.00	1.00	1.00	Yes
	13:38	40	WHT100-4	White noise	1.00	1.00	1.00	
	13:51	21	RRS35	Northridge, Rinaldi Rec. Sta.	0.35	0.35	0.35	
	14:03	40	WHT100-5	White noise	1.00	1.00	1.00	Yes
	15:13	40	WHT100-6	White noise	1.00	1.00	1.00	
	15:25	21	RRS35(XY)88(Z)	Northridge, Rinaldi Rec. Sta.	0.35	0.35	0.88	
	15:34	40	WHT100-7	White noise	1.00	1.00	1.00	Yes
	17:07	40	WHT100-8	White noise	1.00	1.00	1.00	
	17:23	196	IWA70(XY)	Tohoku, Iwanuma	0.70	0.70	0	
	17:35	40	WHT100(X)-2	White noise	1.00	0	0	
	17:43:12		WHT100(Y)-2	White noise	0	1.00	0	
17:52:47		WHT100(Z)-2	White noise	1.00	1.00	1.00	Yes	



## 4.5 Table Motions

The peak accelerations of the target motions and the actual motions generated by the earthquake simulator are compared in Tables 4-6 and 4-7. The target records were obtained from various sources such as the PEER NGA database (Chiou et al. 2008), Huang et al. (2009), and sources within E-Defense; and scaled by the scaled factors given in Tables 4-3 to 4-5. The realized input motions to the structure were generally amplified by the earthquake simulator relative to the target motions, and amplification factors of 50% were not uncommon. Amplification occurred because the recommended iterative response modification technique, which involves gradually increasing the intensity of the motions while making modifications to the control settings, was not used in favor of performing more simulations with a wider variety of earthquakes. However, it was observed that the ground motion excitations were replicated consistently when repeated for the different system configurations.

Amplification was notable during the Northridge-Rinaldi (RRS88) simulation due to its effect on the vertical response of the system. The motion was reproduced similarly for all three building configurations. The acceleration histories of the 3 components of this motion for the hybrid LR configuration are plotted in Figure 4-18. The horizontal amplification occurred at the instant of the large horizontal pulse in the record and the vertical acceleration was amplified at the same instant. Thus, the realized intensity of the Rinaldi motion was much stronger than the intended design level earthquake, and in particular the vertical component of excitation might be considered extreme. On the other hand, motions with similar vertical intensity can be found in the PEER NGA database

(Chiou et al. 2008). Note that the realized intensity of vertical excitation in RRS88(XY) was non-negligible (vertical peak ground acceleration or PGA = 0.05g for the hybrid LR configuration and 0.10g for TP configuration).

The 5% damped response spectra are compared for the target motions and the realized input motions. The ratio between these spectra at periods ranging from 0.01 sec to 5 sec is plotted in Figures 4-19 and 4-20. At periods longer than 0.7 sec, the spectral amplitudes of the realized motions did not differ much from the target motions. At periods less than 0.7 sec, the spectral amplitude of the realized motions in the horizontal direction was generally larger than that of the target motions. The isolation system is controlled by the post-yield properties of the bearings, so that the isolator displacement demands would not be significantly affected by the difference between the realized motions and the target motions. However, the contribution of higher mode effects to structural accelerations may have been amplified in the simulations compared to typical ground motions. The earthquake simulator appeared to amplify the horizontal period components at around 0.2 sec more strongly than components at neighboring periods.

**Table 4-6: Peak Acceleration of Target and Realized Motions for the TP Isolation Configuration**

	Trial	Peak $a_x$ ( $g$ )		Peak $a_y$ ( $g$ )		Peak $a_z$ ( $g$ )	
		Target	Table	Target	Table	Target	Table
TP Configuration	80WSM	0.171	0.169	0.135	0.147	0.174	0.140
	130ELC	0.278	0.293	0.408	0.484	0.263	0.261
	88RRS	0.427	0.586	0.730	1.213	0.722	1.241
	100SYL	0.601	0.674	0.869	1.145	0.519	0.543
	50TAB	0.450	0.585	0.418	0.463	0.327	0.357
	70LGP	0.415	0.445	0.391	0.628	0.641	0.687
	50TCU	0.408	0.453	0.304	0.278	0.000	0.015
	70TCU	0.571	0.648	0.425	0.378	0.000	0.027
	100IWA	0.364	0.409	0.418	0.580	0.000	0.031
	100SAN	0.190	0.231	0.167	0.161	0.000	0.020
	100TAK	0.747	0.789	0.619	0.922	0.288	0.259
	100KJM	0.595	0.680	0.822	0.893	0.340	0.408
	88RRSXY	0.427	0.532	0.730	1.194	0.000	0.098
	80TCU	0.653	0.747	0.486	0.418	0.000	0.034
	80TAB	0.720	0.870	0.670	0.836	0.523	0.593
	90TAB	0.810	0.930	0.753	1.011	0.000	0.102
	100TAB	0.901	0.995	0.837	1.139	0.000	0.120
	100SCT	0.171	0.177	0.101	0.106	0.000	0.017
	115TAK	0.859	0.936	0.712	1.088	0.288	0.278

**Table 4-7: Peak Acceleration of Target and Realized Motions for Hybrid LR Isolation and Fixed-base Configurations**

	Trial	Peak $a_x$ (g)		Peak $a_y$ (g)		Peak $a_z$ (g)	
		Target	Table	Target	Table	Target	Table
Hybrid Configuration	WSM80	0.170	0.195	0.138	0.150	0.209	0.145
	VOG75-1	0.329	0.391	0.213	0.259	0.215	0.214
	VOG100	0.438	0.521	0.284	0.346	0.286	0.297
	VOG125	0.548	0.687	0.355	0.451	0.358	0.368
	VOG150	0.657	0.857	0.426	0.549	0.429	0.437
	VOG175	0.767	1.025	0.497	0.639	0.501	0.493
	DIA80	0.783	0.917	0.543	0.662	0.455	0.452
	DIA95(XY)	0.930	1.118	0.645	0.808	0.000	0.063
	ELC130	0.278	0.300	0.406	0.497	0.259	0.277
	IWA100(XY)	0.363	0.429	0.420	0.590	0.000	0.021
	RRS88(XY)	0.430	0.524	0.733	1.180	0.000	0.051
	RRS88	0.430	0.521	0.733	1.193	0.738	1.257
	VOG75	0.329	0.393	0.213	0.246	0.215	0.220
Fixed-base configuration	80WSM	0.171	0.219	0.135	0.175	0.174	0.136
	35RRSXY	0.170	0.201	0.290	0.398	0.000	0.011
	35RRS	0.170	0.201	0.290	0.406	0.287	0.350
	88RRS	0.170	0.228	0.290	0.409	0.722	1.062
	70IWA	0.255	0.270	0.292	0.373	0.000	0.013

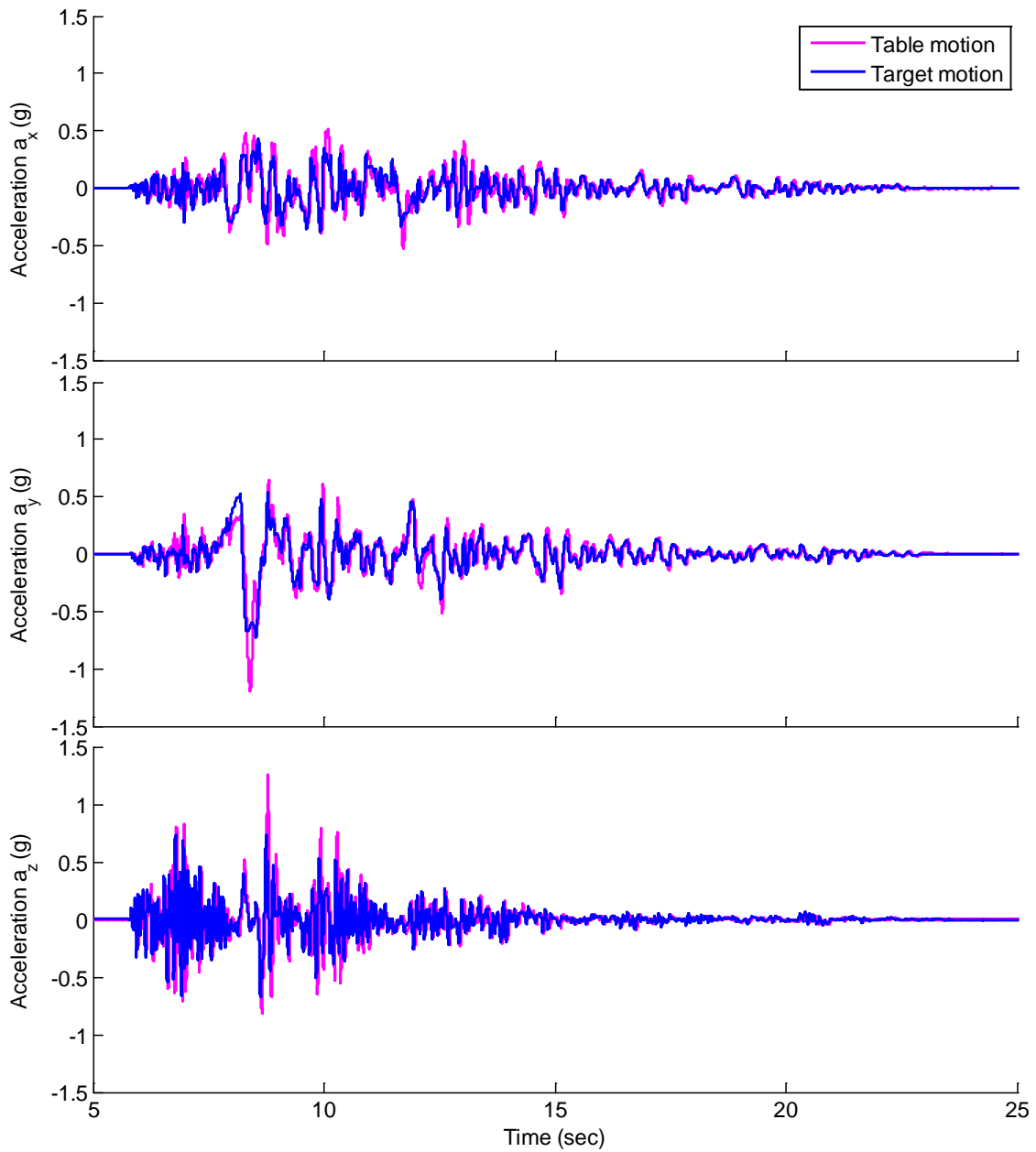


**Figure 4-18: Acceleration history of target and realized RRS88 motion in the hybrid LR isolation configuration test**

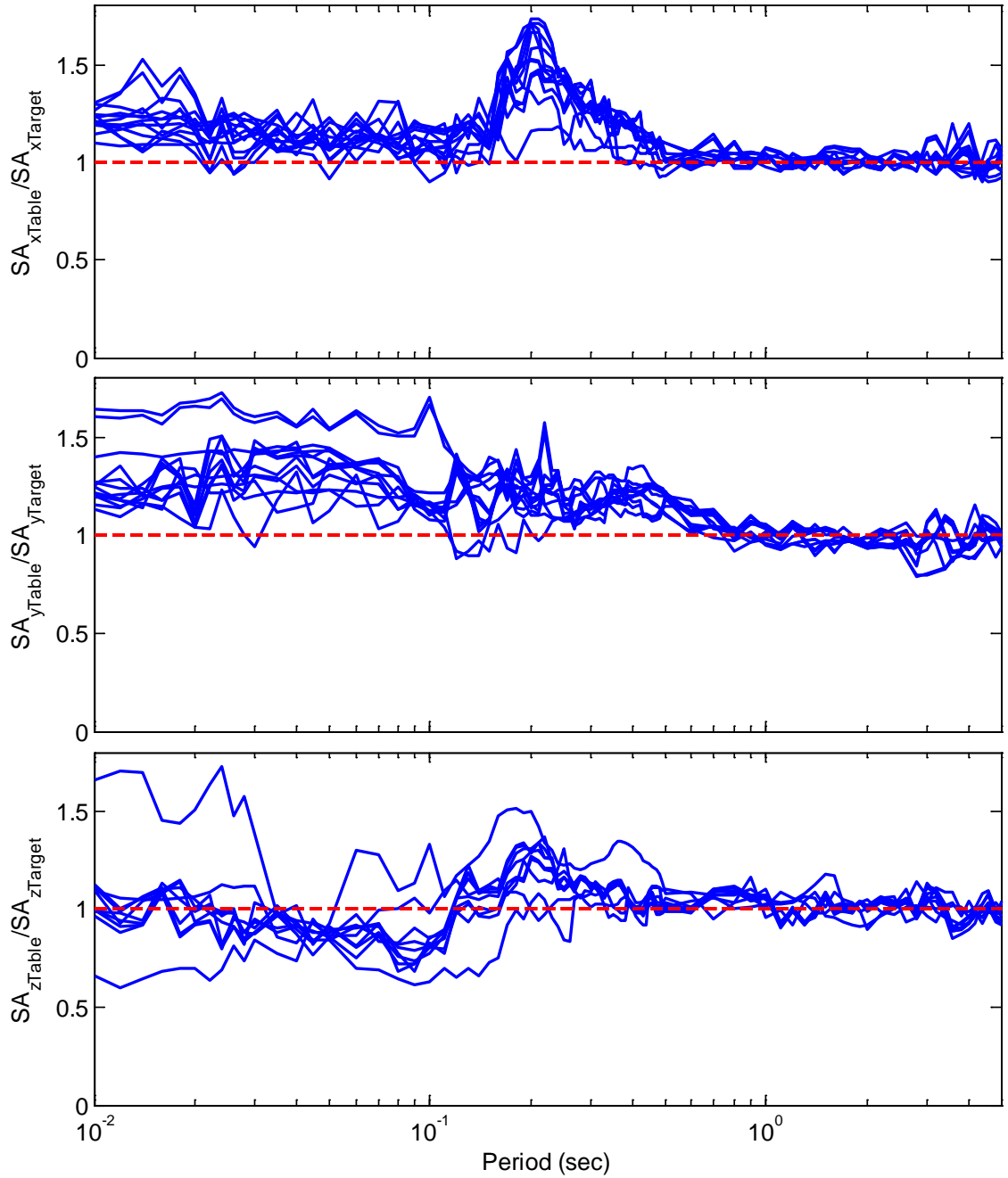


**Figure 4-19: Ratio of realized to target motion 5% damped spectral accelerations – hybrid LR isolation configuration**

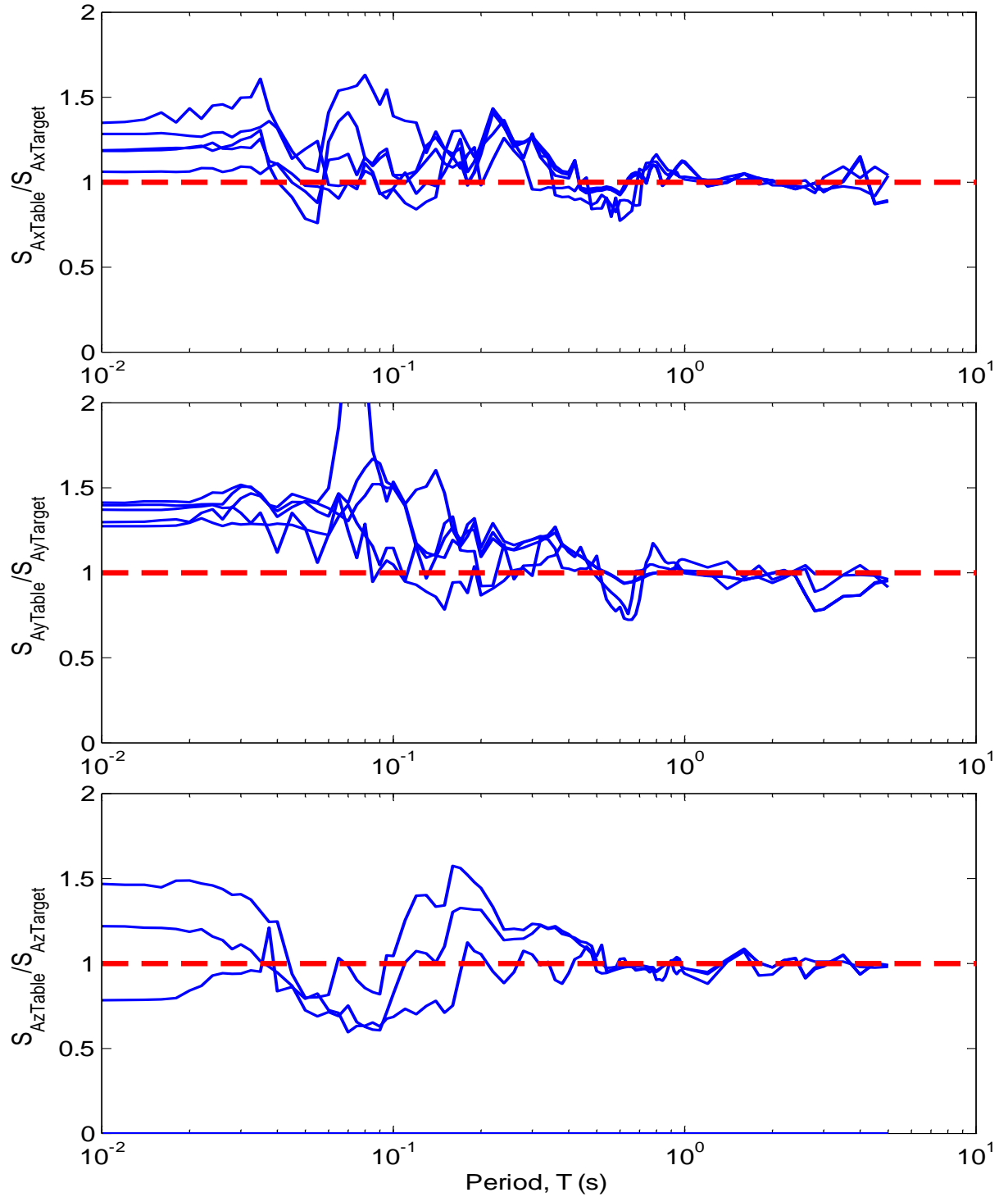


**Figure 4-20: Ratio of realized to target motion 5% damped spectral accelerations – fixed-base configuration**

## 4.6 Derived Responses

### 4.6.1 Horizontal Displacement of the Isolation System

An algorithm to compute the displacements in each isolator from the measured displacements in the string pots is described next. The algorithm accounts for large displacement geometric effects as a result of the large displacement demand in the bearings. From the original and displaced configurations of the isolation system in Figure 4-21, the coordinates  $X_{A'}, Y_{A'} \dots$  of displaced nodes A', B', D', F', G' and H' are:

$$\begin{aligned}
 X_{A'} &= \Delta X + X_A \cos \phi - Y_A \sin \phi \\
 Y_{A'} &= \Delta Y + X_A \sin \phi + Y_A \cos \phi \\
 X_{B'} &= \Delta X + X_B \cos \phi - Y_B \sin \phi \\
 Y_{B'} &= \Delta Y + X_B \sin \phi + Y_B \cos \phi \\
 X_{D'} &= \Delta X + X_D \cos \phi - Y_D \sin \phi \\
 Y_{D'} &= \Delta Y + X_D \sin \phi + Y_D \cos \phi \\
 X_{F'} &= \Delta X + X_F \cos \phi - Y_F \sin \phi \\
 Y_{F'} &= \Delta Y + X_F \sin \phi + Y_F \cos \phi \\
 X_{G'} &= \Delta X + X_G \cos \phi - Y_G \sin \phi \\
 Y_{G'} &= \Delta Y + X_G \sin \phi + Y_G \cos \phi \\
 X_{H'} &= \Delta X + X_H \cos \phi - Y_H \sin \phi \\
 Y_{H'} &= \Delta Y + X_H \sin \phi + Y_H \cos \phi
 \end{aligned} \tag{4.1}$$



where  $\Delta X, \Delta Y$  and  $\phi$  are the displacements and rotation at the center bearing in moving from the original configuration C to the displaced configuration C', with sign convention shown in Figure 4-21(b);  $X_A, Y_A$  are coordinates of the original point A, and so on.

From the displaced configuration in Figure 4-21(b):

$$\begin{aligned}
 (X_{A'} - X_a)^2 + (Y_{A'} - Y_a)^2 &= L_A^2 \\
 (X_{B'} - X_b)^2 + (Y_{B'} - Y_b)^2 &= L_B^2 \\
 (X_{D'} - X_d)^2 + (Y_{D'} - Y_d)^2 &= L_D^2 \\
 (X_{F'} - X_f)^2 + (Y_{F'} - Y_f)^2 &= L_F^2 \\
 (X_{G'} - X_g)^2 + (Y_{G'} - Y_g)^2 &= L_G^2 \\
 (X_{H'} - X_h)^2 + (Y_{H'} - Y_h)^2 &= L_H^2
 \end{aligned} \tag{4.2}$$

where  $X_a, Y_a$  are coordinate of node  $a$ ;  $L_A = L_{A0} + \Delta L_A$  is the distance between  $a$  and  $A'$ ;  $L_{A0}$  is the original length of the transducer and  $\Delta L_A$  is the change in length measured by the transducer.

Substituting Equation (4.1) into Equation (4.2) leads to a system of 6 nonlinear equations to solve for 3 unknown  $\Delta X, \Delta Y$  and  $\phi$ . The system of equations was solved using the `lsqnonlin` command in Matlab, which is applicable to nonlinear least-squares (nonlinear data-fitting) problems. After solving for  $\Delta X, \Delta Y$  and  $\phi$ , the coordinate of the displaced isolators were determined from Equation (4.1). These displacements were determined by subtracting the original coordinates from the displaced coordinates.

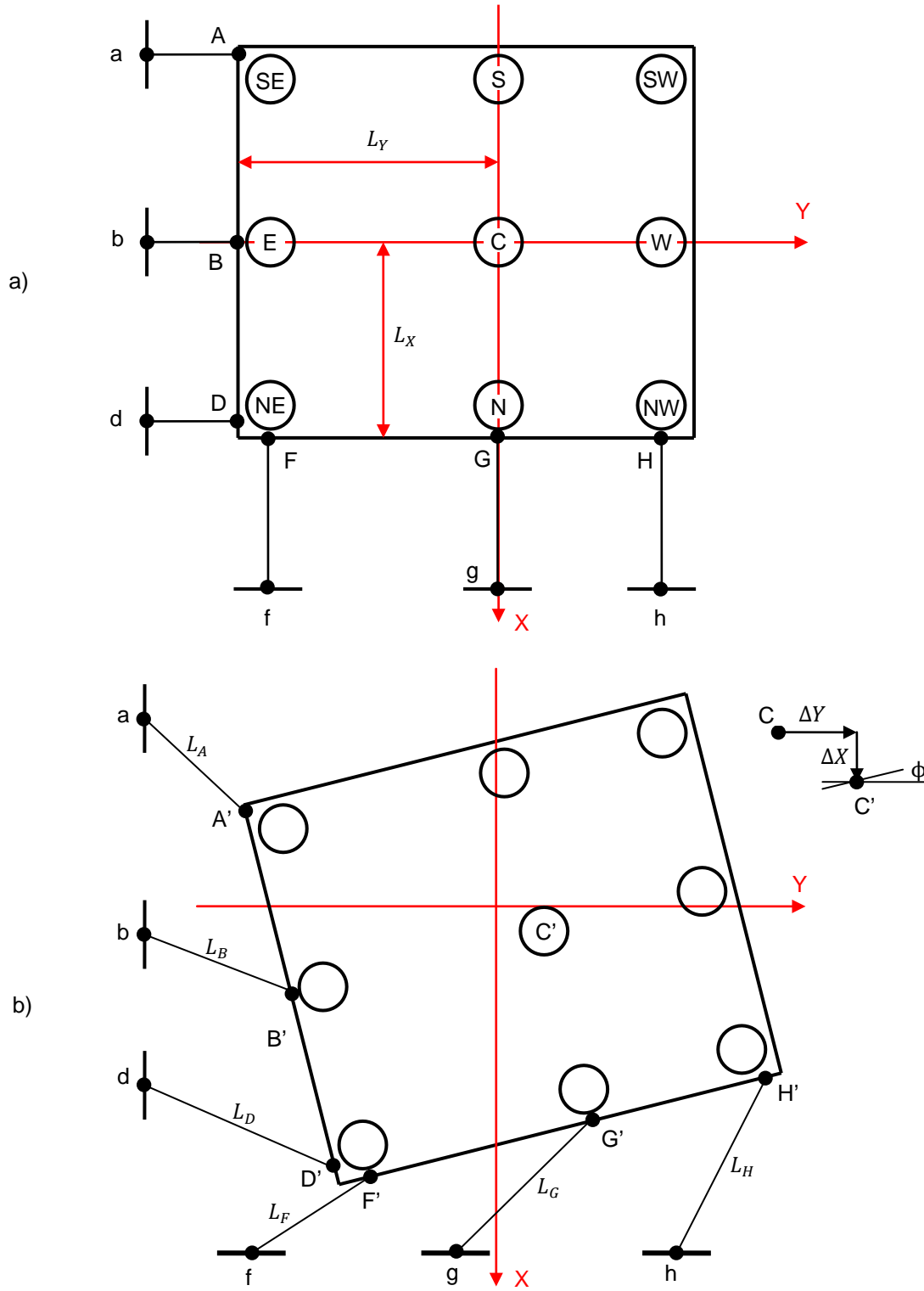


**Figure 4-21: Configurations for solving displacement of the isolation system. (a) original configuration, (b) displaced configuration**

#### 4.6.2 Isolator Forces

The X, Y and Z components of the recorded dynamic force from all load cells of an isolator were added to get the X, Y and Z components of the dynamic reaction at the load cells level. This reaction was then modified by the inertia forces of the connection plate and the bottom concave plate of the bearing to get the dynamic reaction at the isolator level. From the free body diagram in Figure 4-22 the relationships between the dynamic reaction components  $R_X$ ,  $R_Z$  at the isolator level and the dynamic reaction components  $R_{cX}$ ,  $R_{cZ}$  at the load cell level are:

$$\begin{aligned} R_X &= R_{cX} - m_c a_{cX} \\ R_Y &= R_{cY} - m_c a_{cY} \\ R_Z &= R_{cZ} - m_c a_{cZ} \end{aligned} \quad (4.3)$$

where  $m_c$  is the mass of the top plate in the bearing connection assemblies plus the bottom half of the bearing; and  $a_{cX}$ ,  $a_{cY}$  and  $a_{cZ}$  represent the horizontal and vertical accelerations recorded at the top connection plate. The reactions  $R_X$  and  $R_Z$  in Equation (4.3) represent the forces at mid-height of the LR bearing. These reactions are dynamic reactions so that the participation of the gravity load is not included in the equations.

Since vertical acceleration in the top connection plate was not recorded, the vertical acceleration in the earthquake simulator was used for  $a_{cZ}$ , which approximates the load cells as vertically rigid. The vertical acceleration of the simulator platform at every

isolator was extrapolated from the measured acceleration at the center of the platform including the effect of roll and pitch components. The validity of these extrapolation accelerations was checked by comparing the extrapolated acceleration at the 4 corners of the platform to the accelerations recorded at these locations.

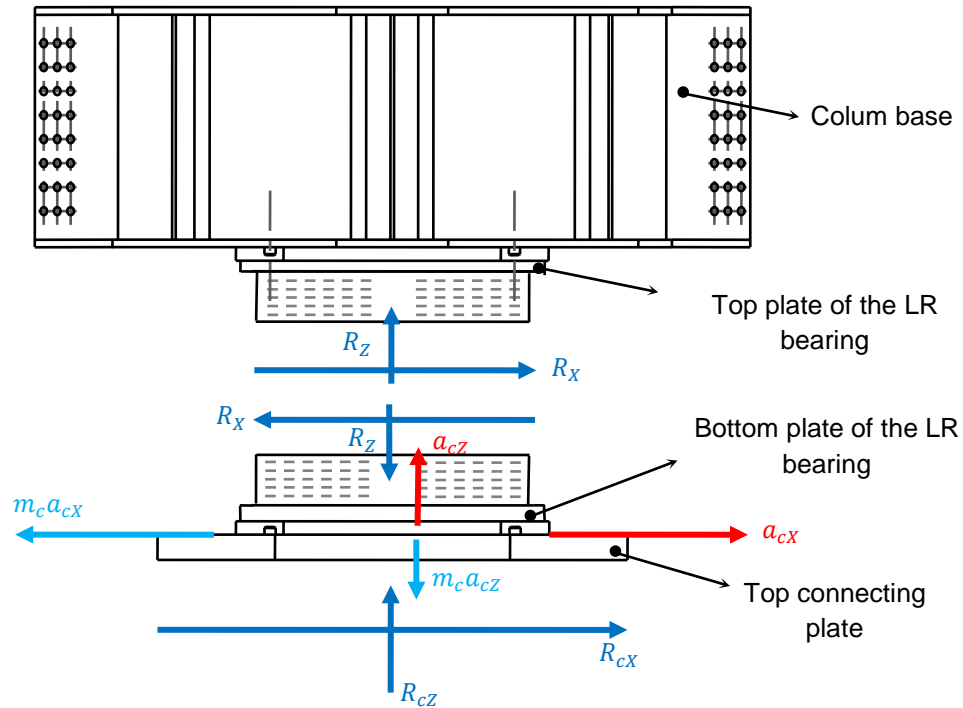


**Figure 4-22: Free body diagram illustrating derivation of isolator reaction**

The vertical force in all load cells was measured before each test series. The load cells were then zeroed before the first simulation of the test series so that only the dynamic force variation was measured during the simulations. The forces were only sampled during the simulation so that any redistribution of forces on the bearings from the original static state were reflected as offsets in the vertical forces at the beginning of each new simulation. The procedure used to measure the initial static forces in the LR bearings was

found to be unreliable; thus, the computed static loads may have errors in them. Fortunately, interpretation of the LR bearing response was not sensitive to the measured vertical force.

### 4.6.3 Horizontal Acceleration and Story Drifts

As shown in Figure 4-11, the horizontal accelerations were measured at the SE, NW and NE corners of each floor. These recorded accelerations were processed to get an average acceleration in each direction, computed as:

$$\begin{aligned} a_{x,avg} &= \frac{1}{3}(a_{xSE} + a_{xNE} + a_{xNW}) \\ a_{y,avg} &= \frac{1}{3}(a_{ySE} + a_{yNE} + a_{yNW}) \end{aligned} \quad (4.4)$$

where  $a_{xSE}$ ,  $a_{ySE}$  are X and Y –components of the horizontal acceleration at the SE corner, and so on. Physically, the average acceleration represents a plan location one third of the way from the geometric center to the NE corner of the building.

The story drift in X- and Y-direction at the geometric center were also interpolated from the measured story drift at the 2 locations shown in Figure 4-23. For instance, the story drifts  $\delta_{xC}$  at (Figure 4-23) or  $\delta_{yC}$  the geometric center were extrapolated from the story drifts at the SE and NW corners  $\delta_{xSE}$ ,  $\delta_{xNW}$ ,  $\delta_{ySE}$ ,  $\delta_{yNW}$  as follows:

$$\begin{aligned} \delta_{xC} &= \delta_{xSE} + \frac{L_1}{L_2}(\delta_{xNW} - \delta_{xSE}) \\ \delta_{yC} &= \delta_{ySE} + \frac{L_1}{L_2}(\delta_{yNW} - \delta_{ySE}) \end{aligned} \quad (4.5)$$

Inconsistencies were observed in the drift sensor measurements, especially under vertical excitation. The vertical slab vibration is believed to have produced rocking of the measurement towers, which distorted the recorded drifts.

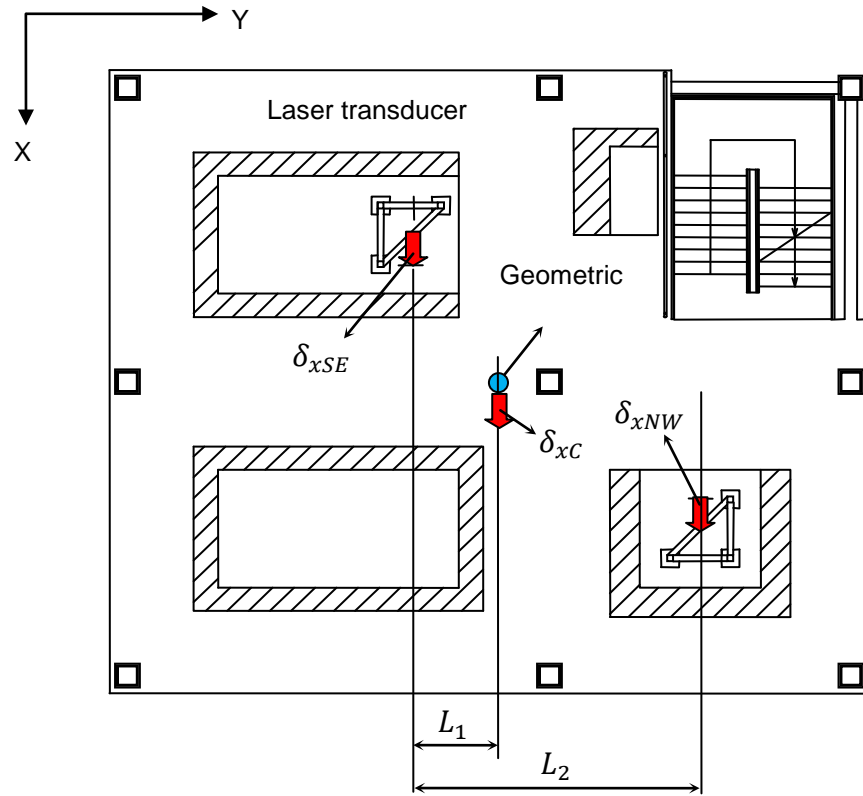


**Figure 4-23: Diagram illustrating the computation of drift at the geometric center**

## **CHAPTER 5: SUMMARY OF EXPERIMENTAL SIMULATION RESULTS FOR THE HYBRID LR ISOLATED BUILDING**

This chapter summarizes the overall response of the building with hybrid LR isolation system, with emphasis on the peak demands of various response parameters observed throughout the experimental program. Response quantities examined include displacement, rotation, shear force, axial force in compression and tension, and residual displacement of the isolators; and floor accelerations and story drifts in the structure.

### **5.1 Isolator Displacements**

The target isolator displacements were 300 mm (11.8 in) for the design base earthquake (DBE) and 600 mm (23.6 in) for beyond DBE. However, as mentioned previously, the maximum isolator displacement targeted in the test program was 550 mm (21.6 in) due to the various safety-related limitations imposed by the test facility (see Section 3.3.1). The DBE motion, VOG100, produced a peak vector sum displacement of 265 mm (10.4 in) and the beyond DBE motion, VOG175, produced a peak vector sum displacement of 505 mm (19.9 in) as shown in Figure 5-1. The peak displacements observed during the Vogtle suite of simulations were slightly lower than numerically predicted, and did not reach the target. However, the displacement demands for the Diablo Canyon suite of simulations were slightly greater than predicted. The scale factor for the largest Diablo Canyon simulation (DIA95(XY)), originally planned for 100%, was adjusted on the day of testing to achieve the target displacement of 550 mm (21.6 in). The peak displacement observed

in any LR bearing during DIA95(XY) was 547 mm (21.5 in). The smallest displacement (88 mm or 3.5 in) was observed during the service level simulation WSM80. The largest vector displacements of the LR bearings relative to the DB and EDB levels are shown in Figure 5-2(a). Over half of the 15 input motions produced peak displacements that exceeded DB level. The displacement for the Vogtle #13 motion was observed to increase approximately linearly as the scaling intensity increased from 75% to 175% of the original input motion (Figure 5-2(b)). Because of the nonlinearity of the isolation system, the displacement demand would not normally be expected to increase linearly with excitation intensity.

The maximum displacements observed in each LR bearing (East (E), South (S), North (N) and West (W)) are summarized in Figure 5-3 for the x-direction, y-direction, and overall peak in any direction, determined as the peak of the vector sum displacement history. The simulations names are abbreviated by numbers in the figure, in order of their sequence, where the correspondence between number and simulation name, the directions that the excitations were applied and the input scale factor is summarized in Table 5-1 for convenience. By way of the small rotation assumption used to process the sensor data and derive individual isolator displacements (Section 4.6.1), the x-direction displacements were identical for the North and South bearings, which had the same y-coordinate, and the y-direction displacements were identical for the East and West bearings, which had the same x-coordinate. The East bearing experienced the largest displacement for most of the simulations (Figure 5-3(c)) due to the observed base rotation (see Section 5.2). The displacement traces (displacement in x-direction versus displacement in y-direction) of



the East LRB are compared for four simulations in Figure 5-4: (a) WSM80, which produced the smallest displacement demand, (b) DIA95(XY), which produced the largest displacement demand, (c) VOG100, which was scaled to DBE intensity, and (d) VOG175, which was scaled to MCE intensity. The displacement observed in WSM80 was trivially small compared to the other simulations, and the large discrepancy in displacements affected the ability to model the LR bearings with a single set of physical parameters (discussed in Chapter 8). The simulations produced both linear and circular displacement orbits in the bearings, the latter of which would be more affected by bidirectional coupling. As mentioned in Section 3.3.2, the Vogtle ground excitation was rotated 11.25 degrees to induce the maximum displacement in a diagonal direction, as observed in Figure 5-4(d).

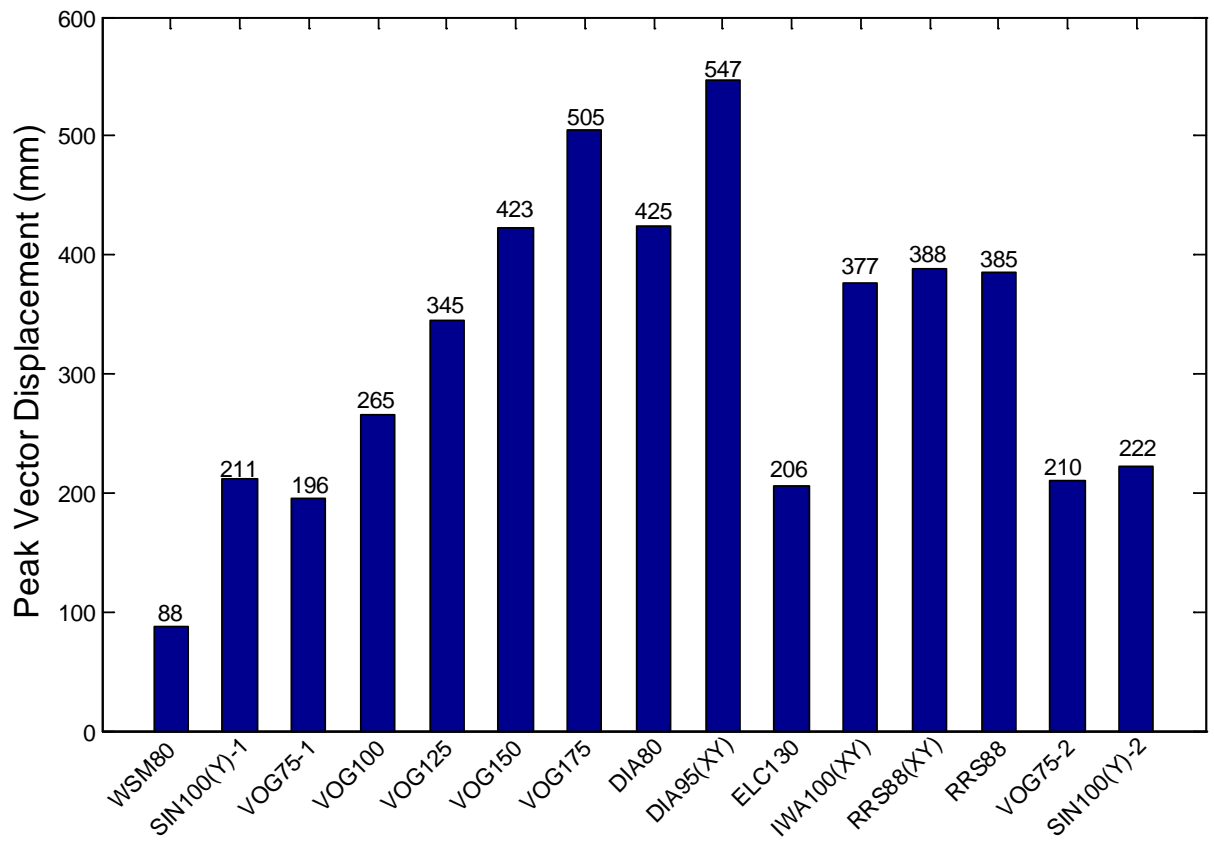


**Figure 5-1: Peak vector sum displacement recorded in any LR bearing for each earthquake simulation**

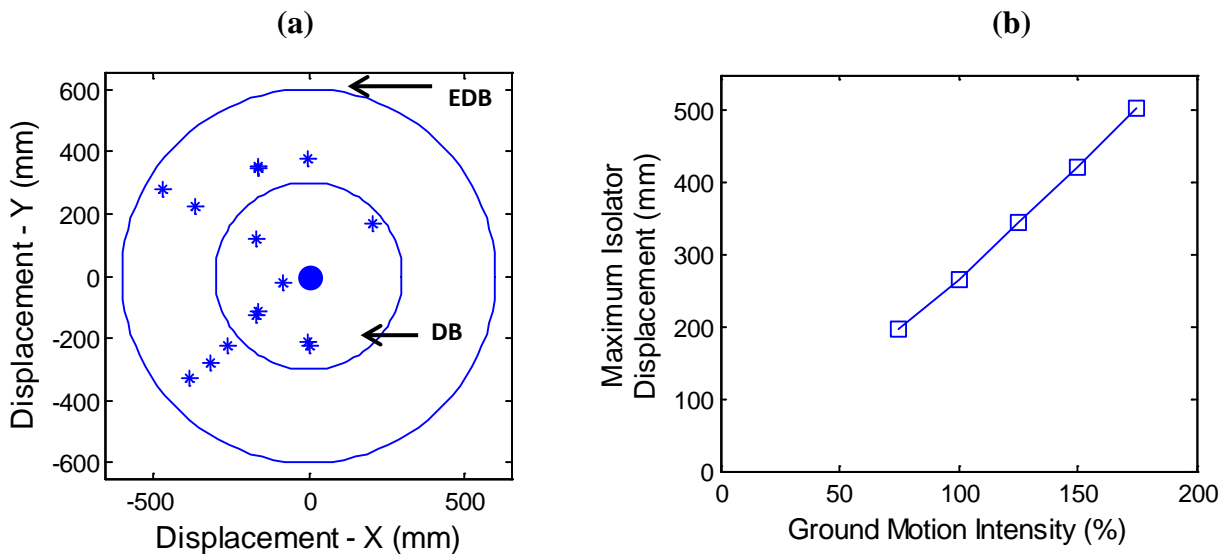


Figure 5-2: Maximum isolator (LR bearing) displacement (a) for each ground excitation relative to DB and EDB levels, (b) versus intensity for Vogtle motions.

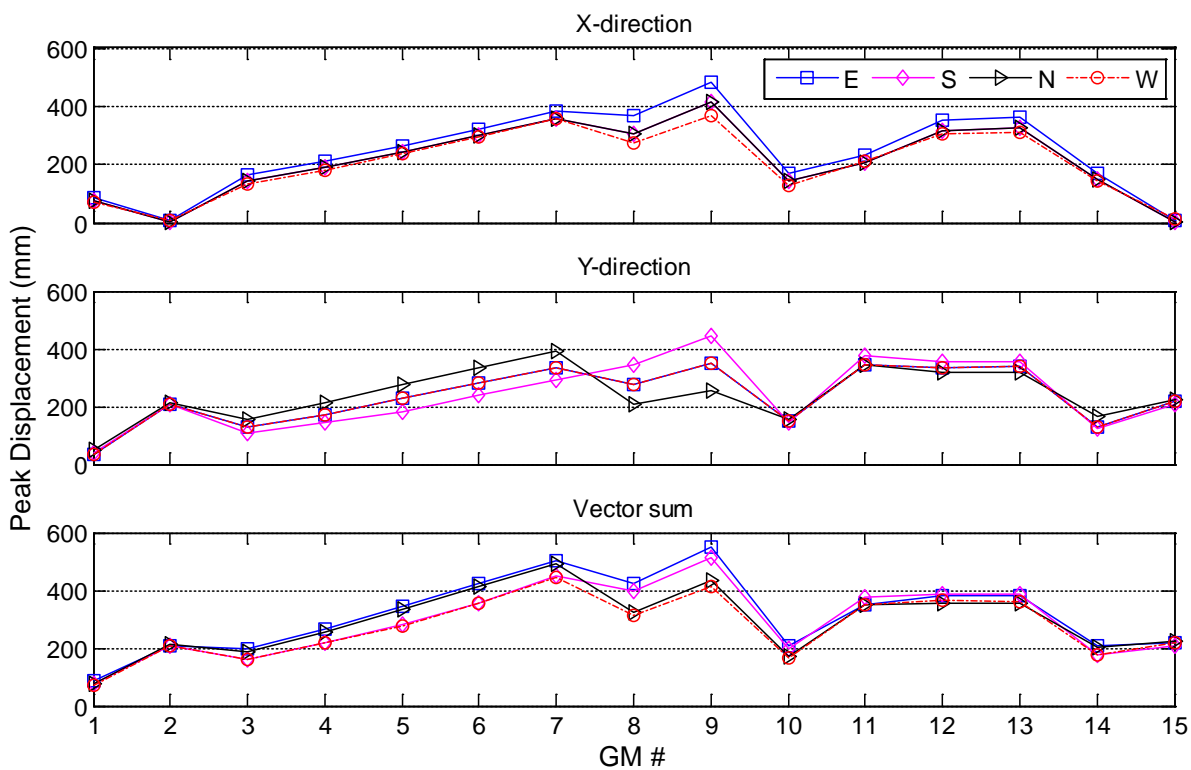
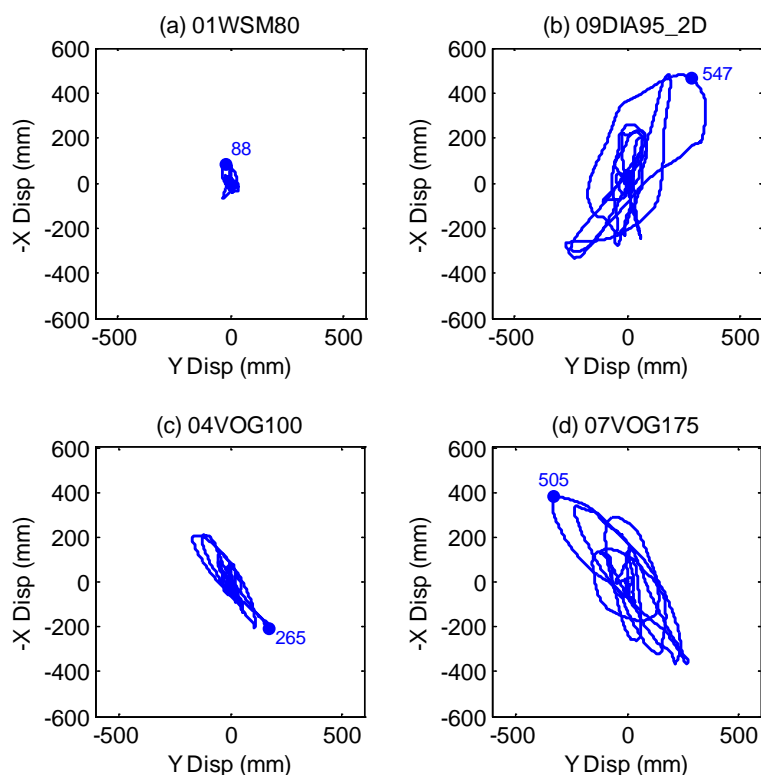


Figure 5-3: X-direction, y-direction and overall peak (vector sum) displacement of each LR bearing for each earthquake simulation

**Table 5-1: List of Ground Motion (GM) Simulations by Number, Name, Abbreviation and the Directions Considered.**

GM #	GM Name	GM Abbreviation	Input Direction	Scale Factor (%)
1	Superstition Hills, Westmorland	WSM80	X, Y, Z	80
2	Sine-wave	SIN100(Y)-1	Y	100
3	Vogtle #13	VOG75-1	X, Y, Z	75
4	Vogtle #13	VOG100	X, Y, Z	100
5	Vogtle #13	VOG125	X, Y, Z	125
6	Vogtle #13	VOG150	X, Y, Z	150
7	Vogtle #13	VOG175	X, Y, Z	175
8	Diablo #15	DIA80	X, Y, Z	80
9	Diablo #15	DIA95(XY)	X, Y	95
10	Imperial Valley, El Centro	ELC130	X, Y, Z	130
11	Tohoku, Iwanuma	IWA100	X, Y, Z	100
12	Northridge, Rinaldi Rec. Sta.	RRS88(XY)	X, Y	88
13	Northridge, Rinaldi Rec. Sta.	RRS88	X, Y, Z	88
14	Vogtle #13	VOG75-2	X, Y, Z	75
15	Sine-wave	SIN100(Y)-2	Y	100



**Figure 5-4: Displacement trace (x vs y-direction displacement) of the East LRB for (a) WSM80, (b) DIA95(XY), (c) VOG100 and (d) VOG175.**

## 5.2 Torsional Response

The dynamic characteristics of the testbed building were affected by stiffness asymmetry resulting from the unequal bays widths (equal to 7 m or 23 ft and 5 m or 16.4 ft) in the y-direction (Section 2.1, Figure 2-2), and various sources of mass eccentricity, the most notable being the asymmetrically configured steel blocks at the roof level (Section 2.3). The level of eccentricity is later quantified while discussing the model development for numerical simulation (Section 7.3). Aside from the supplementary roof weight, the sources of eccentricity were mild and typical of practice. However, as discussed in Section 3.3.2, the restrictions on the experimental setup did not allow for the isolation system to be configured to minimize torsion, unlike the design of a realistic structure with hundreds of isolators. Thus, non-negligible rotation was observed in the hybrid LR isolation system.

The peak rotation angle at the base (isolation system) level for each simulation is summarized in Figure 5-5. The rotation angle observed during the sine wave simulation (SIN100-1 and SIN100-2) was small, since the sine wave was applied unidirectionally in the y-direction (theoretically uncoupled) to minimize the torsional response for bearing characterization. During WSM 80%, which produced the smallest displacement demand, a peak rotation angle of 0.0029 rad was observed, and during VOG175 and DIA95(XY) the largest peak rotation angle of 0.019 rad was observed. The peak rotation was proportional to the peak displacement. The influence of the rotation on the bearing displacements can be observed from the displacement traces of all bearings during the VOG175 motion (Figure 5-6). From the SE to the NW isolator, the displacement traces

transitioned from nearly linear (back and forth) motion to a circular displacement orbit. Furthermore, the peak displacement in the LR bearings varied from 505 mm in LRB-E to 446 mm in LRB-W, which is a 13% variation across the plan. Considering all isolation devices, the peak displacement varied from 531 mm (NE corner) to 427 mm (SW corner), a 24% variation from corner to corner. For the Rinaldi simulation that was repeated at the same scale factor for XY and 3D input, the peak rotation increased 4% from RRS88(XY) to RRS88 (Figure 5-5) while the peak displacement remained about the same, which may have been related to a residual rotation or displacement.

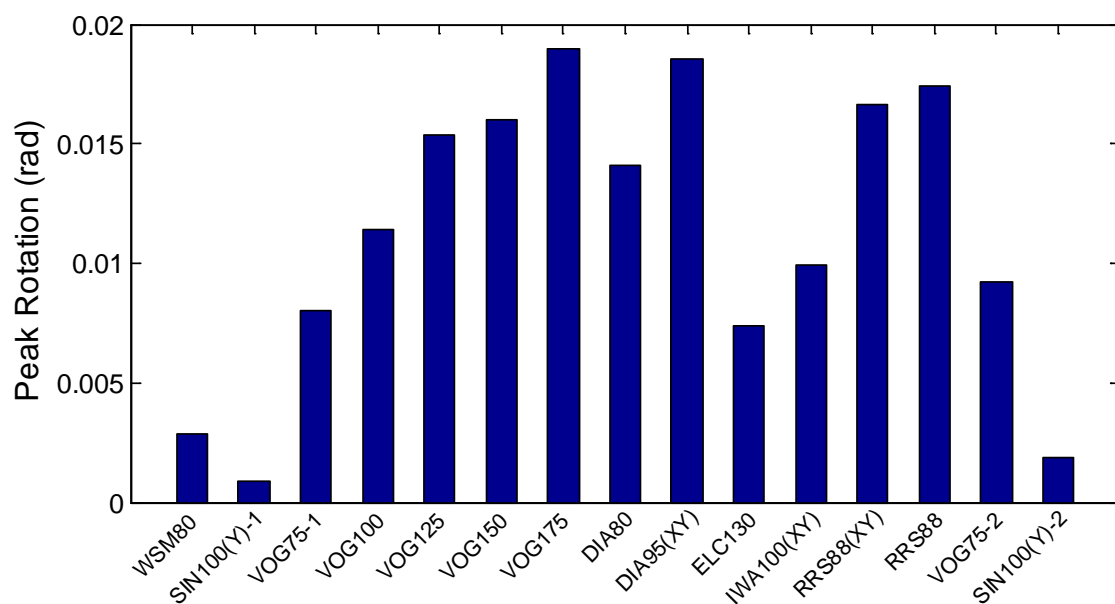


**Figure 5-5: Peak rotation angle of the base for each earthquake simulation**

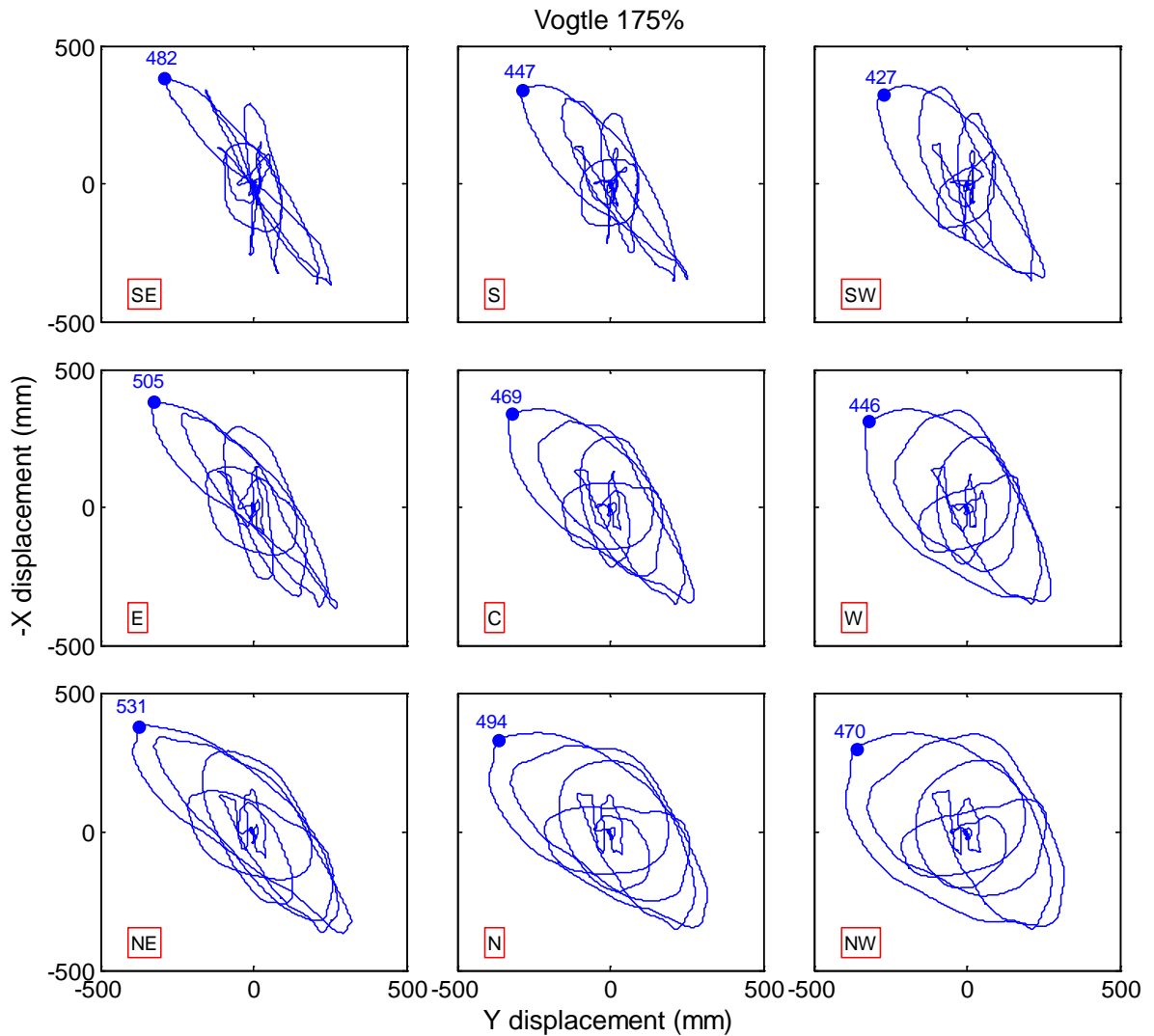


**Figure 5-6: Displacement trace of each isolator during the Vogtle 175% simulation**

The amplification of displacement demand in the experiment due to torsion is compared to the amplification factor prescribed in ASCE 7 (2016) to account for the effects of eccentricity. According to the code, the total displacement  $D_{TM}$  including torsional amplification in terms of the center of rigidity (CR) displacement  $D_M$  is computed by:

$$D_{TM} = D_M \left[ 1 + y \frac{12e}{b^2 + d^2} \right] \quad (5.1)$$

where the amplification factor (bracketed term in Equation (5.1)) is a function of the building plan dimensions  $b$  and  $d$ , the distance  $y$  between the isolation system CR and its outermost element, and the eccentricity  $e$  between the building center of mass and isolation system CR. For this experiment, the effects of torsion were largest for motion in the X-direction, with a computed eccentricity  $e = 0.8$  m (2.6 ft), or 6.6% of the plan dimension. Taking  $b = 10$  m (32.8 ft),  $d = 12$  m (39.4 ft), and  $y = 1.4$  m (4.6 ft) for motion in X direction, the code prescribed amplification factor is 1.26 based on the actual eccentricity. Accidental eccentricity is neglected since the distribution of stiffness and mass in the building is well known.

An experimental peak amplification factor was computed for all input motions with components applied in the X-direction (as listed in Table 4-4). The amplification factor was calculated as:

$$1 + abs\left(\frac{E_x - W_x}{E_x + W_x}\right) \quad (5.2)$$

where  $E_x$  and  $W_x$  are the X-direction displacements recorded in the E and W bearings, respectively. Physically, the amplification factor represents  $1 + \text{rotational displacement} \div \text{average displacement}$ . The amplification factor was computed at two different times: the instant of largest average displacement, labeled “Peak Avg. Disp.”, and the instant of largest peak displacement in either bearing, labeled “Peak East Disp.” (Figure 5-7). The computed amplification factor was shown to be sensitive to the chosen time instant. Taking the “Peak East Disp.” as the worst case scenario, the prescribed code



amplification (neglecting accidental eccentricity) was generally conservative, but within range of the observed data points.

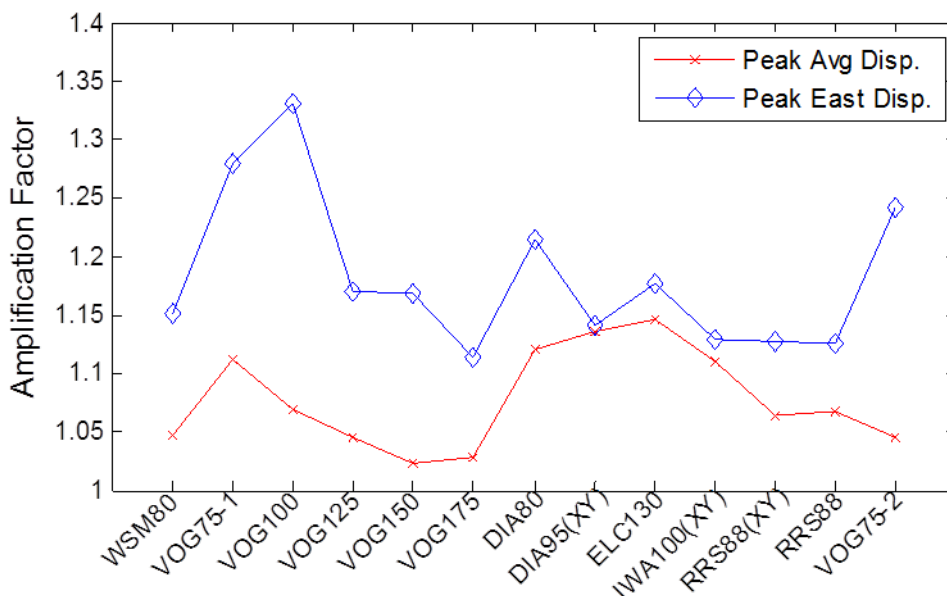


**Figure 5-7: Computed torsion amplification factor for several motions.**

### 5.3 System Base Shear

The total base shear was computed by summing the recorded shear force of the four LR bearings in the x and y-directions, evaluating the vector sum of the x and y-components, and determining the peak over all times steps. This procedure was applied in the two horizontal directions, and from this the peak vector sum was determined. The calculation of the base shear does not include forces in the CL bearings, which were not recorded in this experiment. The forces in the CL bearings were assumed to be negligible as the rated friction coefficient was about 0.005. Although the influence of the CL bearings on the base shear is not certain, there was no evidence to suggest that the forces in the CL

bearings were significant. The peak values of total (vector sum), x and y-direction base shears are listed in Table 5-2 for each simulation. The corresponding values of normalized base shear or base shear coefficient, listed in Table 5-3, were obtained by dividing the total base shear by the total static weight of the building. Figure 5-8 illustrates the results of Table 5-2 graphically. The largest base shear of 1467 kN (328 kips), corresponding to a base shear coefficient of 0.28, was observed during VOG175. Among the other largest base shear coefficients observed were DIA95(XY) (0.28), DIA80 (0.24) and RRS88(XY) and RRS88 (both 0.26).

**Table 5-2: Peak Base Shear for all Simulations: Total, X and Y Directions**

GM #	GM Name	Peak Base Shear (kN)	Peak Base Shear - X (kN)	Peak Base Shear - Y (kN)
1	WSM80	468	467	274
2	SIN100(Y)-1	996	9	996
3	VOG75-1	869	682	665
4	VOG100	1003	831	754
5	VOG125	1163	979	870
6	VOG150	1317	1109	967
7	VOG175	1467	1237	1058
8	DIA80	1271	1064	916
9	DIA95(XY)	1457	1245	965
10	ELC130	851	677	719
11	IWA100(XY)	1212	766	1211
12	RRS88(XY)	1365	1100	1240
13	RRS88	1355	1097	1214
14	VOG75-2	808	645	624
15	SIN100(Y)-2	926	13	926

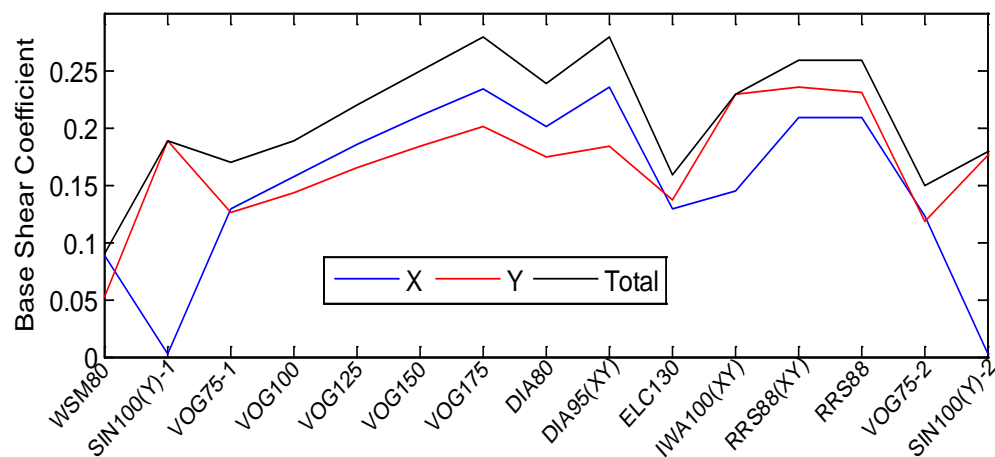


**Figure 5-8: Base shear coefficient for all simulations: total, x and y-directions**

**Table 5-3: Peak Base Shear Coefficient for all Simulations: Total, X and Y Directions.**

GM #	GM Name	Peak Base Shear Coeff.	Peak Base Shear Coeff. - X	Peak Base Shear Coeff. - Y
1	WSM80	0.09	0.09	0.05
2	SIN100	0.19	0.002	0.19
3	VOG75	0.17	0.13	0.13
4	VOG100	0.19	0.16	0.14
5	VOG125	0.22	0.19	0.17
6	VOG150	0.25	0.21	0.18
7	VOG175	0.28	0.24	0.20
8	DIA80	0.24	0.20	0.17
9	DIA95_2D	0.28	0.24	0.18
10	ELC130	0.16	0.13	0.14
11	IWA100	0.23	0.15	0.23
12	RRS88_2D	0.26	0.21	0.24
13	RRS88	0.26	0.21	0.23
14	VOG75	0.15	0.12	0.12
15	SIN100	0.18	0.002	0.18

In Figure 5-9, the base shear coefficient for each motion is superimposed over the backbone force-displacement relation of the LR bearings, using the assumed design properties in Table 3-3. The total force in the LR bearings was observed to exceed the design backbone for displacements less than 300 mm (12 in) and fall below the design backbone for displacements exceeding 300 mm (12 in). As an example, the base shear was approximately proportional to displacement as the intensity was increased from VOG75 to VOG175 simulations (simulations 3 to 7 in Figure 5-9), but with a slope slightly lower than the post-yield stiffness  $K_d$ . The influence of ground motion intensity on the isolator response and modeling assumptions is addressed in Section 8.4.2.

Most simulations followed this trend with the exception of the Rinaldi motions (simulations 12 and 13, RRRS88(XY) and RRS88, in Figure 5-9). Assuming the design backbone curve was an accurate reflection of the bearing response, the observed points should fall below the design curve since the base shear coefficient represented an average bearing shear, while the displacement represented a peak displacement recorded in any LR bearing.

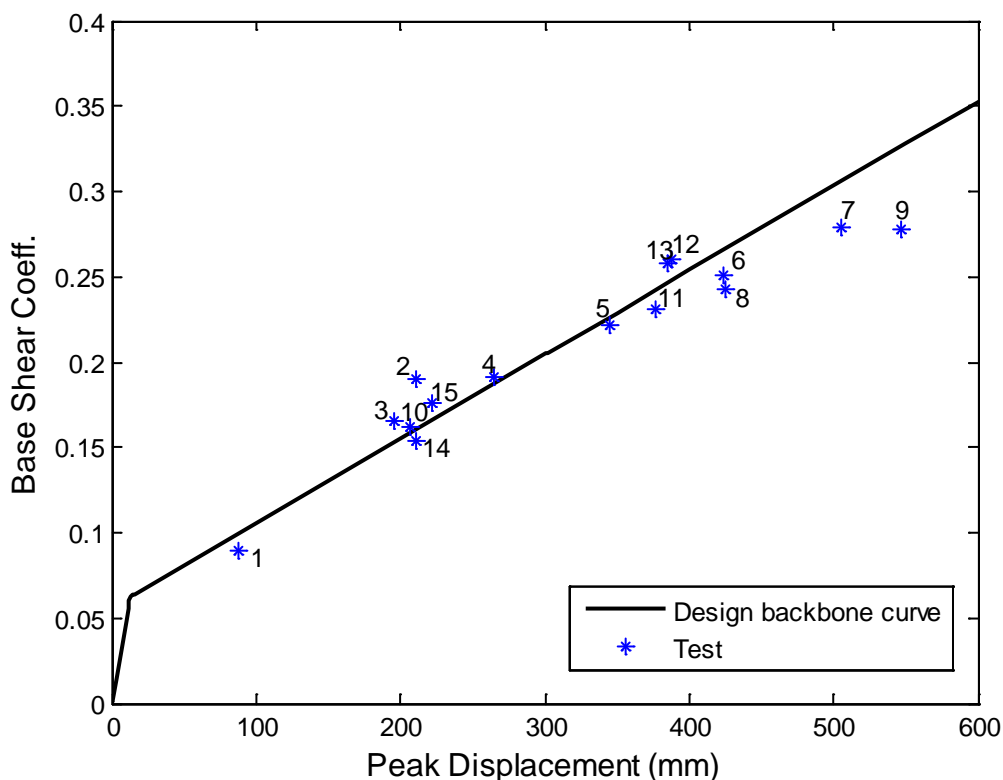


**Figure 5-9: Base shear coefficient for each simulation alongside the design backbone curve.**

#### 5.4 Axial Forces in LR Bearings

The static forces on the LR bearings at the start of the experiments were measured as: East = 435 kN (98 kips), South = 755 kN (170 kips), North = 490 kN (110 kips), and West = 235 kN (53 kips). As discussed in Section 4.3, the measured static loads on the bearings at the beginning of the experiments differed from the expected loads according to tributary area calculations. The actual measured and expected static loads on the LR bearings were compared in Table 4-2. In summary, the portion of the building weight carried by the LR bearings (about 37%) was significantly less than portion of the weight that was expected to be carried by the LR bearings (about 51%). The sources of the

discrepancy could not be identified with certainty, but following are some probable causes: 1) The base of the testbed building was noticeably warped. This caused the weight of the building to be distributed in a different pattern than if the building had been erected on top of the isolation system. 2) The stiffer CL bearings attracted more weight, thus carrying a larger portion than if the weight was balanced on a single type of isolator. Both factors were thought to contribute to the static load distribution measured at the part of the experiment.

The axial forces in the LR bearings varied for each bearing and during each simulation due to a combination of factors including: variation in static forces, overturning, vertical excitation, and load transfer between LR bearings and CL bearings (discussed in Section 6.2). The peak compressive and tensile forces measured in any LR bearing for each simulation are shown in Figures 5-10 and 5-11, respectively. Tension was observed in at least one bearing for seven of the fifteen simulations (Figure 5-10). The largest compressive force in a single bearing was about 2000 kN or 450 kips (about 40% of the static weight of the building) and the largest tensile force was 453 kN (102 kips), both observed during RRS88. The variation in axial force during RRS88 was caused by the vertical excitation. To put this magnitude of tension into perspective, cavitation, or tensile rupture of the rubber matrix, is expected at a negative pressure =  $3G$  (Constantinou et al. 2007), where  $G$  is the shear modulus of the rubber. Taking  $G$  to equal the design value of 0.41 MPa (0.06 ksi) (Table 3-3), the approximate tensile force for cavitation in these LR bearings is 476 kN (107 kips). Although the cavitation limit does not apply at large displacements when the bearing is under combined tension and shear (Kalpakidis et al.,

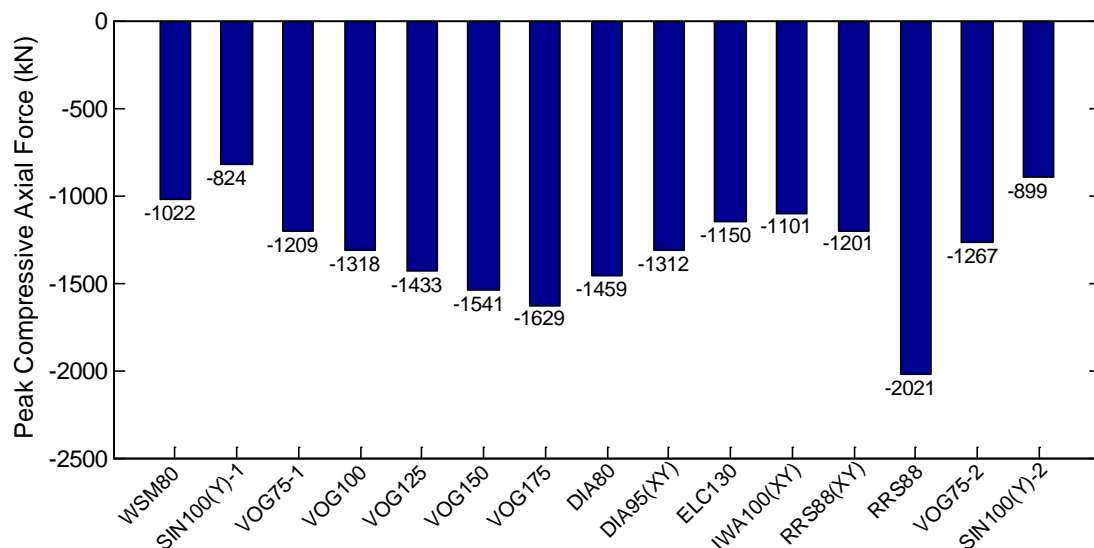
2009b), the measured peak tensile force was substantial. Thus, the East LR bearing may have been on the verge of cavitation, or cavitation may have actually occurred, preventing the peak tensile force from going beyond the observed value.

Figure 5-12 illustrates the peak axial force in compression and tension for each LR bearing in each simulation, both absolute and normalized by the static force in the bearing at the start of the test program. Throughout the simulations, the South bearing was generally subjected to the largest compressive force, and the West bearing was subjected to the smallest compressive force (Figure 5-12(a)), which was in proportion to the static weight carried on the bearings. However, the *normalized* compressive force was largest in the West bearing, which carried the smallest static force, and smallest in the South bearing, which carried the largest static force (Figure 5-12(b)). Thus, the variation in compressive force, computed as a percentage of the static load, increased as the static load decreased. The largest tensile force generally occurred in the East LR bearing (Figure 5-12(c)), which did not carry the greatest or least static force, but was usually subjected to the largest displacement (Figure 5-3). At large lateral displacements, a portion of the axial forces in the LR bearings were observed to transfer to the CL bearings, in some cases causing the LR bearings to be subjected to tension. Since the displacement demands were largest in the East bearing, the largest tensile forces occurred in the East bearing. The phenomenon of load transfer between LR and CL bearings is documented in Section 6.2.

The maximum LR bearing axial load, assumed positive in tension, is plotted against isolator displacement for all earthquake motions (represented by GM #) in Figure 5-13.

The “Peak Disp.” case plots the instantaneous axial load on the bearing at the observed peak LR bearing displacement. The “Max Force” and “Min Force” cases plot the instantaneous isolator displacement at maximum compression and minimum compression (or maximum tension), respectively. The largest compressive force of 2022 kN (455 kips) was observed in the South LR bearing during RRS88 (GM# 13). The bearing critical buckling load was estimated from bearing shear modulus and geometric properties (Weisman et al. 2012). The variation in the critical buckling load with displacement was estimated using the overlapping area rule (Kelly, 2003), which has been shown to be conservative (Kalpakidis et al. 2009a). The expected critical buckling load of the bearing at zero displacement was 14.8 MN (3327 kips). The shaded area in Figure 5-13 identifies the unstable region for which the axial load ( $P$ ) was larger than the critical load ( $P_{crit}$ ) as a function of displacement. During the “Peak Disp.” case, the axial load on the LR bearings never approached  $P_{crit}$ . Peak axial load would generally be expected to occur near a peak displacement, however maximum compression never occurred at an LR bearing displacement greater than 300 mm (11.8 in), and the axial load corresponding to the bearing peak displacement (“Peak Disp.” case) was significantly smaller than the maximum.





**Figure 5-10: Peak compressive force in any LR bearing for each earthquake simulation**

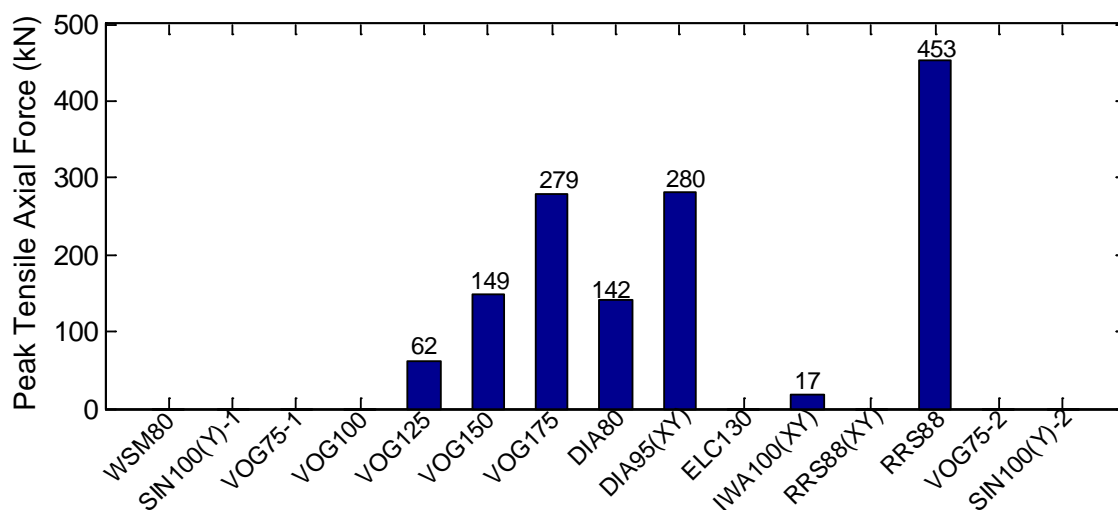


**Figure 5-11: Peak tensile force in any LR bearing for each earthquake simulation. (A tensile force of zero indicates that tension was not observed).**

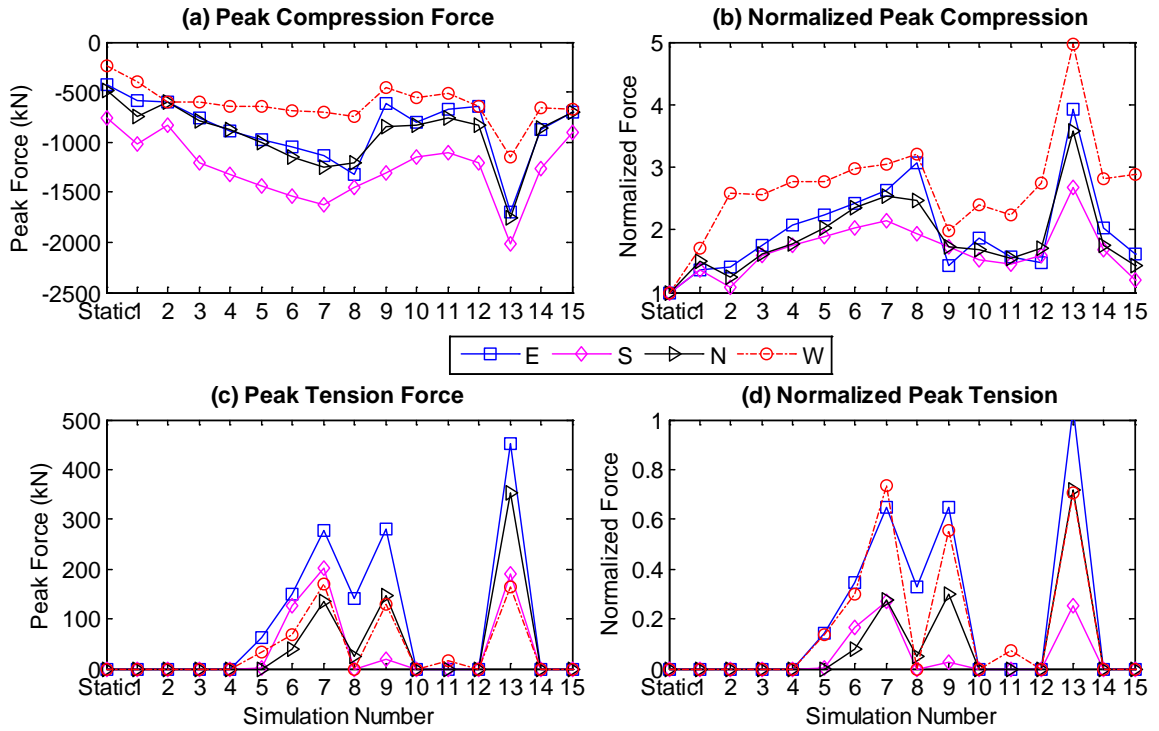


**Figure 5-12: Peak axial forces in each LR bearing for each simulation: (a) Peak compression force, (b) normalized peak compression force, (c) peak tension force, and (d) normalized peak tension force.**

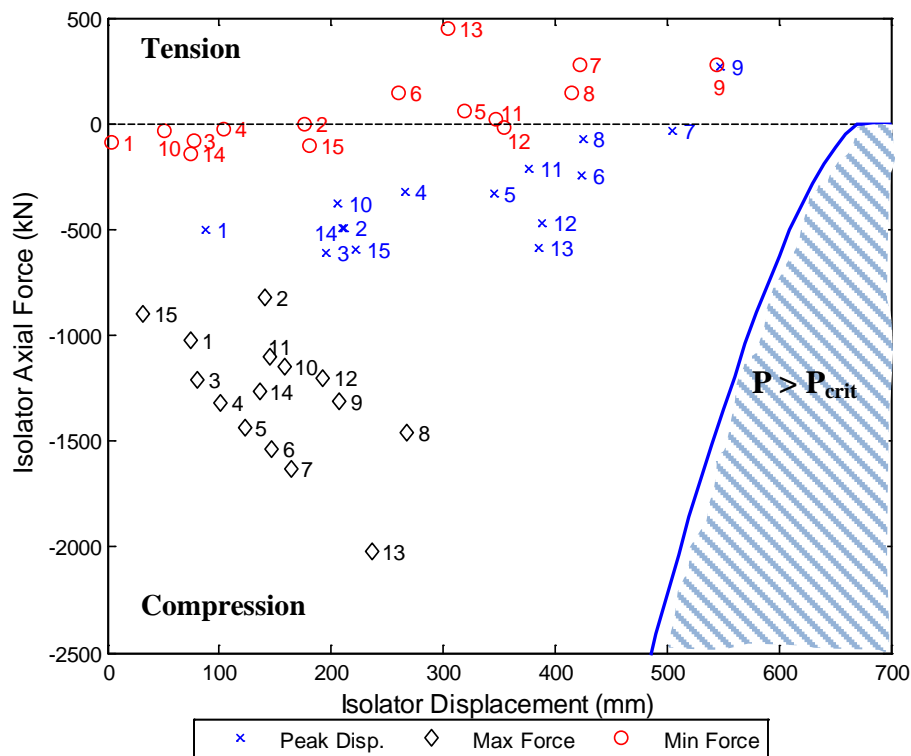


**Figure 5-13: Axial force in the LR bearing at the peak horizontal displacement, and maximum and minimal compressive axial force for each input motion compared to the critical load.**

## 5.5 Isolation System Re-Centering

The displacement recorded at the location of each LR bearing at the end of every simulation – referred to as permanent displacement - is shown in Figure 5-14. Prior to the 8<sup>th</sup> simulation (DIA80), the peak permanent displacement at any isolator location was about 50 mm (0.2 in). A sudden increase in the permanent displacement was observed in the x and y directions at the East and North LRB locations, respectively, at simulation #8. This permanent displacement recorded in the sensors reflected is believed to be a combination of permanent deformation in the bearings and sliding of the steel connecting plate.

From the inspection pictures taken at the end of the 1<sup>st</sup> day of testing which directly followed DIA80 (Figure 5-15), the bottom steel plate of the East LR bearing slid about 11 mm (0.4 in). It cannot be determined whether the slippage occurred during trial 8 or trial 7. However, as later shown in Section 6.1, slippage of the bolts connecting the LR bearing bottom steel plate to the supporting steel hexagonal plate of the load cell occurred as early as the 5<sup>th</sup> trial (VOG125), which led to the sliding of the bottom plate seen in Figure 5-15. If the sliding of the steel plate had not occurred, perhaps the permanent displacement in the bearings would have been limited to that observed in the first few simulations - around 5 mm (0.2 in) - which is insignificant.

Prior relaxation tests performed on LR bearings (Constantinou et al. 2007) suggested that the characteristic strength of LR bearings drops markedly under static conditions. Specifically, a bearing was returned to zero displacement following a sequence of large velocity cyclic loading and an imposed permanent displacement. When returned to zero displacement, the characteristic dropped to about 1/3 of its starting value after 8 minutes and 1/4 of its starting value after 30 minutes. The drop in characteristic strength due to relaxation suggests that permanent displacements in the bearings would disappear over time.

The relaxation effect was evaluated in the present test program by looking for reductions in permanent displacement from the end of one simulation to the start of the next, which is illustrated separately for each bearing in Figure 5-16. Recall that the average time between simulations was about 50 minutes. Figure 5-16 does not indicate consistent reductions in permanent displacements in the sensors from the end of one simulation to

the start of the next that are consistent with a relaxation effect. The changes in permanent displacement may have been inconsistent (sometimes increasing and sometimes decreasing) since the bearing displacements, as computed by the string pots, were not independent but rather constrained to move together through the assumed base diaphragm constraint. Nonetheless, the observed permanent displacements were not significant.

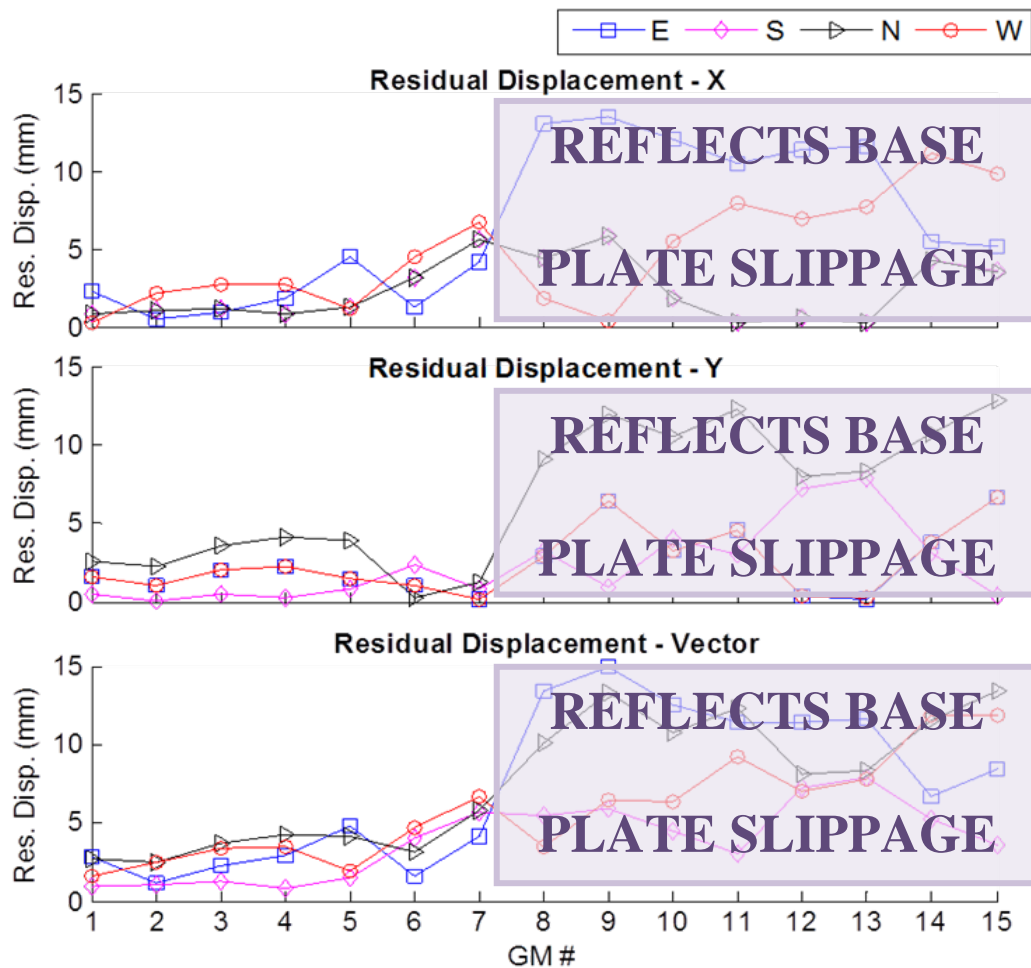


**Figure 5-14:** X-direction, y-direction, and total (vector sum) displacement recorded in each LR bearing at the end of every earthquake simulation.



**Figure 5-15:** Permanent displacement of around 11 mm on the East bearing due to sliding of the bottom steel plate.

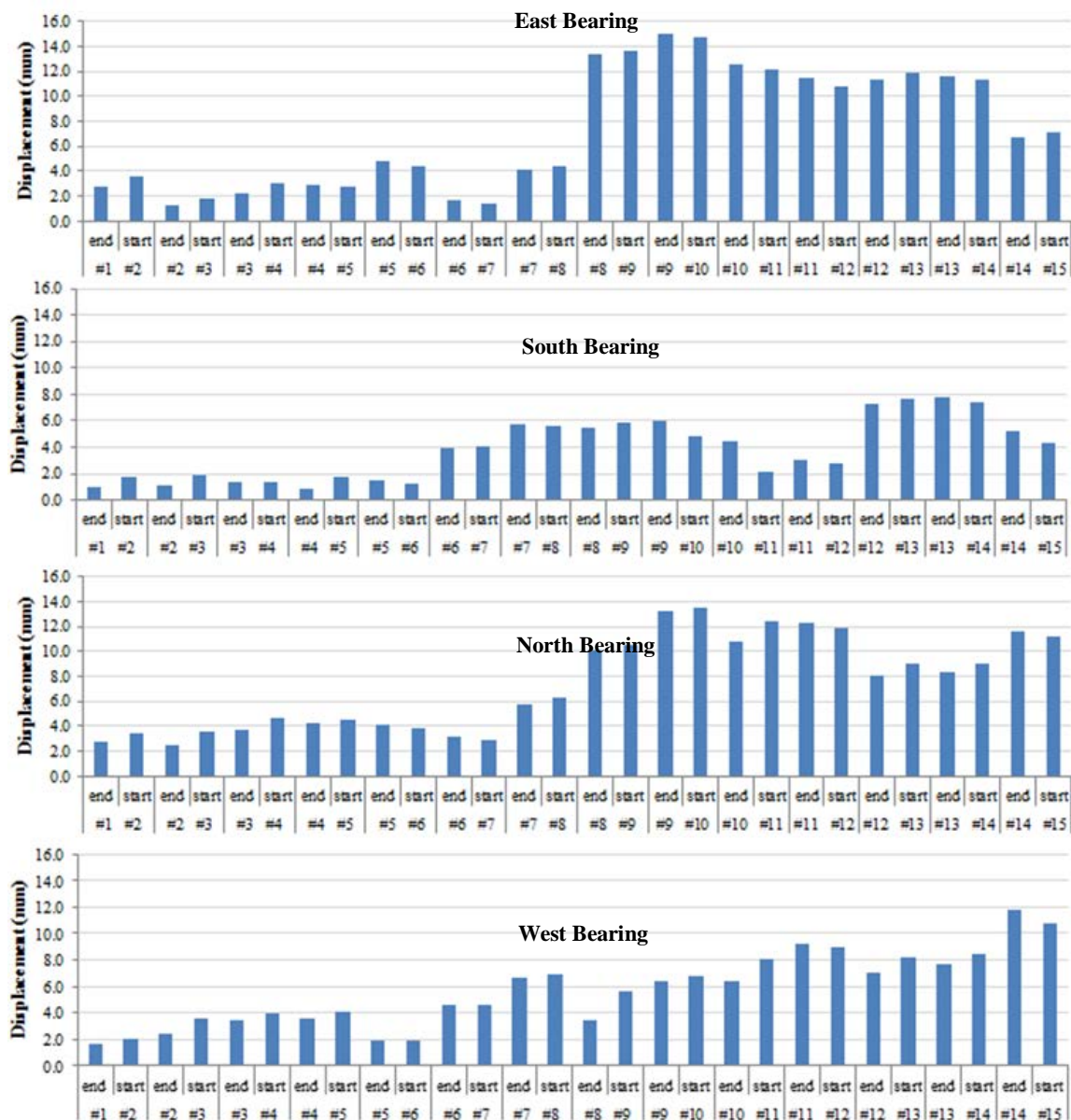


**Figure 5-16: Permanent displacement at the location of each LR bearing at the end of one simulation compared to the beginning of the next.**

## 5.6 Floor Accelerations in the Testbed Building

The peak acceleration profile of the building (peak acceleration versus floor level) in both horizontal directions for all earthquake simulations is shown in Figure 5-17.

Accelerations from multiple sensors were averaged as described in Section 4.6.3 based on the acceleration sensor layout in Figure 4-14. Although most individual simulations are not identified by input excitation, this plot format depicts the range of accelerations observed. The acceleration profile shape was similar for most excitations, which was almost linear from the base through the 4<sup>th</sup> floor followed by an increase in acceleration at the 5<sup>th</sup> and roof floors. The isolation system was very effective in attenuating the acceleration in the superstructure. Outliers are identified in Figure 5-17, which include on the low side: the service level motion Westmorland (WSM80) in both horizontal directions, and the sine wave simulations (SIN100(Y)- 1 & SIN100(Y)-2)) in the x-direction due to the unidirectional input; on the high side: Rinaldi (RRS88) in the y-direction as a result of the strong vertical input.

With the exception of RRS88, larger peak ground accelerations led to greater attenuation of acceleration as expected. Although it cannot represent variability due to ground motion frequency content, the reduction in floor accelerations relative to PGA is often used to quantify the effectiveness of the isolation system. During Diablo 95%, one of the largest motions applied to the system with PGA in the x-direction = 1g, the observed peak roof acceleration was 0.45g, which was a 65% decrease relative to PGA. Excluding the outliers, PGA ranged from around 0.3g to 1g in the x-direction and 0.24g to 1.18g in the y-direction, while base level peak acceleration (just above the isolators) ranged from 0.19g to 0.5g in both directions. For Rinaldi 88, the roof acceleration in the y-direction was greater than the PGA.



To directly investigate the floor acceleration as a function of ground motion intensity, the floor acceleration profiles, both absolute and normalized by PGA, are plotted for the increasing intensity Vogtle excitations (VOG75, VOG100, VOG125, VOG150 and VOG175) in Figure 5-18. Recall that a low pass filter with a cutoff frequency of 50 Hz was applied to all signals (Figure 4-5). The absolute floor accelerations increased consistently with increasing ground intensity, but the normalized accelerations decreased with increasing ground intensity as expected.

The influence of vertical excitation is considered by comparing the absolute and normalized acceleration profiles for Diablo 95% (XY), Diablo 80% and Rinaldi 88% (XY and 3D) (Figure 5-19). Even though the intensity of the Diablo 95% motion was substantially greater than the Diablo 80% motion, the floor accelerations were greater in Diablo 80%, which indicates that vertical excitation affected the recorded horizontal floor acceleration. For the Rinaldi motion, a significant amplification of horizontal floor acceleration was observed for 3D shaking relative to XY (horizontal only) shaking, which suggests a horizontal-vertical coupling phenomenon.

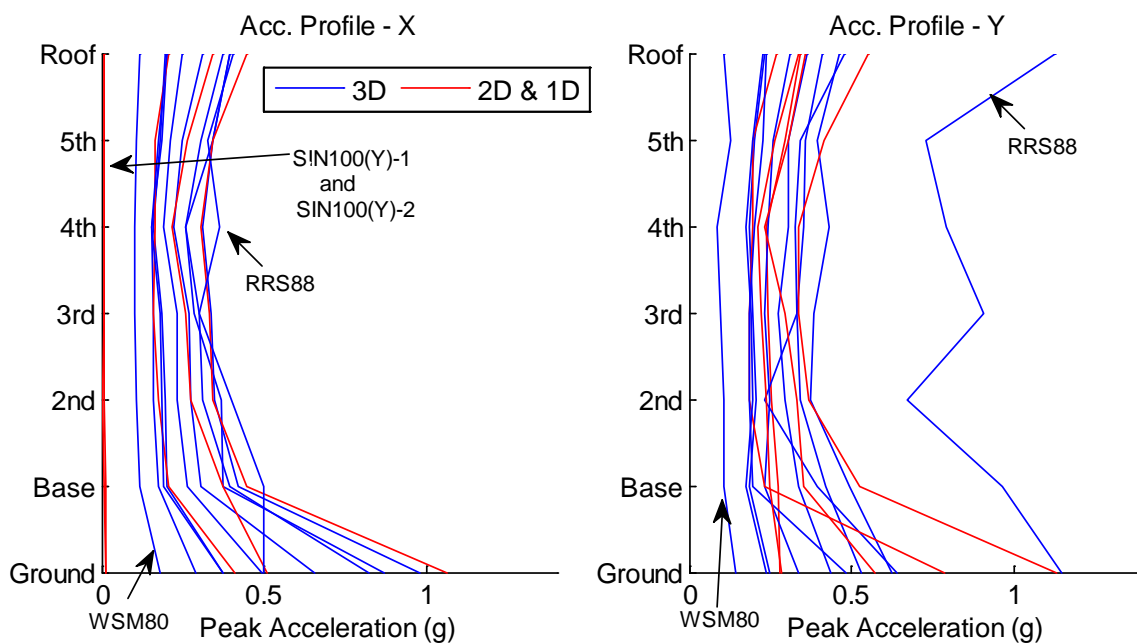


**Figure 5-17: Peak acceleration profile for all simulations in both horizontal directions.**

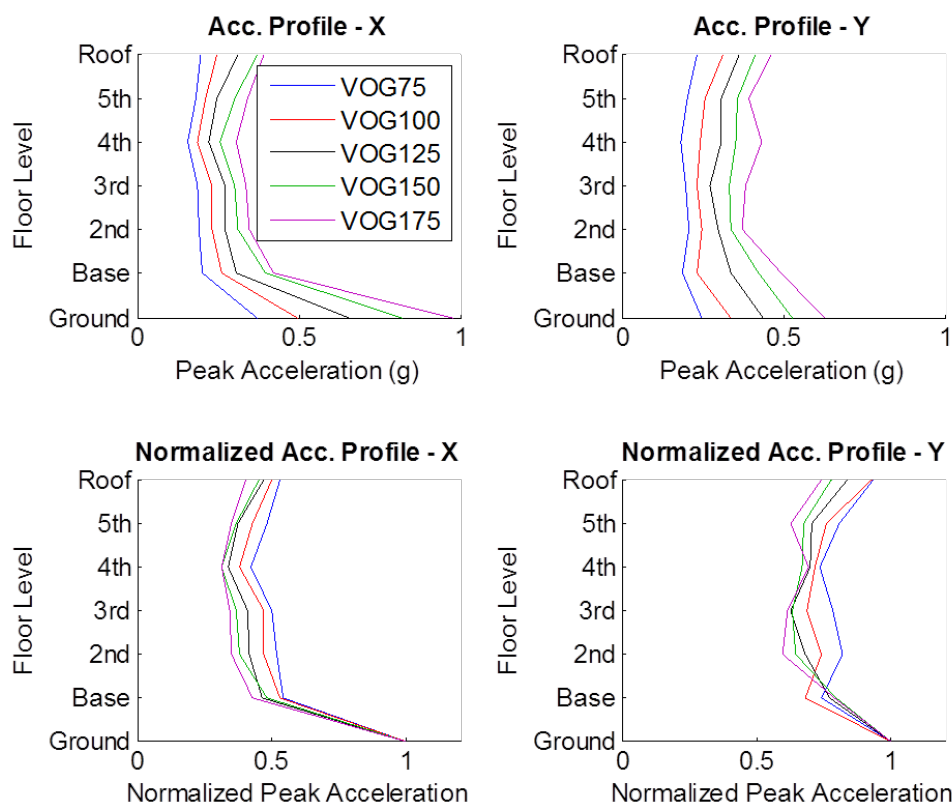


**Figure 5-18: Peak floor acceleration profiles for increasing intensity of Vogtle input excitation (75% - 175%).**

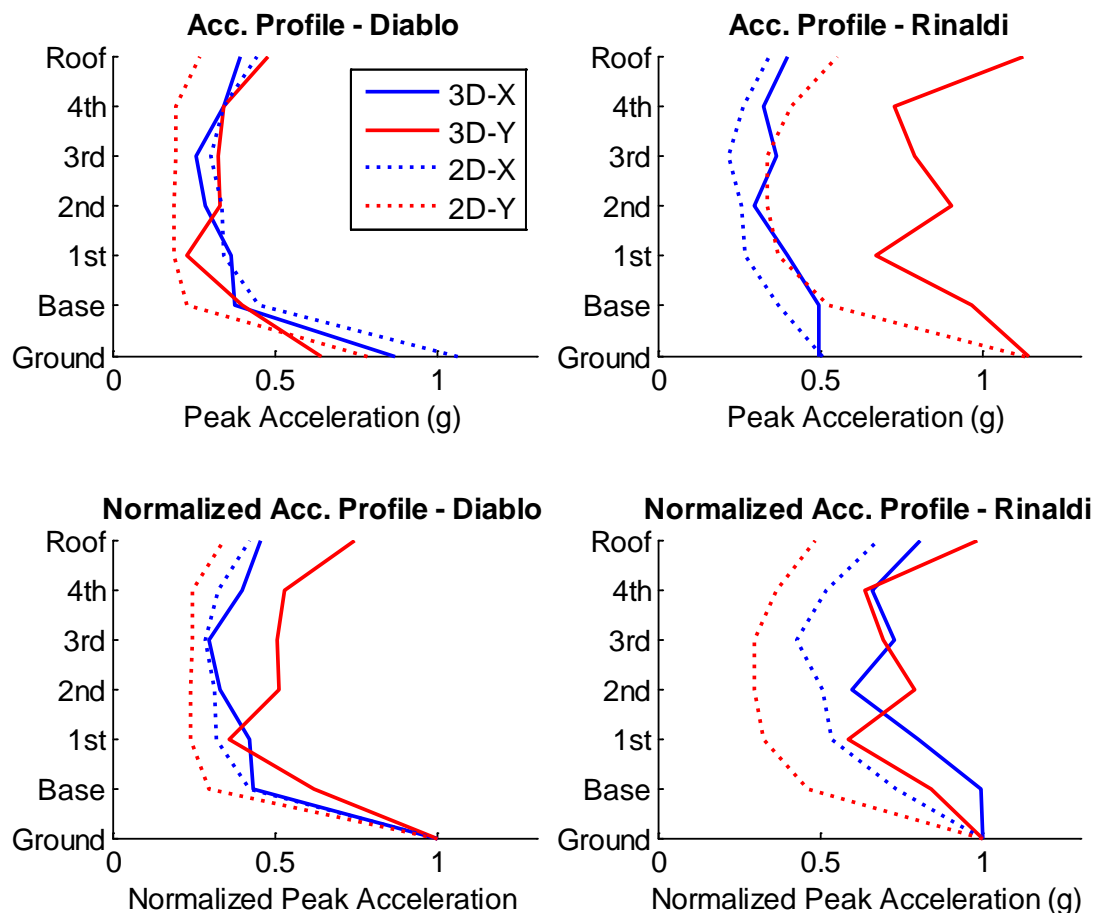


**Figure 5-19:** Peak absolute and normalized acceleration profile comparing XY and 3D excitations for Diablo (95% and 80% respectively) and Rinaldi (88%).

## 5.7 Story Drifts in Testbed Building

The peak story drift profiles (peak drift versus story level) in both horizontal directions for all earthquake simulations are shown in Figure 5-20. The drifts were calculated at the geometric center of each story level as described in Section 4.6.3. The peak drift in either direction occurred in the 2<sup>nd</sup> floor for all simulations, with the exception of both sine wave simulations, which incurred negligible drifts in the x-direction. The story drift

decreased from the 2<sup>nd</sup> floor to the roof level, where the peak roof drift was generally less than the first story drift.

The drifts for both RRS88(XY) and RRS88 in the y-direction were noticeably larger than the drifts observed in any other motion. This increase in drift was due to the predominance of low frequency components associated with the near-fault motion. The input acceleration history for the RRS88 simulation, shown in Figure 4-18, contains a strong pulse with a duration of about 1 sec at the instant of peak acceleration in the y-direction. The relative intensity of ground acceleration in the x and y-directions was consistent with the trend of the drift profiles. Like the accelerations, the drifts increased significantly from RRS2D to RRS3D. The drift in the 5<sup>th</sup> floor was larger than the 4<sup>th</sup> floor in the y-direction for RRS3D, which is consistent with the acceleration profile of Figure 5-19.

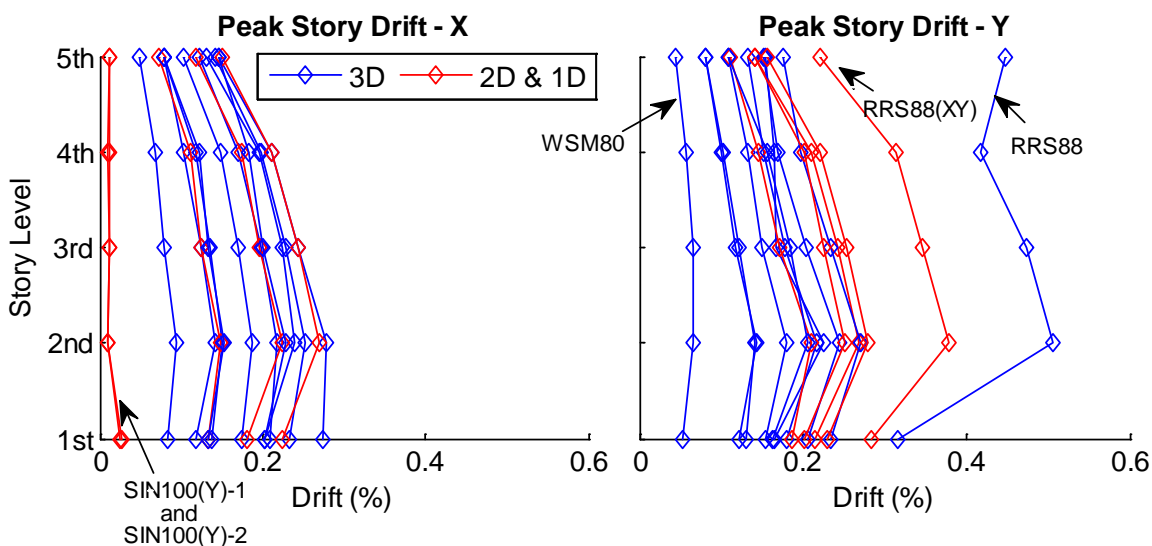


**Figure 5-20: Peak story drift throughout the height of the building for all excitations in x and y directions.**

## 5.8 Summary of Observations

The experimental responses of the LR bearings showed that over half of the trials produced peak isolator displacements that were greater than the design displacement of 300 mm. The largest peak experimental bearing displacement was 547 mm which was very close to the limit displacement imposed by the test facility of 550 mm. Rotation at the base level was observed due to the eccentricity of the mass of the roof of the building and unequal bay widths. The code prescribed amplification factor was shown to be generally conservative when compared to the amplification of displacement demand in the experiment due to torsion. The largest base shear coefficient on the LR bearings observed during the experiment was 0.28. The forces in the CL bearings were not recorded; however, there was no evidence to suggest that the forces in the CL bearings were significant. Individual LR bearing experienced significant tensile forces due to the load transfer between LR and CL bearings. A small residual displacement in the LR bearings was observed due to slippage of the base plate.

The floor acceleration profile in the testbed building obtained from all trials showed that in general it was almost linear from the base through the 4<sup>th</sup> floor followed by an increase in acceleration at the 5<sup>th</sup> and roof floors. Furthermore, it showed that the isolation system was very effective in attenuating the superstructure acceleration. The story drift profile in the testbed building obtained from all trials showed that the peak story drift in general occurred in the 2<sup>nd</sup> floor and decreased with increasing in story level that resulted in the peak roof drift to generally be lower than the first story drift.

## **CHAPTER 6: TECHNICAL RESPONSE OF HYBRID LR ISOLATION SYSTEM**

In this chapter, specific technical aspects germane to the response of the hybrid LR isolation system are explored. This is the first time that LR bearings and CL bearings were tested as a hybrid isolation system on an earthquake simulator. Thus, unique load transfer between the two types of devices and stability aspects of the system are explored in depth. The topics discussed in this chapter include bolt slip, load transfer, and repeatability of the isolation system response after many tests.

### **6.1 Bolt Slip in LR Bearings**

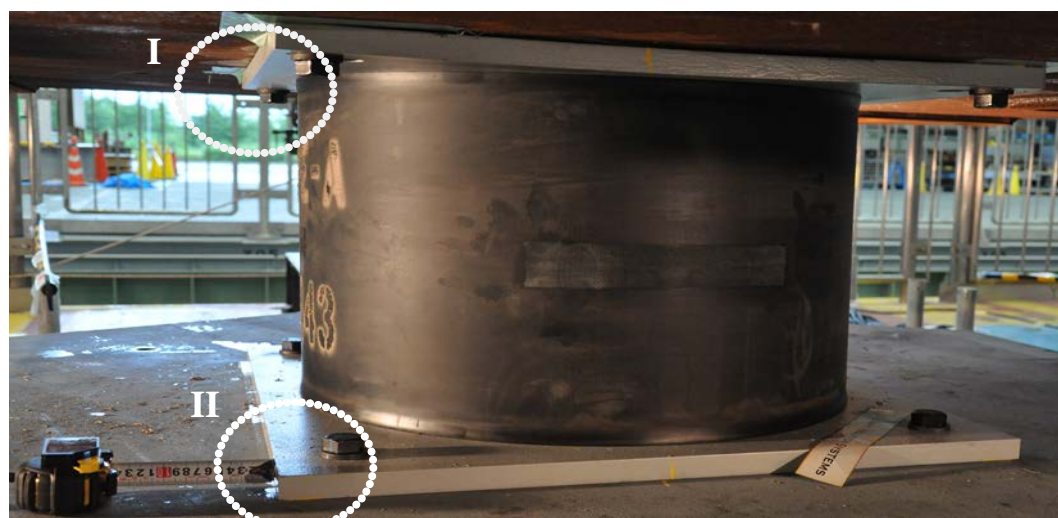
Due to a variety of conditions unique to this experimental program, the bolted connections securing the LR bearings to the structure above and steel connecting plates below did not satisfy slip critical criteria, and slippage of the bolts was observed. The connections were anticipated to reach the slip critical limit at bearing displacements of about 400 to 450 mm (16-18 in), but the bearings were tested out to displacements of 550 mm (22 in). In practice, the bearings would never be designed with low capacity at the connection level. The following factors influenced the connection design: 1) technical difficulties and prohibitive cost associated with drilling and tapping holes in the base of the testbed structure from beneath prompted the project team to select the smallest possible bolt size for the connection. 2) The bolt holes were oversized by 9 mm (0.4 in), deviating from standard practice, to accommodate ease of installation when lowering the

testbed structure by crane over the 9 pre-installed isolators. 3) During pre-test planning and negotiation, when the connection design was finalized, it was doubtful that the bearings would be tested beyond 400 mm (16 in). Since bolt slip can easily be avoided in practice, its occurrence and subsequent influence on the response of the isolated building are documented briefly here for completeness.

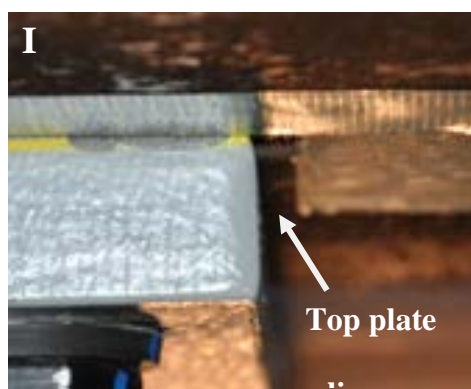
As mentioned above, slippage was observed in the bolts that secured the LR bearing top connecting plate to the base of the structure above and the bottom connecting plate to the steel hex plate of the load cell assembly. Evidence of bolt slip included: 1) loud banging noise heard in-phase with the displacement cycles and subsequently observed instantaneous force drops and/or spikes in the LR bearing forces recorded by the load cells, and 2) movement of the LR bearings relative to the structure above and below observed in post-test inspection, which was shown in Figure 5-15 and is further illustrated in Figure 6-1 below.

The bolt slip was first observed during Vogtle 125%, and continued to be observed throughout the simulation sequence, wherein larger displacements in the bearings increased the instances of bolt slip. Some slip was observed in all four LRBs, but the largest force spikes and drops occurred in the East bearing. Figures 6-2 plot snapshots of the *unfiltered* force history of the East bearing (LRB-E) in the x and y-directions for 8 of the 15 simulations, which are labeled by trial number, the 3 letter abbreviation for the ground motion, and the scale factor. (Recall that, as stated in Chapter 4, all data shown is filtered unless otherwise indicated.) In these figures, the force drops are first observed in Vogtle 125% around 11.5 sec and 12 sec. In the next trial (Vogtle 150%), additional

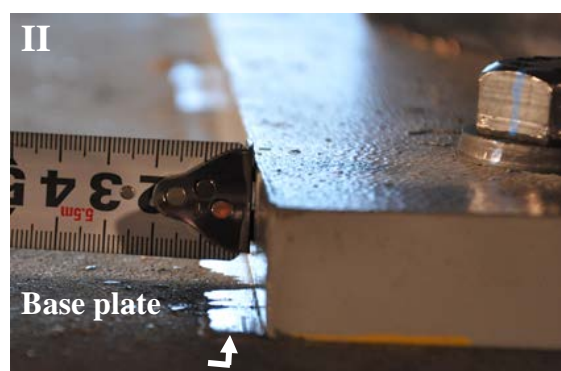
drops are observed at other time instances, and spikes are observed at 11.5 and 12 seconds. Then, in Vogtle 175%, even more spikes and drops are observed. After Vogtle 175%, force drops and spikes continue to appear (e.g. Diablo 80% at about 15 sec) but with decreasing intensity. The drops and spikes are also observed in the bearing hysteresis loops, such as those plotted for LRB-E during Vogtle 125% and Vogtle 150% (Figure 6-3). The force drops and spikes tend to be observed during large displacement cycles just before the peak displacement is reached.



(a)



(b)



(c)

**Figure 6-1: Movement of (a) East LR bearing relative to (b) top and (c) bottom plates.**



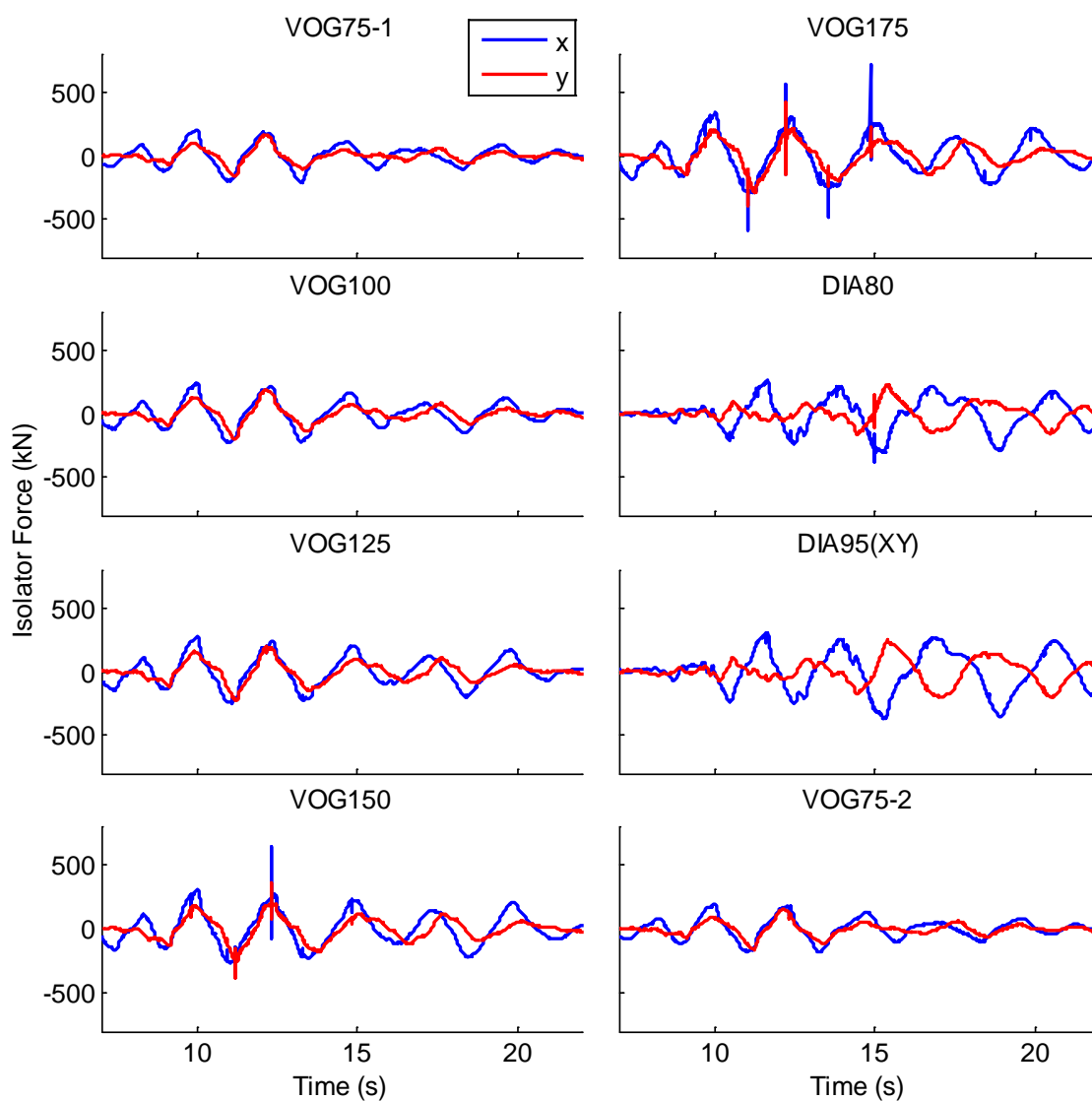


**Figure 6-2:** Horizontal force history of the East bearing (LRB-E) in the x- and y-directions for a subset of the trials.

The horizontal and vertical force histories for all four LR bearings are shown in Figure 6-4 for Vogtle 150%, which demonstrates that the greatest amount of bolt slip occurred in LRB-E. During Vogtle 150%, LRB-E is the only bearing that experienced both substantial force spikes and force drops. Several force drops are observed in LRB-W, but

they are small in intensity compared to LRB-E. Only one small drop/spike for LRB-N (around 12 sec), and two in LRB-S are evident (Figure 6-4).

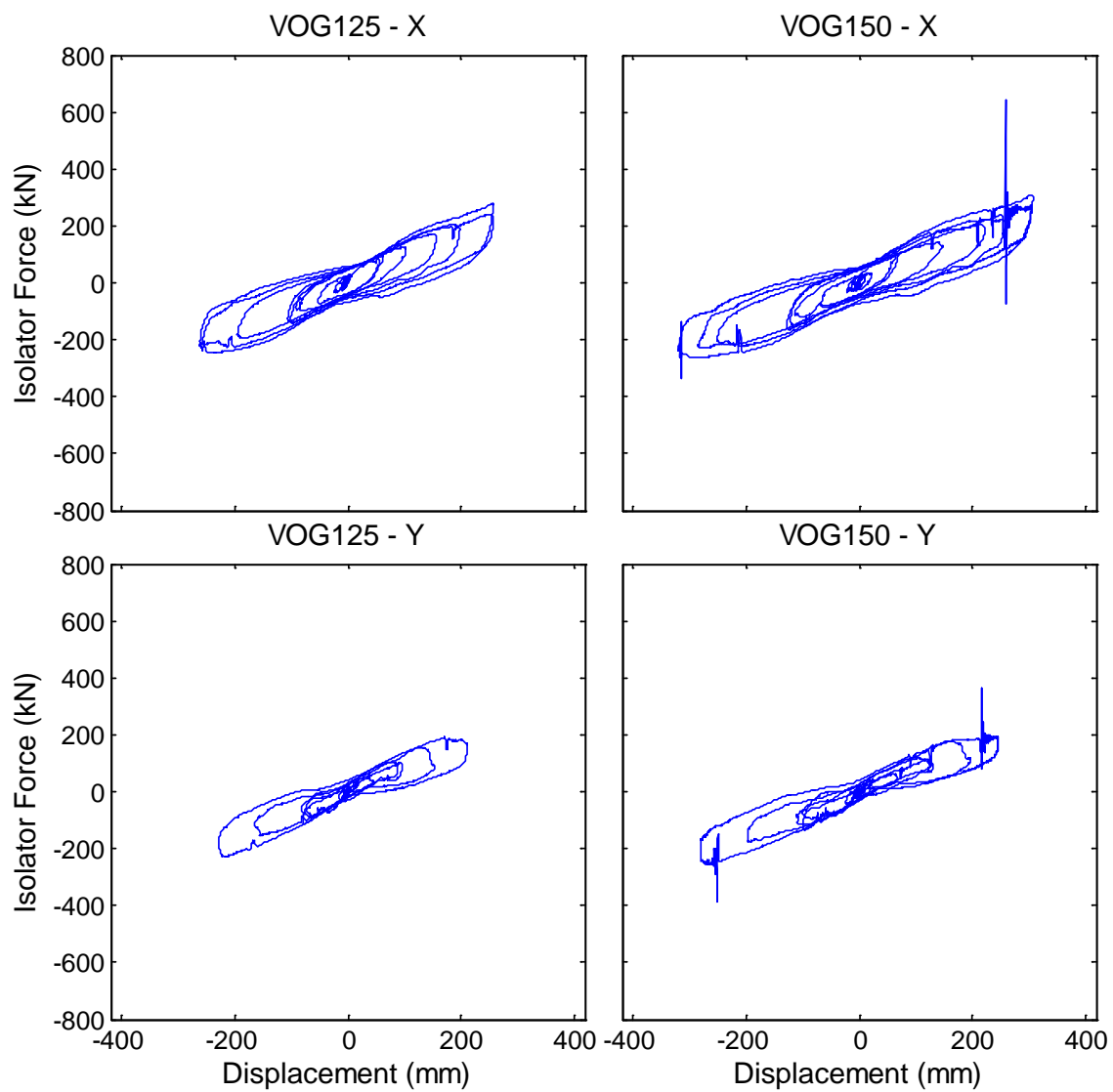
The synchronized vertical force histories of each bearing are also plotted in Figure 6-4 to provide additional insight as to why the bolt slip may have occurred. One proposed theory is that bearing tension contributed to the bolt slip. The addition of CL bearings to the isolation system did not entirely prevent tension in the LR bearings, which is discussed in the next section. During the Vogtle 150% record, tension (bearing vertical force greater than zero in Figure 6-4) is observed more frequently and with larger intensity in LRB-E and LRB-W, which also have the most obvious horizontal force drops/spikes. The instances of bolt slip seen in this figure do not align with the instances of peak tension, but horizontal force drops/spikes always occur after tension has been observed in the bearing. At the same time, LRB-E is subjected to the largest displacement demands (423 mm (16.7 in) in Vogtle 150% compared to 357 mm (14.1 in) in LRB-W), and thus experiences a larger shear force that makes it more susceptible to bolt slip.

Figure 6-5 plots the unfiltered force in LRB-E and unfiltered accelerations in the SE column sensors at all floors in x and y-directions, respectively, for Vogtle 150%. In this figure, a spike in the bearing horizontal force is always preceded by a small force drop. The following explanation is consistent with the drop/spike pattern. After a large tension excursion, the bolts start to slip and move with respect to the oversized holes. The bolt movement stops the bearing movement, causing it to instantaneously unload, corresponding to the first drop in force. If the bolts reach the other side of the oversized hole, an impact occurs, resulting in a force spike and a loud banging noise. Due to the

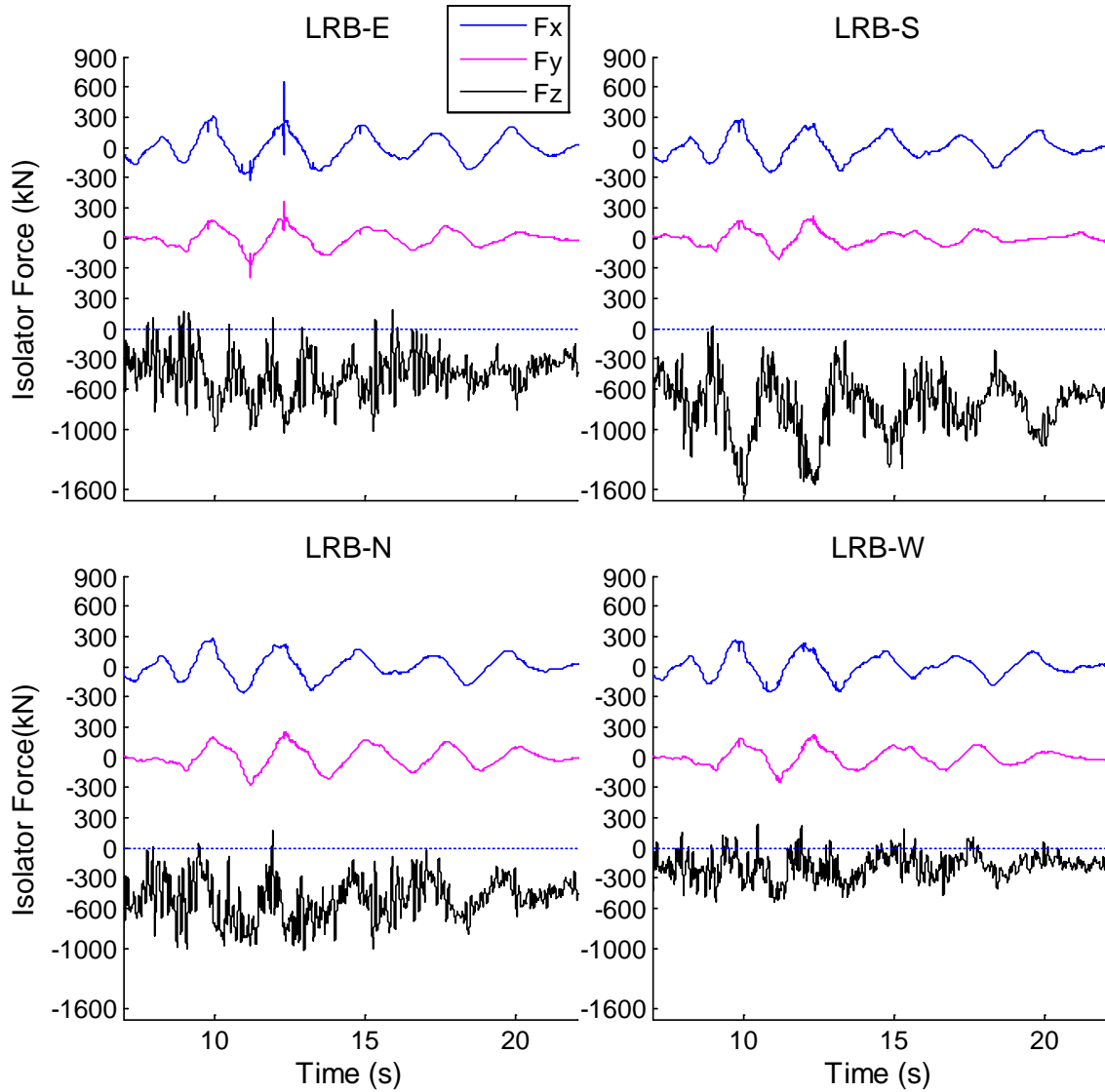
instantaneous nature of the impact, dynamic amplification occurs, causing what appears to be an instantaneous spike/drop, but is actually very high frequency oscillation.

Figure 6-5 also shows that the bolt slip induces a dynamic amplification in the floor accelerations that diminishes with increasing height in the building. The acceleration spikes appear to be timed with the first force drop associated with the start of bolt slip and not the second force spike/drop associated with impact of the bolt against the other side of the hole. In the overall test program, bolt slip (by itself) did not appear to affect the performance of nonstructural components or cause disruption of contents, located on the 4<sup>th</sup> floor and above. There is no evidence of whether nonstructural components on the lower floors would have been affected by the bolt slip. Filtering the recorded force and acceleration data significantly reduced the drops and spikes resulting from bolt slip, but did not completely eliminate them.

In summary, in this experimental program, the bolt slip did not appear to affect the response of the isolation system aside from the drops/spikes in force, and the adverse effects on the structural response were limited. However, the possibility that increased acceleration would affect the response of nonstructural components and contents or compromise performance in any way is an unnecessary risk. The observations from these experiments reinforce the conclusion that bearings should always be designed with slip critical connections, as they routinely are in practice.



**Figure 6-3: X and y-direction hysteresis loops (horizontal force vs. displacement) of the East bearing (LRB-E) during Vogtle 125% and Vogtle 150%.**



**Figure 6-4: Horizontal ( $F_x$  and  $F_y$ ) and vertical ( $F_z$ ) force history of all four LR bearings during Vogtle 150%.**

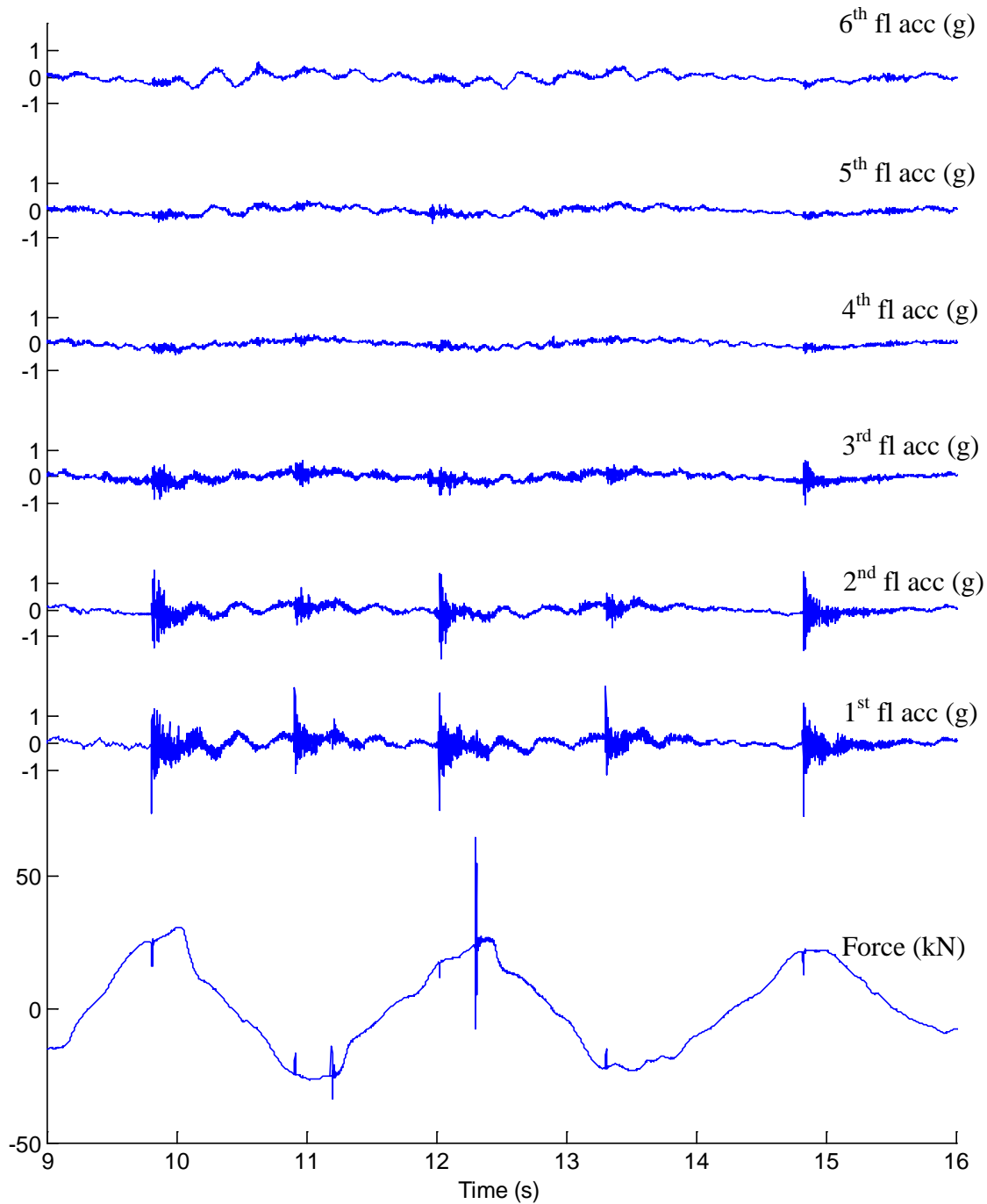


**Figure 6-5:** Propagation of bolt slip through the height of the structure in x-direction during Vogtle 150%; unfiltered horizontal force in LRB-E and 1<sup>st</sup> – 6<sup>th</sup> floor acceleration in SE column.

## 6.2 Transfer of Load Between Bearings

Axial force transfer between the LR bearings and the CL bearings over the course of the simulations was expected. LR bearings, when subjected to combined compressive load and lateral displacement, reduce in height, as shown in Figure 6-6(a), where  $P$  is the axial force and  $\delta$  is the downward deflection or shortening. However, downward movement of the LR bearings is constrained by the rigidity of the base diaphragm and the axial stiffness of the CL bearings, which is about 2.5 times the stiffness of the LR bearings. The constraint generates an upward force  $F$  on the bearings (Figure 6-6(b)), which causes load to redistribute from the LR bearings to other isolators. If  $P$  exceeds  $F$ , a reduction in axial compressive force carried by the LR bearings occurs, while if  $F$  exceeds  $P$  the LR bearing will go into tension to satisfy the base diaphragm constraint. This type of behavior, which is subsequently referred as the “load transfer” effect, can occur at large displacements and is unrelated to system overturning).

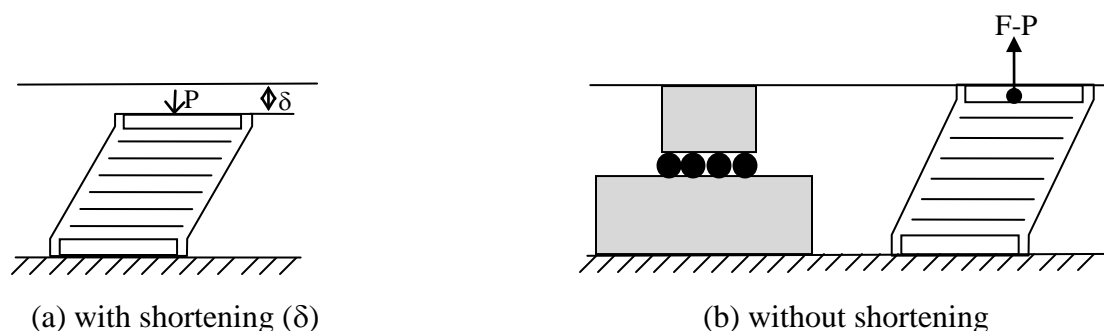


**Figure 6-6: Resultant action on LR bearings as a result of CL bearings and base diaphragm constraint**

Evidence of the load transfer effect was observed during the test program. Histories of isolator displacements and axial forces on individual LR bearings and summed over all LR bearings are shown for three different XY excitations: sine wave input (Figure 6-7), Diablo 95% (Figure 6-8) and Rinaldi 88% (Figure 6-9). The displacements shown have been computed by averaging displacements of LRB-E and LRB-W in the x-direction, and LRB-N and LRB-S in the y-direction; axial force is considered to be positive in tension. Recall that forces acting on the CL bearings were not measured during the experimental program. The sine wave simulation is the simplest to interpret because the input to the building was unidirectional in the y-direction, generating very little torsional response in the isolators. Vertical lines drawn through local (vector sum) peak displacements and extended through the axial force plots demonstrate that every time a peak displacement is reached (either local maximum or local minimum), a corresponding net reduction in total axial force of the 4 LR bearings (black line in Figure 6-7) is observed. The axial forces in individual LR bearings are more complex since overturning effects are present. LRB-N and LRB-S, which being close to the neutral axis of the building plan for y-direction input should not experience much overturning, also appear to consistently unload at every local displacement peak – max or min (Figure 6-7). The instant of least compressive axial force in the bearings does not exactly correspond to the instant of peak displacement shown, but is close enough that the load transfer trend is confirmed. With regard to individual bearings, LRB-W sustains maximum compression for displacements in the positive y-direction and minimum compression for displacements in the negative y-direction, while LRB-E experiences the opposite, which is the expected trend when subjected to overturning related axial force demands (Figure 6-7). Thus, for this



excitation, the overturning effect in LRB-E and LRB-W is stronger than the load transfer effect. However, fluctuation of the axial force between the displacement peaks suggests that both the overturning effect and the load transfer effect are contributing to the response.

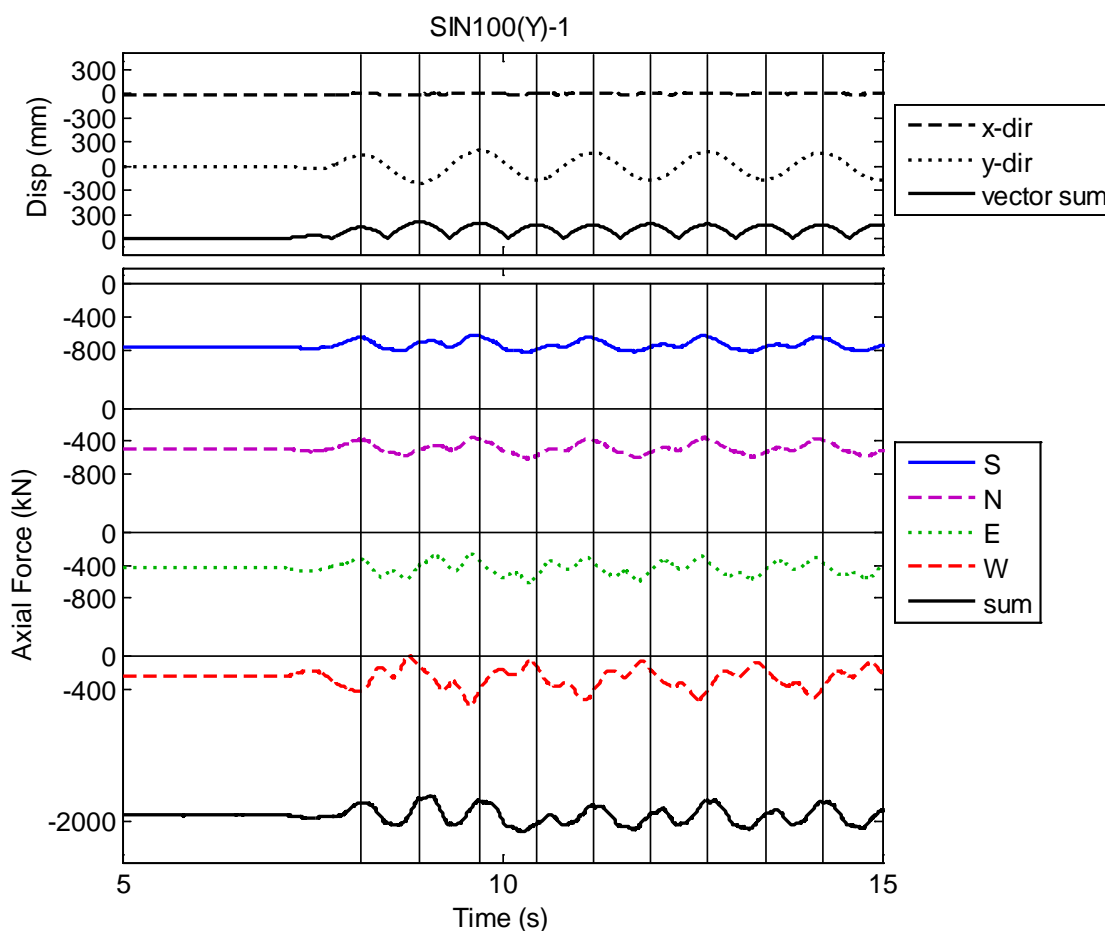


**Figure 6-7:** History of average horizontal displacement (x, y and vector sum), and axial force in individual LR bearings and summed over all LR bearings for Sine Wave (XY).

For Diablo 95% (XY) (Figure 6-8), substantial load transfer, as indicated by axial unloading of the LR bearings, occurs at 4 different time instants corresponding to peak displacements (combination of x and y-direction movement) observed at the center of the building. LRB-E sustains tension at every one of these time instants, and at two different

instants (just after 15 sec and about 19 sec), the total axial force on the LR bearings exceeds 0, indicating that the entire weight of the building has shifted to the CL bearings. The load transfer effect is much more significant for this simulation than the sine wave since the isolator displacement is much larger (550 mm or 22 in compared to 210 mm or 8 in, see Figure 5-1). As a result of the torsional demand on the isolation system discussed previously, the largest displacements are consistently observed in LRB-E, which is also subjected to the greatest tension.

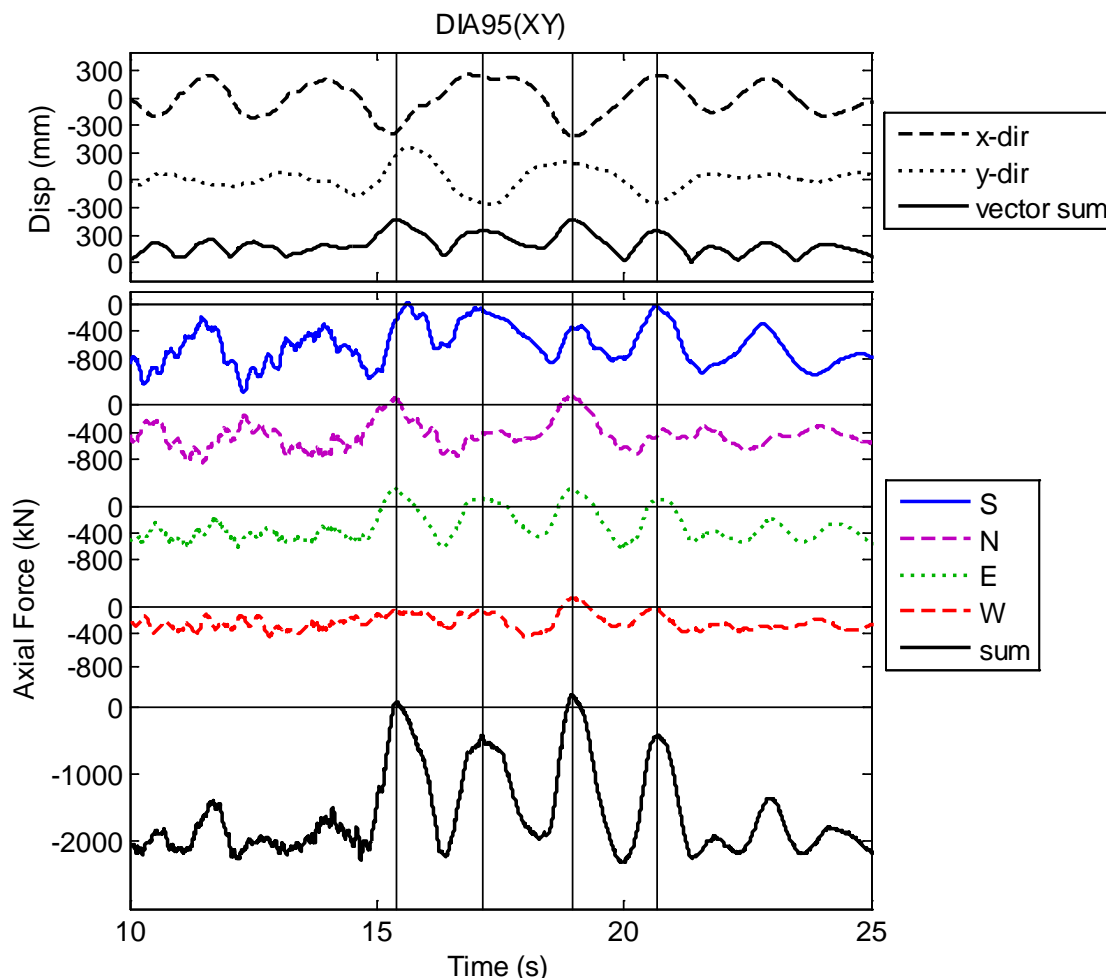


**Figure 6-8:** History of average horizontal displacement (x, y and vector sum), and axial force in individual LR bearings and summed over all LR bearings for Diablo 95% (XY).

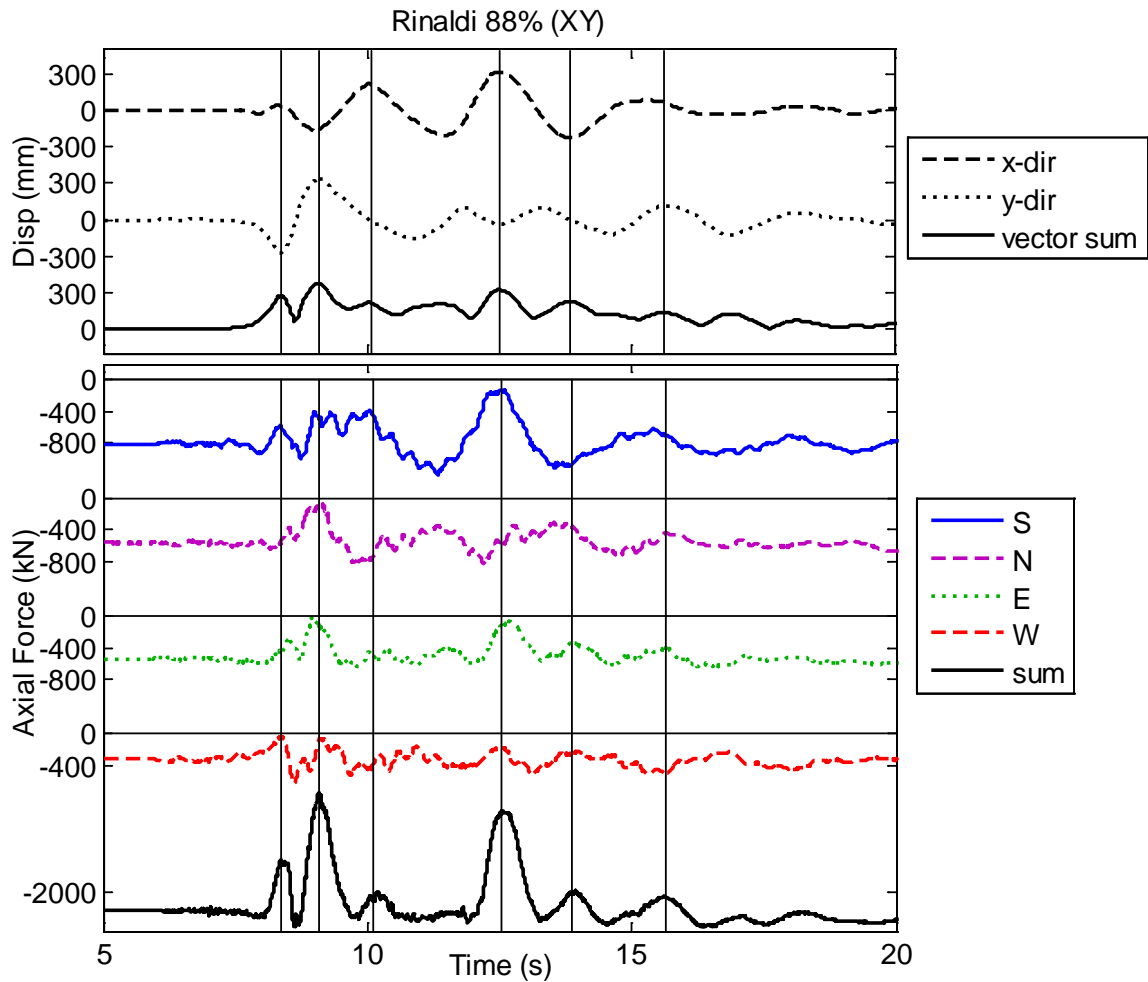


**Figure 6-9:** History of average horizontal displacement (x, y and vector sum), and axial force in individual LR bearings and summed over all LR bearings for Rinaldi 88% (XY).

To understand the extent of load transfer when the isolator displacement is 550 mm, consider that the overlapping area  $A_r$  between the top and bottom areas of a circular bearing at a given displacement is calculated by (AASHTO, 2010):

$$\delta = 2 \cos^{-1} \left( \frac{D_{max}}{D} \right) = 2 * \cos^{-1} \left( \frac{550 \text{ mm}}{698.5 \text{ mm}} \right) = 1.34 \quad (6.1)$$

$$A_r = \frac{D^2}{4} (\delta - \sin \delta) = \frac{698.5^2}{4} (1.34 - \sin(1.34)) = 44920 \text{ mm}^2 \quad (6.2)$$

where  $D$  is the bearing diameter and  $D_{max}$  is the peak displacement. At the peak recorded displacement of 550 mm (22 in), the overlapping area is a small fraction – about 12% – of the total bonded area (383200 mm<sup>2</sup> or 592 in<sup>2</sup>). According to the overlapping area rule (Buckle and Liu 1994), the bearing has sustained an 88% loss in axial force capacity, which confirms that upward forces are generated to counteract the natural shortening in the bearing. The displacement pattern shown in the time series plots of Figure 6-8 (also in Figure 5-4) indicates that the peak displacement cycle occurs along a diagonal (from NE corner to SW corner). Since the load transfer is partially counteracted by the effects of overturning, LRB-N and LRB-E sustain less load transfer (axial unloading) for a positive excursion in  $x$  and a negative excursion in  $y$ , and LRB-S sustains less load transfer for a negative excursion in  $x$  and a positive excursion in  $y$  (Figure 6-8). The trend for LRB-W is inconclusive. The load transfer effect may be stronger than the overturning effect in LRB-W because it carries significantly less static weight than the rest of the LR bearings (Section 5.4). The load transfer effect is also observed during Rinaldi 88% (Figure 6-9), although the less axial force unloading occurs due to the lower peak displacement in Rinaldi (380 mm or 15 in from Figure 5-1).

While the transfer of load between LR bearings and CL bearings is evident for XY simulations, the trends are more difficult to ascertain in 3D simulations that include vertical excitation. In this series, Rinaldi 88% is the only excitation applied both with and without vertical input, thus allowing for the effects of vertical shaking to be directly assessed. Figure 6-10 shows the axial force histories for each of the four bearings and the total for Rinaldi 88%. By inspection, the axial force histories for 3D excitation are rich in

higher frequency content compared to the force histories for XY excitation. Thus, instances of load transfer are less obvious. However, from a direct comparison of the axial forces in Rinaldi 88% (XY) and Rinaldi 88% (Figure 6-11), the 3D forces oscillate about the backbone of the XY forces. Thus, the 3D force variation is essentially equal to the XY force variation augmented by an additional high frequency component. To eliminate the force variation due to vertical excitation, and thus verify the pattern of load transfer for the 3D simulation, a low-pass Butterworth filter with a cutoff frequency of 2 Hz is applied to the total axial force for Rinaldi 88%. This filter has the same shape as that shown in Figure 4-5 when normalized with respect to the cutoff frequency. The 2 Hz cutoff frequency was selected since it preserves the frequencies related to horizontal vibration of the isolation system but eliminates typical frequency of vertical excitation and response. The resulting filtered axial force is shown in Figure 6-11 as a red dashed line superimposed over the unfiltered total axial force. The filtered total axial force for 3D excitation matches that for XY excitation very closely.

Knowing that the trend for 3D excitation can be identified, an XY versus 3D comparison is attempted for the Diablo excitation, where the 3D simulation data is available at a different scale factor (80%) than the XY simulation (95%). The total (vector sum) displacement (computed as described for Figures 6-7 to 6-9), axial forces in each LR bearing, and total axial force (with and without filtering for the 3D simulation) are compared for Diablo 95% (XY) and Diablo 80% in Figure 6-12. The peak displacement demand at the center of the building (Figure 6-12) is about 25% lower in Diablo 80% than Diablo 95% (XY). However, in Diablo 80%, about half of the load transfers from

the LR bearings to the CL bearings, while in Diablo 95% (XY), all of the load transfers from the LR bearings to the CL bearings at two different time instances. This indicates a nonlinear or escalating trend in the amount of load transfer with increasing horizontal displacement. The bearing tensile force demands would need to be analyzed prior to executing Diablo 95% as a 3D simulation; as it stands, almost no tension was observed in Diablo 80% (Figure 6-12).

In the context of the previous information, horizontal displacement and axial force data is presented for Vogtle 175% (Figure 6-13), which represents the largest simultaneous horizontal displacement and vertical excitation. The pattern of load transfer for individual LR bearings is evident even without filtering, and applying filtering to the total force confirms the pattern. Peak tensile demands in individual bearings are not as great for Vogtle 175% as they were for Diablo 95% (XY), for which the bearing displacements are largest, or Rinaldi 88%, for which the vertical excitation input is largest.

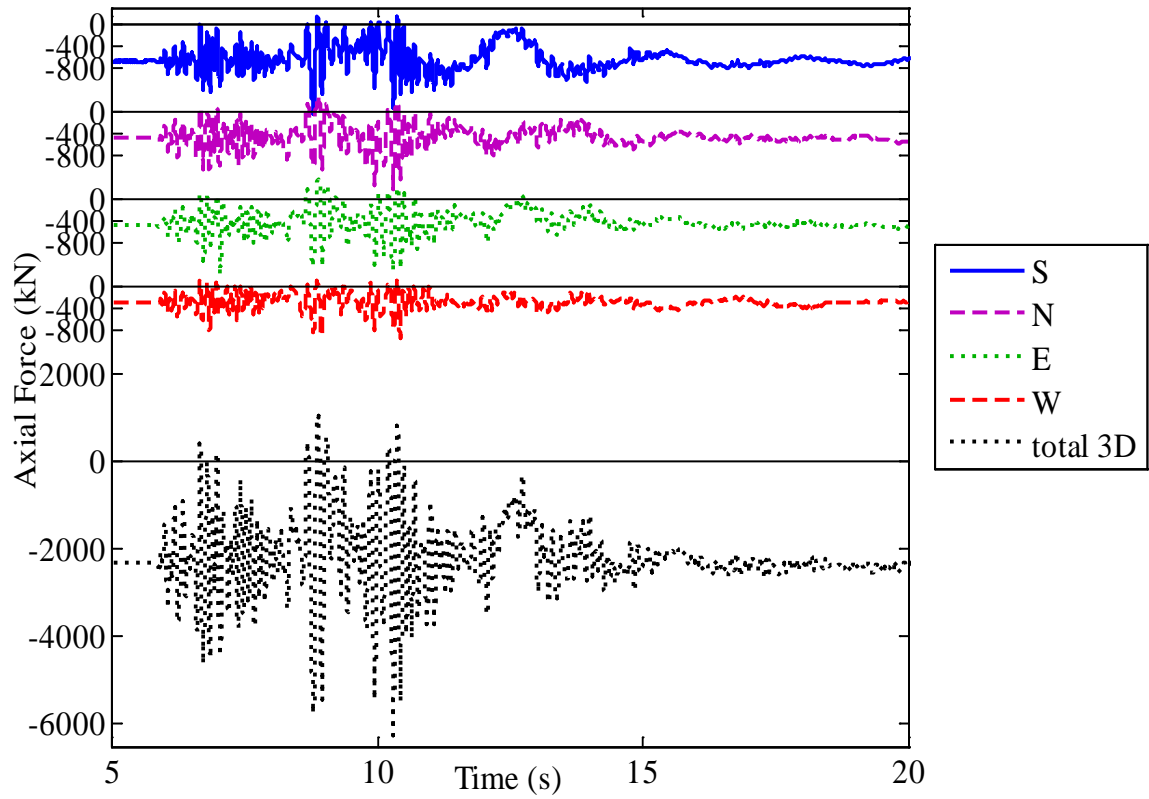


**Figure 6-10:** History of axial force in individual LR bearings and summed over all LR bearings for Rinaldi 88%.

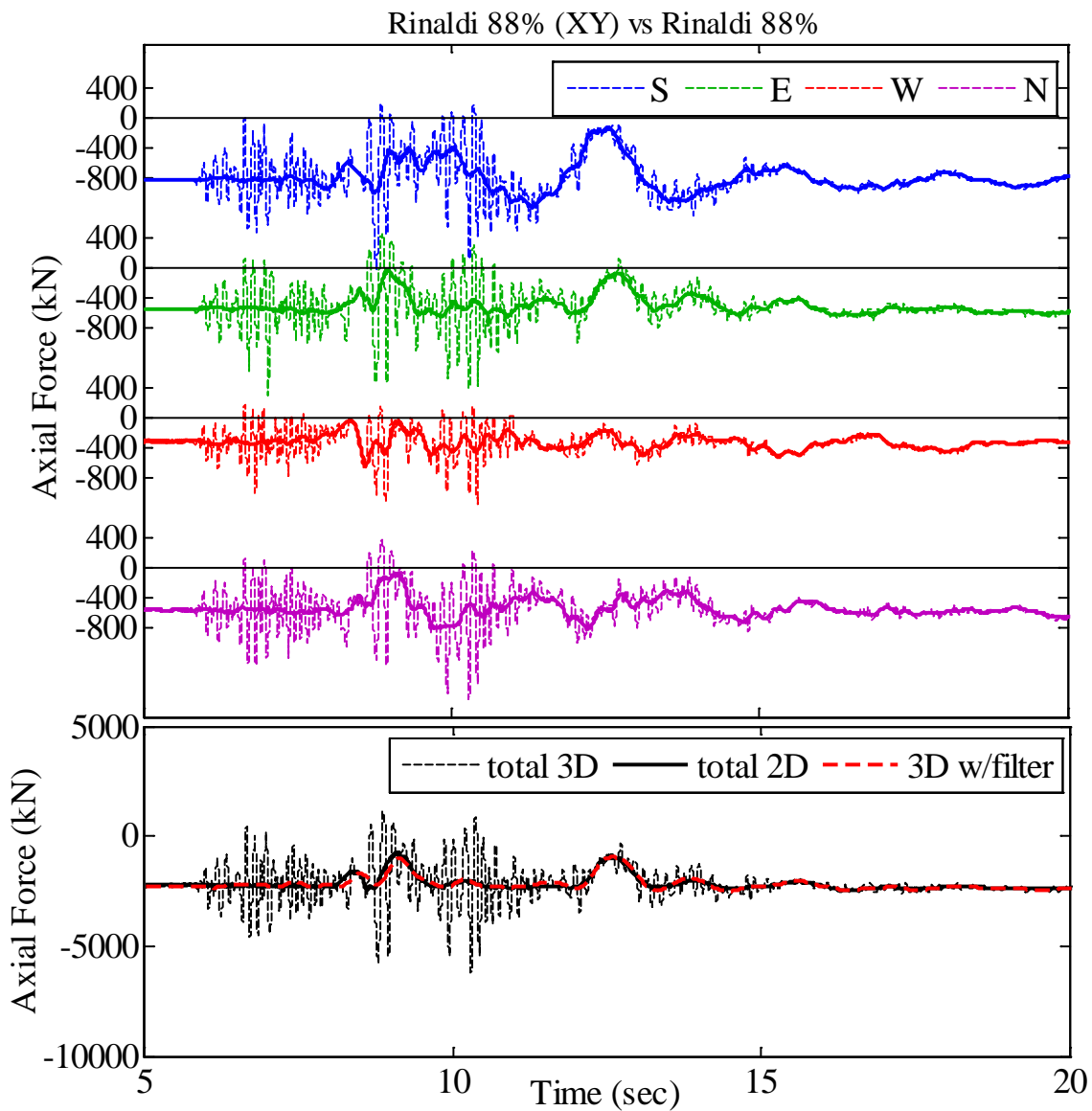


**Figure 6-11: History of axial force in individual LR bearings and summed over all LR bearings comparing Rinaldi 88% – dashed line – and Rinaldi 88% (XY) – solid line. A low pass filter with a cutoff frequency of 2 Hz was applied to the total axial force for Rinaldi 88% and is superimposed over the total, shown as a red dashed line.**



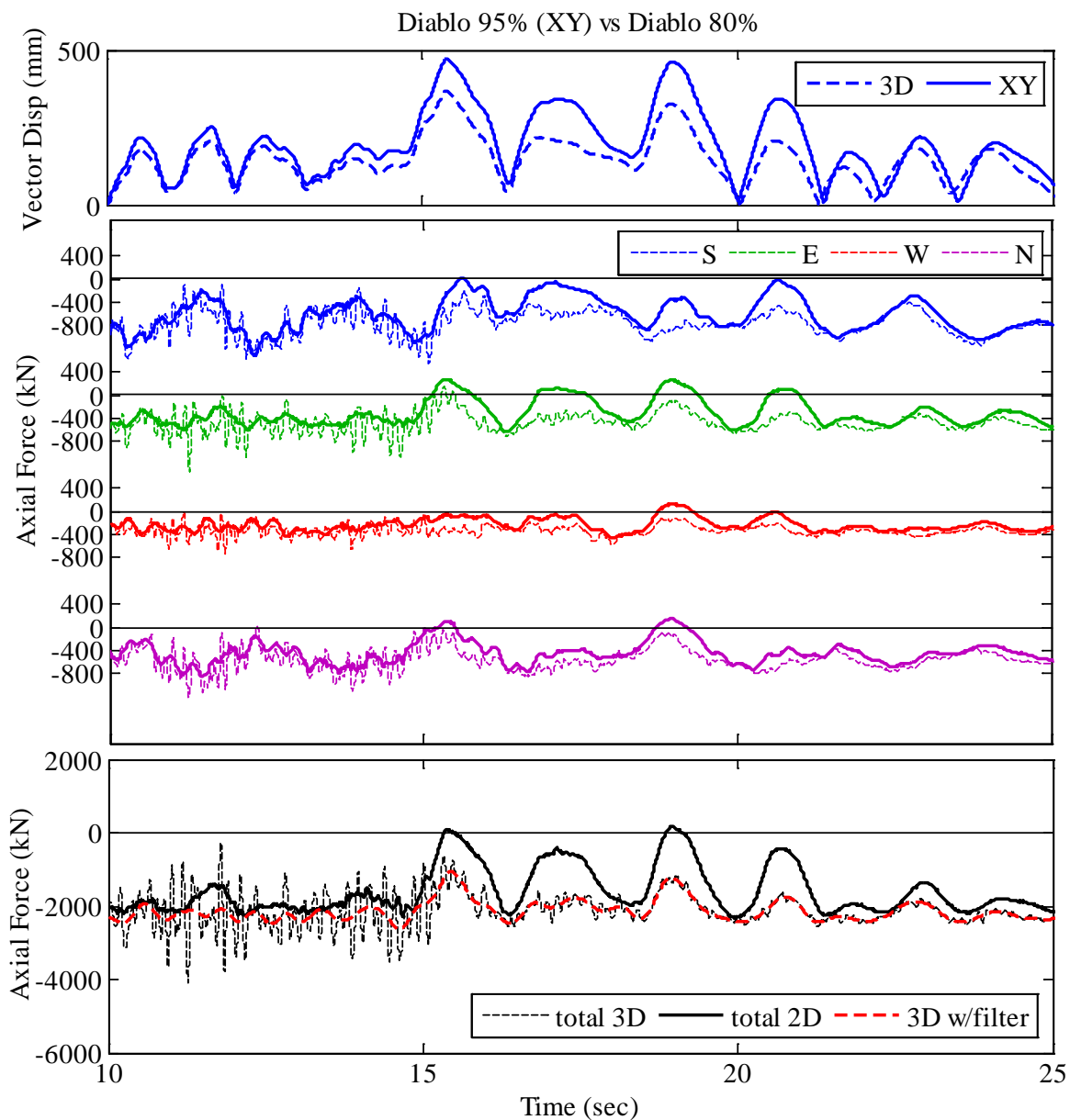


**Figure 6-12:** History of average vector sum displacement at building center, axial force in individual LR bearings and axial force summed over all LR bearings comparing Diablo 95% – dashed line – and Diablo 80% (XY) – solid line. A low pass filter with a cutoff frequency of 2 Hz was applied to the total axial force for Diablo 80% and is superimposed over the total, shown as a red dashed line.

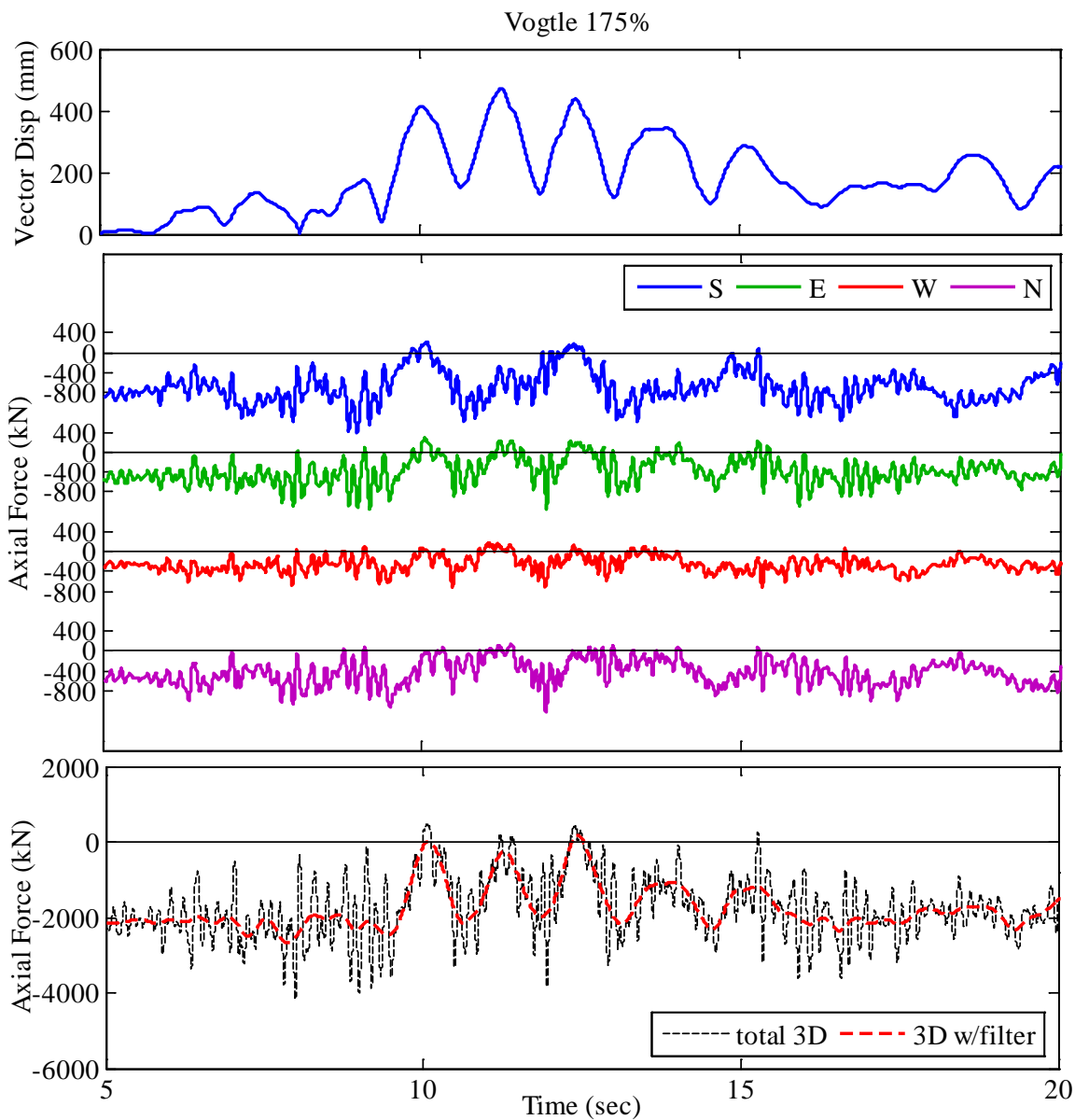


**Figure 6-13:** History of average vector sum displacement at building center, axial force in individual LR bearings and axial force summed over all LR bearings for Vogtle 175%. A low pass filter with a cutoff frequency of 2 Hz was applied to the total axial force and is superimposed over the total, shown as a red dashed line.

While it was demonstrated that force transfers between LR bearings and CL bearings over the course of a simulation, a different pattern emerged between simulations, which

is illustrated in Figure 6-14. This figure shows that the total compressive force carried by the LR bearings always increases from the beginning to the end of the simulation, which means that a small amount of load transfers from the CL bearings to the LR bearings over the course of the simulation. However, from the end of one simulation to the beginning of the next, the total compressive force carried by the LR bearings is consistently observed to decrease (Figure 6-14), which suggests that the original compressive force on the LR bearings would be restored over time. As mentioned before, the time between simulations in a given day was about 50 minutes. At the end of Day 1, the total compressive force increase on the four LR bearings is about 430 kN or 97 kips (about 22% of the original total of 1915 kN or 431 kips). As confirmation of the relaxation effect, the original static load on the LRBs is nearly restored by the start of Day 2; only about 50 kN (11 kips) additional remained (Figure 6-14). Nearly the same pattern is repeated on Day 2, except that additional compressive force accumulates more quickly as larger motions were executed earlier in the day.

Our hypothesis regarding the pattern of axial force transfer between simulations is as follows. When the bearings are constrained at large lateral displacements as depicted in Figure 6-6, the lead is sheared laterally and takes the shape of the slanted cylinder. The height of the slanted cylinder is longer than the height of the cylinder in the undeformed configuration. Upon return to the original position, the slanted cylinder tries to rotate, but the axial load and confinement from the shims force the lead cylinder back to its original height. Immediately upon return to the undeformed configuration, the lead plug exerts some force onto the upper and lower plates, or alternatively a slight height increase is

maintained if the upper and lower plates are not confined. The confining force or height increase causes the LR bearings to temporarily take on additional load. After a short period of time, the force relaxes and the original state is restored. This effect would not be seen if a) the hybrid isolation system used elastomeric bearings instead of LR bearings, b) the base diaphragm was less stiff, or c) the system consisted entirely of LR bearings.

The maximum increase in the static compressive force in the LR bearings due to the effect described above is about 500 kN, which is about a 25% increase relative to the static load carried by the LR bearings at the start of the test program.

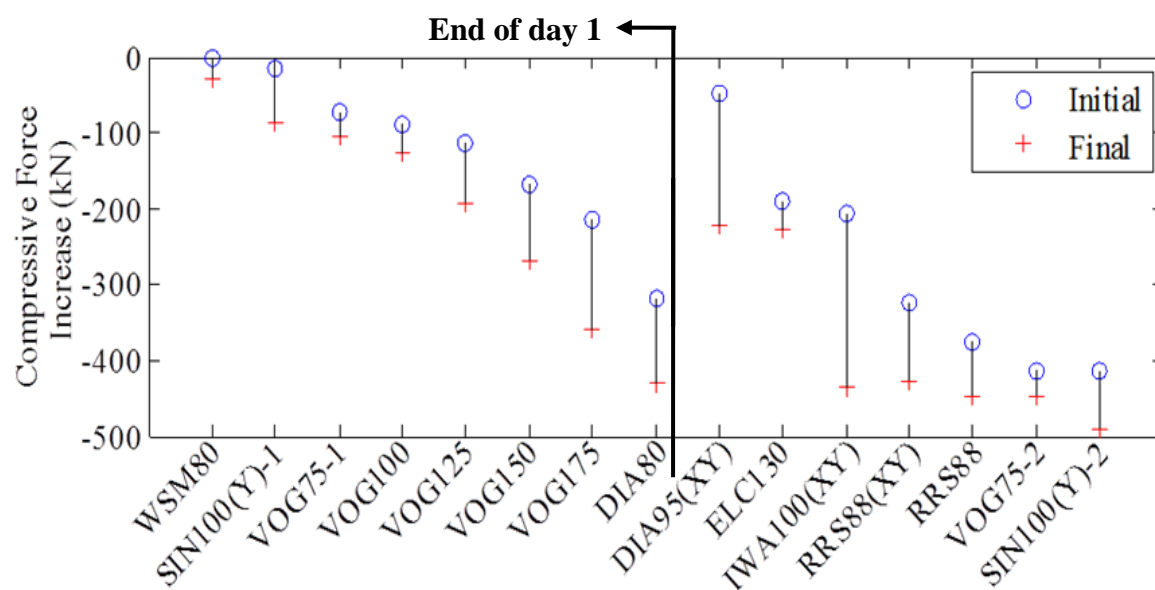


**Figure 6-14:** Relative change in the total (summation over all LR bearings) compressive force

As described in Section 3.2.2, the combination of LR and CL bearings was necessary in this program to provide a sufficient period shift and displacement capacity for the

relatively lightweight structure. Chapters 7, 8, 10 and 11 describe numerical simulation to validate and demonstrate the predictability of the experimental response. However, the prediction of the axial forces in the bearings was not attempted as part of this simulation. The forces in CL bearings cannot be validated since they were not measured.

The observed load transfer in these experiments suggests that the compliance of the devices in a hybrid system must be carefully considered. The experiments have demonstrated that when working with a high stiffness tension capable device, the LR bearings can be subjected to non-negligible tension due to a combination of load transfer and vertical excitation; the tension is not related to overturning. While the load transfer and the resulting tension observed in the LR bearings in these experiments is considered acceptable, the tensile demand on the bearings should be considered during design; see Chapter 10 and 11 for further discussion.

Due to these concerns regarding the load transfer, it is pertinent to consider the likely differences in response between the tested hybrid system and an isolation system composed exclusively of LR bearings. First, suppose the CL bearings were removed from the test setup, and the as-designed LR bearings were located beneath the four corner columns. Further, suppose that the same DBE and beyond DBE motions were posed that produced displacement demands up to 300 mm and 550 mm, respectively. The likely differences in the response of the exclusive LR system and the hybrid LR are discussed as follows.

The effective isolation properties and displacement demands for a DBE are expected to be essentially unchanged for an exclusive LR system. The bearing hysteresis loops in the exclusive LR system and the hybrid LR system are expected to look very similar.

Without CL bearings, individual LR bearings are estimated to sustain overturning induced tensile loads on the order of 200 kN (see Equation (3.4) and related discussion). Based on Figure 5-12, a tensile load on the order of 350 kN was observed in one bearing in this experiment due to the combined effects of load transfer and vertical excitation. Vertical excitation would also increase the peak tensile load in an exclusive LR system, such that the peak tensile demands on individual bearings in the hybrid LR system and in the exclusive LR system are expected to be similar.

If not constrained by the hybrid setup, a simple analysis predicts that one or more bearings may experience a complete loss of horizontal stiffness at the displacement demands of beyond DBE motions (550 mm). As discussed earlier, the bearing overlapping area at 550 mm of displacement is about 12% of the total bonded area (Equation (6.2)), and thus by the overlapping area rule is predicted to reduce to 12% of the bearing critical buckling load in the undeformed configuration (Buckle and Liu 1994). The nominal critical buckling load of the bearings is  $P_{cro} = 12,600$  kN (Figures 3-8 and 3-9 for LR Option 3), and thus the reduced buckling load is  $P_{cr} = 1500$  kN at a displacement of 550 mm. With only 4 LR bearings, the average static load of  $P = 1300$  kN per bearing nearly exceeds the reduced critical buckling load, and thus the bearings are expected to buckle if subjected to compressive force increase due to overturning. In

this case, the reduced horizontal stiffness of the bearing  $K_b$  of the bearing as a function of the nominal stiffness  $K_{bo}$

$$K_b = K_{bo} \left( 1 - \left( \frac{P}{P_{cr}} \right)^2 \right) \quad (6.3)$$

would also tend to zero. As a worst case scenario, buckling and temporary loss of stiffness in one or more bearings could cause a global collapse of the system.

However, emerging studies suggest that the stability capacity of elastomeric bearings at large displacements is much larger than predicted by the overlapping area rule, and the isolation system has remarkable ability to recover from local instabilities in one or more bearings. For example, Sanchez et al. (2012) subjected a rigid block system with 4 one quarter scale natural rubber bearings to ground motions that imposed bearing displacements beyond their theoretical and experimentally observed stability limits. In one instance, one of the bearings was driven to a displacement 1.2 times its diameter and about twice the displacement at which loss of stiffness was observed, and the composite isolation system had a large negative stiffness. The isolation system successfully recovered from this and other excursions into the instability range. In an experimental study of a two-fifth scale 3-span horizontally curved girder bridge with two isolation bearings at each bent and abutment, isolators were shown to remain stable at displacements 1.33 times the bearing diameter (Monzon et al. 2013). At a slightly larger displacement (1.4 times the bearing diameter), both bearings at one abutment experienced a local instability. One bearing was observed to sit down on the bottom plate while the top plate touched the side of the bearing. The other isolators remained

stable because the bent bearings were larger diameter and because the displacement demands at the abutment were larger due to asymmetry in the curved bridge. The system recovered from instability multiple times, and no changes to the isolator hysteretic properties were observed following instability.

Relating these results to a hypothetical test of an exclusive LR isolation system at E-Defense, another possible scenario is that the isolated structure could survive excursions to displacements equal to the bearing diameter (700 mm) and beyond without collapse due to the ability to recover from local instabilities. The potential for recovery would be aided by the fact that displacements on one of the building were consistently observed to be substantially smaller than displacements on the other side due to torsion, and that axial loads on one side of the building would be less than the static loads due to overturning. Both of these variations increase the likelihood that the instabilities are localized, enhancing the chance of a global recovery. As a result of localized instabilities, the bearing hysteresis loops would change substantially compared to the ones observed in these tests, and exhibit negative stiffness loops at large displacements, similar to those observed in Sanchez et al. (2012).

Next, suppose instead that the isolation system were designed without the constraints of the test setup for an actual nuclear facility. Removal of the test constraints implies the following could be achieved. Individual bearings would carry greater static loads, and thus their size (both diameter and bearing height) could be increased without altering the design properties (period and damping) of the system. As a result of the size increase, the target displacement demand for the Vogtle site (about 600 mm) could easily be



accommodated without approaching the stability limit of the bearing. As a result, stable hysteresis loops similar to the ones observed in these tests would be expected.

### **6.3 Repeatability of Isolation System Response after Many Tests**

During the test program, repetitions were conducted for two of the input ground excitations: Sine 100% (Y) and Vogtle 75%. Each of these excitations was applied near the beginning of the test program and then again at the end of the test program for the hybrid LR isolation system. The repetitions were planned to assess the consistency of the isolation system response after the LR bearings had been subjected to many ground motions and to very large ground motions.

The variation in the input signals for these repetitions is assessed in Figures 6-15 and 6-16. Figure 6-15 compares the x and y-direction feedback acceleration at the center of the earthquake simulator (averaged over several accelerometers) for the first and second Sine 100% (Y) and Vogtle 75% simulations. This feedback acceleration is the input acceleration to the isolated structure. Figure 6-16 compares the comparable 5% damped response spectra for the feedback acceleration. Figures 6-15 and 6-16 demonstrate that the input accelerations for the first and second simulations are essentially identical for both Sine 100% (Y) and Vogtle 75%.

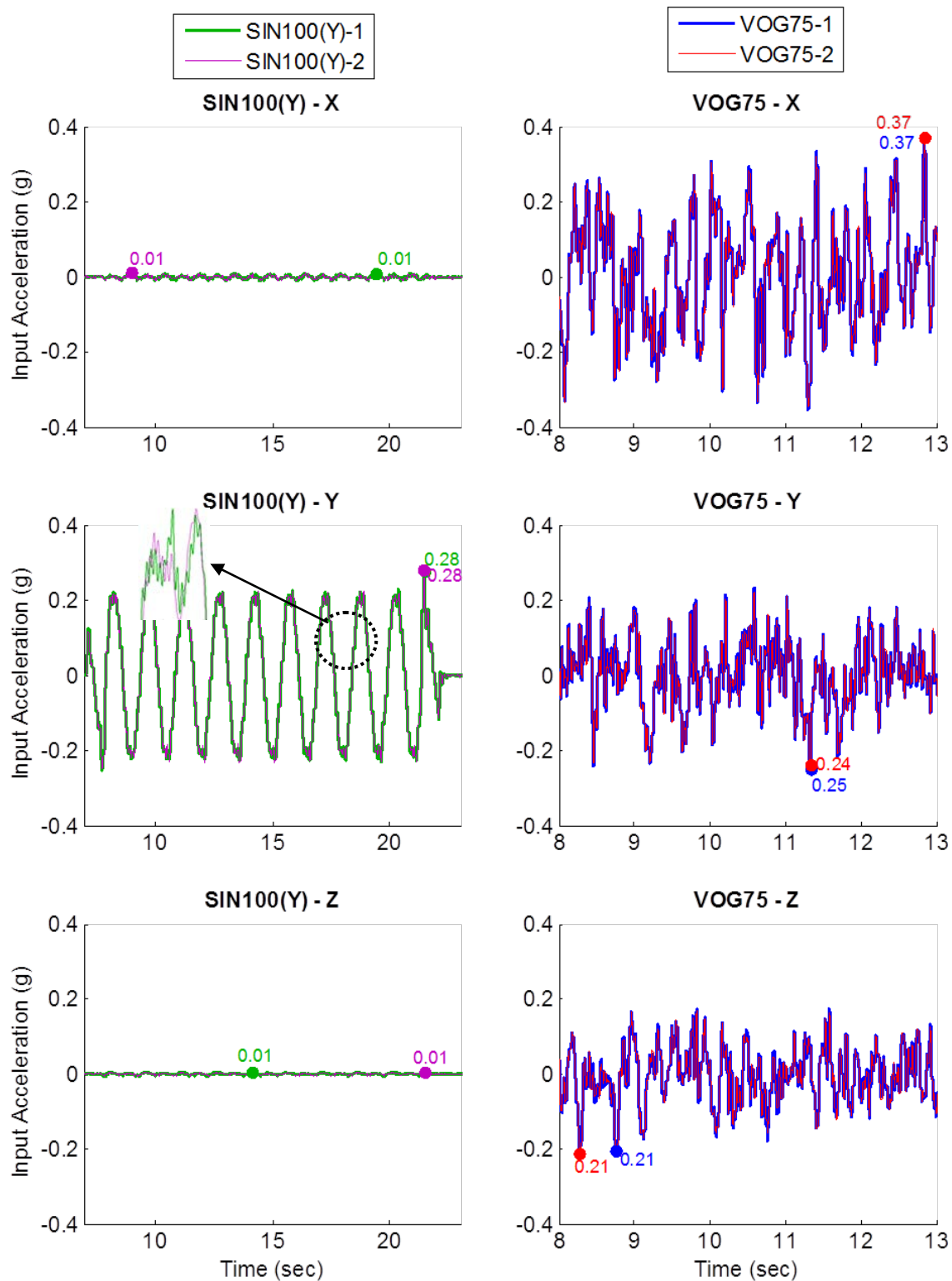


**Figure 6-15: Sample feedback acceleration at the center of the earthquake simulator (averaged over several accelerometers) in the x and y-directions compared for the first and second Sine 100% (Y) and Vogtle 75% simulations.**

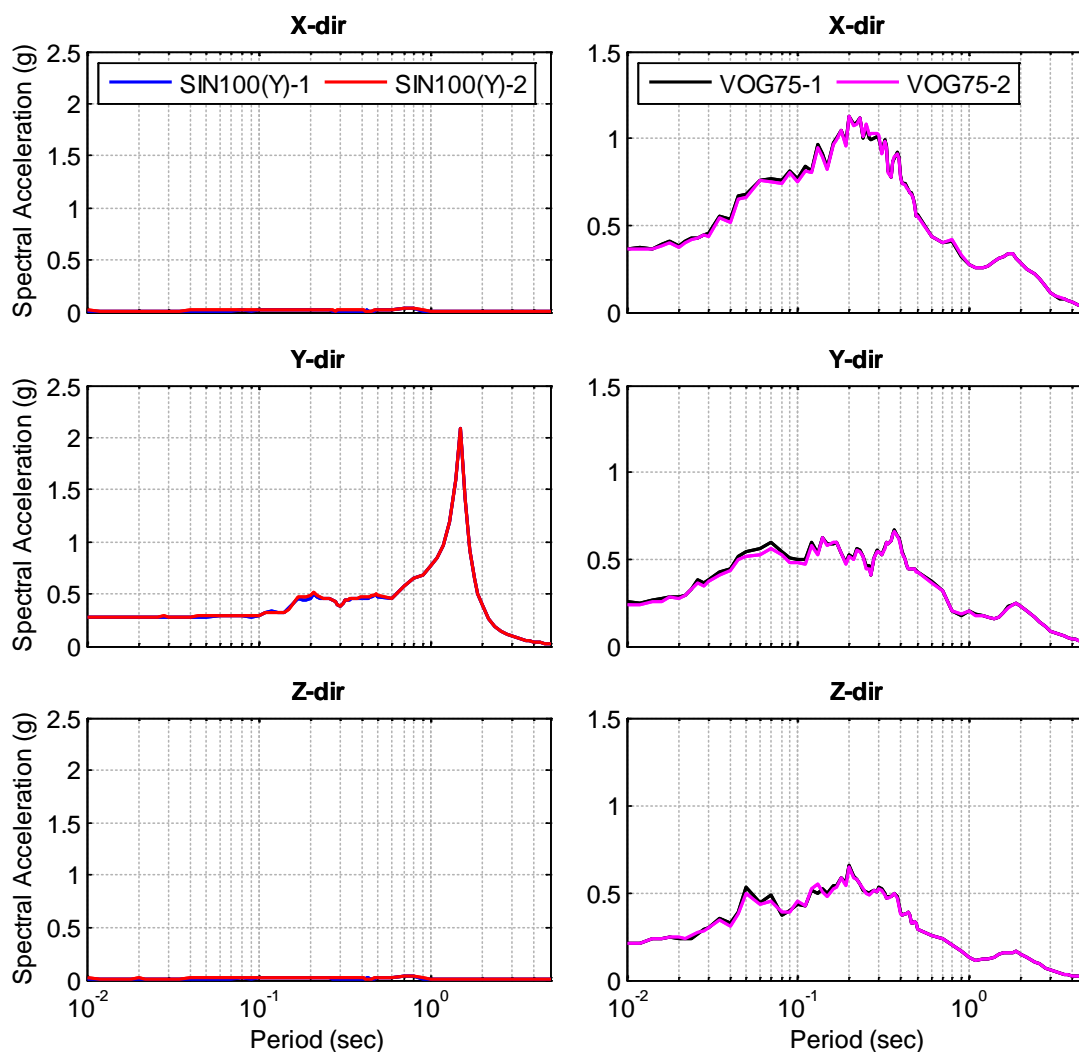


**Figure 6-16: 5% damped response spectra for the feedback acceleration at the center of the earthquake simulator (averaged over several accelerometers) in the x, y and z-directions compared for the first and second Sine 100% (Y) and Vogtle 75% simulations.**

The Sine 100% (Y) excitation is a unidirectional input consisting of several similar amplitude sinusoidal cycles used for characterization of the isolation system. As mentioned in the previous section, the input was applied in the y-direction to minimize torsional response. Minor displacements and forces in the x-direction were observed that had no distinguishable effects on the y-direction hysteresis loops. The y-direction bearing

force versus displacement (hysteresis loops) and y-direction displacement/force histories of all LR bearings are compared for the two Sine 100% (Y) simulations in Figures 6-17 and 6-18, respectively. From the hysteresis loops, a small decrease in bearing force is observed in the second simulation relative to the first (Figure 6-17). This force decrease is most notable as the displacement peak is approached in the negative direction. The peak force cycle-by-cycle is also slightly lower for the second simulation than the first based on the force histories (Figure 6-18), which is true for all LRBs. The observed decrease in the peak force is on the order of 5 to 11% when all LR bearings are considered, which is small.

The following hypothesis is offered to explain the mild variation in bearing response over the two simulations. The characteristic strength of LR bearings is affected by heating and temperature increase in the lead plug (Kalpakidis and Constantinou 2009a). Specifically, the characteristic strength of the lead plug decreases as the temperature increases under repeated cycling. While repetitions performed with the same starting temperature should produce identical response in the bearings, repetitions performed at different starting temperatures would produce slightly different response in the bearings. Since the test program consisted of many simulations in a single day with only 45-50 minutes between simulations, it is likely that 1) the bearings did not have time to cool to the starting temperature between simulations, and 2) the starting temperature for each simulation was different based on the recent simulation history. Consistent with the observations, the starting temperature for the second SIN100 simulation was likely higher than for the first SIN100 simulation, since the second followed a full day of testing including DIA95(XY),

which generated the largest displacement demand, and IWA100(XY), which was more than 4 minutes long.

Although the forces decrease, the overall displacement demands do not increase in the second Sine 100% (Y) simulation. Rather, the hysteresis loop for each bearing shifts slightly to the left in the second simulation so that the negative direction peak increases but the positive direction peak decreases. This shift can be observed in every bearing hysteresis loop except for LRB-S (Figure 6-17), and in the displacement histories (Figure 6-18). The shift could be related to a small residual (permanent) displacement present at the beginning of the second Sine 100% (Y) simulation in some bearings; residual displacement is visible only in LRB-S and LRB-N in the opposite directions (Figure 6-18), which indicates that the permanent displacement is torsional. Recall that a portion of the permanent displacement is believed to be a result of sliding in the connection plates associated with bolt slip (see Sections 5.5 and 6.1). The absolute peak displacement (observed in the negative direction) increases on the order of 3 to 5% in the second simulation when all LR bearings are considered, which is insignificant.

Additional plots are included to evaluate the consistency of the bearing response in the Vogtle 75% simulations, for responses in both directions. X and y-direction bearing force versus displacement (hysteresis loops) are compared for the Vogtle 75% simulations in Figures 6-19 and 6-20, while x and y-direction displacement/force histories of all LR bearings are compared in Figure 6-21 and 6-22. An additional figure (Figure 6-23) indicates the displacement traces (displacement in x versus displacement in y) of all LR bearings for the two Vogtle 75% repetitions. This figure is necessary to evaluate the

consistency of the peak displacement, which is a vector quantity for bidirectional horizontal excitation, over the two Vogtle simulations.

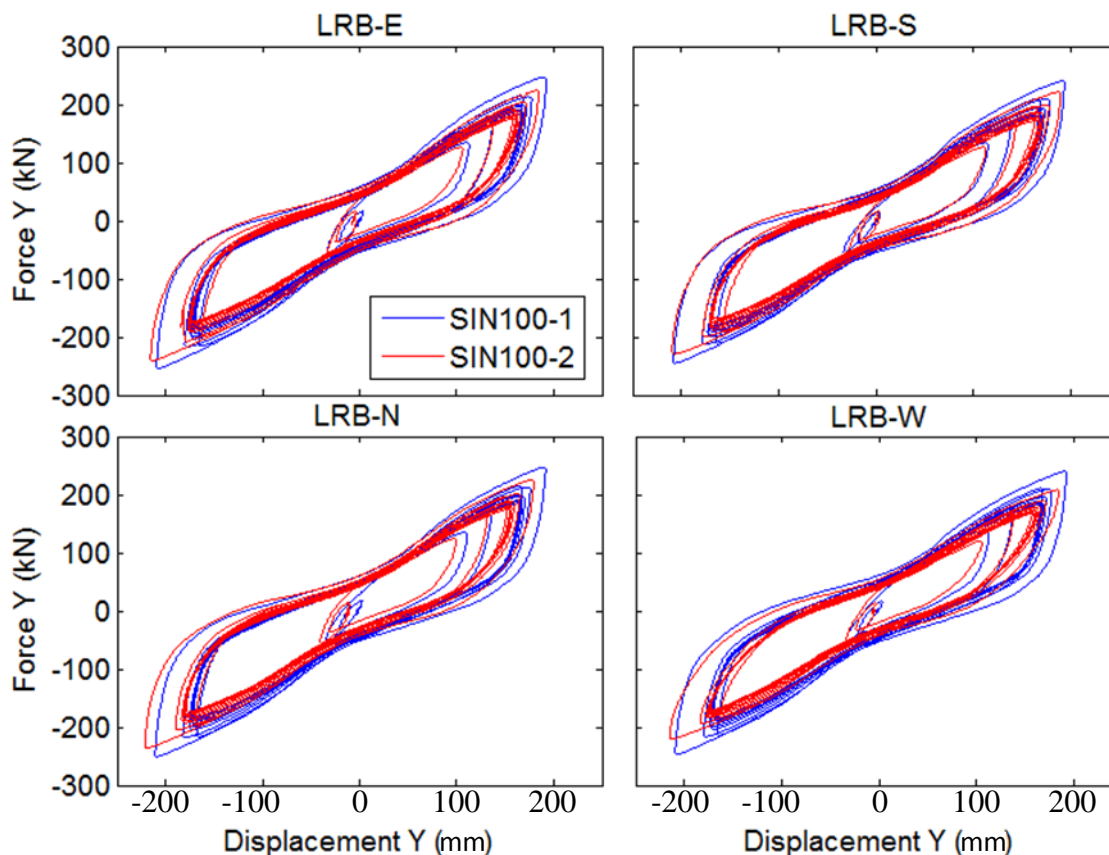


**Figure 6-17: Y-direction force vs. displacement (hysteresis loops) for the 1<sup>st</sup> and 2<sup>nd</sup> simulation of Sine 100%(Y).**

Again, by visual inspection of the hysteresis loops, the forces in the LR bearings decrease slightly for the second repetition of Vogtle 75% relative to the first (Figures 6-19 and 6-20). This reduction in force seems to be smaller for Vogtle 75% than for Sine 100% (Y). The absolute peak displacement increases for each LR bearing in the second simulation relative to the first, but also appears to result from the entire hysteresis loop shifting to the direction of negative displacement rather than a true increase in the displacement

demand. The increase in absolute peak displacement for the second simulation of Vogtle 75% relative to the first is about 8% in all LR bearings (determined from Figure 6-23). Force and displacement histories are very similar when superimposed over each other for the first and second simulations (Figures 6-21 and 6-22).

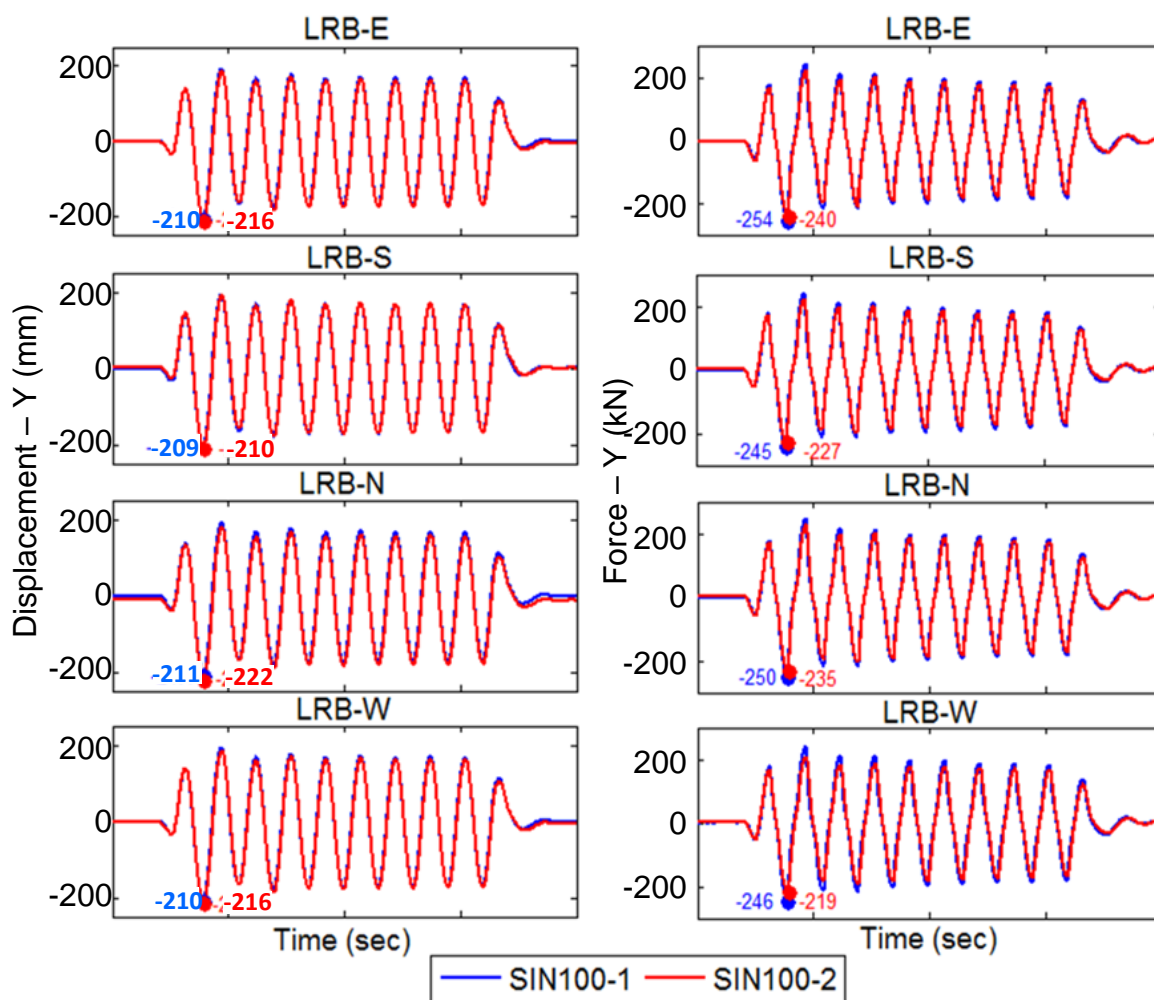


**Figure 6-18:** Y-direction displacement and force histories for the 1<sup>st</sup> and 2<sup>nd</sup> simulation of Sine 100% (Y).

The peak force in the LR bearings also decreases from cycle to cycle while the displacement remains approximately constant over the course of a simulation. This behavior is also indicative of dynamic reduction in yield strength due to heating of the lead plug. This behavior is observed most clearly during the Sine 100% (Y) simulation, which contains several regular displacement cycles of similar amplitude. The hysteresis loops generated during Sine 100% (Y), both first and second simulations, are plotted again for LRB-N in Figure 6-24, where the cycles are individually identified. In this figure, the forces decrease in every cycle, with the greatest reduction between the first and the second cycle. While the total reduction in strength over the 8 cycles of the sine wave is significant, a typical motion includes at most a few cycles of strong amplitude motion. The reduction in strength is difficult to quantify for the other input motions, such as actual earthquake loading, because of the lack of multiple large amplitude cycles at the beginning of the displacement history. However, Vogtle 75% had two large cycles at the beginning of the displacement history and for this motions, a reduction of nearly 8% in  $Q_d$  between the 1<sup>st</sup> and 2<sup>nd</sup> cycles was observed (Figures 6-25). The data for the two sine wave simulations suggests that much, but not all, of the force reduction is recovered between tests.

Related to these observations, predicting the change in characteristic strength of the lead plug over the history of the motion is of interest. Such effects have not been incorporated into our numerical simulation models, discussed in Chapters 7-8, but the following is noteworthy. Kalpakidis and Constantinou (2009a) developed theoretical equations to compute the instantaneous strength and evolution of strength in the lead plug over the



history of the excitation. Kalpakidis et al. (2010) presented a numerical algorithm to incorporate the temperature dependence into a bidirectionally coupled bilinear numerical model of the isolator. The algorithm to compute the temperature increase in a response simulation is based on the dimensions of the lead plug, density and specific heat of lead, thermal diffusivity and thermal conductivity of steel, and a few other calibrated parameters. To improve prediction of the experimental response, heating of the lead plug should be incorporated into the numerical model.

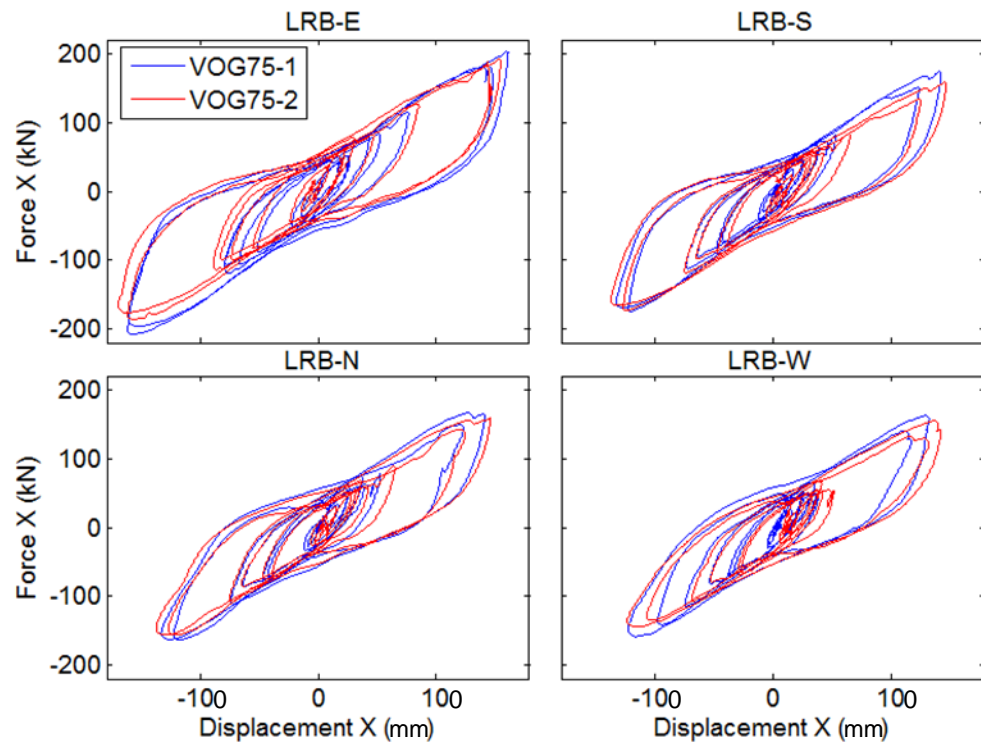


**Figure 6-19: X-direction force vs. displacement (hysteresis loops) for the 1<sup>st</sup> and 2<sup>nd</sup> simulation of Vogtle 75%.**

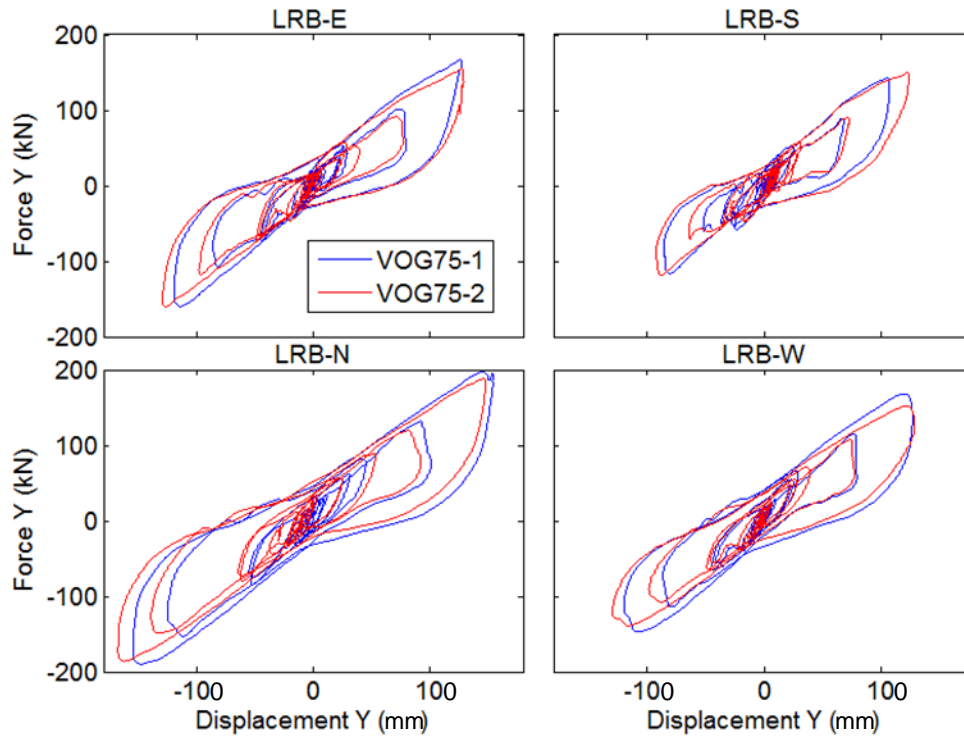


**Figure 6-20: Y-direction force vs. displacement (hysteresis loops) for the 1<sup>st</sup> and 2<sup>nd</sup> simulation of Vogtle 75%.**

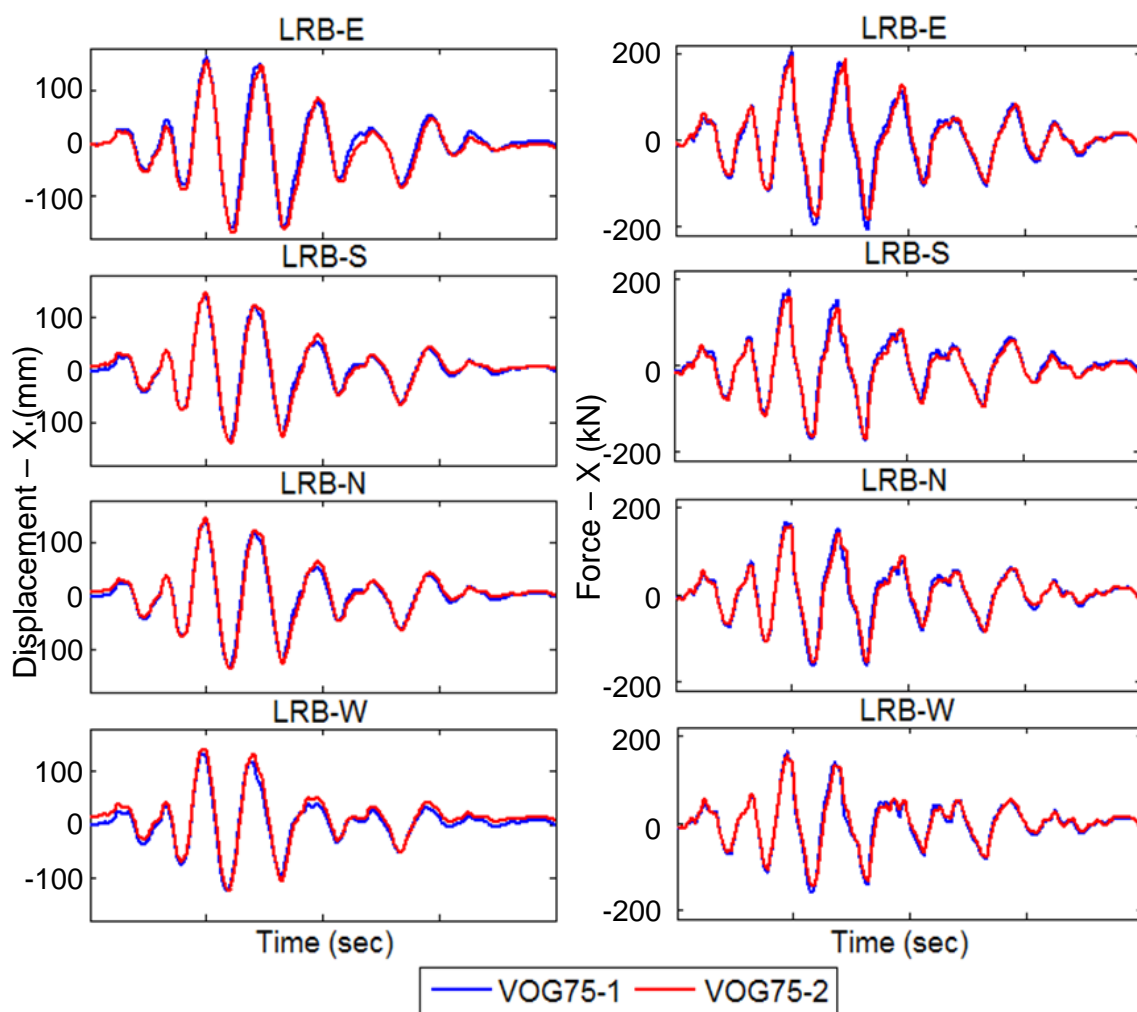


**Figure 6-21:** X-direction displacement and force histories for the 1<sup>st</sup> and 2<sup>nd</sup> simulation of Vogtle 75%.

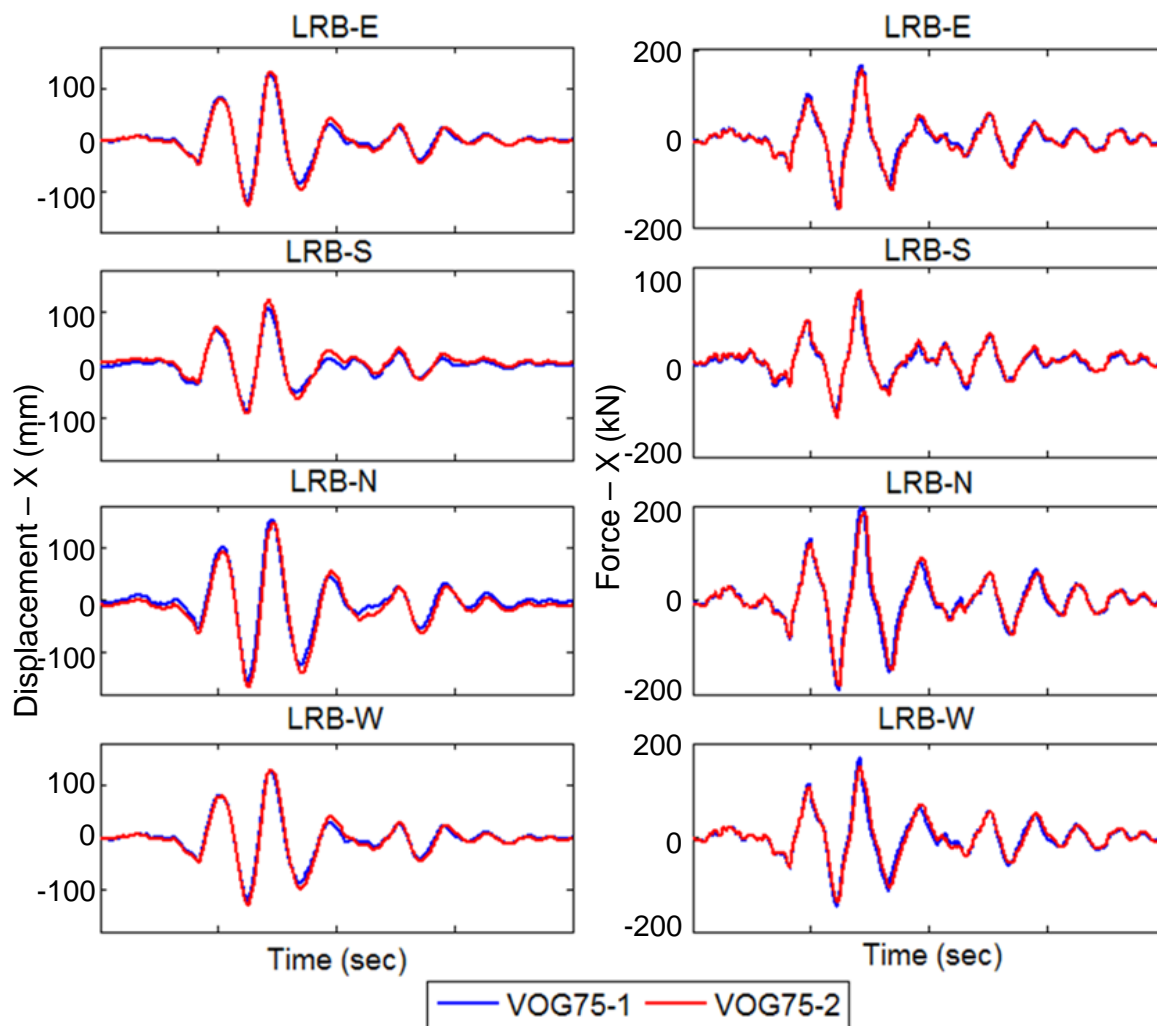


**Figure 6-22:** Y-direction displacement and force histories for the 1<sup>st</sup> and 2<sup>nd</sup> simulation of Vogtle 75%.

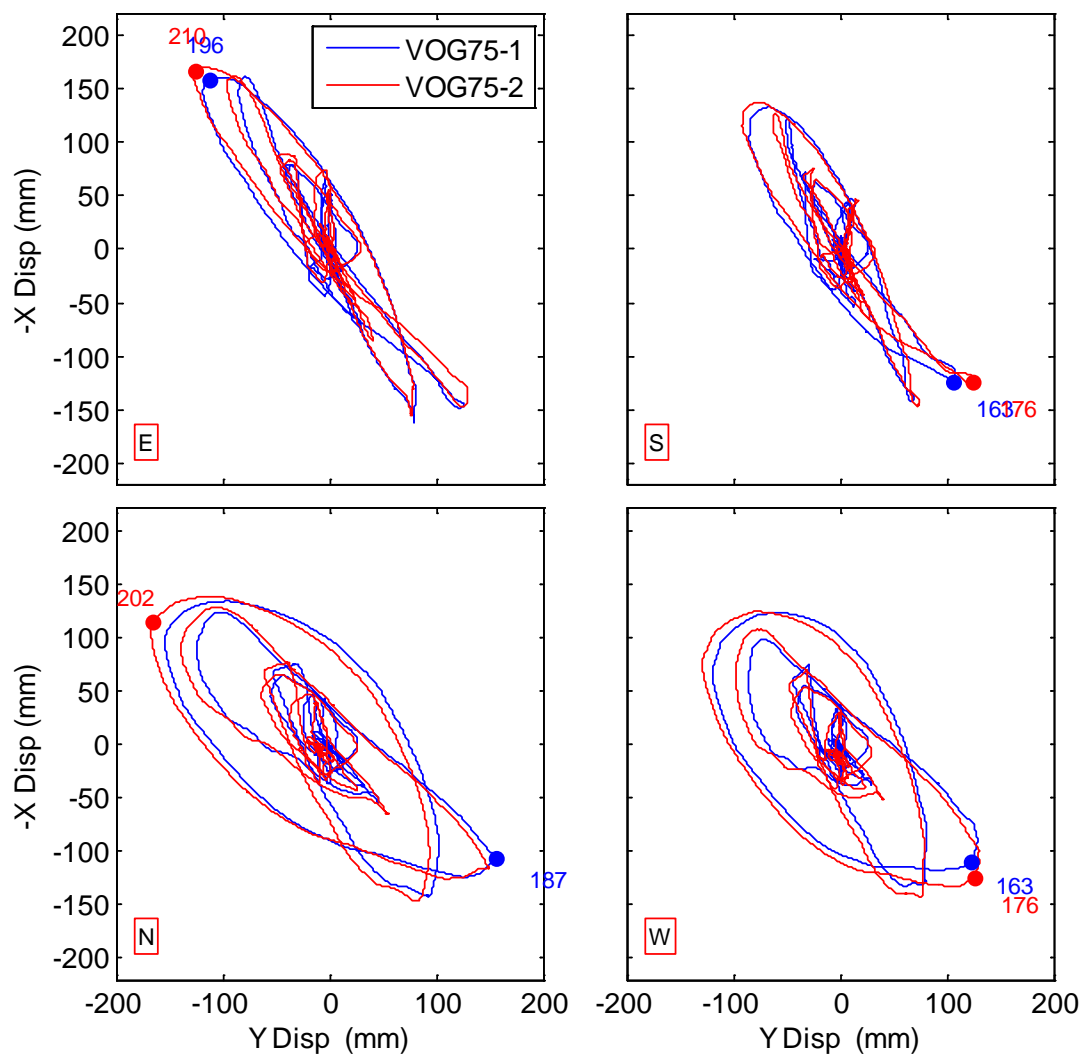


**Figure 6-23: X vs. y-direction displacement (displacement trace) for the 1<sup>st</sup> and 2<sup>nd</sup> simulation of Vogtle 75%.**

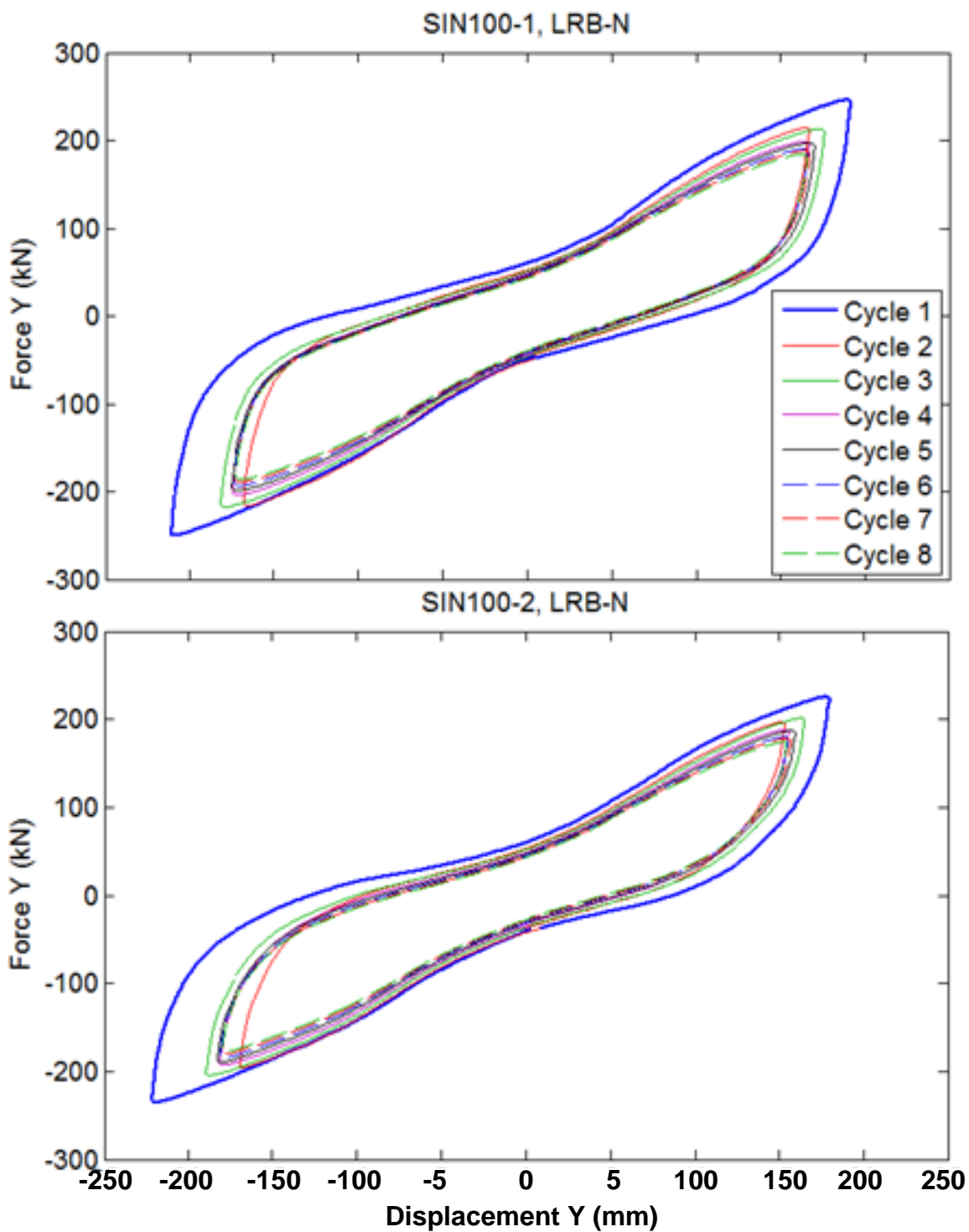
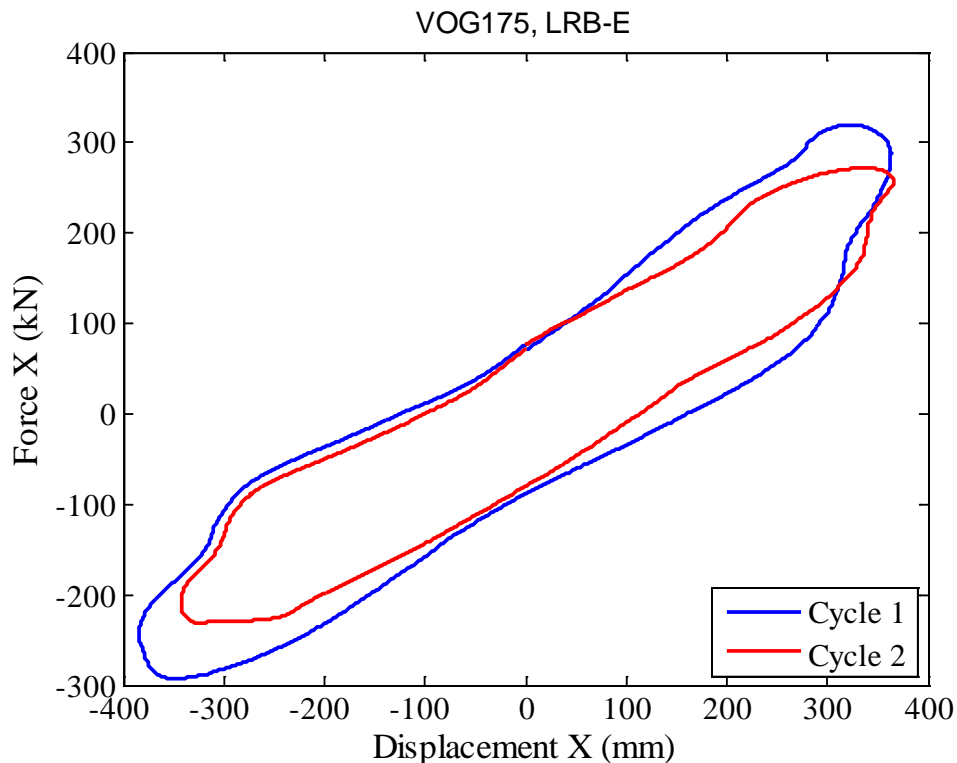


Figure 6-24: Y-direction force vs. displacement (hysteresis loops) identified by cycle for the 1<sup>st</sup> and 2<sup>nd</sup> simulation of Sine 100% (Y).



**Figure 6-25:** X-direction force vs. displacement (hysteresis loops) for the 1<sup>st</sup> and 2<sup>nd</sup> cycles of Vogtle 175%.

#### 6.4 Summary of Observations

The top and bottom bolted connections securing the LR bearings did not meet slip critical criteria due to several unique conditions during this experiment. As a result, bolt slippage occurred during the experiment that resulted in a small residual displacement in the isolation system and large sharp spikes in the horizontal force history of individual LR bearings. However, the bolt slippage did not have a significant influence on the structural response. Axial force from the LR bearings was observed to transfer to the CL bearings at large horizontal displacements, which caused LR bearings to sustain tension during some of the simulations. As the isolation system recentered, axial load transferred

back to the LR bearings from the CL bearings. The experimental response of two input excitations that were tested at the beginning of the test program and then at the end showed that the LR bearing properties remained the same even after the bearings were subjected to many ground motions that produced some large isolator demands. The characteristic strength of the LR bearing was observed to decrease over the duration of an excitation, which is associated with heating of the lead plug.



## **CHAPTER 7: NUMERICAL SIMULATION MODEL OF TESTBED STRUCTURE**

As mentioned before, many aspects of the experimental setup were applicable to the three test configurations (TPB, hybrid, fixed base), and thus not developed directly by the author for the exclusive purposes of this dissertation. As such, some of the information in this chapter is an excerpt from Dao and Ryan (2015) and presented here for completeness.

A model for numerical simulation of the testbed building with the isolation system was developed in OpenSees. The assumptions used in developing the model of the building frame with floor slabs, shown in Figure 7-1(b), are described in this chapter. As an overview, the contribution of floor slabs to the bending stiffness was included in composite beam sections and their in-plane stiffness was accounted for through application of diaphragm constraints. The beam-column connection behavior was represented by a panel zone model. Material nonlinearity was considered through nonlinear material models, and some geometric nonlinearities were included through a P-Delta transformation. Mass and gravity loads were lumped to nodes. Rayleigh damping was applied to the superstructure with additional inter-story dampers to represent energy dissipation. The bearings were represented using the modeling assumptions and characterized parameters of LR bearings and CL bearings described later in Sections 8.1 and 8.2, with calibrated bearing parameters presented in Table 8-4.

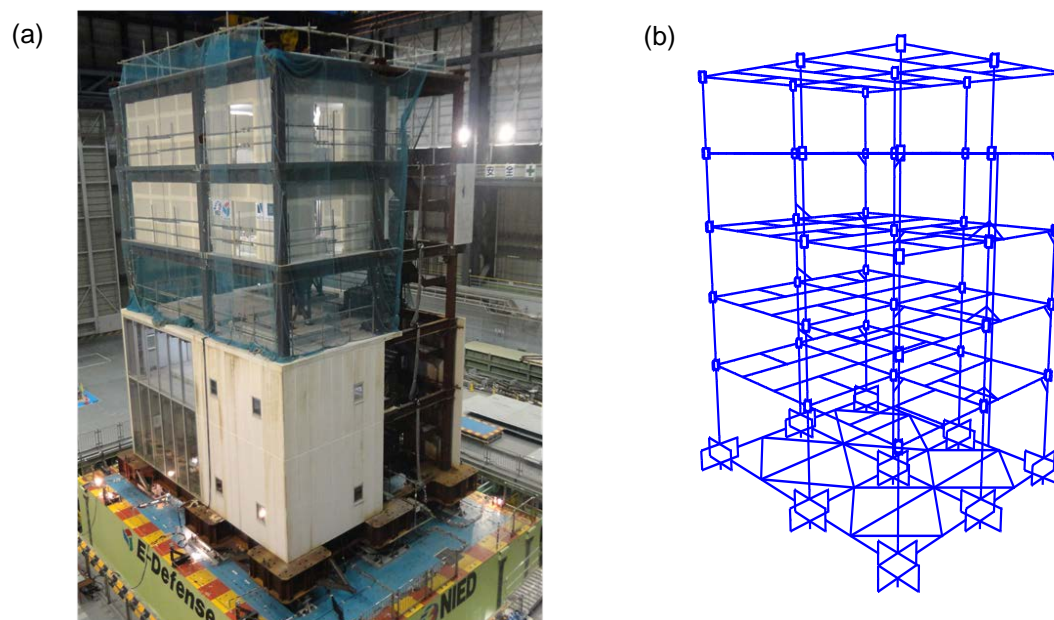


**Figure 7-1: (a) Photo and (b) OpenSees model of the testbed building without isolators**

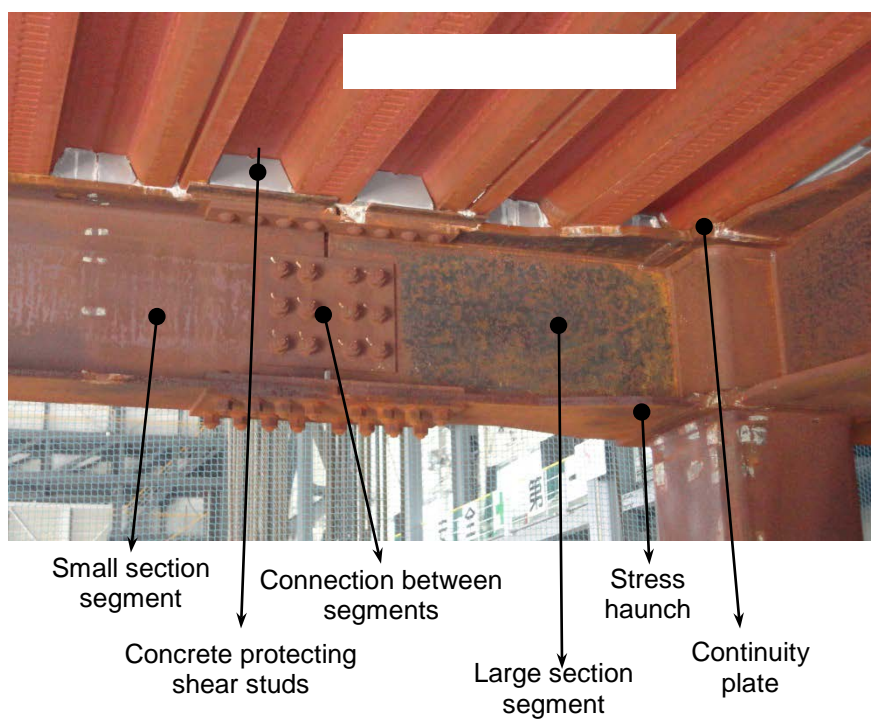


**Figure 7-2: Primary beam, beam-to-column connection, and slab**

## 7.1 Modeling Beams and Columns

The beams of the testbed building were composed of either rolled or built-up I-sections. Primary beams - supported by columns - consisted of a small section segment in the middle bolted to large section segments at the ends, all 400 mm (16 in) deep (Figure 7-2). The beam-column connections were fully restrained moment connections with beam flanges and webs welded to the column face. Generally, the primary beams were haunched at the ends for improved strength, and continuity plates protected the panel zones. Secondary beams - supported by primary beams - were connected to the primary beams through shear tabs. The columns were made of 350 mm (14 in) HSS sections with thickness varying from story to story (Appendix A).

Primary beams were modeled by displacement-based nonlinear frame elements with distributed plasticity. The displacement formulation was selected over advocated force formulations (Neuenhofer and Filippou 1997) to improve the convergence of the numerical simulation. To optimize the performance of displacement-based elements, each beam member was divided into at least 8 elements. Since mass was lumped at the nodes, the discretization also helped to distribute mass over the structure more realistically.

The nonlinear frame elements were accompanied by composite section models to account for the contribution of floor slabs, which were connected to the primary beams through shear studs (Figure 7-2). The effective slab width for each side of the composite section was the minimum of (1) one-eighth of the beam span, (2) one-half the distance between the beams and (3) the distance to the edge of the slab (AISC 2005). Longitudinal slab reinforcement was included in the section model. The Giuffre-Menegotto-Pinto (CEB,

1996) and Kent-Park concrete materials (Kent and Park 1971, Scott et al. 1982) are used to model the stress-strain relations of steel and unconfined concrete (applied to floor slabs), respectively. The tensile resistance of concrete was neglected in the concrete material model.

For these non-symmetric composite sections, when the material behavior becomes nonlinear, the neutral plane of the section moves and the geometric centerline deforms axially under pure bending loads. However, the rigid diaphragm constraint prevents the axial deformation of the centerline, thus introducing an axial force to the bent beam. The axial force changes the behavior of beams significantly, as demonstrated in Figure 7-3(b), where the bending behavior with and without axial deformation restraint are compared for a simply supported 5 m (16 ft) beam element with a composite section driven cyclically at the midpoint. To avoid the unintended effect of axial force on bending of the composite beam sections, the axial and bending behaviors were decoupled through the use of resultant section models for moment-curvature and axial force-strain. The resultant beam section behavior was determined from analysis of the composite fiber sections (e.g. Figure 7-3(a)). As an example, the pure bending cyclic behavior of the composite fiber section determined by section analysis (solid line in Figure 7-4(a)) was approximately represented by combining the steel material model (Figure 7-4(b)) with a hysteresis model (Figure 7-4(c)) in parallel.

Secondary beams of the testbed were modeled as elastic beam elements with elastic composite sections. The secondary beams in the model were also divided into 8 elements to distribute mass realistically.

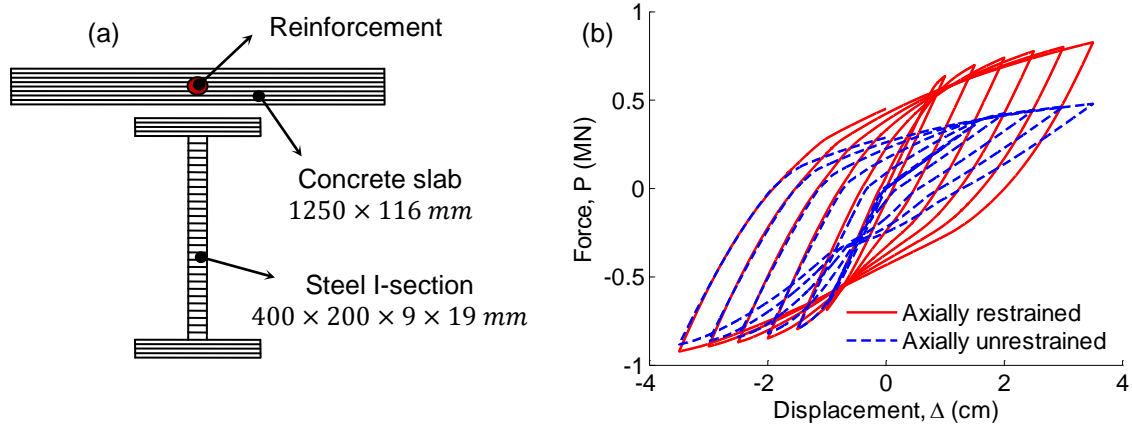


**Figure 7-3: Behavior of a representative composite fiber section beam with and without axial restraint: (a) fiber section geometry and (b) force-displacement relationship**

The testbed columns were also modeled by displacement-based nonlinear frame elements, but fiber sections were used to account for axial force-bending interaction in the columns. Each column member was modeled with 3 elements to improve the performance of the displacement-based elements. Because plasticity is mainly concentrated at the two ends of a column member, the length of the end elements was set equal to the section height (350 mm or 14 in). Three displacement-based elements were shown to give similar moment rotation behavior to the force-based element with 7 integration points (Dao and Ryan 2015).

During the experimental simulation, the response of the testbed frame was essentially elastic. However, the floor system exhibited some nonlinearity due to the cyclic response of concrete between tension and compression. Dao and Ryan (2015) demonstrated that the numerical simulation results more closely matched the experimental data when nonlinear modeling assumptions were considered, compared to an elastic frame model.

Thus, the attention to detail and consideration of nonlinear effects in the model was justified.

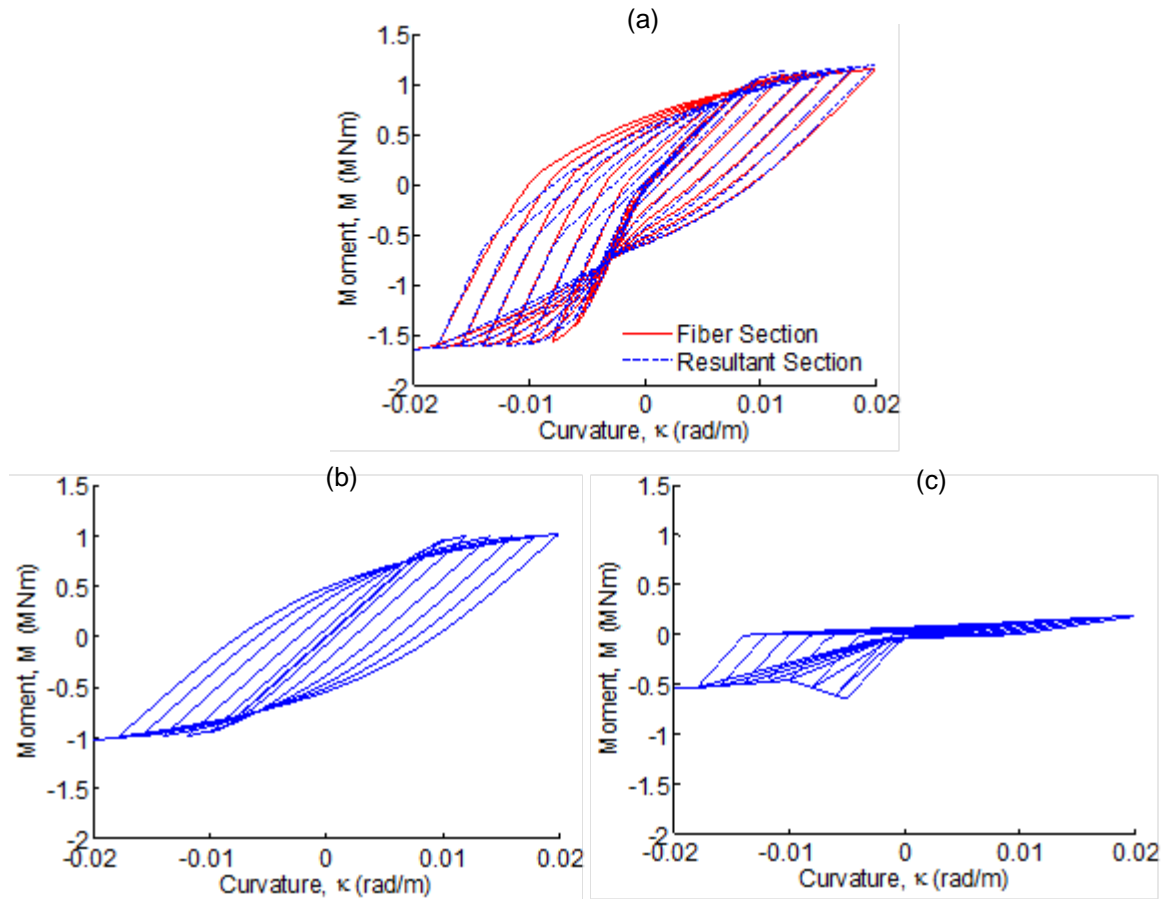


**Figure 7-4: Composite section behavior: (a) moment-curvature relationship of the section, (b) component 1 of resultant section modeled by steel material model, and (c) component 2 of resultant section modeled by hysteresis model**

## 7.2 Modeling Panel Zones

The Krawinkler panel zone model (Krawinkler 1978, Charney and Downs 2004) was used to model the connection between beams and columns. According to this model, each panel zone (Figure 7-5(a)) was modeled by 8 rigid elements and 2 elastic-perfectly plastic

rotational springs, one representing the shear behavior of the panel zone (or the web, lying in the working plane) and one representing the bending behavior of the flanges (perpendicular to the working plane) (Figure 7-5(b)). Since the columns were fully welded to primary beams in both directions, the panel zones in two directions were independently modeled by two Krawinkler panel zone models.

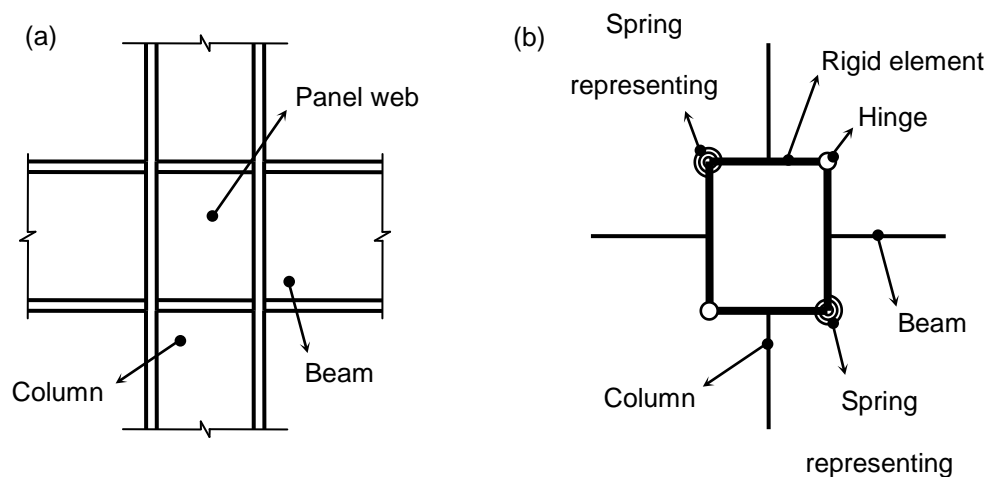


**Figure 7-5: Panel zone model for beam to column connection. (a) beam to column connection, (b) numerical model of panel zone.**

The initial stiffness  $S_P$  and yield strength  $M_{YP}$  of the spring representing the shear behavior of the panel zone web were computed as:

$$S_P = GV_P \quad (7.1)$$

$$M_{YP} = 0.58F_Y V_P \quad (7.2)$$

where:  $G$  = shear modulus of steel,  $V_p$  = volume of the panel zone web, and  $\sigma_Y$  = yield strength of steel material. The initial stiffness  $S_F$  and yield strength  $M_{yF}$  of the spring representing bending of the flanges are:

$$S_F = 0.75Gb_{cf}t_{cf}^2 \quad (7.3)$$

$$M_{yF} = 1.80\sigma_Y b_{cf}t_{cf}^2 \quad (7.4)$$

where:  $b_{cf}$  = flange width of column and  $t_{cf}$  = flange thickness of column.

Elastic axial elements equivalent to the Krawinkler model were also used to model gusset plates (Figure 7-6(a)), which were an integral part of the specimen for attaching dampers in the March 2009 test (Kasai et al., 2010). The dampers were not present during the experimental simulation described in this dissertation. Finite element analysis of a connection with gusset plate subjected to gravity load suggested that the gusset resistance is in the diagonal direction (Figure 7-6(b)), and can be modeled as a diagonal strut. The equivalent elastic stiffness  $k_{truss}$  of the axial element was:

$$k_{truss} = S_p \frac{(x^2 + y^2)}{x^2 y^2} \quad (7.5)$$

where  $x \times y$  = size of the gusset plate and  $S_p$  = initial shear stiffness of the gusset plate (Equation (7.1)).



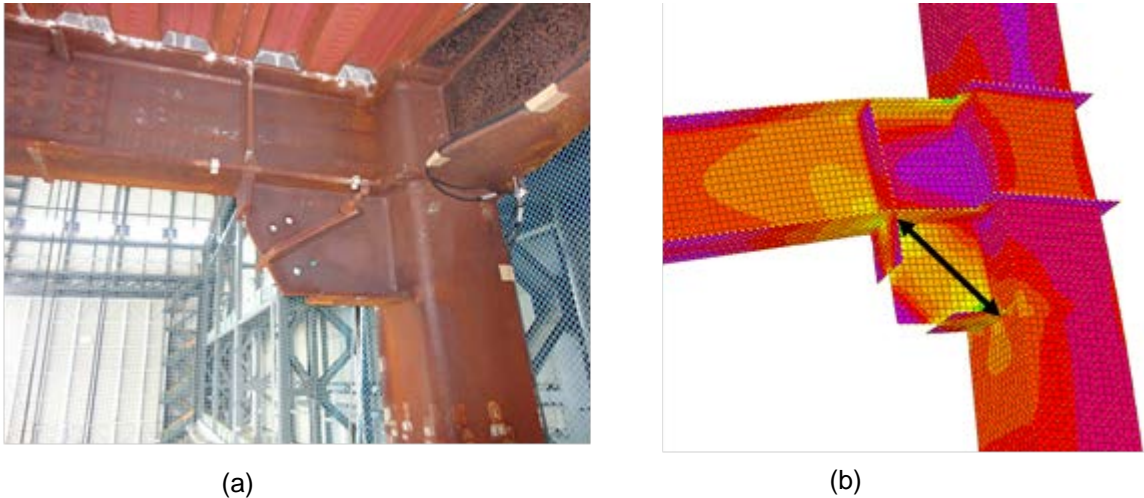


**Figure 7-6:** Gusset plate and its finite element model: (a) gusset plate, (b) Von-Mises stress due to gravity load

### 7.3 Modeling Gravity Load and Mass

As mentioned earlier, the testbed building was modeled as a bare frame without slabs so that gravity loads and mass were applied directly to beams and columns. Static analysis of a SAP2000 model subjected to gravity loads with slabs represented by general shell elements was used to compute beam internal forces and distributed loads. From the shear forces  $V_i$  and  $V_j$  at the two ends of a beam element, the equivalent uniform load  $v$  on the beam element was computed according to:

$$v = \frac{V_i - V_j}{L} \quad (7.6)$$

where  $V_i$  and  $V_j$  are shear forces at the two ends of the element, and  $L$  is the length of the element. The mass of the OpenSees model was directly derived from the computed distributed loads and lumped to every node of the model. Because of the bending

stiffness of the slab, some of the slab gravity load transferred directly to the corner slab nodes. In the OpenSees model, these loads were applied as concentrated loads to the corresponding corners.

Table 7-1 summarizes the weight and the eccentricity of gravity center from the geometric center of the SAP and OpenSees models. The weight of all floors in SAP model, estimated directly from the nominal weight and dimension of all components of the testbed, is shown in column (2). By this approach, the total weight of the testbed building was 5122kN (1151 kips). However, as mentioned earlier, the measured weight of the testbed was actually 5250 kN (1180 kips), which was determined from the uplift investigation of the TP bearings. To match the measured weight, the weight in the numerical frame model was increased by a factor of  $5220/5122 = 1.019$ . The weight increase was assumed to be uniform over all nodes of the model. Column of Table 7-1 (3) indicates the factored weight at all floors applied to the OpenSees model.

Columns (4) and (5) of Table 7-1 indicate the mass eccentricity at every floor, or distance from the geometric center of the building to the center of mass. In general, the center of mass of each floor shifted toward the North-East relative to the geometric center. At the base, the center of mass shifted toward the West due to the weight of the column bases on the West side as well as the staircase on the SouthWest. The Y direction eccentricity at floor 5 increased relative to other floors due to the absence of the staircase in the 5th story. The eccentricity was greatest at the roof due to the added steel blocks. As mentioned previously, this added weight was excessive compared to typical roof mounted equipment and influenced the seismic response of the testbed building.

**Table 7-1: Weight and Eccentricity (Distance from Geometric Center to Center of Mass) of Numerical Simulation Model**

Floor (1)	Weight from SAP (kN) (2)	Modified weight (kN) (3)	Eccentricity	
			X (mm) (4)	Y (mm) (5)
Roof	1153	1175	90	-850
5	771	786	200	-400
4	781	796	210	-240
3	782	797	270	-220
2	792	807	220	-240
Base	842	859	0	310
Sum	5122	5220	160	-320

#### 7.4 Modeling Damping

Rayleigh damping (combining mass and stiffness proportional components) was used to represent energy dissipation in the testbed building, based on specified damping ratios at two different frequencies. The experimental response of the fixed base building to white noise excitations was analyzed to find the periods and damping ratios of natural modes of the structure (Sasaki et al., 2012), which are listed in Table 7-2 for the first 3 modes in both directions. The Rayleigh damping curve passing through damping ratios of 2.2% at periods of 0.70 sec (frequency of 1.43 Hz), corresponding to the first mode period, and 0.15 sec (6.67 Hz) (Figure 7-7), was found to give a good match between experimental and numerical results of the fixed-base building.

Past experiments have shown that the damping ratios determined by the method described above include damping in the hydraulic actuators of the earthquake simulator and thus over-estimate the actual damping in the structural system. If determined from

free vibration analysis, damping ratios on the order of 1% or less are expected for the first few modes of bare steel frame systems (e.g. Uang and Bertero 1986, Whittaker et al. 1990). The damping in the hydraulic actuators was not accounted for in the numerical modeling of the system. However, additional damping in the testbed building was present compared to a bare steel frame due to the concrete floor system, exterior concrete cladding, nonstructural components (partition walls, ceilings and piping system) and contents. Thus, the level of observed damping in the testbed building was partially justified.

The final “best fit” damping coefficients for the building with hybrid LR isolation system were determined by trial and error. The basic strategy behind the selection was to control damping between the periods of 0.1 sec (10 Hz) and 2 sec (0.5 Hz) and, which included the major response components that were observed in the floor spectra (Ryan et al., 2013a). The damping ratios were fixed at 1.9% and 1.93% at 0.15 sec (6.66 Hz) and 2.0 sec (0.5 Hz). The Rayleigh damping curve for the isolated building configuration is compared to that for the fixed-base building configuration in Figure 7-7.

**Table 7-2: Experimentally Determined Natural Periods and Damping Ratios of the Fixed-base Building**

	White noise X		White noise Y		White noise 3D	
	Period (s)	Damping ratio (%)	Period (s)	Damping ratio (%)	Period (s)	Damping ratio (%)
Mode 1 X	0.65	3.3	n/a	n/a	0.68	4.1
Mode 2 X	0.20	1.6	n/a	n/a	0.21	2.0
Mode 3 X	0.11	3.3	n/a	n/a	0.11	3.7
Mode 1 Y	n/a	n/a	0.68	2.5	0.69	3.5
Mode 2 Y	n/a	n/a	0.21	1.7	0.21	1.9
Mode 3 Y	n/a	n/a </td <td>0.11</td> <td>2.6</td> <td>0.11</td> <td>3.6</td>	0.11	2.6	0.11	3.6

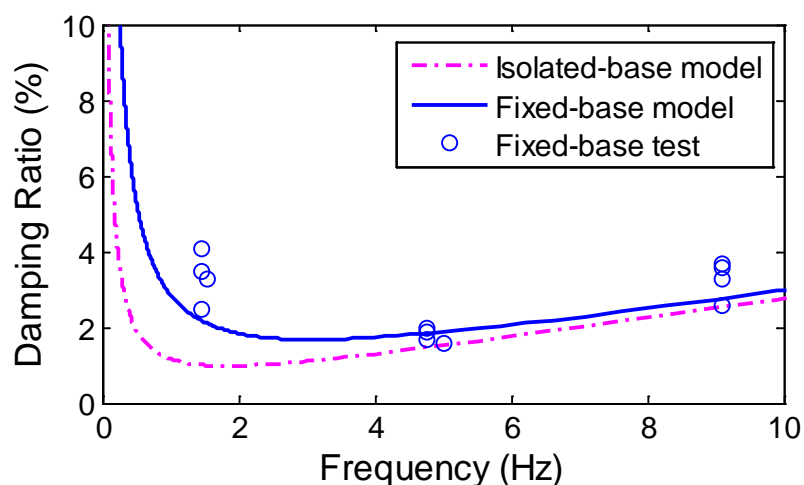


**Figure 7-7: Rayleigh damping model for the fixed-base and hybrid LR isolated building model**

The calibrated Rayleigh damping model produced low damping ratios at frequencies around 3 Hz (Figure 7-7), which were the frequencies of the first structural modes of the isolated structure in both directions, so that these frequency components of the numerically simulated response tended to be amplified compared to the experimental

data. To solve this difficulty, additional dampers were added to apply extra damping to these modes (Dao and Ryan, 2015). From modal analysis, the relative horizontal displacement between the base and roof in the 1<sup>st</sup> structural mode in each direction was observed to be much larger than in other modes. Thus, additional dampers were connected between the center of stiffness nodes at the base and roof in each direction as shown in Figure 7-8. At these locations, the displacements in the 1<sup>st</sup> torsional mode were zero. The damping coefficient  $c$  for the damper in a given direction was computed as (Dao and Ryan 2015):

$$c = \frac{2 \cdot \zeta_n \cdot \omega_n \cdot m_{nn}^*}{\bar{c}_{nn}} \quad (7.7)$$

where  $n$  = mode number of the modified damping mode;  $\zeta_n$  = desired additional damping ratio;  $\omega_n$  = the angular frequency of the  $n^{th}$  mode;  $m_{nn}^*$  = modal mass of the  $n^{th}$  mode; and  $\bar{c}_{nn}$  = a constant dependent on  $n^{th}$  mode shape, computed by:

$$\bar{c}_{nn} = (\phi_{pn} - \phi_{qn})^2 \quad (7.8)$$

where  $\phi_{pn}$ ,  $\phi_{qn}$  = horizontal displacements at base and roof in the  $n^{th}$  mode shape. Computation of  $[\bar{c}_{ij}]$  for the first 14 modes, including off diagonal terms, demonstrated that the extra damping contributed primarily to the intended mode (Dao and Ryan, 2015). The selected value of  $\zeta_n$  for numerical simulation was 2% for the for the hybrid LR isolation configuration.

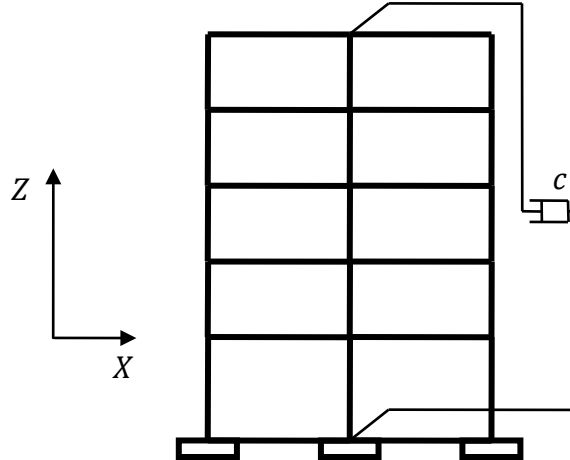


**Figure 7-8:** Additional damper for adjusting the damping coefficient of the 2<sup>nd</sup> mode in the *X* direction

## 7.5 Adjusting Vertical Reaction

As presented in Section 4.3, the warping of the base of the specimen caused the experimental distribution of the vertical load on the bearings to differ than the expected vertical load estimated from the numerical simulation. Therefore, the distribution of the axial load on the numerical simulation was calibrated to better match the experimental response of the LR bearings. As mentioned before, the vertical load on the CL bearings were not recorded, thus in the calibration process the axial force in each CL bearing,  $F_{CLB}$ , were assumed to be one fifth of the difference in the total weight of the building,  $W_T$  and the total (summation over all LR bearings) static weight on the LR bearing,  $W_{T,LRB}$ , as per Equation 7.9.

$$F_{CLB} = \frac{W_T - W_{T,LRB}}{5} \quad (7.9)$$

Then, the procedure of load redistribution, to adjust the axial load on the bearings in the numerical simulation developed by Dao and Ryan (2015) was applied. This procedure is replicated here next for completeness.

Let the actual vertical reaction at bearing  $i$  at the beginning of a test simulation be  $R_{i,test}$  and the vertical reaction at bearing  $i$  in the numerical simulation subjected to gravity load be  $R_{i,0}$ . The additional reaction  $\Delta R_i$  needed at bearing  $i$  so that the initial analytical reaction matches the test data is:

$$\Delta R_i = R_{i,test} - R_{i,0} \quad (7.10)$$

Additional forces were applied to the top of the bearings to increase the reaction at bearing  $i$  in the numerical simulation by  $\Delta R_i$ . The value of these additional forces was determined as follows.

The reaction  $r_{ij}$  was measured from the numerical simulation, where  $r_{ij}$  = reaction at bearing  $i$  ( $i = \overline{1,9}$ ) due to a unit vertical load applied at the top of bearing  $j$  ( $j = \overline{1,9}$ ). It should be noted that:

$$\sum_{i=1}^9 r_{ij} = 1 \quad (7.11)$$

If the behavior of the system remains linear, the vertical reaction at bearing  $i$  caused by a vertical load  $P_j$  applied at the top of bearing  $j$  is:



$$R_{ij} = r_{ij} \cdot P_j \quad (7.12)$$

The total vertical reaction  $R_i$  at bearing  $i$  when each bearing is subjected to a vertical load  $P_j$  is:

$$R_i = \sum_{j=1}^9 r_{ij} \cdot P_j \quad (7.13)$$

Based on Equations (7.10) and (7.13), the additional vertical loads  $P_j$ s needed for adjusting the initial vertical reactions in the numerical simulation such that they match the initial reactions measured from test can be obtained by solving the following system of linear equations:

$$\sum_{j=1}^9 r_{ij} \cdot P_j = \Delta R_i, \quad i = \overline{1,9} \quad (7.14)$$

From Equation (7.10):

$$\sum_{i=1}^9 \Delta R_i = \sum_{i=1}^9 R_{i,test} - \sum_{i=1}^9 R_{i,0} = W_{test} - W_{model} \quad (7.15)$$

where  $W_{test}$  and  $W_{model}$  are the weight of the specimen and the weight of the model, respectively.

If the weight of the model is identical to the weight of the specimen, then:

$$\sum_{i=1}^9 \Delta R_i = 0 \quad (7.16)$$

From Equations (7.14):

$$\sum_{i=1}^9 \sum_{j=1}^9 r_{ij} \cdot P_j = \sum_{i=1}^9 \Delta R_i = 0 \quad (7.17)$$

Or:

$$\sum_{j=1}^9 P_j \sum_{i=1}^9 r_{ij} = 0 \quad (7.18)$$

Introducing Equation (7.11) into Equation (7.18):

$$\sum_{j=1}^9 P_j = 0 \quad (7.19)$$

This means that when the weight of the numerical simulation equals the weight of the specimen, the additional set of loads computed from Equation (7.14) does not change the total vertical load on the structure. Because the initial recorded reactions on the LR bearings changed from simulation to simulation, the analytical reactions were modified independently at the beginning of every simulation.

## **CHAPTER 8: MODEL FOR ISOLATION BEARINGS AND BEARING CHARACTERIZATION**

In this chapter, a basic numerical model that was used to represent and characterize the LR isolation system is presented. The modeling assumptions for the LR bearings and CL bearings are described in Section 8.1 and 8.2, respectively. Section 8.3 estimates the vertical dynamic properties of the system considering the contribution of the load cell assemblies. Section 8.4 details the procedure used by Dynamic Isolation Systems to characterize the parameters of the LR bearings based on cyclic testing (Sec. 8.4.1), which is extended to the test data (Sec. 8.4.2). Section 8.5 compares the experimental and numerical responses of the bearing and the superstructure considering the characterized bearing properties described in Section 8.4.

### **8.1 Lead-Rubber Bearings**

In this basic numerical model, the force-deformation relation of the LR bearings was represented by a combination of spring elements. The horizontal and vertical behavior of the bearing was assumed to be uncoupled. Horizontal-vertical coupling, loss of lateral stiffness, and loss of axial load carrying capacity have been observed in elastomeric bearings under the combination of large horizontal displacements and axial forces (Buckle and Liu 1994, Buckle et al. 2002, Warn and Whittaker 2006). However, the constraint provided by the vertically stiff CL bearings and base diaphragm, documented in Chapter 6, prevented axial shortening and loss of lateral load carrying capacity of the isolation system, which supports the choice of an uncoupled bearing model.

### 8.1.1 Horizontal Direction Modeling Assumptions

The force-displacement relation of the LR bearings in the horizontal direction was idealized as bilinear as shown in Figure 8-1. Numerically, this was implemented as a rate-independent plasticity model with kinematic hardening; defined by the elastic stiffness ( $K_1$ ), yield force ( $F_y$ ), and the kinematic ( $K_H$ ) hardening modulus. These parameters were calculated from the post yield stiffness ( $K_d$ ) and characteristic strength ( $Q_d$ ) according to:

$$K_1 = 10K_d \quad (8.1)$$

$$F_y = Q_d + K_d D_y \quad (8.2)$$

$$K_H = \frac{K_1 K_d}{K_1 - K_d} \quad (8.3)$$

where  $D_y$  is the yield displacement. The values of  $K_d$  and  $Q_d$  selected for numerical simulation are given in Section 8.4. Bidirectional coupling was accounted for through a circular yield surface. Physically, the element was implemented as a `zeroLengthSection` element in OpenSees (2010) incorporating a `Bidirectional` section to directly represent the force-deformation relation of the isolator.

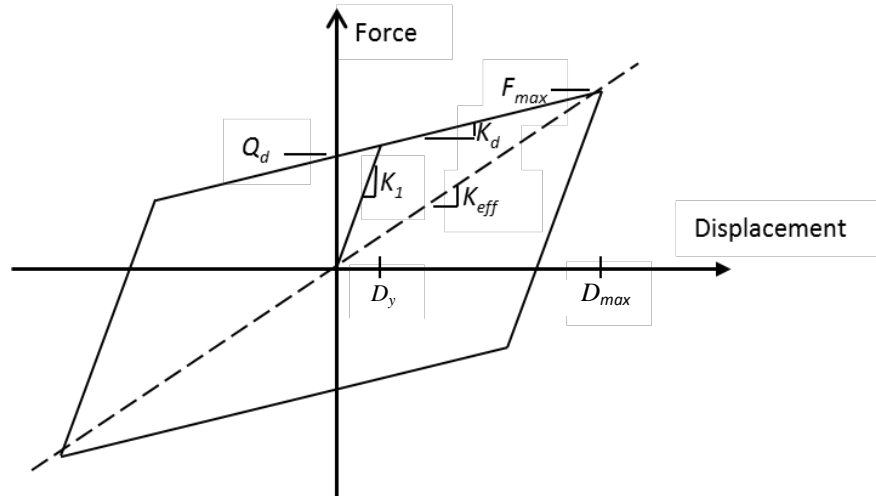


**Figure 8-1: Horizontal force-displacement of LR bearing for numerical simulation**

### 8.1.2 Vertical Direction Modeling Assumptions

In the vertical direction, the force-displacement relation of the LR bearings was idealized as bilinear elastic with different stiffness in tension and compression as recommended by Dynamic Isolation Systems. Physically, the bearings have nominal stiffness in tension but cavitate at relatively low values of tensile pressure (Constantinou et al. 2007). This behavior can be approximately simulated by assuming a low tensile stiffness. Numerically, an elastic-no tension model (Figure 8-2(a)) was combined in parallel with an elastic model (Figure 8-2(b)) to achieve the desired behavior shown in Figure 8-2(c). An effective tension stiffness of 2% of the compression stiffness was assumed. This approach was recommended by Dynamic Isolation Systems as an approximate way to capture the elastic-plastic tension behavior of the bearing and limited tensile capacity.

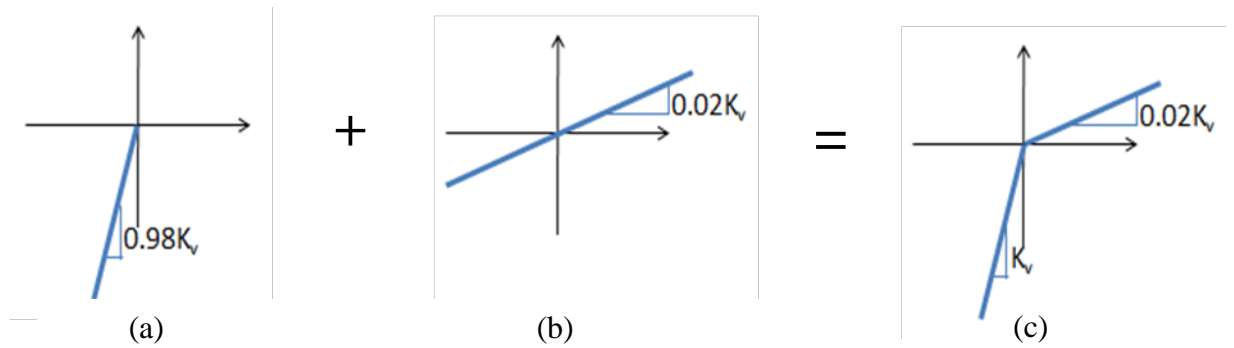


**Figure 8-2: Vertical force-deformation of LR bearing for numerical simulation: (a) elastic-no tension, (b) elastic, and (c) combined**

The nominal vertical stiffness of each LR bearing, as provided by Dynamic Isolation Systems, was  $K_v = 1,500$  kN/mm (8,570 kip/in). The vertical stiffness of the bearings in the numerical simulation model was adjusted by trial and error to 1,000 kN/mm (5,710 kip/in) to indirectly account for the flexibility of the load cell support assemblies described in Section 4.1. This adjusted value was supported by the following approximate calculations. The vertical stiffness of a single Type A load cell – present under three of the four bearings – was given as  $K_{LC} = 8,500$  kN/mm (48,600 kip/in). The vertical stiffness of the steel plates was assumed to be dominated by plate bending as the weight carried by the isolator was shifted to different locations on the steel plate. Assuming the plate acts as a continuous beam spanning several load cells, the plate bending stiffness was computed assuming fixed-fixed boundary conditions with a point load (the weight transferred through the isolator) acting midway between the supports (load cells):

$$K_{plate} = \frac{192EI}{L_{clear}^3} \quad (8.4)$$

where  $E = 200$  GPa (29,000 ksi) is the elastic modulus of steel,  $L_{clear} = 750$  mm (30 in) is the clear length between adjacent load cells, and  $I = bh^3/12$ , using  $b = L_{clear}/2$  and  $h = 100$  mm (4 in) as the plate thickness. With these assumptions, the plate bending stiffness was computed to be  $K_{plate} = 2,800$  kN/mm (19,000 kip/in). Combining the stiffness of an LR bearing, plate, and load cell in series

$$\frac{1}{K_{total}} = \frac{1}{K_v} + \frac{1}{K_{plate}} + \frac{1}{K_{LC}} \quad (8.5)$$

the total vertical stiffness of the bearing load cell assembly was  $K_{total} = 880$  kN/mm (5,030 kip/in), which is close to the assumed value of 1,000 kN/mm (5,710 kip/in). The estimated stiffness of the bearing-load cell assembly was estimated similarly for a TP bearing-load cell assembly, which was in fact further corroborated by a detailed finite element analysis of the assembly (Dao and Ryan, 2015).

## 8.2 Cross Linear Bearing

Similar to the LR bearings, the force-displacement relation of the CL bearings was represented by a combination of spring elements, which were uncoupled in the horizontal and vertical directions. This assumption is not strictly accurate since the CL bearing is a friction device, and thus the horizontal force is proportional to the instantaneous axial force. However, the friction coefficient of the CL bearings was small so that their contribution to the overall base shear was negligible.

### 8.2.1 Horizontal Direction Modeling Assumptions

The force-displacement relation for the CL bearings was assumed to be elastic-perfectly plastic (with a post-yield stiffness of zero) in each horizontal direction as shown in Figure 8-3. The rolling rail system acts independently in each horizontal direction; thus a model with a square interaction surface was used instead of a bidirectionally coupled model. This assumption only affects the first yield mechanism since the model is perfectly plastic. The model initial stiffness of the CL bearing ( $K_{1s}$ ), where yield represents rolling of the bearing, was estimated as:

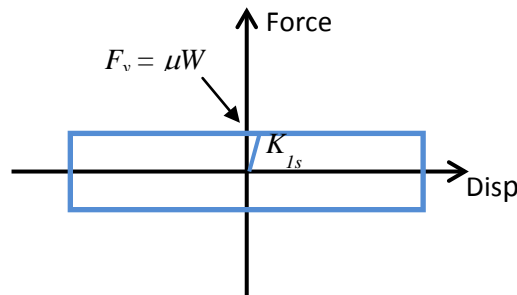


**Figure 8-3: Horizontal force-displacement of CL bearing for numerical simulation**

$$K_{1s} = \frac{\mu W}{D_y} \quad (8.6)$$

where  $\mu$  is the coefficient of friction,  $W$  is the weight (or static vertical force) on each isolator, and  $D_y$  is the yield displacement. The assumed friction coefficient for numerical simulation was 0.0025. Note that this differs from the value listed in Table 3-3, which reflects more recently acquired information about the CL bearing.



Under typical distribution of dead load based on tributary area, the center CL bearing would carry more weight than the CL bearings in corner positions. However, in the tested TP isolation system, the center bearing was lightly loaded compared to several of the other bearings (Dao and Ryan, 2015). The warping at the base of the structure and the shimming procedure used to adjust the loads in the LR bearings affected the load distribution. The static vertical force in individual CL bearings was not measured during the test program. Since load distribution by tributary area was not a reasonable assumption, the total weight carried by the CL bearings (deduced from the weight of the structure and the measured weight on the LR bearings) was distributed evenly to individual CL bearings according to:

$$W = \frac{(W_{total} - \sum W_{LRBs})}{5} \quad (8.7)$$

Because of the uncertainty in the static axial loads in the CL bearings and the sensitivity of load transfer (Section 6.2) to the static equilibrium state, the developed numerical simulation model was not expected to accurately track axial forces in either LR or CL bearings. Trial and error variation of the vertical stiffness of these devices, which affects the balance of forces and load distribution over the isolators, was found to have little consequence to the predicted horizontal response of the isolation system.

### 8.2.2 Vertical Direction

The vertical force-deformation for the CL bearings was modeled using a similar parallel spring model as used for the LR bearing. In this case, the compression ( $K_{vc}$ ) and tension ( $K_{vt}$ ) stiffness were independent values provided by the manufacturer as listed in Table 3-

3. Thus, the composite force-displacement relation was derived from an elastic-no tension spring with stiffness  $K_{vc} - K_{vt}$  (Figure 8.4(a)) and an elastic spring with stiffness  $K_{vt}$  (Figure 8.4(b)) to get the combined behavior of Figure 8.4(c).

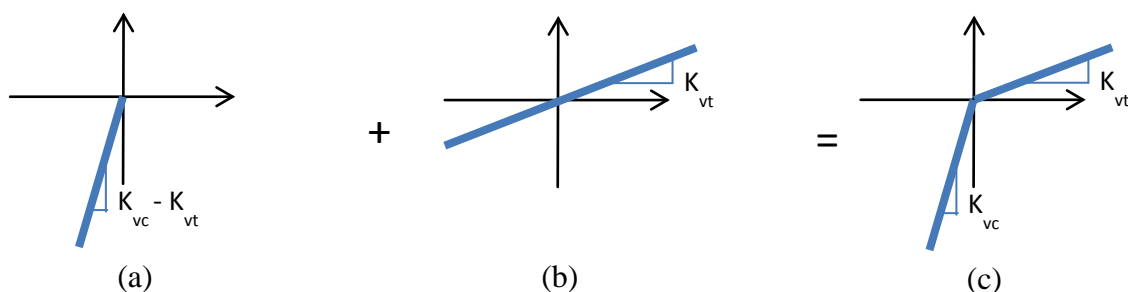


**Figure 8-4: Vertical force-deformation of CL bearing for numerical simulation: (a) elastic-no tension, (b) elastic, and (c) combined**

### 8.3 Composite Vertical Properties of the Isolation System

As part of the investigation, it was considered that due to the flexibility of the load cell assemblies, the vertical stiffness (and fundamental frequency) did not represent a typical isolation system in the vertical direction. The following calculations support the conclusion that the hybrid LR isolation system was not uncharacteristically flexible in the vertical direction.

A typical “rigid body” vertical frequency of an elastomeric isolation system, computed from

$$\omega_{z,rigid} = \sqrt{\frac{g \cdot \sum K_v}{W}} \quad (8.8)$$

ranges from 10-15 Hz (Kasalanati 2012). Recall that the measured weight of the testbed building was 5,220 kN (1,174 kip), and the nominal (manufacturer supplied) vertical

stiffnesses were 1,500 kN/mm (8,565 kip/in) for an LR bearing and 3,470 kN/mm (19,814 kip/in) for a CL bearing. The adjusted vertical stiffness of the LR bearing-load cell assembly was assumed to be 1,000 kN/mm (5,710 kip/in). Ignoring the influence of the CL bearings, suppose the isolation system had consisted of 4 LR bearings, which would be typical for the composite weight of the system, and not supported on load cells - thus representative of the expected field conditions for these LR bearings. The vertical frequency of the isolation system, computed from Equation (8.8), would be about 17 Hz (0.06 sec), which is on the stiff side of typical. Now, suppose the isolation system consisted of 4 LR bearings supported on load cells with the modified stiffness of 1,000 kN/mm (5,710 kip/in). In this case, the frequency would be reduced slightly to 14 Hz (0.07 sec), which is also stiff. However, the actual hybrid system tested in this experimental program, with 4 LR bearings on the load cell assemblies at 1,000 kN/mm (5,710 kip/in) and 5 CL bearings at 3,470 kN/mm (19,814 kip/in), had a vertical frequency of 31 Hz (0.032 sec). Thus, as asserted above, the fundamental vertical frequency of the tested hybrid isolation system was actually quite large, such that the system can be considered sufficiently stiff.

#### **8.4 Characterization of Lead-Rubber Bearings**

To predict the response of the isolation system for design of a nuclear power plant, one would ideally develop the modeling or numerical simulation parameters based on physical properties of the individual isolation devices. As discussed in Chapter 1,  $K_d$  is physically related to the stiffness of rubber and  $Q_d$  is physically related to the strength of the lead plug. For design, a single set of bilinear parameters ( $K_d, Q_d$ ) is generally used to

represent the bearing hysteresis loop over a wide range of displacement, supplemented by bounding analysis.

For the LR bearings tested as part of this experimental program, a single set of simulation parameters did not lead to sufficient accuracy in the model over the range of displacement amplitudes observed in the test program. Factors that may have amplified the disparity in bearing hysteresis loop and best fit model parameters included the following. First, the test program included a few small amplitude simulations, such as Westmorland 80% that did not drive the isolators sufficiently into the nonlinear range to develop the full characteristic strength of the lead plug. Second, the pinching behavior induced by the smaller size lead plug, not seen in typical full scale LR bearings, meant that a bilinear model could not be fit closely to the observed hysteresis loop, which lacked a consistent backbone curve. Thus, more significant parameter variations induced by amplitude changes were observed throughout the test program than would be considered in design.

To obtain a consistently accurate prediction of isolator displacements and forces across the set of trials, the bearing parameters were characterized independently for each simulation in the test program. Characterized bearing properties were determined both for pseudo-static cyclic tests conducted by DIS and for each simulation during the test program at E-Defense.

### 8.4.1 Characterization by Dynamic Isolation Systems

The LR bearings were characterized by Dynamic Isolation Systems in their manufacturing facility prior to shipment to Japan. Bearings were tested in the machine two at a time; each pair of bearings was subjected to cyclic shear tests under constant compressive load and the measured horizontal force represents the sum of the horizontal forces in the two bearings. The tests were displacement controlled, such that the bearings were cycled back and forth to the target maximum displacement in each direction for the desired number of cycles. A series of four tests were conducted at different axial loads and displacements, as summarized in Table 8-1. Test C was added to accommodate E-Defense's safety protocol, given that a displacement demand of 550 mm (22 in) was to be targeted during the tests. Test D was a repeat of Test A and was intended to document any change in hysteresis loops as a result of repeated loading. A minimum fifteen minute interval was inserted after every test. As shown by the rate parameter in Table 8-1, these characterization tests were essentially static and thus do not include any rate effects on the bearing response. In particular, the lead plug heating effects would be smaller in a static simulation than in a high speed cyclic simulation.

**Table 8-1: Compression Shear Test Schedule**

<b>Test ID</b>	<b>Number of Cycles</b>	<b>Axial Load (kN)</b>	<b>D<sub>max</sub> (mm)</b>	<b>Shear Strain %</b>	<b>Rate (cycles/min)</b>
A	3	600	300	125	1.15
B	3	1000	500	208	0.71
C	0.5	100	650	271	0.54
D	3	600	300	125	1.15

In the test report provided by Dynamic Isolation Systems (Appendix E), the isolator properties were determined by fitting a bilinear loop to the recorded hysteretic loop such that the energy dissipated and the effective stiffness of the two loops were equal. The fitted post-yield stiffness ( $K_d$ ) and characteristic strength ( $Q_d$ ) were determined directly from the fitted loop. The fitting procedure is described conceptually by Figure 8-5. The effective stiffness of the isolator ( $K_{eff}$ ) is equal to  $F_{max}/D_{max}$ , where  $D_{max}$  is the maximum isolator displacement and  $F_{max}$  is the maximum force measured in the isolator. If the cycle is unsymmetric, the peak-to-peak stiffness is used rather than the half cycle effective stiffness. The energy dissipated per cycle ( $EDC = \text{area of the loop}$ ) was determined by numerically integrating the force-displacement data. Fixing the corner points ( $F_{max}, D_{max}$  and  $F_{min}, D_{min}$ , which are the minimum isolator force and displacement, respectively) of the numerical simulation to match the test data,  $Q_d$  and  $K_d$  are adjusted until the energy dissipated in a cycle of the theoretical bilinear loop with initial stiffness  $K_I = 10 K_d$  matches the numerically integrated energy dissipated from the recorded data.

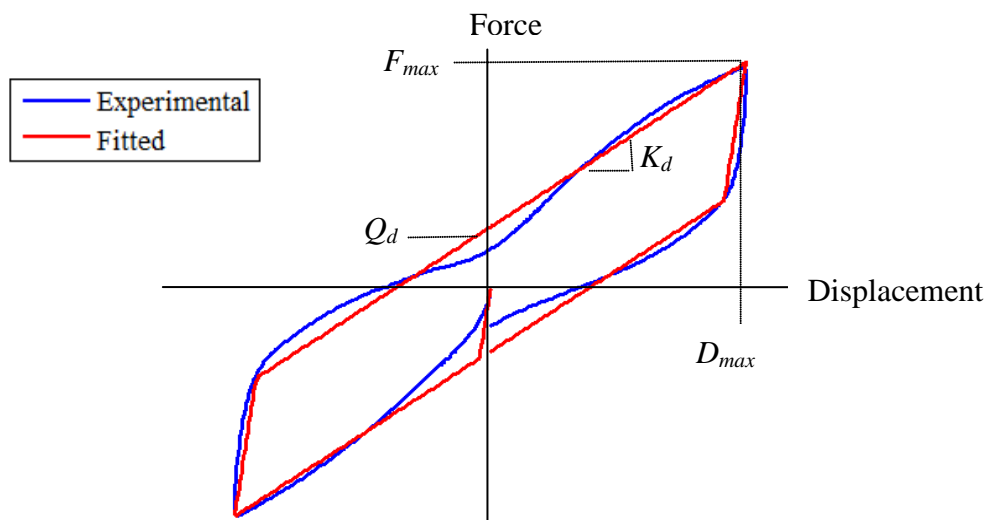


**Figure 8-5: Comparison of fitted hysteresis loop and parameters to test data**

The force-displacement relationship for one of the isolator pairs recorded during the Test A loading protocol is shown in Figure 8-6. Pinching of the hysteresis loop is observed around zero displacement, which is expected when the lead plug is small relative to the diameter of the bearing or simply small on an absolute scale. Pinching may be observed in full size or prototype LR bearings manufactured for real world projects, but far less pronounced than that observed here (Kasalanati, 2012).

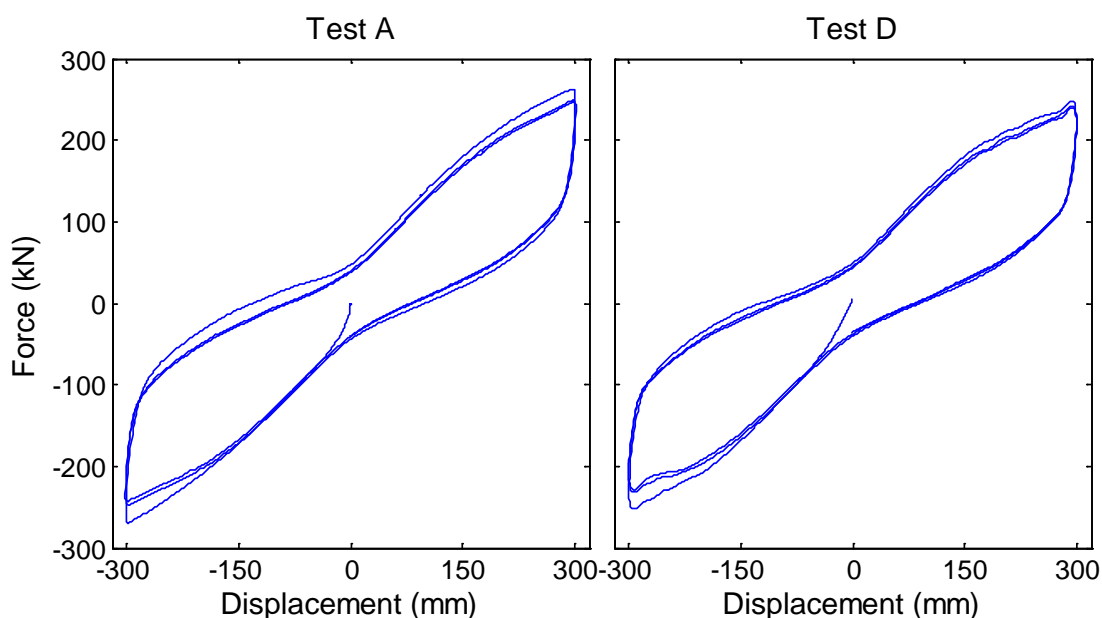


**Figure 8-6: Hysteresis loop of Test A and D for one of the isolation pairs**

The recorded and fitted parameters for the test data (Figure 8-6) are listed in Table 8-2 for each cycle as well as the average over all 3 cycles. The energy dissipation per cycle  $EDC$  and thus fitted  $K_d$  and  $Q_d$  decrease after each cycle, with a large drop noted after the first cycle. As a result of the pinching, the fitted  $Q_d$  is significantly larger (by up to 70%) than the y-axis force intercept of the test data. The characterization procedure was carried out

for each cycle of all four tests. The characterized values for each test (averaged over all cycles and over the two pairs of bearings) are reported in Table 8-3.

**Table 8-2: Recorded and Fitted Parameters for Test A**

Cycle	$D_{max}$ (mm)	$F_{max}$ (kN)	$K_{eff}$ (kN/mm)	$EDC$ (kN.mm)	$K_d$ (kN/mm)	$Q_d$ (kN)
1	301	266	0.88	84550	0.65	71.2
2	302	249	0.82	74860	0.62	62.9
3	302	245	0.81	72060	0.61	60.4
AVERAGE	302	253	0.84	77160	0.63	64.8

**Table 8-3: Characterized Isolator Parameters for all Tests in the Sequence**

Test	Axial Load (kN)	$D_{max}$ (mm)	$K_d$ (kN/mm)	$Q_d$ (kN)	$K_{eff}$ (kN/mm)
A	600	300	0.63	64.7	0.84
B	1000	50	0.51	75.6	0.66
C	100	65	0.55	85.6	0.68
D	600	30	0.58	63.1	0.79

The isolator parameters given in the design specifications (Table 3-3) were stiffness  $K_d = 0.65$  kN/mm (3.7 kip/in), characteristic strength  $Q_d = 65.7$  kN (14.8 kips), and effective stiffness  $K_{eff} = 0.87$  kN/mm (5 kip/in). The fitted parameters are within 4% of the design specifications at a displacement of 300 mm (12 in). Note that the design specifications are just target values set by Dynamic Isolation Systems prior to their manufacture.

#### 8.4.2 Characterization Based on Experimental Data

The characterization of the bearings for the earthquake simulations was complicated by the fact that the experimental data was bidirectional, and the random earthquake excitation did not produce the smooth controlled hysteresis loops of cyclic data. A



procedure to characterize the bearing parameters directly based on bidirectional data was desired, but such procedure was not found in the literature. Thus, the following alternative procedure was implemented to characterize the bearings for each test.

**Step1:** To obtain the best results for a unidirectional characterization procedure, the test data in both directions was rotated to an alternate coordinate system with a main axis that contained the largest displacement cycle of the record. The main axis was identified from the largest single cycle peak-to-peak excursion on the displacement trace. For instance, in Vogtle 100%, the main axis was identified at an approximate 45 degree rotation (Figure 8-7), consistent with the rotation of the input motion to generate the peak displacement demand along the diagonal (Section 3.3). Identification of the main axis was subjective if the displacement trace contained a large circular cycle of motion.

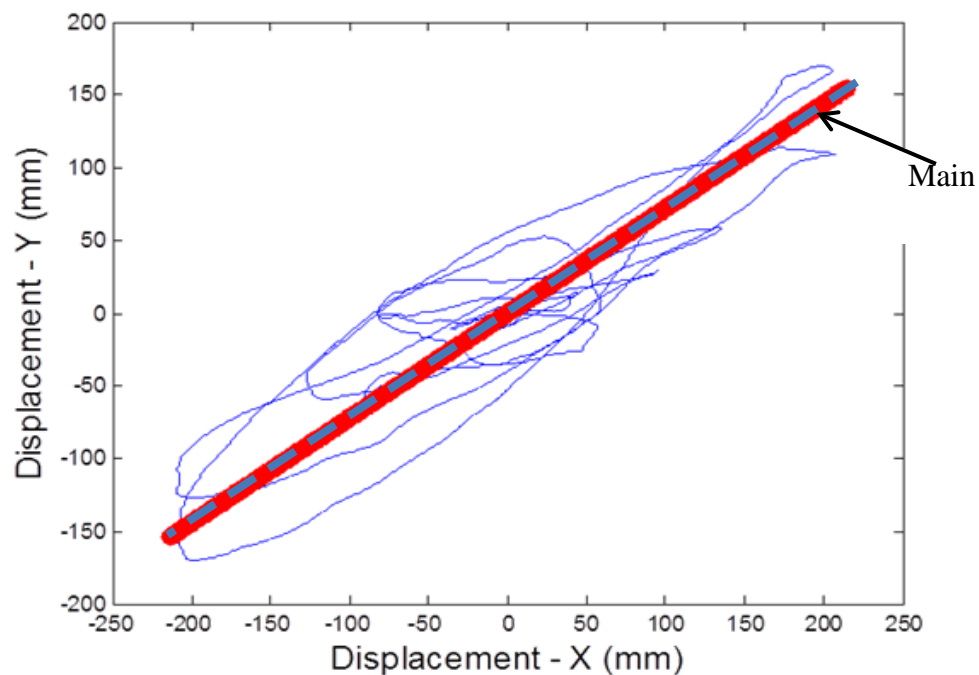


**Figure 8-7: Projection of displacement trace to main axis for Vogtle 100%**

**Step 2:** The isolator displacement history was projected to the main axis direction of the rotated data, and the cycle containing the largest peak-to-peak displacement was selected for characterization. Figure 8-8 shows the selected cycle for LRB-E for Vogtle 100%.

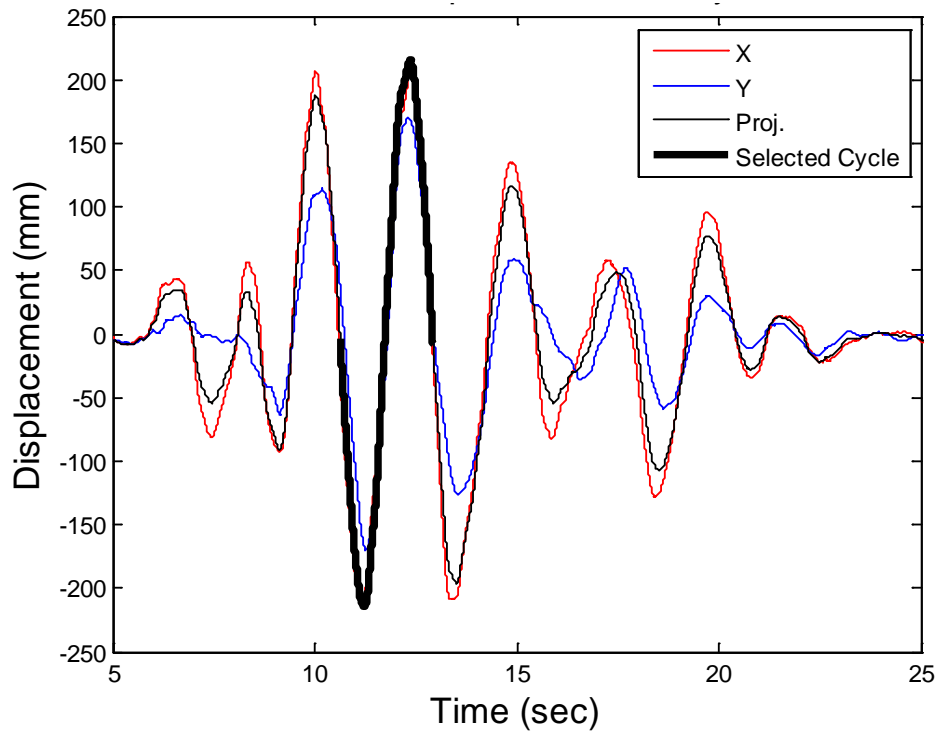


**Figure 8-8:** Selection of cycle for characterization for Vogtle 100%

**Step 3:** The energy dissipated ( $EDC_{test}$ ) for the selected cycle was determined by numerically integrating the shear force versus lateral displacement using a cumulative trapezoidal algorithm.

**Step 4:** The theoretical characteristic strength  $Q_d$ , post-yield stiffness  $K_d$  and yield displacement  $u_y$  were fitted to the projected test data using essentially the same algorithm employed by Dynamic Isolation Systems, and summarized as follows. The energy dissipated in a bilinear force-displacement loop  $EDC_{bilin}$  is determined by:

$$EDC_{bilin} = 4Q_d(D_{peak} - D_y) \quad (8.9)$$

where  $Q_d$  is the characteristic strength,  $D_{peak}$  is absolute peak displacement for the selected cycle, and  $D_y$  is the yield displacement. The energy dissipated during the experiment ( $EDC_{test}$ ) is equated to the theoretical energy dissipated ( $EDC_{bilin}$ ), and Equation 8.9 is rearranged to solve for  $Q_d$ . The yield displacement  $D_y$ , which is unknown, is dropped from the equation and replaced with a calibration factor  $\gamma$  initialized to 1:

$$Q_d = \frac{\gamma * EDC_{test}}{4 * D_{peak}} \quad (8.10)$$

From the estimate of  $Q_d$ , the theoretical post-yield stiffness  $K_d$  and yield displacement  $D_y$  are computed.

$$K_d = \frac{F_{peak} - Q_d}{D_{peak}} \quad (8.11)$$

$$D_y = \frac{Q_d}{K_1 - K_d} \quad (8.12)$$

where,  $F_{peak}$  is the absolute peak force for the selected cycle, and  $K_1 = 10 K_d$ . Equations (8.9) – (8.12) are computed iteratively until convergence is obtained ( $EDC_{bilin} \approx EDC_{test}$ ). If  $EDC_{test} < EDC_{bilin}$ , then  $\gamma$  is decreased by small increments, while if  $EDC_{test} > EDC_{bilin}$ , then  $\gamma$  is increased by small increments.

Once the characterized values were computed by the above procedure, the model parameters (initial stiffness, kinematic hardening modulus and yield force) were computed from Equations 8.1 to 8.3.

The hysteresis loop for the projected experimental data and the fitted loop based on characterized parameters are compared in Figure 8-9 for Vogtle 100%. In Figure 8-9, no obvious bidirectional interaction is observed in the experimental data, which supports the idea that projecting the force-displacement data to a main axis improves the characterization compared to experimental data that has not been projected.

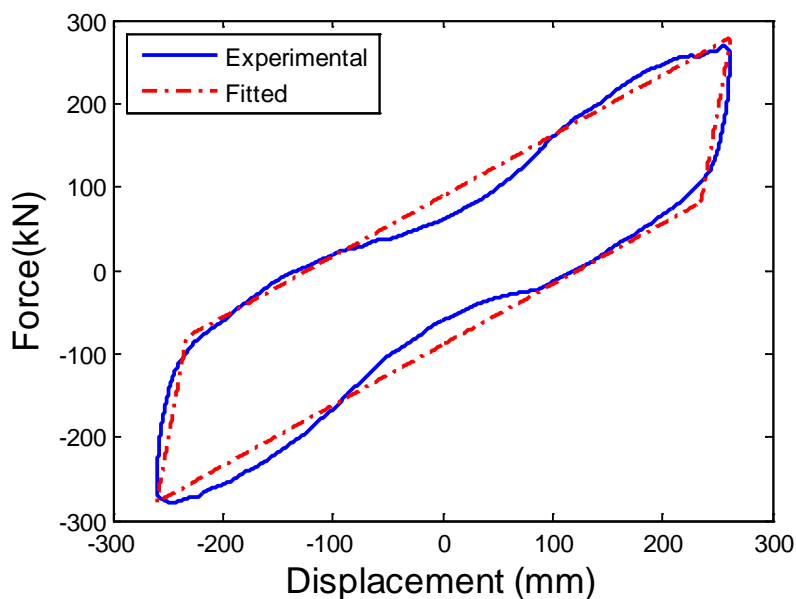


**Figure 8-9:** Hysteresis loop of peak cycle for the projected-direction for East bearing for Vogtle 100%.

The characterized parameters  $Q_d$ ,  $K_d$ ,  $D_y$  for each bearing and the average among all bearings for each simulation are summarized in Table 8-4. The numerical simulation model in OpenSees used the average values listed on the last column for each simulation, with some minor adjustment, which is described momentarily. The range of the parameters varied as follows. The average of  $Q_d$  ranged from 33.4 – 89.4 kN (7 - 20 kip), and the average  $K_d$  ranged from 0.57 – 1.1 kN/mm (3.2 - 6.3 kip/in). However, omitting WSM80 and ELC130, which produced only about 90 mm (4 in) and 210 mm (8 in)

displacement, respectively,  $Q_d$  ranged from 62.0 - 89.4 kN (14.0 – 20.1 kip), and  $K_d$  ranged from 0.57 – 0.82 kN/mm (3.2 – 4.7 kip/in), where the displacement varied from 200 mm (8 in) to 550 mm (22 in). As a comparison, the target specifications at a displacement of 300 mm (12 in) were  $Q_d = 65.7$  kN (14.8 kip) and  $K_d = 0.65$  kN/mm (3.7 kip/in).

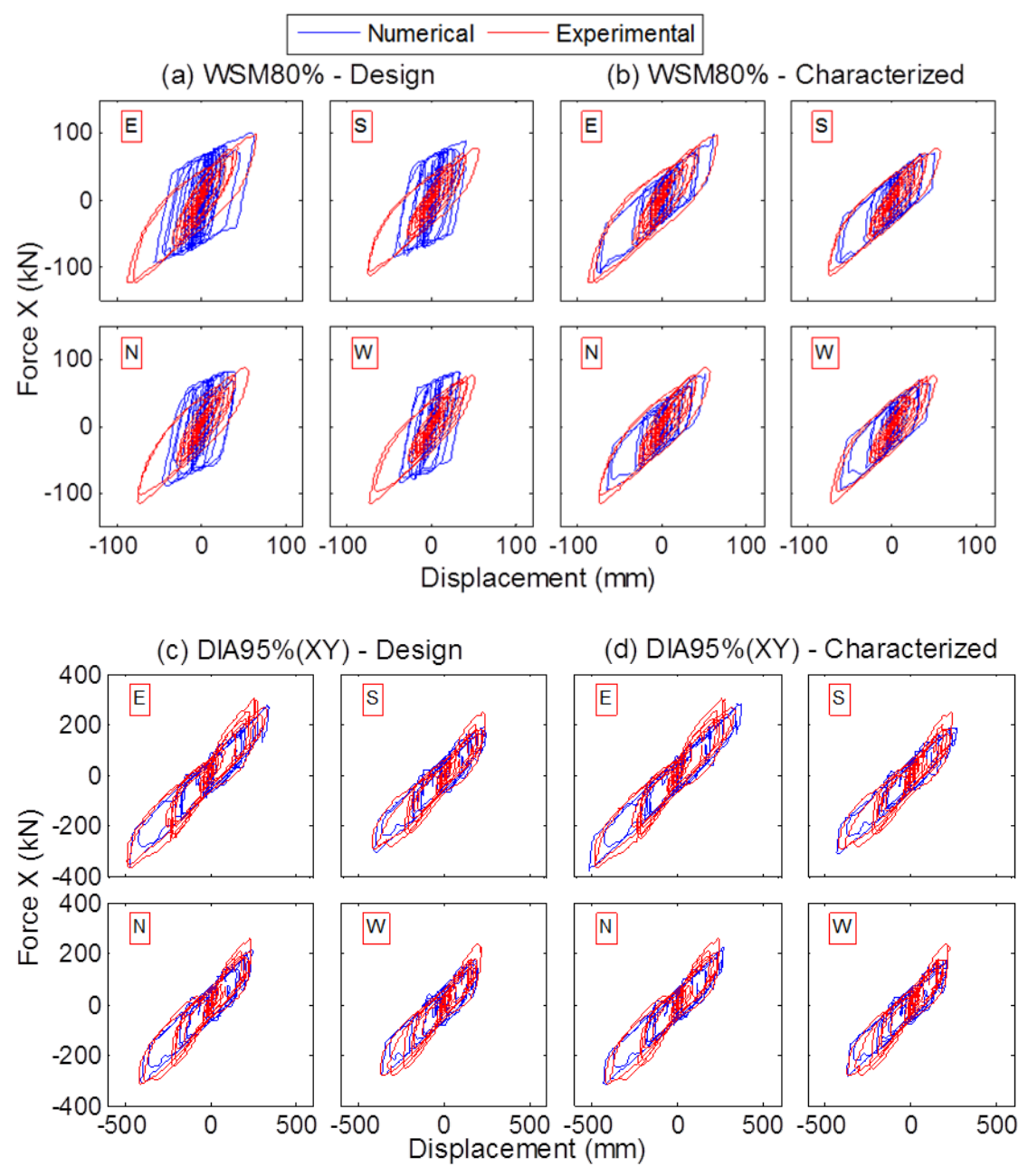
The numerical and experimental simulation hysteresis loops are compared using the design parameters (Figure 8-10(a),(c)) and the parameters determined by characterization (Figure 8-10(b),(d)) for the Westmorland 80% and Diablo 95% (XY) motion. The numerical simulation loops were determined by response history analysis of the complete specimen model (described in Chapter 7) subjected to the recorded table motion. The characterized parameters led to a clear improvement in prediction of the peak displacement for Westmorland 80%. On the other hand, since the characterized and design values of  $Q_d$  and  $K_d$  for Diablo 95% (XY) are about the same, the hysteresis loops and peak displacements generated by the two approaches were similar, as shown in Figure 8-10(c) and (d). Overall, Figure 8-10 confirms that the bilinear model is a reasonable assumption for the behavior of the bearing if the parameters are calibrated for each simulation.

Table 8-4: Characterized Bearing Parameters for Each Earthquake Simulation

Trial #	GM	Isolator	$Q_d$ (kN)	$K_d$ (kN/mm)	$K_I$ (kN/mm)	$D_y$ (mm)	Average
1	WSM80	E	37.1	1.07	10.66	0.04	$F_y = 37.1$ kN $Q_d = 33.4$ kN $K_d = 1.10$ kN/mm
		S	31.5	1.07	10.70	0.03	
		N	33.6	1.10	11.03	0.03	
		W	31.5	1.15	11.51	0.03	
2	SIN100(Y)-1	E	78.2	0.84	8.38	0.10	$F_y = 86.0$ kN $Q_d = 77.4$ kN $K_d = 0.82$ kN/mm
		S	76.3	0.81	8.08	0.10	
		N	77.8	0.82	8.16	0.11	
		W	77.2	0.80	8.04	0.11	
3	VOG75-1	E	77.4	0.82	8.19	0.10	$F_y = 75.5$ kN $Q_d = 67.9$ kN $K_d = 0.82$ kN/mm
		S	61.6	0.87	8.72	0.08	
		N	70.8	0.82	8.18	0.10	
		W	61.8	0.76	7.59	0.09	
4	VOG100	E	86.3	0.74	7.35	0.13	$F_y = 88.6$ kN $Q_d = 79.7$ kN $K_d = 0.74$ kN/mm
		S	77.6	0.77	7.67	0.11	
		N	82.0	0.72	7.15	0.13	
		W	72.9	0.73	7.35	0.11	
5	VOG125	E	91.9	0.64	6.42	0.16	$F_y = 95.3$ kN $Q_d = 85.8$ kN $K_d = 0.65$ kN/mm
		S	83.0	0.64	6.38	0.14	
		N	86.9	0.64	6.43	0.15	
		W	81.3	0.67	6.74	0.13	
6	VOG150	E	92.4	0.60	5.98	0.17	$F_y = 98.5$ kN $Q_d = 88.7$ kN $K_d = 0.59$ kN/mm
		S	87.4	0.56	5.56	0.17	
		N	87.5	0.59	5.91	0.16	
		W	87.3	0.60	5.99	0.16	
7	VOG175	E	92.3	0.60	6.00	0.17	$F_y = 99.4$ kN $Q_d = 89.4$ kN $K_d = 0.57$ kN/mm
		S	90.5	0.54	5.38	0.19	
		N	87.8	0.57	5.67	0.17	
		W	87.1	0.56	5.61	0.17	
8	DIA80	E	79.2	0.66	6.57	0.13	$F_y = 74.8$ kN $Q_d = 67.3$ kN $K_d = 0.66$ kN/mm
		S	64.0	0.63	6.32	0.11	
		N	68.4	0.69	6.85	0.11	
		W	57.6	0.67	6.70	0.10	
9	DIA95(XY)	E	79.9	0.63	6.28	0.14	$F_y = 78.1$ kN $Q_d = 70.3$ kN $K_d = 0.62$ kN/mm
		S	65.7	0.60	5.99	0.12	
		N	74.4	0.62	6.24	0.13	
		W	60.9	0.63	6.30	0.11	
10	ELC130	E	61.0	0.77	7.72	0.09	$F_y = 59.5$ kN $Q_d = 53.5$ kN $K_d = 0.84$ kN/mm
		S	56.6	0.81	8.09	0.08	
		N	48.5	0.88	8.83	0.06	
		W	47.8	0.90	8.96	0.06	

**Table 8-4 (Cont.): Characterized Bearing Parameters for Each Earthquake Simulation**

Trial #	GM	Isolator	$Q_d$ (kN)	$K_d$ (kN/mm)	$K_I$ (kN/mm)	$D_y$ (mm)	Average
11	IWA(XY)	E	81.3	0.67	6.67	0.14	$F_y = 87.6$ kN $Q_d = 78.8$ kN $K_d = 0.63$ kN/mm
		S	80.7	0.59	5.85	0.15	
		N	75.1	0.65	6.52	0.13	
		W	78.0	0.63	6.27	0.14	
12	RRS88(XY)	E	75.5	0.66	6.62	0.13	$F_y = 75.8$ kN $Q_d = 68.2$ kN $K_d = 0.66$ kN/mm
		S	65.1	0.64	6.36	0.11	
		N	68.8	0.67	6.69	0.11	
		W	63.3	0.66	6.59	0.11	
13	RRS88	E	74.3	0.65	6.53	0.13	$F_y = 74.7$ kN $Q_d = 67.2$ kN $K_d = 0.64$ kN/mm
		S	64.5	0.62	6.21	0.12	
		N	67.8	0.65	6.50	0.12	
		W	62.2	0.65	6.47	0.11	
14	VOG75-2	E	69.8	0.76	7.59	0.10	$F_y = 69.5$ kN $Q_d = 62.5$ kN $K_d = 0.74$ kN/mm
		S	61.3	0.76	7.57	0.09	
		N	64.3	0.72	7.25	0.10	
		W	54.8	0.72	7.24	0.08	
15	SIN100(Y)-2	E	75.5	0.77	7.65	0.11	$F_y = 79.7$ kN $Q_d = 71.8$ kN $K_d = 0.74$ kN/mm
		S	74.6	0.73	7.28	0.11	
		N	72.3	0.73	7.31	0.11	
		W	64.6	0.72	7.19	0.10	



**Figure 8-10: Numerical and experimental hysteresis loop using (a),(c) isolator design parameters and (b),(d) characterized parameters.**

The characterized model was calibrated for a cycle close to the peak displacement, but consequently did not improve the response prediction for cycles at smaller displacement. For example, the y-direction hysteresis loop and force history (test versus analysis) are



shown in Figure 8-11 for the first sine wave trial. At small amplitudes (after 22 sec in Fig 8-11(b) and (d)), the actual force in the LR bearing was quite small, indicating the lead plug was not fully engaged. Thus, both numerical models significantly overestimated the force in this range. The characterized model gave a much better prediction of peak force than the design model at the expense of higher force error in the small amplitude part of the record. As another example, the x-direction mean square error in the design model was lower than the characterized model for Vogtle 175%. Based on the displacement history (Figure 8-12), the characterized model better predicted the displacement for the largest cycle (around 10 sec), but the design model better predicted the displacement in subsequent cycles (compare Figures 8-12(a) and (b)).

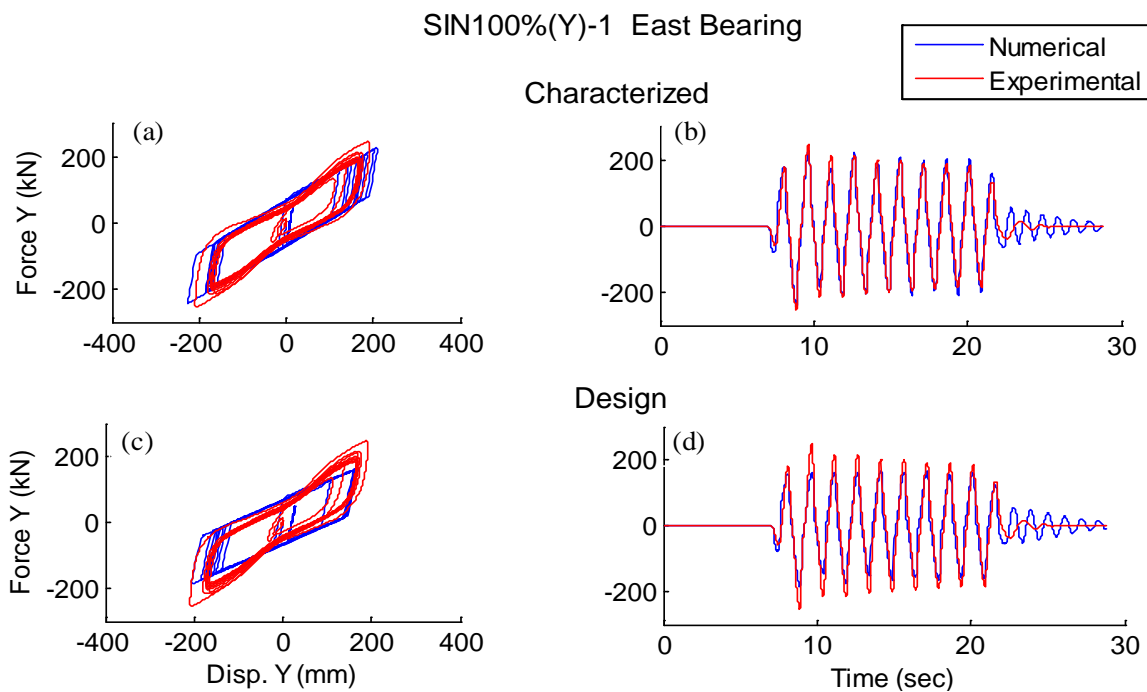


**Figure 8-11: Y-direction hysteresis and force history of test data of the East bearing compared to (a)-(b) characterization model, and (c)-(d) design model for Sine 100%(Y)-1.**

The comparisons illustrate the challenge of predicting the bearing response using a single bilinear model that is insensitive to the characteristic strength variation due to amplitude dependence and temperature change in the lead plug. The challenge was amplified by the pinching in the lead plug, which is not typical of full scale isolation bearings. When the bearing model was calibrated to the largest displacement cycle, it tended to overestimate the force and underestimate the displacement at smaller amplitudes. Development or use of existing models that account for the various effects such as pinching and thermal may significantly improve the fitted response that could be obtained from a model with a single set of parameters. One potential improvement was attempted, which was to model the bearings with trilinear force-deformation that may be able to represent a smoother transition to the fully-yielded state, and thus reduce the energy dissipated in the hysteresis loop for small cycles. This potential improvement was attempted, and is described in the next section.

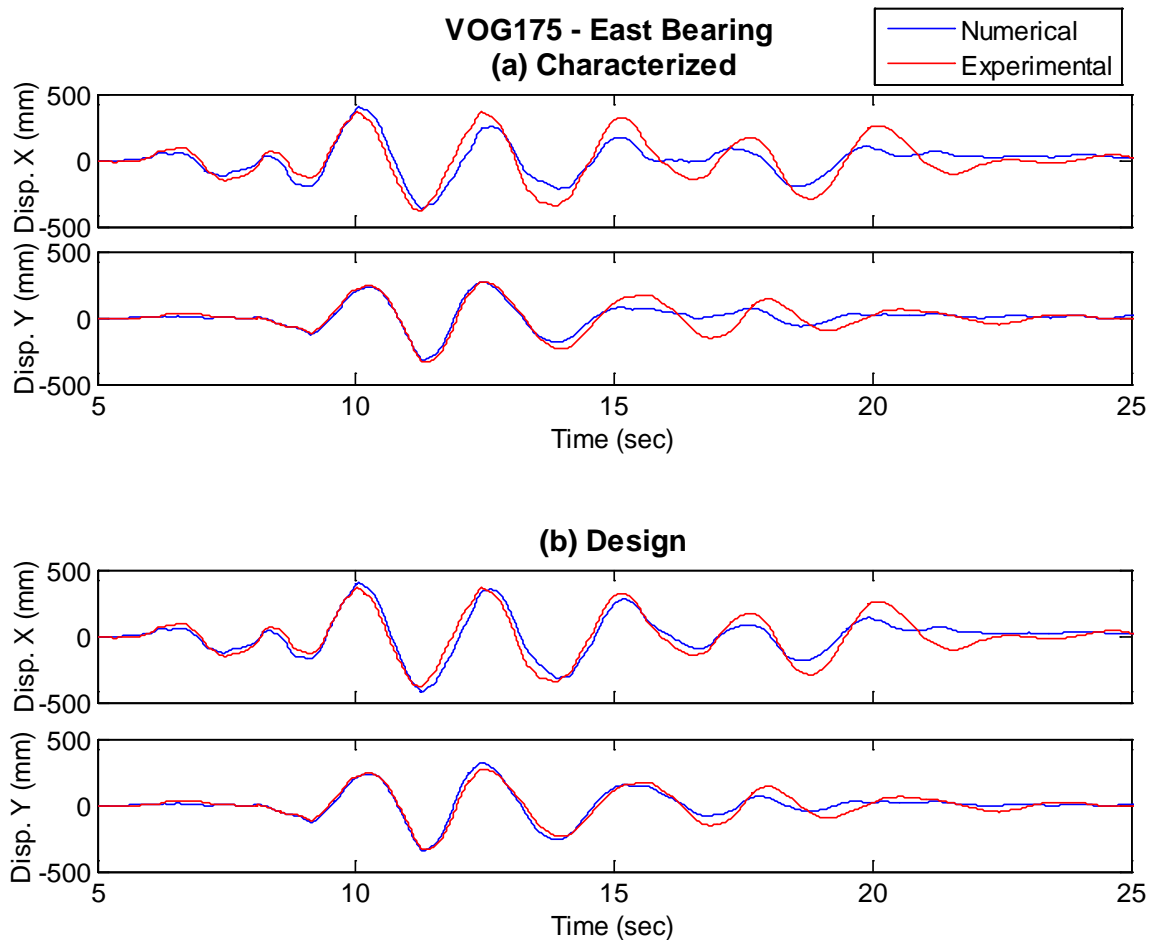


**Figure 8-12: X and y-direction displacement history of experimental data compared to (a) characterized model and (b) design model for Vogtle 175%, East bearing**

### 8.4.3 Trilinear Characterization

The elastic stiffness in a bilinear hysteretic model is determined by the stiffness of the lead plug, and the model assumes that the lead plug stiffness is linear. However, the experimental data exhibited a smooth transition from the linear to the post-yield state (e.g. Sine 100%(Y)-1, Figure 8-13), such that a numerical model defined by a sharp transition from the linear to post-yield state was overly stiff for large displacements. The gradual transition to the yielded state is a reflection of the true behavior of the lead plug

(Figure 8-14). Thus, a trilinear model was attempted to improve the small displacement prediction without altering the large displacement response of the model. (A Bouc-Wen model (Park et al. 1986) is also known for smoothing the transition from the linear to the post-yield state, and is another approach that could have been attempted.)

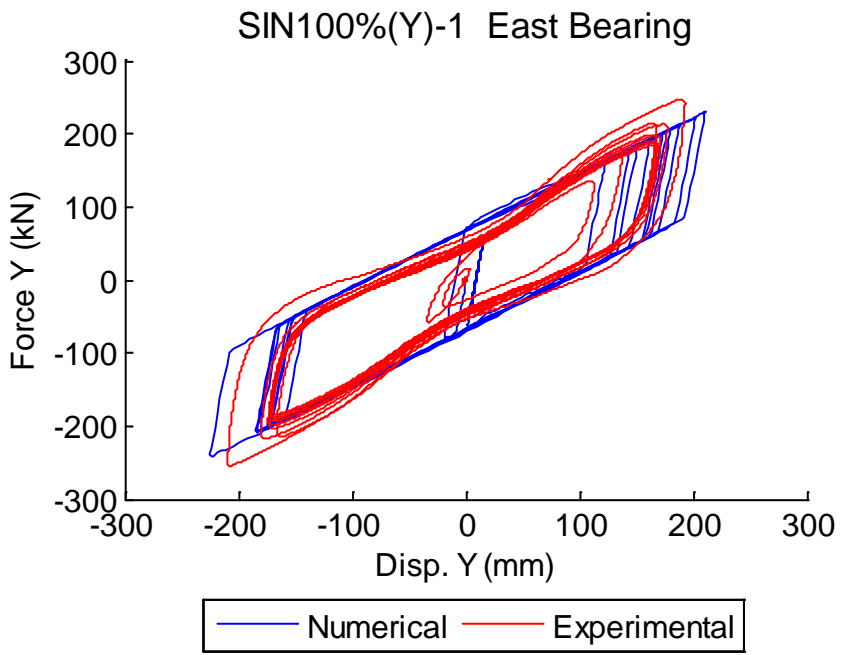


**Figure 8-13:** Force vs. displacement loop for the East LRB in Sine 100% (Y)-1

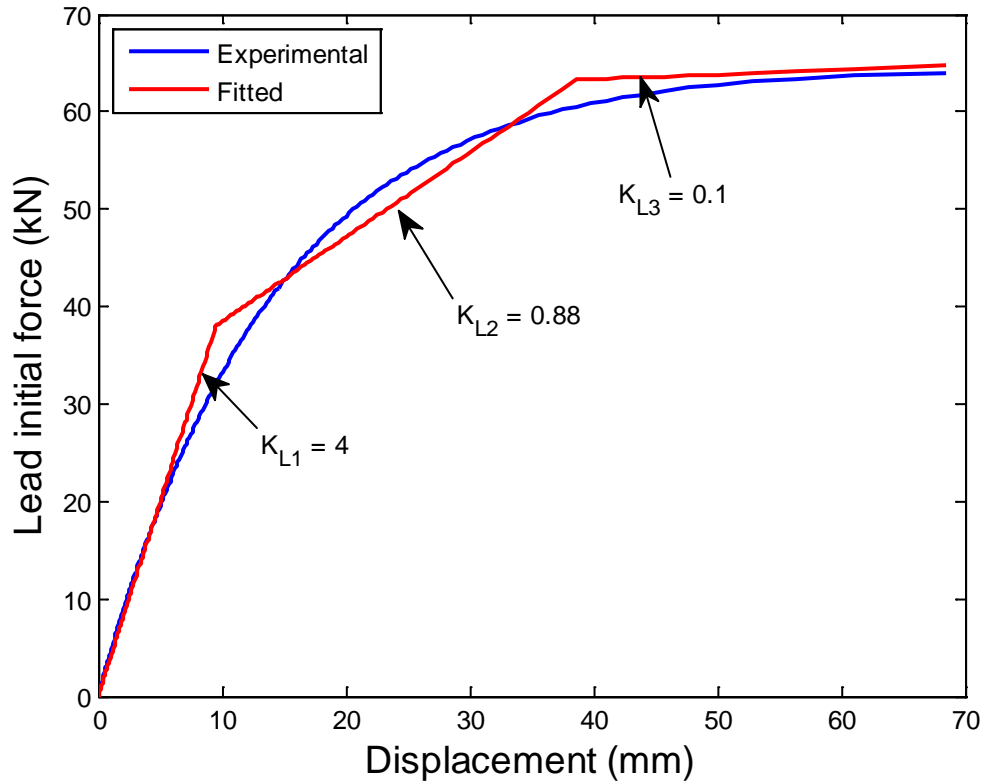


**Figure 8-14: Conceptual force vs. displacement of lead plug for monotonic loading (courtesy of Dynamic Isolation Systems)**

In the trilinear model, the stiffness of the lead-plug was modeled as piecewise linear with stiffness  $K_{L1}$ ,  $K_{L2}$  and  $K_{L3}$ . The values of  $K_{L1}$ ,  $K_{L2}$  and  $K_{L3}$  from Figure 8-14 were selected such that the tangent stiffness for the displacement less than 1 cm and greater than 6 cm matched the experimental data. Then,  $K_{L2}$  was selected such that the same area under the actual curve and the theoretical curve were equal.

The trilinear model was implemented in OpenSees as three bilinear springs in parallel, where each spring was assigned different properties and represented bidirectionally coupled behavior. Springs 1 and 2 represented the stiffness and energy dissipation in the lead plug while Spring 3 represented the stiffness of rubber. Springs 1 and 2 were elastic-

perfectly plastic with initial stiffness and yield force as determined by Figure 8-14. The properties of the third spring representing the rubber were calculated as follows. The elastic stiffness of rubber ( $K_{1,rub}$ ) was computed as

$$K_{1,rub} = K_{1,char} - K_{1,lead} \quad (8.13)$$

where  $K_{1,char}$  is the characterized elastic stiffness described in Section 7.4 and  $K_{1,lead}$  is the elastic stiffness from Figure 8-15. The characteristic strength of rubber  $Q_{d,rub}$  was defined as:

$$Q_{d,rub} = Q_{d,char} - Q_{d,lead} \quad (8.14)$$

where  $Q_{d,char}$  is the characterized characteristic strength described in Section 8.4 and  $Q_{d,lead}$  is the characteristic strength of the lead from Figure 8-15. The yield displacement was defined as:

$$D_{y,rub} = \frac{Q_{d,rub}}{K_{1,rub} - K_{d,char}} \quad (8.15)$$

where  $K_{d,char}$  is the characterized post yield stiffness described in Section 8.4.2. These properties were sufficient to determine the modeling parameters of the spring.

Results for numerical and experimental simulation with both the bilinear and trilinear bearing models are compared in Figure 8-15 for SIN 100(Y)-1 (Figure 8-15(a)-(b)) and Vogtle 100% (Figure 8-15(c)-(d)), where the influence of the multi-linear pivoting can be seen especially in the center of the loop and the large displacement transitions for Sine 100%. The trilinear model led to some improvement in the small displacement hysteresis for SIN100(Y)-1, but the improvement was negligible for Vogtle 100%. The same was

true for the other earthquake simulations. In particular, the trilinear model did not appear to substantially change the prediction of the displacement over the majority of the record, and did not address the primary inconsistency of the model compared to the experimental data, which was the pinching of the lead plug through the center of the loop that extended into the post-yield behavior. Therefore, the trilinear model was not adopted for final numerical simulation to validate the experimental data.

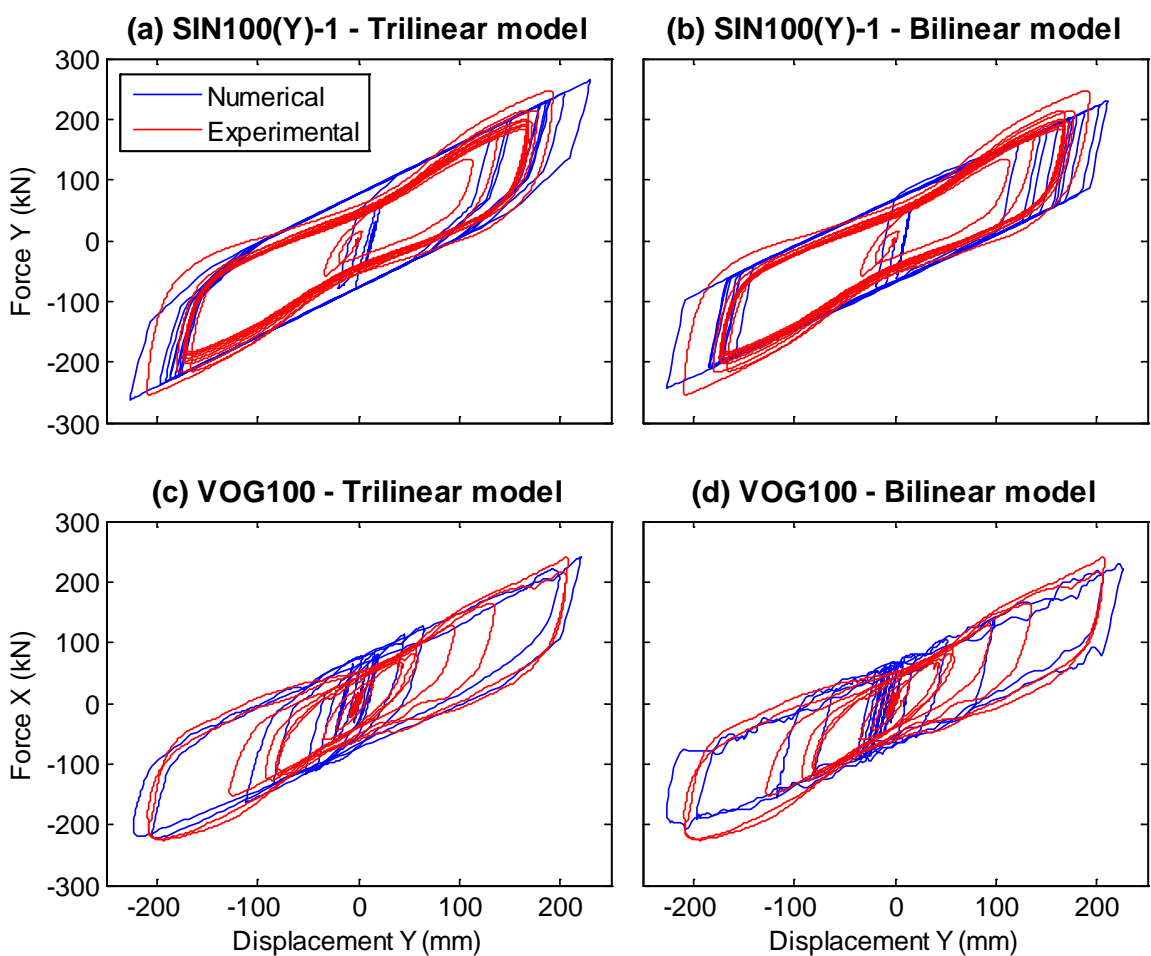


**Figure 8-15: Comparison of numerical and experimental simulation force versus displacement of the East bearing for SIN100(Y)-1 and VOG100 using (a), (c) a trilinear hysteretic model and (b), (d) a bilinear hysteretic model.**

#### 8.4.4 Final Bearing Parameter Selection for Numerical Simulation

One slight modification was made to the characterized bearing parameters used in the final numerical simulation models, which are compared to the experimental results in Section 8.5. The peak displacements using the best fit parameters of Table 8-4 were often below the peak experimentally observed displacements. The problem seemed to result from the fact that the fitted  $Q_d$  (y-intercept) was larger than the actual  $Q_d$  of the LR bearings, thus increasing the energy dissipation at lower amplitudes and suppressing the higher displacement amplitudes from ever being reached. By trial and error, it was observed that decreasing  $Q_d$  by a nominal amount relative to the best fit value improved the displacement prediction. As an example, Figure 8-16 compares simulation results using the best fit characterized model parameters and the model with  $Q_d$  reduced to 85% of the characterized value to the experimental data for Vogtle 100%. The model with reduced  $Q_d$  better predicted the peak displacement amplitude and followed the bearing hysteresis better than the best fit characterized model. Thus, the reduced value of  $Q_d$  was used for all simulation results presented in Section 8.5.



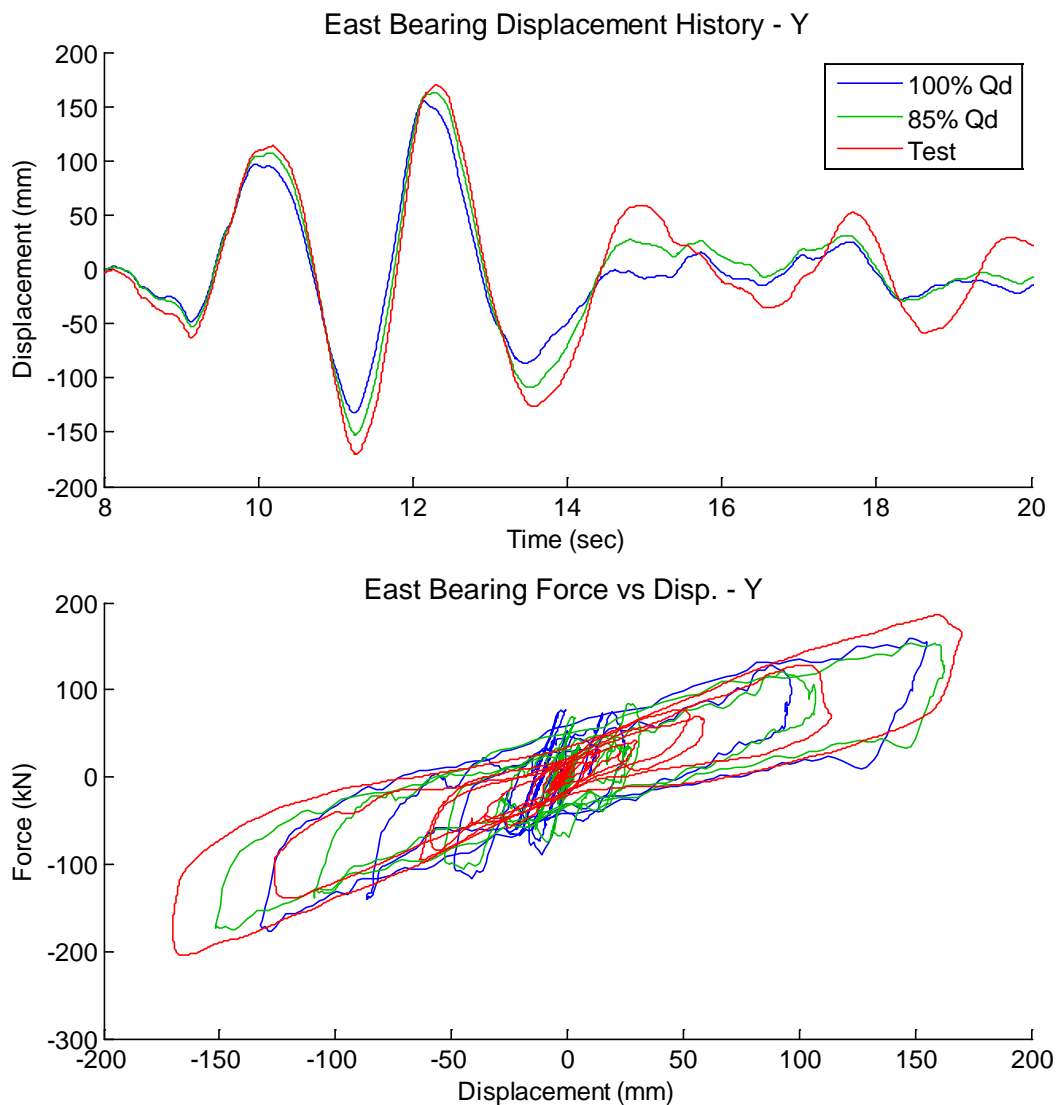


**Figure 8-16:** Comparison of numerical simulation with 100% and 85% characterized values of  $Q_d$  to the experimental data for Vogtle 100%; displacement history and hysteresis loop in the y-direction for the East bearing.

## 8.5. Comparison of Experimental and Numerical Simulation Considering Characterized Bearing Properties

In this section, the predicted responses of the hybrid LR isolated building (both isolation system and structure) using the OpenSees model described above and in Chapter 7 is

compared to the experimental results. Response quantities examined include the isolator displacement and force, story drifts, floor accelerations, and floor response spectra. Four different input excitations have been chosen as a representative variety sample: El Centro 130%, Vogtle 100%, Vogtle 175%, Diablo Canyon 95%. Vogtle was selected because of its great interest to the research sponsor, and two different intensities were chosen to approximately represent the DBE and the beyond DBE. Diablo Canyon was chosen because of its secondary interest to the sponsor, and because it produced the largest displacement demand in the bearings. El Centro was chosen to be representative of a smaller earthquake. The earthquake records used as input to the numerical model are the recorded output at the base of the earthquake simulator. The target ground excitation for Diablo is bidirectional only (XY) excitation, while the other three excitations include vertical input. Reports comparing the experimental and numerical simulation results for every excitation are permanently archived in the NEES Project Warehouse (Ryan et al. 2013a, 2013b, 2013c).

### **8.5.1 Isolator Response**

Demonstration that the isolation system and overall structure demands of safety related nuclear structures can be accurately determined in analysis and design is an important milestone toward the acceptance and implementation of seismic isolation for nuclear structures. As discussed in Section 8.4, replication of the isolation system response using a single bearing model with physically determined parameters may have been limited by circumstances unique to the test program. These circumstances are: 1) the bearings were designed with an unusually small lead plug, resulting in pinching of the bearing

hysteresis loops that is difficult to represent with a single bilinear model. Observation of slight pinching is not uncommon, but the selection of small lead plug has been correlated with greater amounts of pinching. 2) The sequence of closely spaced trials caused heating of the lead plugs. Since the bearing temperature was not measured, the influence of heating on the bearing response cannot be quantified. Under normal field conditions and in a strong earthquake, LR bearings would be activated in an unheated state.

As discussed in Section 8.4, in lieu of numerical simulation with a single bearing model, the bearing modeling parameters for each experimental simulation were independently calibrated to represent the largest displacement cycle that was observed. Use of this technique is helpful to interpret the data from this test program, but does not imply that a single bilinear model with physical parameters would not be suitable over a wide range of intensities in practice. Also discussed in Section 8.4, for all subsequent numerical simulations,  $Q_d$  was equal to 85% of the best fit characterized model, based on the trial-and-error observation that it improves the results.

Displacement traces, displacement histories, and bearing force vs. displacement (hysteresis loops) for the four selected input motions are shown in Figures 8-17 to 8-24. This adjusted characterized model – with its acknowledged limitations – generally predicts the amplitude of the peak vector displacement in each LR bearing quite well; a prediction within 5% of the recorded peak is not uncommon. The model also tends to represent the largest cycles in the displacement traces well, and capture obvious differences among the 4 LR bearings that are the result of the torsion in the system. For example, in Vogtle 100%, the numerical simulation correctly picks up a linear

displacement along a diagonal axis in the East (E) and South (S) bearings, but more of a circular orbit pattern in the North (N) and West (W) bearings (Figure 9-3). Plots of the displacement history best illustrate the accuracy of the model throughout the records. As discussed in Section 8.4, the predicted displacement is most accurate at cycles close to the peak intensity for which it has been optimized. Thus, the numerical prediction of the displacement history is not as accurate over small intensity cycles in large intensity records (e.g. Vogtle 175%, Figure 8-21). However, the peak displacement – which is the most critical response parameter in the isolation system – is predicted very well by the model, and the prediction in the small displacement range is not too important. The numerical simulation also predicts well the peak base rotation angle in the isolation system, which is more sensitive to modeling errors. An example is shown for Vogtle 175% in Figure 8-25, which compares the history of base rotation angle as predicted by numerical and experimental simulation.

The hysteresis loops confirm that, by inspection, the adjusted characterized numerical model is a good fit to the experimental data in most cases, and the fitted value of  $K_d$  looks reasonable. The numerical model tends to underestimate the force at the peak displacement. (e.g. consider the negative excursion of the bearings in both x and y-directions for El Centro, Figure 8-18), which results from the pinching behavior of the hysteresis loops due to a small diameter lead plug. Because of the pinching behavior, the best fit bilinear model parameter for  $Q_d$  exceeds the observed yield strength  $Q_d$  near the center of the loops, but is less than the physical  $Q_d$  (applicable at large displacements). Also, the numerically simulated loops show a tendency to be “wavy” compared to the

experimental data. For example, in the El Centro motion, on the largest negative excursion in the x-direction, the numerically predicted force dips suddenly on the return for all 4 LR bearings, while the actual force recorded during the experimental simulation does not (Figure 8-18). In Vogtle 100%, the numerical hysteresis loops (Figure 8-20) are characterized by rapid up and down variations of force on a large displacement excursion that are absent from the experimental loops. The waviness in the numerical hysteresis loops is believed to be related to the algorithm for bidirectional interaction.

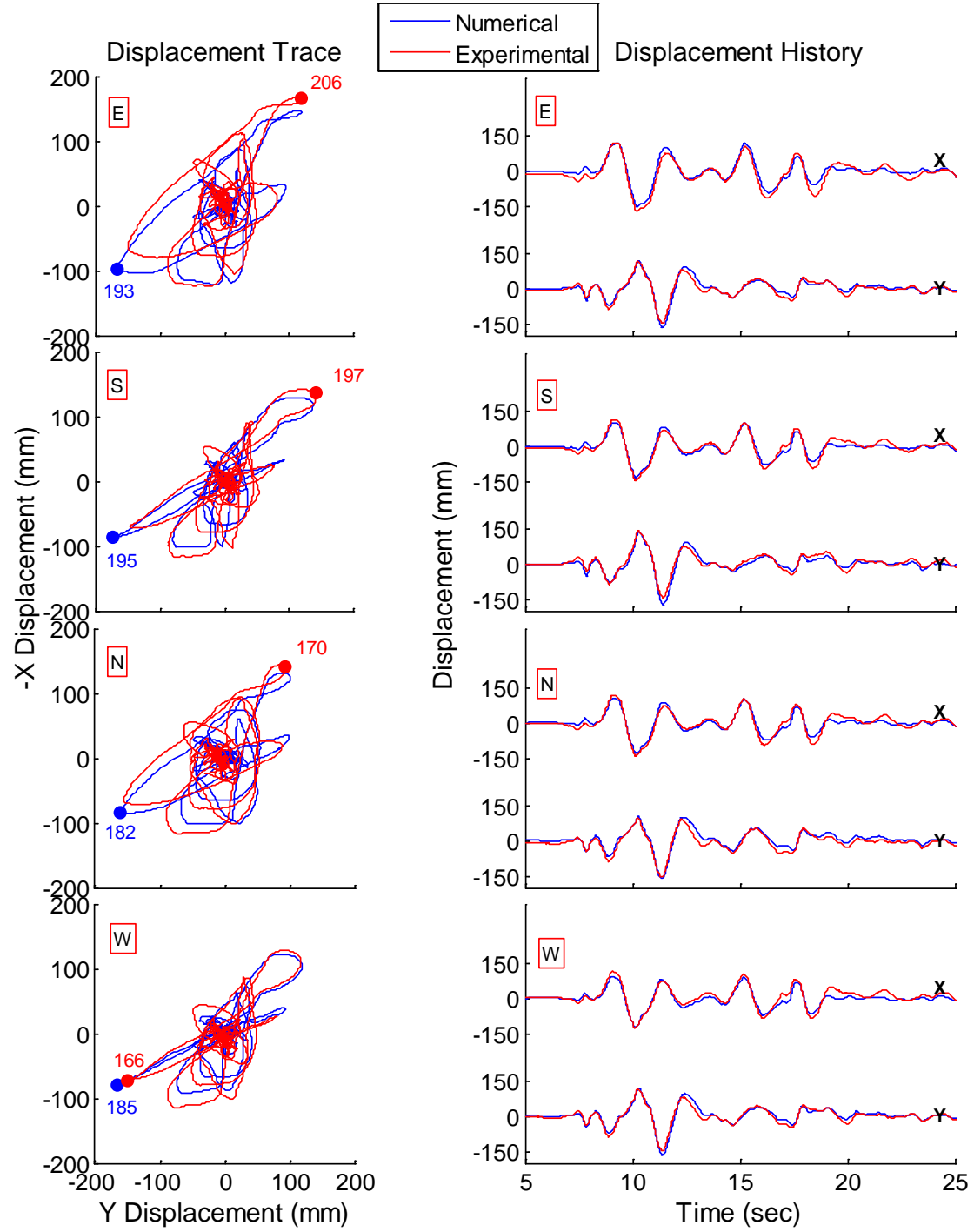


**Figure 8-17: Comparison of numerical and experimental simulation for El Centro 130%; displacement trace and displacement histories (x and y) in each LR bearing, labeled by position (E, S, N, W). Numerical simulation uses the characterized model with 85% of the characterized value for Qd.**

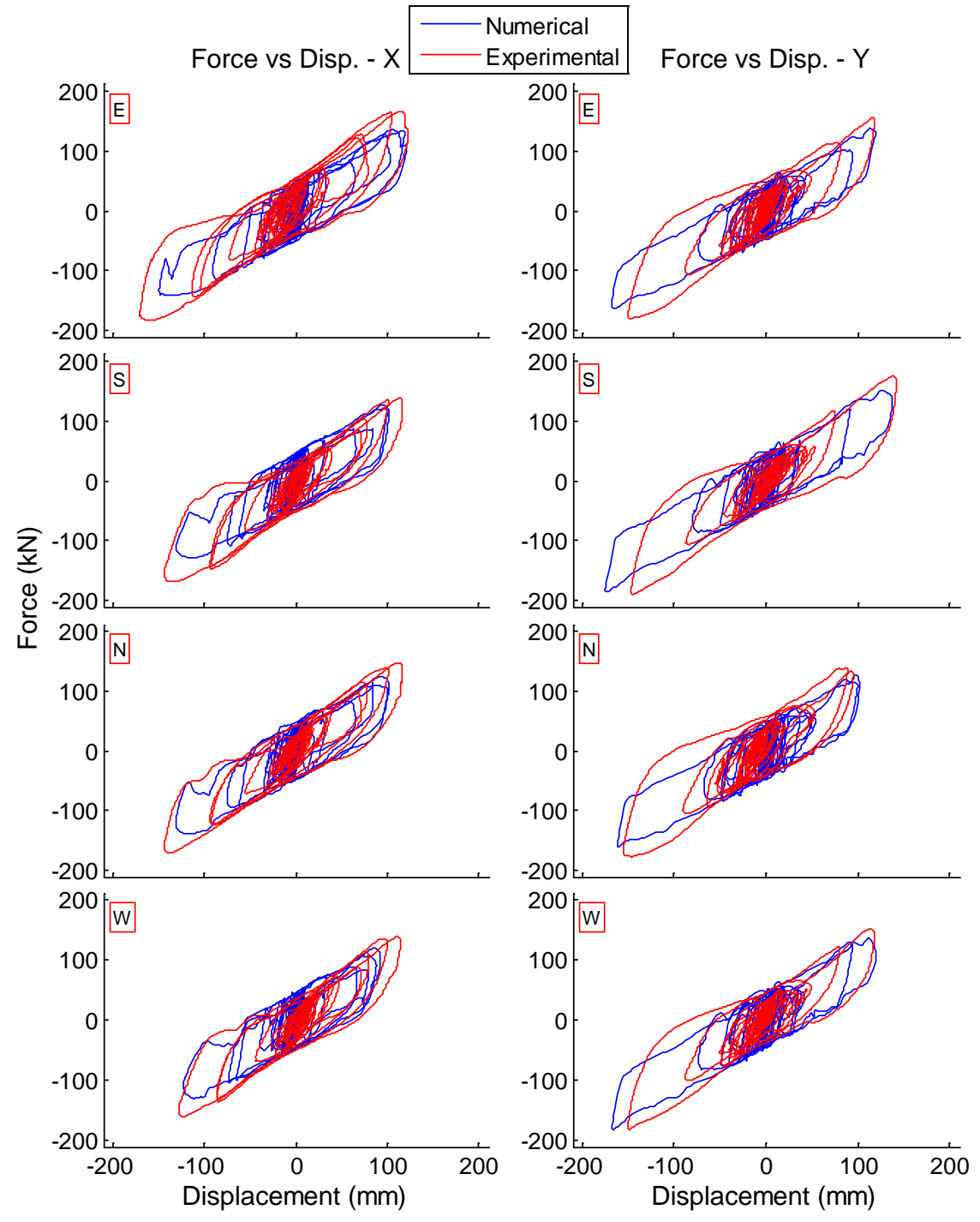


**Figure 8-18:** Comparison of numerical and experimental simulation for El Centro 130%; bearing force vs. displacement or hysteresis loops (x and y) in each LR bearing, labeled by position (E, S, N, W). Numerical simulation uses the characterized model with 85% of the characterized value for Qd.

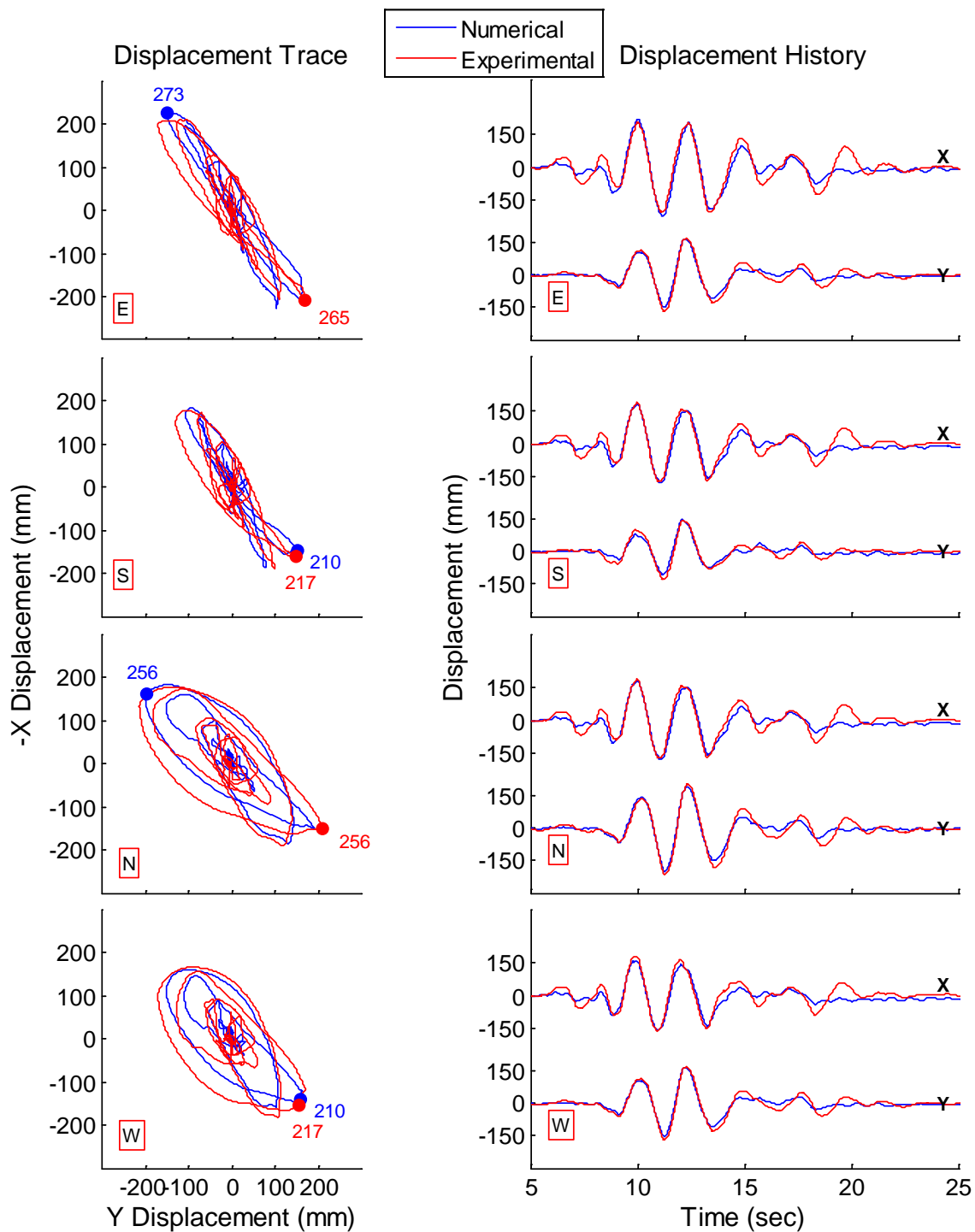


**Figure 8-19:** Comparison of numerical and experimental simulation for Vogtle 100%; displacement trace and displacement histories (x and y) in each LR bearing, labeled by position (E, S, N, W). Numerical simulation uses the characterized model with 85% of the characterized value for  $Q_{it}$ .



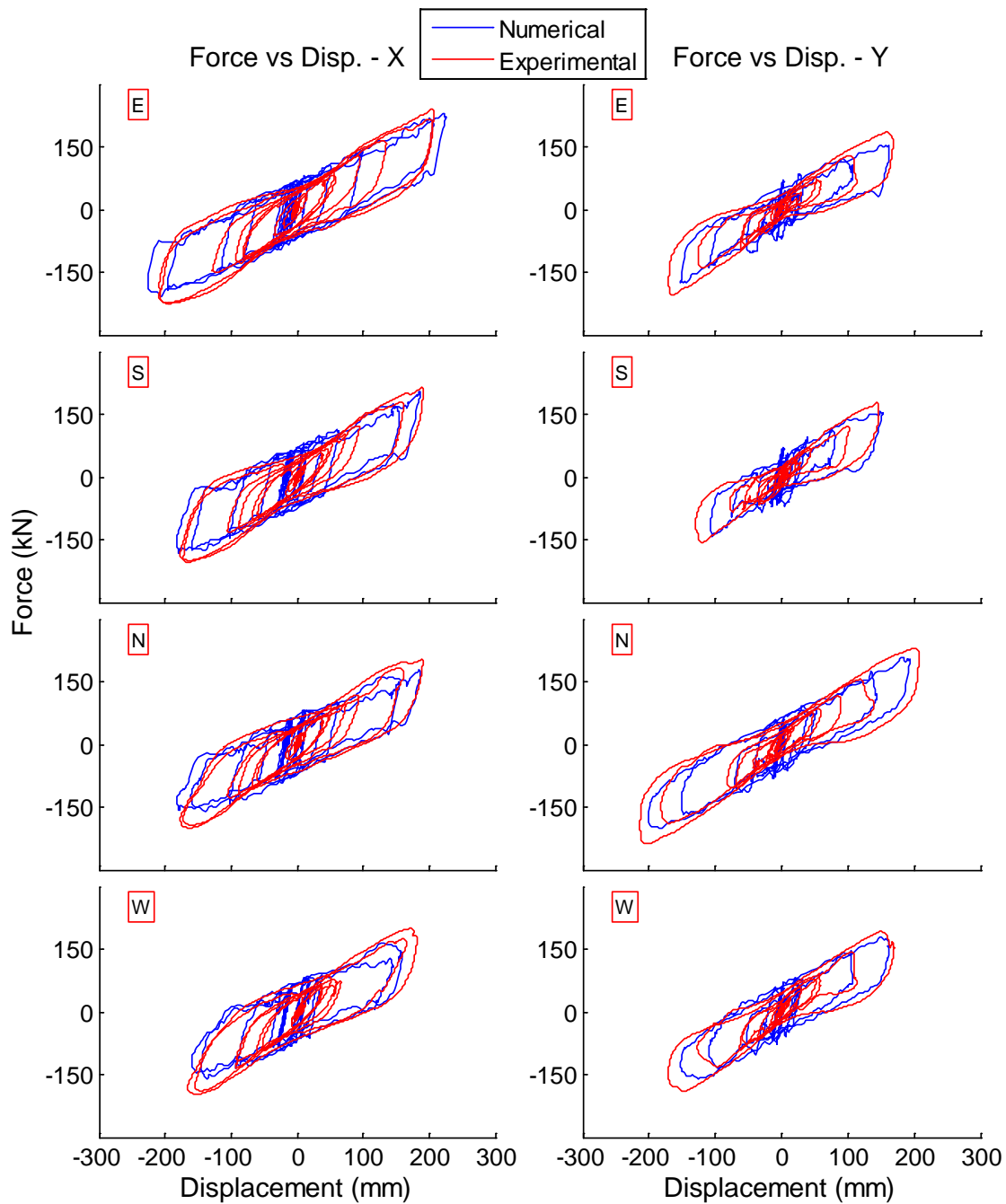


**Figure 8-20: Comparison of numerical and experimental simulation for Vogtle 100%; displacement trace and displacement histories (x and y) in each LR bearing, labeled by position (E, S, N, W). Numerical simulation uses the characterized model with 85% of the characterized value for Qd.**

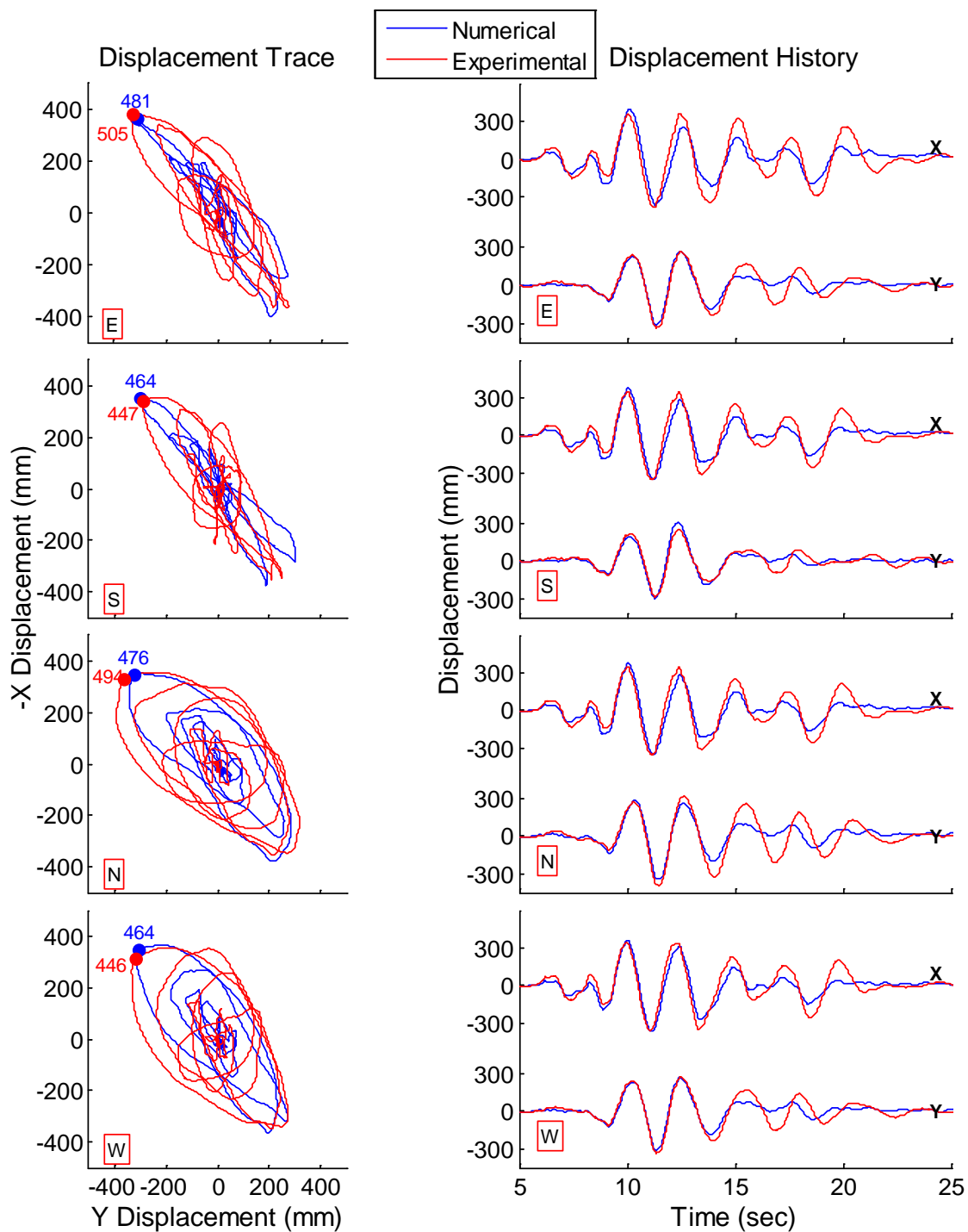


**Figure 8-21: Comparison of numerical and experimental simulation for Vogtle 175%; displacement trace and displacement histories (x and y) in each LR bearing, labeled by position (E, S, N, W). Numerical simulation uses the characterized model with 85% of the characterized value for Qd.**

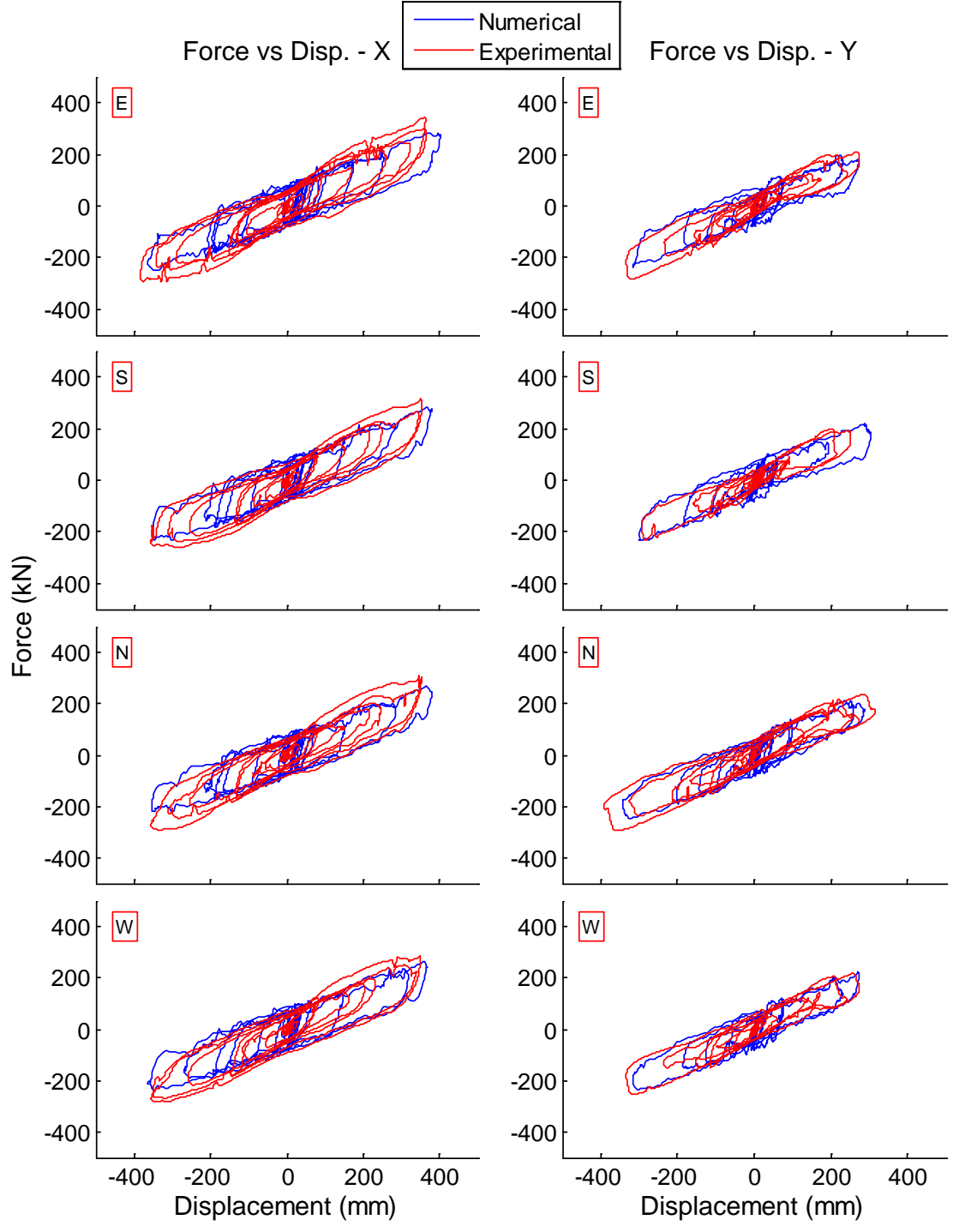


**Figure 8-22:** Comparison of numerical and experimental simulation for Vogtle 175%; displacement trace and displacement histories (x and y) in each LR bearing, labeled by position (E, S, N, W). Numerical simulation uses the characterized model with 85% of the characterized value for  $Q_{it}$ .

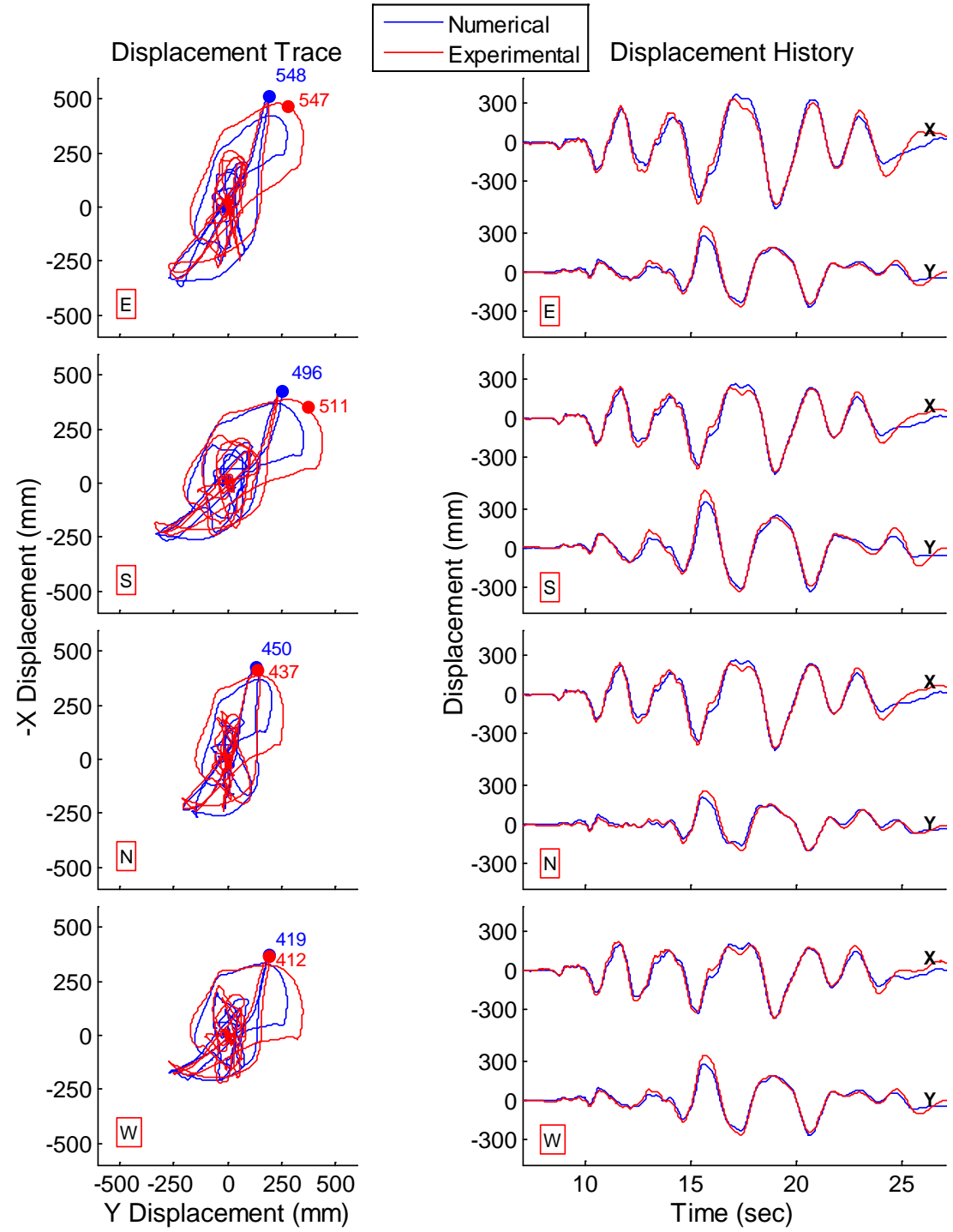


**Figure 8-23:** Comparison of numerical and experimental simulation for Diablo 95%; displacement trace and displacement histories (x and y) in each LR bearing, labeled by position (E, S, N, W). Numerical simulation uses the characterized model with 85% of the characterized value for Qd.

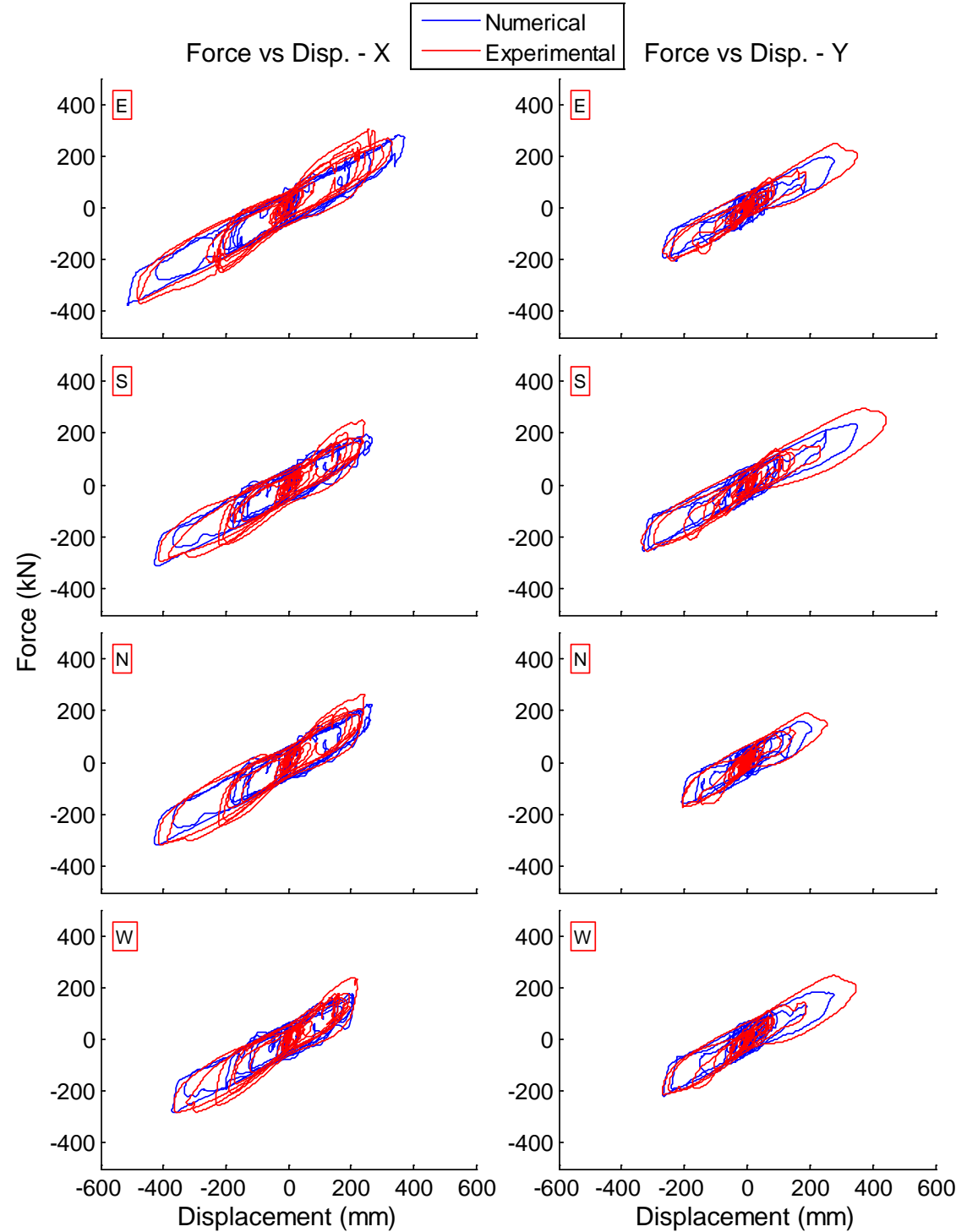


**Figure 8-24:** Comparison of numerical and experimental simulation for Diablo 95%; displacement trace and displacement histories (x and y) in each LR bearing, labeled by position (E, S, N, W). Numerical simulation uses the characterized model with 85% of the characterized value for Qd.

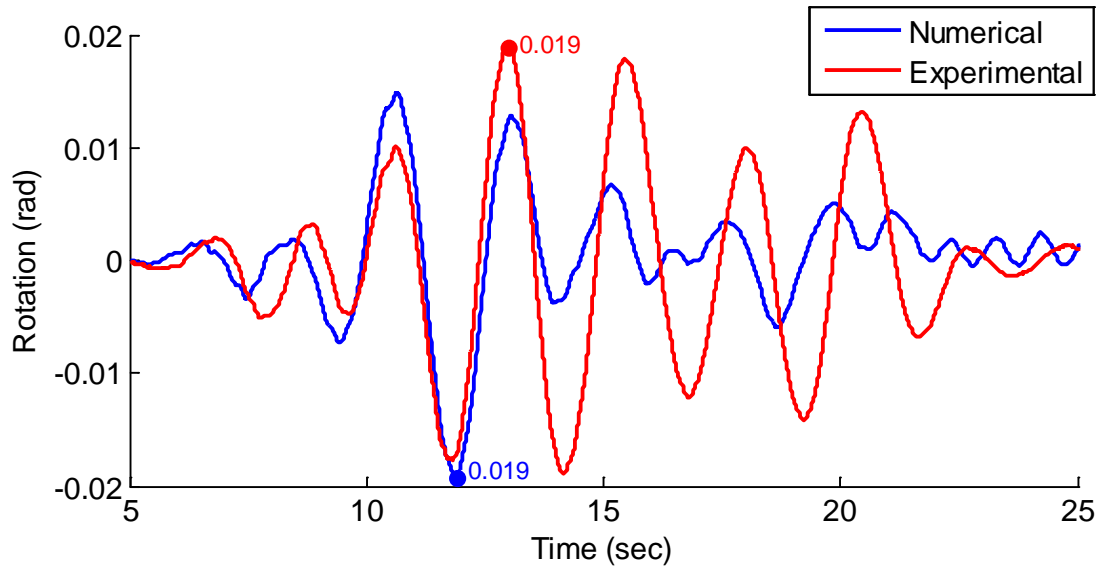


**Figure 8-25:** Comparison of numerical and experimental simulation for Vogtle 175%; history of base rotation angle. Analysis uses the characterized model with 85% of the characterized value for  $Q_d$ .

There is no evidence of loss of axial load carrying capacity in the bearing hysteresis loops. Such evidence would include a decrease of the stiffness at large horizontal displacements that occurred in combination with high overturning induced axial loads, and the inability of the numerical model, which does not include the interaction of horizontal shear and axial force, to simulate the response. Neither of these effects are observed in any of the hysteresis loops. The current numerical model is unable to predict load transfer described in Chapter 6, therefore a new numerical model that can capture some of these effects is investigated in Chapters 10 and 11. In summary, the overall ability of the characterized model to predict the bearing displacement and bearing force is sufficient that this model can be expected to provide insight into the structural response, which is examined next.

### 8.5.2 Structural Response

In this section, the structural responses predicted by the numerical model is compared to those recorded from the sensors. The x and y-direction roof acceleration histories, peak acceleration profiles (peak acceleration vs. story level), 2<sup>nd</sup> story drift histories, and peak drift profiles (peak drift vs. story level) are plotted for the four selected input motions in Figures 8-26 to 8-29. The response quantities are reported at the geometric center of the structure, obtained for the experimental data by averaging or linear interpolation of the filtered data from multiple sensors. The roof and 2<sup>nd</sup> story are chosen for plotting the acceleration and drift histories because the largest demands are observed at these locations, respectively.

Both low and high frequency vibrations are visible in the roof acceleration and 2<sup>nd</sup> story drift histories (Figures 8-26 to 8-29). The low frequency vibration appears as a slow moving wave at the isolation frequency that determines the amplitude of oscillation, while the higher frequency motions appear as rapid oscillations about the slower moving wave. As expected, the low frequency motion is strong in the drift histories, but obscured by higher frequency components in the acceleration histories. The observed isolation frequency is lower for El Centro (Figure 8-26) than for the other records, to reflect the nonlinearity of the system and thus the change in frequency with amplitude. A second component, strong in all signals, is deduced by visual inspection to be around 3 Hz (0.33 sec), and thus represents the first structural mode.

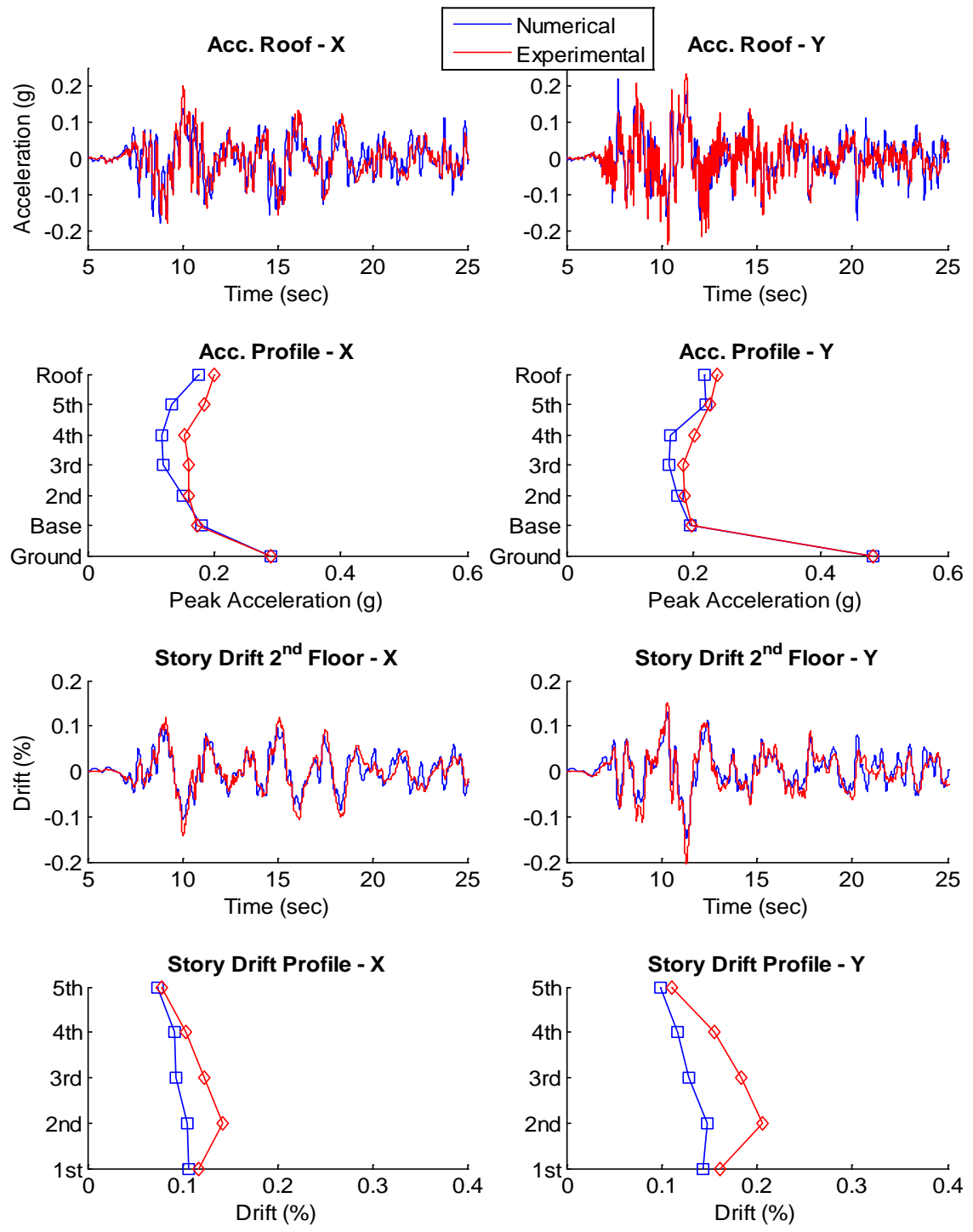


**Figure 8-26:** Comparison of numerical and experimental simulation for El Centro 130%; x and y-direction roof acceleration histories, peak acceleration profiles, 2<sup>nd</sup> story drift histories, and peak drift profiles. Numerical simulation uses the characterized model with 85% of the characterized value for Qd.



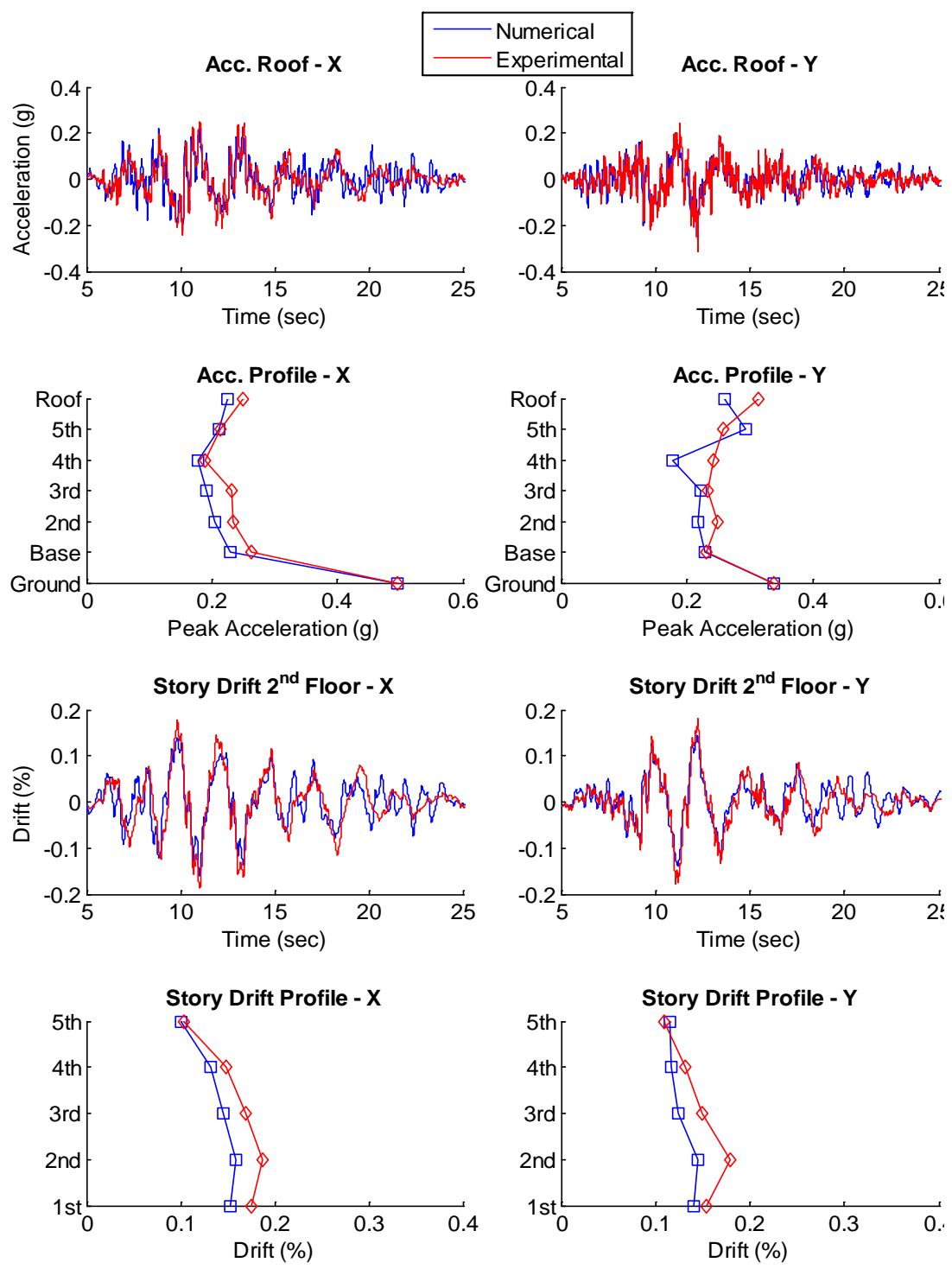


**Figure 8-27: Comparison of numerical and experimental simulation for Vogtle 100%; x and y-direction roof acceleration histories, peak acceleration profiles, 2nd story drift histories, and peak drift profiles. Numerical simulation uses the characterized model with 85% of the characterized value for Qd.**

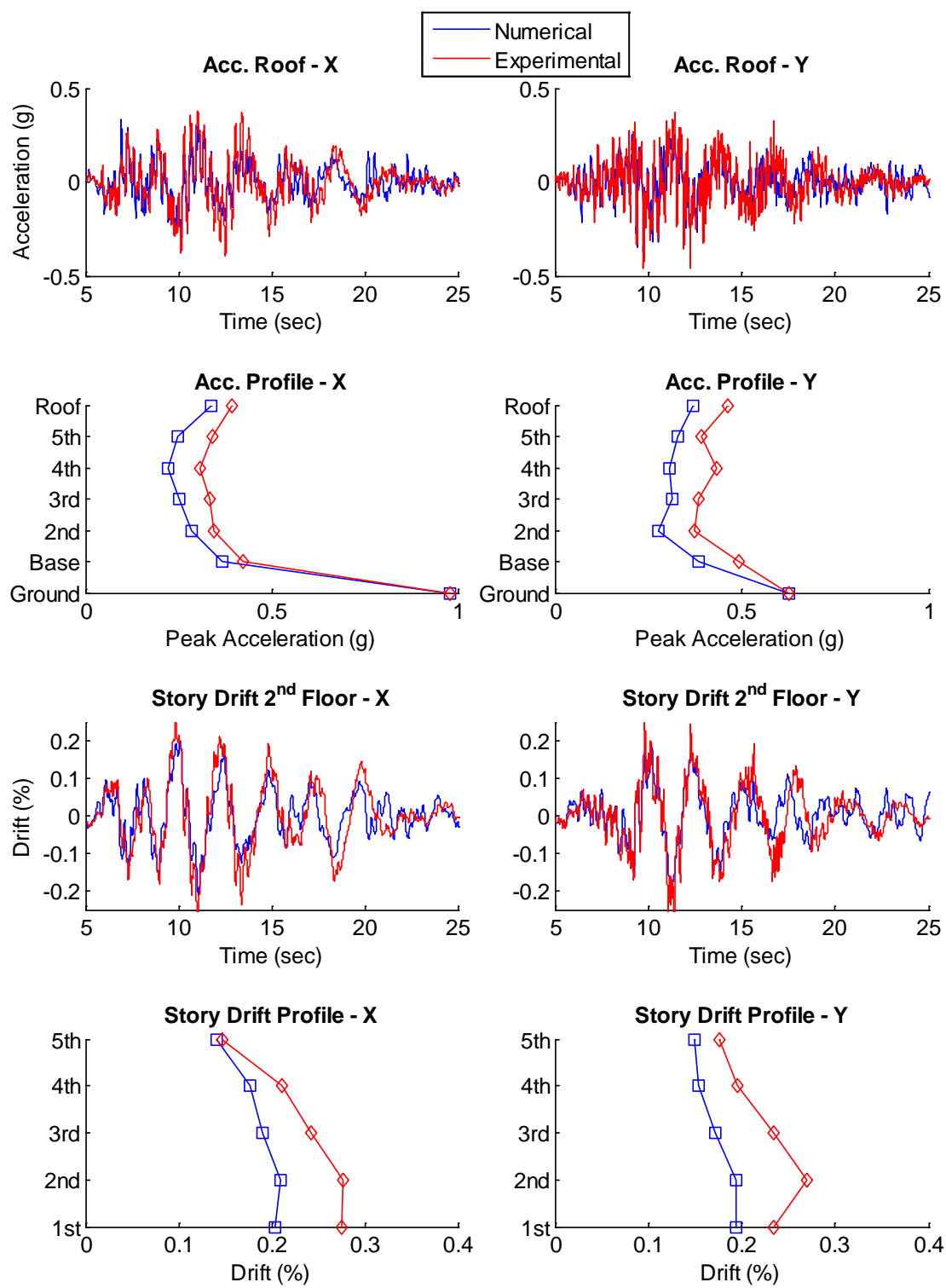


**Figure 8-28: Comparison of numerical and experimental simulation for Vogtle 175%; x and y-direction roof acceleration histories, peak acceleration profiles, 2nd story drift histories, and peak drift profiles. Numerical simulation uses the characterized model with 85% of the characterized value for Qd.**

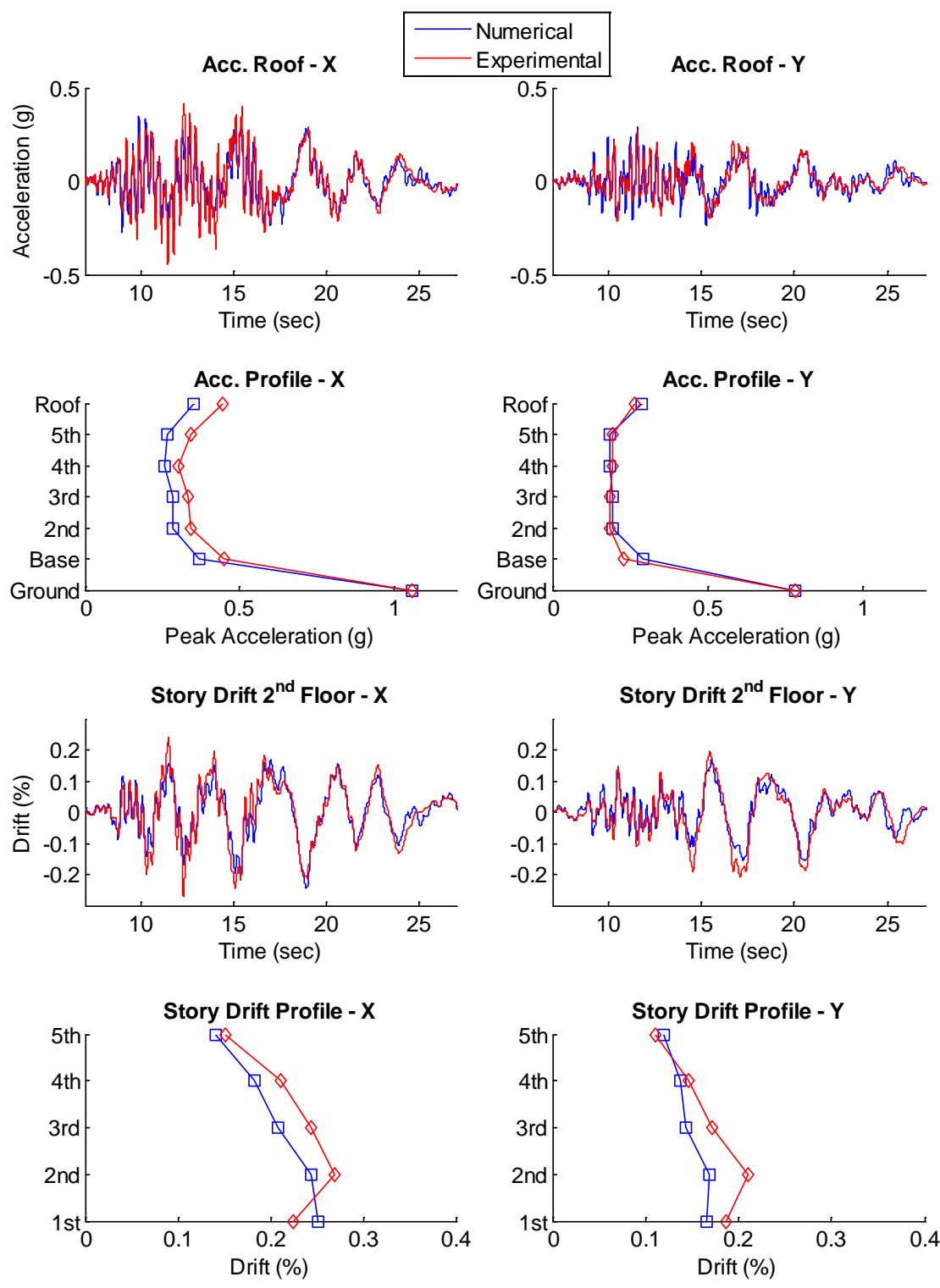


**Figure 8-29: Comparison of numerical and experimental simulation for Diablo 95%; x and y-direction roof acceleration histories, peak acceleration profiles, 2nd story drift histories, and peak drift profiles. Numerical simulation uses the characterized model with 85% of the characterized value for Qd.**

The frequency components in the experimental response histories are clearly replicated in the numerically simulated responses, which is strong validation of the accuracy of the numerical simulation. The peak amplitude of response histories are difficult to simulate numerically due to inevitable noise and spikes in recorded experimental data, as well as the sensitivity of the response to the low values of damping in the calibrated numerical model. Given these difficulties, the numerically simulated peak amplitudes of floor acceleration and story drift are quite accurate, generally within about 20% of the experimentally observed values.

As further indication of the effectiveness of the numerical simulation, the numerically simulated acceleration profiles generally follow the trends observed in the experimental acceleration profiles. For instance, for all of the records except Diablo 95% (Figure 8-29), the accelerations in the y-direction are larger than in the x-direction, replicated in both experimental and numerical simulation data. The acceleration profile pattern in the x-direction is characterized by maxima at the base and the roof and a minimum at the 4<sup>th</sup> floor. This pattern is clearly indicative of the combination of an isolation mode (uniform) and a first structural mode (linear with a node at the 4<sup>th</sup> floor). A larger slope in the acceleration profile (or greater difference between the maximum and minimum acceleration over the height) indicates greater participation of the first structural mode. The shape of the acceleration profile through these control points is more jagged in the lower intensity motions (El Centro 130% and Vogtle 100%, Figures 8-26 and 8-27) and smoother in the larger motions (Vogtle 175% and Diablo 95%, Figures 8-28 and 8-29). All these trends are well captured by numerical simulation. In the y-direction, the

acceleration profile shapes from the experimental data are not as consistent from record to record, which suggests that other modes may be participating. The numerical simulation seems to pick up a false peak at the 5<sup>th</sup> floor in the y-direction for some records such as Vogtle 100% (Figure 8-27).

Strong higher mode participation is observed in the floor accelerations, which is a consequence of the low amount of energy dissipation in the steel frame. As described in Section 7.6, the Rayleigh damping model has been calibrated for 1.9% at the representative higher mode frequency of 6.6 Hz (0.15 sec). Measured damping ratios on the order of 1-2% are reasonable for a steel frame system that remains linear.

Overall, the numerical simulation matches the experimental data with sufficient accuracy to a) build confidence in the modeling techniques used by the profession, and b) provide insight to help interpret the response of the test structure, as has been described above.

As discussed in Chapter 2, a nuclear facility would be substantially stiffer than the tested steel moment frame structure, with a natural period in the range of 0.1 to 0.25 sec, while the tested structure natural period exceeded 0.6 sec. Relative to the experimental data shown here, a stiffer structure with the same isolation period would experience lower overall accelerations and reduced higher mode effects. The expected evidence of reduced higher mode effects is a) reduced high frequency vibration in the acceleration histories (Figures 8-26 to 8-29), and b) acceleration profiles that are more uniform (i.e. identical accelerations at all levels from base to roof (Figures 8-26 to 8-29)). In addition, higher mode effects may be reduced as a result of a simpler (single story) structural configuration. Without simulation, the extent of acceleration reduction cannot be

predicted, but it is expected to be significant. These general trends can be verified by fundamental textbooks on the theory of seismic isolation (e.g. Kelly 1997, Chopra 2012).

## CHAPTER 9: ESTIMATING PEAK ISOLATION SYSTEM DEMANDS THROUGH BOUNDING ANALYSIS

### 9.1 Introduction

The bearing properties  $K_d$  and  $Q_d$  of the LR bearing have been shown to vary significantly due to effects such as aging, temperature of the lead core, wear, and history of loading (Constantinou et al., 1999, 2007; Kalpakidis et al., 2009a, 2009b). Since the exact state of the bearing at the time of a seismic event is unknown, probable maximum and minimum values of  $K_d$  and  $Q_d$  were suggested by Constantinou et al. (1999). The lower and upper bound values of  $K_d$  and  $Q_d$  are determined with the use of system property modification factors or  $\lambda$ -factors (Constantinou et al., 2007). These  $\lambda$ -factors are multipliers to the nominal design parameters to account for variation in isolation system properties. Typically, the force-displacement loop using upper bound properties results in the largest force demand and describes the behavior of aged bearings while the force-displacement loop using lower bound properties results in the largest displacement demands on the isolator and describes the behavior of new bearings (Constantinou et al. 2011). Thus, in general, the upper bound properties are used to estimate the base shear demands, while the lower bound properties are used to estimate the displacement demands.

Bounding values have been implemented for over a decade for the analysis and design of seismically isolated bridges in the American Association of State Highway and Transportation Officials (AASHTO) design guidelines (AASHTO, 1999). Currently, it is

anticipated that a more rigorous bounding analysis with  $\lambda$ -factors similar to those in AASHTO will be adopted in the new edition of the American Society of Civil Engineers ASCE 7 guidelines for the analysis and design of buildings (ASCE, 2016) and ASCE 41 for the rehabilitation of existing buildings (ASCE, 2017) with seismic isolation systems. In these implementations, the upper and lower bound properties are to be applied separately to the numerical model and the governing response of each simulation case used for design (ASCE, 2016).

Independent factors have been devised to account for various property variation effects and their multiplication results in a combined factor with a certain level of conservatism (ASCE 7, 2016). In ASCE 7 (ASCE, 2016), the sources of system property uncertainty are divided into the following three  $\lambda$ -factors:

1. Aging and environmental effects, denoted as  $\lambda_{ae}$ ,
2. Variation that may be observed in prototype testing due to rate of loading, axial force and temperature variation of the bearing, and scragging, denoted as  $\lambda_{test}$  and,
3. Expected variation on the average properties of a group of same sized isolators due to uncertainty in the manufacturing process, denoted as  $\lambda_{spec}$ .

Each of these  $\lambda$ -factors has a maximum and minimum value that when combined according to the following results in the maximum ( $\lambda_{max}$ ) and minimum ( $\lambda_{min}$ ) property modification factors:

$$\lambda_{max} = (1 + (0.75(\lambda_{ae,max} - 1)))\lambda_{test,max} \lambda_{spec,max} \geq 1.8 \quad (9.1)$$



$$\lambda_{\min} = (1 - (0.75(1 - \lambda_{ae,\min})))\lambda_{test,\min}\lambda_{spec,\min} \leq 0.60 \quad (9.2)$$

The upper bound bearing properties ( $K_{d,max}$  and  $Q_{d,max}$ ) and lower bound ( $K_{d,min}$  and  $Q_{d,min}$ ) are then determined by multiplying  $\lambda_{\max}$  and  $\lambda_{\min}$  by the design parameters  $K_d$  and  $Q_d$ , from Equations 9.3 - 9.6.

$$K_{d,max} = \lambda_{K_d,max} K_d \quad (9.3)$$

$$K_{d,min} = \lambda_{K_d,min} K_d \quad (9.4)$$

$$Q_{d,max} = \lambda_{Q_d,max} Q_d \quad (9.5)$$

$$Q_{d,min} = \lambda_{Q_d,min} Q_d \quad (9.6)$$

Default  $\lambda$ -factors are provided in ASCE7-16 for  $K_d$  and  $Q_d$  for commonly used isolation systems. The default values provided for LR bearings are listed in Table 9-1.

**Table 9-1: Default Maximum and Minimum  $\lambda$ -factors for  $K_d$  and  $Q_d$  (ASCE7-16)**

Variables	$K_d$	$Q_d$
$\lambda_{ae,max}$ ( $\lambda_{ae,min}$ )	1.10 (1.00)	1.00 (1.00)
$\lambda_{test,max}$ ( $\lambda_{test,min}$ )	1.03 (0.98)	1.30 (0.95)
$\lambda_{spec,max}$ ( $\lambda_{spec,min}$ )	1.15 (0.85)	1.15 (0.85)

The preferred approach in determining the  $\lambda$ -factors, as opposed to using default values, is through rigorous testing of the materials used in the manufacturing process, and dynamic prototype tests of a full size bearing (ASCE, 2016). Prototype tests are a series

of tests performed by the bearing manufacturer on the isolation device that confirms the design bearing properties at the specific design load and displacement for the given application. These tests are conducted in accordance with Section 17.8.2 in the ASCE guidelines. Examples of tests to be performed in a prototype test are: twenty fully reversed cycles of loading at a lateral force corresponding to the wind design force; three fully reversed cycles of loading at 25%, 50%, 67% and 100% of the total maximum displacement; and at least 10 continuous fully reversed cycles of loading at 75% of the total maximum displacement (ASCE, 2016).

During the design phase of a project, the default  $\lambda$ -factors can be used in the preliminary analysis of the model. Once the bearings are manufactured, the registered design professional and bearing manufacturer can choose to use  $\lambda$ -factors that directly correlate to results obtained from the prototype tests of the bearing. In this case, the maximum and minimum limits of Equations (9.1) and (9.2) may be overridden, provided that the new limits are approved by the registered design professional and bearing manufacturer. In the case where prototype tests are not available, alternative procedures may be used to estimate the nominal bearing properties for LR bearing and friction pendulum isolators based on available test data for similar bearings (Constantinou et al., 2011). Ultimately, the registered design professional and peer-reviewer are responsible for determining the final values to be used on a project-product basis.

For the E-Defense experiment, a smaller set of prototype tests than required for design was agreed upon among the investigators. This included testing the LR bearing to a peak displacement of 300 mm, 500 mm and 650 mm, while subjecting it to different axial

loads (Table 8-1). The tests with peak displacement of 300 mm and 500 mm had three full cycles, while the 650 mm peak displacement test consisted of one half cycle (Table 8-1). Recall that a detailed explanation of the prototype test and characterization procedure of the LR bearings by the manufacturer was presented in Section 8.4.1. The same characterization procedure, applied to bearing hysteresis loops recorded during the experiment (Section 8.4.2), showed that the measured  $K_d$  and  $Q_d$  varied significantly between excitations. As a result, a single set of characterized bearing parameters was not effective to represent the force-displacement loop for all simulations (Table 7-4) and to predict peak displacement and force demands. This chapter investigates whether the lower and upper bound methodology being proposed in ASCE 7 (ASCE, 2016), when applied to the numerical model, can predict the observed peaks of the force-displacement loop observed in the experiment.

## 9.2 Determining $\lambda_{test}$ from Prototype Test Data

In general, a set of  $\lambda_{test}$  factors for  $K_d$  and  $Q_d$  can be determined by using the prototype test data. Guidance on how to determine  $\lambda$ -factors based on the prototype test is presented in the section “*C17.8.4 Determination of Isolator Unit Test Properties for Design*” of the proposed ASCE 7 (2016) code. The guidelines assume a full set of prototype test data, which, as mentioned above, consists of several fully reversed cycles at different displacement amplitudes and subjected to different axial loads (ASCE, 2016). Since the prototype test data for the E-Defense project was incomplete, a different approach was used to determine an effective  $\lambda_{test}$  as described later.

The average fitted post-yield stiffness and characteristic strength of the prototype test for peak displacements of 300 mm and 500 mm, originally presented in Section 8.4, are relisted in Table 9-2 for convenience. The design values of  $K_d$  and  $Q_d$  are 0.65 kN/mm and 65.7 kN, respectively, which were determined from a pre-manufacture design specification.

**Table 9-2: Average Characterized Isolator Parameters for  $D_{max} = 300$  mm and 500 mm**

Test	Axial Load (kN)	$D_{max}$ (mm)	$K_{d,fit}$ (kN/mm)	$Q_{d,fit}$ (kN)
A	600	300	0.63	64.7
B	1000	500	0.51	75.6

The variation in fitted  $K_{d,fit}$  and  $Q_{d,fit}$  for each cycle (loop) of each prototype test normalized by the design values (i.e.  $\lambda_{test}^{K_d} = K_{d,fit}/K_{d,des}$  and  $\lambda_{test}^{Q_d} = Q_{d,fit}/Q_{d,des}$ ) is plotted in Figure 9-1(a). The values of  $\lambda_{test}^{K_d}$  ranged from 0.87-1.00 and 0.75-0.81 for a peak displacement of 300 mm and 500 mm, respectively, while the values of  $\lambda_{test}^{Q_d}$  ranged from 0.91-1.09 for 300 mm and 1.09-1.24 for 500 mm. From Table 9-2 and Figure 9-1(a), the average post-yield stiffness of the 500 mm force-displacement loops was lower than the loops with peak displacement of 300 mm. On the contrary, the average characteristic strength was higher for the 500 mm than for the 300 mm force-displacement loop. The variation in post-yield stiffness can be further observed in the comparison of the 300 mm and 500 mm force-displacement loops (Figure 9-1(b)). Pinching of the force-displacement loop is evident in Figure 9-1(b), which resulted in a significantly lower measured characteristic strength than the design value. Although bearing properties are

known to be displacement dependent, pinching is believed to have contributed to the variation in the values of  $K_{d,fit}$  and  $Q_{d,fit}$ .

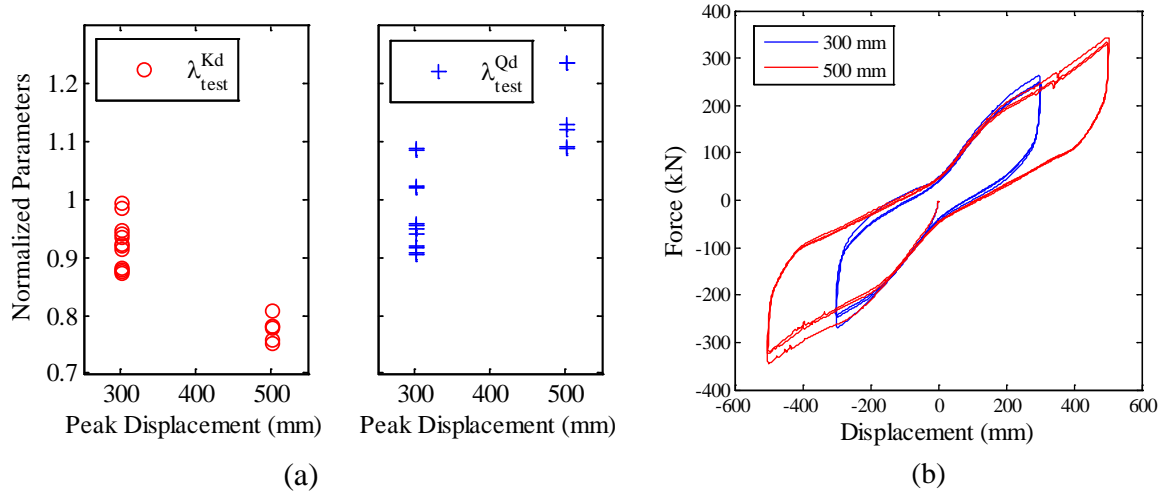


**Figure 9-1: (a) variation in the normalized  $\lambda_{test}^{Kd}$  and  $\lambda_{test}^{Qd}$  observed during the manufacturer prototype test, (b) force-displacement loop of prototype test for 300 mm (Trial ID A) and 500 mm (Trial ID B)**

Due to the reduced set of prototype tests for the E-Defense project, an alternative approach to determine  $\lambda_{test}$  was desired, and three methods were considered as follows:

- Method 1: Use the default values listed in Table 9-1.
- Method 2: Apply the variation in  $K_{d,fit}$  and  $Q_{d,fit}$  observed during the prototype test (Figure 9-1(a)) to determine the maximum and minimum  $\lambda_{test}$ . The overall maximum values of  $\lambda_{test}^{Kd}$  and  $\lambda_{test}^{Qd}$  (1.00 and 1.24, respectively) were assigned to  $\lambda_{test,max}$ , and the overall minimum values of  $\lambda_{test}^{Kd}$  and  $\lambda_{test}^{Qd}$  (0.75 and 0.91, respectively) were assigned to  $\lambda_{test,min}$ .

- Method 3: *Apply amplitude dependent  $\lambda_{test}$  factors based on the variation of bearing properties observed in the E-Defense experiment.* Because the bearing properties change based on displacement, the ground motions used in the E-Defense experiment (Table 5-1) were divided into bins according to the recorded bearing peak displacement of the motion. Then,  $\lambda_{test}$ -factors were determined for each bin as follows:
  - Bin 1: The experimental trials with peak displacement in any LR bearing ranging between 150-350 mm were included in this bin. These trials were: SIN100(Y)-1, VOG75-1, VOG100, VOG125, ELC130, and IWA100(XY). The repetitions of SIN100 and VOG75, that is, SIN100(Y)-2 and VOG75-2, were not included since they were expected to lead to similar results to the first excitation. The  $\lambda_{test}$ -factors applied to these trials were taken from the prototype test factors  $\lambda_{test}^{K_d}$  and  $\lambda_{test}^{Q_d}$  at peak displacement of 300 mm (Figure 9-1(a)). Thus, the relative maximum values of  $\lambda_{test}^{K_d}$  and  $\lambda_{test}^{Q_d}$  (1.00 and 1.09, respectively) were assigned to  $\lambda_{test,max}$ , and the relative minimum values of  $\lambda_{test}^{K_d}$  and  $\lambda_{test}^{Q_d}$  (0.87 and 0.91, respectively) were assigned to  $\lambda_{test,min}$ .
  - Bin 2: The experimental trials with peak displacement in any LR bearing ranging between 350-500 mm were included in this bin. These were: VOG150, VOG175, DIA80, DIA95(XY), RRS88(XY), and RRS88. The  $\lambda_{test}$ -factors applied to these trials were taken from the prototype test factors  $\lambda_{test}^{K_d}$  and  $\lambda_{test}^{Q_d}$  at peak displacement of 500 mm (Figure 9-1(a)).

Thus, the relative maximum values of  $\lambda_{test}^{K_d}$  and  $\lambda_{test}^{Q_d}$  (0.81 and 1.24, respectively) were assigned to  $\lambda_{test,max}$ , and the relative minimum values of  $\lambda_{test}^{K_d}$  and  $\lambda_{test}^{Q_d}$  (0.75 and 1.09, respectively) were assigned to  $\lambda_{test,min}$ .

For the methods listed above, Method 1 can be used when the prototype test data is not yet available, to estimate the upper and lower bound force-displacement loop. However, applicable variants of Method 2 or Method 3 can be considered once the prototype test data is available. ASCE 7 (ASCE, 2016) should normally be followed for a more rigorous determination of  $\lambda_{test}$  than considered here due to the reduced set of prototype tests available for the E-Defense experiment. Method 3 investigates if the force and displacement demands can be more reliably bounded when amplitude dependence of the variation in bearing parameters is considered. The amplitude dependence can be obtained from a complete prototype test where the bearing is subjected to a variety of displacement amplitudes.

### **9.3 Comparison of Numerical and Experimental Data Considering Bounding Values**

The bounding methodology presented above was investigated to determine if by including the upper and lower  $\lambda$ -factors in the numerical simulations, the simulations can bound the peak bearing force and displacement observed during the experiment. For this investigation, the numerical model described in Chapter 8 was utilized and the force-displacement response of the LR bearing during numerical simulation was recorded. In

the model, the design values  $K_{d,des}$  and  $Q_{d,des}$  were multiplied by the  $\lambda_{max}$ -factor for the upper bound (UB) analysis and  $\lambda_{min}$ -factor for the lower bound (LB) analysis.

The LR bearings were fabricated shortly before the experiment; therefore, the effects of aging and environmental conditions were not considered applicable for this experiment.

Thus,  $\lambda_{ae,max} = \lambda_{ae,min} = 1$  in Equations 9.1 and 9.2. As a result, these equations can be simplified and written as the product of  $\lambda_{test}$  and  $\lambda_{spec}$ :

$$\lambda_{max} = \lambda_{test,max} \lambda_{spec,max} \quad (9.7)$$

$$\lambda_{min} = \lambda_{test,min} \lambda_{spec,min} \quad (9.8)$$

noting that the  $\lambda$ -factor values multiplied by  $K_{d,des}$  are generally different than the  $\lambda$ -factor values multiplied by  $Q_{d,des}$ .

The bounding analysis was applied for each of the three methods listed above. The numerical values for the UB and LB of  $\lambda_{test}$ ,  $\lambda_{spec}$  and  $\lambda$  ( $\lambda_{max}$  or  $\lambda_{min}$ ) factors for  $K_d$  and  $Q_d$  for each method are listed in Table 9-3. In summary, “Method 1-UB” and “Method 1-LB” cases considered default maximum and minimum  $\lambda$ -factors (Table 9-1). “Method 2-UB”, “Method 2-LB”, “Method 3-UB”, and “Method 3-LB” cases considered the maximum and minimum  $\lambda_{test}$  value determined from the prototype test, as described above, and  $\lambda_{spec}$  from the ASCE 7, (ASCE, 2016) default values (Table 9-1). The last column of Table 9-3 lists the  $\lambda$  multipliers to the design values  $K_{d,des}$  and  $Q_{d,des}$  that were applied in the numerical simulation.



The numerical peak bearing displacement and peak base shear (summed over all LR bearings) were determined for the design case and the three methods by applying the  $\lambda$  parameters in the numerical simulation model. Figure 9-2 presents results for UB analysis and Figure 9-3 presents results for LB analysis. In these figures, the circular markers (labeled by the GM #) represent the numerical response normalized by the peak experimental response for individual trials, plotted against the corresponding experimental peak bearing displacement. The peak displacements were determined as the largest displacement in any LR bearing. Analysis using the design values of  $K_d$  and  $Q_d$  is included for reference, thus  $\lambda = 1$ . A normalized response  $> 1$  means that the numerically predicted response was larger than that observed in the experiment and the bounding analysis is considered effective. All ground motions were included with the exception of WSM80, due to its low peak isolator displacement, and VOG75-2 and SIN100-2, which produced responses similar to VOG75-1 and SIN100-1, respectively. Moreover, for better comparison, since the data is plotted in scatter format, the median (solid line) and  $\pm$  one standard deviation (dashed lines) determined from linear regression analysis were also plotted.

The results presented in Figure 9-2 show that in general, Method 1-UB produced larger peak base shear than the experiment, in particular for GM# 2, 6, 7, 12 and 13. The trend of the normalized base shear using Method 2-UB is similar to Method 1-UB. Moreover, the Design case produced normalized base shear  $< 1$  for eleven out of twelve trials, while five out of twelve trials produced normalized base shear  $> 1$  for Method 1-UB and four out of twelve trials produced normalized base shear  $> 1$  for Method 2-UB. For Method 3-

UB, all trials produced normalized base shear  $< 1$  and four trials (GM# 6, 7, 8 and 9) actually produced lower peak normalized base shear than the Design case (Figure 9-2).

**Table 9-3: Bounding Cases Considered for the Numerical Simulation**

Case Name		$\lambda_{test}$	$\lambda_{spec}$	$\lambda$
<b>Method 1-UB</b>	$K_d$	1.03	1.15	1.18
	$Q_d$	1.3	1.15	1.50
<b>Method 1-LB</b>	$K_d$	0.98	0.85	0.83
	$Q_d$	0.95	0.85	0.81
<b>Method 2-UB</b>	$K_d$	1.00	1.15	1.15
	$Q_d$	1.24	1.15	1.43
<b>Method 2-LB</b>	$K_d$	0.75	0.85	0.64
	$Q_d$	0.91	0.85	0.77
<b>Method 3-UB</b> <b>Bin 1</b>	$K_d$	1.00	1.15	1.15
	$Q_d$	1.09	1.15	1.25
<b>Method 3-LB</b> <b>Bin 1</b>	$K_d$	0.87	0.85	0.74
	$Q_d$	0.91	0.85	0.77
<b>Method 3-UB</b> <b>Bin 2</b>	$K_d$	0.81	1.15	0.93
	$Q_d$	1.24	1.15	1.43
<b>Method 3-LB</b> <b>Bin 2</b>	$K_d$	0.75	0.85	0.64
	$Q_d$	1.09	0.85	0.93

Moreover, the median (solid line) of Method 3-UB is nearly constant, suggesting that the normalized base shear is independent of the peak displacement. On the contrary, the medians of the Design, Method 1-UB, and Method 2-UB, are linear, or the normalized peak base shear increases with peak displacement (Figure 9-2). Although the UB analysis does not tend to govern the peak displacement, the normalized displacement obtained

from the UB analysis is also plotted in Figure 9-2 to show that the peak displacements of most of the trials in Methods 1-UB, 2-UB and 3-UB are lower than the Design case.

The results presented in Figure 9-3 for LB analysis show that for all cases, only two out of twelve trials produced normalized displacement  $> 1$ . However, the trials with normalized peak displacement  $> 1$  for the Design case were GM# 6 and 7, while for each LB method were GM# 8 and 9. The normalized displacements for Methods 1-LB, 2-LB, and 3-LB are larger than the Design for all trials with exception of GM# 2, 5 and 6 (Figure 9-3). The median lines of Method 1-LB, 2-LB and 3-LB are increasing, thus, suggesting that in general the numerical peak displacement will increase in a LB analysis with increase in peak displacement. Although the LB analysis does not tend to govern the base shear, the normalized base shear obtained from the LB analysis is also plotted in Figure 9-3 to show that all cases produced normalized peak base shear  $< 1$  for all trials.

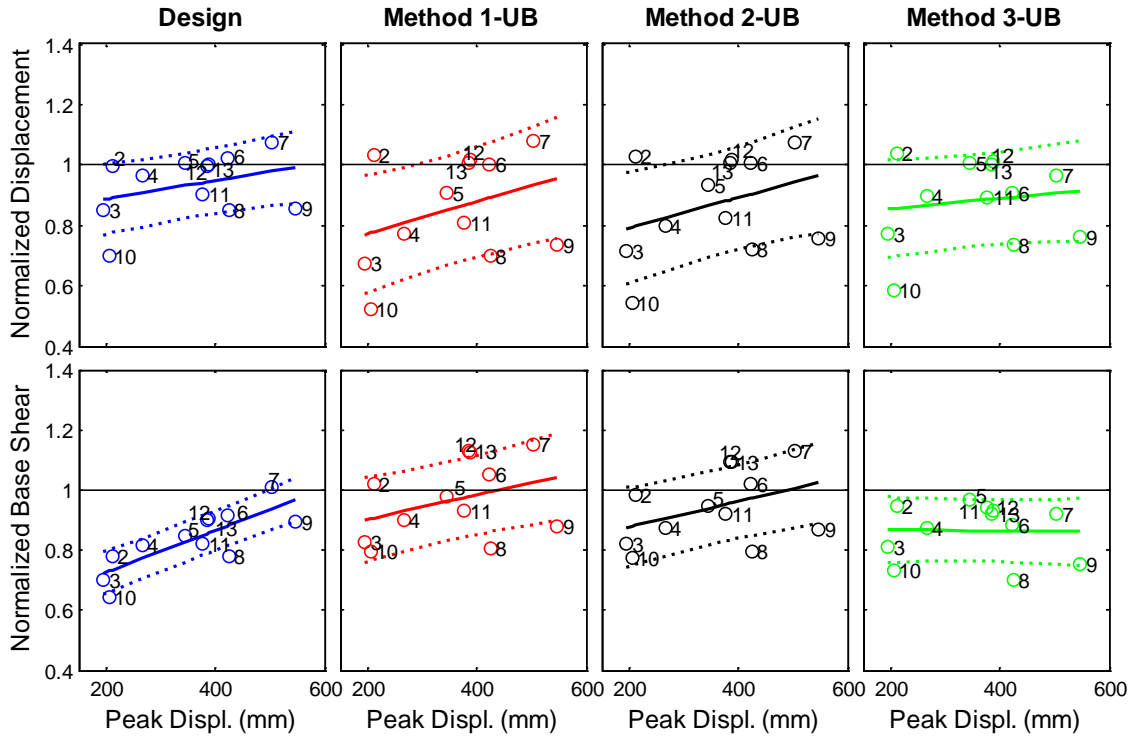


**Figure 9-2: Normalized displacement and total base shear plotted against experimental peak displacement for all ground motions with exception of WMS80, VOG75-2, SIN100-2 for all methods using UB parameters and design values.**

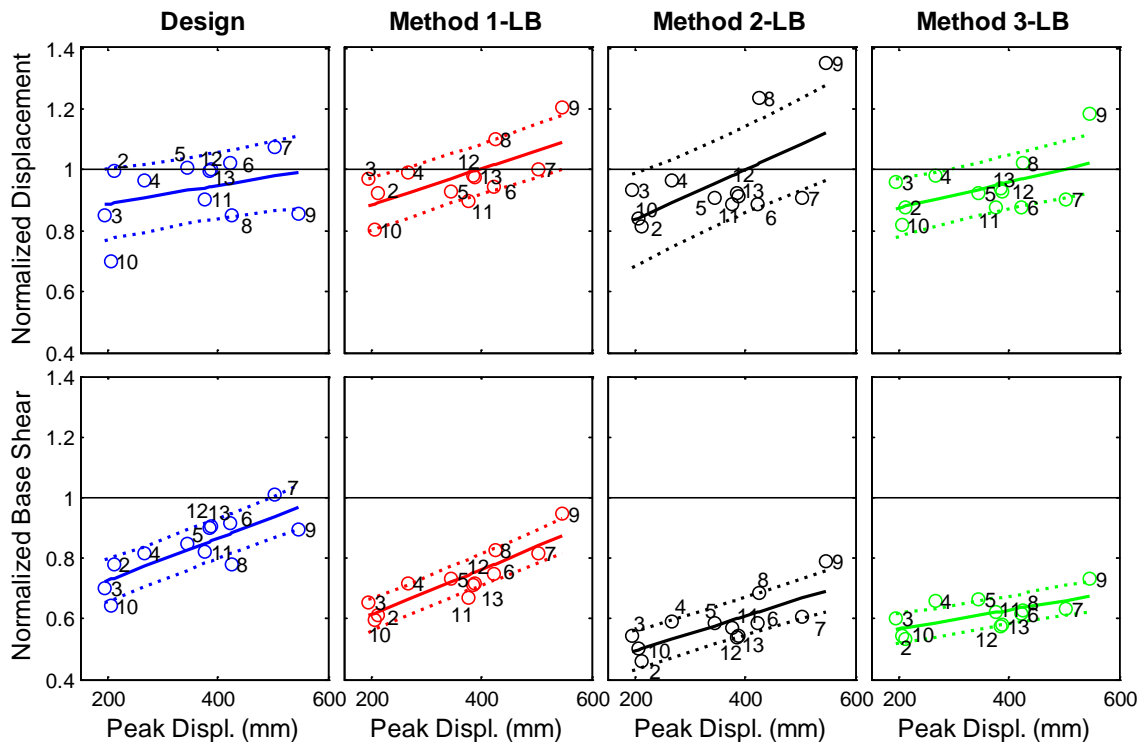


**Figure 9-3: Normalized displacement and total base shear plotted against experimental peak displacement for all ground motions with exception of WMS80, VOG75-2, SIN100-2 for all methods using LB parameters and design values.**

Figures 9-4 and 9-5 present a further breakdown of the results of Method 3 for UB and LB analysis, respectively. The normalized responses determined for Bin 1 and Bin 2 separately are shown in the first and second column subplots of Figures 9-4 and 9-5, and responses combined into a single bin (Combined) are shown in the last column subplots of Figures 9-4 and 9-5. The Combined plot replicates Method 3-UB and Method 3-LB in Figures 9-2 and 9-3, respectively.

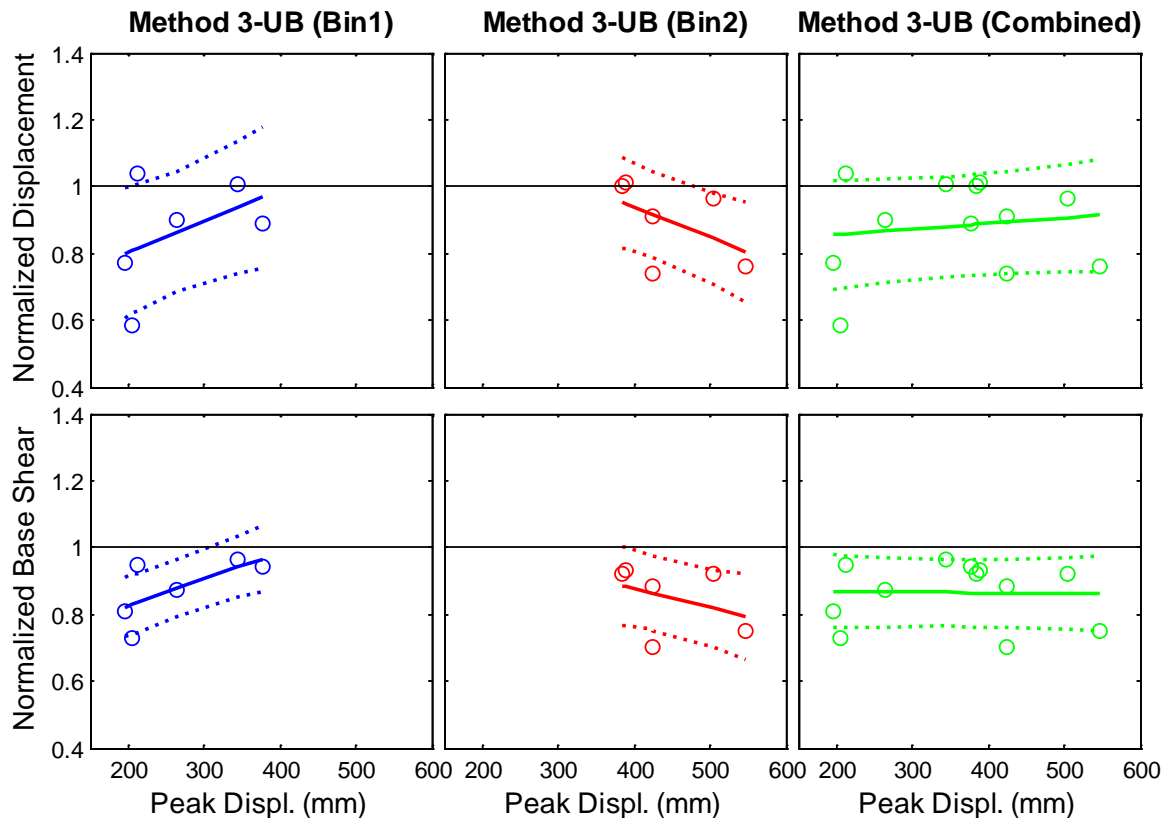


**Figure 9-4: Comparison of normalized displacement and base shear plotted against experimental peak displacement for Method 3 Bin1, Bin 2 and Bin Combined using UB parameters.**

From Figure 9-4 is observed that Method 3-UB (Bin1) produced normalized base shear  $< 1$  for all trials and the median normalized base shear increases as the peak displacement increases. Method 3-UB (Bin2) also produced normalized base shear  $< 1$  for all trials, and the median base shear decreases as the peak displacement increases (Figure 9-4). The normalized displacement of Method 3-LB (Bin1) produced a normalized displacement  $< 1$  for all trials with a nearly constant median (Figure 9-5). For Method 3-LB (Bin2), only two trials produced normalized displacement  $> 1$  with a median with increasing slope. Furthermore, as mentioned before, although peak displacement is often governed by the

LB analysis, and peak base shear often governed by the UB analysis, the normalized displacement for Methods 3-UB are shown in Figure 9-4 and the normalized base shear for Methods 3-LB are shown in Figure 9-5. Figure 9-4 shows that the normalized displacements from Method 3-UB (Bin1), Method 3-UB (Bin2), and Method 3-UB (Combined) produced medians that have similar slope to the normalized base shear. Likewise, Method 3-LB (Bin1), Method 3-LB (Bin2), and Method 3-LB (Combined) produced medians for the normalized base shear that have similar slope to the medians for the normalized displacement (Figure 9-5).

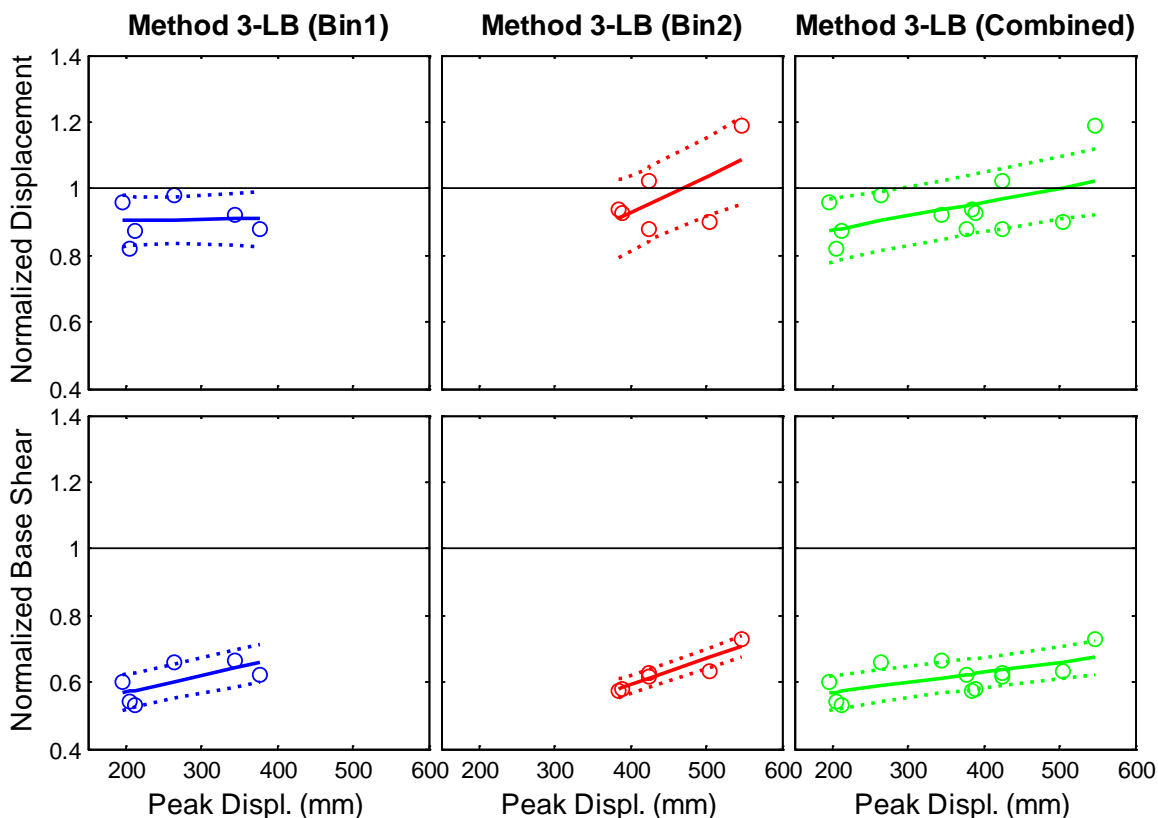


**Figure 9-5: Comparison of normalized displacement and total base shear plotted against experimental peak displacement for Method 3 Bin1, Bin 2 and Bin Combined using LB parameters.**

The median normalized displacement and normalized base shear determined from the linear regression analysis for the three bounding methods and the reference design case are plotted in a single plot for the UB and LB (Figure 9-6). Recall that the bounding analysis is considered effective if peak base shear and peak displacements can be conservatively predicted relative to the experiment, i.e. the normalized response  $\geq 1$ . Figure 9-6 shows that Method 1-UB in general produces peak base shear most likely to conservatively estimate the experimental peak base shear compared to other methods, while Method 1-LB in general produces peak displacements most likely to conservatively estimate the experimental peak displacement. Compared to Method 1, Method 2 produced slightly lower normalized base shear using UB analysis, and in general lower normalized displacement using LB analysis, and therefore was not as effective. The linear increasing median of Methods 1 and 2 suggests that conservative responses can be obtained at large peak displacements, which often controls the design. The normalized base shear from the UB analysis was similar for Methods 1 and 2 because the  $\lambda$ -factor used for both  $K_d$  and  $Q_d$  were similar in value (Table 9-3). Method 3-UB and LB produced even lower normalized base shear and displacement, respectively, relative to Methods 1 and 2. Moreover, Method 3 is ineffective in predicting the base shear for peak displacements larger than about 370 mm as it gives lower peak values than the Design case.



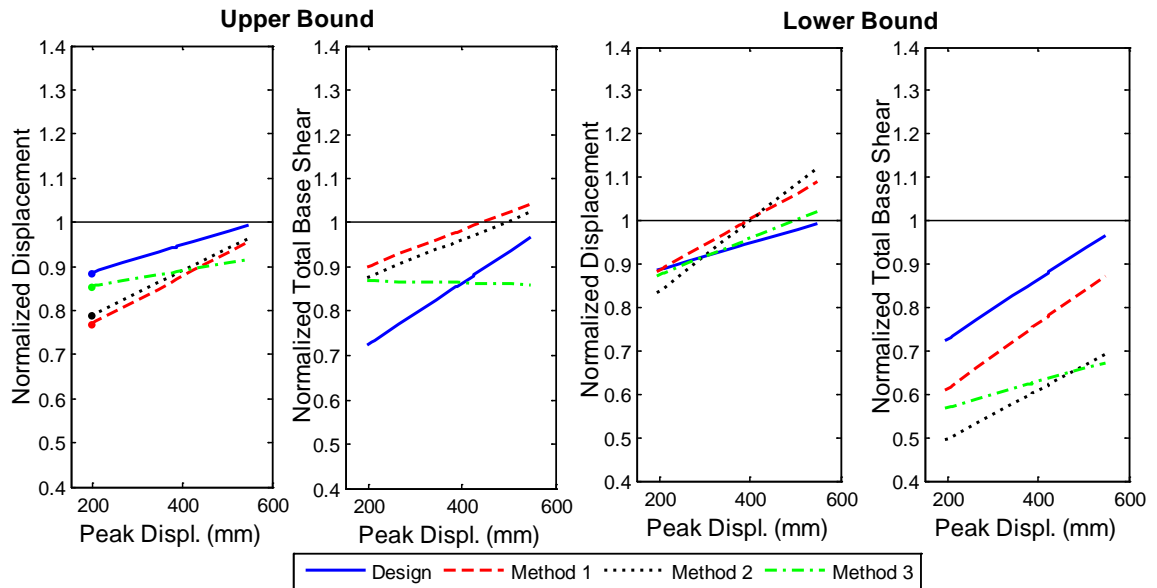


**Figure 9-6: Comparison of the median determined from regression analysis for all methods using UB and LB parameters.**

In general, Method 1 produced peak responses that were closest to the experimental than the other methods. Therefore, the peak (vector sum) force and displacement in any isolator produced during the experiment, by the Design, Method1-UB and Method1-LB are summarized in Figure 9-7 for GM# 2 through GM# 13. Although for some trials the peak isolator force from Method1-UB was lower than the experiment, it was in general higher than the Design case (Figure 9-7(a)). For Method1-LB, the peak isolator displacement for most trials (seven out of twelve) was lower than design case (Figure 9-7(b)).

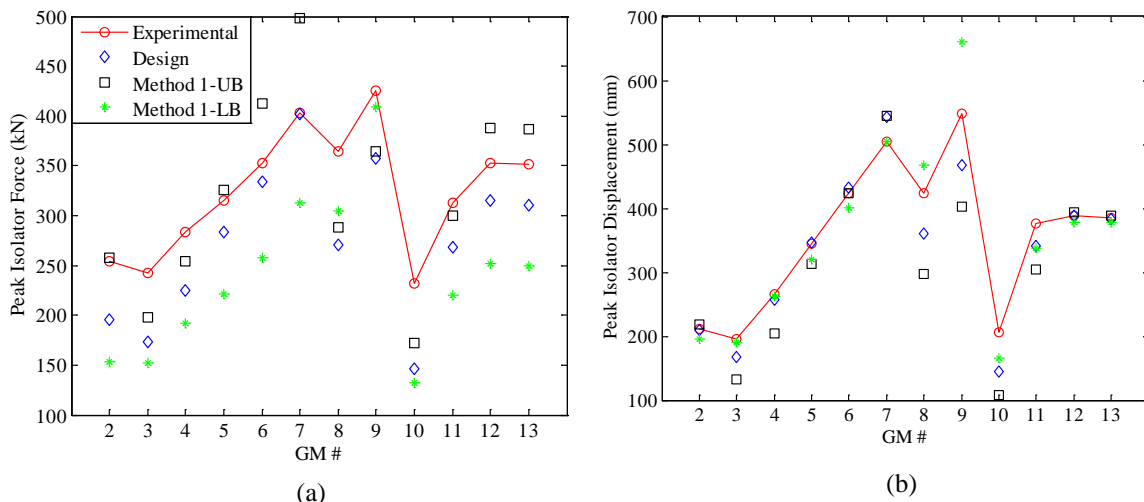


**Figure 9-7: (a) Peak isolator force and (b) peak isolator displacement obtained experimentally, and from Design, Method1-UB, and Method1-LB of selected ground motions.**

## 9.4 Bound Analysis

The discussion presented in Section 9-3 suggests that the UB and LB analysis cannot reliably bound the base shear and the displacements for all methods considered, and that generally Method 1 produced closest responses to the experimental. Therefore, the response of individual trials considering Method 1 is presented in this section to further investigate the apparent inability of the bounding analysis to reliably bound the peak base shear and peak displacement.

The prototype test force-displacement loop for peak displacements of 300 mm and 500 mm are compared with an idealized force-displacement loop for the Design, Method 1-UB and Method 1-LB parameters in Figures 9-8(a) and 9-8(b), respectively. The force-displacement loops were generated using a rate-independent plasticity model. Figure 9-8 shows that the UB loop envelopes the experimental and design loops (i.e. has larger force

at every displacement), and the LB loop is enveloped by the experimental and design loops (i.e. has smaller force at every displacement). This suggests that as long as the numerical peak displacement is the same as the experimental peak displacement, UB analysis will bound the numerical peak base shear.

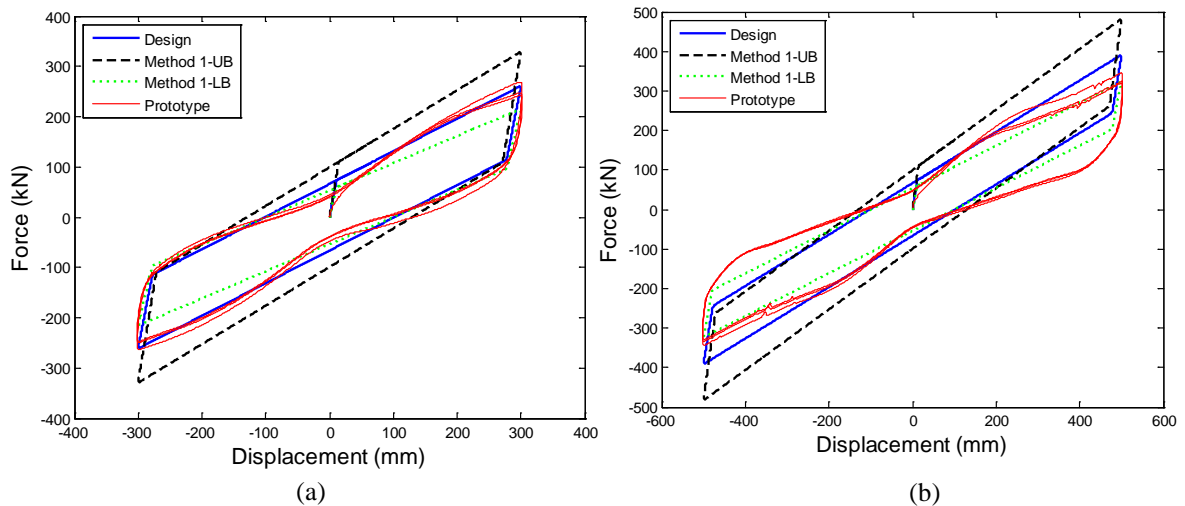


**Figure 9-8: Idealized force-displacement loop for Design, Method 1-UB, and Method 1-LB compared with prototype loop for a peak displacement of (a) 300 mm and (b) 500 mm.**

During numerical simulation, the peak displacement in the force-displacement loop of the UB and LB analysis are expected to differ from the peak displacement of the design case. Next, the peak displacement of the UB and LB analysis are estimated from the design spectrum for the UB and LB properties. The procedure to compute the UB and LB spectrum based peak displacement is summarized as follows:

Step 1: The isolator effective stiffness,  $K_{eff}$ , was computed from Equation 9.9 applying  $\lambda$ -factors for  $K_d$  and  $Q_d$  for Method 1 from Table 9-3 that are in agreement with the type of bound analysis being computed, and assuming a  $D_{max}$ .

$$K_{eff} = \frac{\lambda_{Q_d} Q_{d,des}}{D_{max}} + \lambda_{K_d} K_{d,des} \quad (9.9)$$

Step 2: The maximum isolator force,  $F_{max}$ , was computed from Equation 9.10 and the effective period,  $T_{eff}$ , from Equation 9.11, where  $W$  is the weight on the bearing, and  $g$  is the gravitational acceleration.

$$F_{max} = K_{eff} D_{max} \quad (9.10)$$

$$T_{eff} = 2\pi \sqrt{\frac{W}{gK_{eff}}} \quad (9.11)$$

Step 3: The viscous damping ratio  $\zeta$  is computed from Equation 9.12 assuming that the UB or LB loops have the same yield displacement,  $D_y$ , as the design loop (Table 3-3). The damping coefficient,  $B_L$ , is computed from Equation 9.13, and a new maximum isolator displacement  $D_{iso}$  from Equation 9.14. Then, the  $D_{max}$  from Step 1 is equated to  $D_{iso}$  from Equation 9-14 and iterated until they are equal.

$$\zeta = \frac{2\lambda_{Q_d} Q_{d,des}}{\pi F_{max}} \left( 1 - \frac{D_y}{D_{max}} \right) \quad (9.12)$$

$$B_L = \left( \frac{\zeta}{0.05} \right)^{0.3} \quad (9.13)$$

$$D_{iso} = \frac{g}{4\pi^2} \frac{S_{M1} T_{eff}}{B_L} \quad (9.14)$$

The spectrum based force-displacement loops for the UB and LB analysis determined from Equations 9.9 to 9.14 are compared with the design loop in Figure 9-9. This figure shows that the peak displacement obtained from the UB analysis (376 mm) can be significantly lower than the design case (500 mm), and the peak displacement obtained from the LB analysis (581 mm) tends to increase. As a consequence of the decrease in peak displacement in an UB analysis, the peak base shear produced by the UB analysis can be lower than the design case.

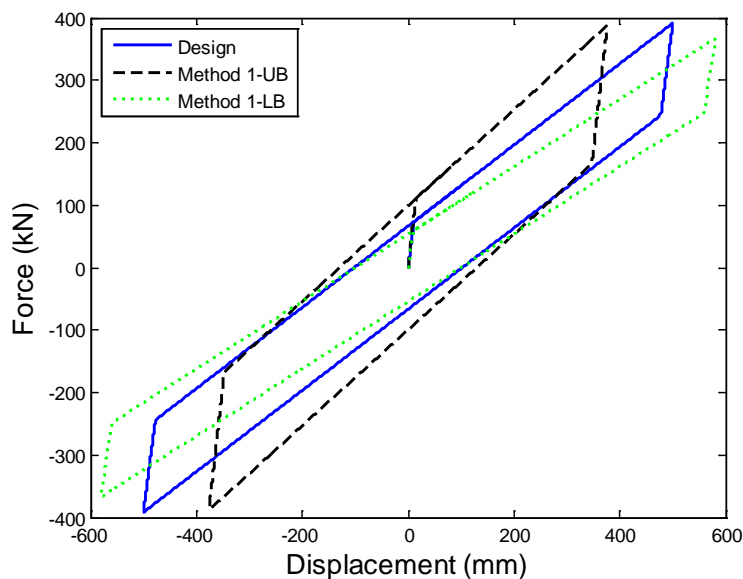


**Figure 9-9: Idealized force-displacement loop considering the Design, Method1-UB and Method1-LB bearing parameters for a design peak displacement of 500 mm.**

The Design, Method 1-UB and Method 1-LB smoothed hysteresis loops with equivalent displacement demands are compared with the response of DIA95(XY) in the projected direction for the bearing that produced the largest base shear in Figure 9-10. The projected direction was considered, as opposed to considering each force-displacement loop in x or y, as a way to compare a bidirectional response to a unidirectional response.

The projected direction was determined using a similar approach to that presented in Section 8.4.2. The results from Figure 9-10 also suggest that Method 1-UB as well as the Design case bound the peak base shear, which was not observed in Figure 9-2, where the numerical model was used and Method 1-UB and Design cases both produced lower peak base shear than the experimental for DIA95(XY).

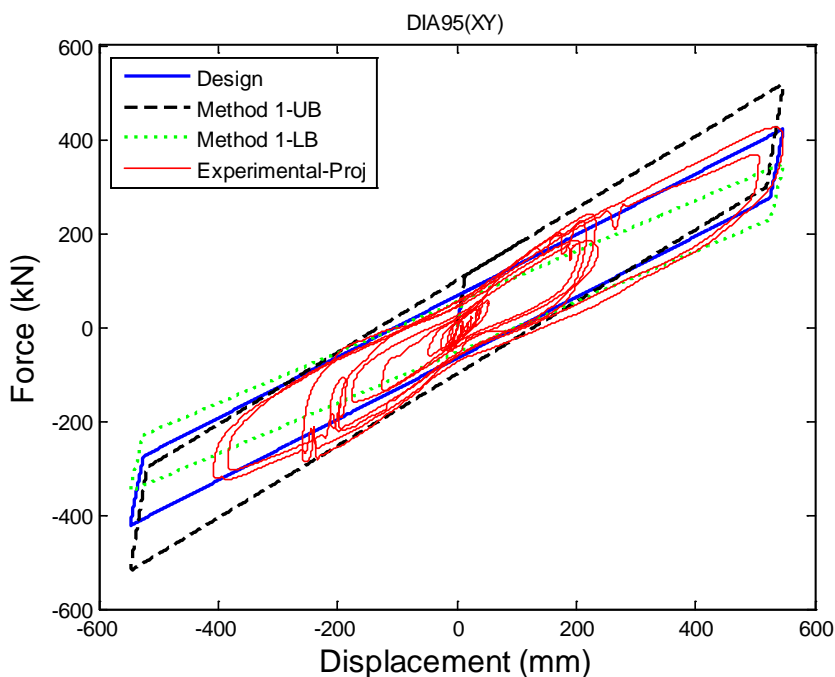


**Figure 9-10: Comparison of the Design, Method 1-UB and Method 1-LB smoothed hysteresis loops with the response of DIA95(XY) in the projected direction.**

Figure 9-10 showed that smooth UB and LB force displacement loops are expected to bound the peak responses, while in reality they may not due to discrepancies in amplitude and loop characteristics that occur during numerical simulation. Trial DIA95(XY) led to the largest experimental peak displacement and VOG175 the second largest, while SIN100(Y)-1 and ELC130 had lower peak displacement at around 200 mm (Figure 9-2). Since DIA95(XY) and ELC130 produced normalized base shear  $< 1$  for the UB analysis

(Figure 9-2) and VOG175 and SIN100(Y)-1 produced normalized base shear near 1 or > 1, these four motions are further investigated.

The variation in peak displacement for the UB and LB analysis for DIA95(XY) and VOG175 can be observed in Figures 9-11 and 9-12, respectively, where the experimental force-displacement loops in the projected, x, and y-directions are compared with the Design, Method1-UB and Method1-LB cases. The force-displacement loops presented hereon were determined as the largest response in any LR bearing. The x and y-direction loops for DIA95(XY) are included in Figure 9-11 to confirm that the projected response is representative of the overall response of the bearing. Figure 9-11 shows that the UB and LB loops computed by the numerical model generally provided similar bounding behavior to the smooth idealized loops. In addition, peak displacement increased with LB and base shear increased with UB when compared with the Design case, which is the basis of bounding analysis theory. Figure 9-11 shows that the Design case underpredicted the peak displacement, while the LB analysis produced larger peak displacement than the Design case, thus bounding the experimental peak displacement as desired. However, the peak displacement for the UB analysis is significantly lower when compared with the peak displacement from the Design case, producing a lower force than the Design case, and therefore could not bound the force observed in the experiment. The opposite trend is observed for VOG175 in Figure 9-12. UB analysis produced larger peak displacement than the Design case and the experimentally observed displacement, which resulted in a larger peak base shear than observed experimentally. Consequently, the UB analysis bounded both displacement and force, while the LB analysis actually produced lower

peak displacement than the Design case and thus did not factor into the result (Figure 9-12). A similar trend is observed with SIN100(Y)-1 and ELC130. These two trials produced near the same experimental peak displacement, however, Method1-UB produced peak base shear that was larger than the experimental for SIN100(Y)-1 (Figure 9-13) and lower for ELC130 (Figure 9-14). Moreover, the peak displacement in Method1-UB is larger than Method1-LB for SIN100(Y)-1.



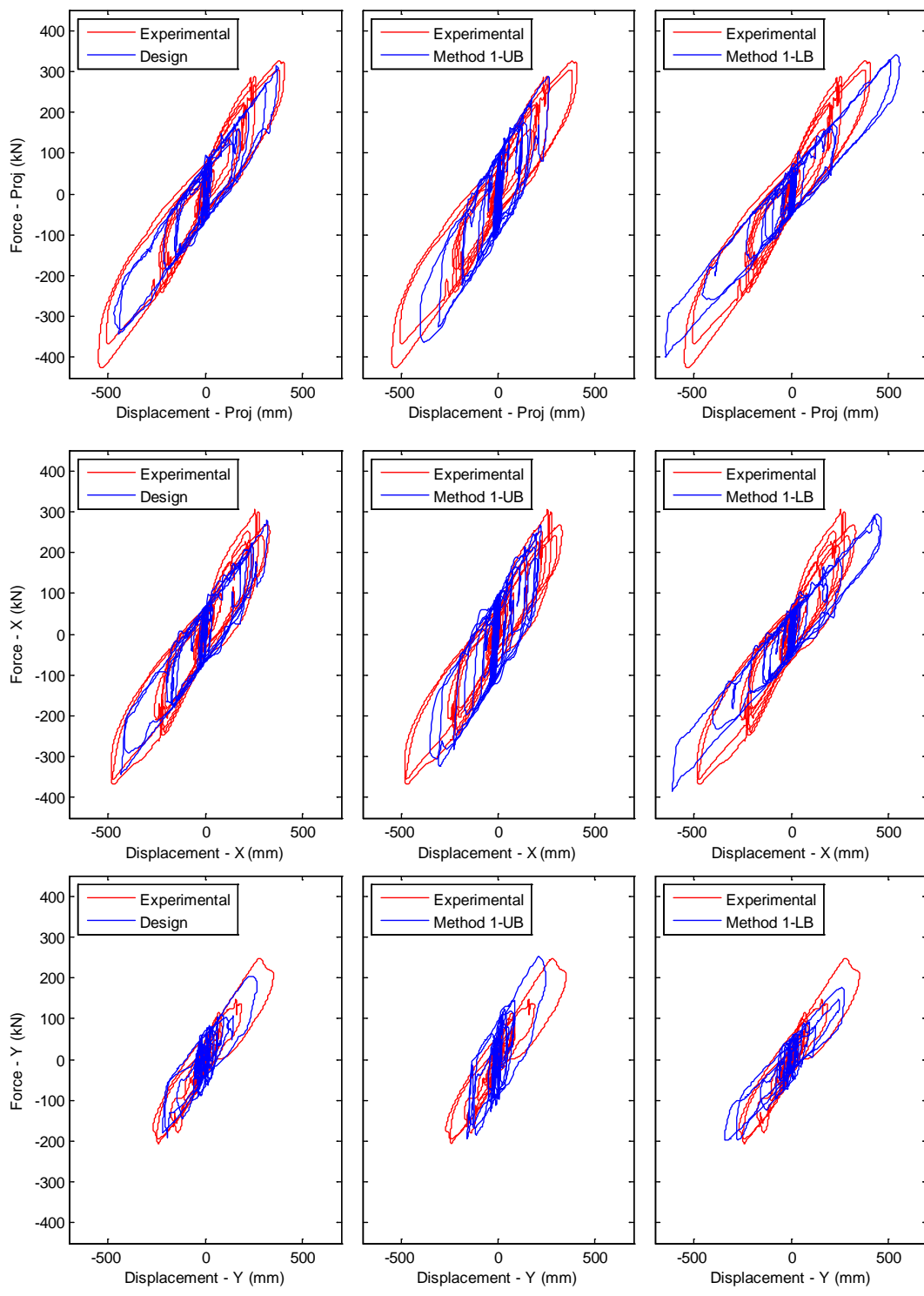


**Figure 9-11: Comparison of experimental force-displacement loop with Design, Method1-UB and Method1-LB in the projected, x- and y-directions for DIA95(XY).**

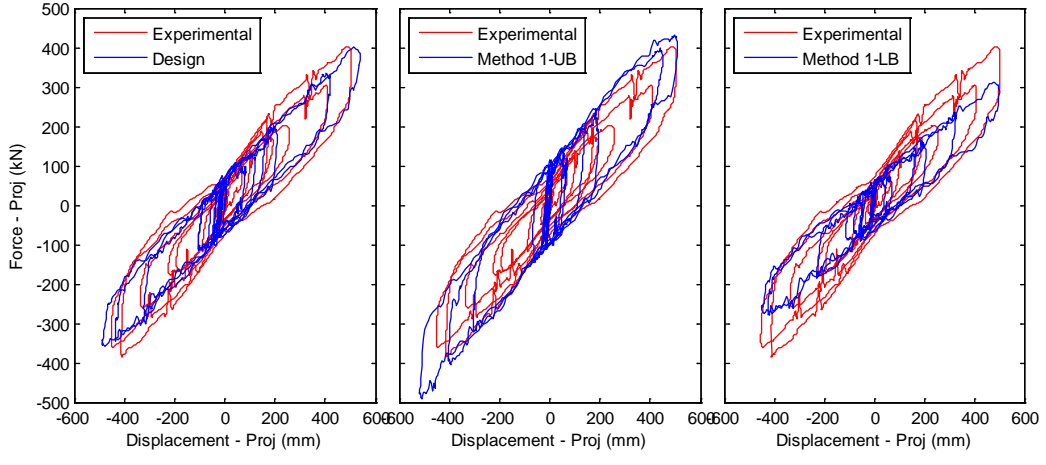


**Figure 9-12: Comparison of experimental force-displacement loop with Design, Method1-UB and Method1-LB in the projected directions for VOG175.**

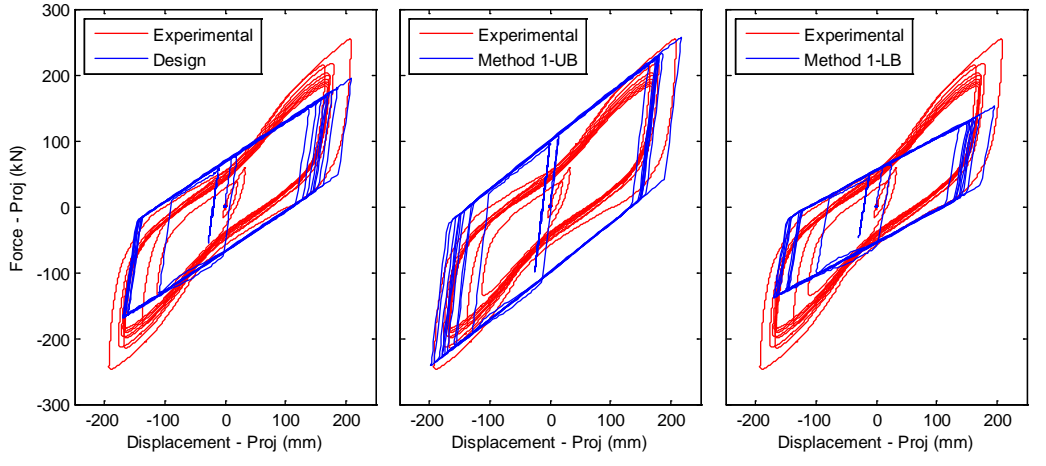


**Figure 9-13: Comparison of experimental force-displacement loop with Design, Method1-UB and Method1-LB in the projected directions for SIN100(Y)-1.**

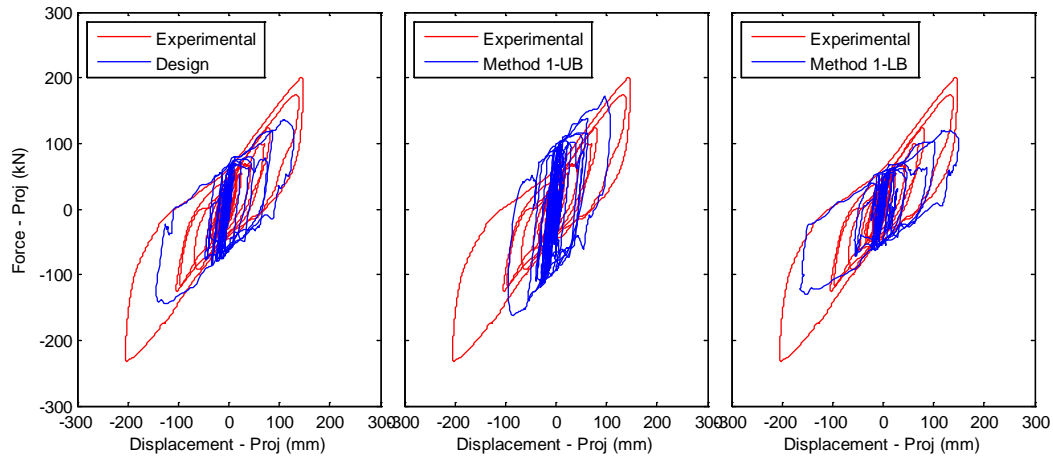


**Figure 9-14: Comparison of experimental force-displacement loop with Design, Method1-UB and Method1-LB in the projected directions for ELC130.**

The 5% damped spectral displacement for DIA95(XY), VOG175, SIN100(Y)-1, and ELC130 is shown in Figure 9-15. In this figure, the circles represent the effective period of the system associated with the recorded peak displacement of each simulation where design properties were considered. Figure 9-15 shows that the spectral displacements of VOG175 and SIN100 are decreasing, while the spectral displacements of DIA95(XY) and ELC130 are increasing around their effective periods. Furthermore, the effective period of DIA95(XY) occurs at a local max, where the spectral displacement is relatively decreasing on both sides of the effective period, therefore, bounding the responses of this motion is not feasible. Motions like VOG175 that have sharply decreasing displacement with increasing period are ideal for bounding analysis, since the displacement, and hence base shear, will increase significantly with the upper bound analysis. On the contrary, the steadily increasing displacement with increasing in period seen around the effective period of ELC130, shows that the displacement, and hence base shear, will decrease with

the upper bound analysis. Similar observations to VOG175 can be made for SIN100(Y)-1.

Since the spectral displacement of ELC130 is representative of most real excitations, and the bounding analysis did not bound the responses for this motion, the bounding analysis procedure seems to be unreliable in general.

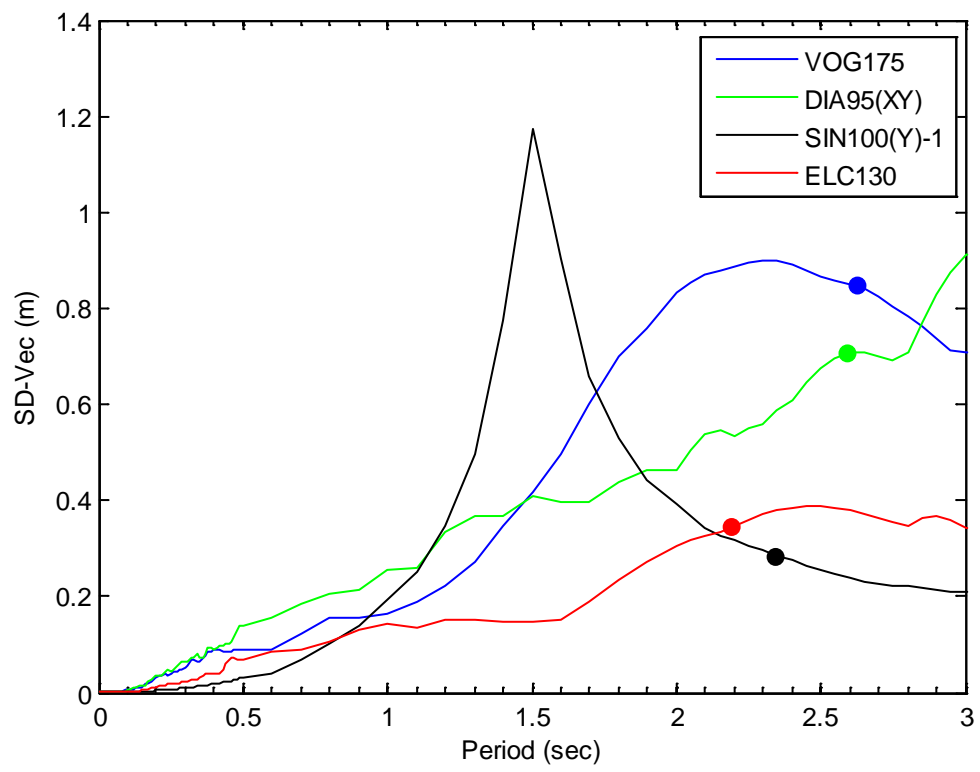


Figure 9-15: 5% damped displacement spectrum for VOG175, DIA95(XY), SIN100(Y)-1, and ELC130.

### 9.5 Summary of Observations

In summary, the results from the bounding analysis suggest that the UB cannot reliably bound peak force when the peak displacement is significantly reduced and the LB cannot

reliably bound peak displacement as LB sometimes produces lower displacement than the design case. Furthermore, the bound analysis responses show that sometimes larger displacements can be obtained from an UB analysis than from a LB analysis and design case. Therefore, in general, the bounding analysis procedures are not 100% reliable to bound the responses. However, the revised bounding analysis procedure recommended in ASCE 7 (ASCE, 2016) that considers the responses of both UB and LB to bound both peak displacements and peak forces, is found to be an improvement over current practices.

## **CHAPTER 10: MODEL OF MULTIPLE SPRING LEAD-RUBBER BEARING**

Although the lead-rubber bearing model presented in Section 8.1 was able to capture the general behavior of the LR bearing observed in the experiment, it was unable to predict more specific behaviors such as the load transfer presented in Section 6.2. The initial horizontal stiffness of the LR bearing model from Section 8.1 does not change based on the influence of the vertical load nor does it account for the decrease in bearing height with increasing in horizontal displacement. As a consequence, the load transfer behavior could not be captured.

Bearing models that consider the change in horizontal and vertical stiffness based on horizontal displacement and vertical load have been proposed. The numerical model generated by Koh and Kelly (1987, 1988, 1989) was fundamental for the advance in modeling elastomeric and LR bearings. The Koh-Kelly model is a linear model based on small displacements and rotations that accounts for axial load effect on the horizontal stiffness. A variation of the Koh-Kelly model was developed by Nagarajaiah et al. (1999) where large displacements, large rotations, and nonlinearity of rubber are considered. Moreover, this model predicts the reduction of critical load with increasing horizontal displacement and the reduction in horizontal stiffness due to the increase in horizontal displacement and axial load. Koh-Kelly linear model was also modified by Iizuka (2000) to introduce finite deformation and nonlinear springs to predict the large-deformation behavior such as hardening, load deterioration and buckling phenomena of LR bearings. A nonlinear numerical model for LR bearings was further developed by Ryan et al.

(2005) to account for the relation between axial loads and lateral/vertical response of the bearings by modifying Koh-Kelly model with a bilinear hysteretic relationship and an empirical equation for bearing yield strength. The numerical model developed by these authors was implemented in OpenSees. The LeadRubber X Model is currently the most recent numerical model implemented in OpenSees (Kumar et al. 2014). In this model, the effect of the axial load on the horizontal behavior is considered indirectly by selecting mechanical properties in the horizontal and vertical directions that are dependent on each other.

Recent research in the behavior of LR bearings led to advanced numerical models, where the horizontal and vertical bearing behavior are represented by multiple vertical and/or multiple shear springs (Yamamoto et al 2009; Kikuchi et al. 2010; Han et al. 2014). In the numerical multi-spring model developed by Yamamoto et al. (2009) in 2D and Kikuchi et al. (2010) in 3D, the vertical behavior is modeled by a series of axial springs at the top and bottom boundaries to represent the individual fibers of the bearing's cross-section area and the horizontal behavior is modeled by multiple shear springs at the mid-height of the bearing to represent the biaxial behavior of the LR bearing (Figure 10-1). The top and bottom series of axial springs are connected at mid-height with the shear spring by vertical rigid elements that represent the height of the bearing. In this model, the interaction between the shear and axial forces are a function of the variation of the vertical load that occurs under severe loading, such as earthquake loading. The Yamamoto and Kikuchi multi-spring model was implemented in OpenSees as the KikuchiBearing element to predict the behavior of LR bearings in 3D.

Since the Yamamoto and Kikuchi models rely on a number of experimentally calibrated parameters, Han et al. (2014) presented an alternative approach to modeling the behavior of elastomeric bearings that doesn't rely on experimentally calibrated parameters, making it more practical for design purposes. In Han et al. (2014) model, a number of vertical springs, each with a bilinear constitutive relationship, are placed at the bottom boundary and together represent the rotational behavior of the bearing as shown in Figure 10-2. However, this model was not implemented in OpenSees. Therefore, there was a need for an LR bearing model that doesn't rely on experimentally calibrated parameters, that considered the change in horizontal stiffness due to the variation in axial load in three-dimensions to capture the load transfer, and that could be used in the OpenSees framework. To achieve all these requirements, the multi-spring LR bearing (MS-LRB) model was developed and is described in this section. The MS-LRB model is an adaptation of the Kikuchi bearing model taking into consideration the work by Han et al. (2014).



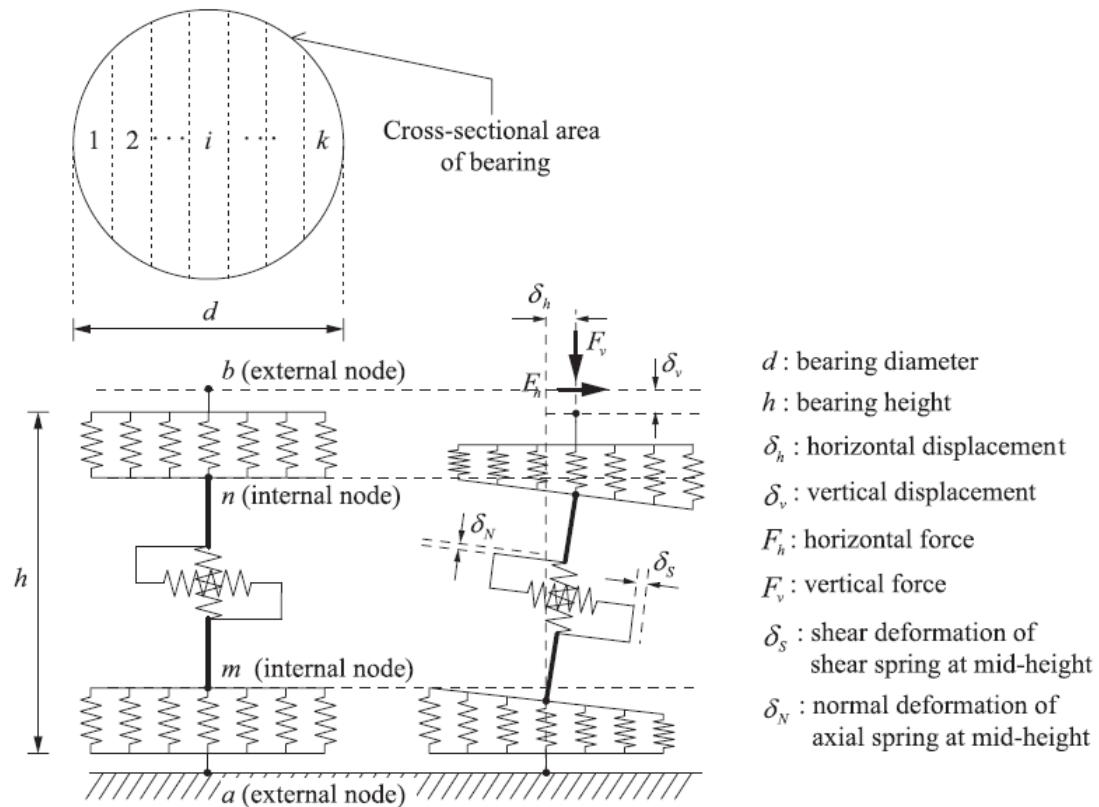


**Figure 10-1: Multi-spring mechanical model (Yamamoto et al 2009; Kikuchi et al. 2010)**

The primary objective of using the MS-LRB model was to account for the vertical movement of the bearing in order to capture the horizontal-vertical displacement interaction of the system that was observed in the experiment. The vertical movement occurs through the rotation of the bearing shear layers when subjected to a combination of horizontal displacement and axial force. A secondary objective was to construct the MS-LRB model using existing materials and elements in OpenSees such that the mechanics is transparent and the implementation can be easily modified by the user. Moreover, as the research in the behavior of lead-rubber bearings expands, new elements and materials are constantly being developed in OpenSees. Therefore, the newer and

improved elements and materials can be applied in the MS-LRB model, in order to best suit the needs in the analytical model. Moreover, since the elements can be easily modified, the MS-LRB can be formulated as a 2D or 3D model, which is beneficial for users that have superstructure models in 2D or 3D.

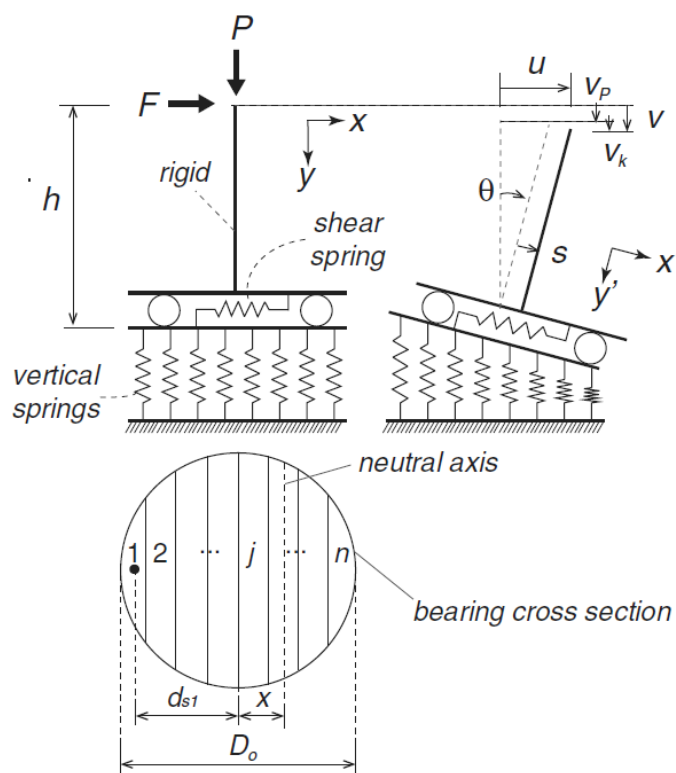


**Figure 10-2: Mechanistic model for elastomeric bearing (Han et al. 2014)**

The construction of the MS-LRB is described in Section 10.1. The modeling assumptions and elements used in the vertical and horizontal directions are described in Section 10.1.1 and Section 10.1.2, respectively. The validation of the properties and behavior of a single DOF MS-LRB model is presented in 10.2. The validation of the MS-LRB model in combination with the slider model described in Section 8.1 is presented in Section 10.3. In Chapter 11, the experimental bearing responses are compared with those determined

through computational simulation of the building model using MS-LRB elements for the LRBs.

## 10.1 Construction of the MS-LRB Model

The mechanics of the MS-LRB model in 2D is represented in Figure 10-3. The planar spring assemblage of the MS-LRB model, which is comprised of a series of vertical springs at the top and bottom boundaries connected by rigid elements, a shear layer, and a plastic spring, is shown in Figure 10-3(a) for the undeformed configuration. The number of vertical springs can vary based on the desired accuracy of the numerical analysis. In the MS-LRB model, the axial load is transferred from the top series of vertical springs to the bottom, via the vertical rigid beams and a rigid element in the shear layer as described in Section 10.1.1. The shear behavior of the LR bearing is modeled by two trusses in the shear layer and a plastic spring. The trusses and plastic spring represent the rubber and lead plug behavior, respectively of the LR bearing, as described in Section 10.1.2.

The bottommost nodes of the bottom series of vertical springs have a fixed boundary condition, that is, there is no translation and rotation about the x-, y- and z-directions. These constraints were specified since the LR bearings were placed underneath the building where the base of the bearings was fixed against any movement. However, these constraints can be modified to allow movement at the base of the bearing if desired. The top center node of the bottom series of vertical springs is constrained from translation in the x- and y-directions and rotation about the z-direction. Furthermore, the center nodes of the top series of vertical springs are constrained such that they have the same translation in the x- and y-directions, and rotation about the z-axis. These constraints

were necessary to ensure that the horizontal displacement occurred only at the shear layer without the addition of more elements.

The horizontal displacement,  $\delta_h$ , and a total vertical deformation,  $\delta_v$ , due to simultaneously applying a vertical force,  $P$ , and shear force,  $F$ , at the top of the model, are shown in Figure 10-3(b). In this figure,  $\delta_v$  represents the total height reduction of the bearing that is a summation of the initial deformation due to the applied load  $P$  and the vertical deformation that results from the rotation that occurs in the vertical springs (Han et al., 2014).

To represent the 3D behavior of the LR bearing, the planar spring assemblage (Figure 10-3(a)) can be built in any direction, that is, parallel to the x- and y-axis or any arbitrary rotation from the x-axis. To assess what type of MS-LRB model provided responses that better matched the experimental, two configurations of the MS-LRB are considered in this study. For the first configuration, hereon referred to as MS2, the model is constructed by placing two planar spring assemblage perpendicular to each other, that is, x- and y-directions using the same coordinate system from the superstructure (Figure 10-4(a-b)). For the second configuration, hereon referred to as MS4, additional planar spring assemblages are placed at  $\pm 45$  degrees from the x-axis (Figure 10-4(c-d)). For both MS2 and MS4 configurations, the planar spring assemblages are connected through the center nodes in both top and bottom series of vertical springs. As a result of the number of planar spring assemblages considered in each model, the two configurations have different numbers of vertical springs. The nodes for the vertical springs are represented by black squares in Figures 10-4(a) and 10-4(c). As will be shown in Chapter 11, the two

bearing configurations are adequate to understand the behavior of the MS-LRB model and predict the bearing response with reasonable accuracy. However, as mentioned before, refined bearing configurations with more vertical springs should be considered until there is minimal variation in bearing response with refinement. The validation of the MS2 will be presented in this chapter to demonstrate that the most (compared to MS4) basic numerical model can predict the nature of the horizontal and vertical behavior of the LR bearing.

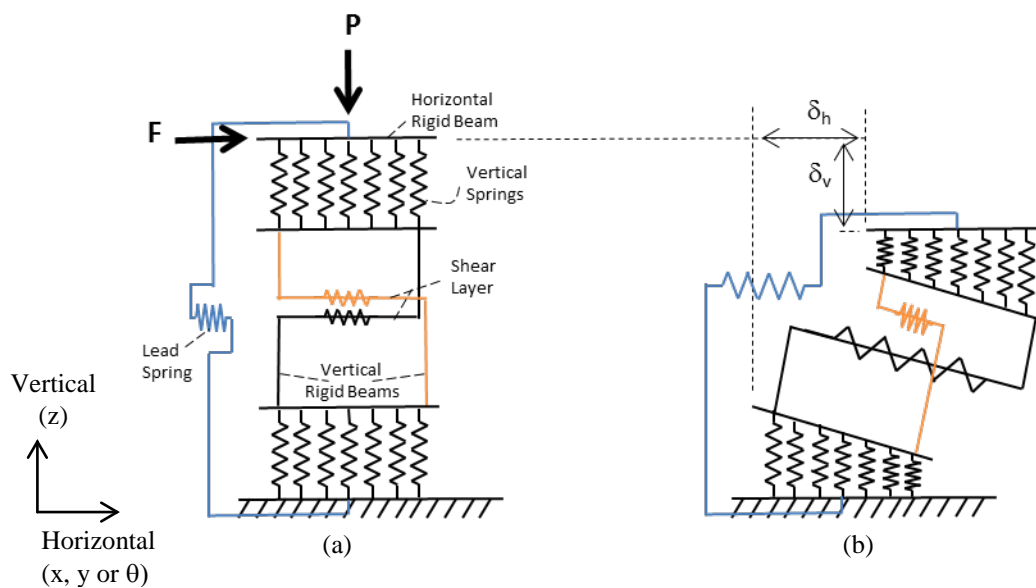


**Figure 10-3: (a) undeformed multiple spring model, (b) multiple spring model under vertical and horizontal deformations.**

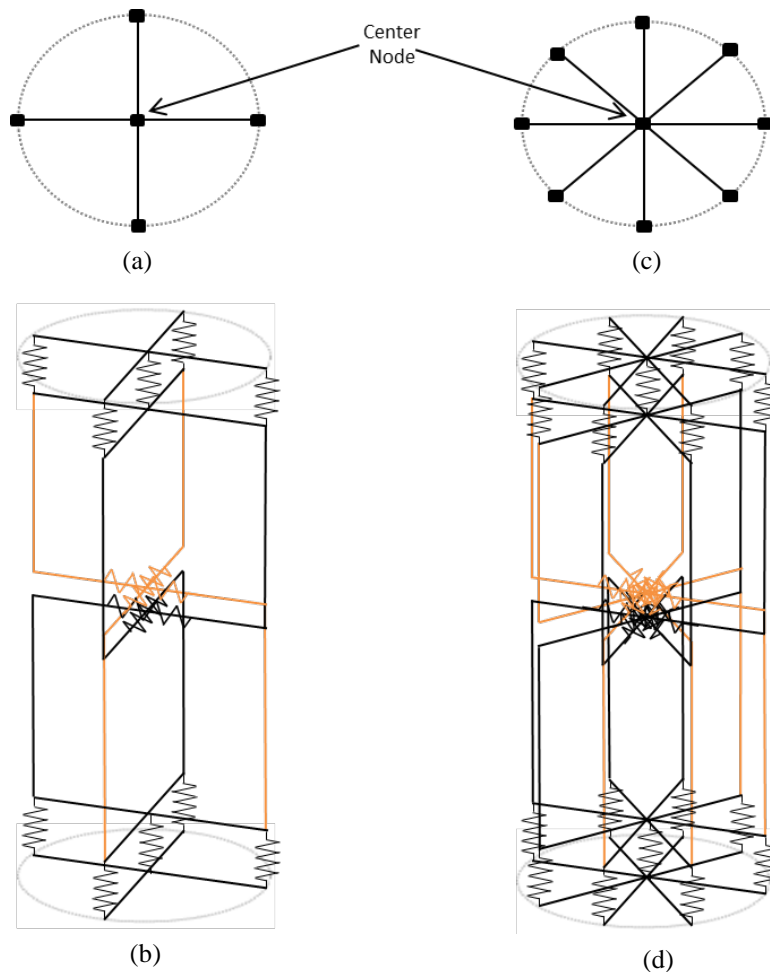


**Figure 10-4:** (a-b) MS2 with shear springs in two directions (X and Y), (c-d) MS4 with shear springs in four directions (X, Y and  $\pm 45^\circ$  from x-axis)

### 10.1.1 Vertical Direction

Load transfers vertically through the bearing from the top to the bottom series of vertical springs by the two top and two bottom rigid beams, and two horizontal beams in the shear layer (Figure 10-5(a)). The horizontal beams in the shear layer have no axial stiffness, but are rigid in shear and bending, hereafter referred to as rigid shear beams (Figure 10-5(b)). The axial load is applied at the top center node of the bearing and distributed to the top series of vertical springs in proportion to their stiffnesses. The load

then transfers to the two top rigid beams, then to the two rigid shear beams, then to the two bottom rigid beams, then finally to the bottom series of vertical springs, and is once again distributed according to the spring stiffnesses. Two sets of vertical rigid beams and rigid shear beams are needed to supplement the double truss configuration as explained in Section 10.1.2.

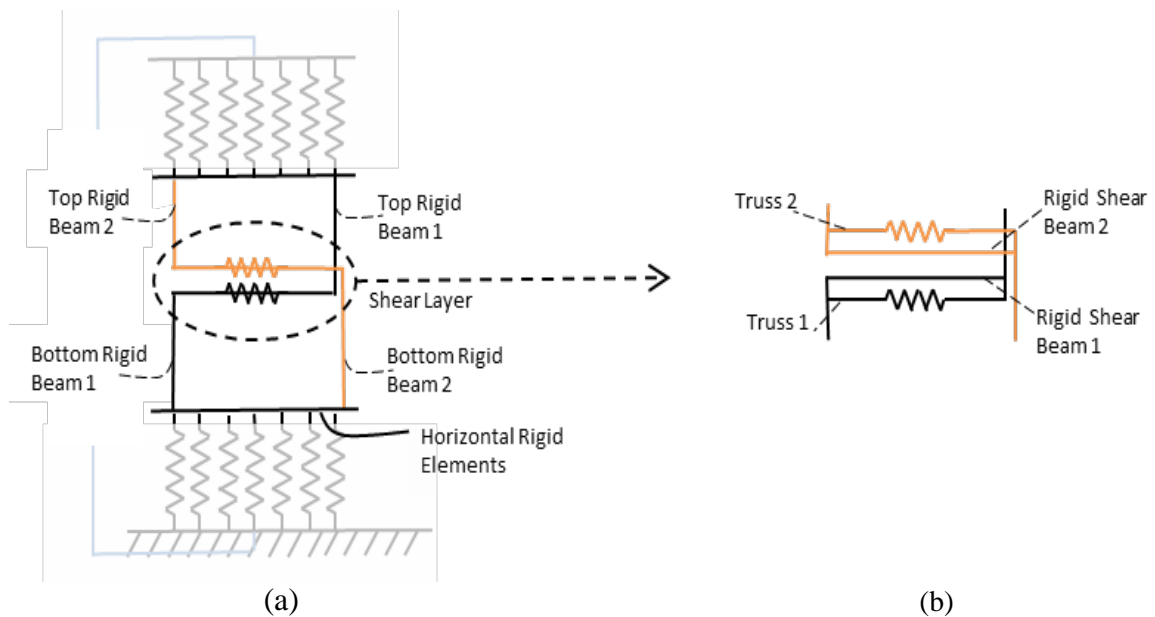


**Figure 10-5: (a) Axial load transfer elements, (b) elements in shear layer**

Vertical Springs: The vertical springs were built using zeroLength elements with an elastic material. The force-displacement relationship of the spring is shown in Figure 10-6. For validation of the element, the tension and compression stiffness of the bearing was assumed to be the same. This assumption was made in order to validate the numerical simulation in comparison to theoretical vertical behavior, since the vertical stiffness is assumed to be the same in tension and compression in the theoretical equations (Kelly, 1997). Furthermore, this force-displacement relationship had to be considered instead of

the one presented in Section 8.1.2 for convergence of the model. Moreover, as mentioned before, the vertical stiffness of the LR bearing in the experiment was observed to be lower than the design vertical stiffness from Table 3-3, as a result of the flexibility provided by the load cells (Section 8.1.2). Therefore, the reduced vertical stiffness,  $K_{vr} = 1000$  kN/mm, was also applied in numerical simulation using the MS-LRB bearing model. The stiffness on each vertical spring,  $K_{vj}$ , was defined to be proportional to its tributary area acting on the cross-section of the bearing, such that the summation of the stiffnesses in the vertical springs equaled  $2K_{vr}$  as shown in Equation 10.1. The factor of two multiplying  $K_{vr}$  is applied because the top and bottom layer of vertical springs in the MS2 act in series as explained later.

$$2K_{vr} = \sum_j K_{vj} \quad (10.1)$$

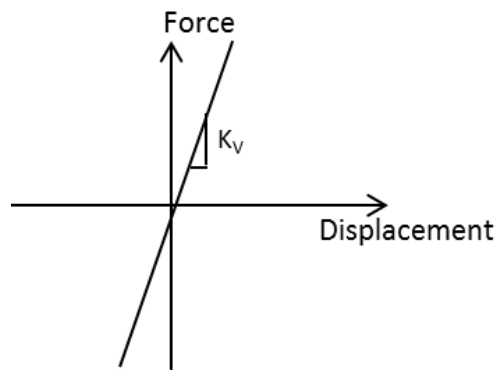


**Figure 10-6: Force-displacement relationship for vertical springs.**



Horizontal Rigid Elements: The vertical springs were connected by horizontal rigid elements (Figure 10-3(a) and Figure 10-5(a)) that were constructed from elasticBeamColumn elements that had large stiffnesses in all directions: axially, in-plane and out-of-plane bending, and torsional. A linear coordinate transformation was applied to the horizontal rigid elements.

Top and Bottom Rigid Beams: The top and bottom rigid beams (Figure 10-5(a)) were constructed from elasticBeamColumn elements that had large stiffnesses in all directions: axially, in-plane and out-of-plane bending, and torsional. A linear coordinate transformation was applied to these rigid beams. The two top rigid beams translated horizontally, while the horizontal movement of the two bottom rigid beams was nearly zero.

Rigid Shear Beams: The main purpose of the rigid shear beams (Figure 10-5(b)) was to transfer the axial load from the top to the bottom vertical rigid beams, without adding any stiffness in the horizontal direction. To achieve this goal, the rigid shear beams were made from elasticBeamColumn elements with nearly zero stiffness for axial and out-of-plane bending, and large stiffness for in-plane bending and torsion. A corotational coordinate transformation was used for the rigid shear beams to capture the exact geometric transformation of the beam stiffness as the bearing deformed horizontally and the rigid shear beam rotated through the horizontal deformation. Moreover, the corotational coordinate transformation was necessary to accompany the corotational truss elements as explained later.

### 10.1.2 Horizontal Direction

The horizontal stiffness of the LR bearing was modeled by a plastic spring (Figure 10-3) and a double truss configuration (Figure 10-5(b)). The elastomeric and lead plug behaviors of the LR bearing were modeled separately in order to capture the bidirectionally coupled behavior of the lead plug by a single element. The force-displacement relationship of the elastomeric component/rubber (truss), lead plug (plastic spring), and their combined response are shown in Figure 10-7.

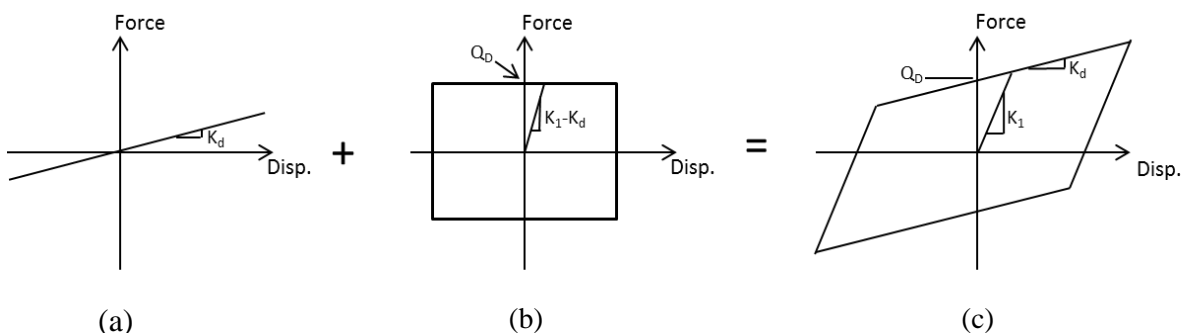


**Figure 10-7: Horizontal force-displacement of LR bearing: (a) rubber, (b) lead plug, (c) combined**

*Truss*: The elastomeric behavior of the LR bearing was modeled using corotational trusses with an elastic material (Figure 10-7(a)). The stiffness of the truss elements was defined such that the total horizontal stiffness of the trusses in any direction was equal to the post-yield stiffness  $K_d$ .

A double truss configuration that has two trusses in each direction, instead of a single truss configuration with only one truss in each direction, was used in order to remove

unrealistic bidirectional movement of the model when subjected to a unidirectional loading. This behavior is illustrated for the MS2 configuration. The forces generated on the truss due to a unidirectional load and the relative deformation across the nodes are shown in Figures 10-8(a) and 10-8(b) for the single and double truss configurations, respectively. In Figure 10-8, the forces are only shown for the nodes where the horizontal movement occurs and the reaction forces generated at the other nodes are not shown but understood to be present. Furthermore, in Figure 10-8, the squares represent the nodes connecting the truss to the bottom rigid beams (Figure 10-5(a)), while the circles represent the nodes connecting the truss to the top rigid beams. Moreover, in Figure 10-8(b) the two trusses in the x- and y-directions are physically on top of each other but shown adjacent for clarity. When the single truss configuration is subjected to displacement in the x-direction, the truss oriented in the x-direction develops an axial force of  $F_{1x}$ , while the truss oriented in the y-direction develops an axial force,  $F_2$ , along the length of the truss that has components  $F_{2x}$  and  $F_{2y}$  in the x- and y-directions, respectively (Figure 10-8(a)). The  $F_{2y}$  component is large and will cause the MS2 system to also move in the y-direction, which is non-physical. In contrast, when the double shear truss configuration is subjected to a displacement in the x-direction, the two trusses oriented in the x-direction develop axial forces,  $F_{1x}$ ,  $F_{2x}$ , while the two trusses oriented in the y-direction develop axial forces,  $F_3$  and  $F_4$  along the length of the truss with components  $F_{3x}$  and  $F_{4x}$  in the x-direction and components  $F_{3y}$  and  $F_{4y}$  in the y-direction, respectively (Figure 10-8(b)). The y-components of forces  $F_3$  and  $F_4$  will sum to zero since  $F_{3y}$  is in the positive y-direction and  $F_{4y}$  is in the negative y-direction, thus,

eliminating undesirable rotation in the system. Therefore, the double shear truss configuration was implemented in the bearing model.

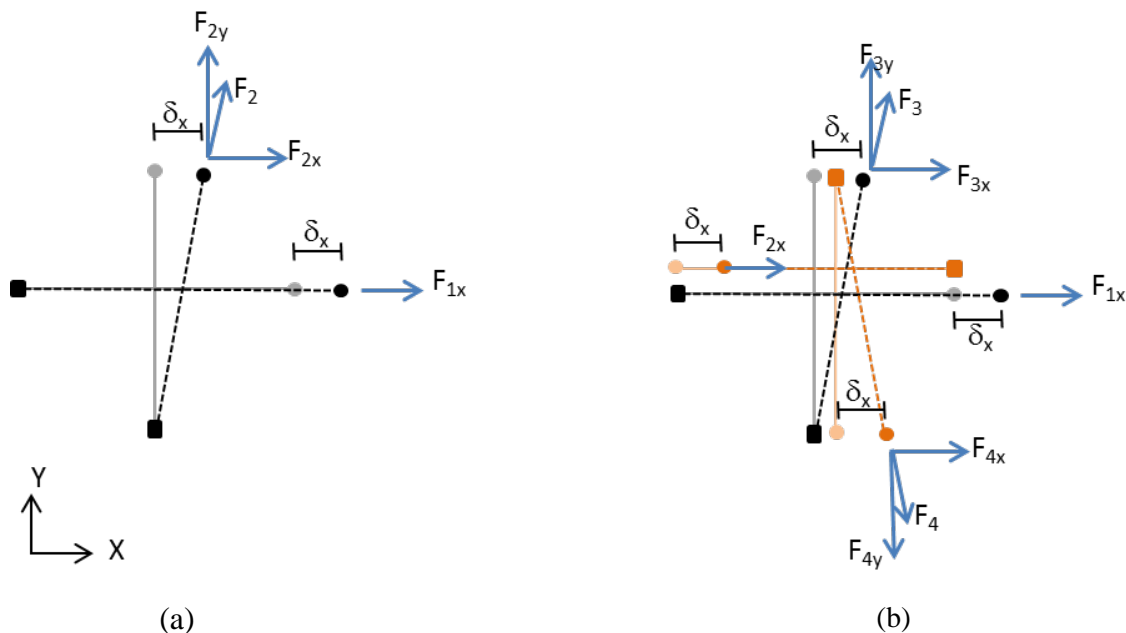


**Figure 10-8: Forces generated in a (a) single vs (b) double truss configuration subjected to a horizontal displacement in the x-direction**

*Plastic Spring:* The lead plug behavior was modeled using a zeroLengthSection element with a bidirectional section that has an elastic-perfectly plastic force-displacement relationship as shown in Figure 10-7(b). The initial stiffness of the plastic spring was equal to the difference between the initial stiffness of the LR bearing,  $K_I$ , and the post-yield stiffness  $K_d$  in Figure 10-7(c). The yield force of the plastic spring was equal to the characteristic strength,  $Q_d$ , of the LR bearing. The design properties from Table 3-3 were assigned to  $K_I$ ,  $K_d$  and  $Q_d$ . Furthermore, in OpenSees, the bidirectional section can

include isotropic and kinematic hardening. These associated isotropic and kinematic hardening moduli were defined to be zero to impose the perfectly plastic response.

## **10.2 Validating a Single MS2 Bearing Model**

The MS2 bearing model was implemented in a single bearing system that consists of a 3D MS2 bearing element fixed at the base and attached to a mass with DOFs in x, y and z (Figure 10-9). In addition to the constraints specified in Section 10.1, the center node of the topmost layer of vertical springs was constrained against rotation in any direction; that is, rotations about x-, y- and z-axes were prevented. This additional constraint was necessary to constrain all rigid body modes in the single bearing system and is not needed in a model where multiple bearings are connected by a rigid base frame. The single bearing system was subjected to an excitation in each horizontal and the vertical direction to confirm that the expected stiffness of the elements was produced, and the axial and shear force were distributed through the elements as expected.

Results showed that convergence of the MS2 model was sensitive to the applied stiffness of the elements used to represent rigid behavior as well as the applied damping parameters. Therefore, the stiffness of the rigid elements in the single MS2 model was adjusted to achieve convergence in conjunction with the Rayleigh damping model described in Section 7.5, while ensuring sufficient rigidity of the rigid elements. This was necessary since ultimately the single bearing system was going to be implemented with the model of the superstructure described in Chapter 7. The allowable stiffness of the rigid shear beam to achieve convergence was shown to be the most sensitive to damping. Damping was applied to all elements of the MS2 model.

The script for the numerical simulation of the MS2 model and an example of its application in OpenSees is presented in Appendix F.

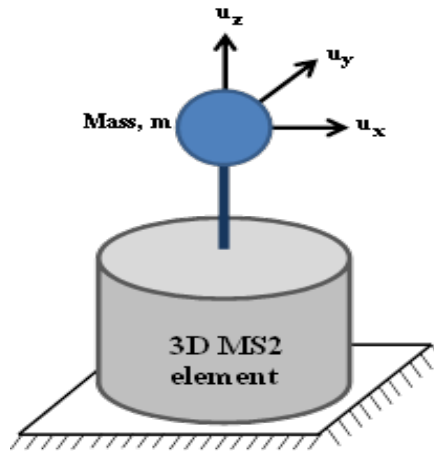


**Figure 10-9: Single bearing system for validation of MS2**

### 10.2.1 Validation of Horizontal Behavior

To confirm that the stiffness of the trusses represented the rubber behavior in each direction, and that the plastic spring represented the lead plug behavior, the single MS2 bearing element was subjected to a controlled cyclic displacement history in the x and y-directions independently and the force-displacement relationship was recorded. The stiffness of each truss was equal to half of  $K_{d,des}$ , (or 0.325 kN/mm) such that the double truss configuration post yield stiffness is 0.65 kN/mm. For the plastic spring, the bidirectional section properties were stiffness = 5.85 kN/mm and yield force  $Q_d = 65.7$  kN. The axial force on the MS2 was equal to 583 kN, which represents 1/9 of the total weight on the building (5250 kN). Figure 10-10 shows the force-displacement relationship of the trusses, the plastic spring, and the combined response due to applying the excitation in the global y-direction. All responses from the controlled cyclic

displacement history in the x-direction produced identical plots as the ones shown in Figure 10-9, and therefore are not presented here. The x-component of the total horizontal force through the shear layer of the bearing was determined by summing the x-components of the forces on the two trusses oriented in the x- and the two trusses oriented in the y-direction. Likewise, the y-component of the total horizontal force through the shear layer of the bearing was determined by summing the y-components of the forces on the two trusses oriented in the x- and y-directions. Therefore, the combined response of the trusses and plastic spring reproduced the horizontal stiffness of the bearing in any direction.

The bidirectional behavior of the MS2 bearing model was investigated by subjecting the single bearing system to an axial force of 583 kN and to the y-component of SIN100(Y)-1 simultaneously in both x- and y- directions and the force-displacement relationship recorded for the truss, the plastic spring and the combined response, as shown in Figure 10-11. As expected, the truss and plastic spring produced responses in the x-direction that were nearly identical to the responses in the y-direction (Figure 10-11). Moreover, the MS2 model produces force in the truss that is not linear in the x- and y-directions (Figure 10-12(a)) due to the large horizontal rotation of the truss elements when the bearing is subjected to a diagonal motion ( $45^\circ$  from x-axis). However, if the MS4 model is subjected to the same loading conditions, this undesired behavior is no longer present and the response of the truss in x- and y-directions are once again linear as shown in Figure 10-12(b). The bidirectionality of the MS2 model was further confirmed by subjecting the

model to DIA95(XY) and observing the circular yield surface produced by the plastic spring response (Figure 10-13).

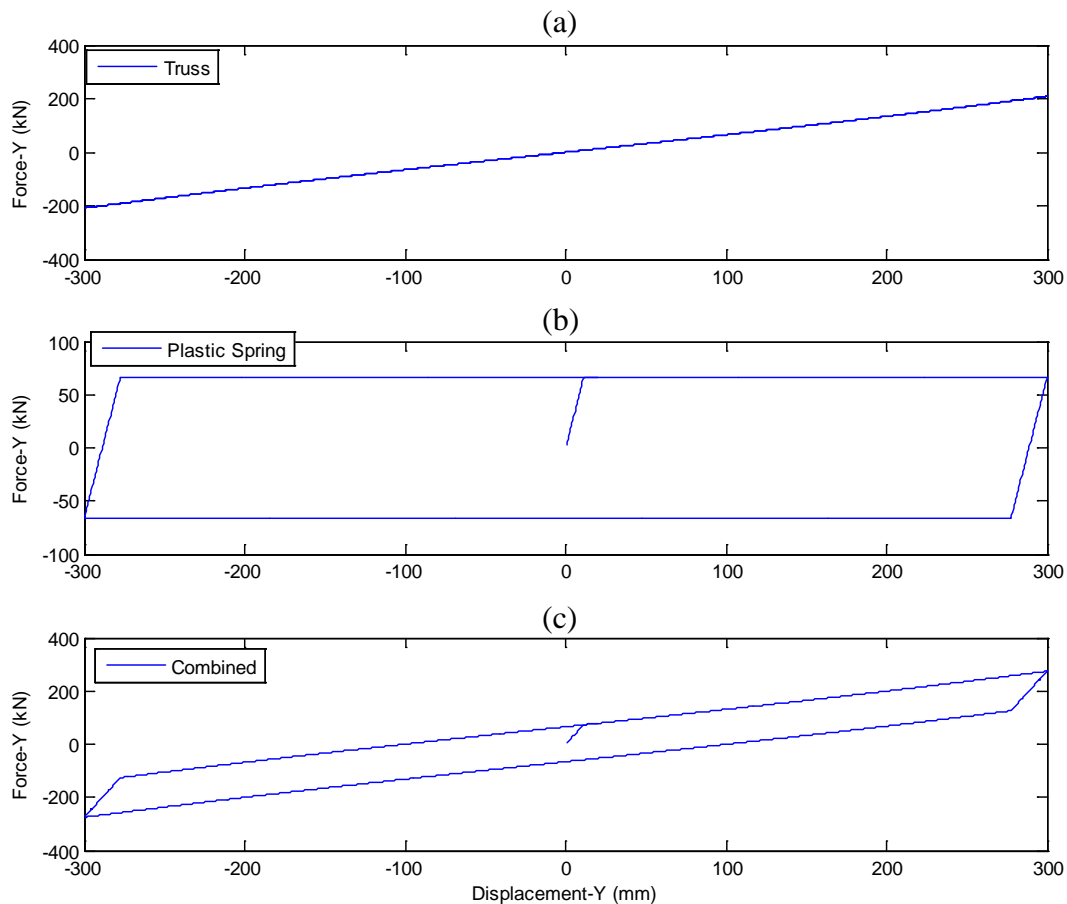


**Figure 10-10: Force-displacement relationship for the truss, plastic spring, and composite due to a controlled cyclic displacement history analysis in the y-direction of the MS2 model.**



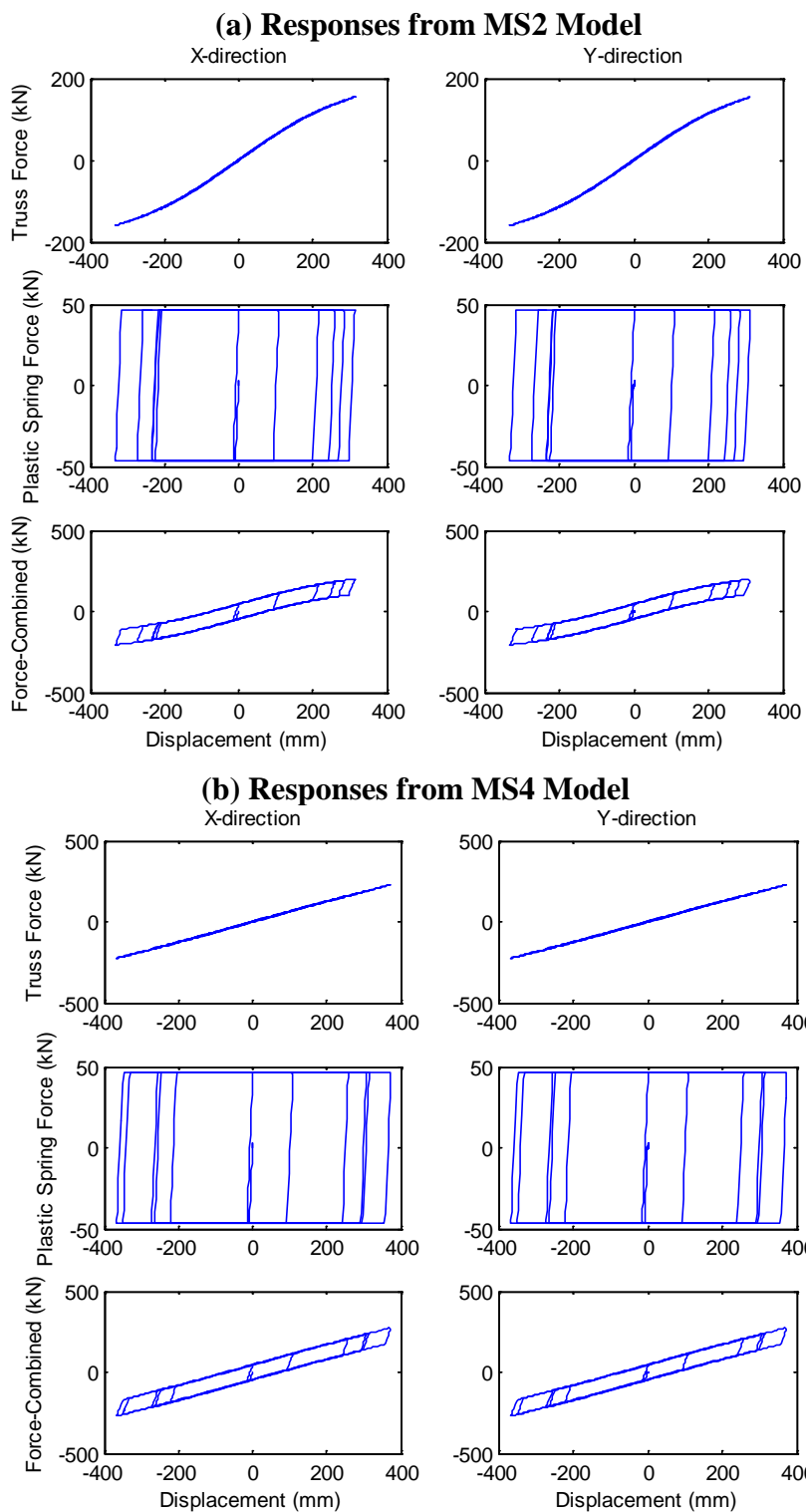


**Figure 10-11: Force-displacement relationship for the truss, plastic spring, and composite from subjecting (a) the MS2 model and (b) the MS4 model to the y-component of SIN100(Y)-1 simultaneously in the x- and y-direction.**

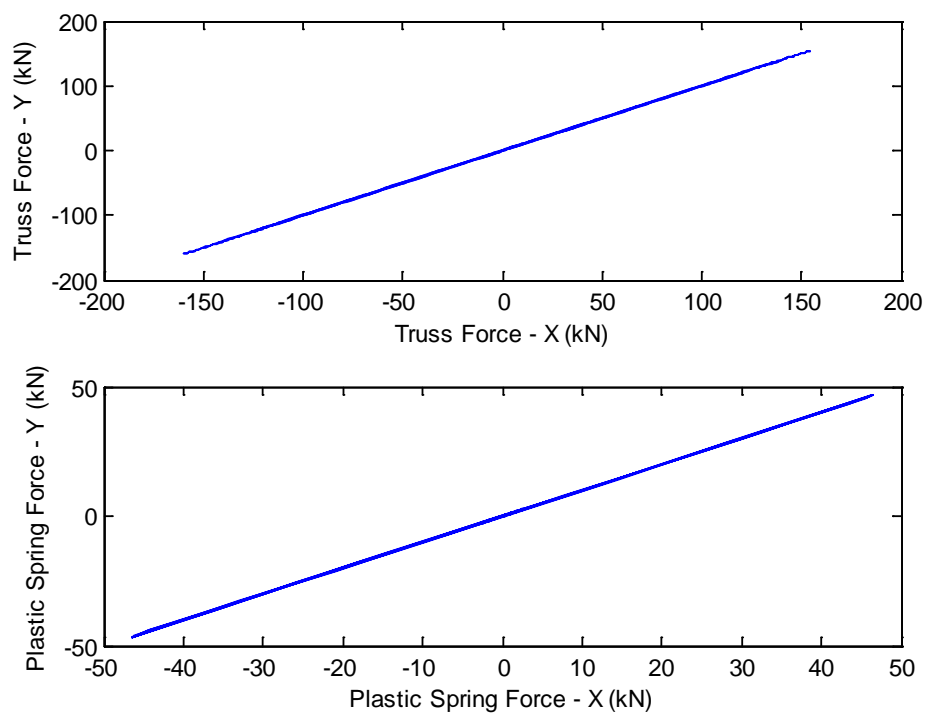


**Figure 10-12: Truss and plastic spring force trace from subjecting the MS2 model to the y-component of SIN100(Y)-1 simultaneously in the x- and y-direction.**

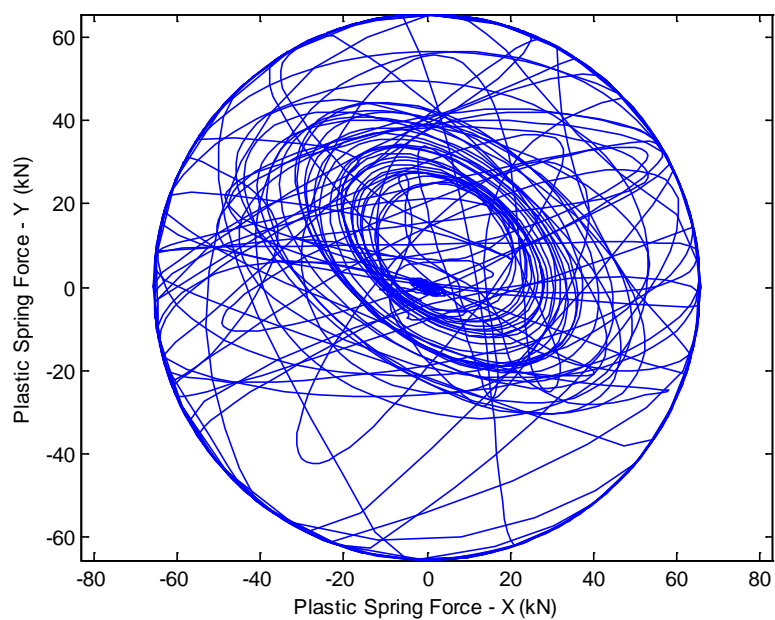


**Figure 10-13: Yield surface of MS2 model.**

### 10.2.2 Validation of Vertical Behavior

To validate the vertical behavior, the single MS2 bearing element was subjected to cyclic vertical displacement in the z-direction. The force-displacement relationship of the MS2 model in the vertical direction is shown in Figure 10-14 for one of the center vertical springs, one of the edge vertical springs, and the total (summed over all springs in a layer). Recall that the MS2 bearing model has one center vertical spring and four edge vertical springs in each layer (Figure 10-4). As mentioned earlier, the vertical stiffness of the center and edge vertical springs were based on the tributary area and as a result, the stiffness of the center vertical spring was larger than the edge vertical springs as shown in Figure 10-14. Because the top and bottom layer of vertical springs act in series, the composite stiffness of each layer was defined to be twice the total desired vertical stiffness of the bearing, and the stiffness of each spring was adjusted accordingly. Therefore, the stiffness of each edge spring (four in each vertical spring layer,  $0.2K_{vr} = 200$  kN/mm), the stiffness of each center spring (one in each vertical spring layer,  $1.2K_{vr} = 1,200$  kN/mm), and the composite stiffness of each layer ( $2K_{vr} = 2,000$  kN/mm) are validated by the force-displacement relations shown in Figure 10-14.

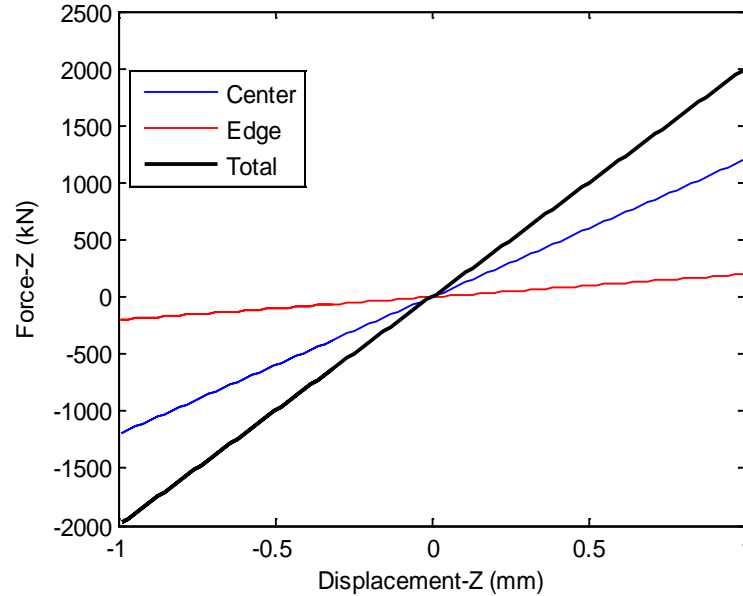


**Figure 10-14: Force-displacement relationship of MS2 model in the vertical direction for the center and edge vertical springs.**

The vertical force-deformation behavior of the bearing is affected by coupling due to combined horizontal and vertical loading. The overall downward movement of the top of the bearing can be determined from the downward movement due to the static gravity load (first term in Equation 10.2) and an additional downward movement that occurs due to a horizontal displacement of the bearings (second term in Equation 10.2) (Kelly, 1997):

$$\delta_v = \frac{Ph}{E_c A_s} + \frac{(GA_s + P)}{P_E} \frac{\delta_h^2}{h} \quad (10.2)$$

In Equation 10.2,  $P$  is the axial load on the bearing,  $h$  is the total height of the bearing,  $E_c$  is the compression modulus,  $G$  is the shear modulus, and  $\delta_h$  is the horizontal deformation at the top of the bearing.  $A_s = A^*h/T_r$ , where  $T_r$  is the total rubber thickness, is an

increased bearing area that accounts for the steel shims of the bearing that do not deform in the composite (steel plus rubber) system (Kelly, 1997).  $P_E$  is the Euler buckling load determined by:

$$P_E = \frac{\pi^2 EI_s}{h^2} \quad (10.3)$$

where  $EI_s$  is the effective bending stiffness for a composite (steel plus rubber) bearing, according to:

$$EI_s = \frac{1}{3} E_c I \frac{h}{T_r} \quad (10.4)$$

which is based on the compression modulus, moment of inertia,  $I$ , and the ratio of the total height of the bearing to  $T_r$ .

The theoretical downward movement of the top of the bearing (based on Equation 10.2) and the numerical downward movement that occurs during a controlled cyclic horizontal displacement history are compared in Figure 10-15. The values considered in the calculation of the theoretical vertical movement were:  $P = 583$  kN,  $h = 460$  mm,  $A_s = 0.734$  m<sup>2</sup>,  $G = 0.414$  MPa,  $T_r = 240$  mm,  $I = 0.012$  m<sup>4</sup> and  $E_c = 0.63$  kN/mm<sup>2</sup> which was determined from Equation 10.5 in order to match the reduced vertical stiffness,  $K_{vr}$ , used in the numerical model.

$$E_c = \frac{K_{vr} h}{A_s} \quad (10.5)$$

The applied axial load in the numerical simulation was held constant during the controlled cyclic displacement history and equal to 583 kN, which is about 7% of the critical load that corresponds to the calibrated value of  $K_{vr}$ . The small difference in values between the two curves in Figure 10-15 is a result of making the stiffness of the rigid shear beam lower than required to achieve convergence of the bearing model during a dynamic analysis. As the stiffness of the rigid shear beam is increased toward infinity, the theoretical and numerical downward movement of the bearing converge to the same value as shown in Figure 10-16.

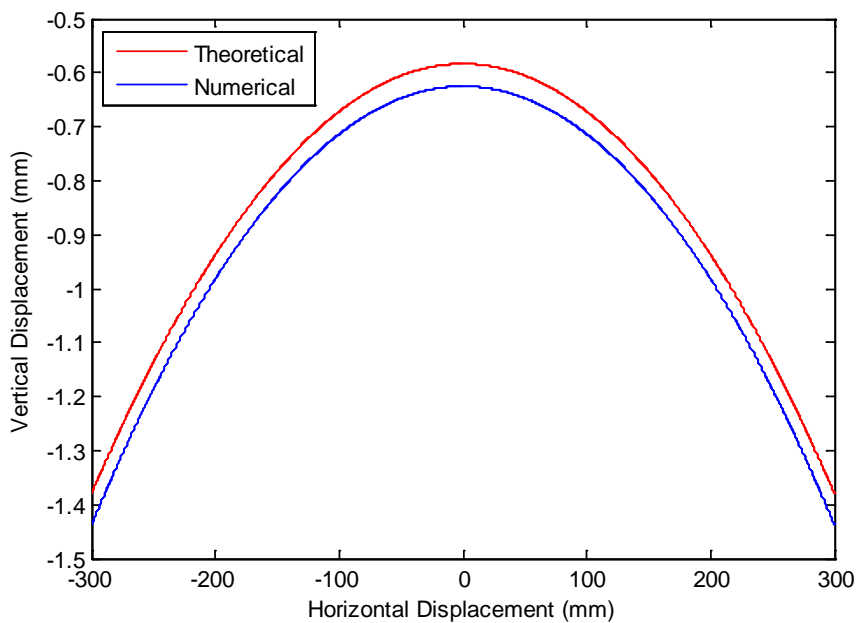


**Figure 10-15: Vertical vs horizontal bearing displacement using low rigidity for the MS2 rigid shear beam.**

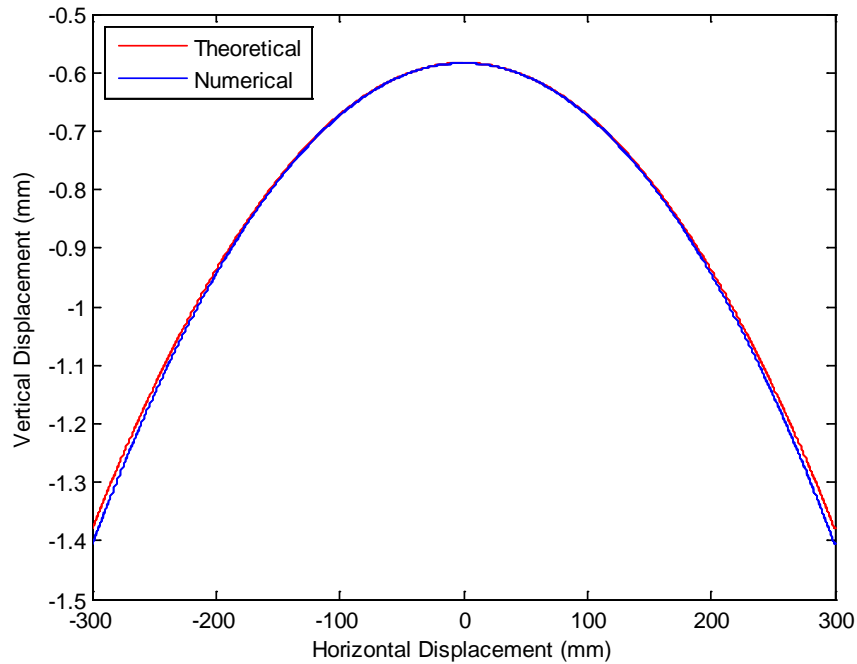


**Figure 10-16: Vertical vs horizontal bearing displacement using high rigidity for the MS2 rigid shear beams.**

### 10.2.3 Validation of Horizontal-Vertical Coupling

The effect of the vertical load on the horizontal stiffness of the bearing was also validated for a single MS2 bearing model. The bearing was subjected to cyclic horizontal displacement at different values of the vertical load that vary as a ratio of the critical load ( $P_{cr}$ ), where  $P_{cr}$  was determined from Equation 10.6. Using the value of  $G$ ,  $A_s$  and the equation to compute  $P_E$  that were presented in Section 10.2.2 yielded to  $P_{cr} = 8141$  kN.

$$P_{cr} = \sqrt{GA_s P_E} \quad (10.6)$$

Figure 10-17 shows the force-displacement relationship of the bearing for different values of  $P_{cr}$ . In Figure 10-17, the decrease in horizontal stiffness due to an increase in

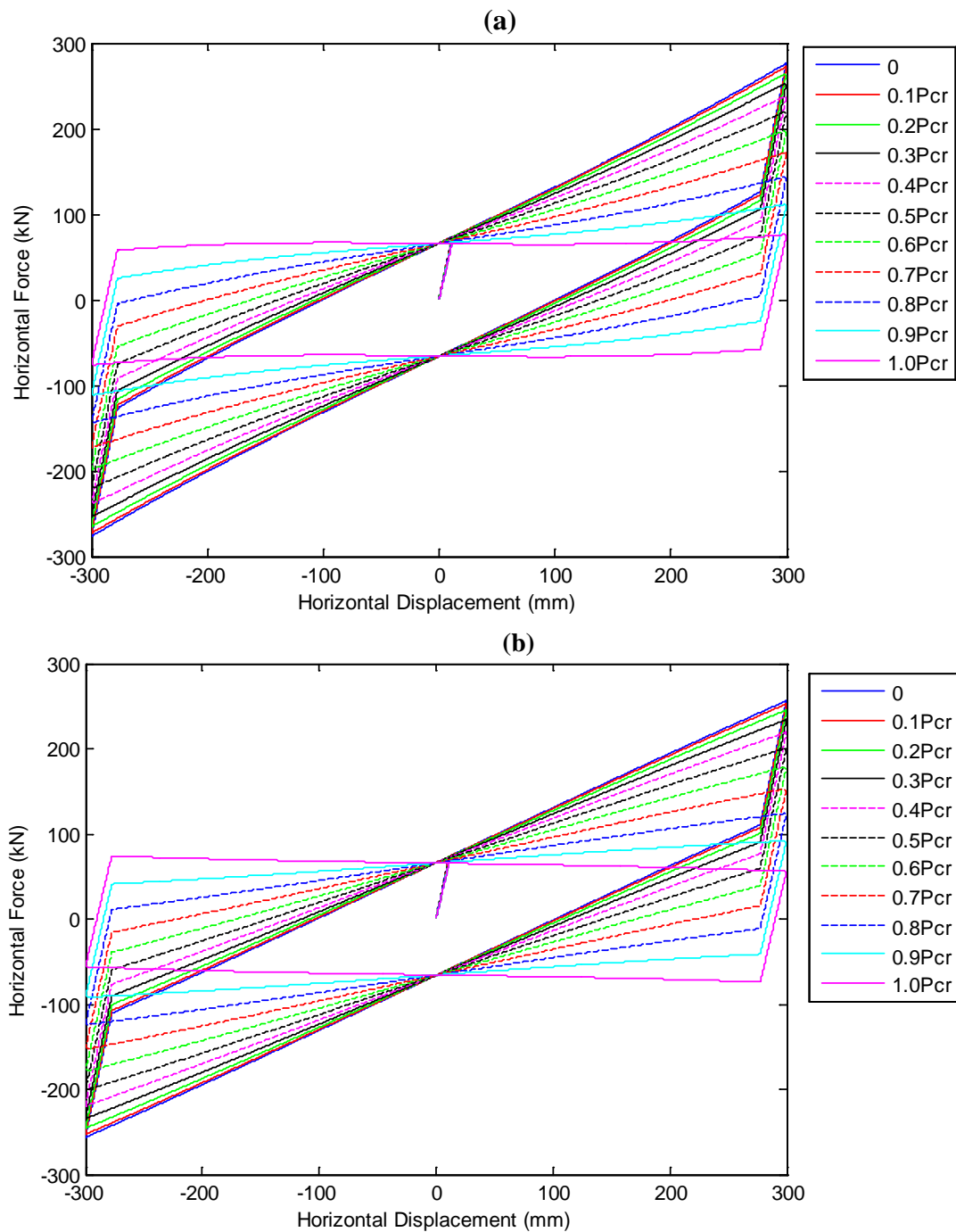
axial load is evident for the MS2 and MS4 bearing models. From Figure 10-17(a) is observed a small nonlinearity in the post-yield stiffness of the MS2 model. The nonlinearity in the post-yield stiffness is significantly reduced in the MS4 model (Figure 10-17(b)).

The decrease in horizontal stiffness is further confirmed when compared with the expected decrease in post-yield horizontal stiffness based on theoretical equations. The theoretical post-yield horizontal stiffness,  $K_H$ , due to an axial load,  $P$ , can be estimated by (Kelly, 1997):

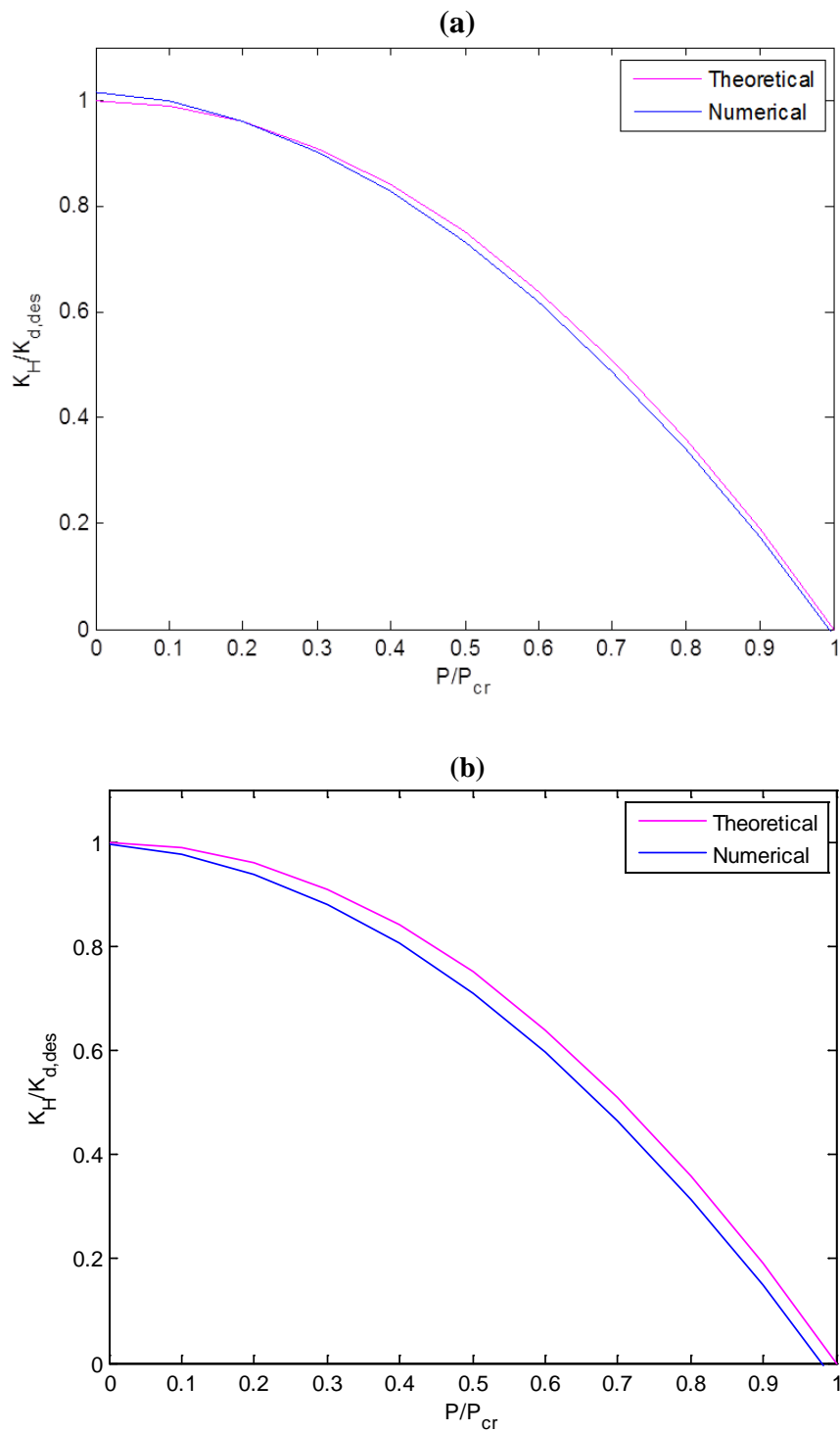
$$K_H = \frac{GA_s}{h} \left[ 1 - \left( \frac{P}{P_{cr}} \right)^2 \right] \quad (10.7)$$

Figure 10-18 shows the change in horizontal stiffness based on theoretical computations (Equation 10.7), and based on the numerical results obtained from the single MS2 model. In this figure, the horizontal stiffness is normalized by the design post-yield stiffness and plotted against the applied load as a ratio of  $P_{cr}$ . The numerical horizontal stiffness was determined as the slope just after yielding occurred, to avoid the observed nonlinearity in the post-yield stiffness of the MS2 model (Figure 10-17(a)). The MS2 and MS4 models predict with reasonable accuracy the decrease in horizontal stiffness when compared to the theoretical (Figure 10-18).





**Figure 10-17: Force-displacement relationship of (a) MS2 and (b) MS4 models with varying axial force as a function of  $P_{cr}$ .**



**Figure 10-18: Theoretical vs numerical influence of the axial load on the horizontal stiffness for the (a) MS2 and (b) MS4 model.**

### 10.3 Validating the MS-LRB in a Simplified Single-Story Model

After the properties of the elements in the single MS2 bearing model were determined and the model was confirmed to predict the general behavior of a lead-rubber bearing, the next step was to implement the single MS2 bearing model in the numerical model of the testbed structure in combination with the CL bearing model to see if the load transfer could be predicted. The dynamic simulations of the numerical model of the testbed structure presented in Chapter 7 - referred to in this chapter as the test specimen (TS) model, required significant time to be processed. Therefore, a simplified version of the TS Model, referred as the simplified single-story (SSS) model, was created for testing and validation of the MS2 model in conjunction with the superstructure and CL bearing models. The OpenSees model of the SSS superstructure with the MS2 isolators is shown in Figure 10-19.

The beams, columns and base frame of the SSS superstructure model were modeled as rigid elements. However, the rigidity of the base frame significantly influenced how the axial loads were distributed amongst the bearings. Thus, the vertical reactions of the isolators were adjusted following the same procedure explained in Section 7.5 so that the static load on the LR bearings of the numerical model matched the experimental static load.

In addition to validating the MS2 bearing model capability to predict the load transfer, another objective of utilizing the SSS model was to see if this simplified model could accurately estimate the LR bearing response compared to the TS model. This information is beneficial for practicing engineers, since a simplified model such as the SSS model can

be used during the initial design stages of a project where a complete numerical model is not yet feasible. The assessment of what bearing model best predicts the experimental response and whether the SSS model gives reasonable prediction of the observed bearing response is presented in Chapter 11, where the responses of the numerical models are compared with the experimental response.

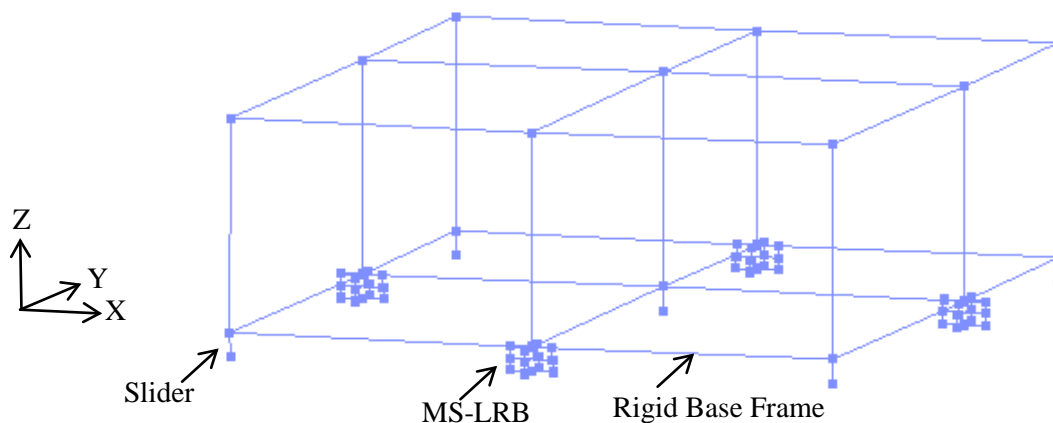


**Figure 10-19: OpenSees model of a simplified single-story structure with MS2 and CL isolators.**

### 10.3.1 Validation of Horizontal Behavior

The force-displacement loop of each LR bearing due to a controlled cyclic displacement history in the y-direction is shown in Figure 10-20. The top and bottom nodes of the center column were displaced horizontally in the y-direction such that the superstructure moved rigidly to represent the first isolation mode. The force in the truss, plastic spring and combined response for the East bearing is shown in Figure 10-20. The force in the truss and plastic spring for the East LR bearing were very similar to those for the North, South and West LR bearings, which resulted in a combined response for all LR bearings to be nearly identical as shown in Figure 10-21. From this figure is noted that the East

and West bearings do not reach the same displacement demands, which is most likely due to torsion in the system. The response of the East bearing modeled by the MS2 Model during the controlled cyclic displacement history in the y-direction when applied to the SSS model (Figure 10-20) is comparable to the response of the MS2 bearing in the single bearing system under similar numerical simulation (Figure 10-10).

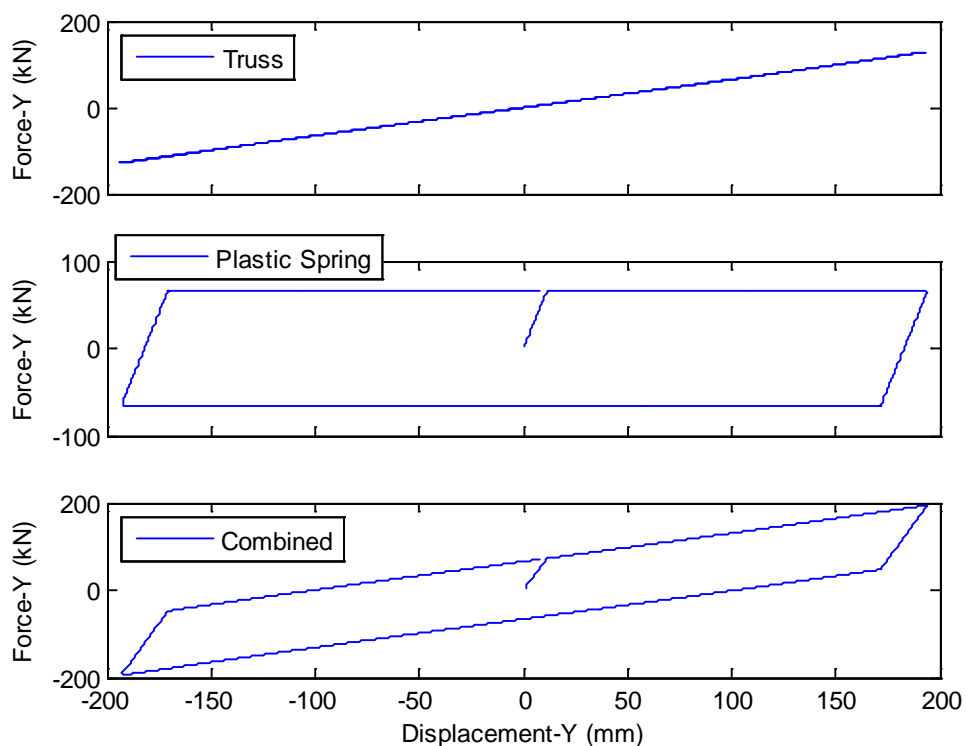


**Figure 10-20: Force-displacement relationship for the truss, plastic spring, and composite in the East bearing due to a controlled cyclic displacement history of the SSS Model in the y-direction.**

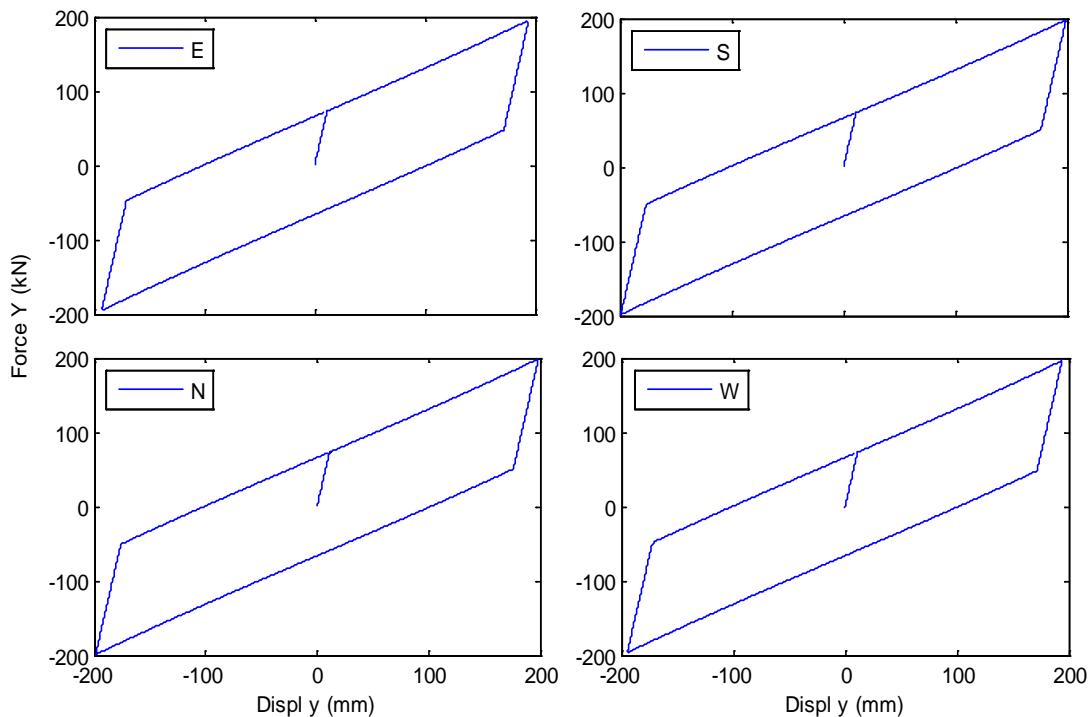


**Figure 10-21: Force-displacement loops for each LR bearing in the SSS model due to a controlled cyclic displacement history in the y-direction.**

### 10.3.2 Validation of Horizontal Behavior

The numerical downward movement of the top of each LR bearing due to a controlled cyclic displacement history on the MS2 model is compared with the theoretical downward movement in Figure 10-22. Response of same system using MS4, not shown for brevity, is nearly identical. In Figure 10-22, the bearings are represented by their location in accordance with Figure 3-5. As mentioned in Section 10.2.2, the vertical displacement of the bearing is sensitive to the stiffness of the rigid shear beam, which was assigned a softer value than desired to achieve convergence in the SSS and TS models. As a result, the numerical model predicts a slightly larger vertical displacement due to the static axial load than the theoretical. Since the static axial load is different on

each LR bearing, the magnitude of the static vertical displacement is also different on each LR bearing as observed in Figure 10-22. Furthermore, when the SSS model is displaced towards the West, the axial force in LRB-W increases, while the axial force in the LRB-E decreases in comparison to the static load, due to overturning in the system. Overturning effects are observed in the vertical movement of the LRB-E and LRB-W, where the East LR bearing develops a larger vertical displacement as the bearings move in the negative horizontal direction, while the West LR bearing develops a larger vertical displacement in the positive horizontal direction. A slight hysteretic loop is developed in LRB-E and LRB-W that is most likely caused by the variation in axial force. Since LRB-S and LRB-N are near the center of the building, these bearings are unaffected by overturning and do not develop a hysteresis loop as seen in the other two LR bearings (Figure 10-22). Moreover, LRB-S and LRB-N developed a peak vertical displacement in the negative horizontal direction that is similar to the peak vertical displacement in the positive horizontal direction.

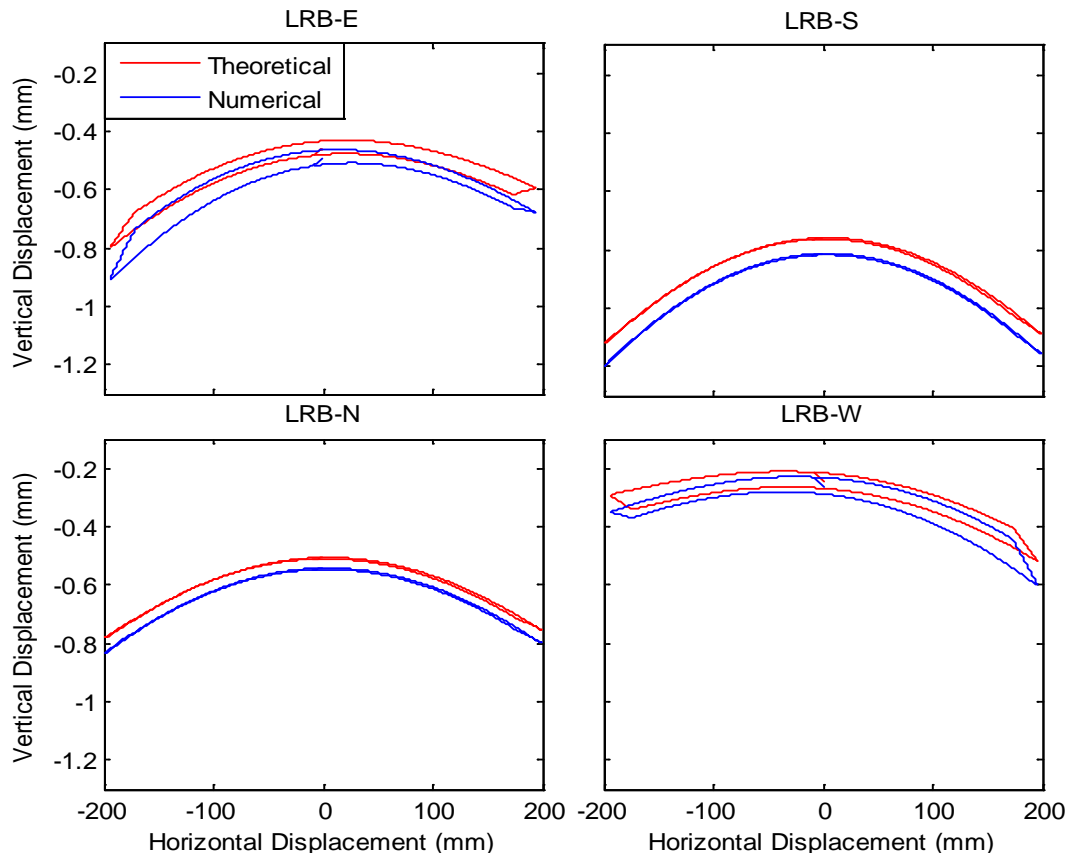


**Figure 10-22: Theoretical vs numerical vertical bearing displacement due to a controlled cyclic displacement history.**

The displacement and axial force history of each LR bearing when the SSS model is subjected to a cycle of horizontal displacement in the y-direction is shown in Figure 10-23. The horizontal displacement is similar for all LR bearings as shown in Figures 10-23 (a), (c), (e) and (g). The influence of overturning and load transfer effects on the axial force of individual bearings can be observed. Figures 10-23(d) and 10-23(f) show that the axial forces on the LRB-N and LRB-S decrease as the horizontal displacement of the bearings increases in either the positive or negative direction. The decrease in axial force on these bearings is caused by the load transfer effect, that is, the axial force is transferred from the LR bearings to the CL bearings with increase in horizontal displacement. Then,



as the bearings move back to the recentered or undeformed configuration, the original axial load is restored. Since LRB-N and LRB-S are located near the building centerline for loading in the y-direction, overturning effects are negligible and cannot be observed in the axial load response.

Overturning effects dominate the axial force histories of LRB-E and LRB-W. Overturning is observed as an increase in axial force for LRB-E (Figure 10-23(b)) and a decrease in axial force for LRB-W (Figure 10-23(h)) as the bearings develop a negative horizontal displacement (or moves toward East). Furthermore, as the bearings develop a positive horizontal displacement (or moves toward West), the axial force on the LRB-W increases while the axial force on LRB-E decreases. Although not as visually obvious, the load transfer effect is also present in the vertical response of LRB-E (Figure 10-23(b)). The axial force on LRB-E, at a static displacement, starts around 465 kN, then increases to only 500 kN at the peak positive horizontal displacement, because the increase in axial force due to overturning is partially offset by the load transfer effects. However, at the peak negative horizontal displacement, the axial force on LRB-E unloads by a much larger amount to about 350 kN, which results from a positive combination of overturning and the load transfer effect. Similar observation can be made for the LRB-W; that is, the axial load on LRB-W (Figure 10-23(h)) is influenced by overturning and load transfer effects. As further evidence of the horizontal-vertical interaction provided by the MS2 bearing mechanics, a sudden shift in axial force around peak horizontal displacements is observed for LRB-E and LRB-W (Figures 10-23(b) and 10-23(h)). During a displacement reversal, the horizontal stiffness of the bearing suddenly increases

from  $K_d$  to  $K_I$ , as seen in the horizontal force-displacement loop of the bearing (Figure 10-7(c)), which causes the sudden shift in the axial force.

The total (sum over all LR bearings) axial force in the LR bearings as the bearings are displaced horizontally is shown in Figure 10-24. This figure shows a net reduction in axial force of nearly 150 kN in the LR bearings as the horizontal displacement increases that is solely caused by load transfer effects, since overturning effects do not affect the total axial force. Furthermore, Figure 10-24 shows that the LR bearings regained axial force as the bearings recenter. Therefore, the MS2 model predicts load transfer effects, which is confirmed by the increase and decrease in total axial force on the LR bearings with change in horizontal displacement (Figure 10-24).

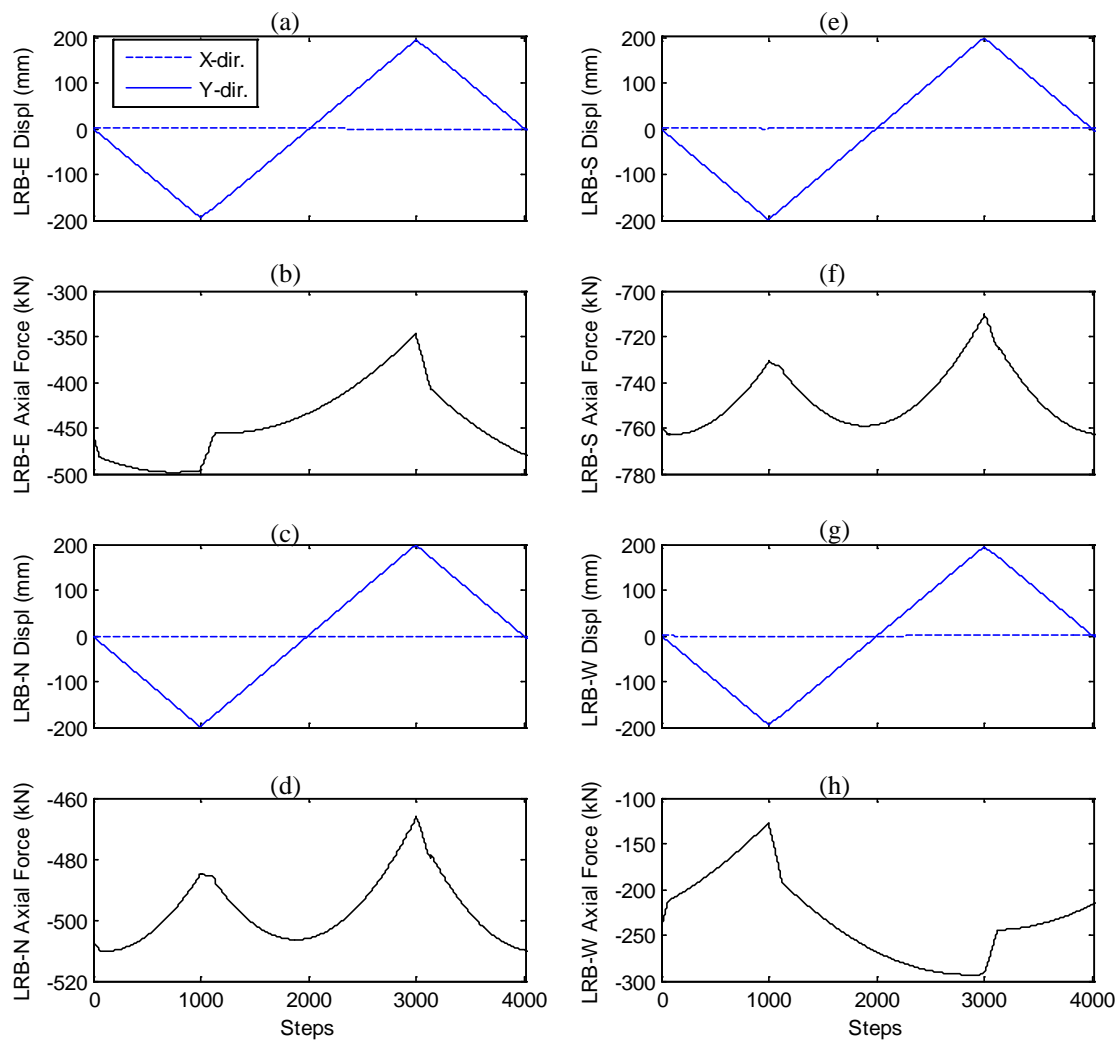


**Figure 10-23: Displacement and vertical force history of each LR bearing due to a horizontal displacement in the y-direction of the SSS model.**

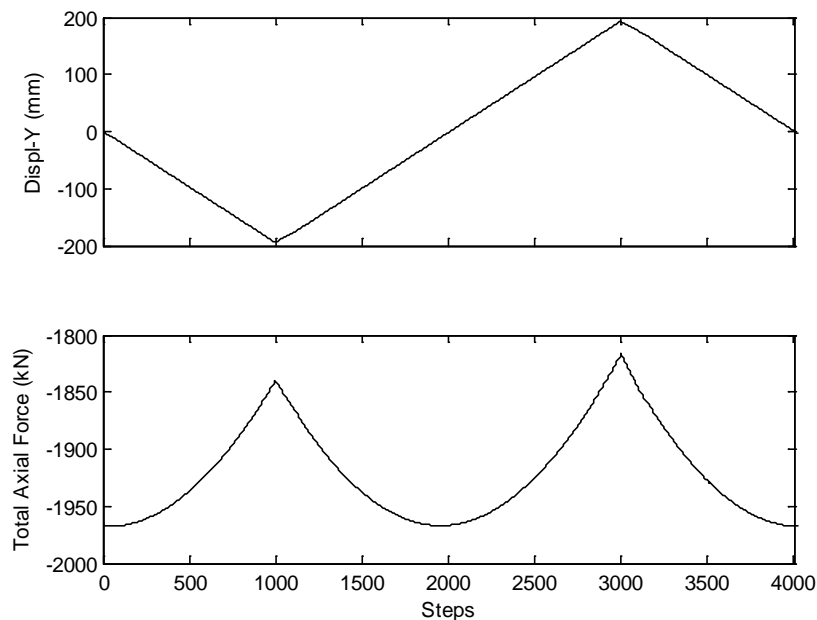


**Figure 10-24: Load transfer in the SSS model due to a horizontal displacement.**

## 10.4 Summary of Observations

In summary, a multi-spring MS-LRB model that can account for horizontal and vertical interaction was developed and validated in this chapter. The validation was focused on the MS2 model, as opposed to the MS4 model, to demonstrate the reliability of this simplest MS-LRB model. The single MS2 model was shown, in general, to accurately predict the response of the LR bearing in the vertical and horizontal directions when compared with the theoretical responses. The accuracy in LR bearing response was obtained despite the adjustments made to the rigidity of some of the model elements in order to achieve convergence when the MS2 model is combined with the TS model. Furthermore, the MS2 model produces an artificial nonlinearity in the horizontal force-displacement for bidirectional loading that can be mediated by adding more truss

elements across the shear layer (MS4). The MS2 model is able to predict some load transfer between LR bearings and CL bearings (Figure 10-24) in the SSS model. Therefore, overall, the MS2 bearing has potential, relative to the numerical model presented in Section 8.1, to predict the load-transfer behavior of the hybrid isolation system observed in the experiment. The ability of the MS-LRB model to reproduce the load transfer effect is the subject of the next chapter.

## CHAPTER 11: COMPARISON OF EXPERIMENTAL AND THREE NUMERICAL LR BEARINGS RESPONSES

In this chapter, the numerically computed responses using the LR bearing model described in Chapter 8, hereon referred to as the “uncoupled” bearing model, and the two configurations of the multiple spring bearing models described in Chapter 10, named MS2 and MS4, are compared with the experimentally observed responses.

The design bearing properties were assumed in the horizontal direction for all three bearing models. The design bearing properties were used, rather than the characterized bearing properties (Section 8.4), because generally these are the properties considered by registered design professionals. Moreover, the comparison between the experimental and numerical LR bearing responses for the uncoupled bearing model with characterized bearing parameters was presented in Section 8.5.

An elastic-perfectly plastic force-displacement relationship in the vertical direction (Figure 11-1(a)) was considered here for the three bearing models as opposed to the elastic (Figure 11-1(b)) and bilinear (Figure 11-1(c)) relationships used in Chapters 10 and 8, respectively. In Figure 11-1(a), the yield force,  $F_y$ , was equal to three times the initial shear modulus times the LR bearing cross sectional area ( $F_y = 476$  kN), and the bearing vertical stiffness equaled the reduced vertical stiffness,  $K_{vr} = 1,000$  kN/mm. The reduced vertical stiffness was used to account for the flexibility of the load cells (Section 8.1.2). The elastic-perfectly plastic relationship was considered to account more explicitly for the nonlinearity that occurs when the LR bearing goes into tension (Han et

al., 2014), while retaining a level of practicality. Furthermore, the bilinear vertical force-displacement relationship considered in Chapter 8 (Figure 11-1(c)) was not successfully applied to the MS2 and MS4 bearing models due to convergence issues.

For the MS2 and MS4 bearing models, all other parameters and material properties were the same as the ones specified in Sections 10.2 and 10.3, except the distribution of stiffness among the vertical spring elements. For the responses reported in this chapter, the stiffnesses assigned to each center and edge vertical spring of the single MS2 model were  $1.5K_{vr}$  and  $0.125K_{vr}$ , respectively, as opposed to  $1.2K_{vr}$  and  $0.2K_{vr}$  (Section 10.2.2). For the MS4 bearing model, since it has double the number of vertical springs, the stiffnesses of the edge vertical springs were equal to half of those for the MS2 bearing model (i.e.  $0.0625K_{vr}$ ), while the stiffnesses for the center vertical springs were unchanged from the MS2 bearing model (i.e.  $1.2K_{vr}$ ). Recalling that the top and bottom layers of vertical springs in the MS2 and MS4 bearing models act in series, the composite stiffness of each layer was defined to be twice the total desired vertical stiffness. These modifications were considered in order to achieve a better match between the numerical and experimental LR bearing responses, particularly the observed load transfer.

Sections 11.1.1 to 11.1.4 show the comparison between experimental and numerical LR bearing responses for the uncoupled, single MS2, and MS4 bearing models in combination with the CL bearing model (Section 8.2) and the test specimen model (Chapter 7). The influence of the reduced vertical spring stiffness distribution on the load transfer effect is presented in Section 11.1.5. The structural response produced by the three bearing models is compared with the experimental in Section 11.1.6. The

limitations and alternative construction of the MS2 and MS4 bearing models are presented in Section 11.2. A summary of observations is presented in Section 11.3.

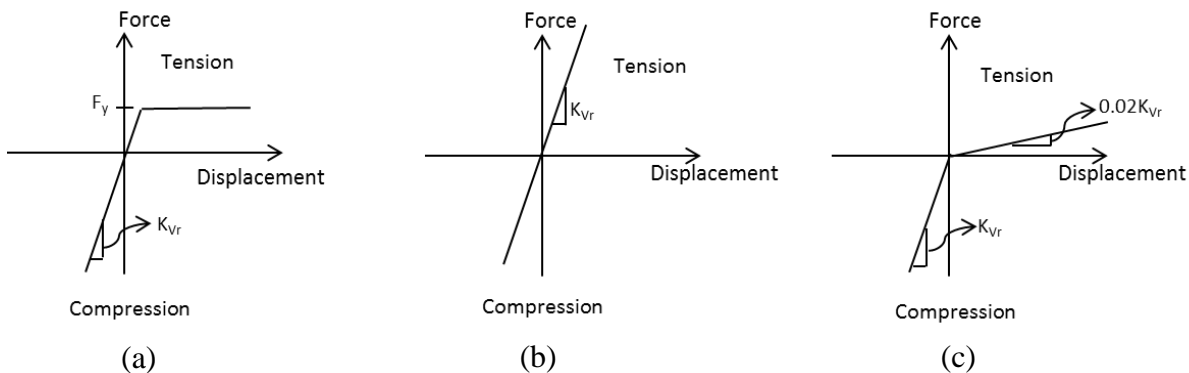


**Figure 11-1: (a) Elastic-perfectly plastic, (b) elastic, (c) bilinear force-displacement relationship in the vertical direction.**

### 11.1 Test Specimen Model Combined with Three LR Bearing Models

The LR bearing responses obtained from the three numerical bearing models is compared with the experimentally observed responses for Sine 100% (Y), Diablo 95% (XY), Vogtle 100%, and Rinaldi 88% (XY) in Sections 11.1.1 – 11.1.4. These excitations were selected to analyze the general behavior of the LR bearing both in the horizontal and vertical direction. The responses of the LR bearing presented here are: displacement history in x- and y-directions, displacement trace, horizontal force history (both in x- and y-directions), vertical force history, and force-displacement loops in x- and y-directions.

#### 11.1.1 Sine 100% (Y) - 1

The displacement history for the three numerical bearing models (uncoupled, MS2, and MS4) are compared with the experimental displacement histories in Figure 11-2 for Sine 100% (Y)-1. This figure shows that the three bearing models are able to predict the



experimental displacement history in y-direction for all bearings with similar accuracy. The magnitude of the peak displacement of the numerical simulation is very close in value to the experimental peak displacement as shown in Figure 11-3. Likewise, all three bearing models produce similar force history in x- and y-directions that in general closely match the experimental force history for all LR bearings (Figure 11-4). However, the experimental peak vector force is underestimated by all of the numerical models as shown in the comparison of the force-displacement loop in the y-direction (Figure 11-5). The force-displacement loop in the x-direction is not presented here, since Sine 100% (Y) was a unidirectional excitation in the y-direction.

The vertical force histories on each LR bearing and the total (summed over all LR bearings) are shown in Figure 11-6. This figure shows that the MS2 and MS4 bearing models predict the experimental vertical force and load transfer effect, represented by the peak reduction in total vertical force, quite well. On the contrary, the uncoupled bearing model does not predict the load transfer effect. The ability for the MS2 and MS4 bearing models to predict the load transfer is strongly related to the ability of the numerical model to predict the bearing displacement. A closer look at the displacement history for MS2 and MS4 models shows that the cycles where the bearing displacement is overestimated (around 8, 12 and 15 seconds in Figure 11-2), resulted in the change in total vertical force also to be overestimated (around 8, 12 and 15 seconds in Figure 11-6). Likewise, during the cycles where the displacement is underestimated, the change in total vertical force is also underestimated.

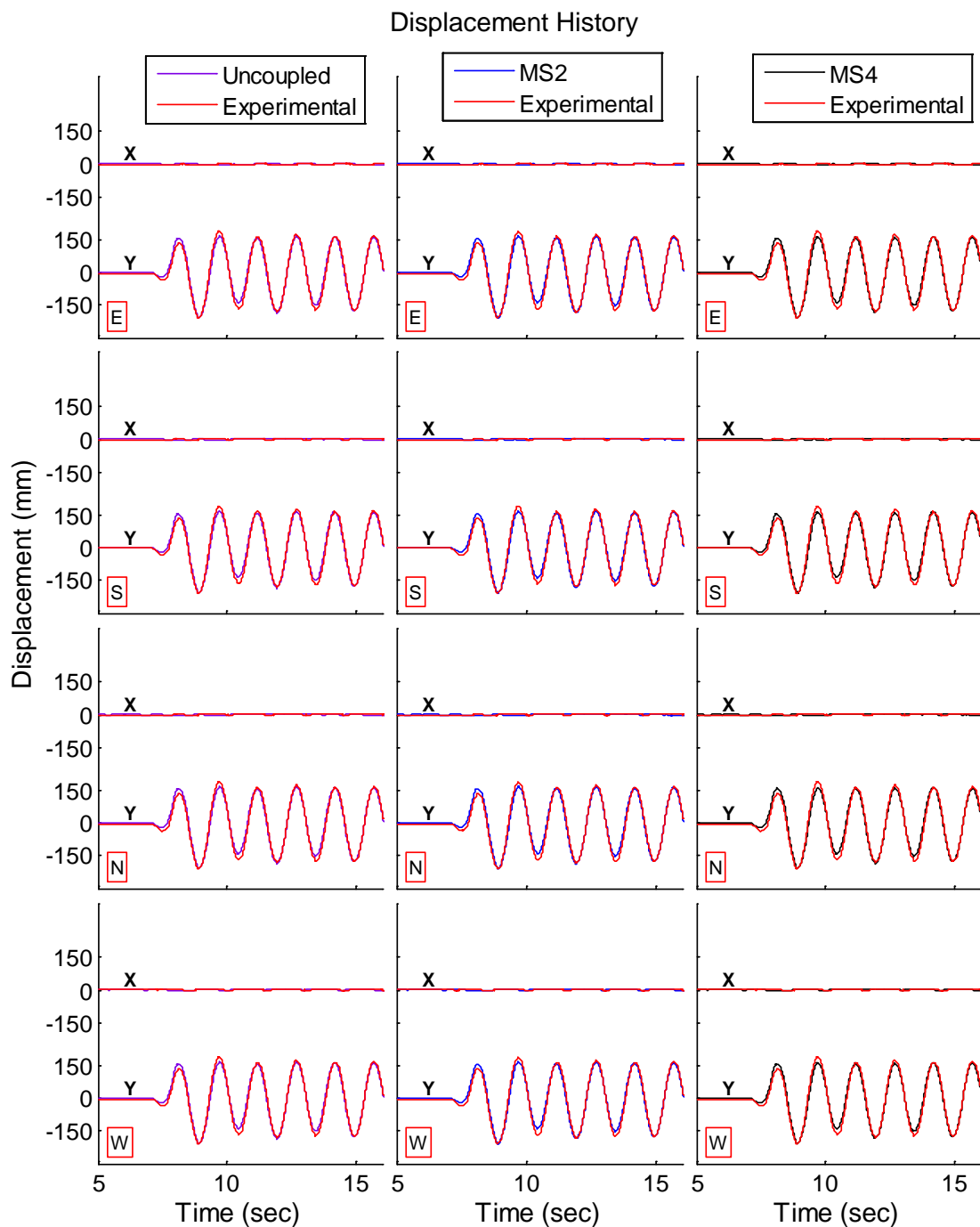


**Figure 11-2: Comparison of experimental and numerical simulation for Sine 100%; displacement history in each LR bearing, labeled by position (E, S, N, W). Numerical simulation of uncoupled, MS2, and MS4 LR bearing models.**

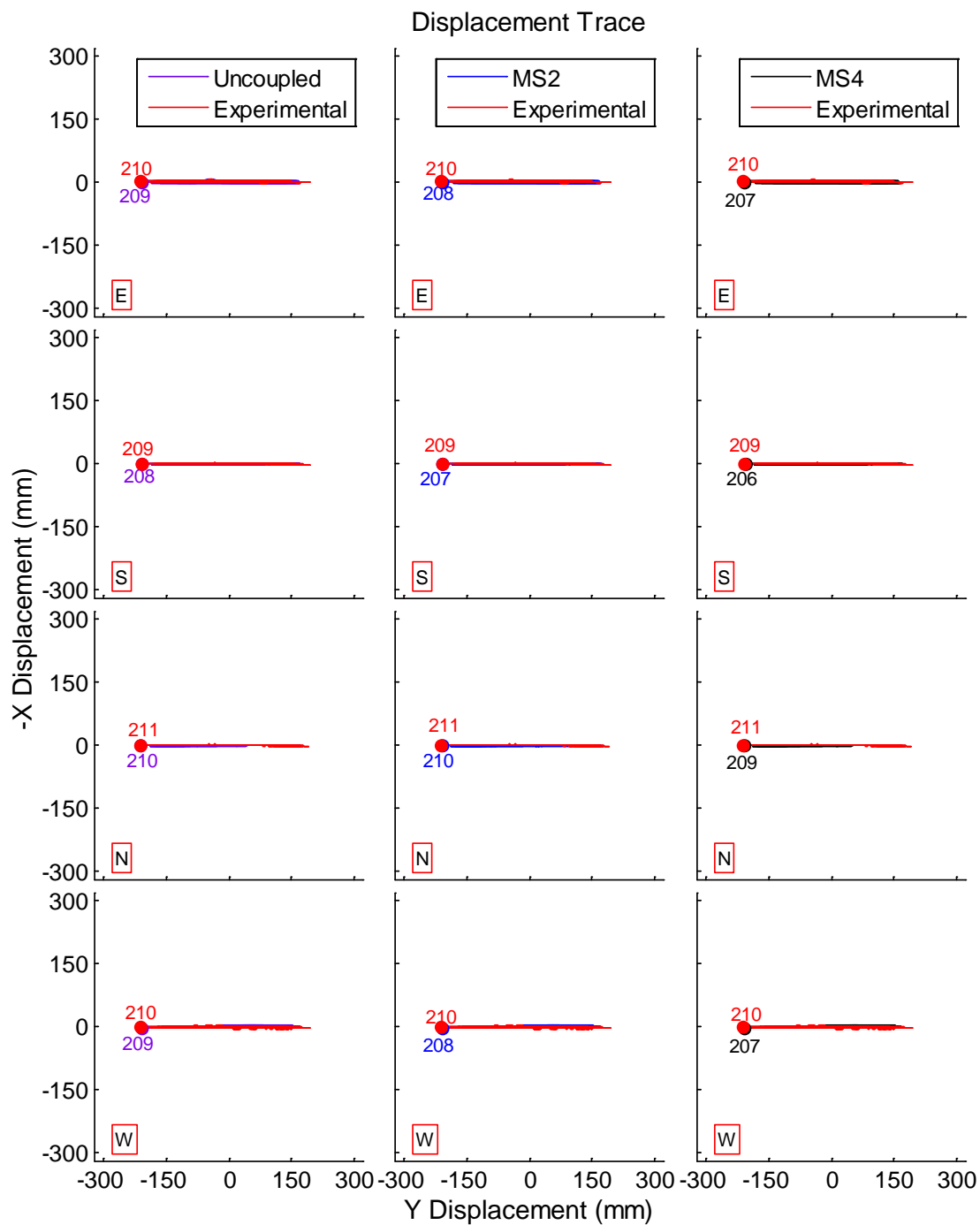


**Figure 11-3: Comparison of experimental and numerical simulation for Sine 100%; displacement trace in each LR bearing, labeled by position (E, S, N, W). Numerical simulation of uncoupled, MS2, and MS4 LR bearing models.**

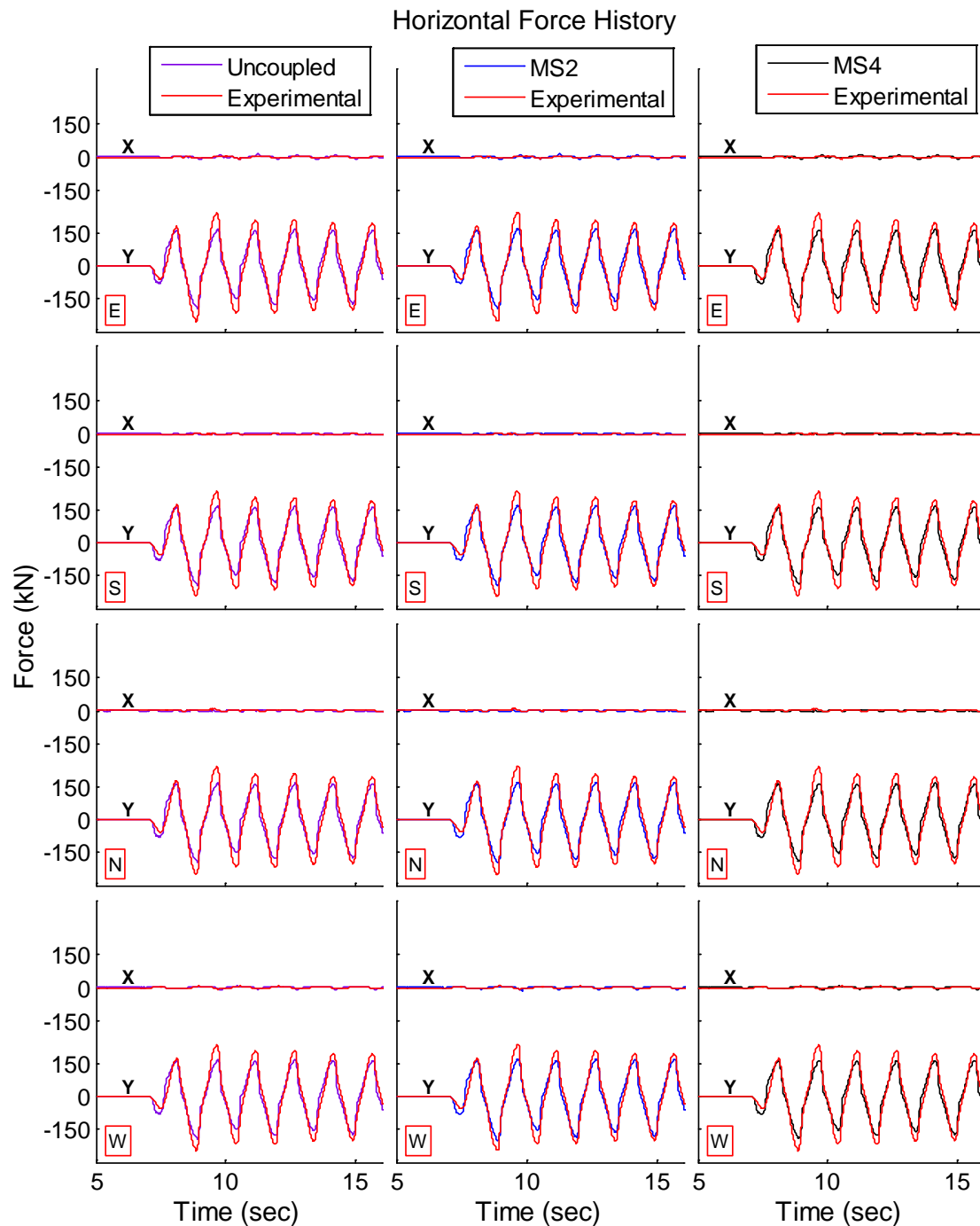


**Figure 11-4: Comparison of experimental and numerical simulation for Sine 100%; horizontal force history (x and y) in each LR bearing, labeled by position (E, S, N, W). Numerical simulation of uncoupled, MS2, and MS4 LR bearing models.**

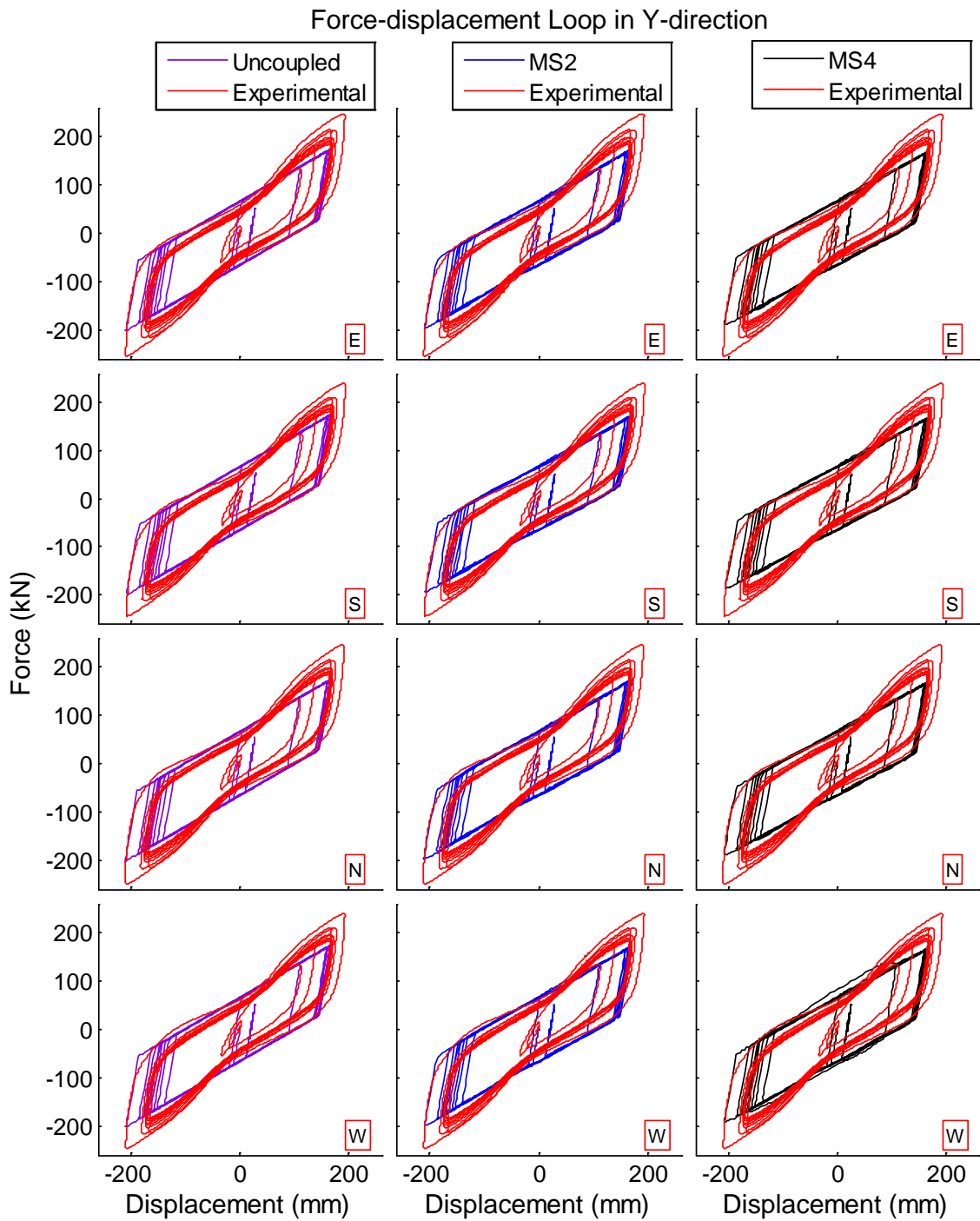


**Figure 11-5: Comparison of experimental and numerical simulation for Sine 100%; force-displacement loop in y-direction in each LR bearing, labeled by position (E, S, N, W). Numerical simulation of uncoupled, MS2, and MS4 LR bearing models.**

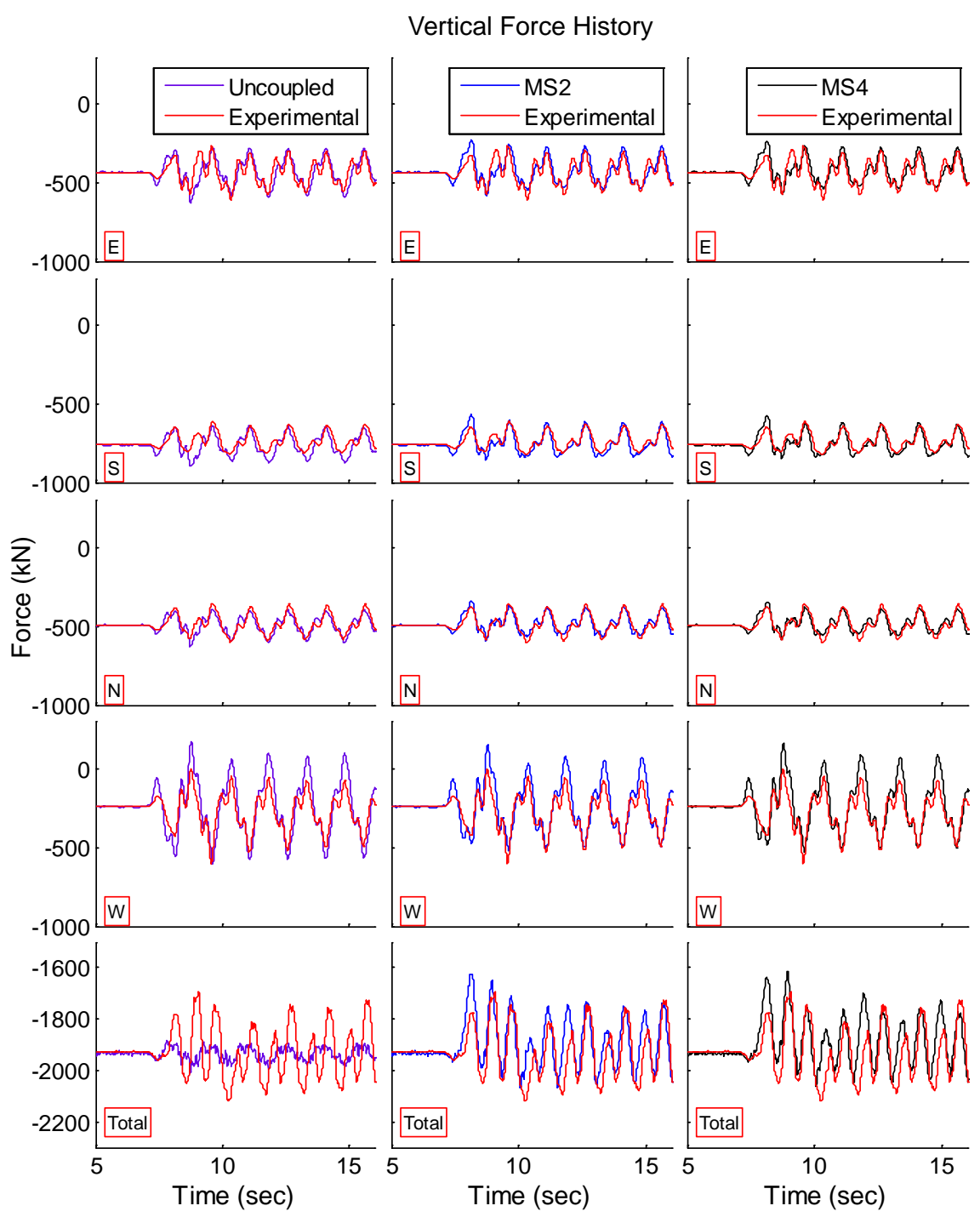


**Figure 11-6: Comparison of experimental and numerical simulation for Sine 100%; vertical force history in each LR bearing, labeled by position (E, S, N, W). Numerical simulation of uncoupled, MS2, and MS4 LR bearing models.**

### 11.1.2 Diablo 95% (XY)

The displacement histories and displacement traces for Diablo 95% (XY) for the three numerical bearing models (uncoupled, MS2, and MS4) are compared with the experimental response in Figures 11-7 and 11-8, respectively. These figures show that the three bearing models are able to predict the experimental displacement for all bearings quite well. In general, the MS2 and MS4 bearing models produced displacements that are slightly closer to the experimental displacements for all LR bearings when compared to the uncoupled bearing model (Figures 11-7 and 11-8). All three bearing models underestimate the experimental peak displacement in any LR bearing (Figure 11-8). The three bearing models produced similar force history in x- and y-directions that closely matched the experimental force history for all LR bearings, yet the numerical models underestimate the peak horizontal force in the x- or y-directions for all bearings (Figures 11-9 to 11-11). The MS4 bearing model produced in general better force-displacement loops, when compared to the uncoupled and MS2 models, in particular near the peak displacement in the positive direction (Figures 11-10 and 11-11).

The vertical force histories on each LR bearing and the total (summed over all LR bearings) are shown in Figure 11-12. This figure shows that the three models are unable to closely match the experimental vertical force for all LR bearings. The uncoupled bearing model is worst in predicting the vertical force in the LR bearings when compared to MS2 and MS4 models, because it is unable to predict the load transfer that occurred between the LR and CL bearings as observed in the total vertical force plot in Figure 11-12. The load transfer effect is visually seen in Figure 11-12 as a peak decrease in the

experimental total vertical force between 15 and 21 seconds. A closer look at the displacement history produced by the MS2 and MS4 bearing models show that displacement is underestimated every time there is a peak reduction in total vertical force (Figure 11-12), which resulted in the load transfer to be underestimated. Furthermore, the numerical models did not predict the experimentally observed tension in the LR bearings, which was primarily caused by the load transfer effect.



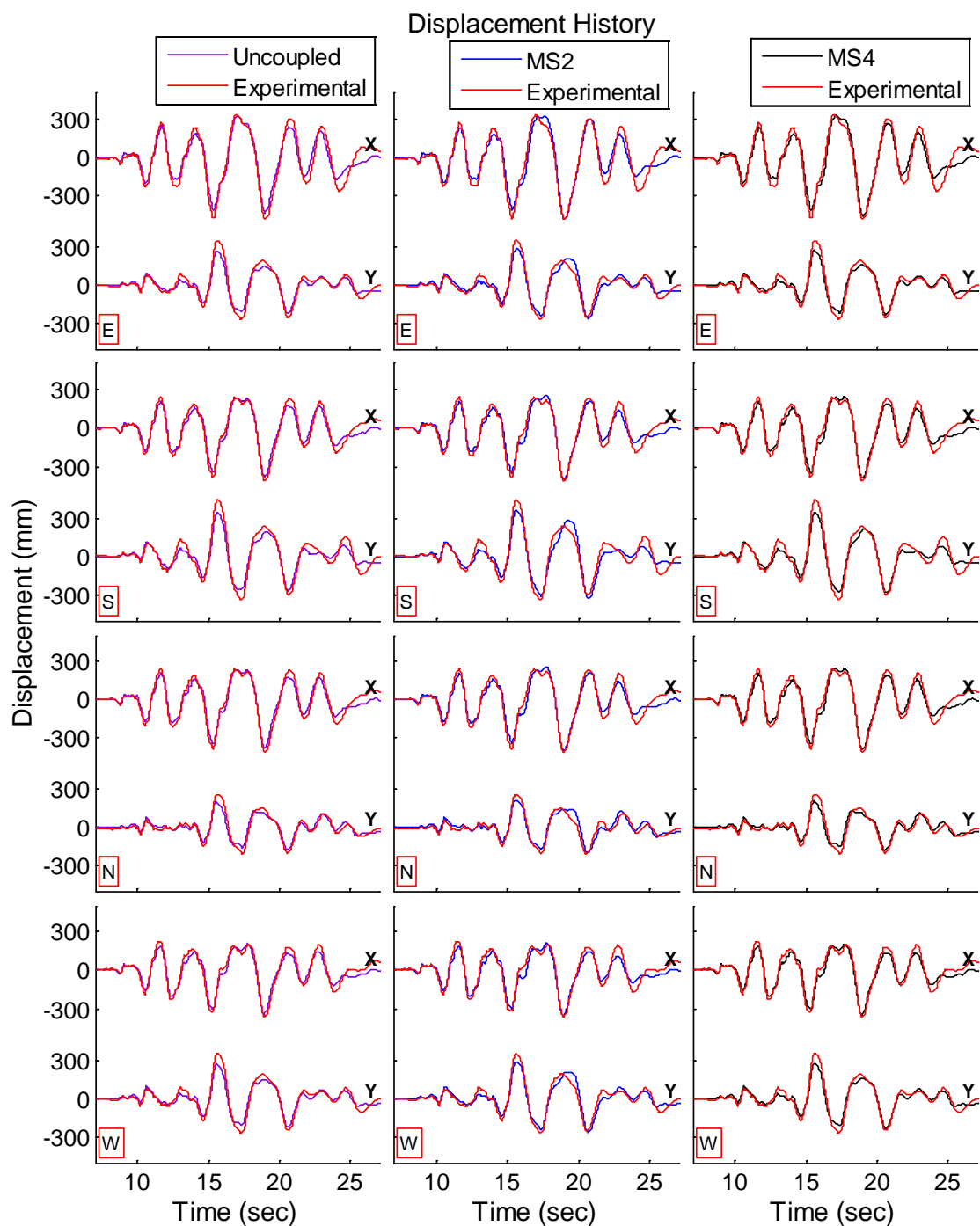


**Figure 11-7: Comparison of experimental and numerical simulation for Diablo 95% (XY); displacement history in each LR bearing, labeled by position (E, S, N, W). Numerical simulation of uncoupled, MS2, and MS4 LR bearing models.**

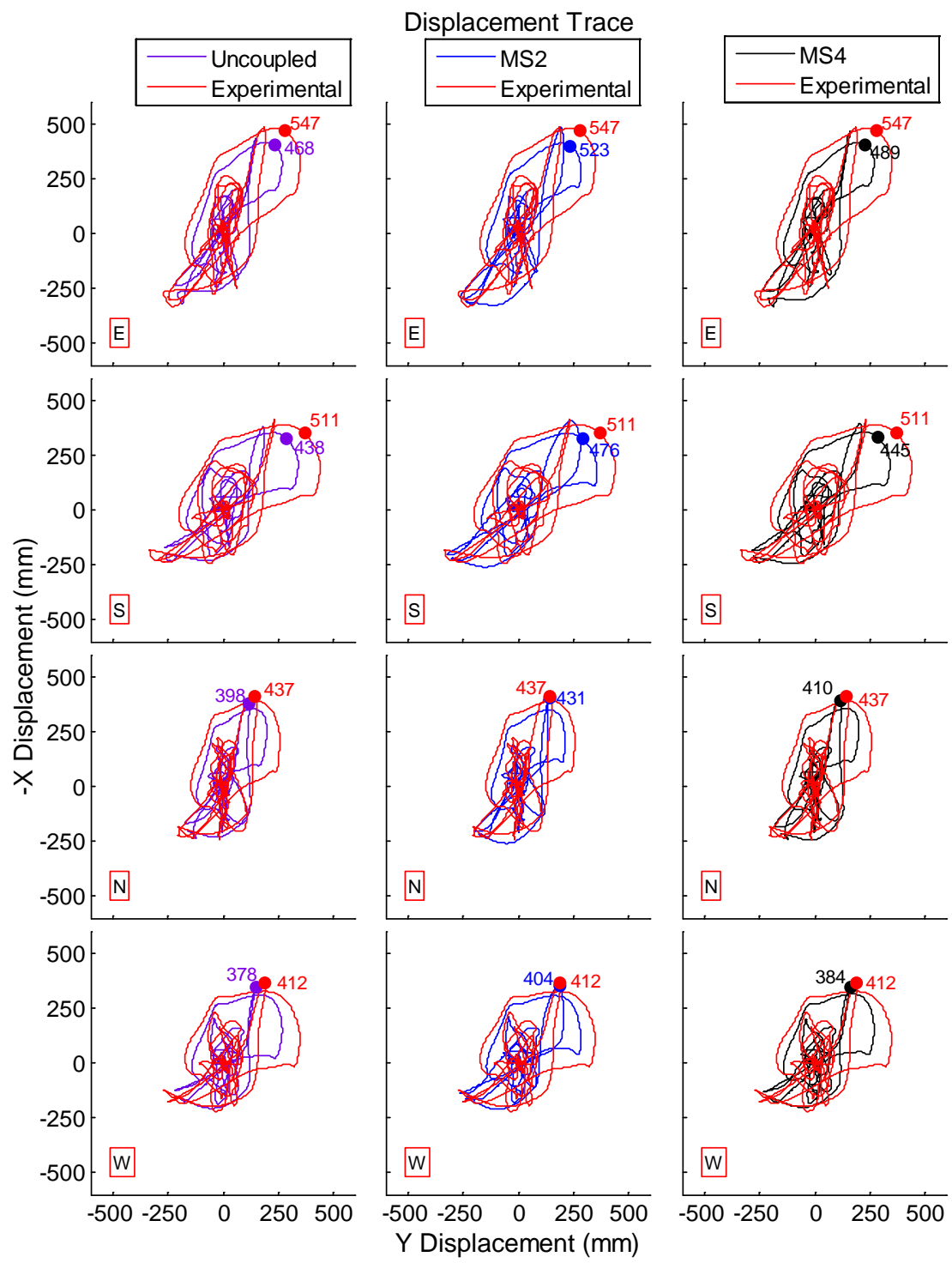


**Figure 11-8: Comparison of experimental and numerical simulation for Diablo 95% (XY); displacement trace in each LR bearing, labeled by position (E, S, N, W). Numerical simulation of uncoupled, MS2, and MS4 LR bearing models.**

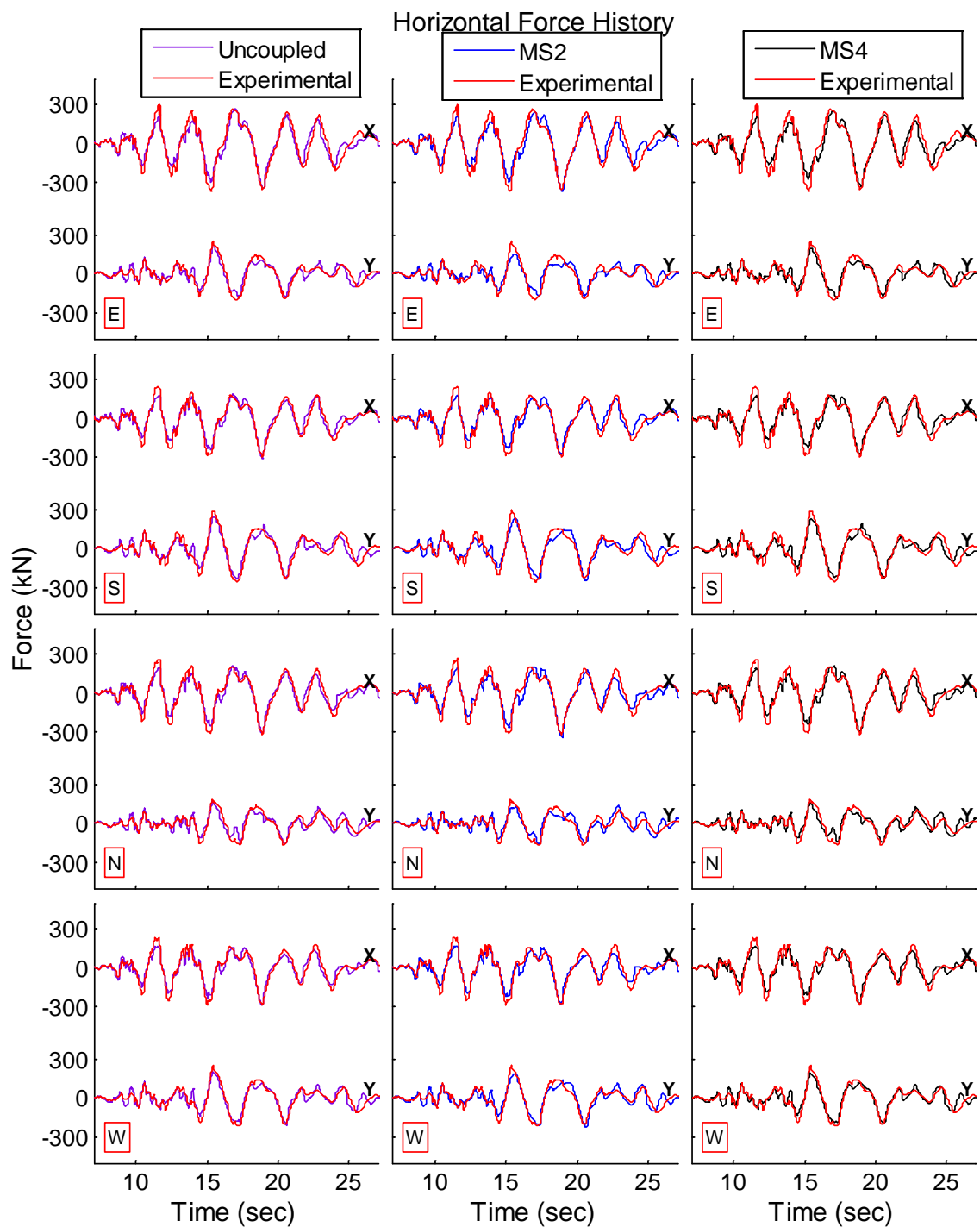


**Figure 11-9: Comparison of experimental and numerical simulation for Diablo 95% (XY); horizontal force history (x and y) in each LR bearing, labeled by position (E, S, N, W). Numerical simulation of uncoupled, MS2, and MS4 LR bearing models.**

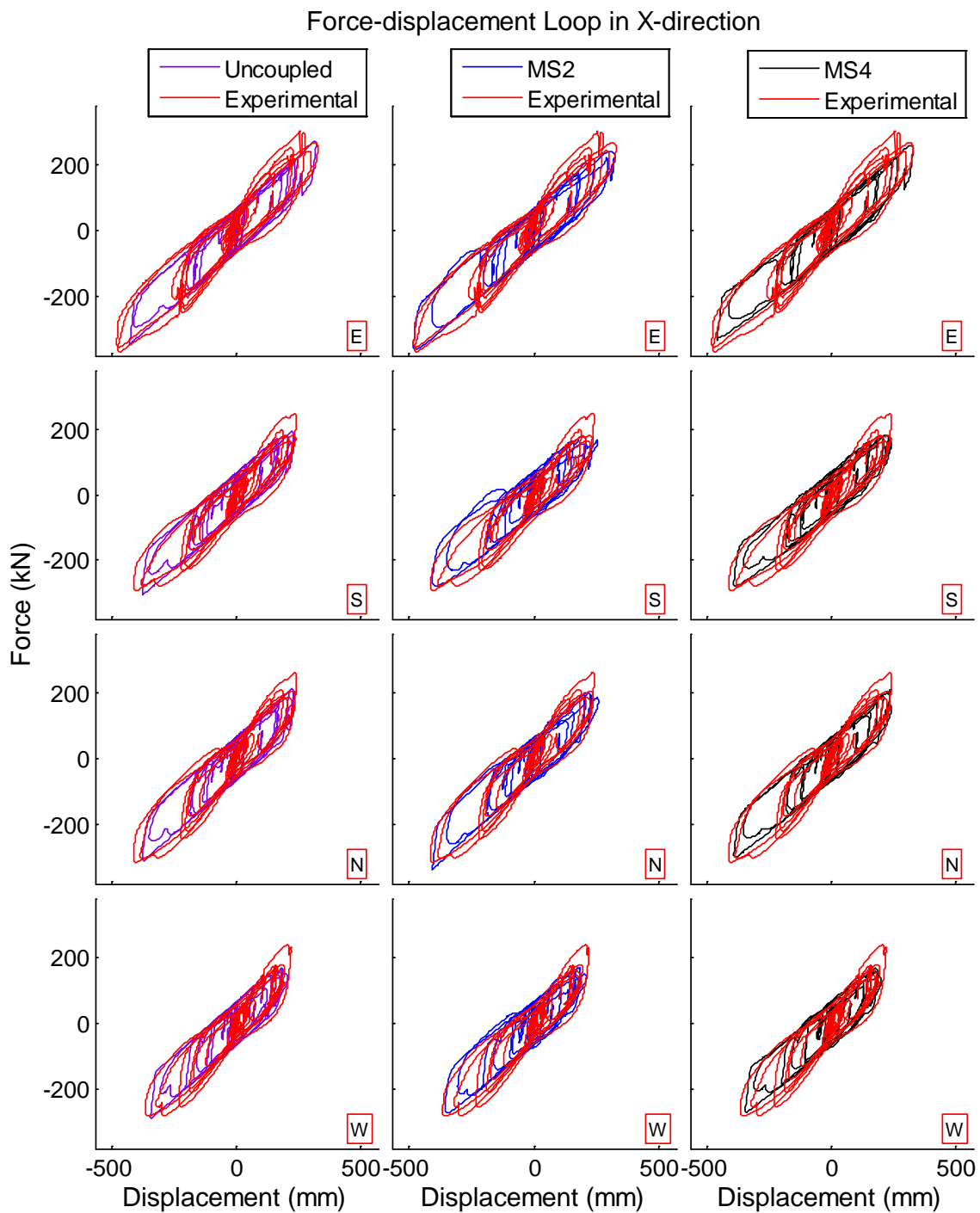


**Figure 11-10: Comparison of experimental and numerical simulation for Diablo 95% (XY); force-displacement loop in x-direction in each LR bearing, labeled by position (E, S, N, W). Numerical simulation of uncoupled, MS2, and MS4 LR bearing models.**

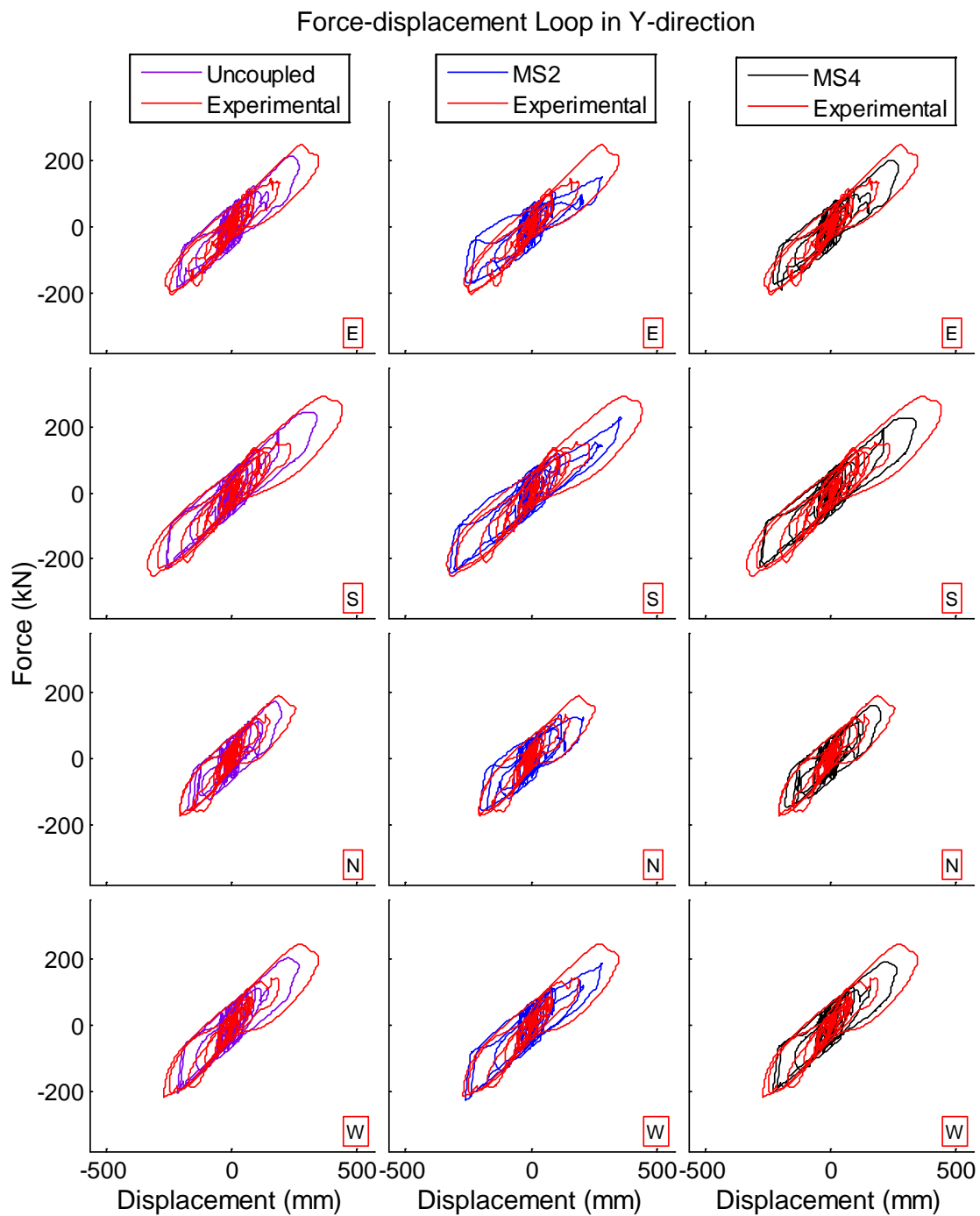


**Figure 11-11: Comparison of experimental and numerical simulation for Diablo 95% (XY); force-displacement loop in y-direction in each LR bearing, labeled by position (E, S, N, W). Numerical simulation of uncoupled, MS2, and MS4 LR bearing models.**

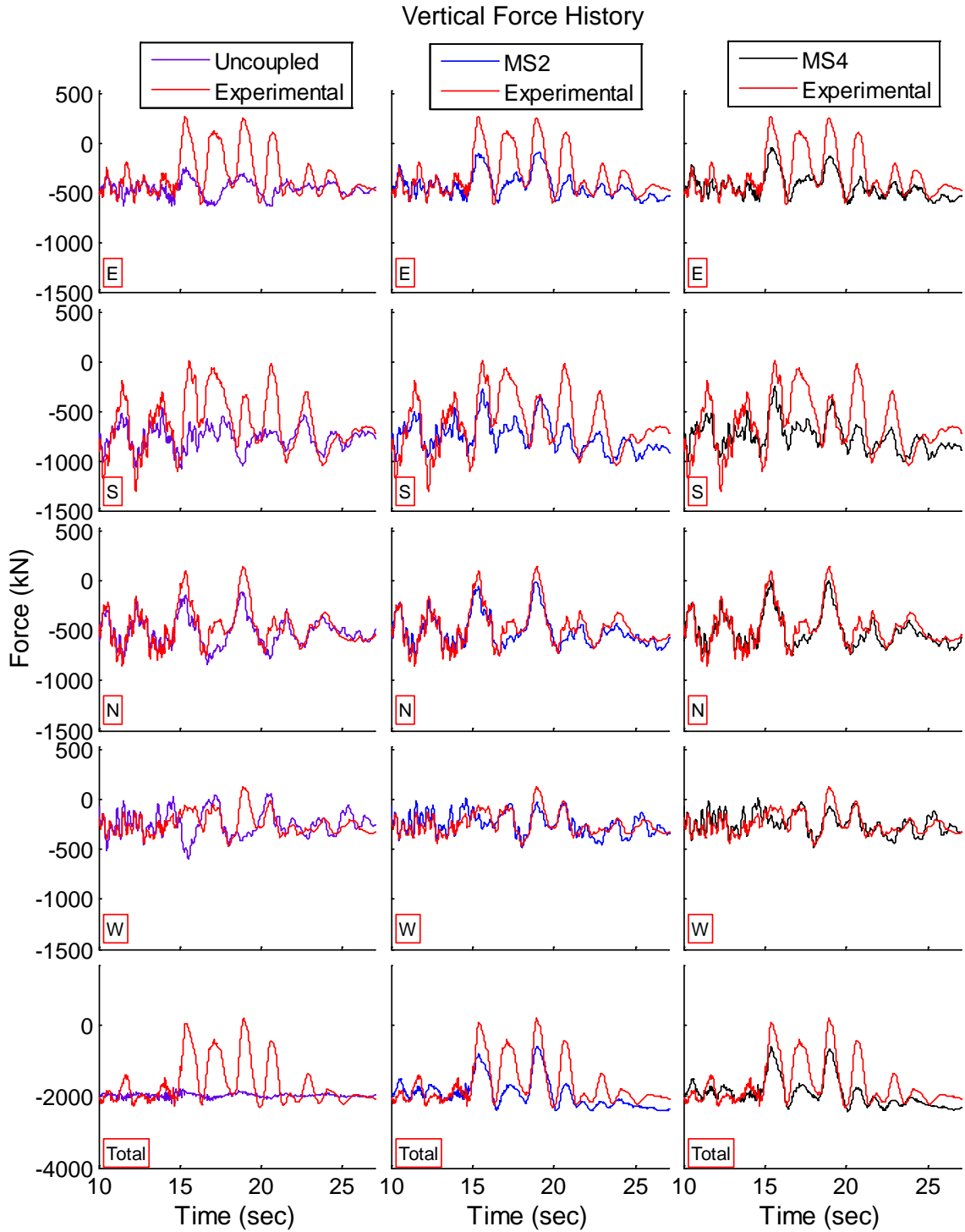


**Figure 11-12: Comparison of experimental and numerical simulation for Diablo 95% (XY); vertical force history in each LR bearing, labeled by position (E, S, N, W). Numerical simulation of uncoupled, MS2, and MS4 LR bearing models.**

### 11.1.3 Vogtle 100%

The displacement history in x- and y-directions produced by the MS2 and MS4 bearing models closely match the experimental displacement histories and are similar to the displacement histories produced by the uncoupled bearing model for Vogtle 100% (Figure 11-13). The numerical models did not predict the cycle where the largest peak displacement occurs, thus, the experimental peak displacement was underestimated by all of the numerical models (Figure 11-14). The three bearing models produced similar force history in x- and y-directions that in general closely matches the experimental force history for all LR bearings (Figure 11-15). For Vogtle 100%, the force-displacement relationship of the LR bearings produced by the three numerical models were similar (Figure 11-16 and Figure 11-17).

The vertical force histories on each LR bearing and the total (summed over all LR bearings) are shown in Figure 11-18. To eliminate the force variation due to vertical excitation and verify the load transfer effect for a 3D excitation, a low-pass Butterworth filter with a cutoff frequency of 2 Hz was applied to the vertical force in each LR bearing as well as the total vertical force as shown in Figure 11-19. As mentioned in Section 6.2, this filter has the same shape as that shown in Figure 4-5 when normalized with respect to the cutoff frequency. The 2Hz cutoff frequency was selected since it preserves the frequencies related to horizontal vibration of the isolation system but eliminates typical frequency of vertical excitation and response. A close match of the total vertical force is obtained between the experimental and the MS4 bearing model (Figure 11-19) when compared to the MS2 and uncoupled models. The two significant instances of reduction

in vertical force (around 10 and 12 seconds) due to load transfer effects are predicted by the MS2 and MS4 bearing models, while the uncoupled bearing model does not capture the load transfer effect at all (total force plot in Figure 11-19). As mentioned before, the ability for the numerical model to predict the load transfer is closely related to the prediction of the bearing displacement. The MS2 and MS4 bearing models in general accurately predict the displacement around 10 seconds (Figure 11-13); therefore, the peak reduction in the total vertical force around 10 seconds is well predicted by these models. On the contrary, the displacement around 12 seconds is underestimated by the MS2 and MS4 models (Figure 11-13), therefore, the peak reduction in total vertical force around 12 seconds is also underestimated for these models (Figure 11-19). Furthermore, the total reduction in experimental vertical force around 14 seconds is significantly underestimated by the MS2 and MS4 models because the numerical displacements are significantly underestimated around 14 seconds.



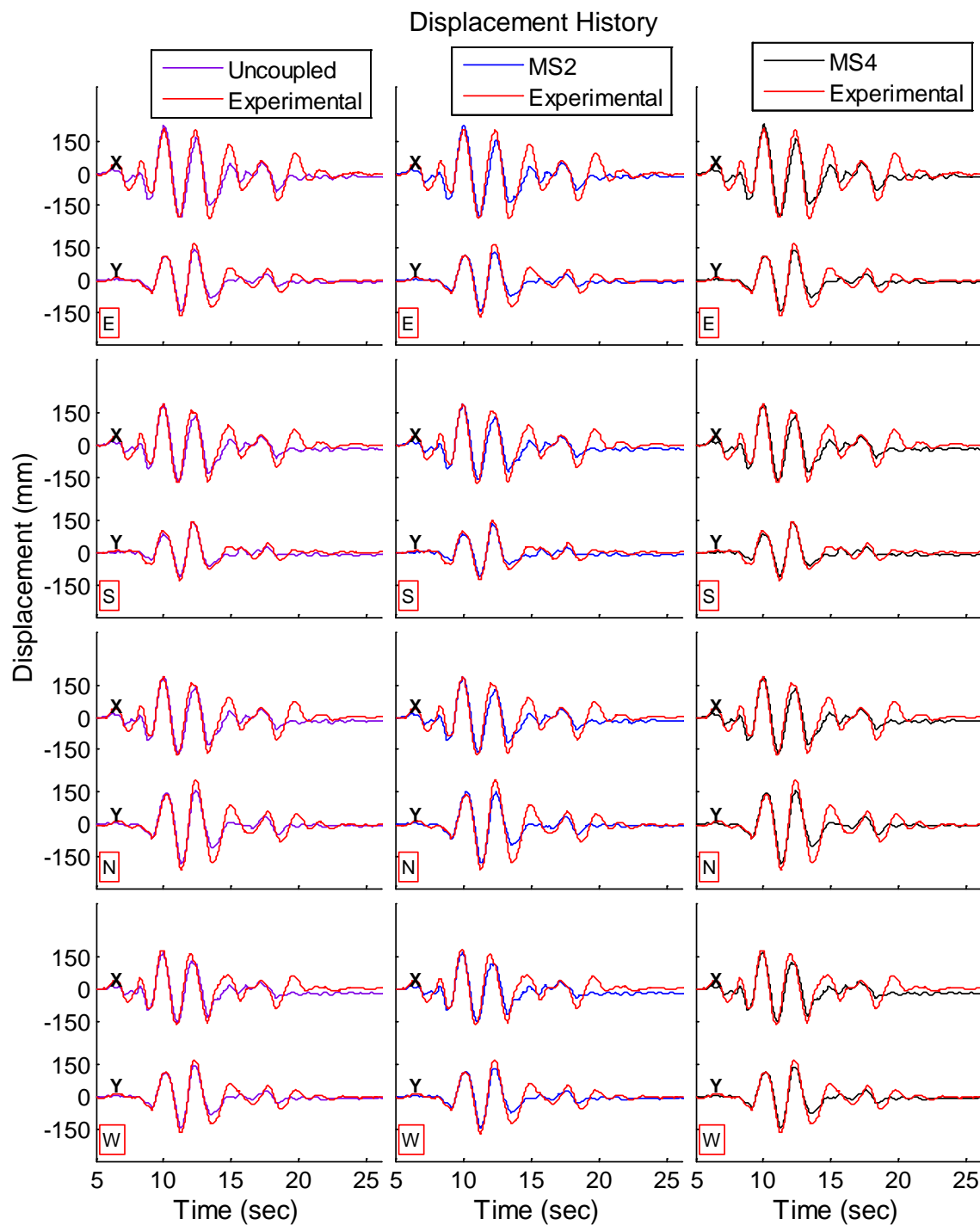


**Figure 11-13: Comparison of experimental and numerical simulation for Vogtle 100%; displacement history in each LR bearing, labeled by position (E, S, N, W). Numerical simulation of uncoupled, MS2, and MS4 LR bearing models.**

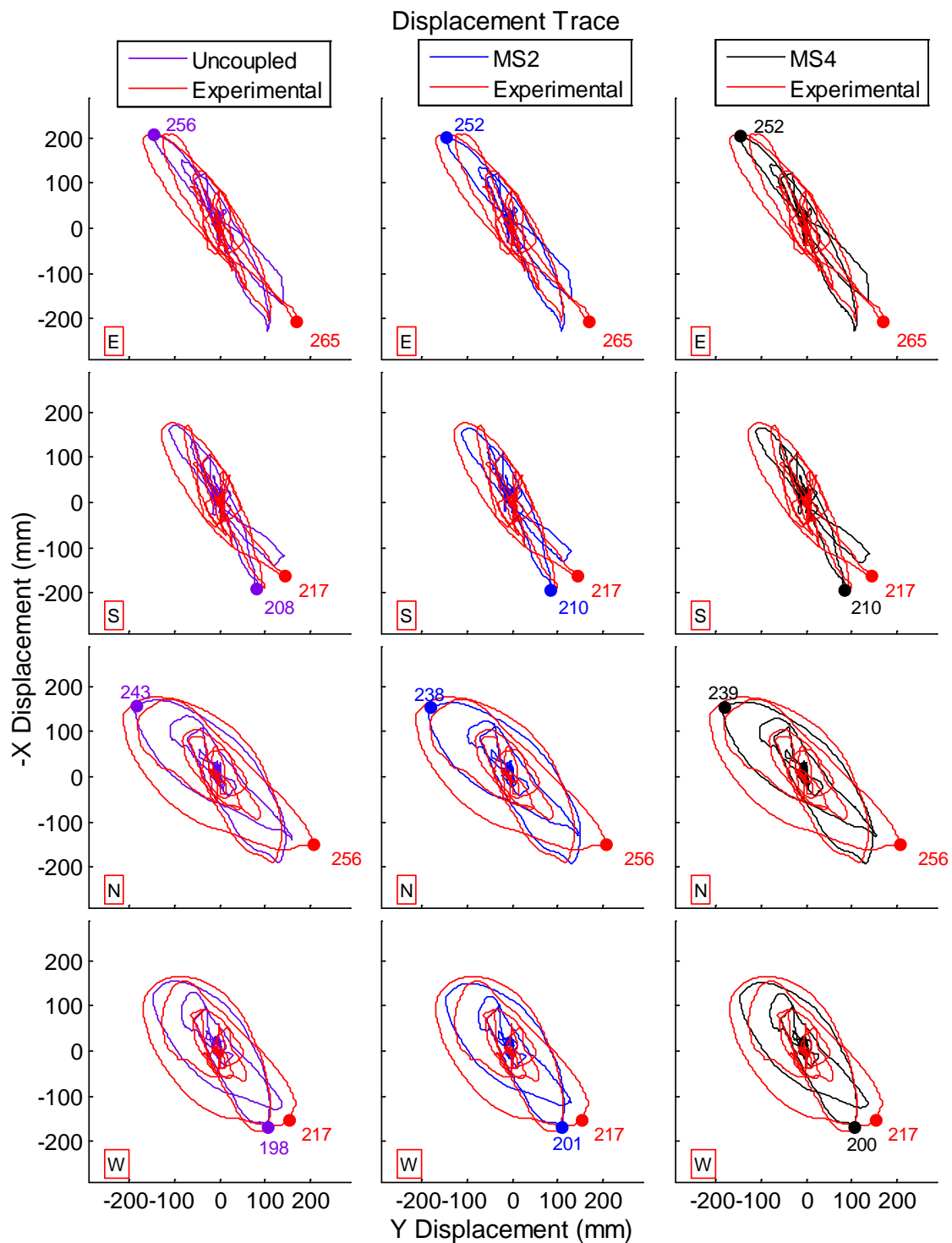


**Figure 11-14: Comparison of experimental and numerical simulation for Vogtle 100%; displacement trace in each LR bearing, labeled by position (E, S, N, W). Numerical simulation of uncoupled, MS2, and MS4 LR bearing models.**

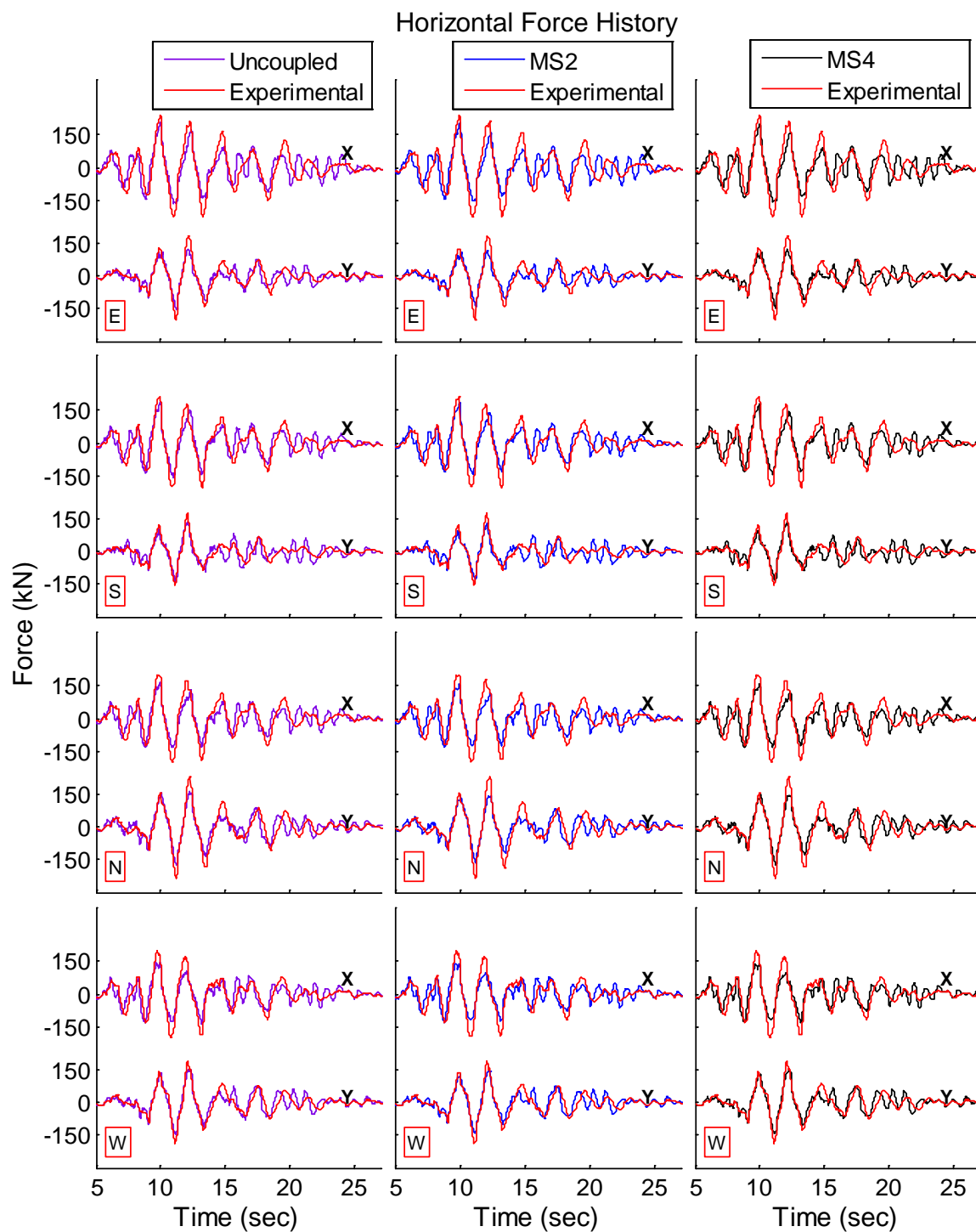


**Figure 11-15: Comparison of experimental and numerical simulation for Vogtle 100%; horizontal force history (x and y) in each LR bearing, labeled by position (E, S, N, W). Numerical simulation of uncoupled, MS2, and MS4 LR bearing models.**

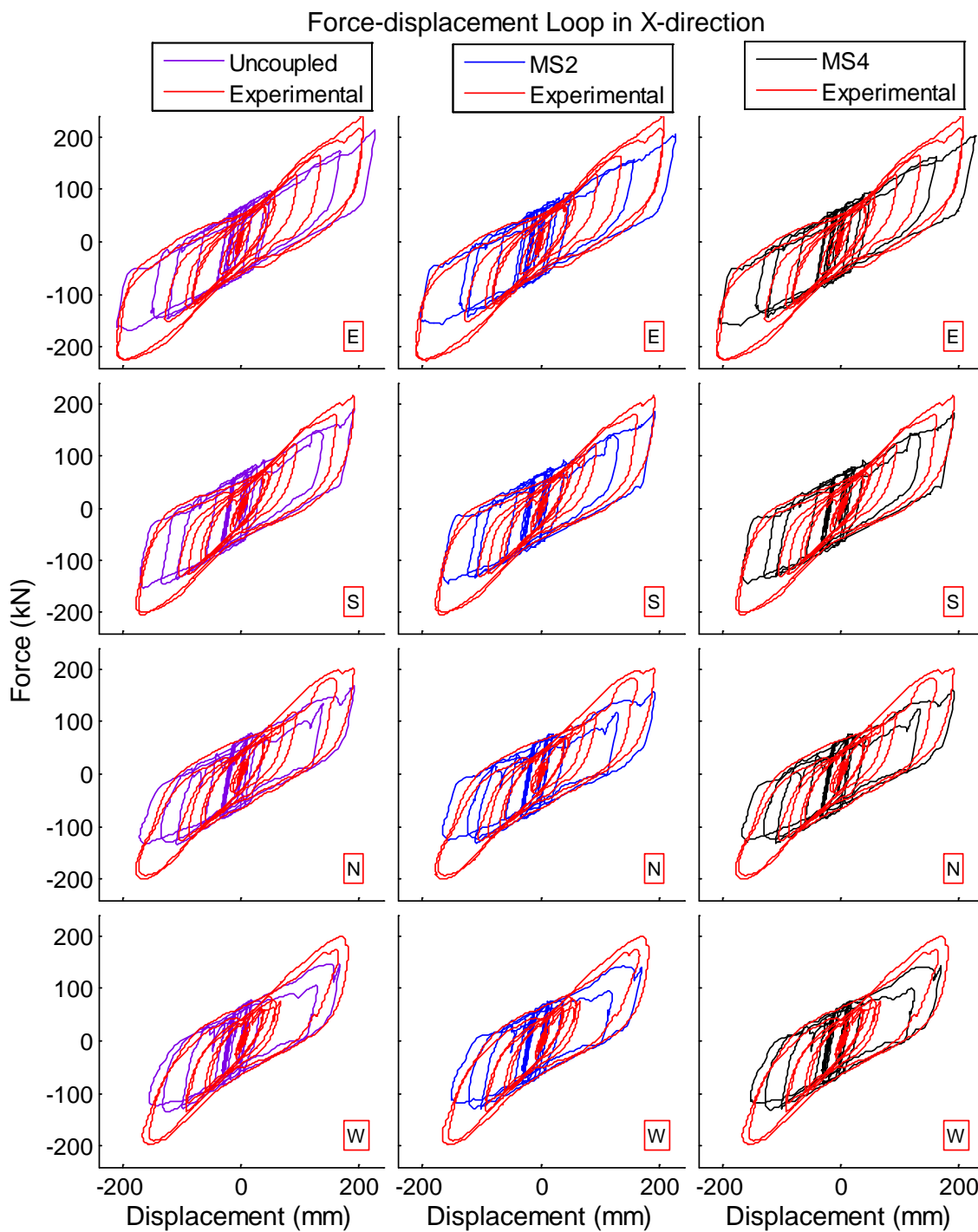


**Figure 11-16: Comparison of experimental and numerical simulation for Vogtle 100%; force-displacement loop in x-direction in each LR bearing, labeled by position (E, S, N, W). Numerical simulation of uncoupled, MS2, and MS4 LR bearing models.**

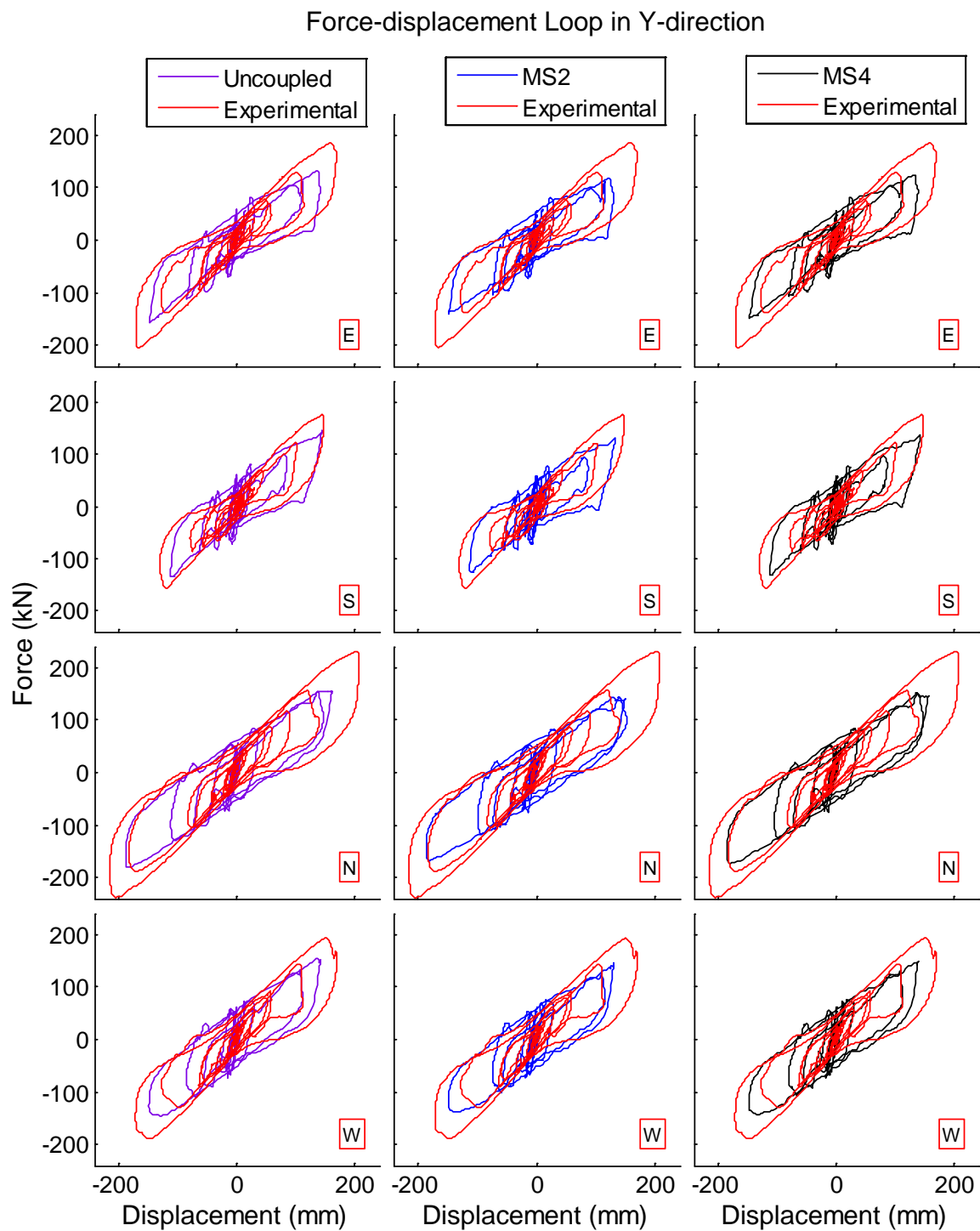


**Figure 11-17: Comparison of experimental and numerical simulation for Vogtle 100%; force-displacement loop in y-direction in each LR bearing, labeled by position (E, S, N, W). Numerical simulation of uncoupled, MS2, and MS4 LR bearing models.**

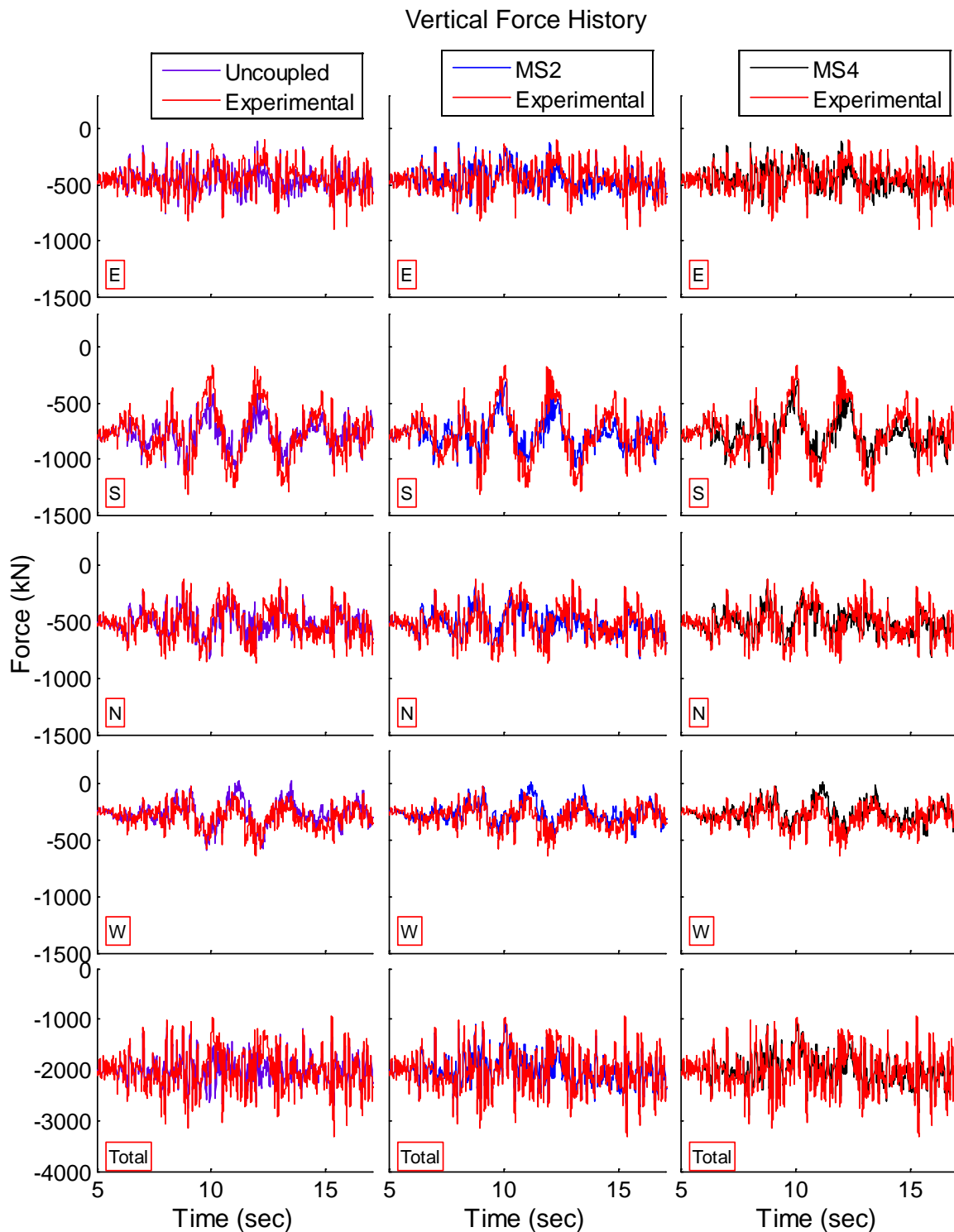


**Figure 11-18: Comparison of experimental and numerical simulation for Vogtle 100%; vertical force history in each LR bearing, labeled by position (E, S, N, W). Numerical simulation of uncoupled, MS2, and MS4 LR bearing models.**

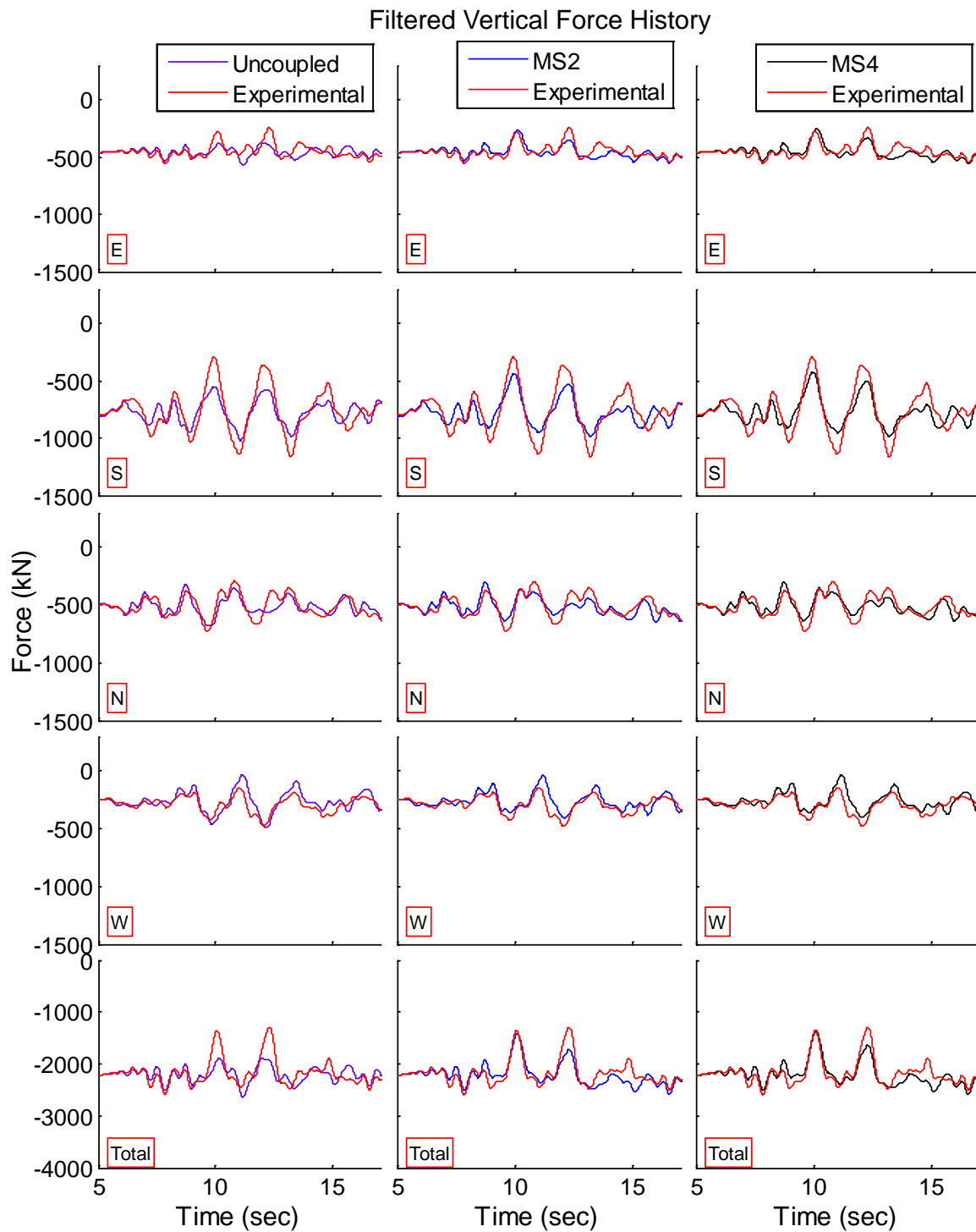


**Figure 11-19: Comparison of experimental and numerical simulation for Vogtle 100%; vertical force history in each LR bearing, labeled by position (E, S, N, W). Numerical simulation of uncoupled, MS2, and MS4 LR bearing models. A low pass filter with a cutoff frequency of 2 Hz was applied to the vertical force.**

#### 11.1.4 Rinaldi 88% (XY)

The displacement histories and displacement traces for the three numerical bearing models (uncoupled, MS2, and MS4) are compared to the equivalent experimental responses in Figure 11-20 and Figure 11-21, respectively, for Rinaldi 88% (XY). These figures show that the uncoupled and MS4 bearing models produced displacements that are similar to each other and closely match the experimental, while the MS2 model is worst in predicting the bearings displacement. Peak horizontal force in x- and y-directions is not predicted by any of the numerical models (Figures 11-23 and 11-24).

The vertical force histories of each LR bearing and the total (summed over all LR bearings) are shown in Figure 11-24. Similar to the vertical response for the other excitations presented above, the uncoupled model does not predict the load transfer effect (see total vertical force plot in Figure 11-24), and the load transfer in general is accurately predicted by the MS2 and MS4 bearing models when the bearings displacements are accurately predicted. For this motion, a comparison between the displacement and vertical force histories shows that the first peak reduction in total vertical force (around 8.5 seconds) due to load transfer is well predicted by the MS2 and MS4 bearing models because the displacement was also well predicted. Likewise, the other two large peak reductions in total vertical force (around 9.5 and 13 seconds) due to load transfer are underestimated because the displacements were also underestimated. Furthermore, an increase in vertical force around 12 seconds is produced by the MS2 and MS4 bearing models that caused a downward shift in the vertical force history that is unrealistic.



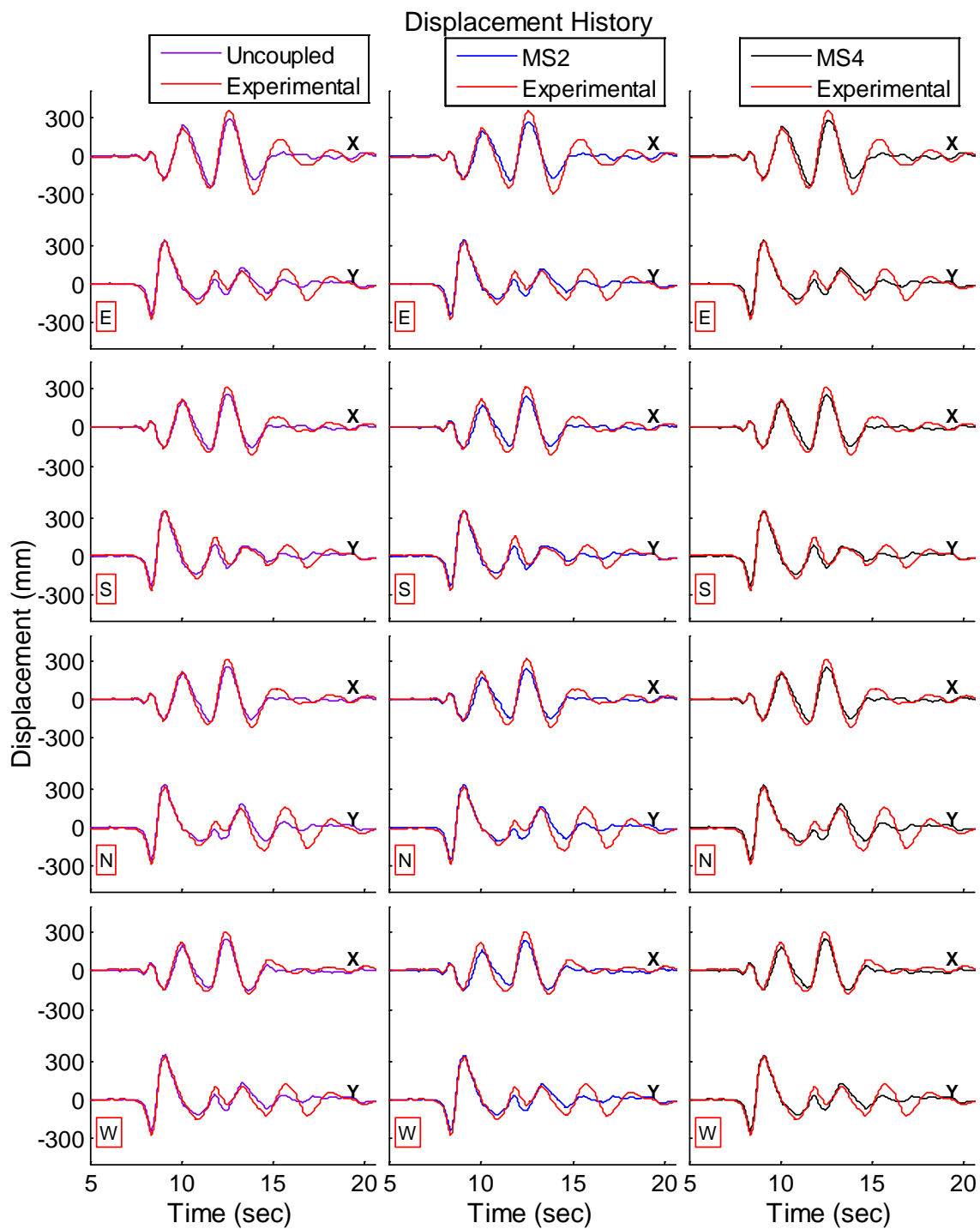


**Figure 11-20: Comparison of experimental and numerical simulation for Rinaldi 88% (XY); displacement history in each LR bearing, labeled by position (E, S, N, W). Numerical simulation of uncoupled, MS2, and MS4 LR bearing models.**

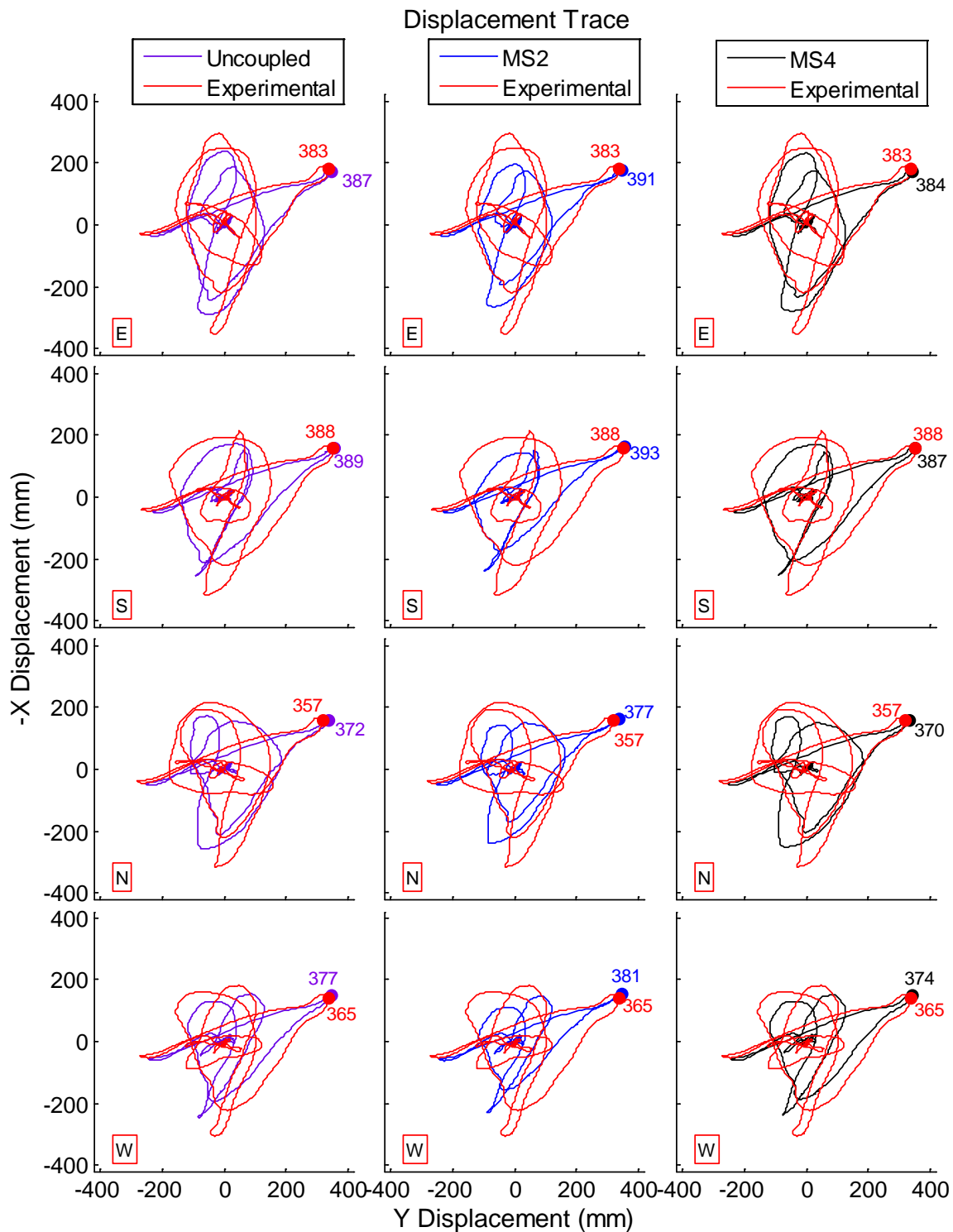


**Figure 11-21: Comparison of experimental and numerical simulation for Rinaldi 88% (XY); displacement trace in each LR bearing, labeled by position (E, S, N, W). Numerical simulation of uncoupled, MS2, and MS4 LR bearing models.**

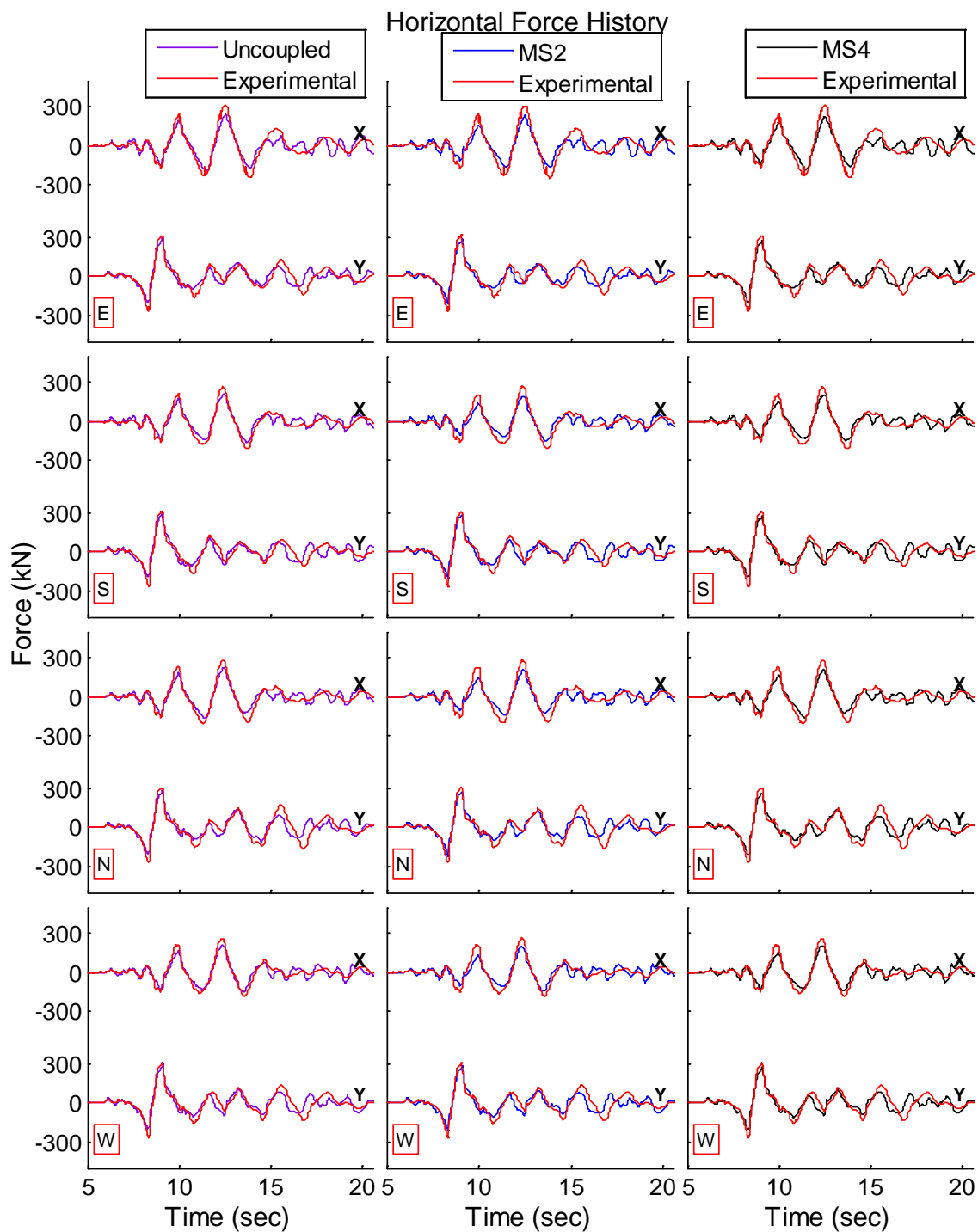


**Figure 11-22: Comparison of experimental and numerical simulation for Rinaldi 88% (XY); horizontal force history (x and y) in each LR bearing, labeled by position (E, S, N, W). Numerical simulation of uncoupled, MS2, and MS4 LR bearing models.**

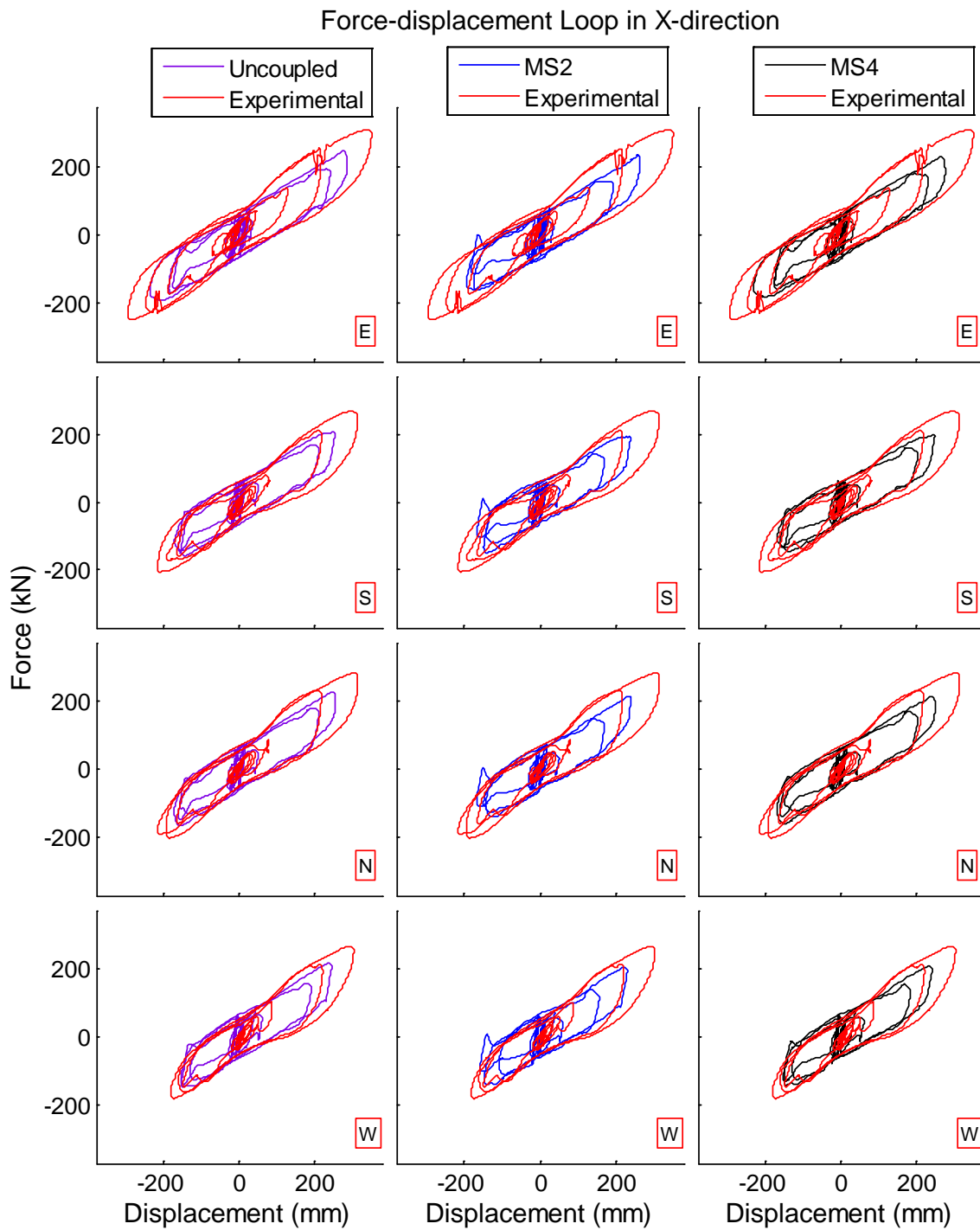


**Figure 11-23: Comparison of experimental and numerical simulation for Rinaldi 88% (XY); force-displacement loop in x-direction in each LR bearing, labeled by position (E, S, N, W). Numerical simulation of uncoupled, MS2, and MS4 LR bearing models.**

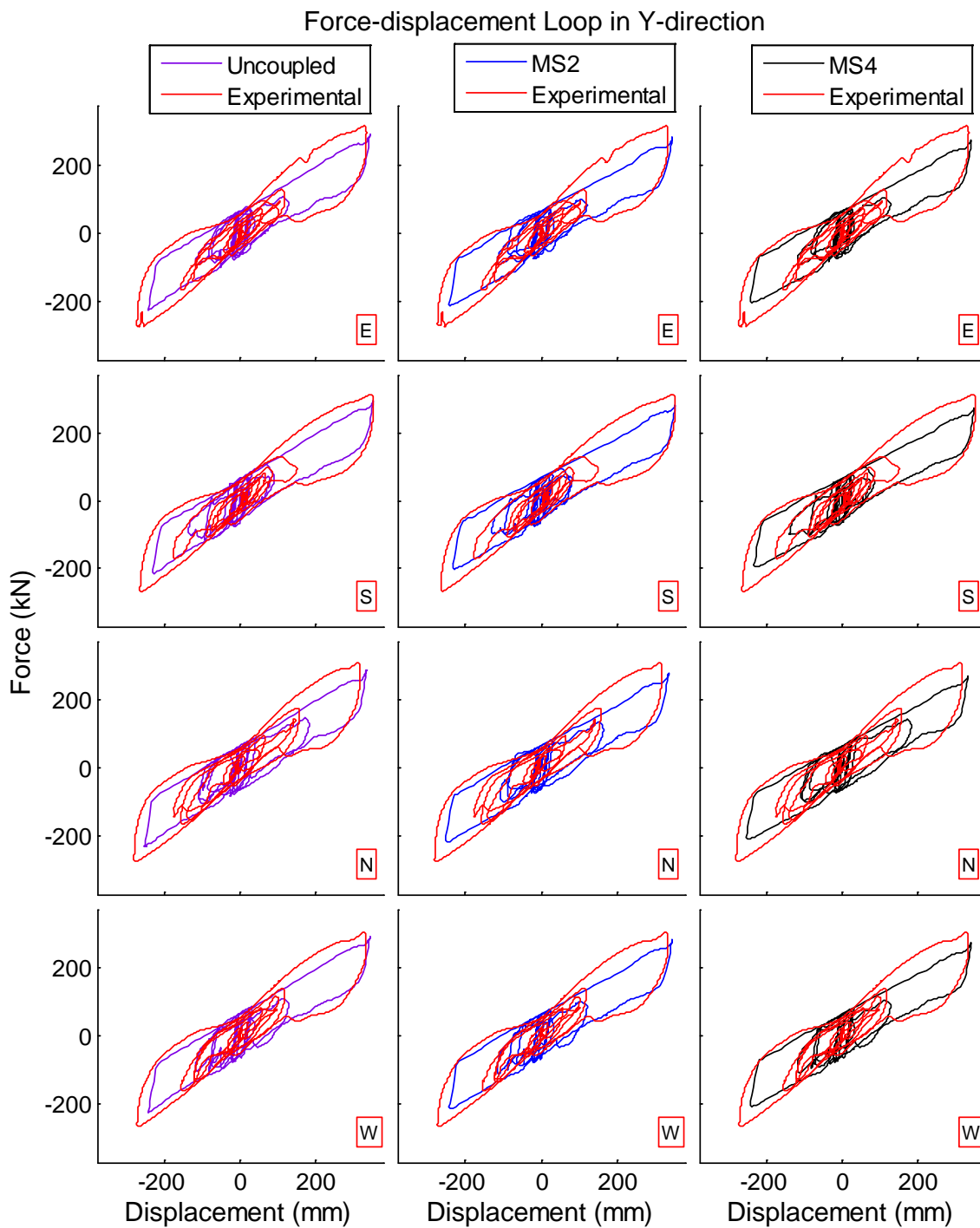


**Figure 11-24: Comparison of experimental and numerical simulation for Rinaldi 88% (XY); force-displacement loop in y-direction in each LR bearing, labeled by position (E, S, N, W). Numerical simulation of uncoupled, MS2, and MS4 LR bearing models.**

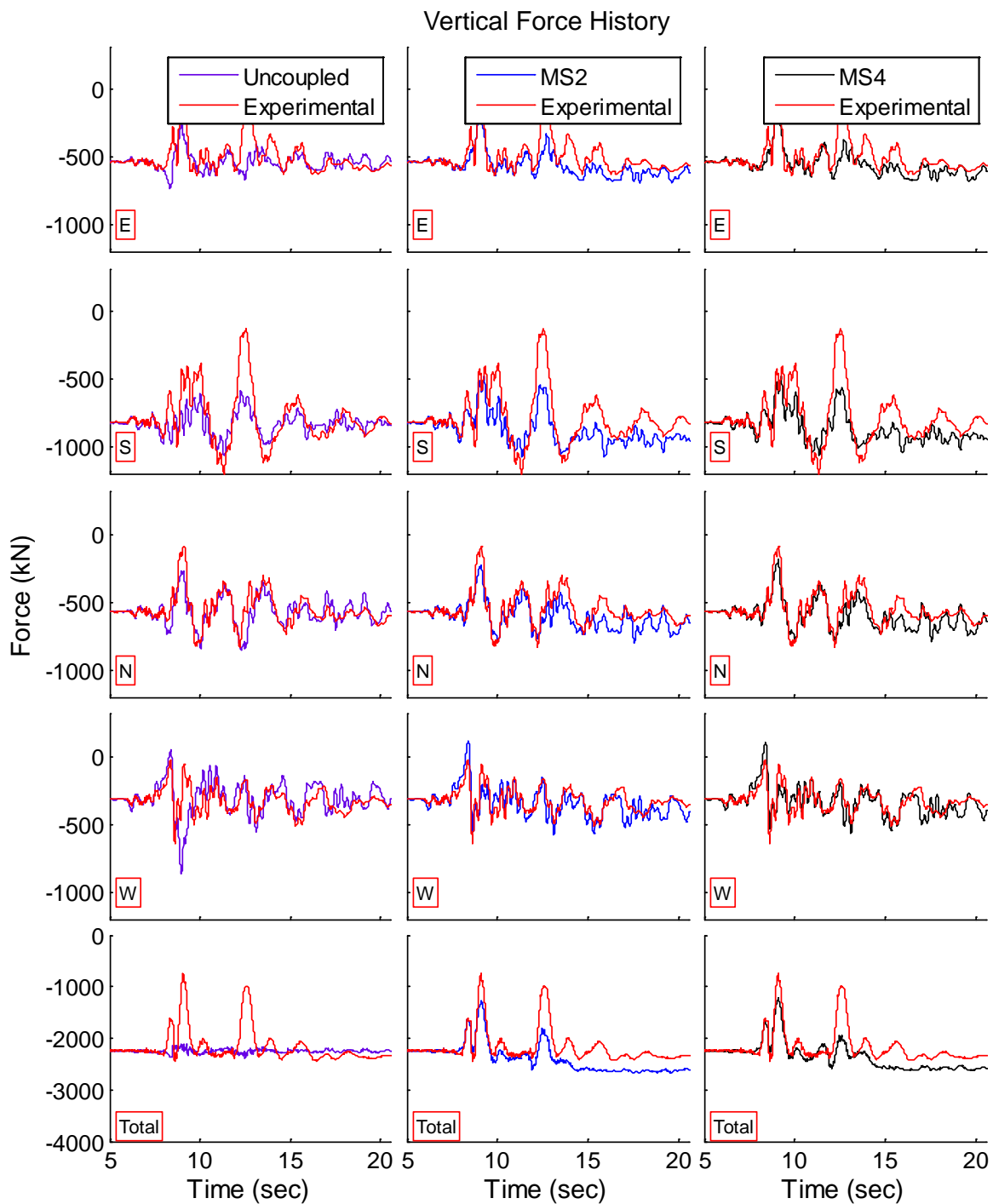


**Figure 11-25: Comparison of experimental and numerical simulation for Rinaldi 88% (XY); vertical force history in each LR bearing, labeled by position (E, S, N, W). Numerical simulation of uncoupled, MS2, and MS4 LR bearing models.**

### 11.1.5 Calibration of Vertical Springs Stiffness in the MS2 and MS4 Bearing Models

As mentioned before, the ability for the numerical model to predict the load transfer effect is strongly related to the ability of the numerical model to predict the bearing displacement. However, the prediction of the load transfer is also affected by the distribution of vertical stiffness among the vertical spring elements. In other words, distribution of spring stiffness may be calibrated to more closely match the experimental results.

The assigned distribution of stiffness to the vertical springs used in the MS2 and MS4 bearing models that were presented above were selected to best match, on average, the experimental vertical response of the four motions presented in Sections 11.1.1 to 11.1.4. However, alternative distributions might be selected to best match the load transfer for a particular excitation, as shown in Figure 11-26 for Diablo 95% (XY), Figure 11-27 for Sine 100% (Y), and Figure 11-28 for Rinaldi 88% (XY). The comparison for Vogtle 100% is not presented since the observations presented are similar to the other three excitations, which are easily visualized. In these figures, the term in parentheses on the numerical plot legend represents the value assigned to the stiffness of the center vertical springs in the MS2 bearing model. The assigned stiffness of the edge vertical springs was in agreement with the stiffness of the center springs to obtain a consistent total vertical stiffness of the LR bearing.

For Diablo 95% (XY), a much closer match to the experimental load transfer can be obtained if the stiffness of the center and edge vertical springs are assigned to be  $1.8K_{vr}$  and  $0.05K_{vr}$ , respectively (Figure 11-26(c)), as opposed to the ratios used in the responses

presented in Section 11.1.2 (Figure 11-26(b)). However, with these same distribution factors, the load transfer for Sine 100% and is Rinaldi 88%(XY) is overestimated (Figure 11-27(c) and Figure 11-28(c)). Furthermore, although the ratio of  $1.25 K_{vr}$  for the center vertical springs was considered for the responses presented in Chapter 10, this ratio was not considered in this chapter because it underpredicted the load transfer for the four excitations investigated above as shown in Figures 11-26(a), 11-27(a), and 11-28(a) for three excitations.

Similar behavior is observed with the MS4 bearing model; that is, the prediction of load transfer changes by varying the vertical stiffness distribution on the vertical spring elements, thus, these plots are not presented here.

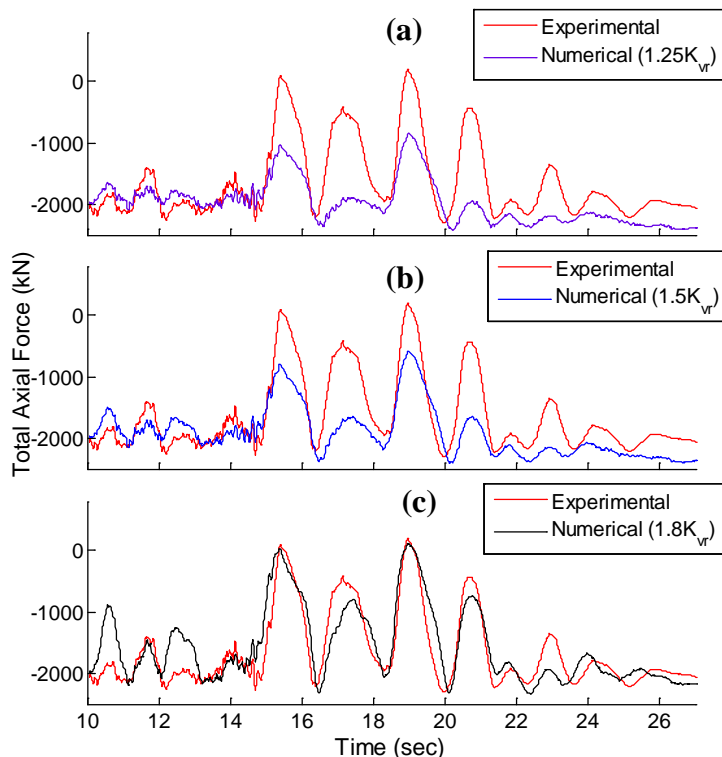


**Figure 11-26: Calibration of vertical spring stiffness in the MS2 bearing model for Diablo 95% (XY).**



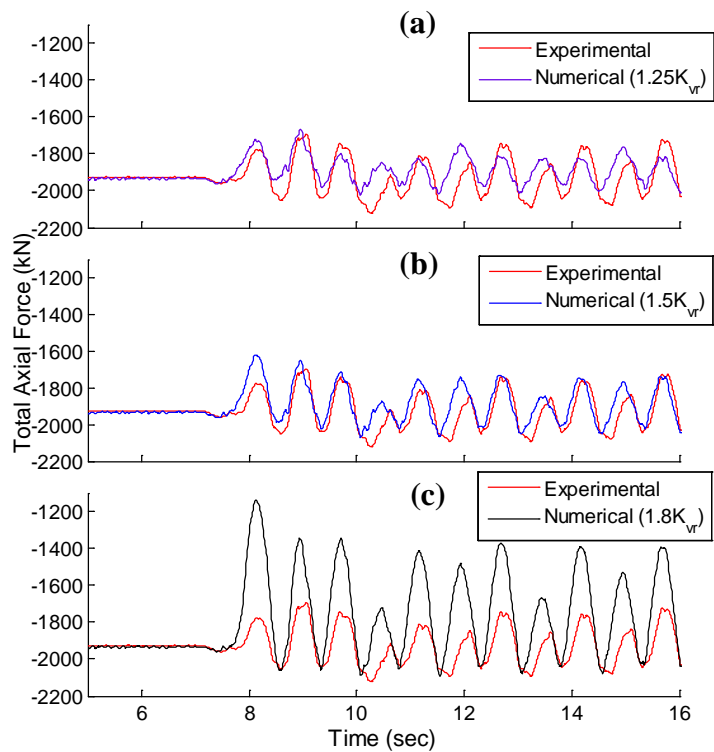


**Figure 11-27: Calibration of vertical spring stiffness in the MS2 bearing model for Sine 100% (Y).**

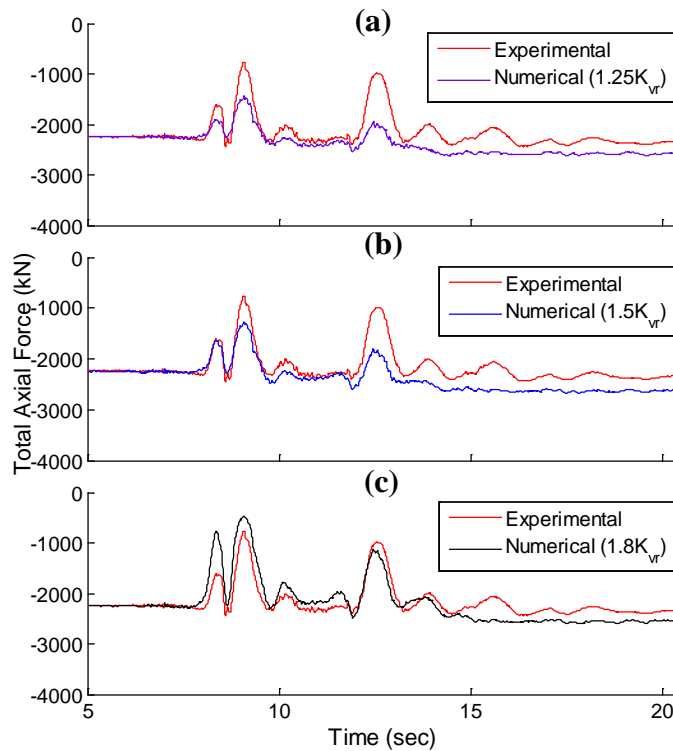


**Figure 11-28: Calibration of vertical spring stiffness in the MS2 bearing model for Rinaldi 88% (XY).**

### 11.1.6 Structural Response

In this section, the structural responses predicted by the uncoupled, MS2, and MS4 bearing models are compared to the experimental structural responses. The x- and y-direction roof acceleration histories, peak acceleration profiles (peak acceleration vs. story level), 2<sup>nd</sup> story drift histories, and peak drift profiles (peak drift vs. story level) are plotted for Diablo 95% (XY) and Vogtle 100% in Figures 11-26 to 11-29. These two excitations were selected as representative of a 2D and a 3D excitation that produced peak displacement near DB and EDB levels, resulting in significant load transfer between the LR bearings and CL bearings (Figures 11-12 and 11-19).

The structural responses produced by the TS structure model (Chapter 7) incorporating the three bearing models are nearly identical to each other for Vogtle 100% and Diablo 95% (XY), thus suggesting that as expected, the load transfer effect had no influence in the structural horizontal acceleration and story drift. Furthermore, the numerical structural response produced by the TS structure model (Chapter 7) incorporating the uncoupled bearing model is also nearly identical to the structural response produced by the TS structure model (Chapter 7) incorporating the uncoupled bearing model that used the characterized bearing properties presented. Recall that the TS structural response of the characterized uncoupled bearings model was presented in Section 8.5.3 for Vogtle 100% (Figure 8-27), Diablo 95% (XY) (Figure 8-29), as well as El Centro 130% (Figure 8-26), and Vogtle 175% (Figure 8-28). Therefore, the assessment and reliability of the numerical bearing model to predict the experimental structural responses presented in Section 8.5.3 are also valid here.

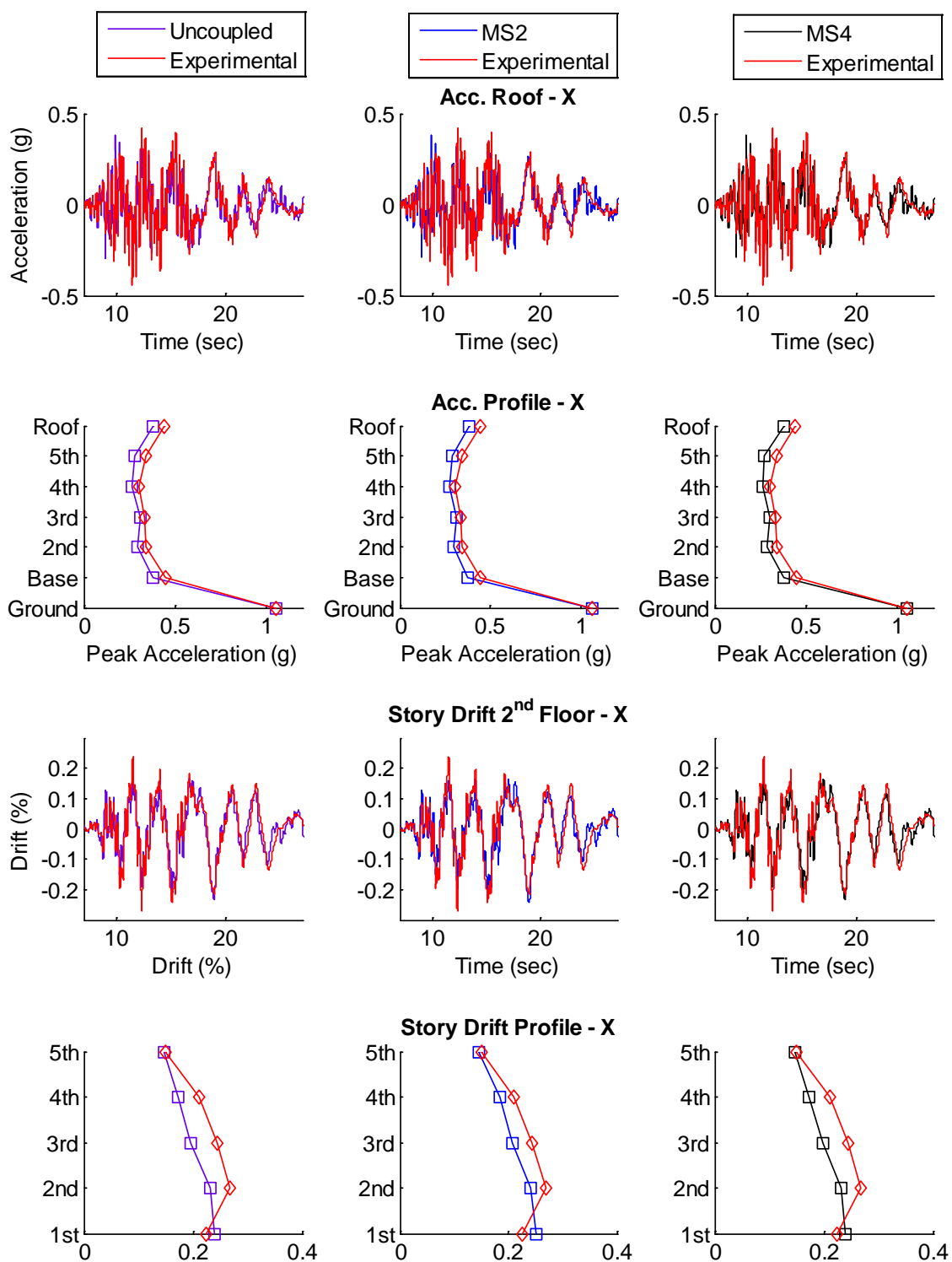


**Figure 11-26: Comparison of experimental and numerical simulation for Diablo 95% (XY); x-direction roof acceleration histories, peak acceleration profiles, 2<sup>nd</sup> story drift histories, and peak drift profiles. Numerical simulation of uncoupled, MS2, and MS4 LR bearing models.**

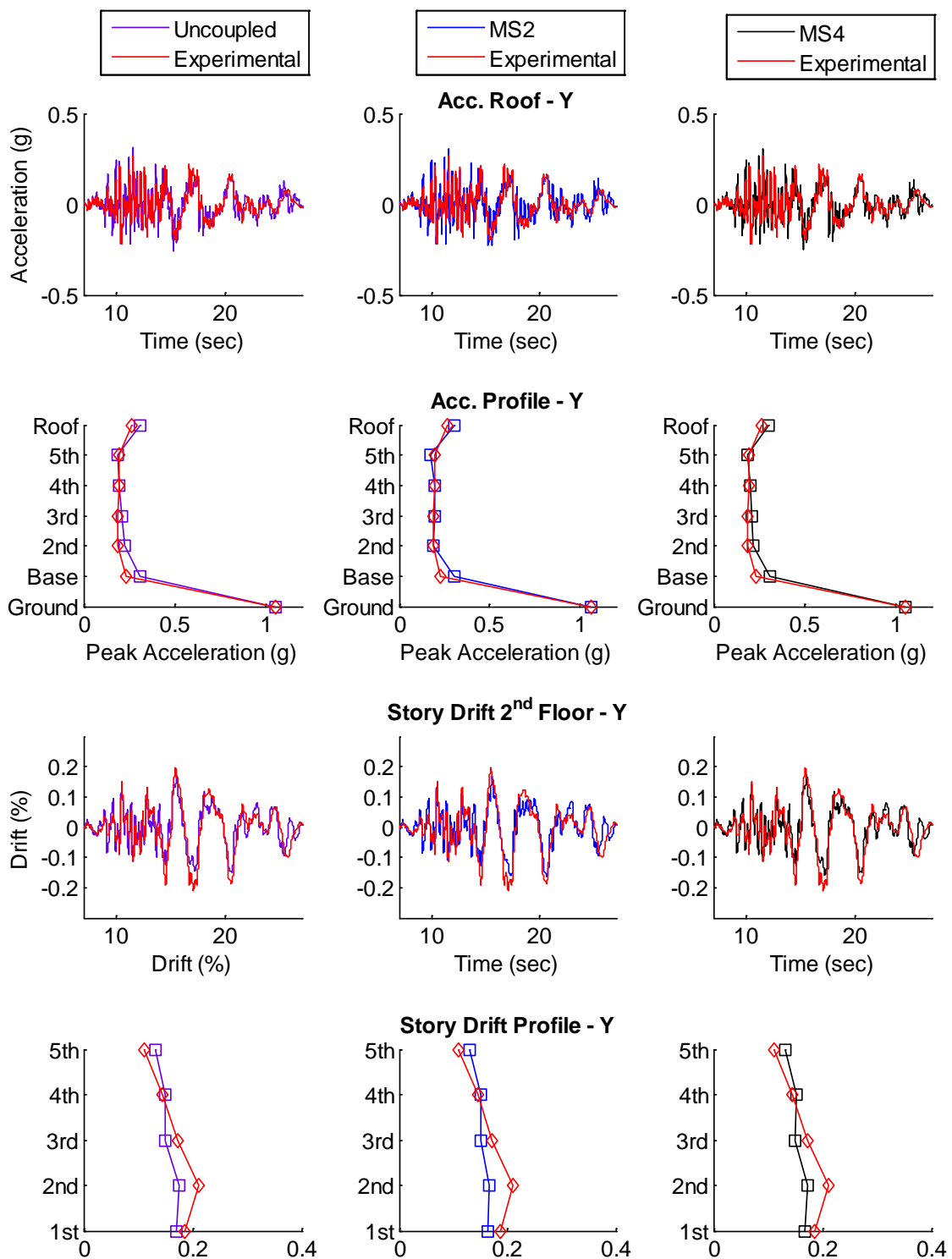


**Figure 11-27: Comparison of experimental and numerical simulation for Diablo 95% (XY); y-direction roof acceleration histories, peak acceleration profiles, 2<sup>nd</sup> story drift histories, and peak drift profiles. Numerical simulation of uncoupled, MS2, and MS4 LR bearing models.**

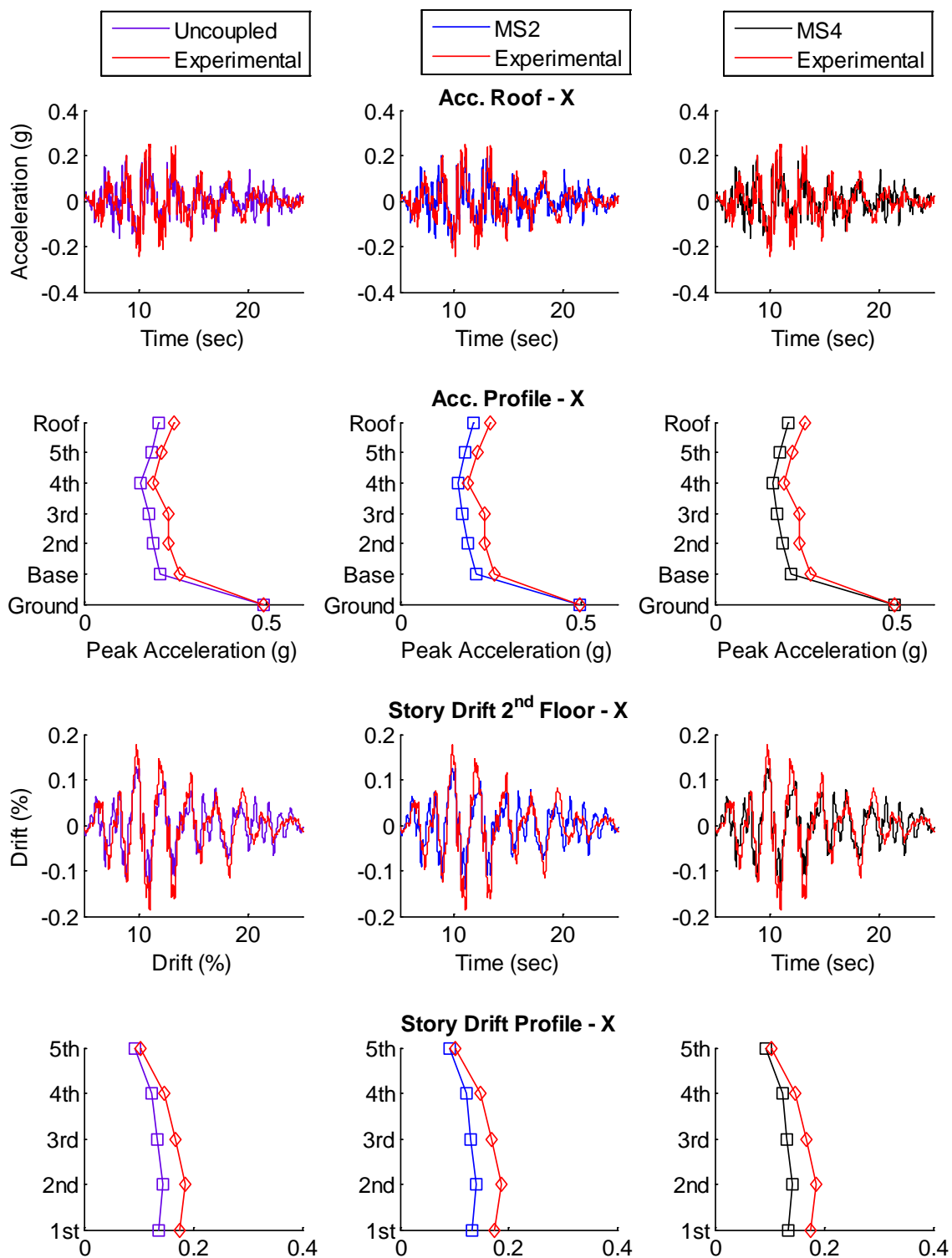


**Figure 11-28: Comparison of experimental and numerical simulation for Vogtle 100%; x-direction roof acceleration histories, peak acceleration profiles, 2<sup>nd</sup> story drift histories, and peak drift profiles. Numerical simulation of uncoupled, MS2, and MS4 LR bearing models.**

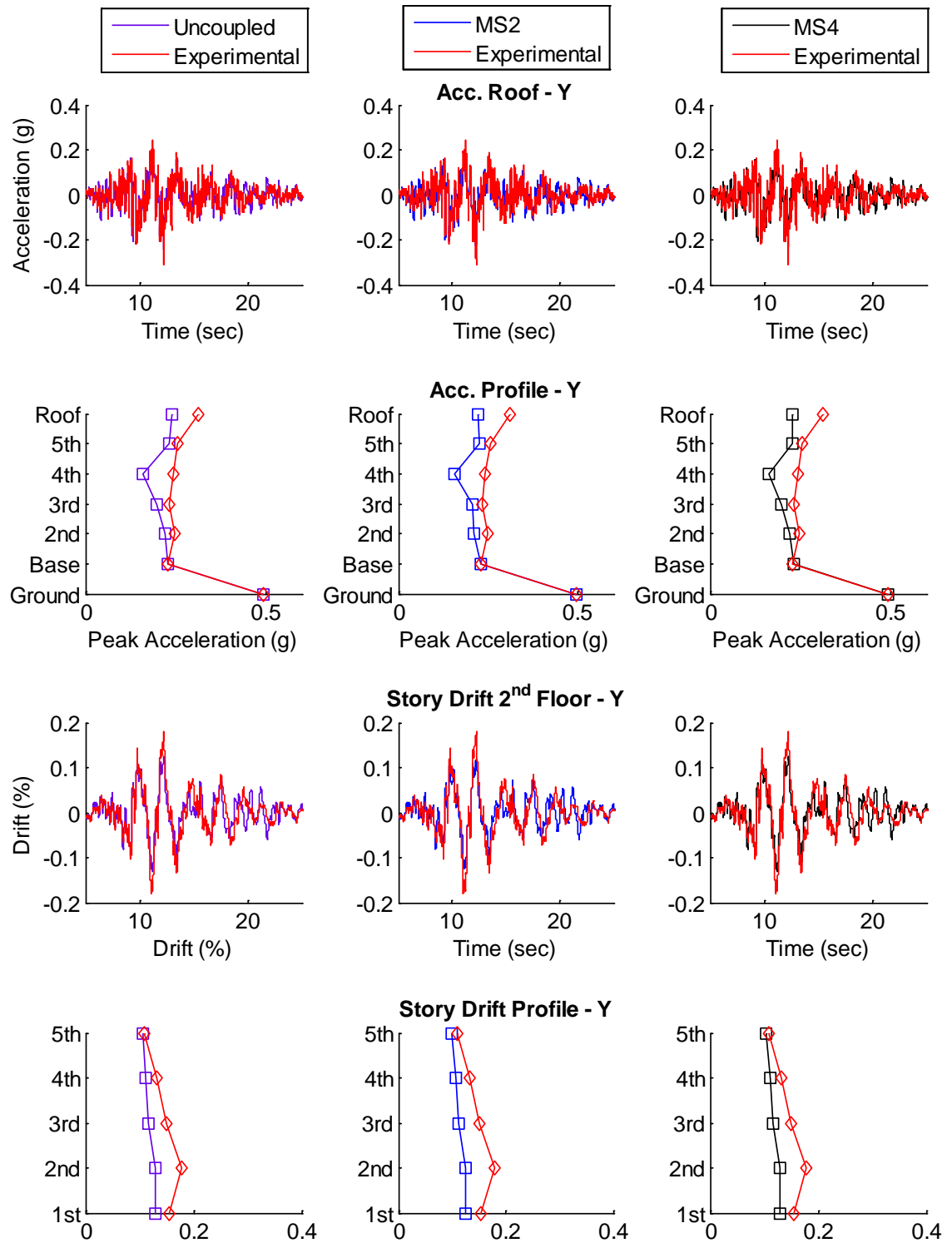


**Figure 11-29: Comparison of experimental and numerical simulation for Vogtle 100%; y-direction roof acceleration histories, peak acceleration profiles, 2<sup>nd</sup> story drift histories, and peak drift profiles. Numerical simulation of uncoupled, MS2, and MS4 LR bearing models.**

## 11.2 Alternative Construction of the MS-LRB model

As mentioned before, the two configurations of the MS-LRB model, named MS2 and MS4, and the material models considered here and in Chapter 10 were selected to provide the simplest numerical bearing model able to predict in general the LR bearing response both in the horizontal and vertical directions. However, refined configurations of the MS-LRB model with increased number of vertical springs and planar spring assemblages (Section 10.1), and improved material models should be considered until there is minimal variation to the LR bearing response with refinement.

Increasing the number of vertical springs and planar spring assemblage (Section 10.1) most likely will eliminate the need to calibrate the distribution of the vertical stiffness. Furthermore, by increasing the number of vertical springs, perhaps a bilinear force-displacement relationship (Figure 11-1(c)) could be applied in the vertical direction without any convergence constraints.

Refined material properties in both vertical and horizontal directions should be considered. As mentioned in Section 6-3, the uncoupled bearing model does not capture the force degradation due to heating of the lead plug that was observed in the experimental force-displacement loop for Sine 100% (Y) (Figure 11-5). Likewise, the MS2 and MS4 bearing models were not able to capture the force degradation behavior. However, this behavior can potentially be predicted with the use of improved material models that incorporate effects such as temperature variation of the lead plug, such as the KikuchiAikenLRB Material model currently available in Opensees. Caution should be used when making any changes to the MS-LRB bearing model. As an example, the



KikuchiAikenLRB material model produces a nonlinear hysteretic force-displacement relationship, thus, if this material is used with the truss element, the plastic spring is no longer needed. Other changes to the numerical bearing model might be necessary when combined with other material models; therefore, the user should carefully study the numerical bearing model prior to any modifications.

### **11.3 Summary of Observations**

The response of the LR bearing produced by three numerical bearing models was compared with the experimentally observed response for Sine 100% (Y), Diablo 95% (XY), Vogtle 100%, and Rinaldi 88% (XY) in Section 11.1. The results presented showed that the horizontal displacement and horizontal force of the LR bearings produced by the uncoupled, MS2, and MS4 bearing models tended to be similar to each other, with on average a slightly more accurate prediction with the MS4 bearing model. In general, the experimental peak displacement was closely matched by the numerical simulations of the three bearing models, while all three numerical models underestimated the peak horizontal force for all these four excitations.

The load transfer between the LR bearings and CL bearings that was recorded during the experiment was predicted by the MS2 and MS4 bearing models during Sine 100% (Y), Diablo 95% (XY), Vogtle 100%, and Rinaldi 88% (XY), while the uncoupled bearing model did not predict the load transfer effect. The reduction in total vertical force is better predicted when the numerical model accurately predicts the horizontal displacement. However, prediction of the load transfer effect is highly influenced by the distribution of

the vertical stiffness to the vertical spring elements. The load transfer effect did not influence the response of the structure as shown in Section 11.1.6.

Alternative constructions to the MS-LRB bearing model were presented in Section 11.2. However, the numerical model should be carefully studied prior to making any modifications as it may require reformulating the structure of the spring assemblage.

## CHAPTER 12: CONCLUSIONS

As documented in this dissertation, a hybrid elastomeric isolation system using lead-rubber (LR) bearings and cross-linear (CL) bearings was designed for a 5-story moment frame building and tested under a variety of earthquake excitations at E-Defense. The isolation system was designed to sustain displacement demands representative of extended or beyond design basis shaking at a potential nuclear site in central and eastern U.S. The experimentally observed response of the LR bearings was calibrated to a bidirectionally coupled, bilinear hysteretic model in the horizontal direction that is uncoupled to the response in the vertical direction. This bearing model represents current numerical approaches used by registered design professionals. However, this model could not predict the experimentally observed load transfer between the LR bearings and CL bearings, referred as the load transfer effect, thus, leading to the development of a three-dimensional multi-spring LR bearing model that couples the response of the horizontal and vertical directions. A realistic numerical simulation model of the 5-story building with isolators was built, tested and calibrated. This dissertation has documented the overall test results, unique response characteristics of the hybrid isolation system, and the comparison of the experimental data to the numerical simulations of the building using two distinct numerical LR bearing models: (1) a bidirectionally coupled, bilinear hysteretic model with uncoupled response in the horizontal and vertical directions, referred as the uncoupled bearing model, and (2) a bidirectionally coupled, bilinear hysteretic model with coupled response in the horizontal and vertical directions, referred

as the multi-spring bearing model. Furthermore, the revised bounding analysis methodology proposed in ASCE 7 (ASCE, 2016) was investigated.

## **12.1 Characteristics of Lead-Rubber Bearing Response**

The following behaviors, many of which have been observed before, were observed in the response of LR bearings during this test program.

1. Pinching near the center of the measured bearing hysteresis loop, attributed to the small size of the lead plug;
2. Loss of characteristic strength over the duration of an excitation, associated with heating of the lead plug;
3. Slight fluctuation of shear force during high frequency axial force variation; thought to be insignificant;
4. Small (negligible) permanent displacements at the end of the records;
5. Significant base rotation demands due to the inability to configure the system appropriately for torsion;
6. No loss of shear resistance at large displacements due to the stabilizing influence of the CL bearings;
7. Transfer of axial forces from LR bearings to CL bearings at large displacements, causing the LR bearings to sustain tension;

Items 1-5 are not believed to be influenced by the presence of CL bearings. With regard to item 6, the stabilizing influence of the CL bearings prevented the loss of shear resistance of the LR bearings at displacement demands beyond their theoretically

computed stability limits in this experiment. Normally, a system composed only of LR bearings can be designed to stay well within the stability limits, and under this scenario similar behavior would be expected. Item 7 is a behavior unique to the hybrid LR system.

## **12.2 Hybrid Lead-Rubber (LR) and Cross-Linear (CL) Bearing**

### **System**

A hybrid isolation system of LR bearings and CL bearings was designed for the test program instead of a pure elastomeric isolation system to overcome the constraints of the utilized experimental setup. While a hybrid system can overcome stability issues, the vertical force demands in individual bearings can be large due to load transfer between the two types of devices (LR bearings and CL bearings).

The hybrid system was chosen for the following reasons. First, due to the light weight of the testbed structure, it was not possible to simultaneously provide the desired period elongation and the desired displacement demands with LR bearings alone. Second, the CL bearings provided significant tension resistance, which was needed to accommodate the expected tensile demands according to preliminary calculations. Third, the CL bearings provided overall stability to the isolation system at large horizontal displacements.

In these tests, the hybrid system resulted in significant axial load transfer between the two types of devices; specifically, load redistributed from the LR bearings to the CL bearings as the lateral displacement increased, because the rigidity of the base diaphragm constrained the free downward movement of the LR bearings. As a positive benefit, the

hybrid system eliminated the potential that the shear behavior of the LR bearings was affected by stability and post-buckling behavior. However, the tradeoff was that the tensile and compressive demands in the CL bearings were quite large, as they carried all the overturning induced axial forces, and significant tensile demands were observed in the LR bearings, which were constrained by the base diaphragm.

### **12.3 Predictability of the System Response**

Predictability of the bearing and structural response is an important requirement for the application of seismic isolation. Thus, two methods of predicting the horizontal behavior of the LR bearing observed during the experiment were investigated. The first considered the calibration of the numerical model to match the experimental data, and the second followed the design provisions proposed in ASCE 7 (ASCE, 2016) to bound the experimental response through bounding analysis.

A single amplitude-independent model that has parameters based on physical theory is desirable to represent the response of the isolation system. Such an approach might be possible in general, but was not possible in this study due to the pinching of the hysteresis loops near zero displacement, which was a result of the small size of the lead plug and the observed load transfer between the LR bearings and CL bearings. Therefore, the bearings were modeled using the uncoupled bearing model that represents current numerical approaches used by registered professionals, to evaluate the accuracy of a readily available model to predict the bearing response. The uncoupled bearing model does not capture the bearing displacement amplitude dependence in the horizontal direction, thus, the parameters of the bilinear model were calibrated independently for each simulation as

a means to investigate the experimental data. Using the calibrated model, the predicted horizontal displacement demand of the isolators was within 10% of the observed experimental displacement. When the uncoupled bearing model was calibrated for the peak displacement cycle, it did not capture the history of the displacement over smaller cycles very well. Another limitation to the uncoupled bearing model was that it did not capture the load transfer between the LR bearings and CL bearings observed during the experiment, leading to the development of a multi-spring bearing model.

The bounding analysis methodology proposed by ASCE 7 (ASCE, 2016) was not 100% reliable to bound the experimentally observed peak horizontal displacement and peak base shear of the LR bearings. A limiting factor of the bounding analysis to bound peak responses was related to the spectral variation of the excitations. The upper bound analysis that generally is applied to bound base shear was effective to bound the peak responses of excitations that produced a decreasing spectral displacement with increasing period. On the contrary, excitations that produced steadily increasing spectral displacement with increase in period showed that the bearing displacement decreases with an upper bound analysis. Depending on how much the displacement demand decreases, the base shear may also decrease. However, despite this limitation, the new bounding analysis procedure that considers the responses of both upper bound and lower bound to bound both peak displacements and peak forces, was found to be an improvement over current design practices.

A close match between the simulated and experimental responses such as story drifts and floor accelerations was obtained with the uncoupled bearing model.

### 12.3 Development and Response of a Multi-Spring Bearing Model

Improved models are available that can capture the interaction between the horizontal and vertical behaviors of the LR bearing. However, these models are often experimentally calibrated and cannot be easily modified. Therefore, for practical design application, an LR bearing model was needed that did not rely on experimentally calibrated parameters, that considered the change in horizontal stiffness due to the variation in axial load in three-dimensions to capture the load transfer, that has transparent mechanics, and that has implementation easily modifiable by the user. To achieve all these goals, the multi-spring bearing model was developed. The multi-spring bearing model was validated and calibrated to reproduce the experimental responses. The horizontal displacements and forces of the LR bearing produced by the multi-spring bearing model were on average nearly identical to the responses produced by the uncharacterized uncoupled bearing model. The responses produced by both numerical models led to a close match to the experimental response. The load transfer effect, which was easily observed in the total (summed over all LR bearings) vertical force history, was only captured by the multi-spring bearing model. As a result, the multi-spring bearing model produced vertical forces that closely matched the experimental vertical response, while the uncoupled bearing model produced vertical responses that did not accurately match the experimental response.

The horizontal responses of the superstructure produced by the uncoupled and multi-spring bearing models were identical, thus suggesting that as expected the load transfer effect had no influence in the structural horizontal acceleration and story drift. The



influence of the load transfer in the vertical response of the superstructure was outside the scope of this dissertation.

The results presented in this dissertation showed that the hybrid LR isolation system has many advantages such as overall stability of the isolation system at large horizontal displacements, and tensile resistance to overturning demands. However, the results also showed that the observed load transfer effect can cause significant tension in individual LR bearings in a hybrid LR isolation system. Thus, it is recommended that improved LR bearing models that can predict the load transfer effect, such as the multi-spring bearing model developed here, be considered for design. Neglecting the load transfer effect may lead to significant underestimation of the vertical force demands on the bearing devices.

## REFERENCES

1. Al-Hussaini TM, Constantinou MC, Zayas VA (1994). *Seismic Isolation of Multi-Story Frame Structures Using Spherical Sliding Isolation System*, Technical Report NCEER-94-0007, State University of New York at Buffalo: Buffalo, NY, USA.
2. American Association of State Highway and Transportation Officials (AASHTO) (1999). “Guide Specifications for Seismic Isolation Design”, Washington, DC, USA.
3. American Association of State Highway and Transportation Officials (AASHTO), (2010). *Guide Specification for Seismic Isolation Design*, 3<sup>rd</sup> Edition.
4. American Institute of Steel Construction (AISC), (2005). *Steel Construction Manual*, 13<sup>rd</sup> edition.
5. American Society of Civil Engineers (ASCE), (2008). *Seismic Design Criteria for Structures, Systems and Components in Nuclear Facilities*, ASCE 43-05, ASCE, Reston, VA.
6. American Society of Civil Engineers (ASCE), (2010). *Minimum Design Loads for Buildings and Other Structures*, ASCE/SEI 7-10, ASCE, Reston, VA.
7. American Society of Civil Engineers (ASCE), (2016). *Minimum Design Loads for Buildings and Other Structures*, ASCE/SEI 7-16, ASCE, Reston, VA.
8. American Society of Civil Engineers (ASCE) (2017). “Seismic rehabilitation of existing buildings.” ASCE/SEI 41, ASCE, Reston, VA.

9. Buckle IG, Liu H (1994). "Experimental determination of critical loads of elastomeric isolators at high shear strain", *NCEER Bull.*, 8(3):1–5.
10. Buckle IG, Nagarajaiah S, Ferrell K (2002). "Stability of elastomeric isolation bearings: Experimental study", *ASCE J. Struct. Eng.* 128:3–11.
11. Charney FA, Downs WM (2004). "Modeling procedures for panel zone deformations in moment resisting frames", *Proc., ECCS/AISC workshop: Connections in Steel Structures V*, Amsterdam, Netherlands.
12. Chiou B, Darragh R, Gregor N, Silva W (2008). "NGA project strong-motion database", *Earthquake Spectra*, 24(1):23–44.
13. Chopra AK (2012). *Dynamics of Structures: Theory and Applications to Earthquake Engineering*, Fourth Edition, Prentice Hall.
14. Clark PW, Aiken ID, Kelly JM (1997). *Experimental Studies of the Ultimate Behavior of Seismically Isolated Structures*, Report No. UCB/EERC-97/18, University of California: Berkeley, CA, USA.
15. Comite Euro-international du Beton (CEB), (1996). *RC Clements under Cyclic Loading, State of the Art Report*. Thomas Telford Publications, London, England.
16. Constantinou MC, Mokha AS, Reinhorn AM (1990). *Experimental and Analytical Study of a Combined Sliding Disc Bearing and Helical Steel Spring Isolation System*, Technical Report NCEER-90-0019, State University of New York at Buffalo: Buffalo, NY, USA.

17. Constantinou MC, Tsopelas P, Kasalanati A, Wolff ED (1999). "Property modification factors for seismic isolation bearings." MCEER-99-0012, Multidisciplinary Center for Earthquake Engineering Research, Buffalo, NY, USA.
18. Constantinou MC, Whittaker AS, Kalpakidis Y, Fenz DM, Warn GP (2007). *Performance of Seismic Isolation Hardware under Service and Seismic Loading*, Technical Report MCEER-07-0012, Multidisciplinary Center for Earthquake Engineering Research, State University of New York at Buffalo: Buffalo, NY, USA.
19. Constantinou MC, Kalpakidis I, Filiatrault A, Ecker Lay RA (2011). "LRFD-Based Analysis and Design Procedures for Bridge Bearings and Seismic Isolators." MCEER-11-0004, Multidisciplinary Center for Earthquake Engineering Research, Buffalo, NY, USA.
20. Dao ND, Ryan KL (2015). *Seismic Response of a Full-scale 5-story Steel Frame Building Isolated by Triple Pendulum Bearings under 3D Excitations*, Technical Report CCEER-15-1, Center for Civil Engineering Earthquake Research, University of Nevada, Reno, NV, USA.
21. Griffith MC, Kelly JM, Coveney VA, Koh CG (1988a). *Experimental Evaluation of Seismic Isolation of Medium-Rise Structures Subjected to Uplift*, Report No. UCB-EERC 88-02, University of California: Berkeley, CA, USA.
22. Griffith MC, Aiken ID, Kelly JM (1988b). *Experimental Evaluation of Seismic Isolation of a 9-story Braced Steel Frame Subjected to Uplift*, Report No. UCB-EERC 88-05, University of California: Berkeley, CA, USA.

23. Griffith MC, Aiken ID, Kelly JM (1990). “Displacement control and uplift restraint for base-isolated structures”, *ASCE J. Struct. Eng.*, 116:1135–1148.
24. Han X, Warn G (2014). “Mechanistic model for simulating critical behavior in elastomeric bearings”, *J. Struct. Eng.* 10.1061/(ASCE)ST.1943-541X.0001084.
25. Huang NY, Whittaker AS, Kennedy RP, Mayes RL (2009) “Assessment of Base-Isolated Nuclear Structures for Design and Beyond-Design Basis Earthquake Shaking”, *Tech. Report MCEER-09-0008*, University at Buffalo.
26. Iizuka, M (2000) “A macroscopic model for predicting large-deformation behaviors of laminated rubber bearings”, *Eng. Struct.*, 22(4), 323-334.
27. Kalpakidis IV, Constantinou MC (2009a). “Effects of heating on the behavior of lead-rubber bearings. I: Theory”, *J. Struct. Eng.* 135:1440–1449.
28. Kalpakidis IV, Constantinou MC (2009b). “Effects of heating on the behavior of lead-rubber bearings. II: Verification of theory”, *J. Struct. Eng.* 135:1450–1461.
29. Kalpakidis IV, Constantinou MC, Whittaker AS (2010). “Modeling strength degradation in lead-rubber bearings under earthquake shaking”, *Earthq. Eng. Struct. Dyn.* 39:1533–1549.
30. Kasai K, Ooki Y, Ishii M, Ozaki H, Ito H, Motoyui S, Hikino T, Sato E (2008). “Value-added 5-story steel frame and its components: Part 1 – full scale damper tests and analyses”, *Proc., 14th World Conference on Earthquake Engineering*, Beijing, China.

31. Kasai K, Ito H, Ooki Y, Hikino T, Kajiwara K, Motoyui S, Ozaki H, Ishii M (2010). “Full scale shake table tests of 5-story steel building with various dampers,” *Proc., 7th Intern. Conf. on Urban Earthquake Engin. & 5th Intern. Conf. on Earthquake Engin.* Tokyo Inst. Tech., Tokyo, Japan.
32. Kasai K, Murata S, Kato F, Hikino T, and Ooki Y (2011). “Evaluation rule for vibration period, damping, and mode vector of buildings tested by a shake table with inevitable rocking motions.” *J. Struct. Const. Eng.*, AIJ, 76(270):2031-2040. (In Japanese).
33. Kasai K (2011). Personal Communication.
34. Kasalanati A, Constantinou MC (2005). “Testing and modeling of prestressed isolators”, *ASCE J. Struct. Eng.* 131:857–866.
35. Kasalanati A (2012). Personal Communication.
36. Kelly JM, Skinner MS, Beucke KE (1980a). *Experimental Testing of an Energy Absorbing Seismic Isolation System*, Report No. UCB/EERC-80/35, University of California, Berkeley: CA, USA.
37. Kelly JM, Beucke KE, Skinner MS (1980b). *Experimental Testing of a Friction Damped Aseismic Base Isolation System with Fail-safe Characteristics*, Report No. UCB/EERC-80/18, University of California: Berkeley, USA.
38. Kelly JM, Hodder SB (1981). *Experimental Study of Lead and Elastomeric Dampers for Base Isolation Systems*, Report No. UCB/EERC-81/16, University of California: Berkeley, CA, USA.

39. Kelly JM (1988). *Base Isolation in Japan*, Report No. UCB/EERC-88/20, University of California: Berkeley, CA, USA.
40. Kelly JM, Chalhoub MS (1990). *Earthquake Simulator Testing of a Combined Sliding Bearing and Rubber Bearing Isolation System*, Report No. UCB/EERC-87/04, University of California: Berkeley, CA, USA.
41. Kelly JM (1997). *Earthquake-Resistant Design with Rubber*, 2<sup>nd</sup> Edition, Springer-Verlag.
42. Kent DC, Park R (1971). Flexural members with confined concrete. *Journal of the Structural Division, Proceedings of the ASCE* 97(ST7): 1969-1990.
43. Kikuchi M, Nakamura T, Aiken ID (2010). “Three-dimensional analysis for square seismic isolation bearings under large shear deformations and high axial loads”, *Earthq. Eng. Struct. Dyn.* 39:1513–1531.
44. Koh CG, Kelly JM (1987). *Effects of axial load on elastomeric isolation bearings*, Rep. No. UCB/EERC-86/12, Earthquake Engineering Research Center, Univ. of California, Berkeley, Calif.
45. Koh CG, Kelly JM (1988). “A simple mechanical model for elastomeric bearings used in base isolation”, *Int. J. Mech. Sci.* 30(12): 933-943.
46. Koh CG, Kelly JM (1989). “Viscoelastic stability model for elastomeric isolation bearings”, *ASCE J. Struct. Eng.* 115(2): 285-302.
47. Krawinkler H (1978). “Shear in beam-column joints in seismic design of steel frames”, *Engineering Journal (AISC)*, 15(3): 82-91.

48. Kumar M, Whittaker A, Constantinou M (2014). "An advanced numerical model of elastomeric seismic isolation bearings", *Earthq. Eng. Struct. Dyn.* 43(13): 1955-1974.
49. Malushte S and Whittaker AS (2005). "Survey of past base isolation applications in nuclear power plants and challenges to industry/regulatory acceptance." *Proc. 18th International Conference on Structural Mechanics in Reactor Technology*, Beijing, China.
50. McGuire RK, Silva WJ and Costantino CJ (2001). *Technical Basis for Revision of Regulatory Guidance on Design Ground Motions: Hazard- and Risk-Consistent Ground Motion Spectra Guidelines*, NUREG/CR-6728, U.S. Nuclear Regulatory Commission, Washington, D.C.
51. Mokha A, Constantinou MC, Reinhorn AM (1988). *Teflon Bearings in Aseismic Base Isolation: Experimental Studies and Analytical Modeling*, Technical Report NCEER-88-0038, State University of New York at Buffalo: Buffalo, NY, USA.
52. Mokha A, Constantinou MC, Reinhorn AM (1990). *Experimental Study and Analytical Prediction of Earthquake Response of a Sliding Isolation System with Spherical Surface*, Technical Report NCEER-90-0020, State University of New York at Buffalo: Buffalo, NY, USA.
53. Monzon EV, Buckle IG, Itani AM (2013). *Seismic Performance of Curved Steel Plate Girder Bridges with Seismic Isolation*, Report CCEER 13-06. Center for Civil Engineering Earthquake Research, University of Nevada, Reno, May, 2013.



54. Nagarajaiah S, Ferrell K (1999). “Stability of elastomeric isolation bearings”, *J. Struct. Eng.* 125:946–954.
55. Neuenhofer A, Filippou FC (1997). “Evaluation of nonlinear frame finite-element models”, *Journal of Structural Engineering* (ASCE), 123(7): 958-966.
56. Nishiyama I, Okawa I, Fukuyama H, Okuda Y (2011). “Building damage by the 2011 off the Pacific coast of Tohoku earthquake and coping activities by NILIM and BRI collaborated with the administration,” *A Report to the U.S.-Japan Cooperative Program in Natural Resources (UJNR) Panel on Wind and Seismic Effects*, Japan Public Works Research Institute. Retrieved May 15, 2012, From [http://www.kenken.go.jp/english/contents/topics/pdf/report\\_ujnr2011.pdf](http://www.kenken.go.jp/english/contents/topics/pdf/report_ujnr2011.pdf)
57. Open System for Earthquake Engineering Simulation (OpenSees), Version 2.2.2. Pacific Earthquake Engineering Research Center, University of California, Berkeley. Retrieved May 15, 2010, From <http://opensees.berkeley.edu/>.
58. Park YJ, Wen YK, Ang AH-S (1986). “Random vibration of hysteretic systems under bi-directional ground motions”, *Earthquake Engineering and Structural Dynamics* 14:543–557.
59. Ryan KL, Kelly JM, Chopra AK (2005). “Nonlinear model for lead-rubber bearings including axial-load effects”, *J. Eng. Mech.* 131:1270–1278.
60. Ryan, KL, Coria CB, Dao ND (2013a). *Large Scale Earthquake Simulation of a Hybrid Lead Rubber Isolation System Designed under Nuclear Seismicity Considerations*, Technical Report CCEER-13-09, Center for Civil Engineering Earthquake Research, University of Nevada, Reno, NV, USA

61. Ryan KL, Sato E, Sasaki T, Okazaki T, Guzman JP, Dao ND, Soroushian S, Coria CB (2013b). "Full Scale 5-story Building with Triple Pendulum Bearings at E-Defense", Network for Earthquake Engineering Simulation (database), Dataset, DOI:10.4231/D3X34MR7R
62. Ryan KL, Sato E, Sasaki T, Okazaki T, Guzman JP Dao ND, Soroushian S, Coria CB (2013c). "Full Scale 5-story Building with LRB/CLB Isolation System at E-Defense", Network for Earthquake Engineering Simulation (database), Dataset, DOI:10.4231/D3SB3WZ43
63. Ryan KL, Sato E, Sasaki T, Okazaki T, Guzman JP, Dao ND, Soroushian S, Coria CB (2013d). "Full Scale 5-story Building in Fixed-Base Condition at E-Defense", Network for Earthquake Engineering Simulation (database), Dataset, DOI:10.4231/D3NP1WJ3P
64. Sanchez J, Masroor A, Mosqueda G, Ryan KL (2012). "Static and dynamic stability of elastomeric bearings for seismic protection of structures", *J. Struct. Eng.*, In Press.
65. Sasaki T, Sato E, Ryan KL, Okazaki T, Mahin SA, and Kajiwara K (2012). "NEES/E-Defense base isolation tests: Effectiveness of friction pendulum and lead-rubber bearing systems", *Proc., 15th World Conference on Earthquake Engineering*, Lisbon.
66. Sato N, Kato A, Fukushima Y, Iizuka M (2002). "Shaking table tests on failure characteristics of base isolation system for a DFBR plant", *Nuclear Eng. Des.*, 212:293–305.

67. Sato E, Furukawa S, Kakehi A, Nakashima M (2011). “Full-scale shaking table test for examination of safety and functionality of base-isolated medical facilities”, *Earthq. Eng. Struct. Dyn.* 40:1435–1453.
68. Scott BD, Park R, Priestley MJN (1982). “Stress-strain behavior of concrete confined by overlapping hoops at low and high strain rates”, *ACI Journal Proceedings*, 79(1): 13-27.
69. Soroushian S, Ryan KL, Maragakis M, Sato E, Sasaki T, Okazaki T, Tedesco L, Zaghi AE, Mosqueda G, Alvarez D (2012). “Seismic response of ceiling/sprinkler piping nonstructural systems in NEES TIPS/NEES nonstructural/NIED collaborative tests on a full scale 5-story building”, In *Proceedings of the 2012 ASCE Structures Congress*, Chicago, IL, USA, 29–31 March.
70. Tagawa Y and Kajiwara K (2007). “Controller development for the E-Defense shaking table”, Proc. IMechE Vol. 221, Part I, *J. Systems and Control Engineering*.
71. Takaoka E, Takenaka Y, Nimura A (2011). “Shaking table tests and analysis method on ultimate behavior of slender base-isolated structure supported by laminated rubber bearings”, *Earthq. Eng. Struct. Dyn.* 40:551–570.
72. Uang C-M, Bertero VB (1986). *Earthquake Simulation Tests and Associated Studies of a 0.3-Scale Model of a Six-Story Concentrically Braced Steel Structure*, Report No. UCB/EERC-86/10; University of California: Berkeley, CA, USA.
73. U.S. Code of Federal Regulations (CFR), (2011). Title 10, Part 50, Domestic Licensing of Production and Utilization Facilities, General Design Criterion (GDC) 2, Design Bases for Protection Against Natural Phenomena in Appendix A, General

- Design Criteria for Nuclear Power Plants, U.S. Nuclear Regulatory Commission, Washington, D.C.
74. Warn GP, Whittaker AS (2006). *A Study of the Coupled Horizontal-Vertical Behavior of Elastomeric and Lead-Rubber Seismic Isolation Bearings*, Technical Report MCEER-07-0012, Multidisciplinary Center for Earthquake Engineering Research, State University of New York at Buffalo: Buffalo, NY, USA.
75. Warn GP, Whittaker AS, Constantinou MC (2007). “Vertical stiffness of elastomeric and lead-rubber seismic isolation bearings”, *ASCE J. Struct. Eng.* 133:1227–1236.
76. Warn GP, Ryan KL (2012). “A review of seismic isolation for buildings: historical developments and research needs”, *Buildings (Open Access)*, In Press.
77. Weisman J, Warn GP (2012). “Stability of Elastomeric and Lead-Rubber Seismic Isolation Bearings”, *J. Struct. Eng.*, 138(2), 215–223.
78. Whittaker AS, Uang C-M, Bertero VB (1990). *An Experimental Study of the Behavior of Dual Steel Systems*, Report No. UCB/EERC-88/14; University of California: Berkeley, CA, USA.
79. Yamamoto S, Kikuchi M, Ueda M, Aiken ID (2009). “A mechanical model for elastomeric seismic isolation bearings including the influence of axial load”, *Earthq. Eng. Struct. Dyn.* 38:157–180.
80. Zayas V, Low S, Mahin S (1987). *The FPS Earthquake Resisting System*, Report No. UCB/EERC-87/01; University of California: Berkeley, CA, USA.

## APPENDIX A

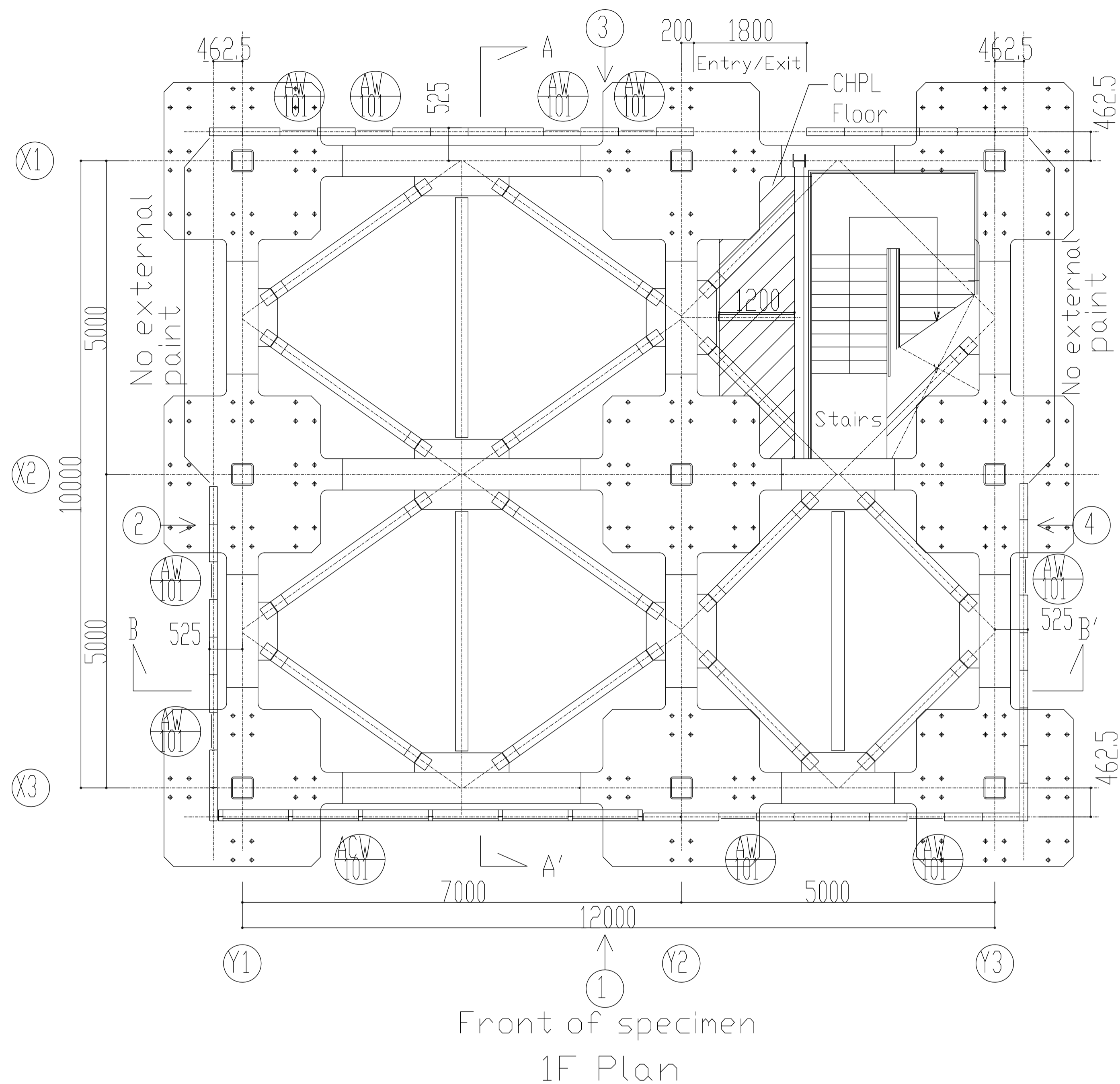
### Design & Construction Drawing for Testing of Value-Added Damped Building

Building Isolated with Hybrid Lead-Rubber Isolation System

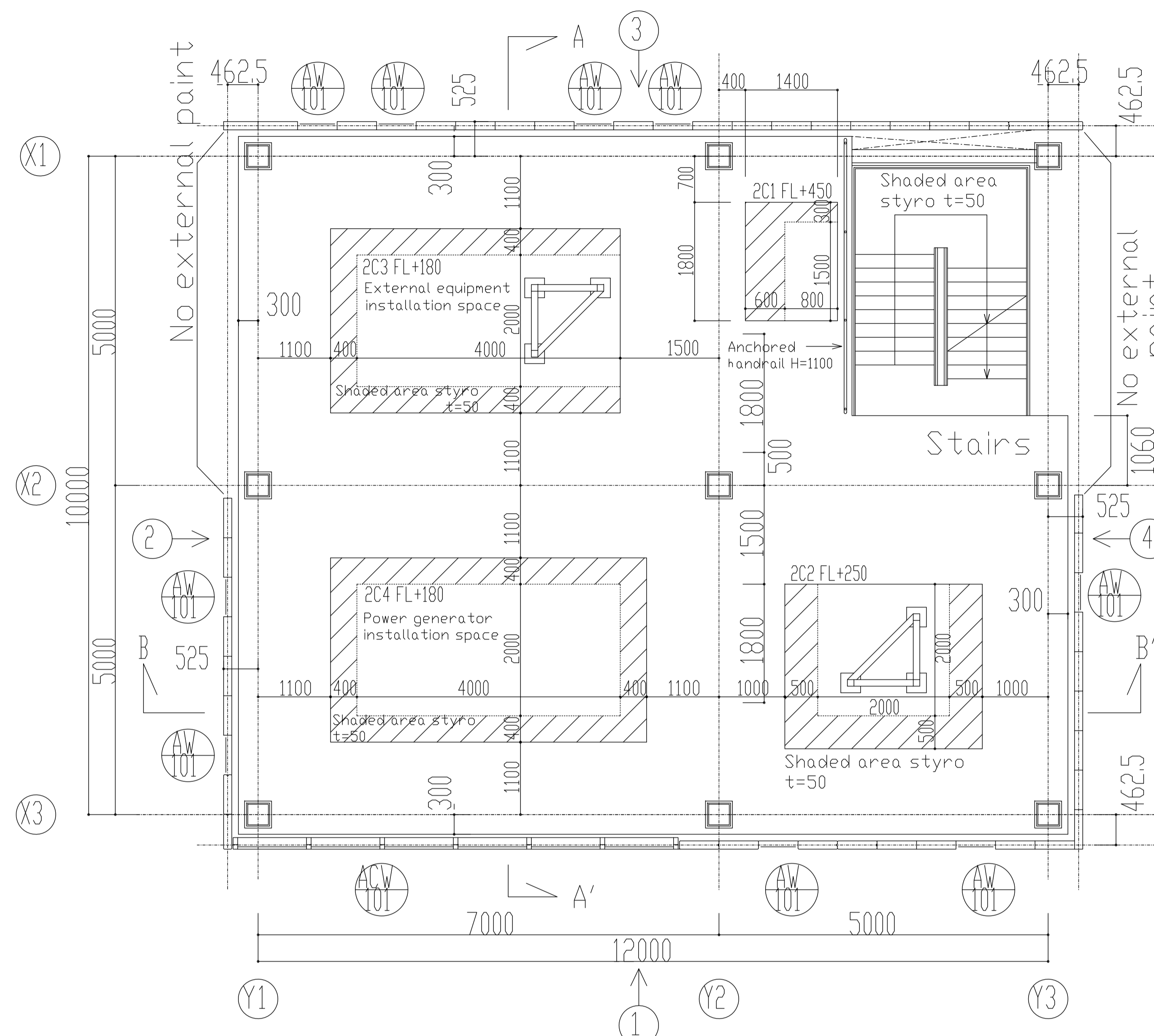
Originals developed by the National Research Institute for Earth Science and Disaster Prevention  
Hyogo Earthquake Engineering Research Center for Value Added Building Project, December 8,  
2008

Modified by NEES TIPS project for NEES/E-Defense Collaborative Test Program on Innovative  
Isolation Systems, 2011-2012

<b>Architectural Drawings</b>		<b>Structural Drawings</b>	
A-001	1F, 2F Plan	S-001	Structure and Particular Specification
A-001a	3F, 4F Plan	S-002	Beam Plans, Framing Elevation
A-002	5F, R Plan	S-003	Material Cross-Sections
A-003c	Elevation 1	S-004	Steel Joint Standard, Test Hoisting Equipment
A-004	Elevation 2	S-005	1F Column Base
A-005	Section	S-006	Steel Structure (1)
A-006	Detailed Area 1	S-007	Steel Structure (2)
A-006a	Detailed Area 2	S-008	Stud, Bolt Layout
A-007	Stair Floor	S-009	QL Deck Layout
A-008	Shaking Table Layout	S-010	High Deck Layout



Front of specimen  
1F Plan



Front of specimen  
2F Plan

Internal Specification

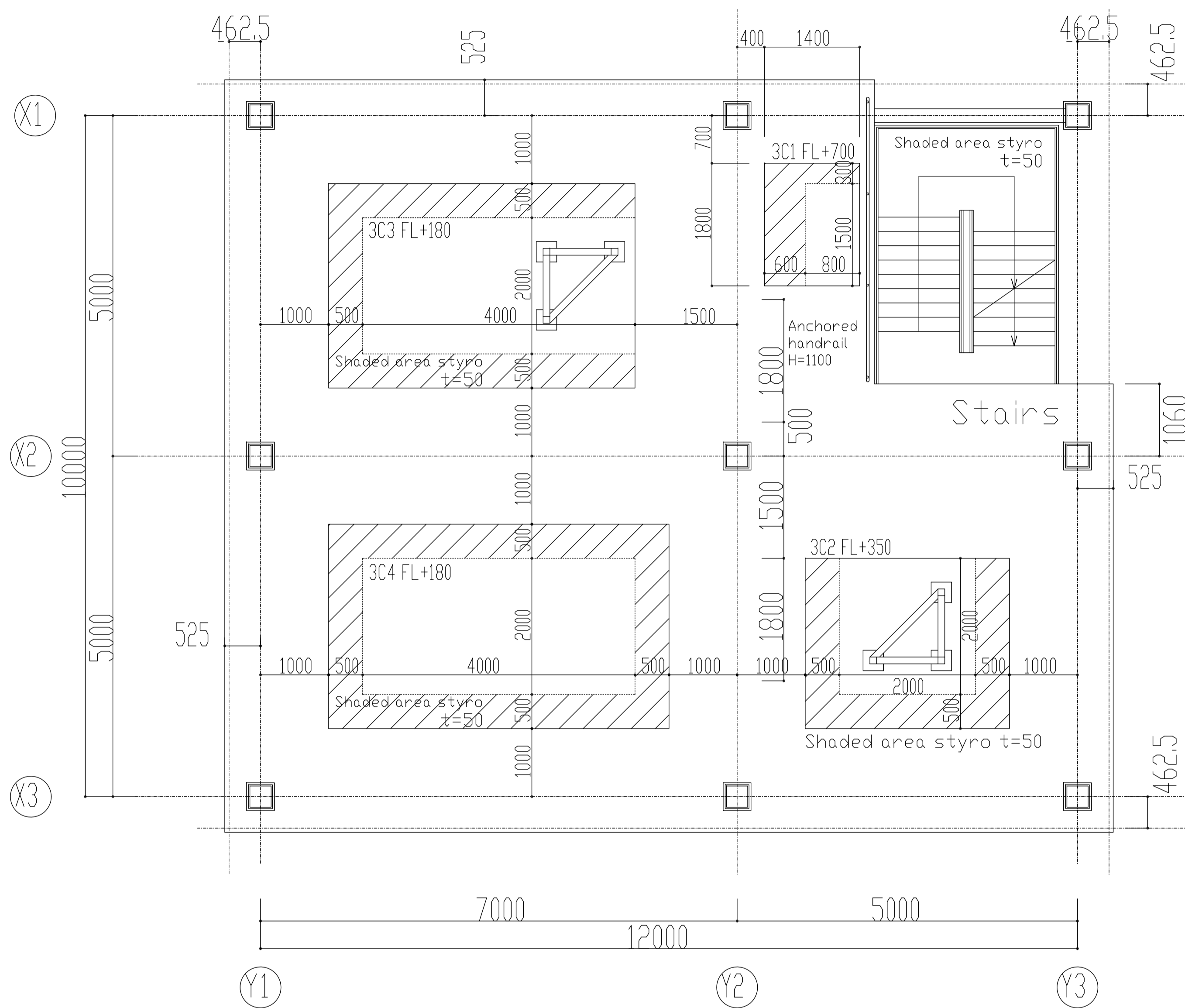
Room	Floor	Baseboard	Wall	Ceiling
Office	-	-	Plaster board t=9.5+12.5 LGS Backing	Installed only for non value-added experiment
Stairwell	Mortar finish with wood float	-	-	-

Fittings

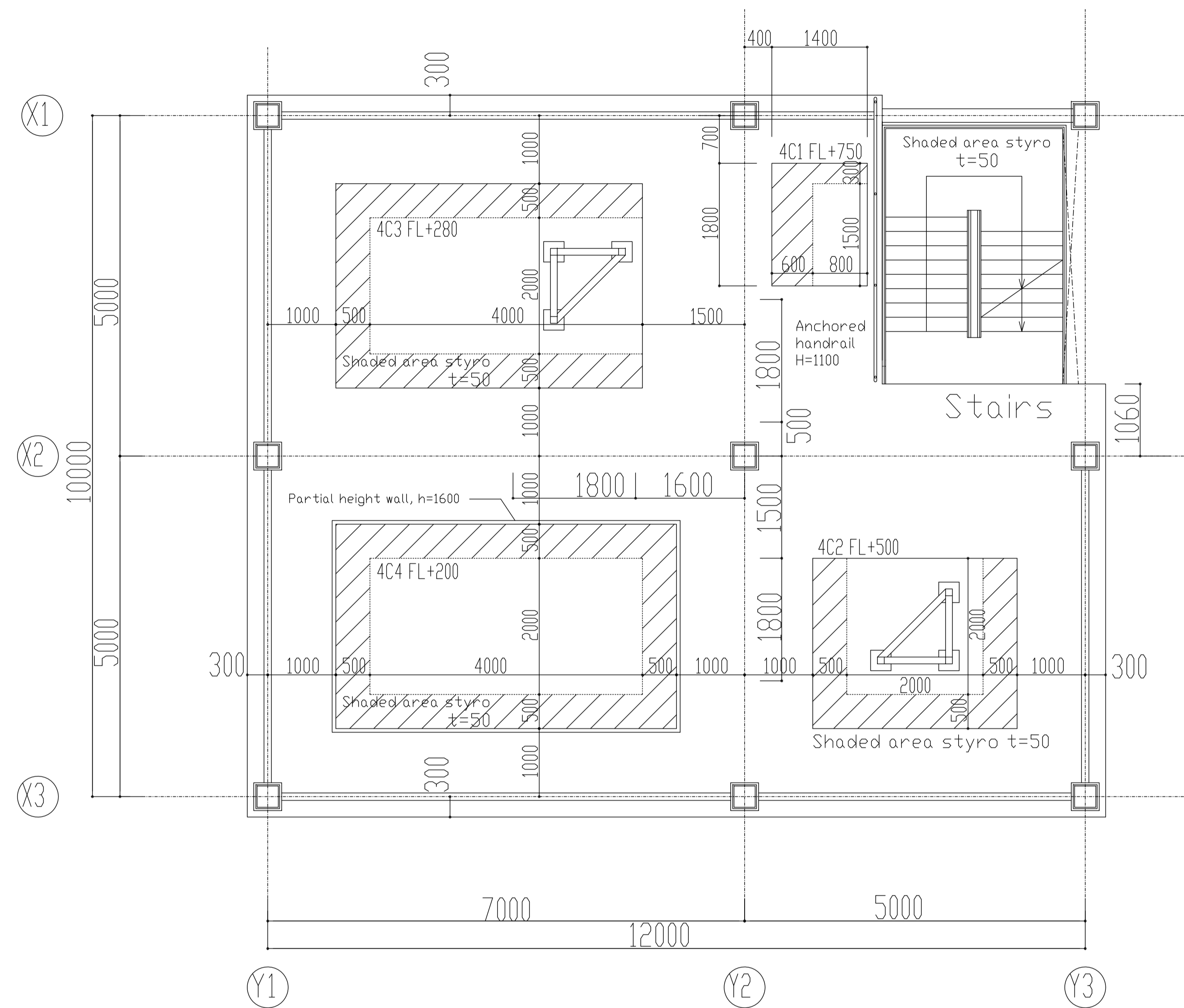
Code (Material)	Region	Type, Structure	Internal Dimensions (WxH)	Material, Finish	Note
AW101	4F-5F	Fixed window	W560xH560	Aluminum alumite	Glass FL-6
ACW101	4F-5F	Refer to Elevation	Fixed window	Aluminum alumite	Glass FL-10
AW101	2F-5F	Double sliding window	W1800xH2100	Steel	Glass FL-8 Threshold plate: steel t=2.0

Revised	///
///	///
///	///
///	///
///	///
///	///

National Research Institute for Earth Science and Disaster Prevention Hyogo Earthquake Engineering Research Center		2
Value-added Five-story Steel Frame Experiment Specimen Design Drawing		2008.11.7
1F, 2F Plan	A1:1/50 A3:1/100	A-001

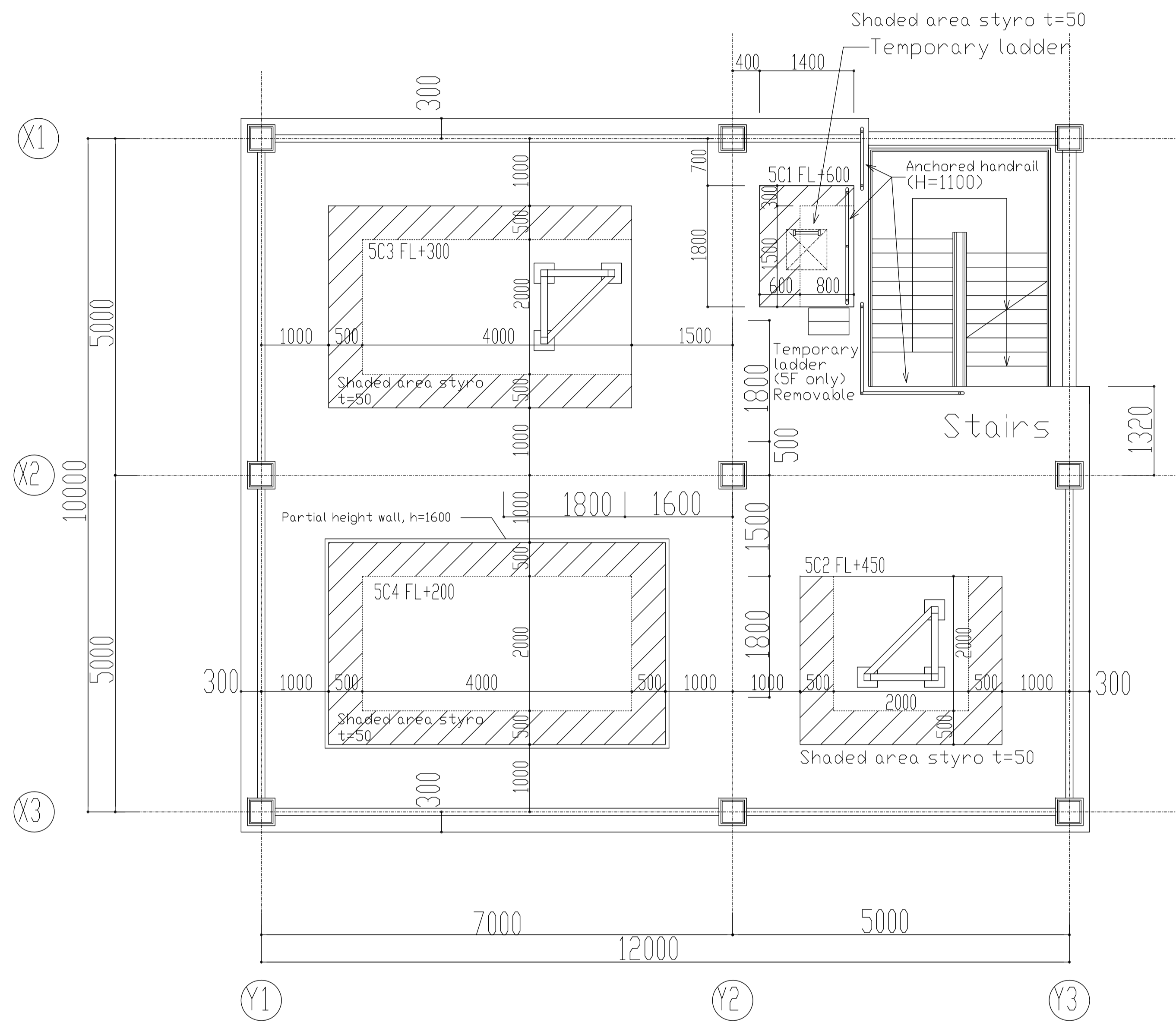


Front of specimen  
3F Plan

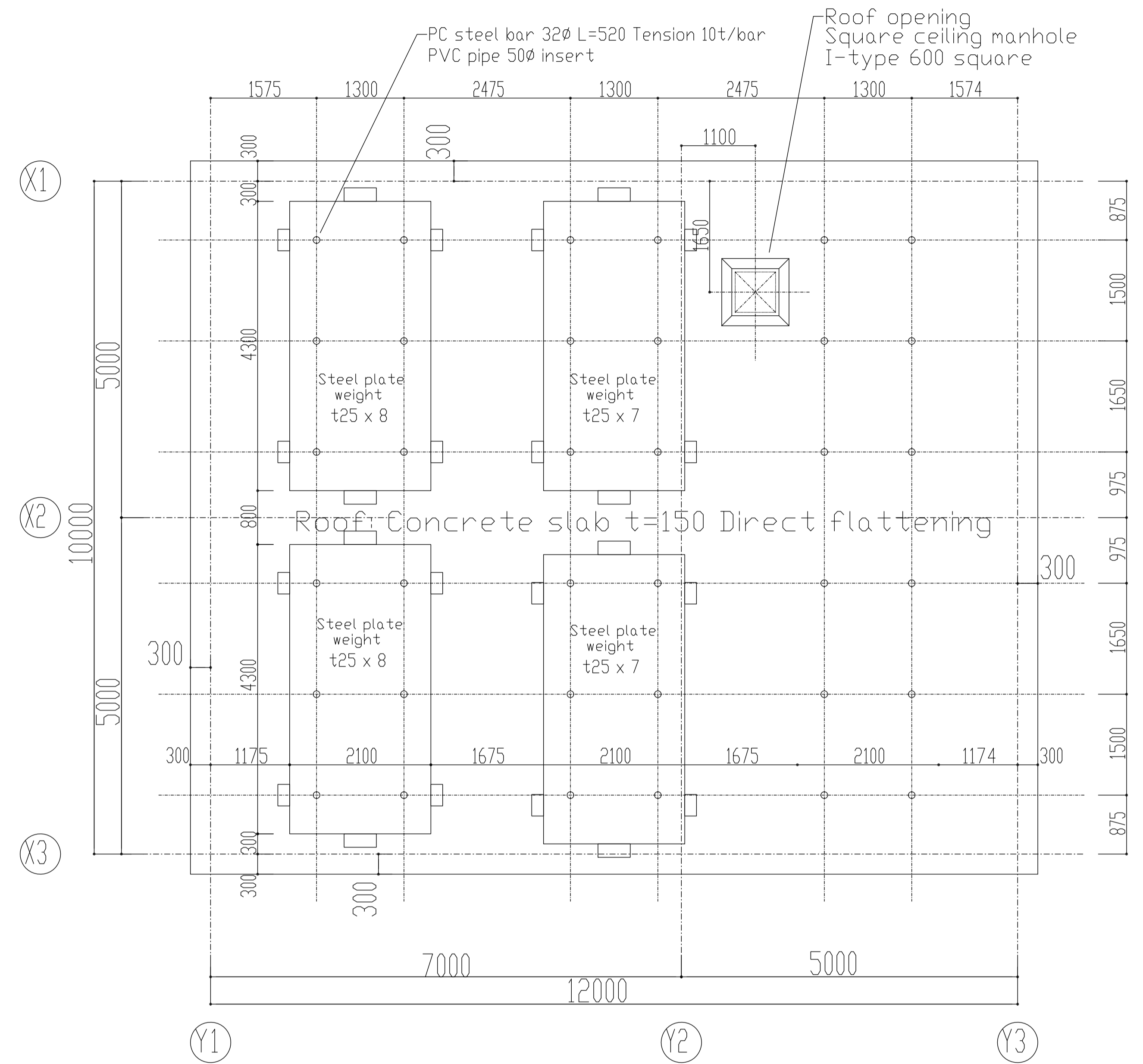


Front of specimen  
4F Plan

Revised	///
	///
	///
	///
	///
	///



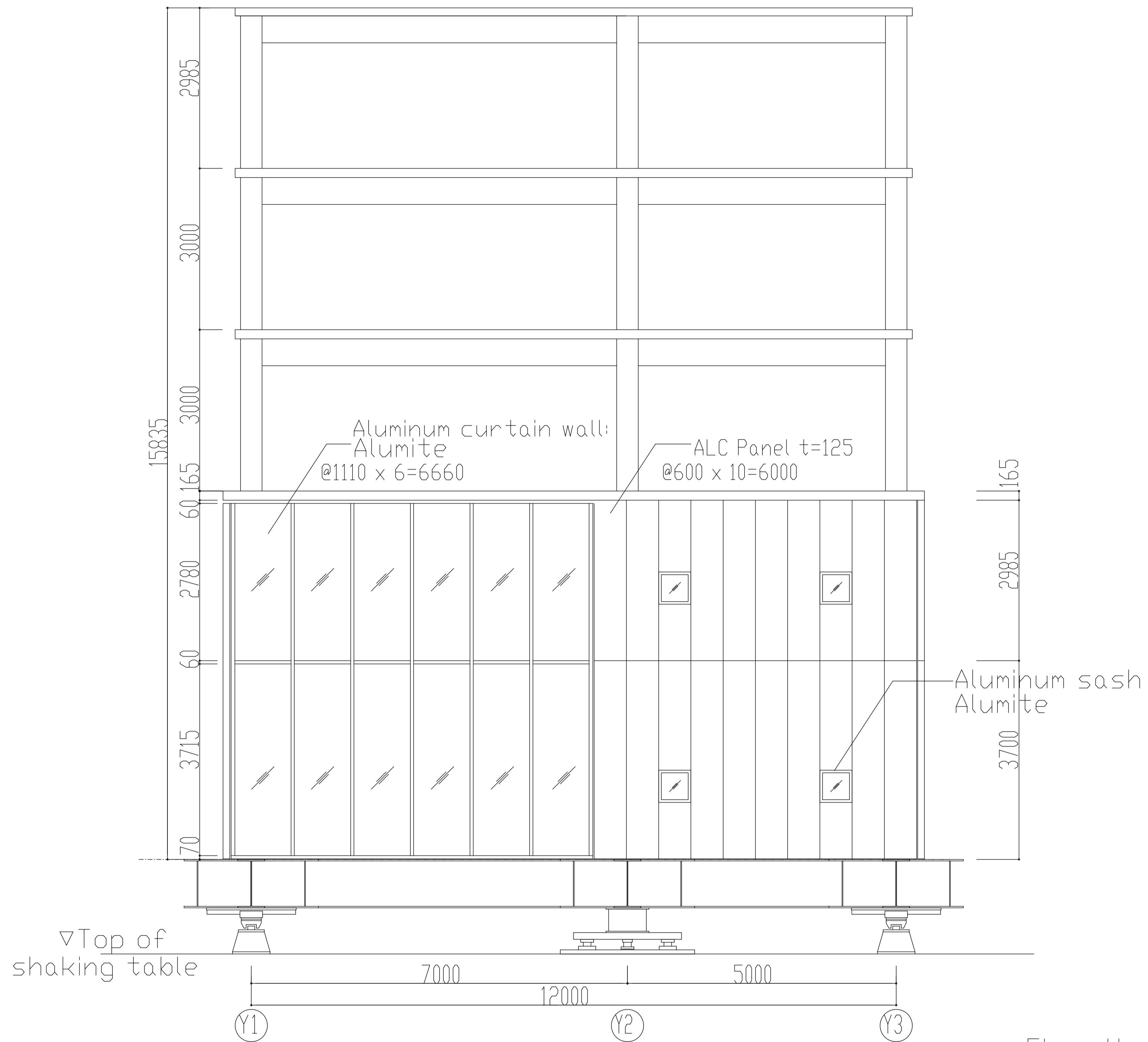
Front of specimen  
5F Plan



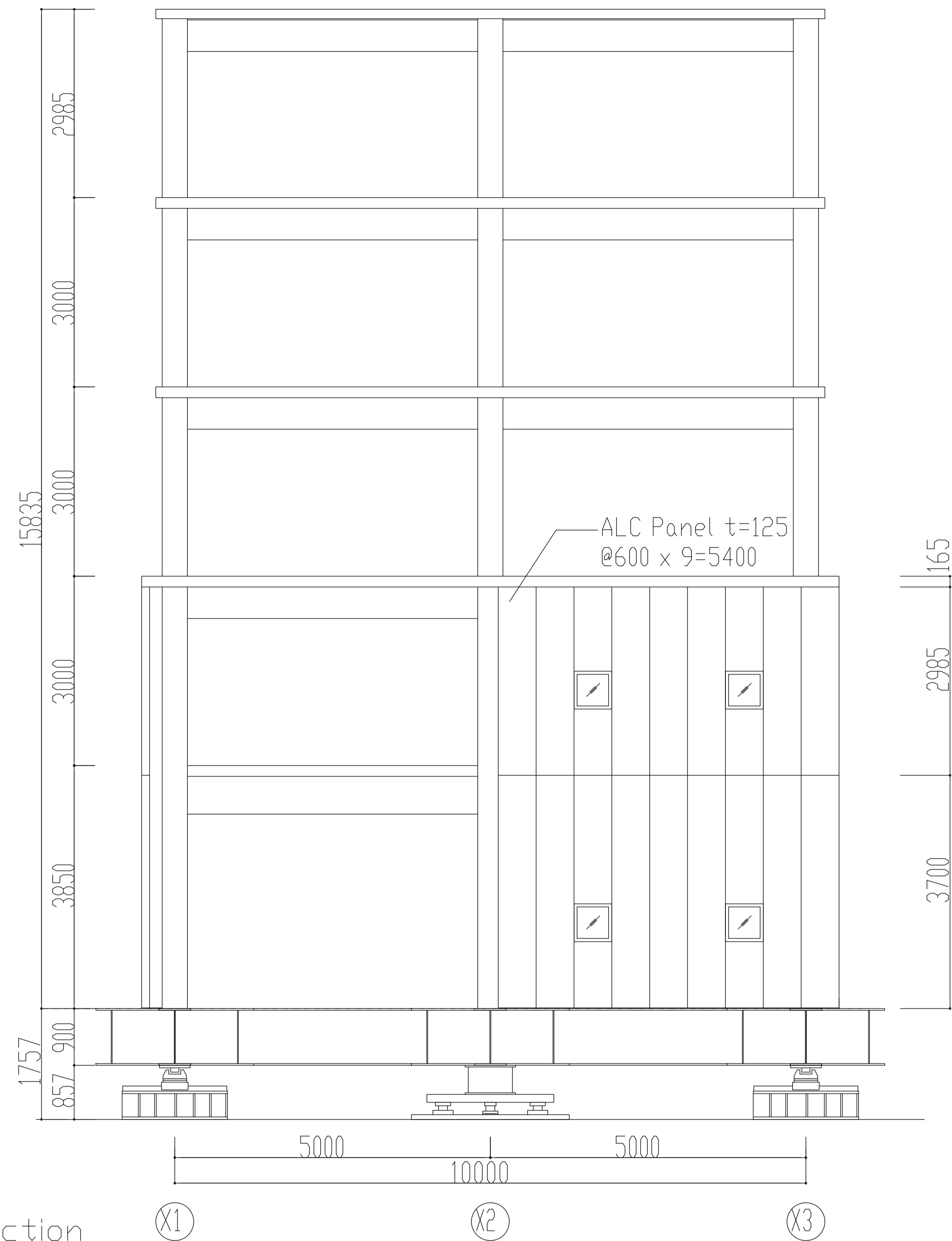
Front of specimen  
RF Plan

Revised	///
	///
	///
	///
	///
	///



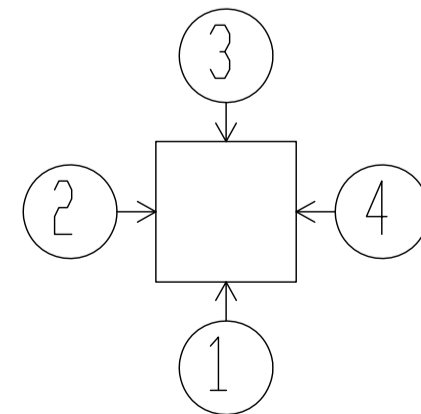


Elevation 1 (Front of specimen)



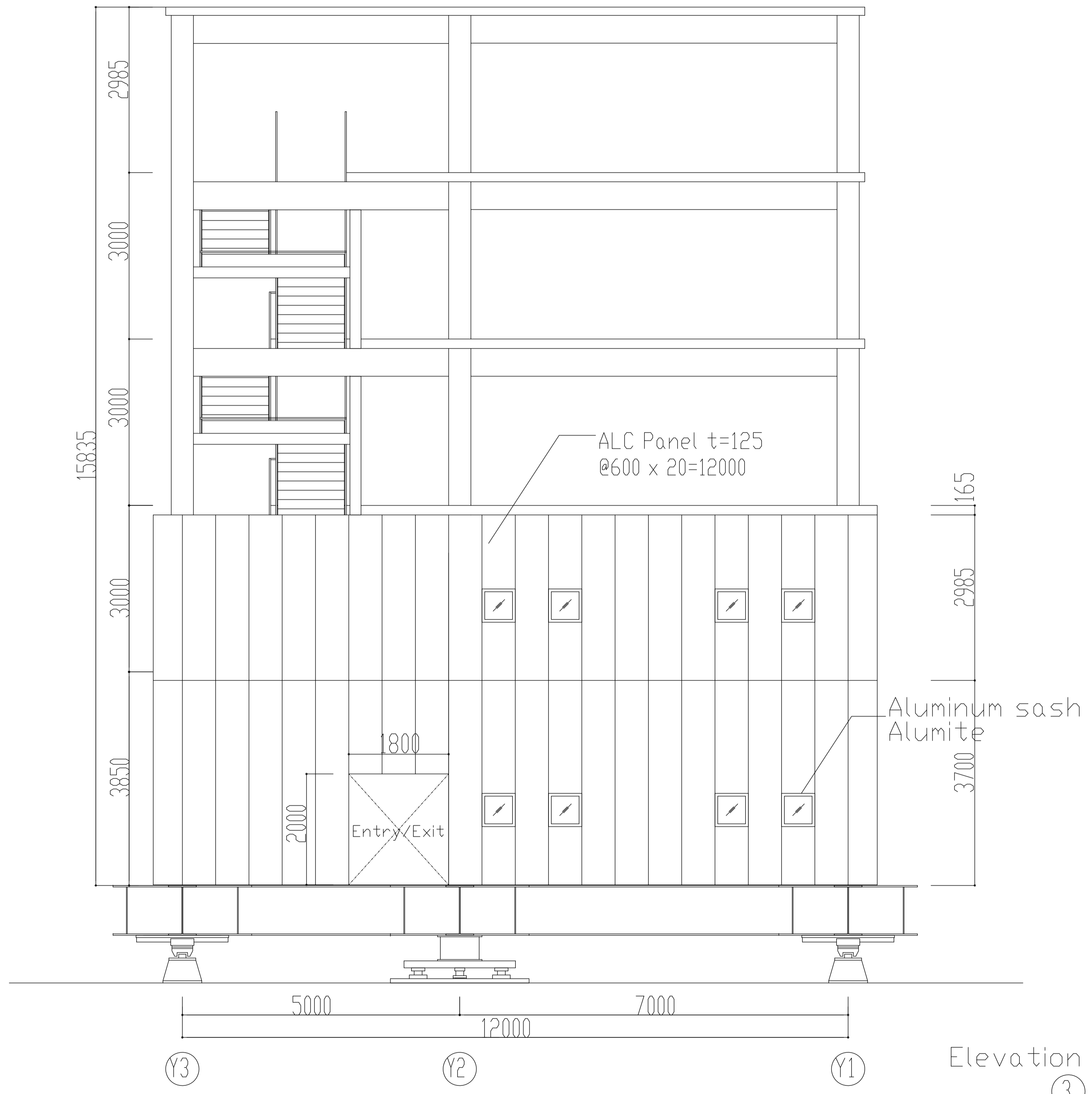
Elevation 2

Elevation direction

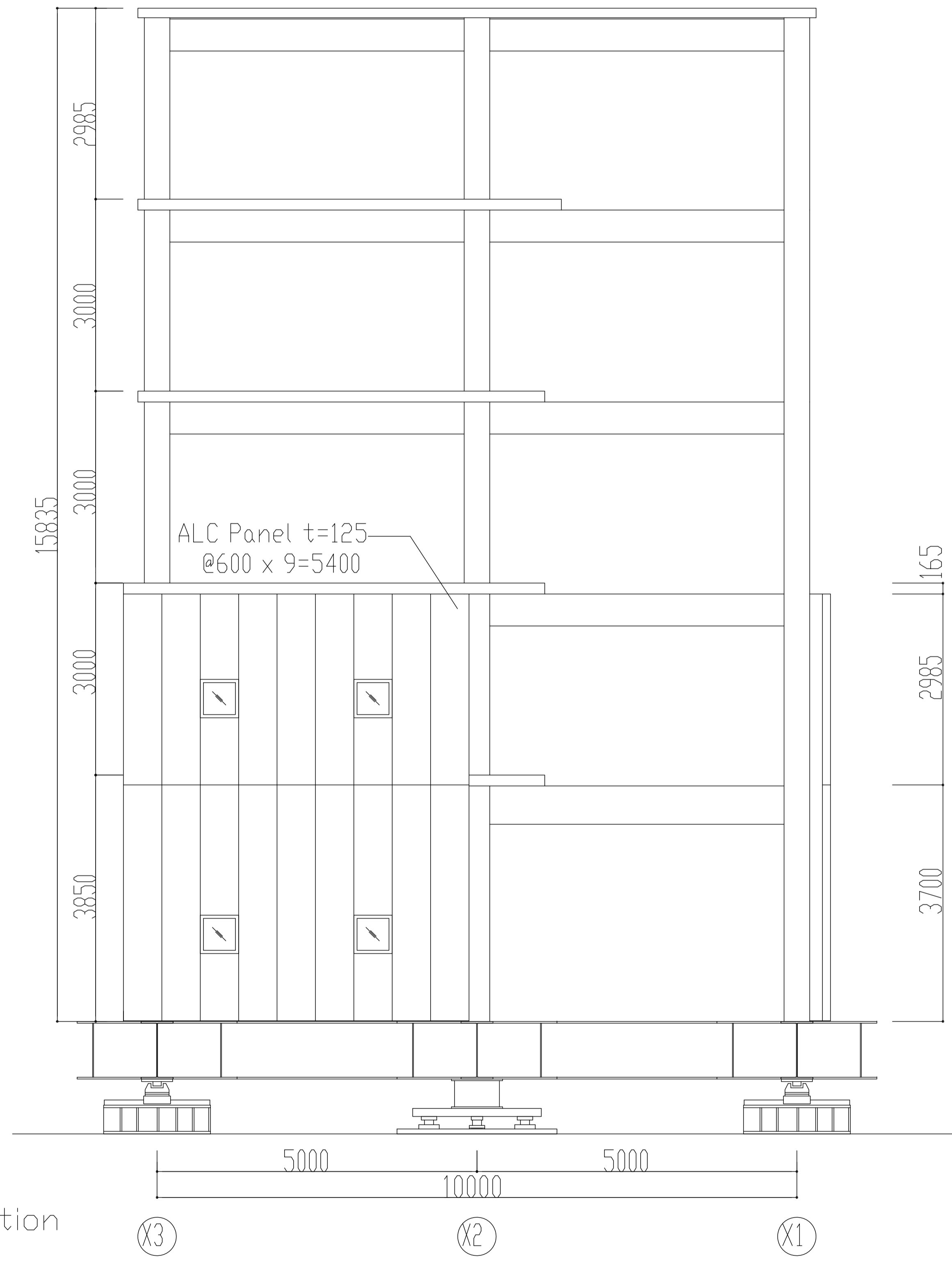


Front of specimen

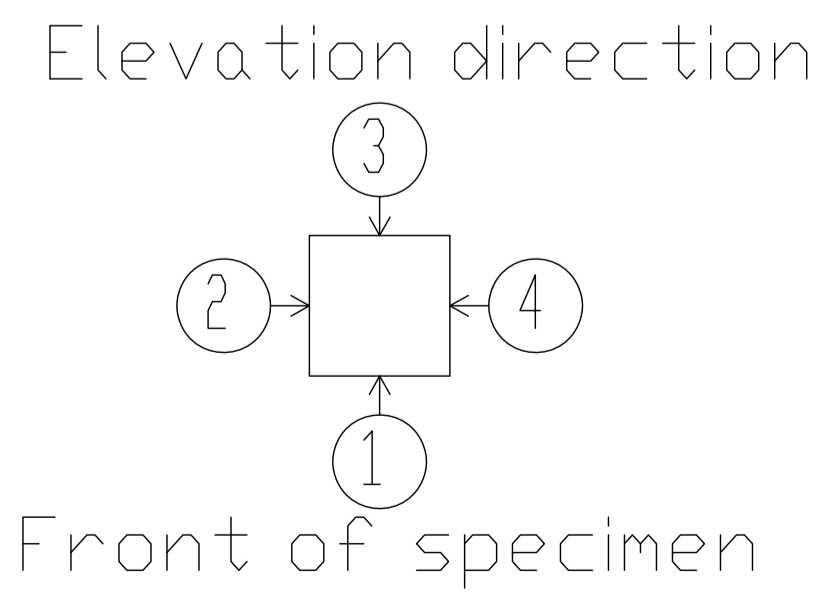
Revised	///
///	///
///	///
///	///
///	///
///	///



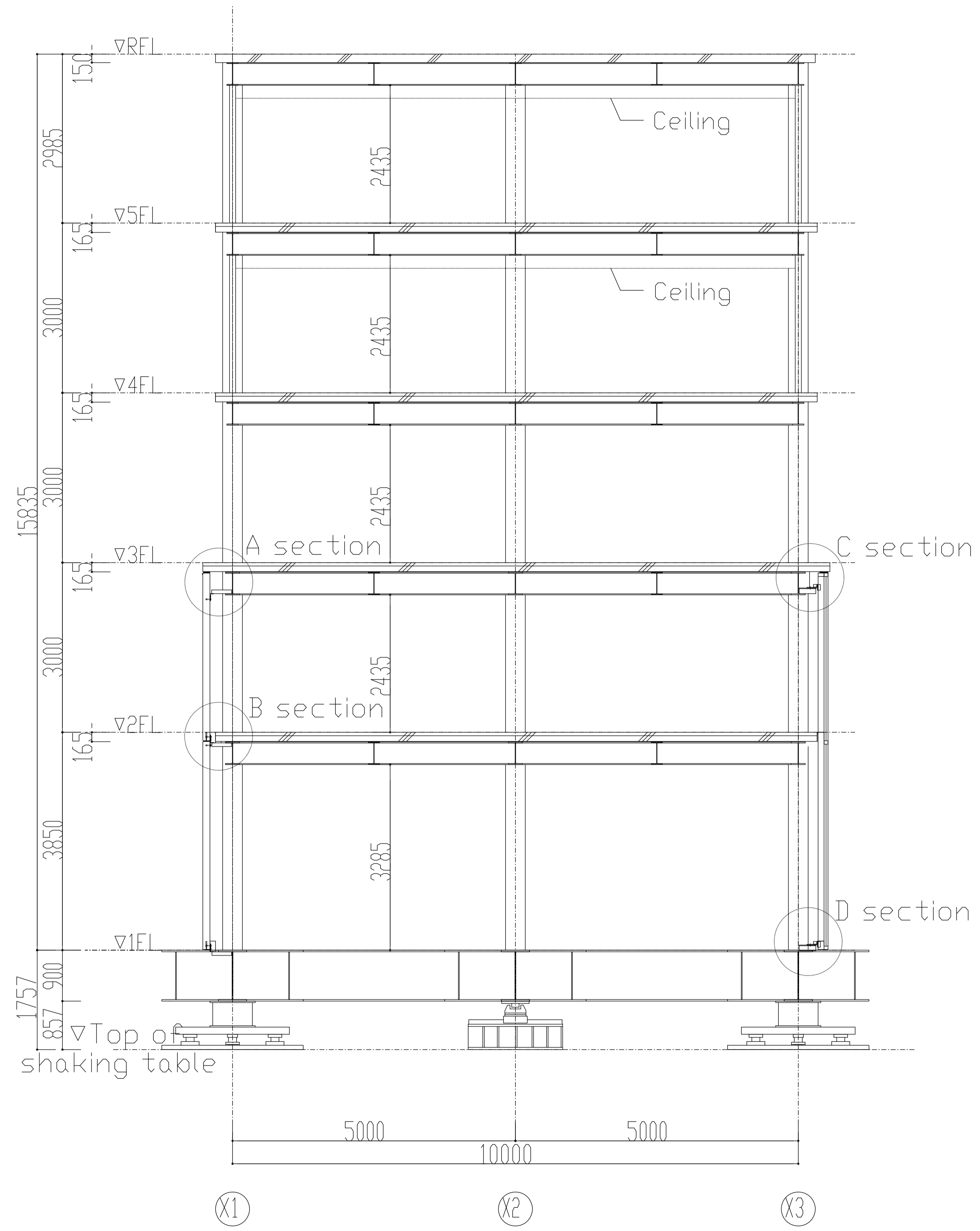
Elevation 3



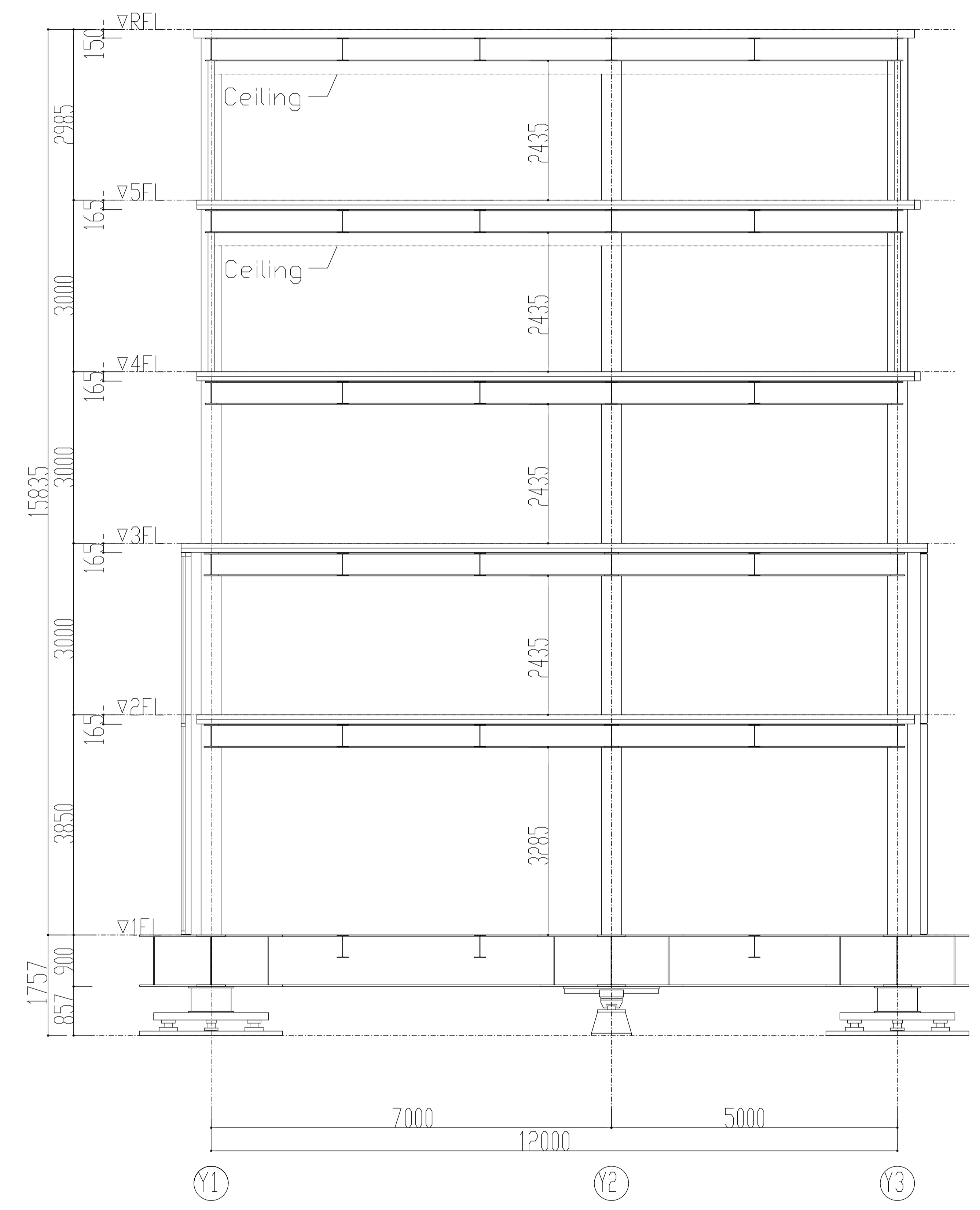
Elevation 4



Revised	///
	///
	///
	///
	///
	///

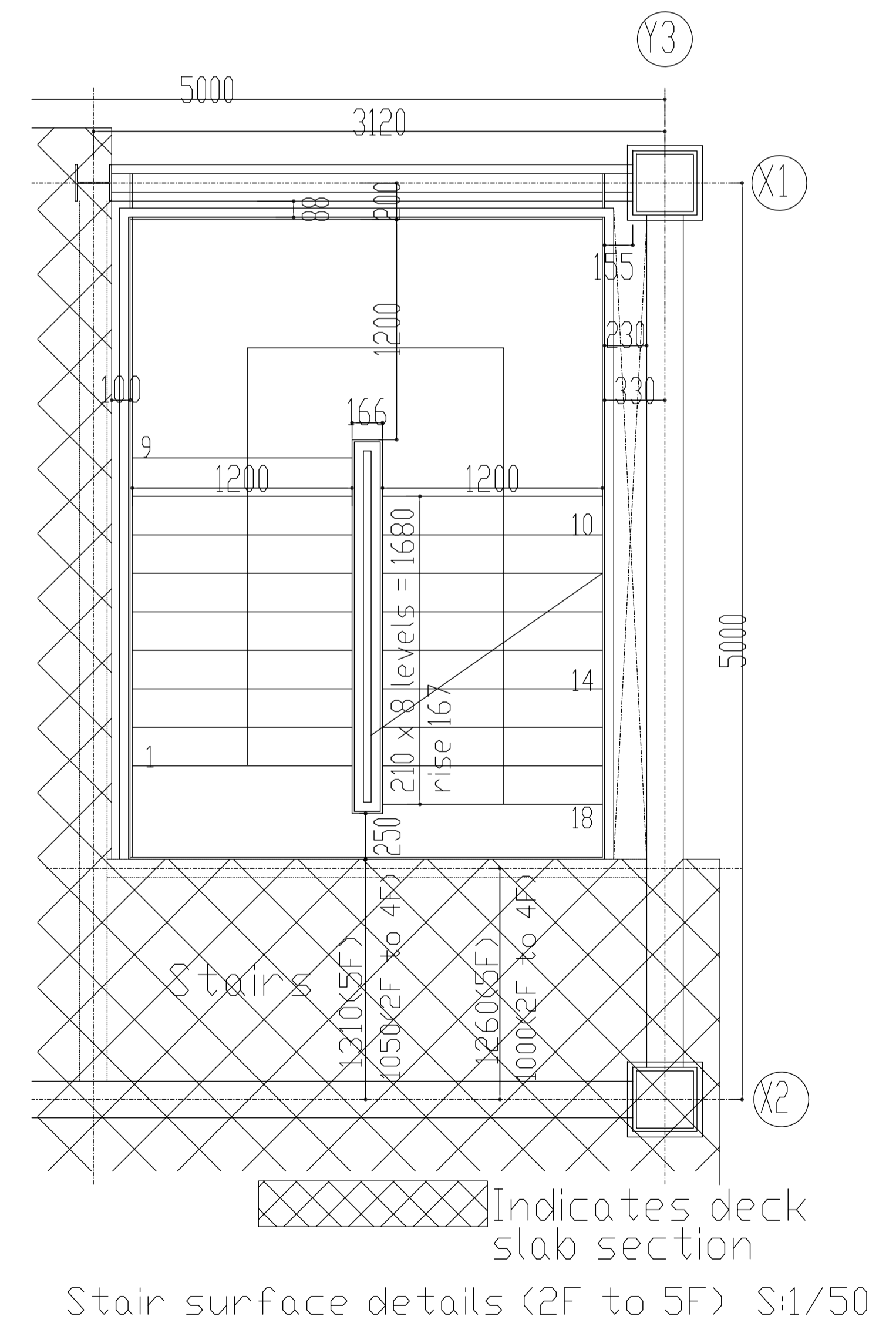
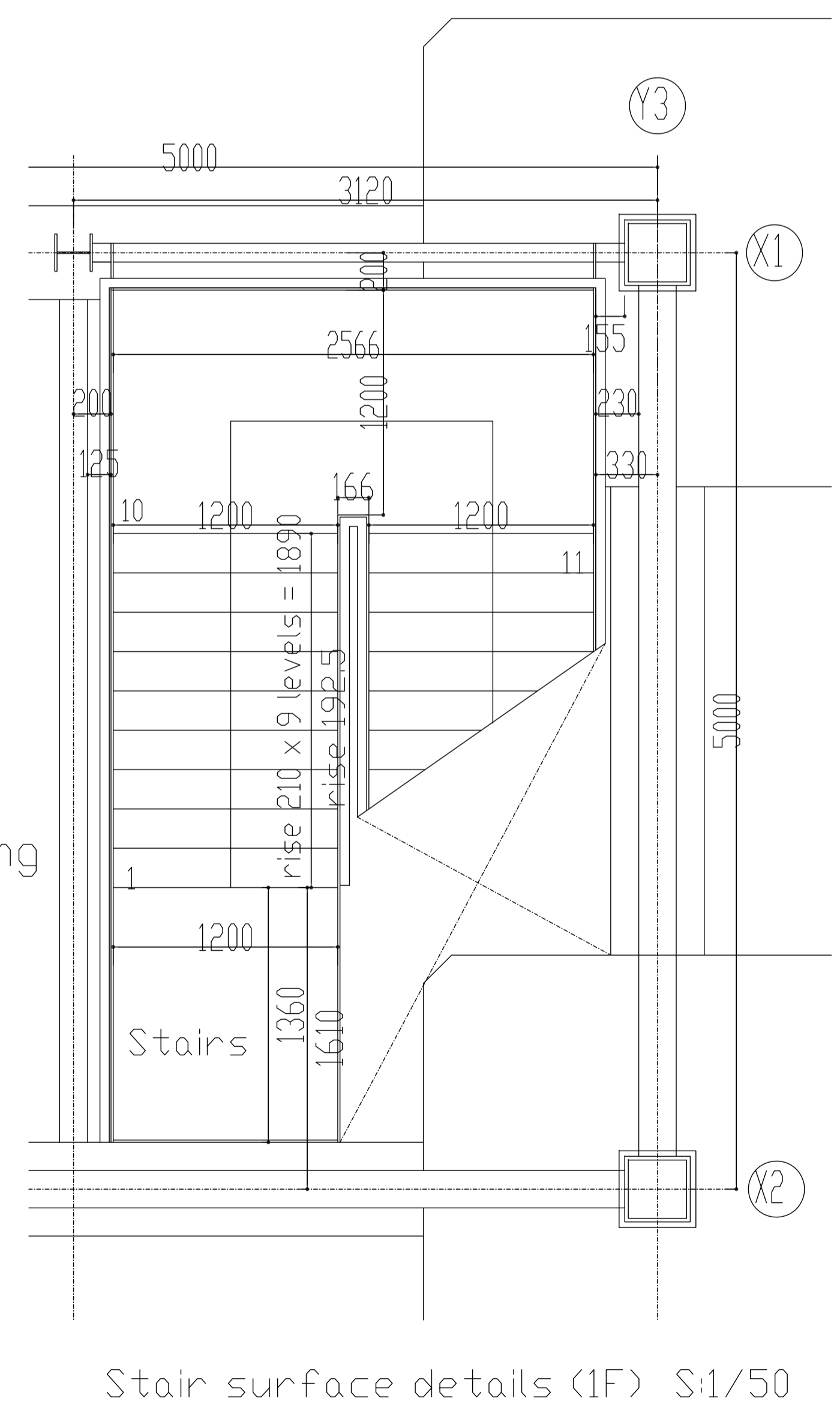
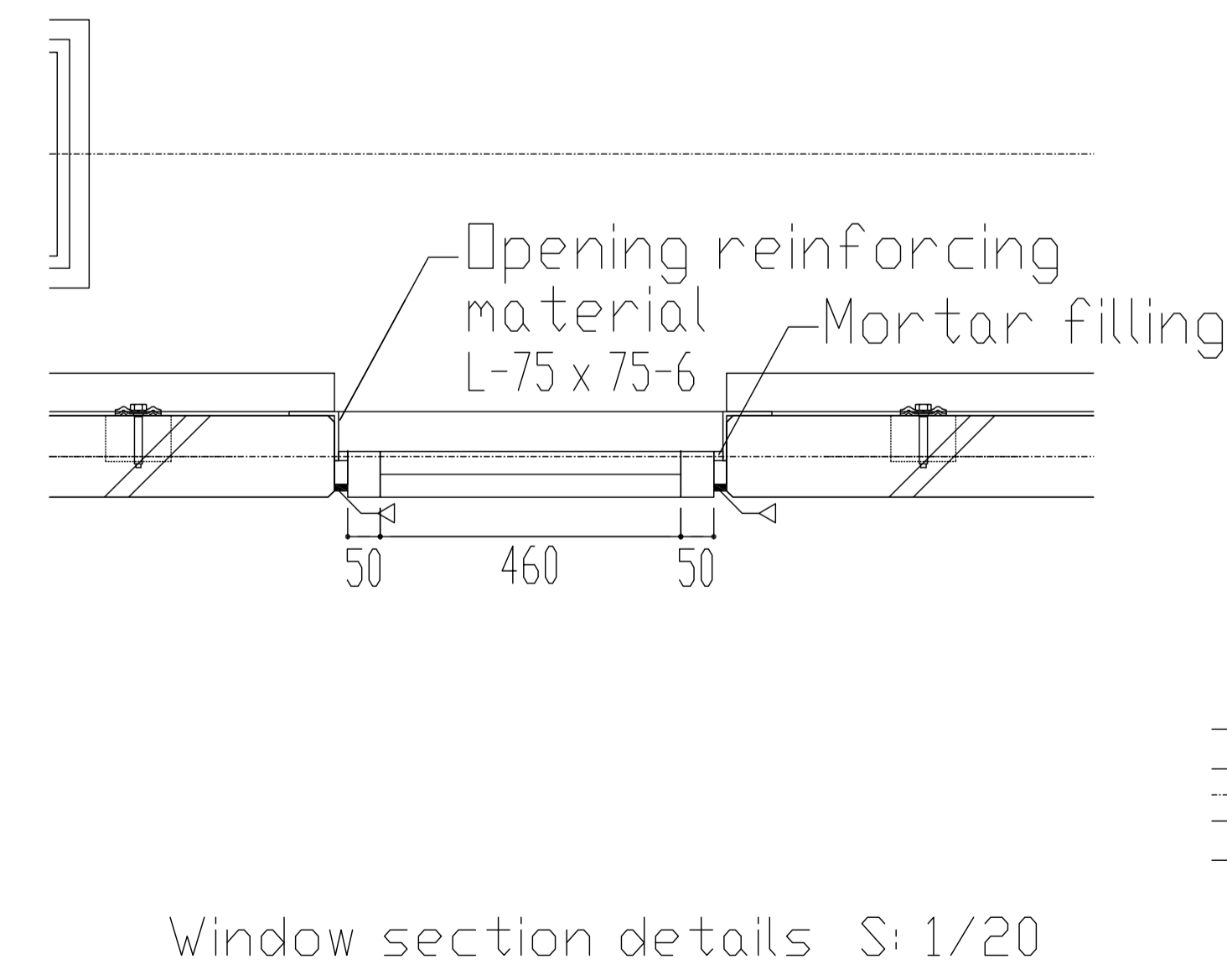
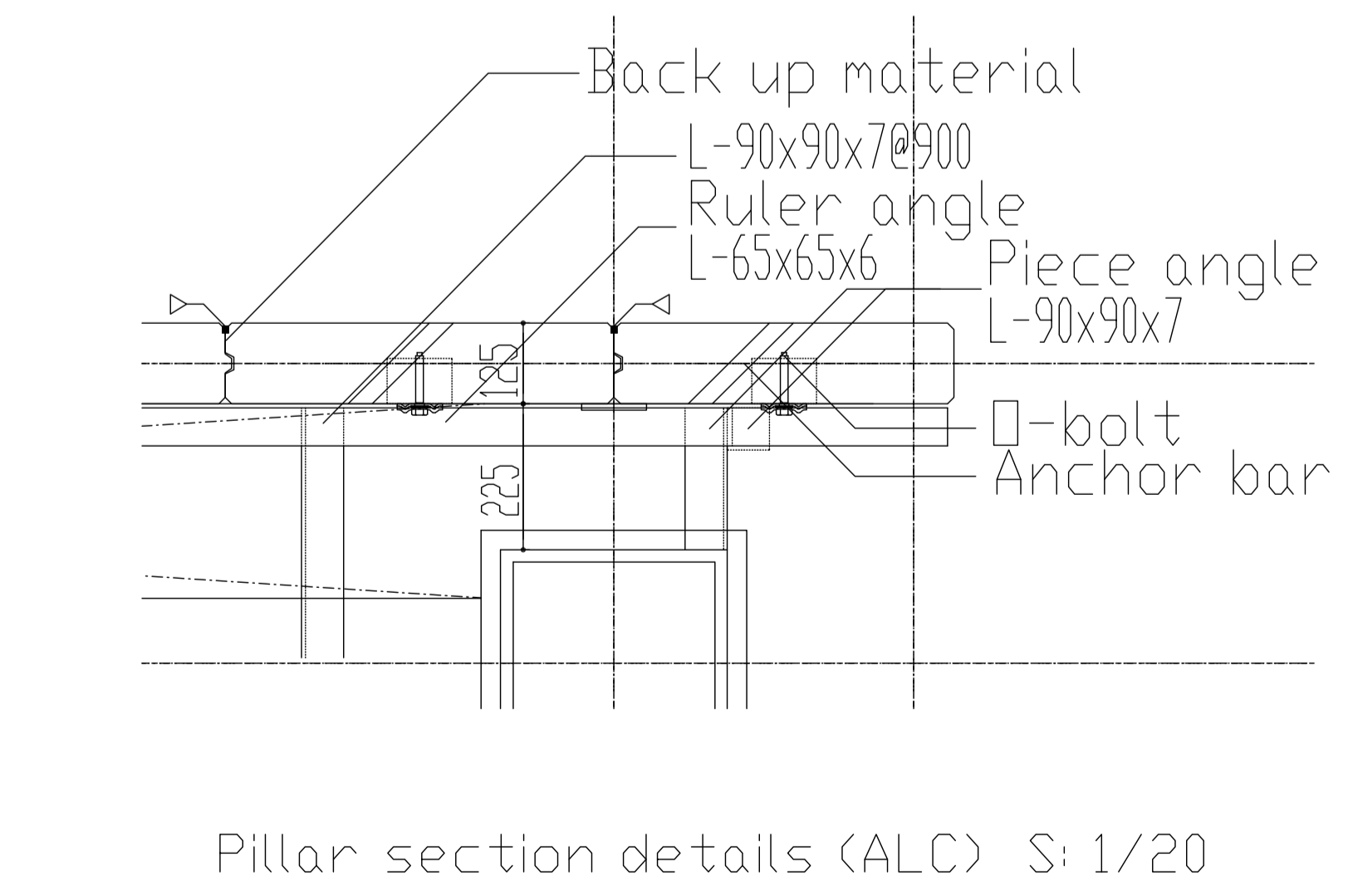
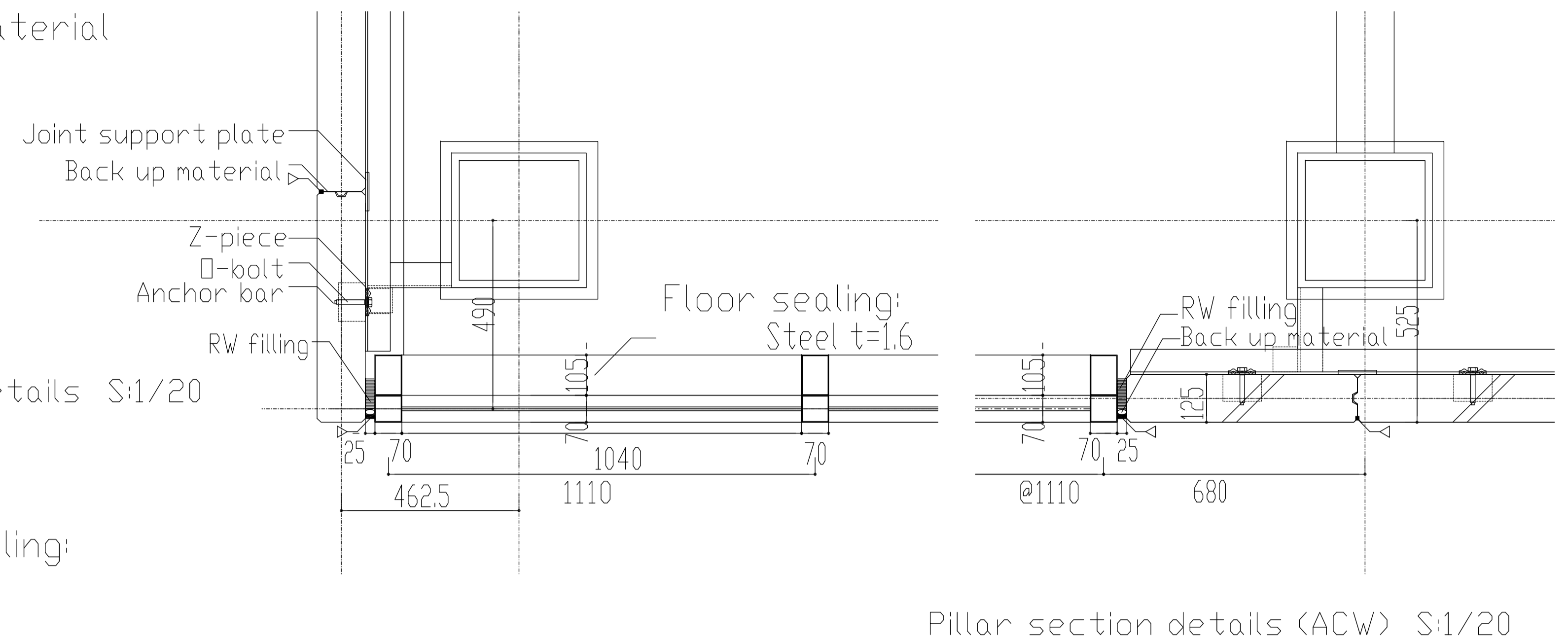
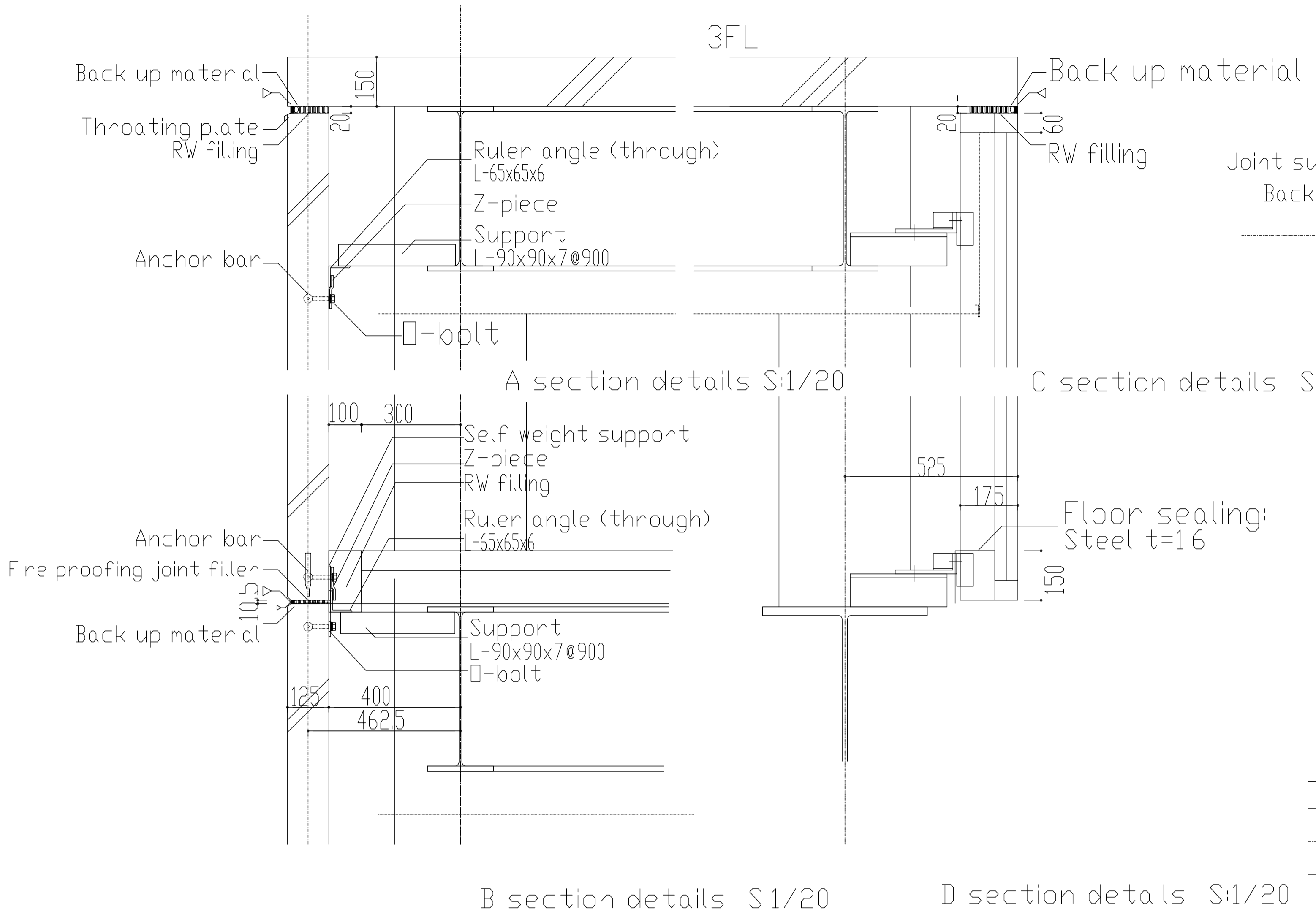


A-A' Section



B-B' Section

Revised	///
	///
	///
	///
	///
	///



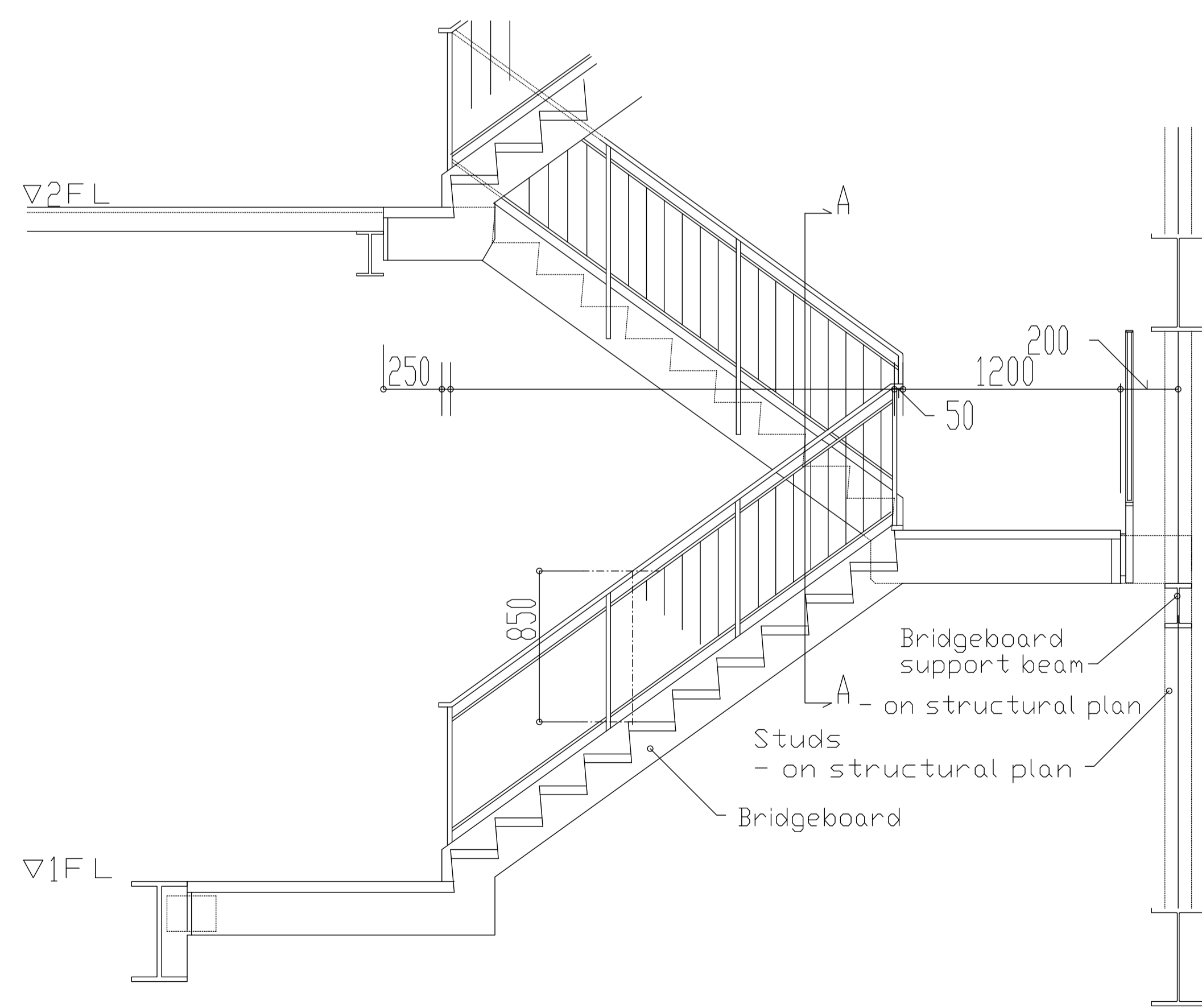
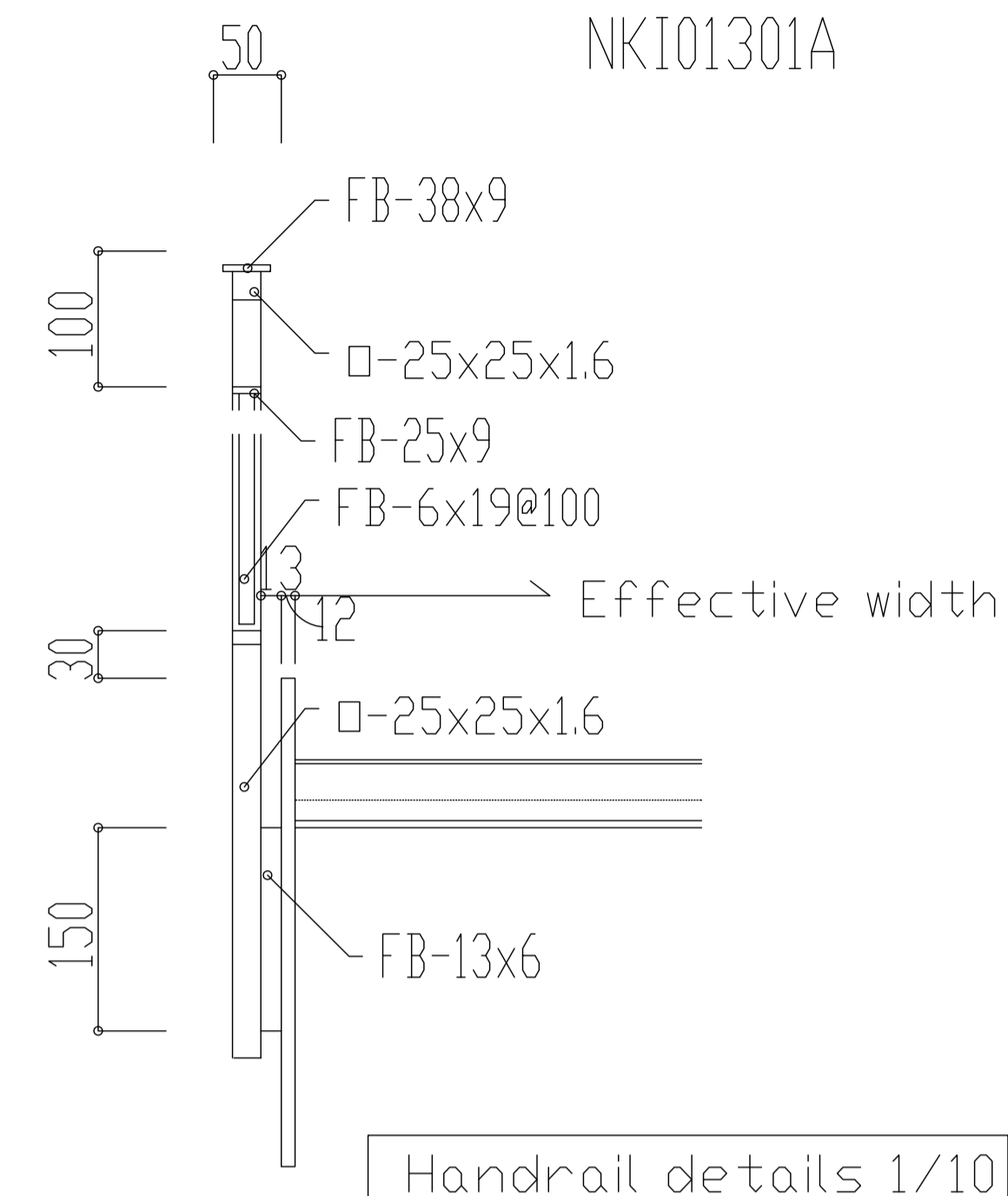
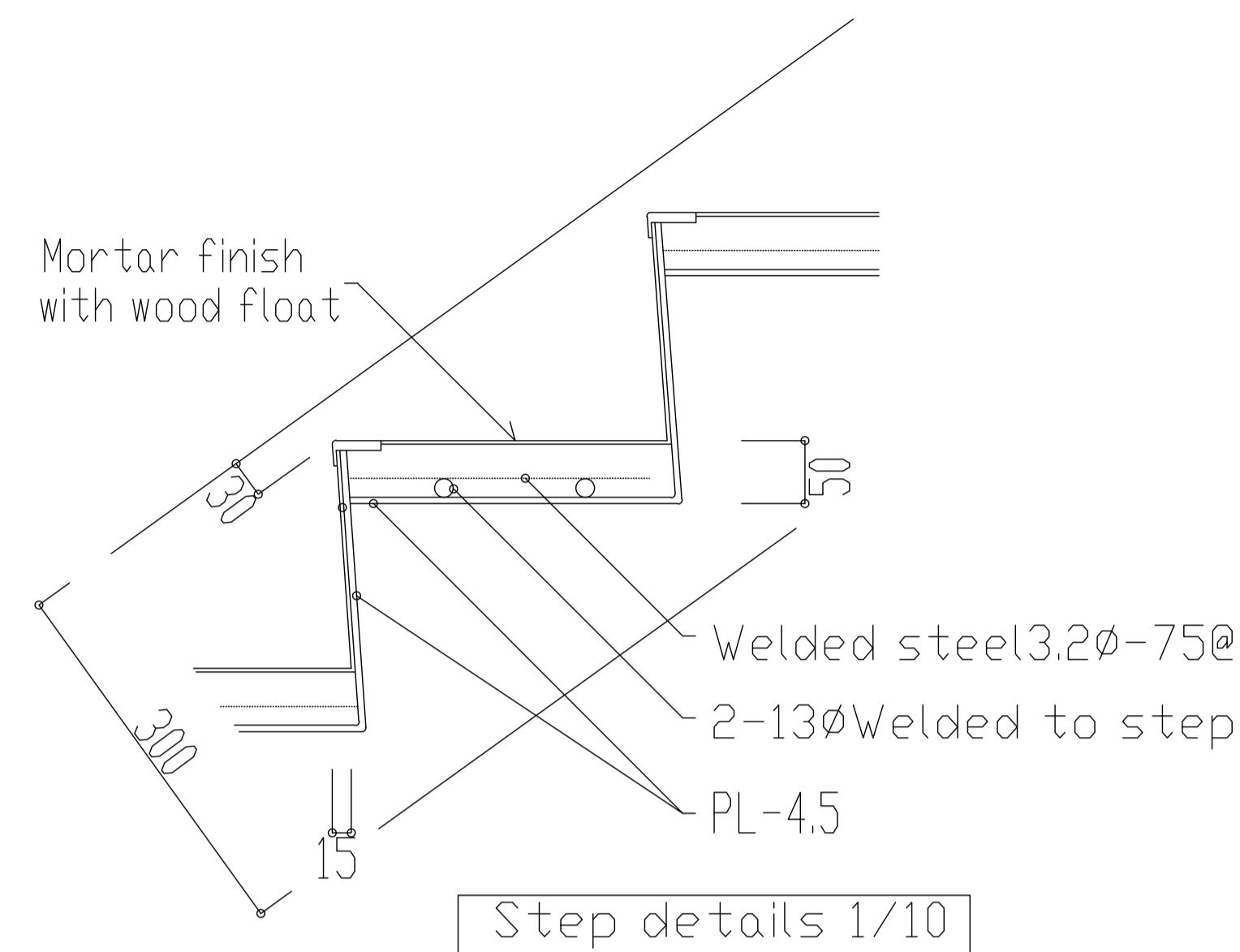
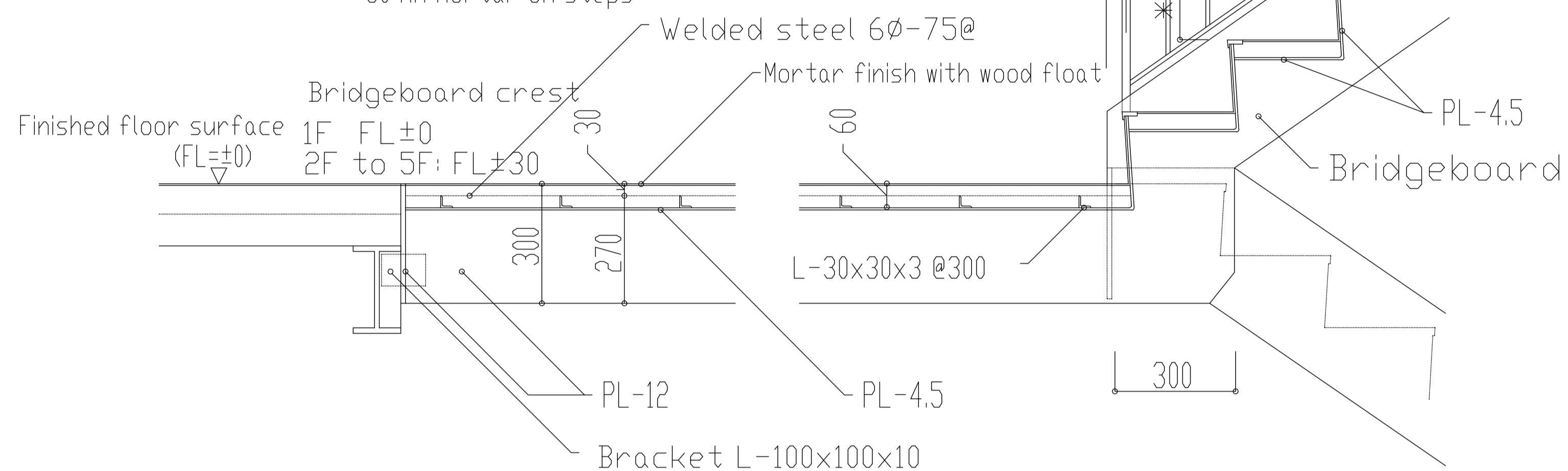
Revised	///
///	///
///	///
///	///
///	///
///	///



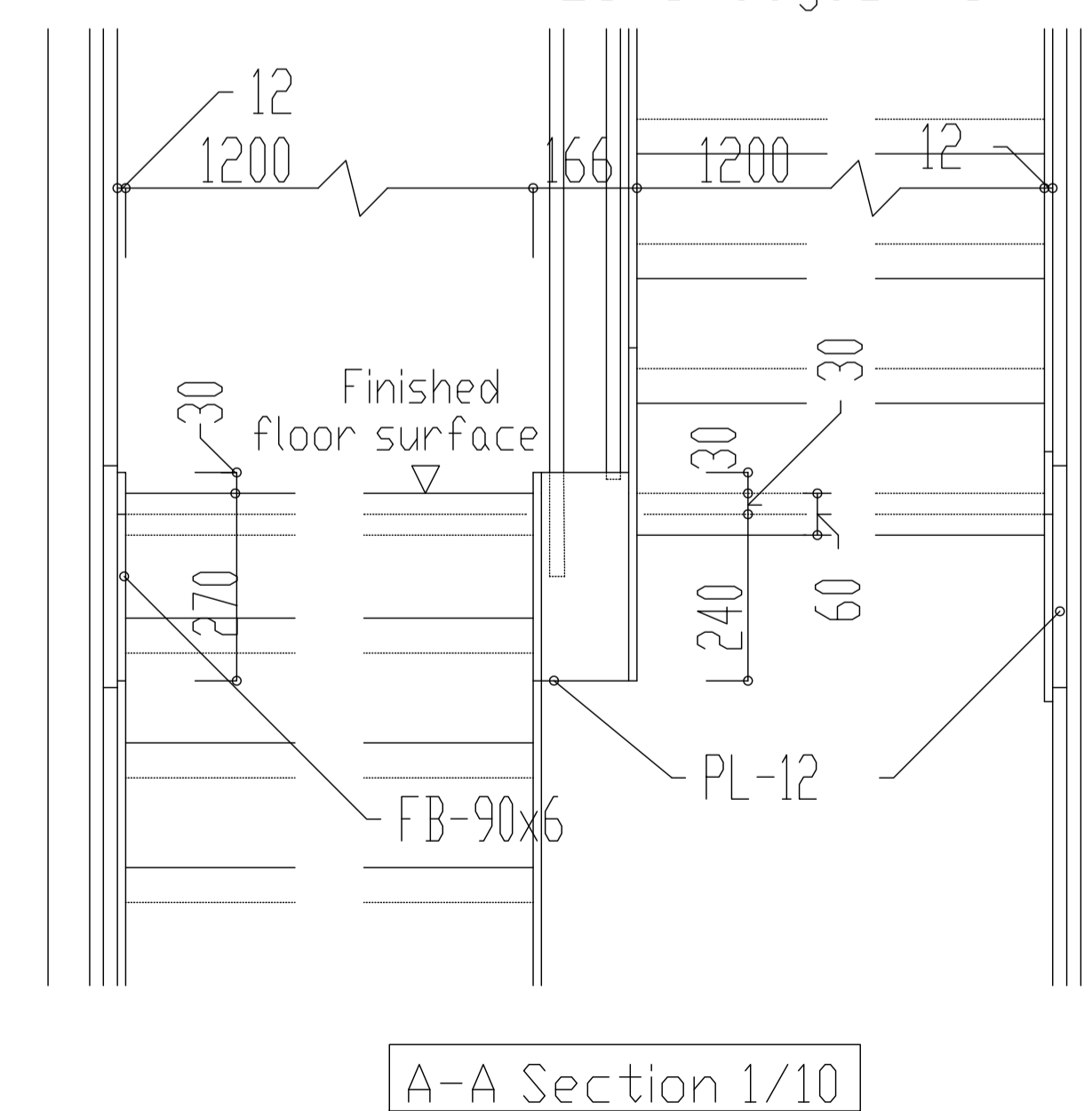
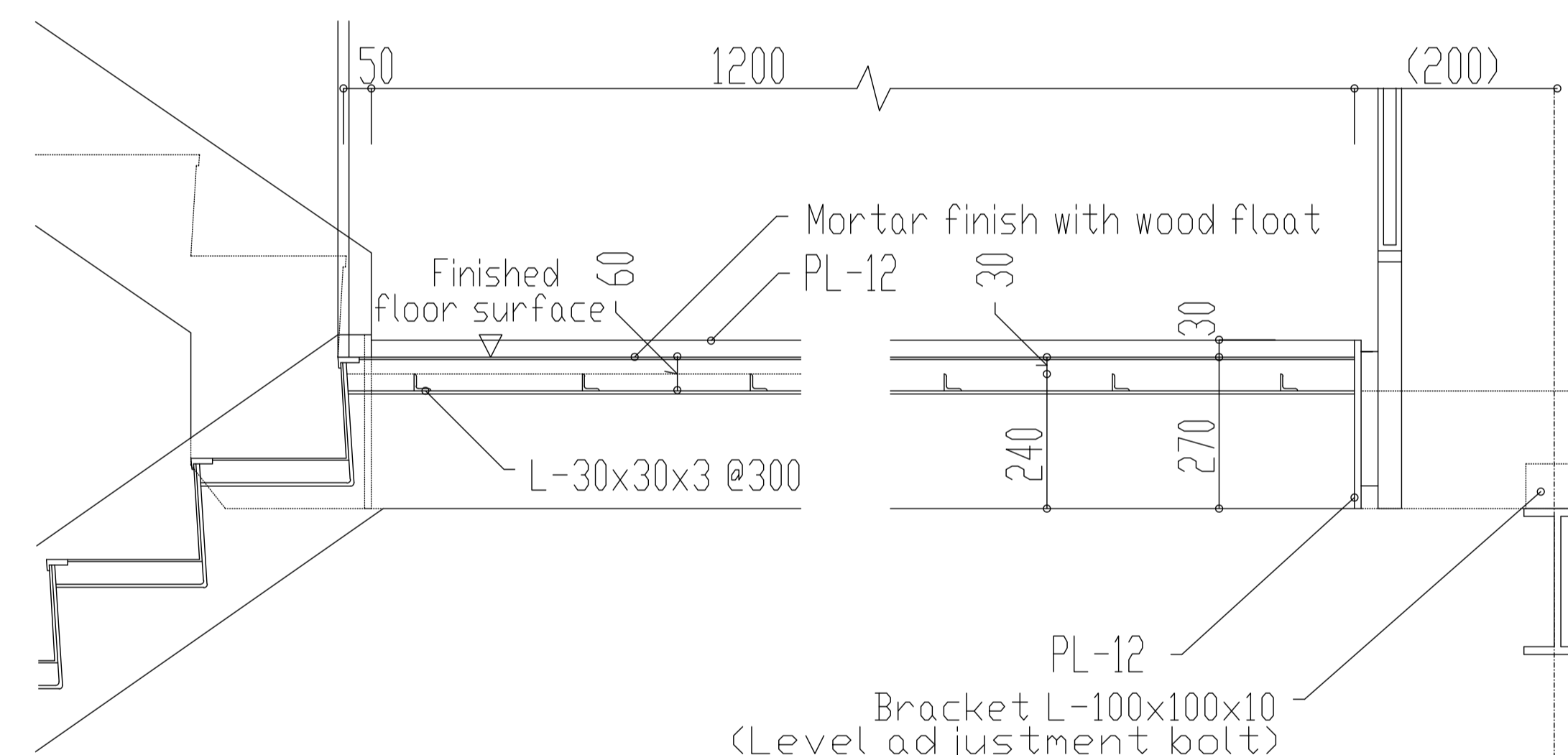
Bridgeboard required cross-section for each stair width and span (SS400)

Stair width \ Bridgeboard span	≤1.2m	≤1.6m	≤1.8m	≤2.0m	≤2.2m
≤6m	PL-12x300	PL-12x300	PL-12x300	PL-16x300	PL-16x300
≤7m	PL-12x300	PL-16x300	PL-16x300	PL-19x300	PL-19x300
≤8m	PL-16x300	PL-22x300 PL-16x350	PL-25x300 PL-16x350	PL-28x300 PL-19x350	PL-28x300 PL-19x350

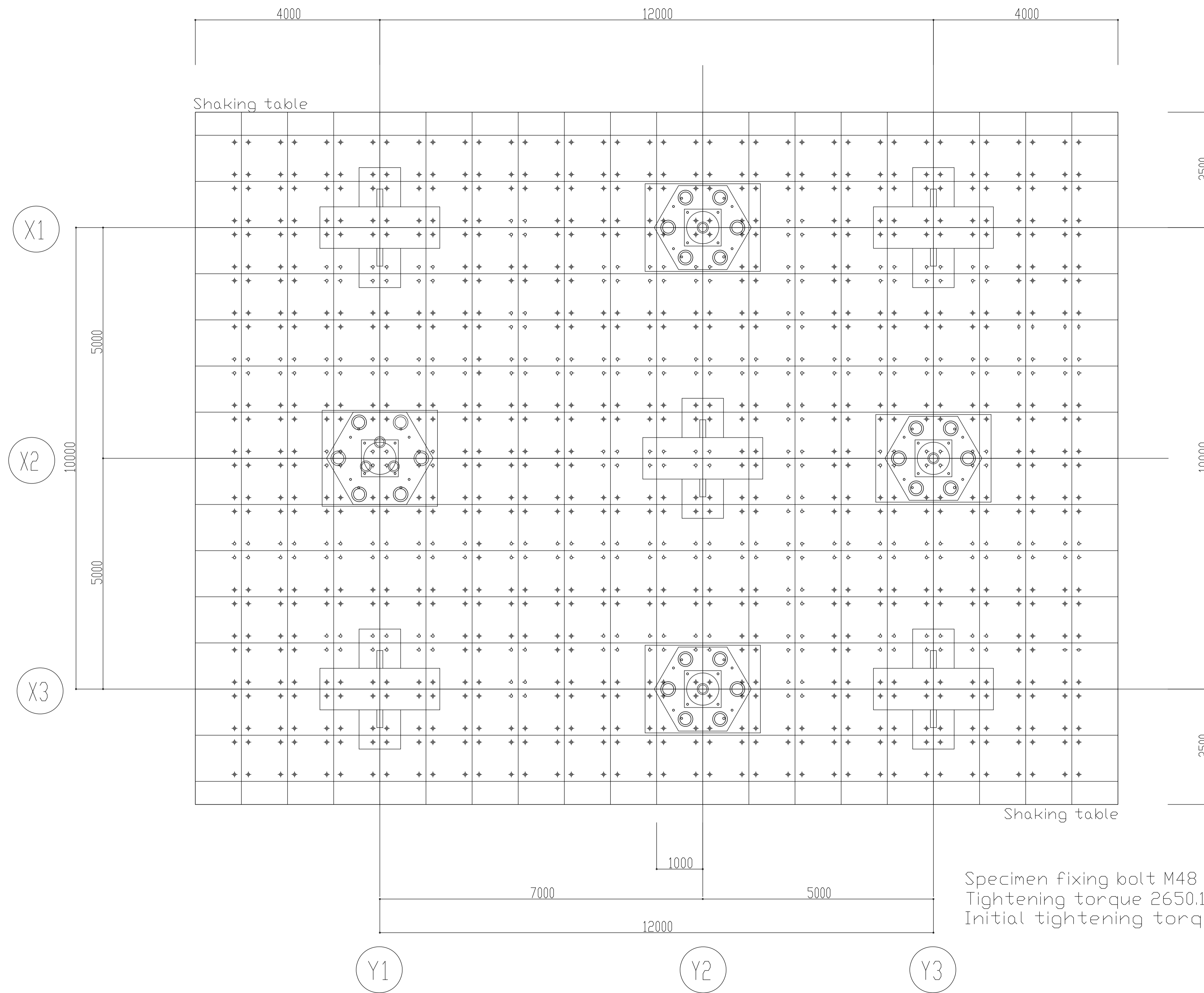
\* Hypothetical conditions - if there is a bridgeboard at each end of the stair width  
 - load weight of 3500 KN/m<sup>2</sup>  
 - 60 mm mortar on steps



\* On different plan



Revised	



Specimen fixing bolt M48 S45C,L=1570  
 Tightening torque 2650.15Nm  
 Initial tightening torque 42.470Nm(Using bolt tensioner)

# Measurement Control Tower Side

Revised	///
	///
	///
	///
	///
	///

National Research Institute for Earth Science and Disaster Prevention Hyogo Earthquake Engineering Research Center Value-added Five-story Steel Frame Experiment Specimen Design Drawing	11
Shaking Table Layout A1:1/50 A3:1/100	2008.11.7
	A-008







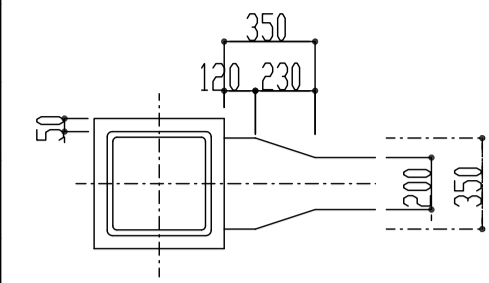
Items with no mark are as follows:  
 1. Steel quality is SN490B.  
 2. D marks: SM490 material

Code	G1 (Value-added plane)	G2 (Non value-added plane)		G3 (Non value-added plane)	
Area	Full Section	End	Center	End	Center
R F	H-400x200x9x12	BH-400x200x9x12	H-400x200x9x12	BH-400x200x9x16	H-400x200x9x12
5 F	BH-400x200x12x16	BH-400x200x9x16	H-400x200x9x12	BH-400x200x9x16	H-400x200x9x12
4 F	BH-400x200x12x19	BH-400x200x9x19	H-400x200x9x16	BH-400x200x9x19	H-400x200x9x16
3 F	H-400x200x12x22	BH-400x200x9x19	H-400x200x9x16	BH-400x200x9x19	H-400x200x9x16
2 F	H-400x200x12x22	BH-400x200x9x19	H-400x200x9x16	BH-400x200x9x19	H-400x200x9x16
1 F	○BH-900x500x16x28	○BH-900x500x16x28		○BH-900x500x16x28	
Note	No Stress Haunch	Stress haunch installed on the 2F to RF beam flanges as shown on the right		Stress haunch installed on the 2F to RF beam flanges as shown on the right	

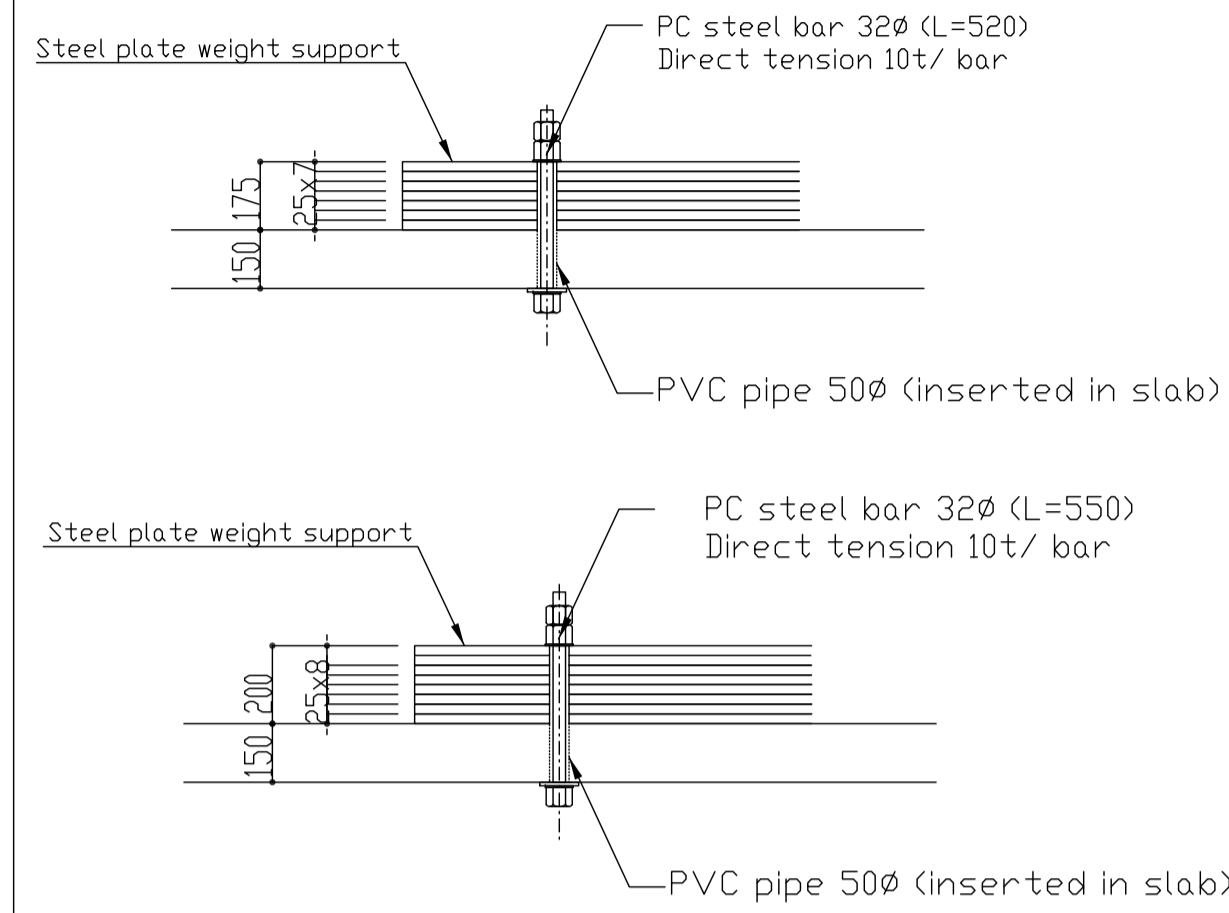
  

Code	G11 (Value-added plane)	G12 (Non value-added plane)		G13 (Non value-added plane)	
Area	Full Section	End	Center	End	Center
R F	H-400x200x9x12	BH-400x200x9x12	H-400x200x9x12	BH-400x200x9x12	H-400x200x9x12
5 F	BH-400x200x12x16	BH-400x200x9x16	H-400x200x9x12	BH-400x200x9x16	H-400x200x9x12
4 F	BH-400x200x12x16	BH-400x200x9x19	H-400x200x9x16	BH-400x200x9x19	H-400x200x9x16
3 F	BH-400x200x12x19	BH-400x200x9x19	H-400x200x9x16	BH-400x200x9x19	H-400x200x9x16
2 F	H-400x200x12x22	BH-400x200x9x19	H-400x200x9x16	BH-400x200x9x19	H-400x200x9x16
1 F	○BH-900x500x16x28	○BH-900x500x16x28		○BH-900x500x16x28	
Note	No Stress Haunch	Stress haunch installed on the 2F to RF beam flanges as shown on the right		Stress haunch installed on the 2F to RF beam flanges as shown on the right	

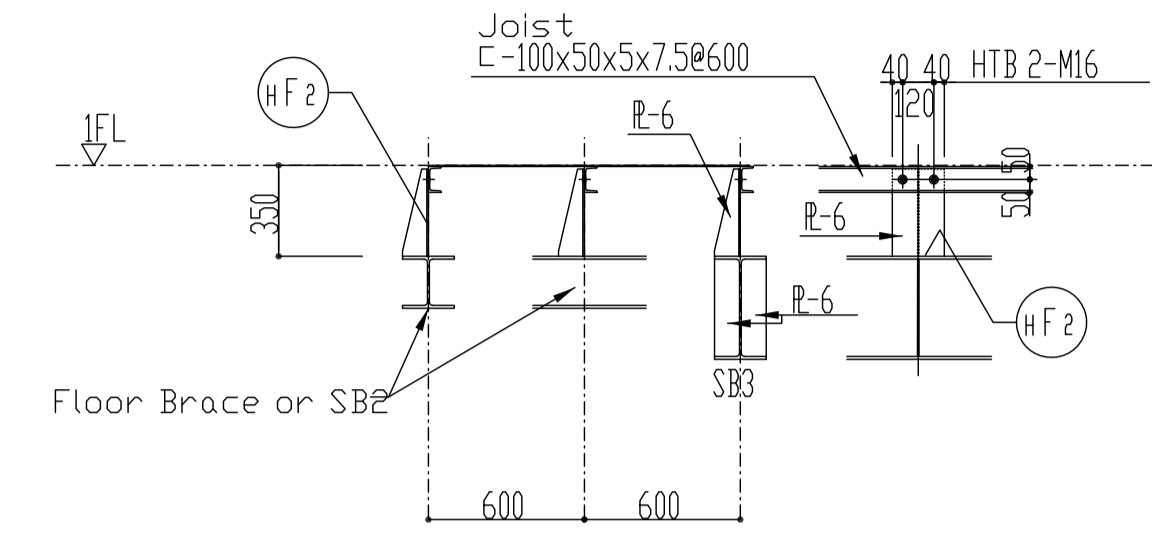
Detail of stress haunch



Roof Steel Plate Weight Attachment Guidelines



1F Hall Floor Details



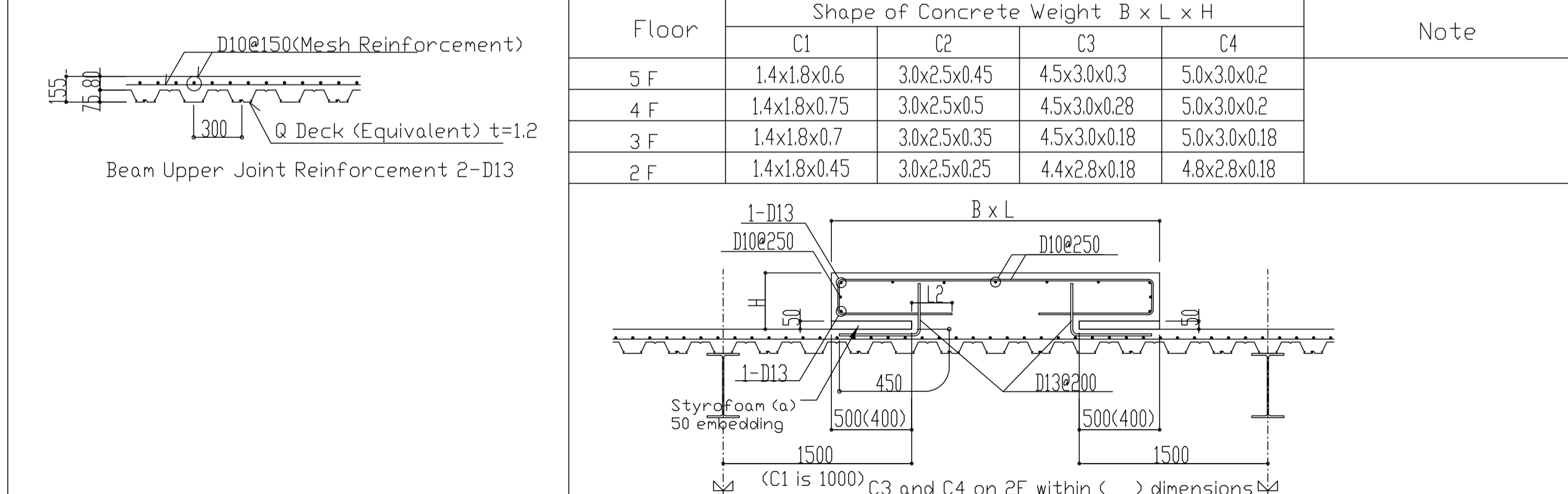
Steel Column Section

Code	C1	C2	C3	Note
RFL				(Note) Steel quality is BCR295.
5FL				
4FL	□-350x350x12x12	□-350x350x12x12	□-350x350x12x12	
3FL	□-350x350x16x16	□-350x350x16x16	□-350x350x19x19	
2FL		□-350x350x19x19		
1FL	□-350x350x19x19	□-350x350x22x22	□-350x350x22x22	

Floor Slab Section

Code	Slab Thickness	Area	short direction reinforcement bar		long direction reinforcement bar		Note
			End, Center	End, Center	End, Center	End, Center	
SI	150	Upper reinforcement Lower reinforcement	D13@200 D13@200	D13@200 D13@200	D10, D13@200 D10, D13@200	D10, D13@200 D10, D13@200	Flat deck is used instead of sacrifice formwork t=1.2
Sta	155	Upper reinforcement Lower reinforcement	D13@200 D13@200	D13@200 D13@200	D10, D13@200 D10, D13@200	D10, D13@200 D10, D13@200	
DS1							

2F to 5F Floor Anchoring



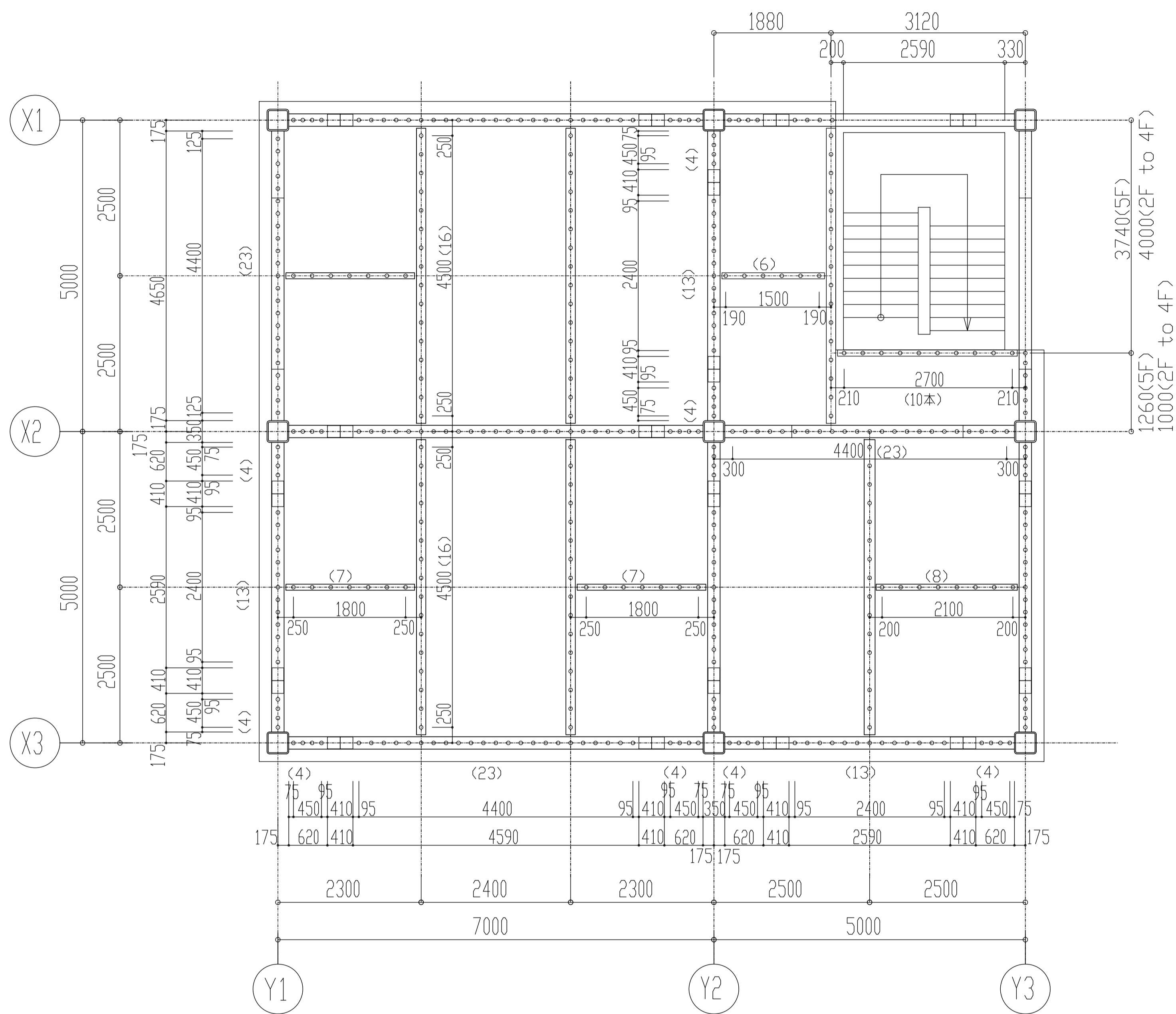
Revised	///
///	///
///	///
///	///
///	///
///	///





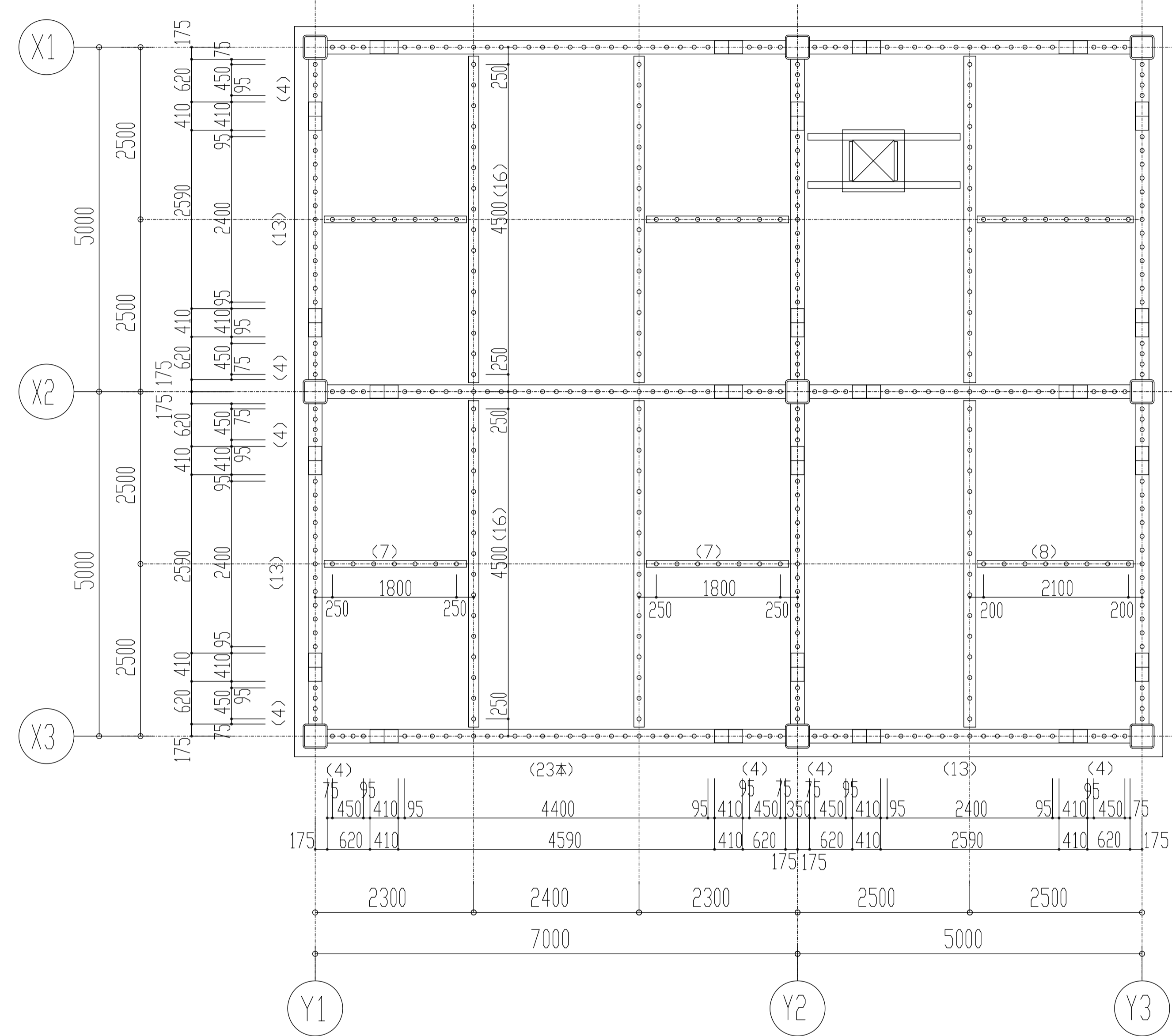






2F to 5F Beam Layout S=1:50

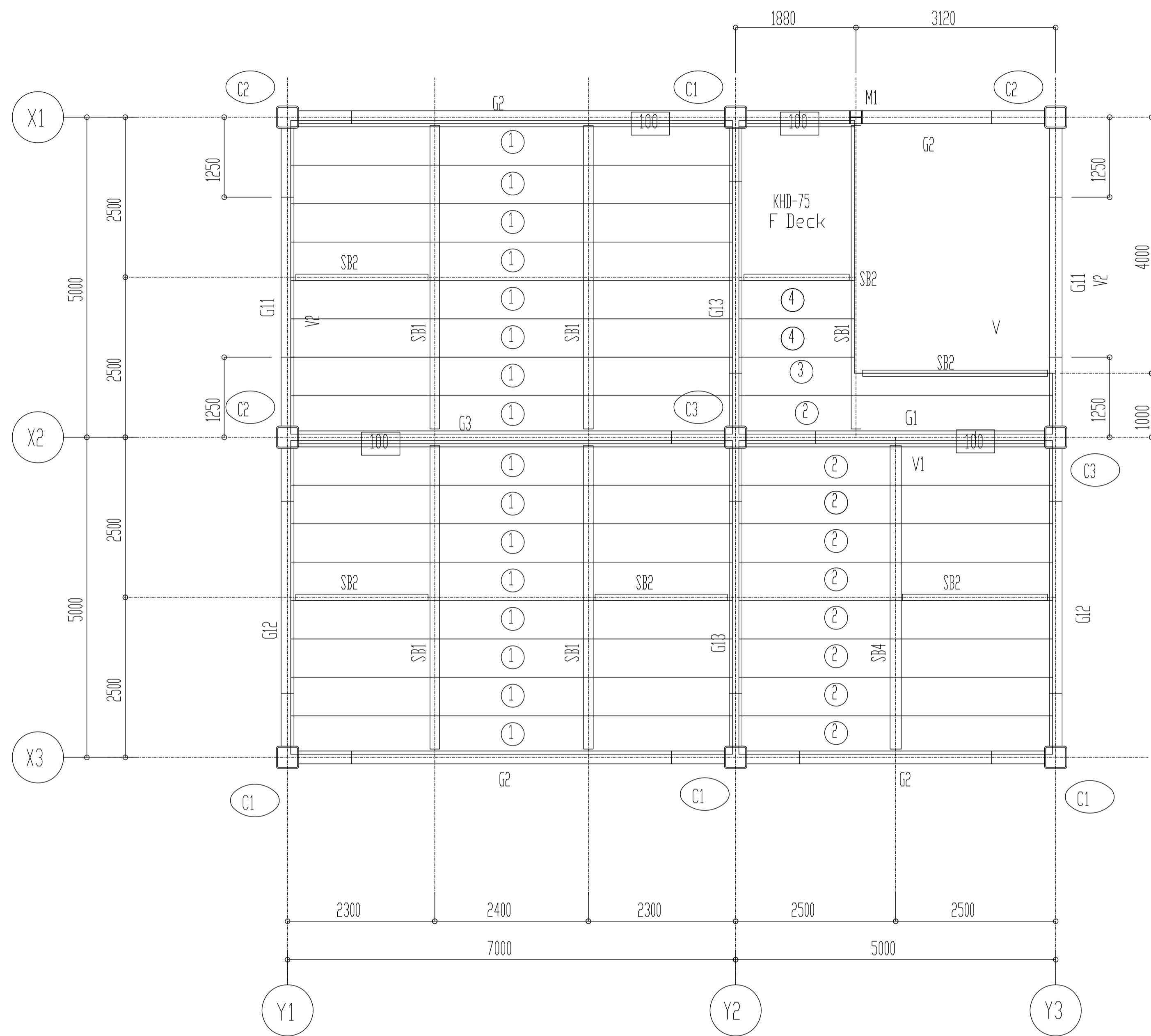
Headed stud D19 L=110  
 \* Girders@200, Small Beams@300  
 \* Detail and placement of girder end haunch is based on 14(S-003)



RF Beam Layout S=1:50

Headed stud D19 L=110  
 \* Girders@200, Small Beams@300  
 \* Detail and placement of girder end haunch is based on 14(S-003)

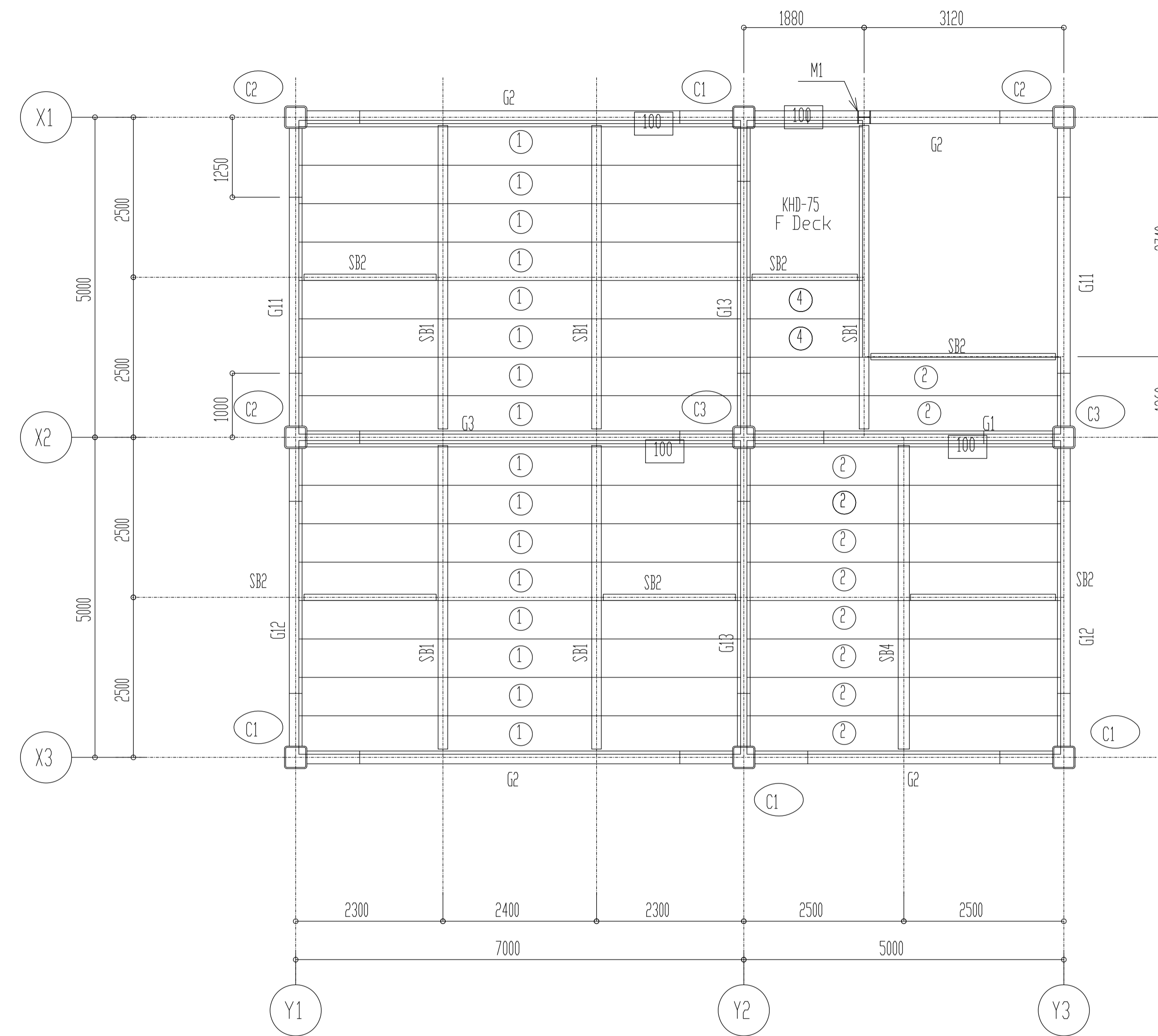
Revised	///
	///
	///
	///
	///
	///



2F, 3F, 4F Beam Structure

Items with no marks are as follows:

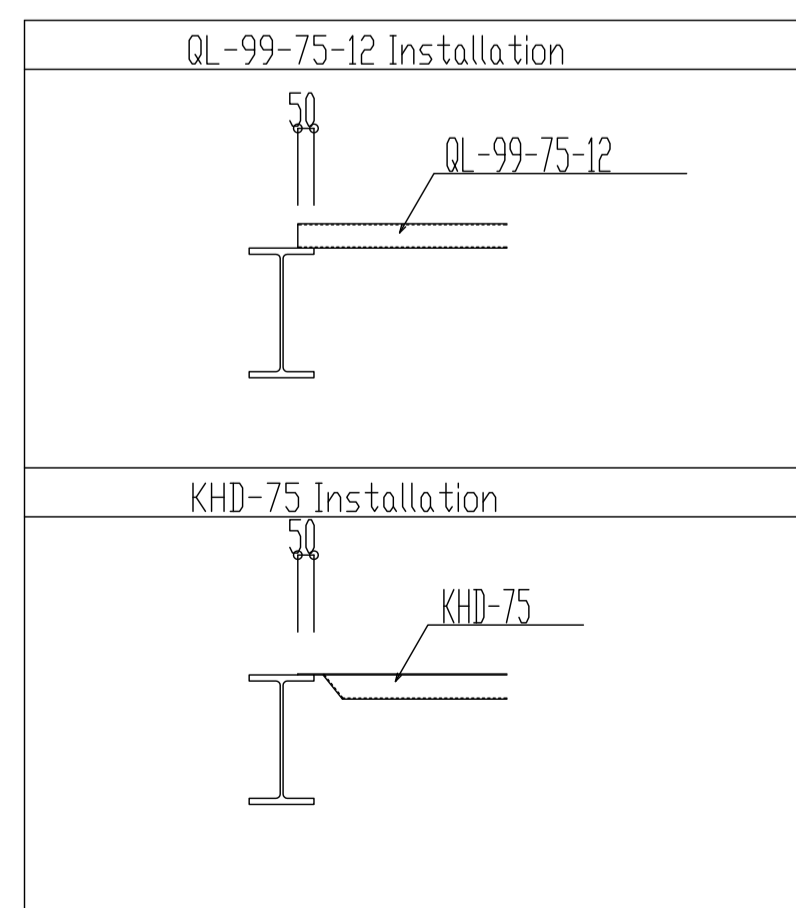
1. Ceiling beam is FL-165.
  2. Bracket length is 1000 from center of pillar.
  3. Detail and placement of girder
- end haunch is based on 14(S-003)



5F Beam Structure

Items with no marks are as follows:

1. Ceiling beam is FL-165.
  2. Bracket length is 1000 from center of pillar.
  3. Detail and placement of girder
- end haunch is based on 14(S-003)

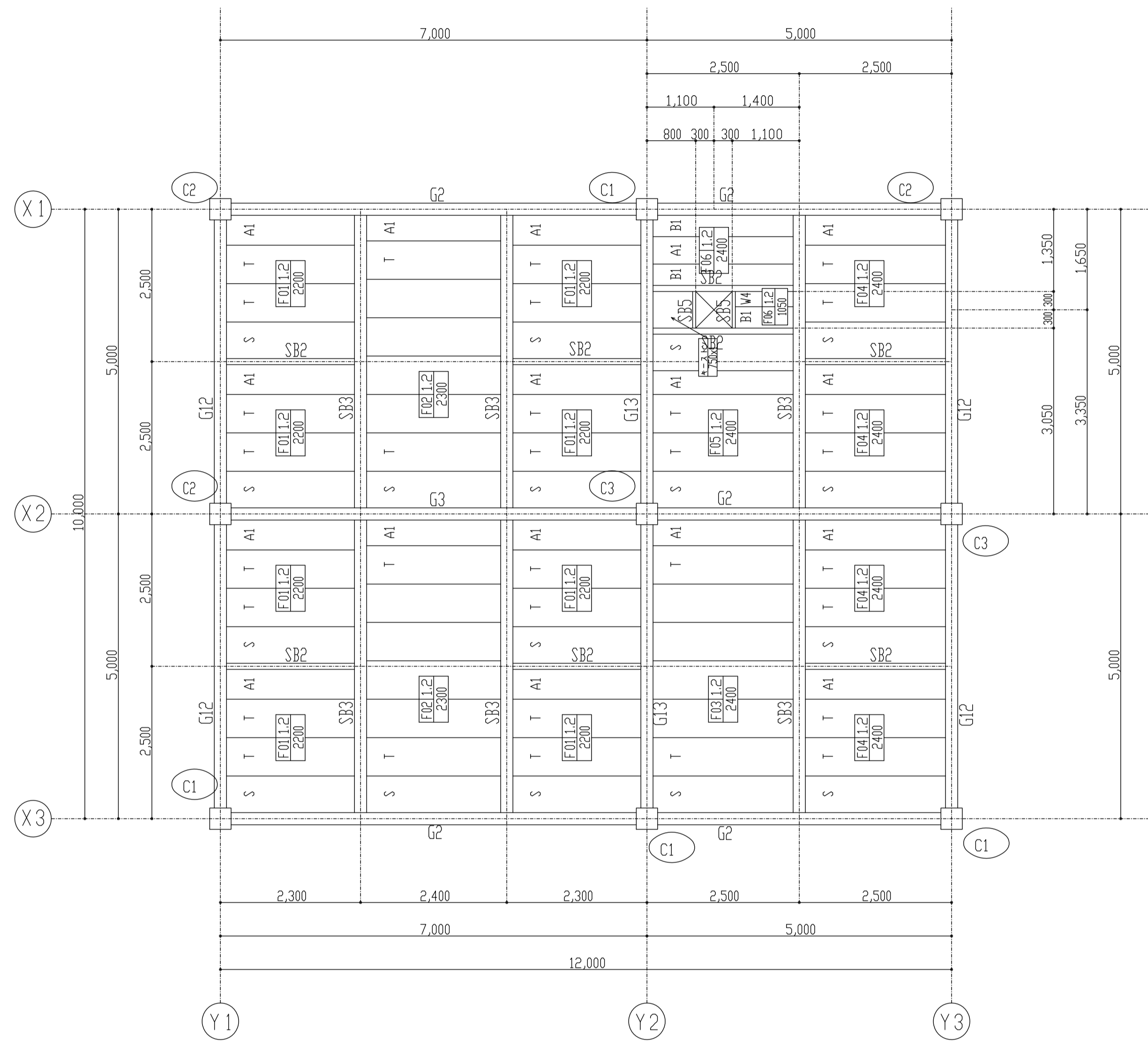


2F, 3F, 4F, 5F Deck Allocation Quantity

Code	Length	No.	Q Deck Allocation Quantity				QL-99-75-12 (12)	Note
			2F	3F	4F	5F		
①	6900	64	16	16	16	16		
②	4900	37	9	9	9	10		
③	4900	3	1	1	1	0	Cutout (2)	
④	1805	24	6	6	6	6		
100	6900	8	2	2	2	2	Adjustment Plate	
100	4900	4	1	1	1	1	Adjustment Plate	
100	1805	4	1	1	1	1	Adjustment Plate	

Revised	///
///	///
///	///
///	///
///	///
///	///

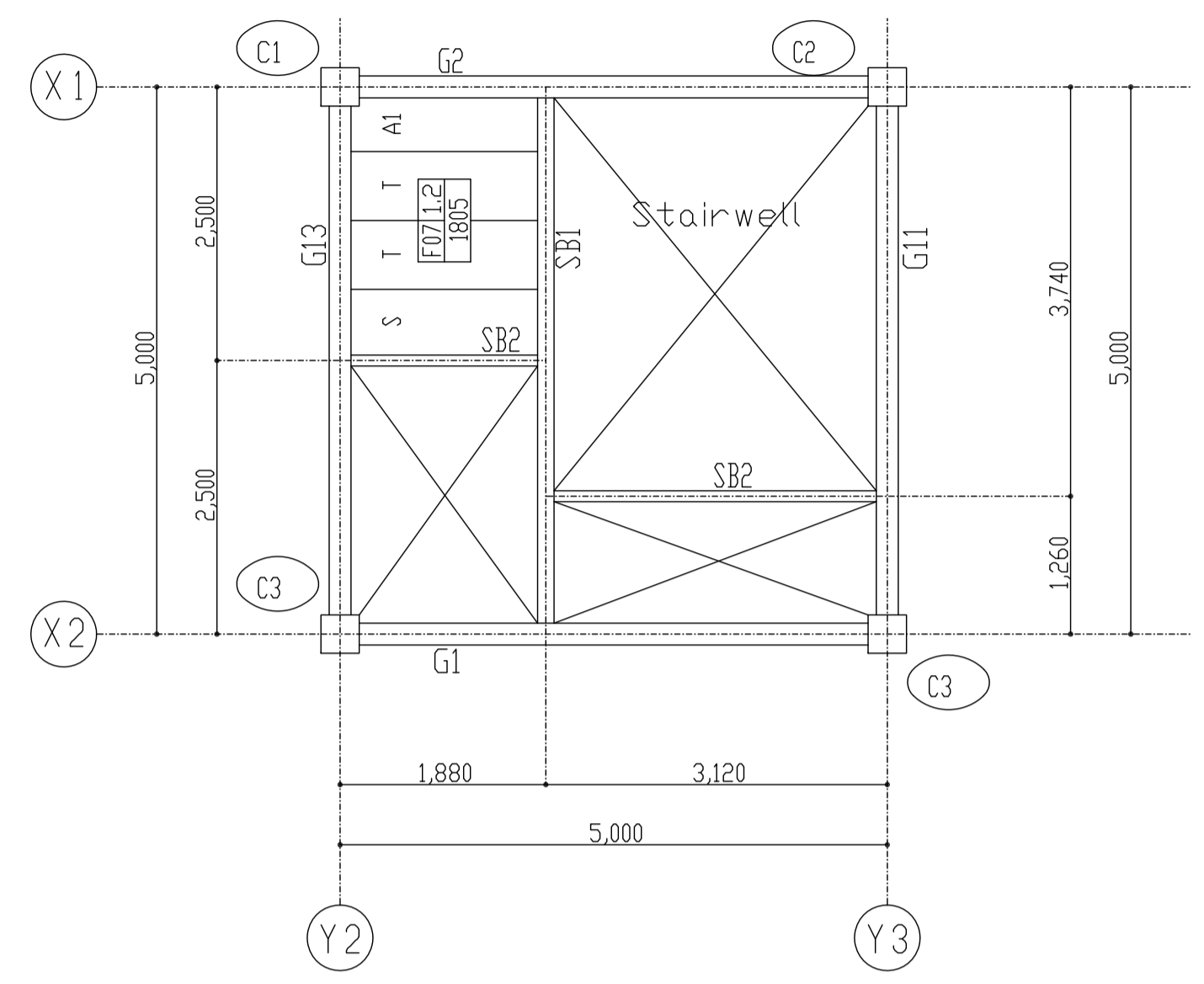




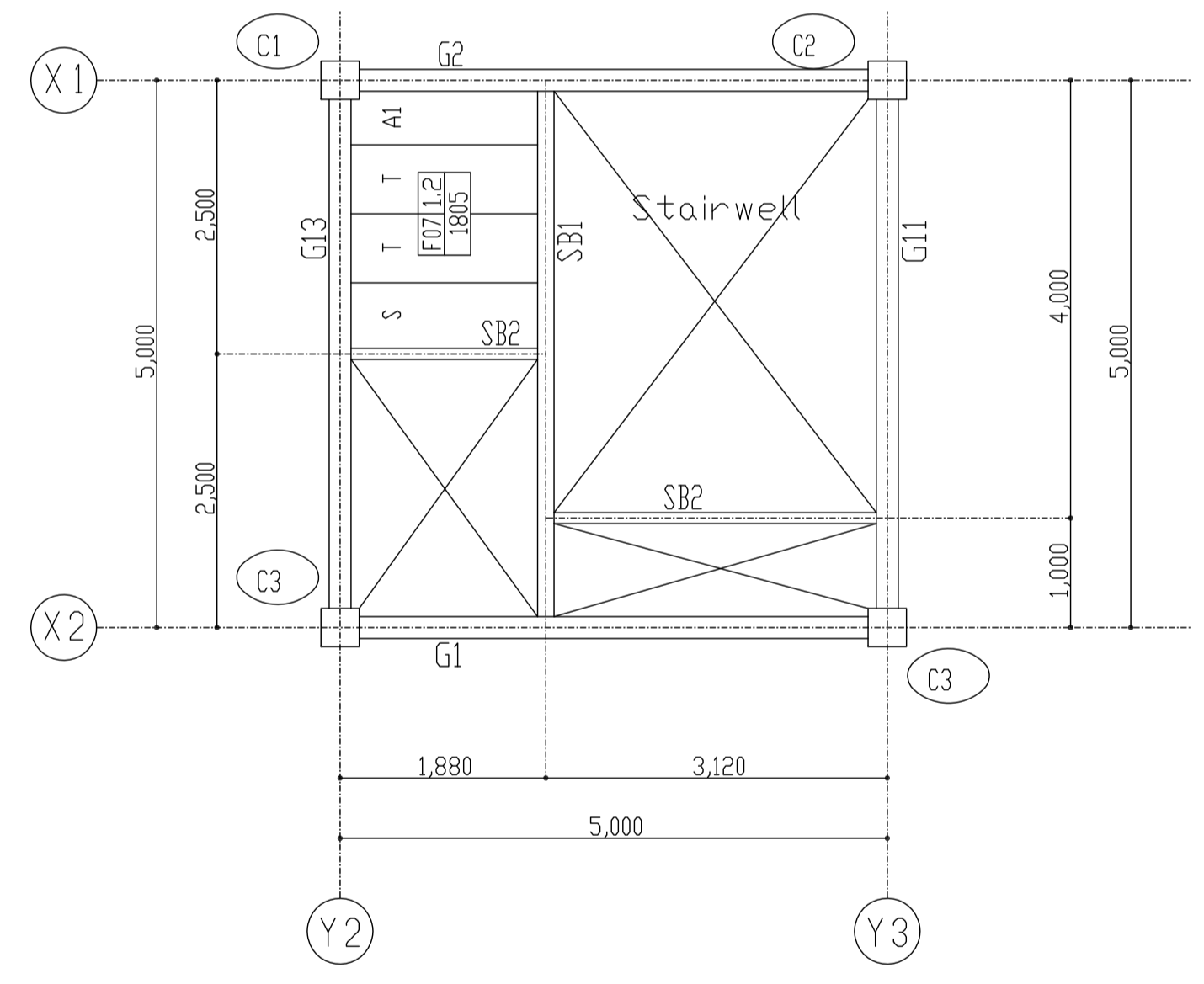
RF Floor High Deck Allocation

**RF Beam Structure**

- Items with no marks are as follows:
1. Ceiling beam is FL-150.
  2. Bracket length is 1000 from center of pillar.
  3. Detail and placement of girder end haunch is based on 14(S-003)



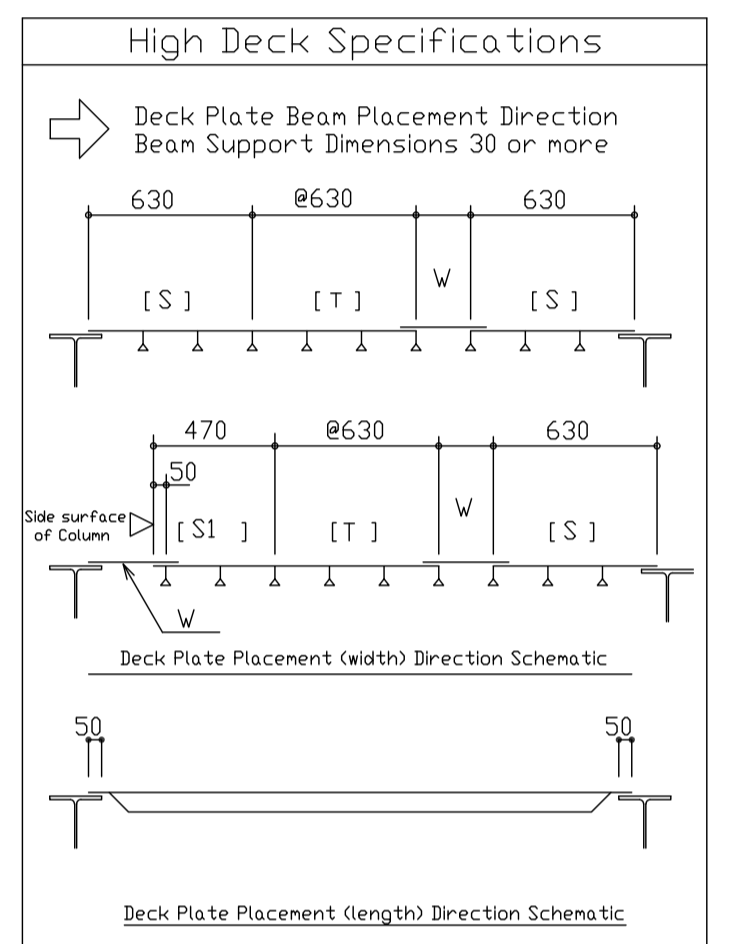
5F Floor High Deck Allocation



2F to 4F Floor High Deck Allocation

High Deck Span Tolerance						
Span	Deck	0.8	1.0	1.2	1.4	1.6
150		2,452	2,766	2,921	3,041	3,149

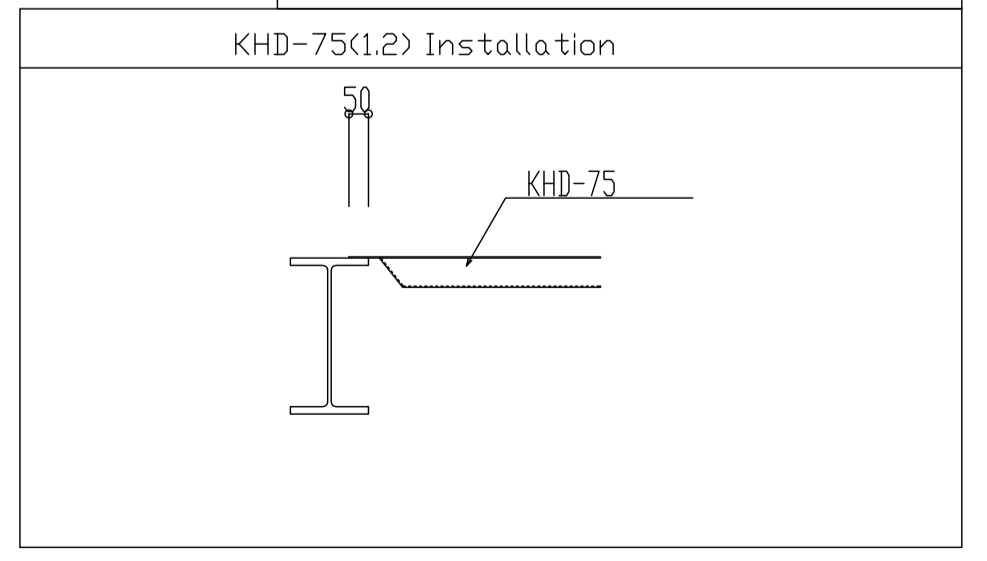
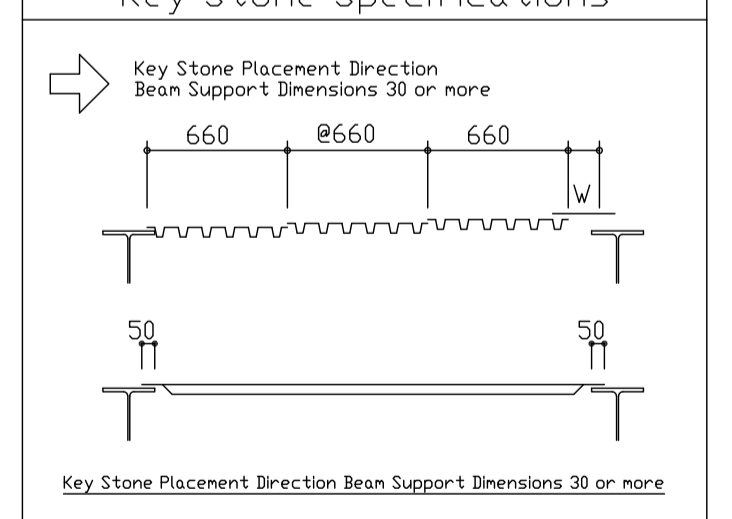
Figures indicate clear span



Materials		
T (general) Type	S Type	S1 Type
A1 Type	B1 Type	Adjustment Plate
		W2 (t-68) W3 (t-12) W4 (t-16)

**Common Legend**

	Slab No.	Deck Plate Thickness
	Deck Length	
	Support	
	Deck Support	
	SRC Beam Width	
	S Beam Width	
	High Deck Adjustment Plate	
	Slab Thickness (without special note)	



Revised	///
	///
	///
	///
	///
	///

## APPENDIX B

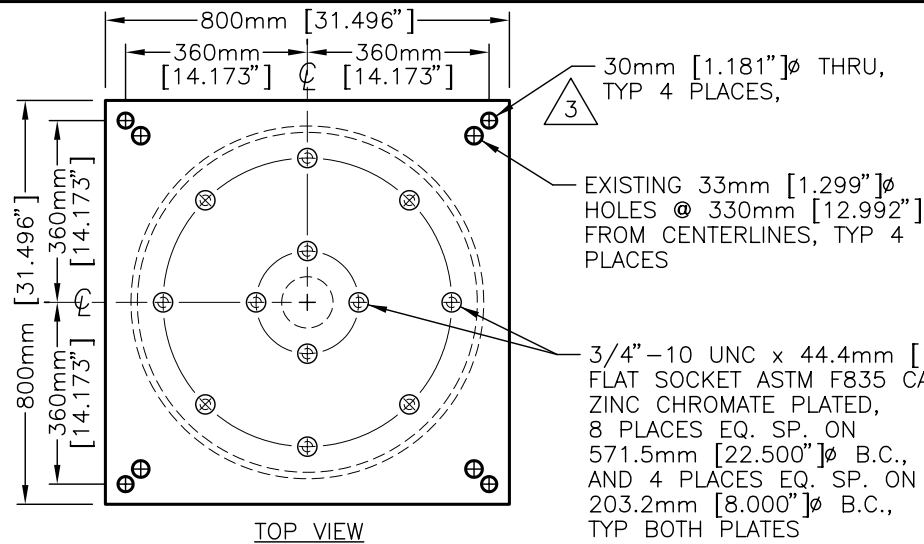
### **Drawings and Specifications for Lead-Rubber Bearings and Cross Linear Bearings**

Building Isolated with Hybrid Lead-Rubber Isolation System

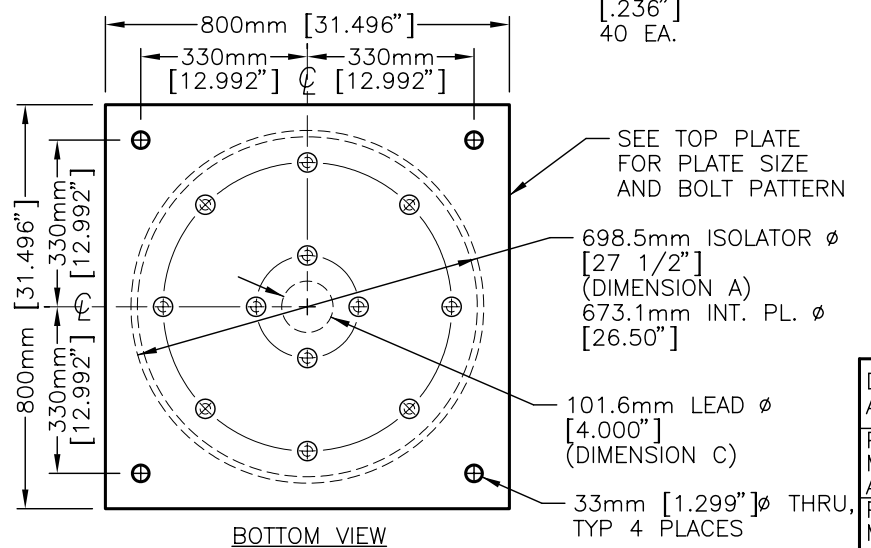
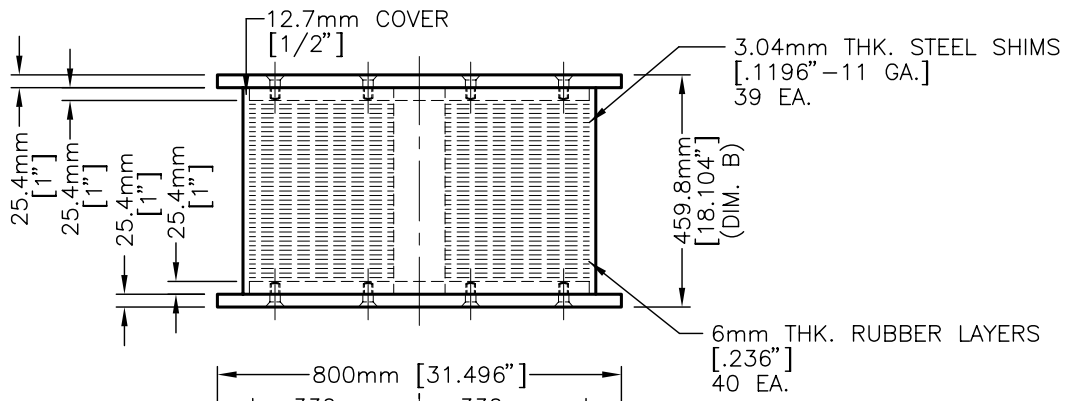
Contributed by Dynamic Isolation Systems, Inc. and Aseismic Devices Co., Ltd.

Developed for NEES/E-Defense Collaborative Test Program on Innovative Isolation Systems, 2011-2012

<b>List of Documents</b>	<b>Contributor</b>
Type A Isolator (LRB Drawing)	Dynamic Isolation Systems, Inc.
Isolator Design Calculations	Dynamic Isolation Systems, Inc.
CLB 250 (CLB Drawing)	Aseismic Devices Co., Ltd.
CLB Specification	Aseismic Devices Co., Ltd.



TOP VIEW



BOTTOM VIEW

REVISION STATUS			
APPR	REV	DATE	DESCRIPTION
AK	A	5/6/11	ISSUED FOR INFORMATION
AK	B	6/7/11	GEN. REV.-REISSUED FOR INFORMATION
TN	0	6/10/11	REV. DWG. #-ISSUED FOR APPROVAL
MG	1	6/10/11	ISSUED FOR FABRICATION
AK	2	6/24/11	REV. EXT. ENDPL-REISSUED FOR APPROVAL
AK	3	6/29/11	REV. EXT. ENDPL-REISSUED FOR APPROVAL

- NOTES:
- MATERIALS:  
ALL STEEL PL's ASTM A36.  
ALL STEEL SHIMS ASTM A1011 GR. 36.  
INTERNAL RUBBER IS DIS TYPE T.  
EXTERNAL RUBBER IS DIS TYPE E100S.
  - DIMENSIONS ARE IN UNITS NOTED.  
DIMENSIONS IN BRACKETS ARE EQUIVALENTS FOR REFERENCE ONLY.
  - DO NOT SCALE THIS DRAWING.
  - FINISH: TO BE DETERMINED.

ISOLATOR DIMENSION TABLE			
		TYPE A ISOLATOR	
		C698.5/459.8/101.6	
QUANTITY		4+0	
		TARGET	
		TOL./ALLOWABLE	
A	Isolator Diameter	698.5mm $\pm$ 2mm	$\pm$ 4mm
B	Overall Isolator Ht.	459.8mm $\pm$ 4mm	$\pm$ 6.35mm
C	Lead Core Diameter	101.6mm	$\pm$ 2mm
D	Parallelity	1/300	1/200
Estimated Weight		1,864 lb./847 kg	
Measurements are taken at 20°C.			

- GENERAL TOLERANCES:
- ENDPLATE OVERALL DIMENSIONS:  $\pm$  3.18mm.
  - BOLT HOLE LOCATIONS:  $\pm$  0.8mm.
  - PLATE THICKNESS:  $\pm$  1.6mm.
  - PLATE FLATNESS:  $\pm$  3.18mm.

THIS DRAWING IS THE PROPERTY OF DYNAMIC ISOLATION SYSTEMS, INC. INFORMATION AND KNOW-HOW HEREON ARE CONFIDENTIAL AND MAY NOT BE USED, REPRODUCED OR REVEALED TO OTHERS EXCEPT IN ACCORDANCE WITH THE CONTRACT OR OTHER WRITTEN PERMISSION OF DYNAMIC ISOLATION SYSTEMS, INC. ANY REPRODUCTIONS IN WHOLE OR IN PART SHALL INCLUDE THIS NOTATION.

DESIGNER APPROVAL	AK
PROJECT MANAGER APPROVAL	-
PLANT MANAGER APPROVAL	MG

**DYNAMIC ISOLATION SYSTEMS**

DIS SEISMIC ISOLATORS  
NRC Project at EDefense  
Type A Isolator  
**DWG. NO. 152-100** SHEET: 1 of 1  
ORIG: 5/6/11

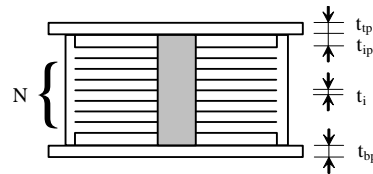


## Isolator Design Calculations

**Job No. :** \_\_\_\_\_ **Job :** EDefense - Final **By :** AK **Date :** June 9, 2011  
**Client :** \_\_\_\_\_ **Subject :** Seismic Isolator Calculations, LRB **Checked :** \_\_\_\_\_ **Date :** \_\_\_\_\_

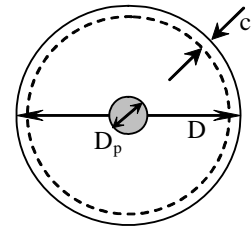
### Rubber Properties

Rubber Shear Modulus  $G := 0.060 \cdot \text{ksi}$   $G = 0.414 \text{ MPa}$   
 Rubber's Elongation-at-break  $\epsilon_u := 5.5$



### Bearing Dimensions

Overall Diameter  $D := 27.5 \cdot \text{in}$   $D = 698.5 \text{ mm}$   
 Number of Rubber Layers  $N := 40$   
 Lead Diameter  $D_p := 4.0 \cdot \text{in}$   $D_p = 101.6 \text{ mm}$   
 Shim Thickness  $t_s := 0.1196 \cdot \text{in}$   $t_s = 3 \text{ mm}$   
 Layer Thickness  $t_i := 0.236 \cdot \text{in}$   $t_i = 6 \text{ mm}$   
 Side Cover Rubber Thickness  $c_s := 0.5 \cdot \text{in}$   $c_s = 12.7 \text{ mm}$   
 Top Mounting Plate Thickness  $t_{tp} := 1 \cdot \text{in}$   $t_{tp} = 25.4 \text{ mm}$   
 Bottom Mounting Plate Thickness  $t_{bp} := 1 \cdot \text{in}$   $t_{bp} = 25.4 \text{ mm}$   
 Internal Plate Thickness  $t_{ip} := 1 \cdot \text{in}$   $t_{ip} = 25.4 \text{ mm}$   
 Isolator Height  $H_{isol} := N \cdot t_i + (N - 1) \cdot t_s + t_{bp} + t_{tp} + 2 \cdot t_{ip}$   $H_{isol} = 18.104 \text{ in}$   $H_{isol} = 460 \text{ mm}$



800 mm SQ Ext plates; 4 x 1"  $\phi$  Ext holes, 8 x 0.75"  $\phi$  internal connection

### Design Displacement

Design Displacement  $D_D := 300 \cdot \text{mm}$  Properties are checked at this displacement.  
 Maximum Displacement  $D_{TM} := 600 \cdot \text{mm}$  Capacity is checked at this displacement.

### Project Loads

Rotation applied on the bearing  $\theta_0 := 0.0$   $\theta_{DTM} := 0.0$  No rotations are applied on the isolators  
 Load at undeformed condition  $P_{zero} := 50 \cdot t$  Assumed  
 Load at maximum displacement  $P_{DTM} := 50 \cdot t$

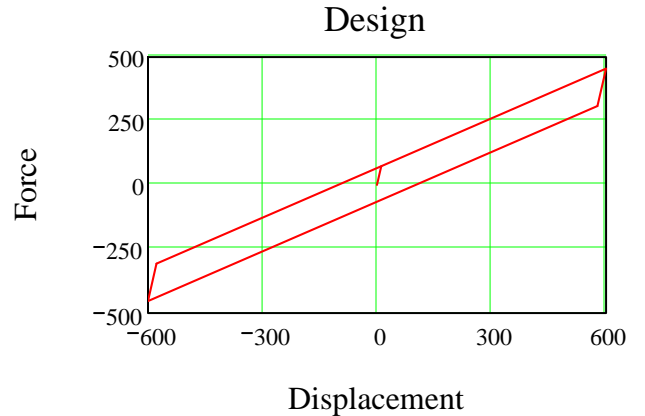
**Summary**

**Isolator Dimensions**

Overall Diameter	D = 27.5 in	D = 698.5 mm
Number of Rubber Layers	N = 40	N = 40
Lead Diameter	D <sub>p</sub> = 4 in	D <sub>p</sub> = 101.6 mm
Shim Thickness	t <sub>s</sub> = 0.12 in	t <sub>s</sub> = 3 mm
Layer Thickness	t <sub>i</sub> = 0.236 in	t <sub>i</sub> = 6 mm
Side Cover Rubber Thickness	c <sub>s</sub> = 0.5 in	c <sub>s</sub> = 12.7 mm
Top Mounting Plate Thickness	t <sub>tp</sub> = 1 in	t <sub>tp</sub> = 25.4 mm
Bottom Mounting Plate Thickness	t <sub>bp</sub> = 1 in	t <sub>bp</sub> = 25.4 mm
Internal Plate Thickness	t <sub>ip</sub> = 1 in	t <sub>ip</sub> = 25.4 mm
Isolator Overall Height	H <sub>isol</sub> = 18.104 in	H <sub>isol</sub> = 459.9 mm

**Isolator Properties**

Design Maximum Displacement	D <sub>D</sub> = 300 mm
Maximum Corner Displacement	D <sub>TM</sub> = 600 mm
Yielded Stiffness	K <sub>d</sub> = 0.65 $\frac{\text{kN}}{\text{mm}}$
Elastic Stiffness	K <sub>e</sub> = 6.5 $\frac{\text{kN}}{\text{mm}}$
Characteristic Strength	Q <sub>d</sub> = 65.7 kN
Yield Force	F <sub>y</sub> = 73 kN
Yield Displacement	Δ <sub>y</sub> = 11.28 mm
Vertical Stiffness	K <sub>v</sub> = 1500 $\frac{\text{kN}}{\text{mm}}$
Shear Force	F <sub>max</sub> (D <sub>D</sub> ) = 259.8 kN
Effective Stiffness	K <sub>eff</sub> (D <sub>D</sub> ) = 0.87 $\frac{\text{kN}}{\text{mm}}$
Energy Dissipated per Cycle	EDC(D <sub>D</sub> ) = 76 kN·m



Equivalent Viscous Damping Ratio at Design Displacement	$\beta(D_D) = 0.155$	$\beta_m(D_{TM}) = 0.094$
Shear Strain in Rubber at Design Displacement	$\gamma(D_D) = 1.25$	
Shear Strain in Rubber at Maximum Displacement	$\gamma(D_{TM}) = 2.5$	
Allowable Load at Undeformed Condition (with a FS of 3.0)	Pallowable <sub>zero</sub> = 4197 kN	
Allowable Load at Maximum Displacement	Pallowable <sub>D<sub>TM</sub></sub> = 532 kN	

**Summary**

**Isolator Dimensions**

Overall Diameter	$D = 27.5 \text{ in}$	$D = 698.5 \text{ mm}$
Number of Rubber Layers	$N = 40$	$N = 40$
Lead Diameter	$D_p = 4 \text{ in}$	$D_p = 101.6 \text{ mm}$
Shim Thickness	$t_s = 0.12 \text{ in}$	$t_s = 3 \text{ mm}$
Layer Thickness	$t_i = 0.236 \text{ in}$	$t_i = 6 \text{ mm}$
Side Cover Rubber Thickness	$c_s = 0.5 \text{ in}$	$c_s = 12.7 \text{ mm}$
Isolator Overall Height	$H_{isol} = 18.104 \text{ in}$	$H_{isol} = 459.9 \text{ mm}$
Yielded Stiffness	$K_d = 3.7 \frac{\text{kip}}{\text{in}}$	$K_d = 0.6 \frac{\text{kN}}{\text{mm}}$
Elastic Stiffness	$K_e = 37 \frac{\text{kip}}{\text{in}}$	$K_e = 6.5 \frac{\text{kN}}{\text{mm}}$
Characteristic Strength	$Q_d = 14.8 \text{ kip}$	$Q_d = 65.7 \text{ kN}$
Yield Force	$F_y = 16.4 \text{ kip}$	$F_y = 73 \text{ kN}$
Yield Displacement	$\Delta_y = 0.44 \text{ in}$	$\Delta_y = 11.28 \text{ mm}$
Vertical Stiffness	$K_v = 8566 \frac{\text{kip}}{\text{in}}$	$K_v = 1500 \frac{\text{kN}}{\text{mm}}$
Undisplaced condition	$Pallowable_{zero} = 4197 \text{ kN}$	FS of 3.0

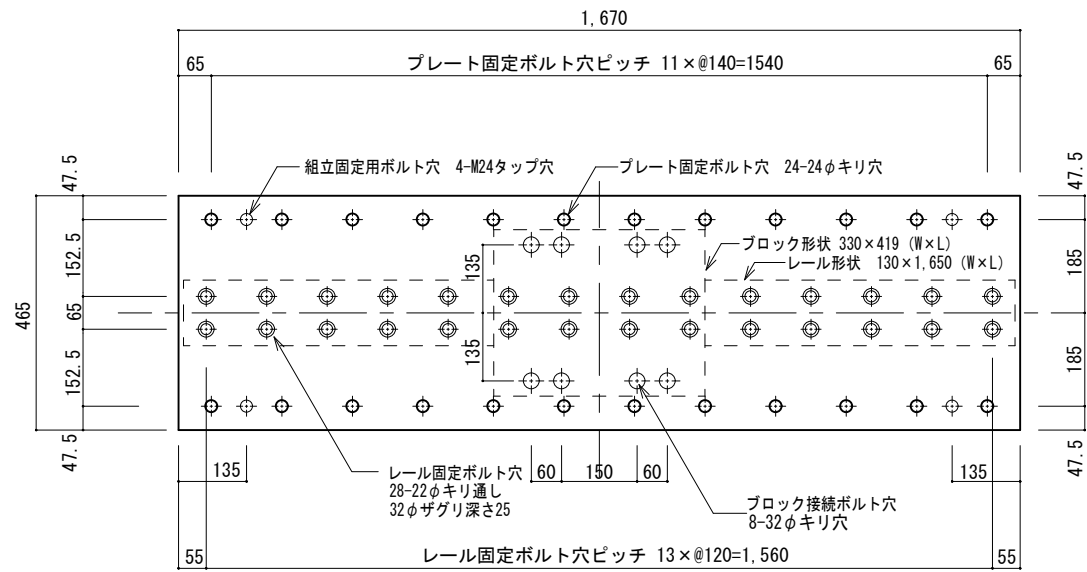
**Displacement**

$D_{TM} := 300 \text{ mm}$
$D_{TM} := 350 \text{ mm}$
$D_{TM} := 400 \text{ mm}$
$D_{TM} := 450 \text{ mm}$
$D_{TM} := 475 \text{ mm}$
$D_{TM} := 500 \text{ mm}$
$D_{TM} := 525 \text{ mm}$
$D_{TM} := 550 \text{ mm}$
$D_{TM} := 575 \text{ mm}$
$D_{TM} := 600 \text{ mm}$

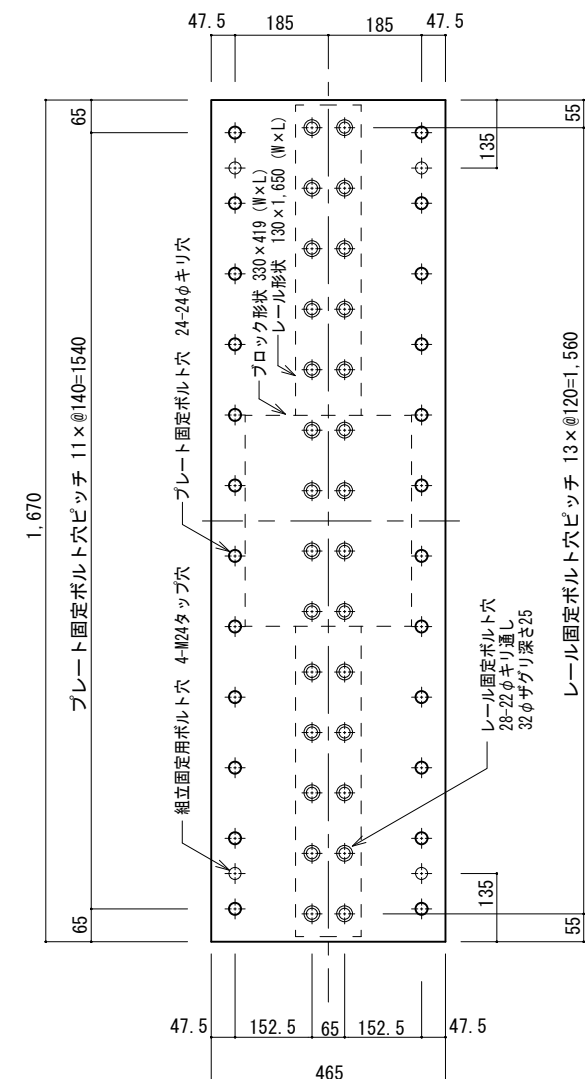
**Minimum of buckling, elastomer limit or a stress limit**

$Pallowable(D_{TM}) = 4795 \text{ kN}$
$Pallowable(D_{TM}) = 4648 \text{ kN}$
$Pallowable(D_{TM}) = 3659 \text{ kN}$
$Pallowable(D_{TM}) = 2736 \text{ kN}$
$Pallowable(D_{TM}) = 2304 \text{ kN}$
$Pallowable(D_{TM}) = 1893 \text{ kN}$
$Pallowable(D_{TM}) = 1507 \text{ kN}$
$Pallowable(D_{TM}) = 1149 \text{ kN}$
$Pallowable(D_{TM}) = 822 \text{ kN}$
$Pallowable(D_{TM}) = 532 \text{ kN}$

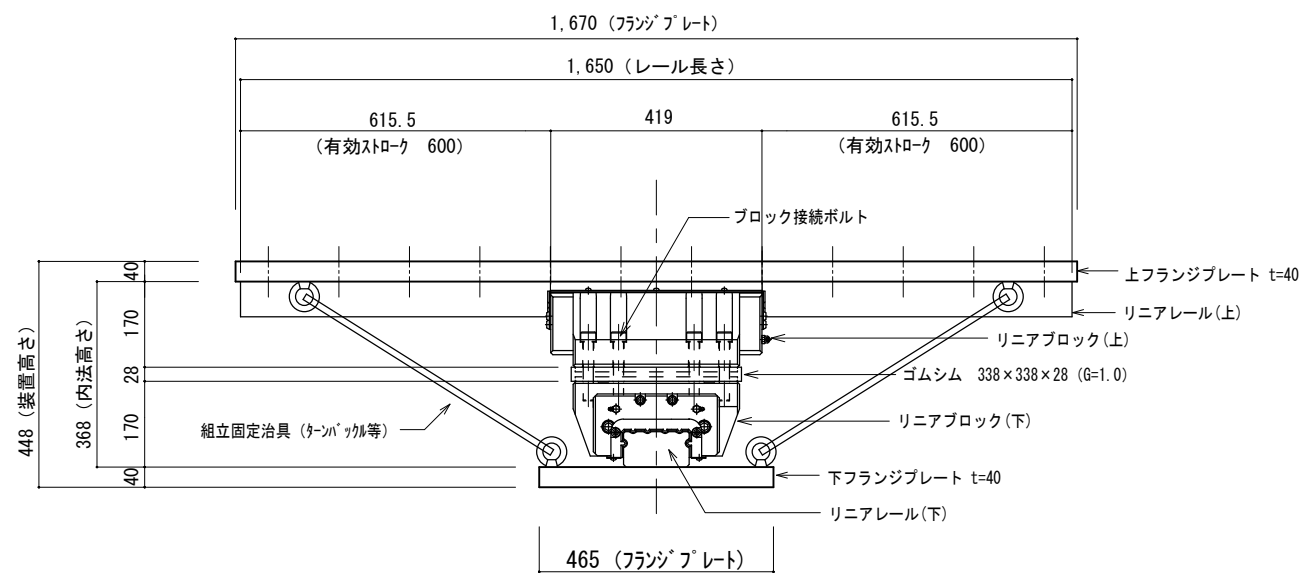
材質・仕様	
リニアブロック	THK5SP S55C [JIS G4051(機械構造用炭素鋼材)より焼入性を向上]
リニアレール	THK5SP S55C [JIS G4051(機械構造用炭素鋼材)より焼入性を向上]
負荷ボール	SUU2 JIS G4805 (高炭素クロム軸受鋼材)
ゴム	天然ゴム (G=1.0)
シムプレート	SUS304 JIS G4304 (熱間圧延ステンレス鋼板及び鋼帯)
フランジプレート	SS400 JIS G3101 (一般構造用圧延鋼材)
ブロック接続ボルト	六角穴付きボルト M20 強度区分10.9
レール固定ボルト	六角穴付きボルト M20 強度区分10.9
プレート固定ボルト	別途
ブロック防錆処理	エポキシ樹脂系塗装 (58012BD-15ﾌﾟﾗｯｸN) 70μm
レール防錆処理	エポキシ樹脂系塗装 (58012BD-15ﾌﾟﾗｯｸN) 40μm
プレート防錆処理	エポキシ樹脂系塗装170μm以上 (接触部は、露出部から20mmまでとする)



CLB250 上フランジプレート



CLB250 下フランジプレート



CLB250 全体組立断面図

CLB免震装置 形状・寸法・重量リスト

装置タイプ	部位	リニアレール・ブロック					フランジプレート				ゴムシム			総重量(kg)	数量(基)	
		呼び番号	レール長(mm)	内法高さ(mm)	数	ブロック接続ボルト(六角穴付)	重量(kg)	長×幅(mm)	厚(mm)	レール固定ボルト(六角穴付)	重量(kg)	長×幅(mm)	厚(mm)			重量(kg)
CLB250	上	JUP250B	1,650	368	1	8-M20 L=120	226	1,670×465	40	28-M20 @120 L=55	244	338×338	28	16	954	5
	下	JUP250A	1,650													

工事名称				
図面名称	CLB250製作図	SCALE	DATE	FILE NAME
		1/15	2011/6/2	CLB250-600
製図		<b>ASEISMIC DEVICES CO., LTD.</b> 株式会社 免制震デバイス 東京都千代田区飯田橋2-1-10 TUGビル4階		

表-6.2 材料の寸法諸元 (標準セット:CLB099~CLB780)

基本型番		CLB099	CLB133	CLB250	CLB385	CLB500	CLB780
Compression Load Load for Friction Coefficient	基準荷重:kN	972	1300	2451	3775	4903	7649
	静定格荷重 Po, tPo:kN	972	1300	2451	3775	4903	7649
Short Term Permissible Load Marginal Permissible Load Kv	短期許容荷重 P <sub>AS</sub> , tP <sub>AS</sub> :kN	687	919	833	1324	1716	2649
	限界強度(荷重) P <sub>cr</sub> , tP <sub>cr</sub> :kN	1944	2600	4902	7550	9806	15298
	引張	188	257	410	481	588	880
	圧縮	3246	4342	8186	12609	16376	25548
	引張	282	385	615	722	882	1320
	圧縮	2106	2242	3471	5171	6120	7957
外形寸法 (mm)	引張	262	282	245	315	388	468
	M	90	105	170	210	235	290
	W	215	260	330	410	465	560
	L	300.4	322.8	419	519	584	722
ブロック寸法 (mm)	H	264	308	448	538	599	730
	Σ Bi	2×92.5	2×110	2×60+150	2×80+180	2×90+200	2×110+250
	C	185	220	270	340	380	470
	N-S	6-M16	6-M18	8-M20	8-M24	8-M27	8-M30
レール寸法 (mm)	W <sub>1</sub>	85	100	130	160	180	230
	M <sub>1</sub>	48	57	70	85	98	120
	M <sub>d</sub>	M22	M24	2×M20	2×M24	2×M27	2×M30
	P	90	105	120	150	150	200
負荷ボール	D <sub>w</sub> (mm)	11.113	13.494	16.669	20.638	23.813	30.163
	個(溝数)	21×(2×2)	20×(2×2)	19×(4×2)	19×(4×2)	19×(4×2)	18×(4×2)
	ρ (%)	51	51	52	52	52	52
ゴムシム	P <sub>t</sub> (mm)	7	9	9	9	9	9
	G(N/mm <sup>2</sup> )	0.8	1.0	1.0	1.0	1.0	1.2
	T <sub>r</sub> (mm)	6	8	10	10	11	12
フランジPL (mm)	W <sub>FP</sub> ×T <sub>FP</sub>	425×32	465×36	465×40	555×45	630×50	740×60
	ボルト&ピッチ	2-M20@125	2-M22@150	2-M22@140	2-M24@150	2-M27@150	2-M30@200

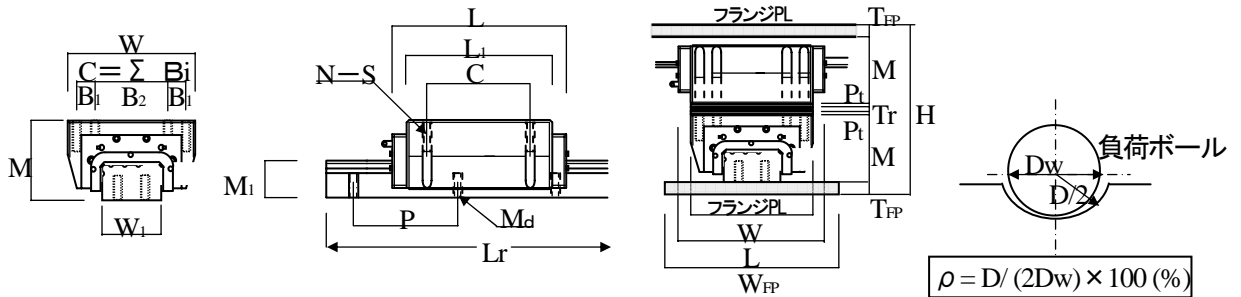


図-3.2 寸法記号



表-6.4 材料の寸法諸元 (引張セット:CLB133H~CLB780H)

基本型番		CLB133H	CLB250H	CLB385H	CLB500H	CLB780H
基準荷重:kN		1300	2451	3775	4903	7649
静定格荷重 P <sub>o</sub> , tP <sub>o</sub> :kN	圧縮	1300	2451	3775	4903	7649
	引張	919	833	1324	1716	2649
短期許容荷重 P <sub>AS</sub> , tP <sub>AS</sub> :kN	圧縮	2600	4902	7550	9806	15298
	引張	557	948	1366	1777	2171
限界強度(荷重) P <sub>cr</sub> , tP <sub>cr</sub> :kN	圧縮	4342	8186	12609	16376	25548
	引張	836	1422	2049	2665	3257
鉛直剛性 kN/mm	圧縮	2242	3471	5171	6120	7957
	引張	282	245	315	388	468
外形寸法 (mm)	M	105	170	210	235	290
	W	260	330	410	465	560
	L	322.8	419	519	584	722
	H	336	478	578	649	770
ブロック寸法(mm)	Σ B <sub>i</sub>	2×110	2×60+150	2×80+180	2×90+200	2×110+250
	C	220	270	340	380	470
	N-S	6-M18	8-M20	8-M24	8-M27	8-M30
レール寸法 (mm)	W <sub>1</sub>	100	130	160	180	230
	M <sub>1</sub>	57	70	85	98	120
	M <sub>d</sub>	M24	2×M20	2×M24	2×M27	2×M30
	P	105	120	150	150	200
負荷ボール	D <sub>w</sub> (mm)	13.494	16.669	20.638	23.813	30.163
	個(溝数)	20×(2×2)	19×(4×2)	19×(4×2)	19×(4×2)	18×(4×2)
	ρ (%)	51	52	52	52	52
ゴムシム	P <sub>t</sub> (mm)	9	9	9	9	9
	G(N/mm <sup>2</sup> )	1.0	1.0	1.0	1.0	1.2
	T <sub>r</sub> (mm)	8	10	10	11	12
フランジPL (mm)	W <sub>FP</sub> ×T <sub>FP</sub>	465×50	465×55	555×65	630×75	740×80
	ボレット&ピッチ	2-M22@150	2-M22@140	2-M24@150	2-M27@150	2-M30@200

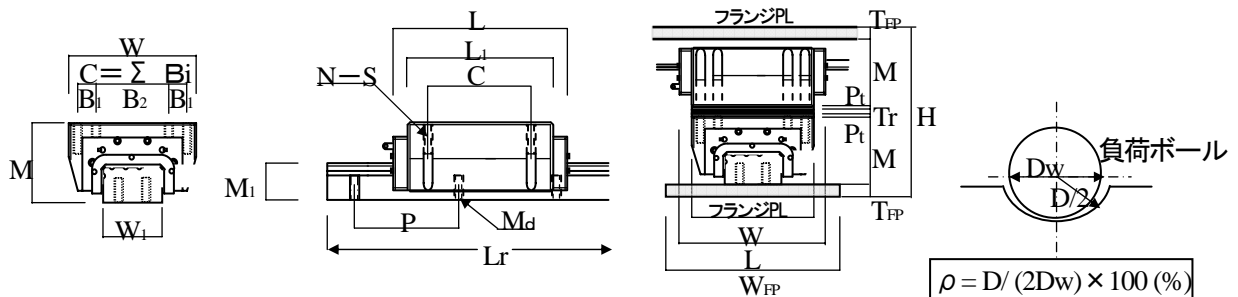


図-3.4 寸法記号

### 8.3 免震材料の設置精度の基準

表-10 設置精度の基準値

項目	精度基準	備考(検査法、許容の根拠)	
設置時	錆び、傷、汚れ	なし	目視検査
	ブロック位置ずれ	±5mm以下	(図-6.1)：限界変形量確保
	レール傾斜角 $\theta_x$	$\theta_x \leq 1/500 \text{ rad}$	(図-6.3、6.4)：限界：10/1000 rad
	レール直交傾斜角 $\theta_y$	$\theta_y \leq 1/500 \text{ rad}$	(図-6.5、6.6)：限界：10/1000 rad
	レール振れ角 $\theta_z$	$\theta_z \leq 1/300 \text{ rad}$	(図-6.7、6.8)：振れ限界：18/1000 rad
	構造芯平行ずれ、振れずれ	±5mm以下、かつ $\theta_z \leq 1/300 \text{ rad}$	解析との整合性確保の為
	設置レベル差 $\Delta h$	$\Delta h \leq \pm 0.01H$ 、かつ $\Delta h \leq 1.5 \text{ mm}$	$\Delta h$ ：設計レベルとの差分、施工精度 (図-6.2)
* レベルおよび JIS1 級メジャーによる		(図-6.2)	

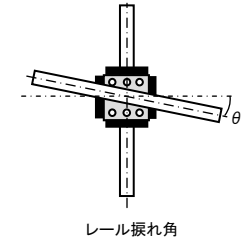


図 6.7 レール振れ角の定義

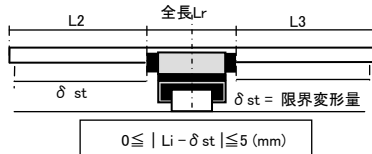


図 6.1 ブロック位置ずれ測定法

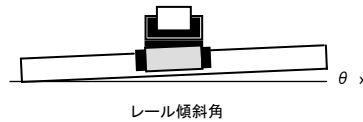


図 6.3 レール傾斜角の定義

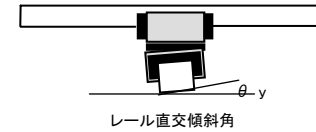


図 6.5 レール直交傾斜角の定義

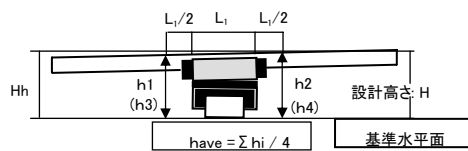


図 6.2 設置レベル差測定法

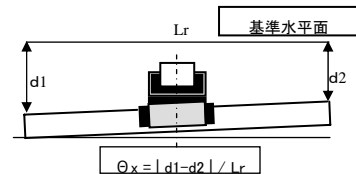


図 6.4 レール傾斜角の測定法

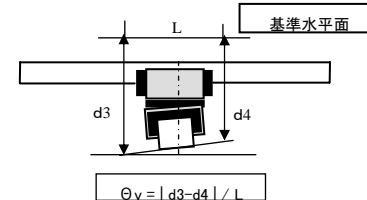


図 6.6 レール直交傾斜角の測定法

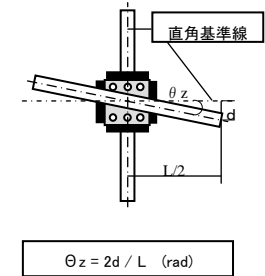


図 6.8 レール振れ角の測定法

### 8.4 免震材料の取付部材料強度及び剛性を確保するための地震時設計クライテリア

表-11 地震時設計の基準値

項目	精度基準	備考(検査法、許容の根拠)
装置の傾斜	レール傾斜角 $\theta_x$	$\theta_x \leq 8/1000 \text{ rad}$ 限界角：10/1000rad (図-6.3、6.4)、設置誤差考慮
	レール直交傾斜角 $\theta_y$	$\theta_y \leq 8/1000 \text{ rad}$ 限界角：10/1000rad (図-6.5、6.6)、設置誤差考慮
	レール振れ角 $\theta_z$	$\theta_z \leq 14/1000 \text{ rad}$ 振れ限界：18/1000rad (図-6.7、6.8) 単体の静的許容モーメント( $M_0$ )時に 18/1000rad (CLB250)

## APPENDIX C

### **Drawings for Load Cell Assemblies and Connection to the Simulator Platform**

Building Isolated with Hybrid Lead-Rubber Isolation System

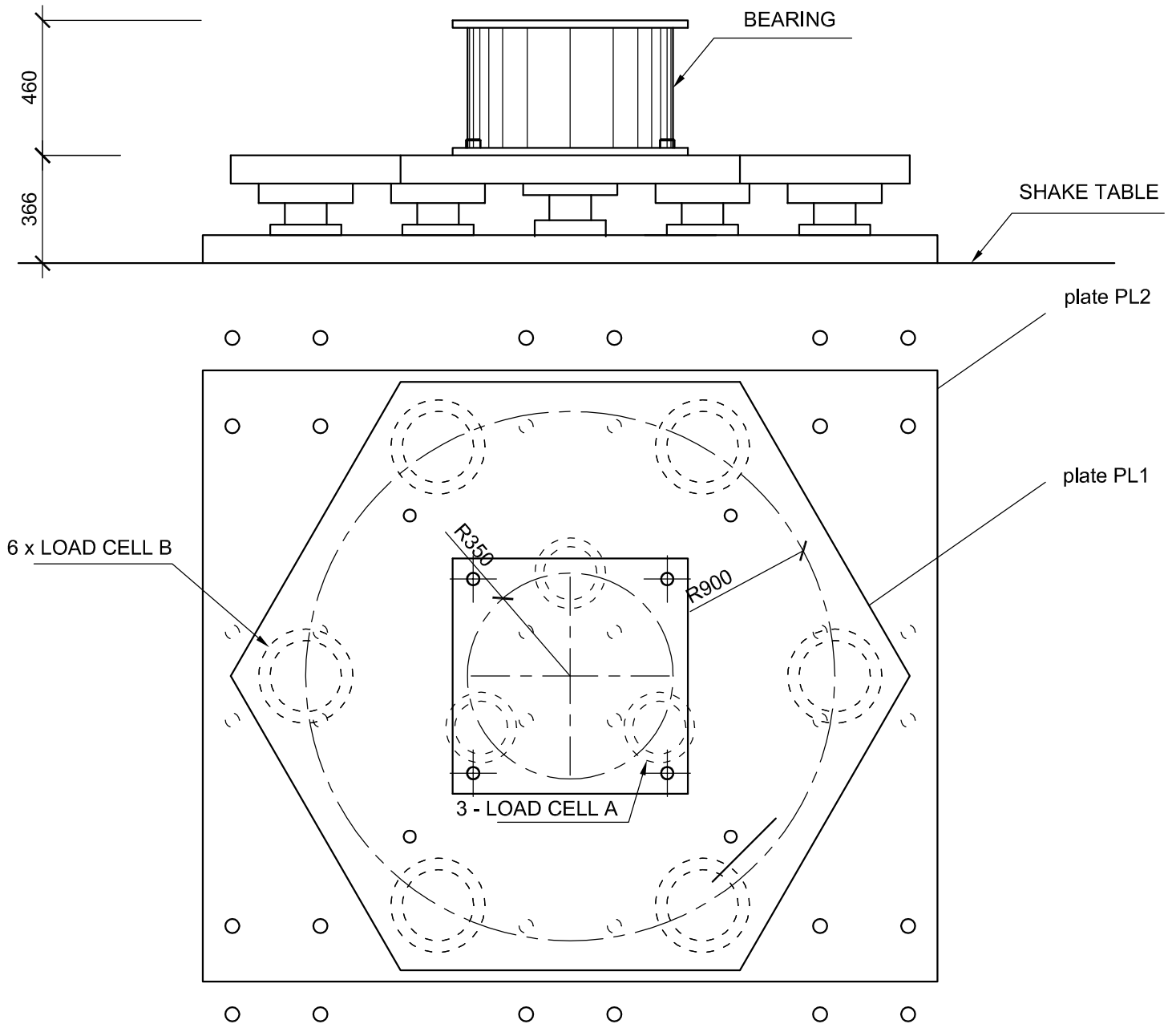
Developed by NEES TIPS Project for NEES/E-Defense Collaborative Test Program on

Innovative Isolation Systems, 2011-2012

Lead Contributor: Nhan D. Dao

#### **Connection Drawings**

B-001	Connecting Plate PL1 – East Column
B-002	Connecting Plate PL1 – East Column
B-003	Connecting Plate PL2 – East Column and Placer
B-004	Connecting Plate PL2 – North, South, West Columns
B-005	Connecting Plate PL2 – North, South, West Columns
B-006	Connecting Plate PL2 – North, South, West Columns
B-007	Elevation of Load Cell Connection
B-008	Connecting Bearing to Structure



**BEARING CONNECTION - EAST COLUMN (1 UNIT)**

SCALE: 1/20



UNIVERSITY OF NEVADA, RENO  
1664 N. Virginia St, Reno, NV 89557

EXPERIMENTAL EVALUATION OF  
AN INNOVATIVE ISOLATION SYSTEM  
FOR A LIGHTWEIGHT STEEL MOMENT FRAME BUILDING

CONNECTING PLATE PL1 - EAST COLUMN

Drawing: B-001  
Scale: As Shown  
Drawn by: N. D. Dao  
Checked by:  
Date: 28 Apr 2011

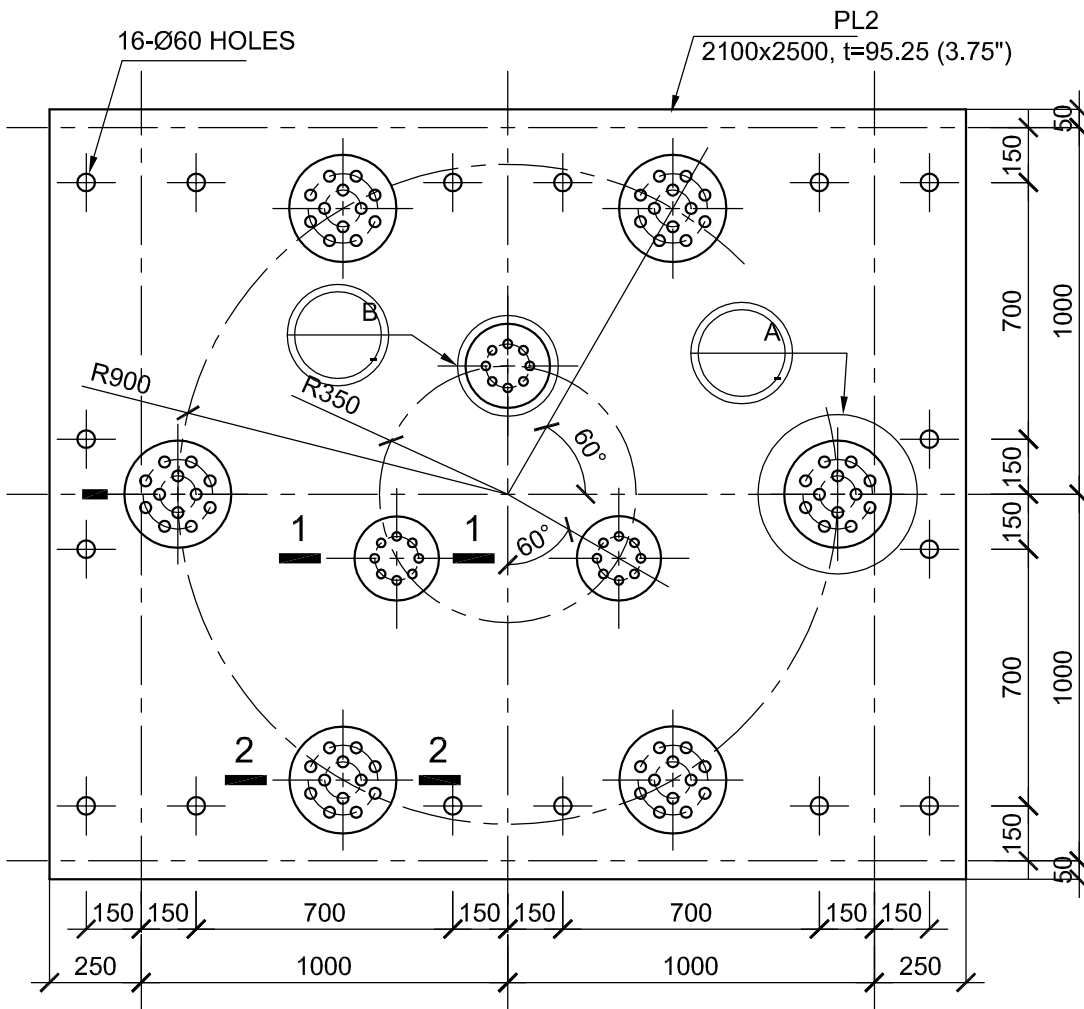
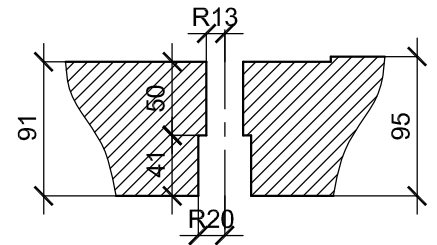


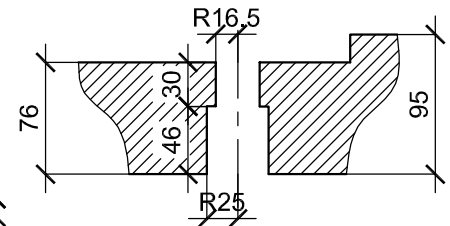
**PLATE PL2 - EAST COLUMN (1 UNIT)**

SCALE: 1/20



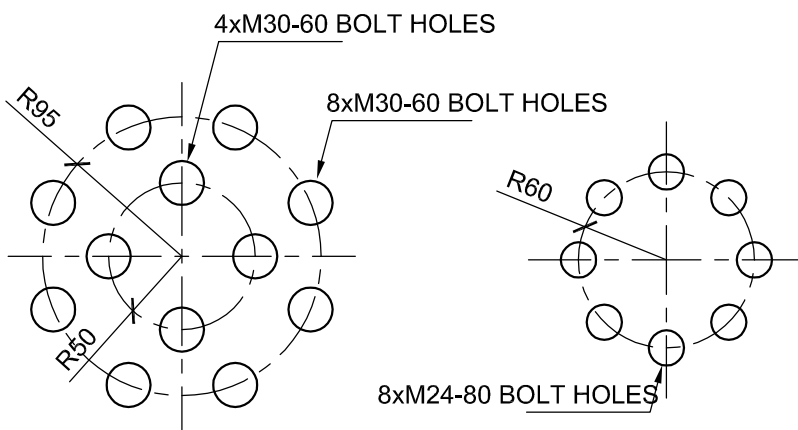
**M24-80 BOLT HOLE**

SCALE: 1/5



**M30-60 BOLT HOLE**

SCALE: 1/5

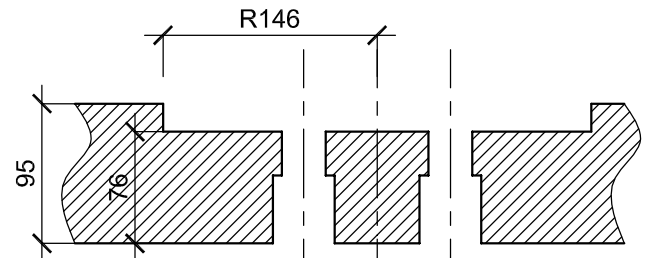


**DETAIL A**

SCALE: 1/5

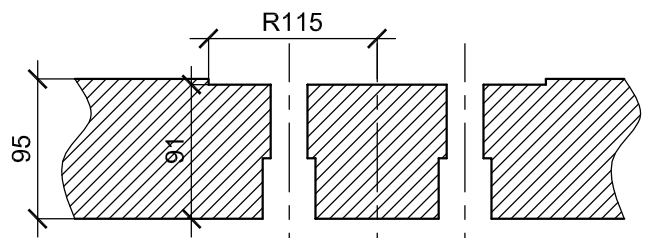
**DETAIL B**

SCALE: 1/5



**SECTION 2-2**

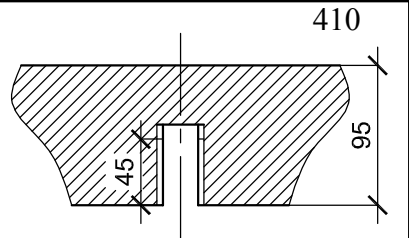
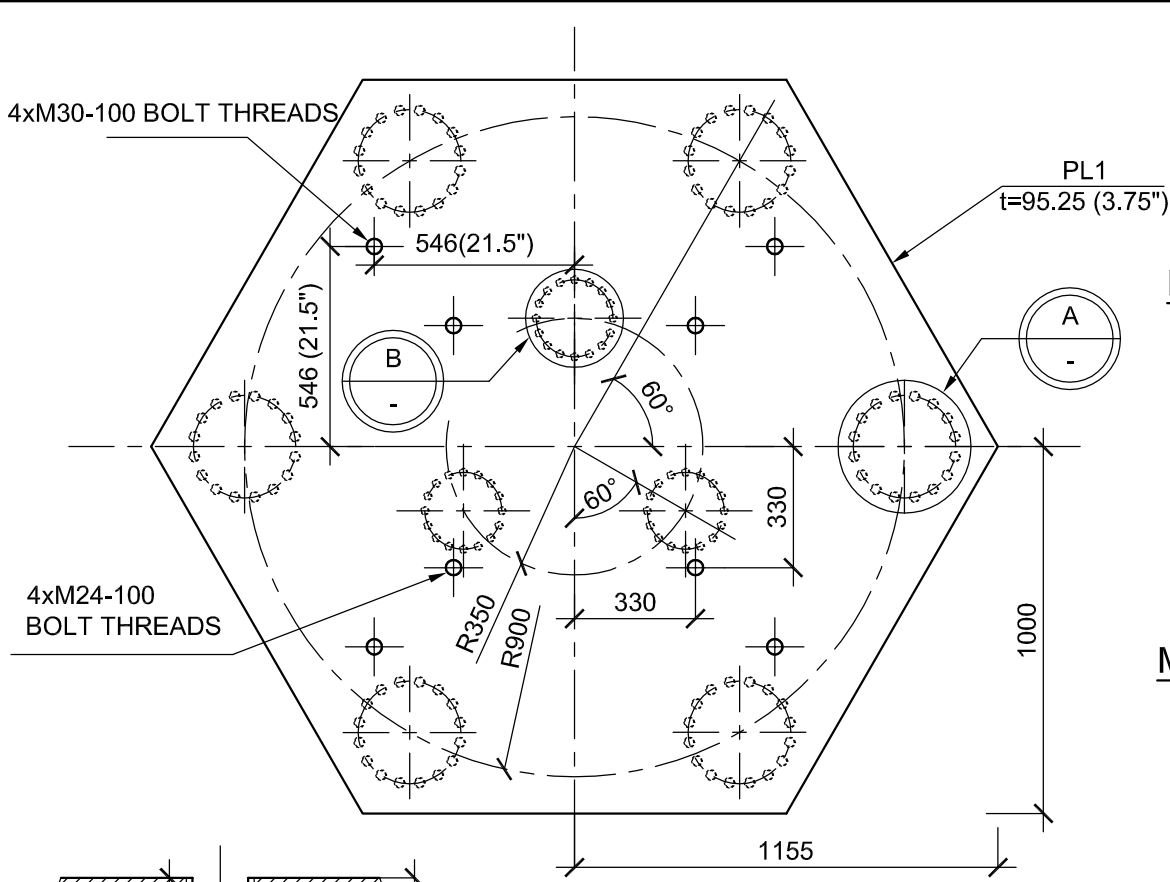
SCALE: 1/5



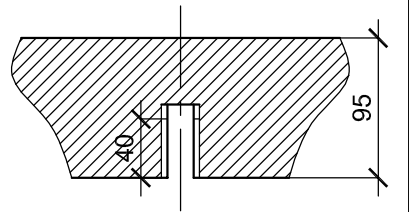
**SECTION 1-1**

SCALE: 1/5

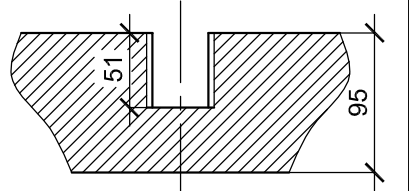




**M24-100 BOLT THREAD**  
SCALE: 1/5



**M18-80 BOLT THREAD**  
SCALE: 1/5



**M30-100 BOLT THREAD**  
SCALE: 1/5

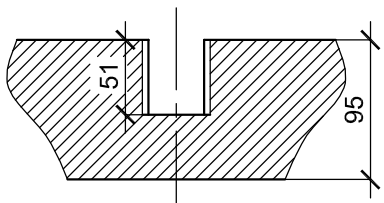
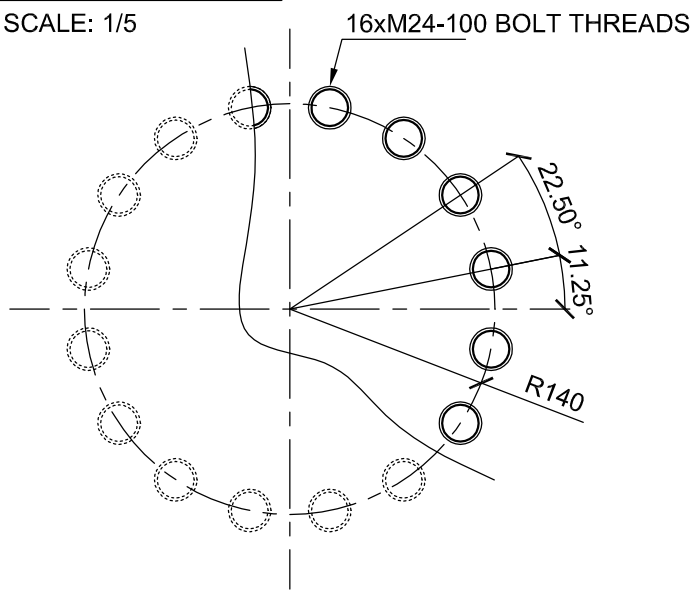
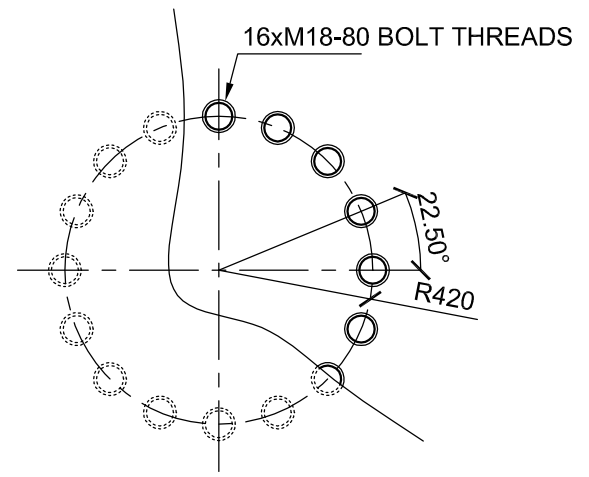


**PLATE PL1 - EAST COLUMN (1 UNIT)**  
SCALE: 1/20

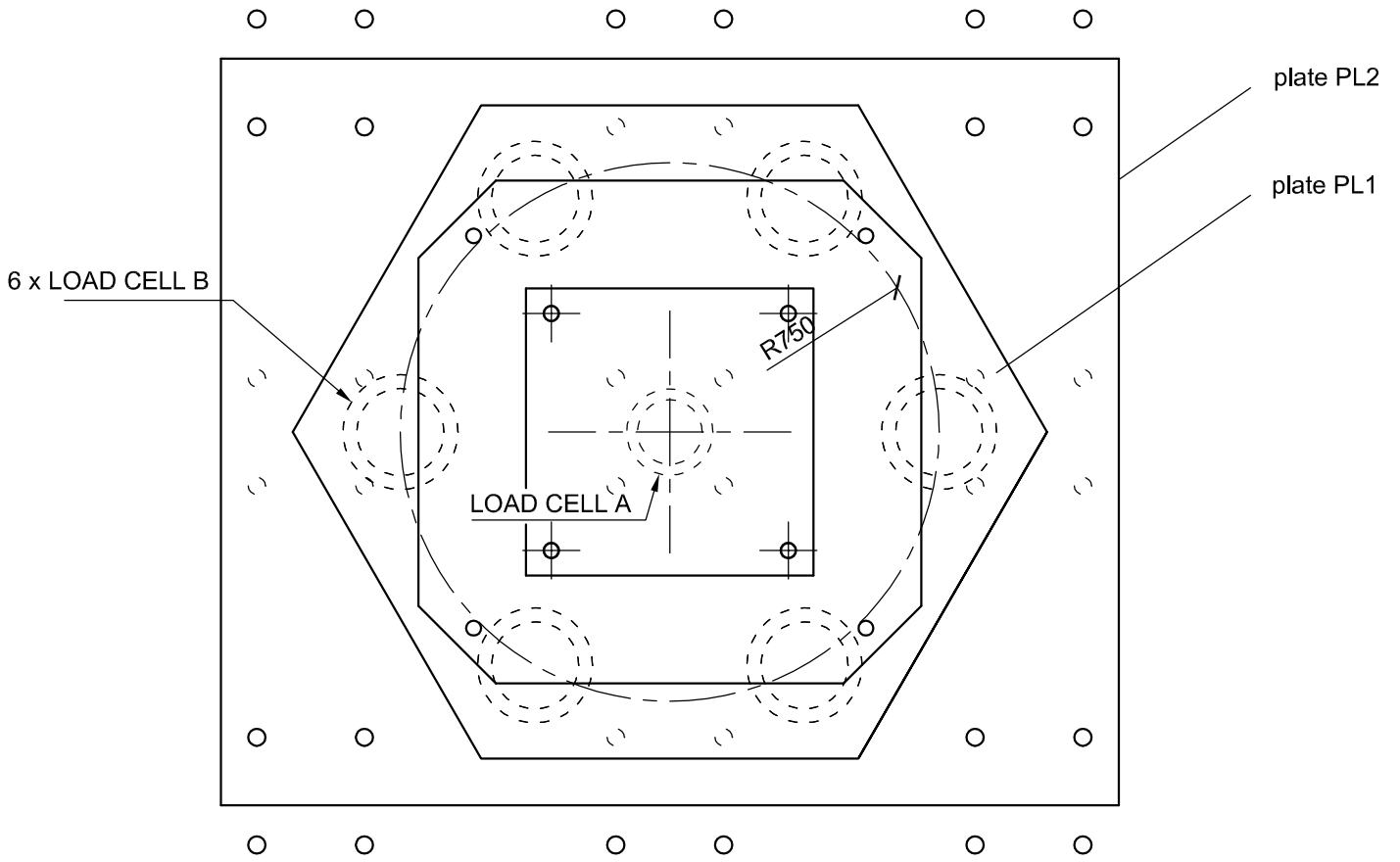
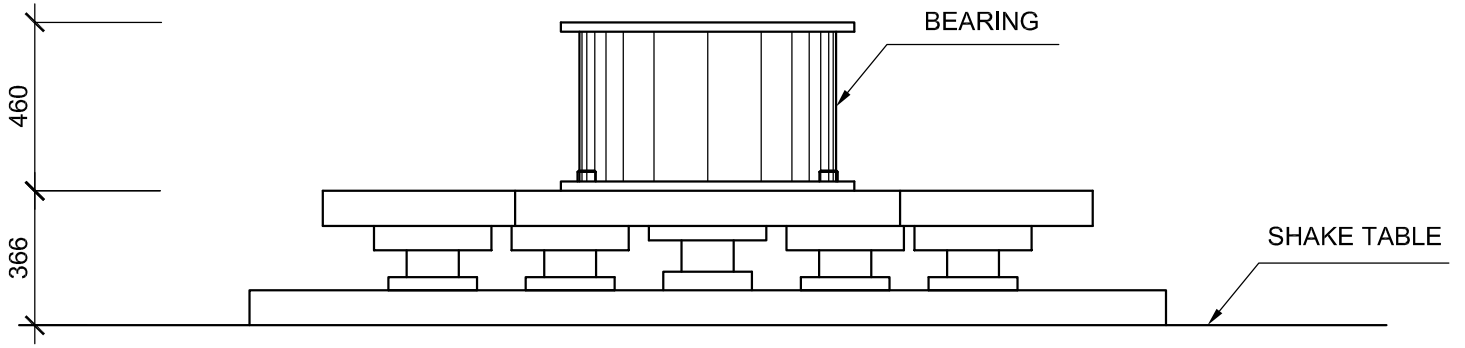
**M24-100 BOLT THREAD**  
SCALE: 1/5



**DETAIL A**  
SCALE: 1/5



**DETAIL B**  
SCALE: 1/5



**BEARING CONNECTION - N, S, W COLUMNS (3 UNITS)**

SCALE: 1/20



UNIVERSITY OF NEVADA, RENO  
1664 N. Virginia St, Reno, NV 89557

EXPERIMENTAL EVALUATION OF  
AN INNOVATIVE ISOLATION SYSTEM  
FOR A LIGHTWEIGHT STEEL MOMENT FRAME BUILDING

CONNECTING PLATE PL2 -  
NORTH, SOUTH, WEST COLUMNS

Drawing: B-004  
Scale: As Shown  
Drawn by: N. D. Dao  
Checked by:  
Date: 28 Apr 2011

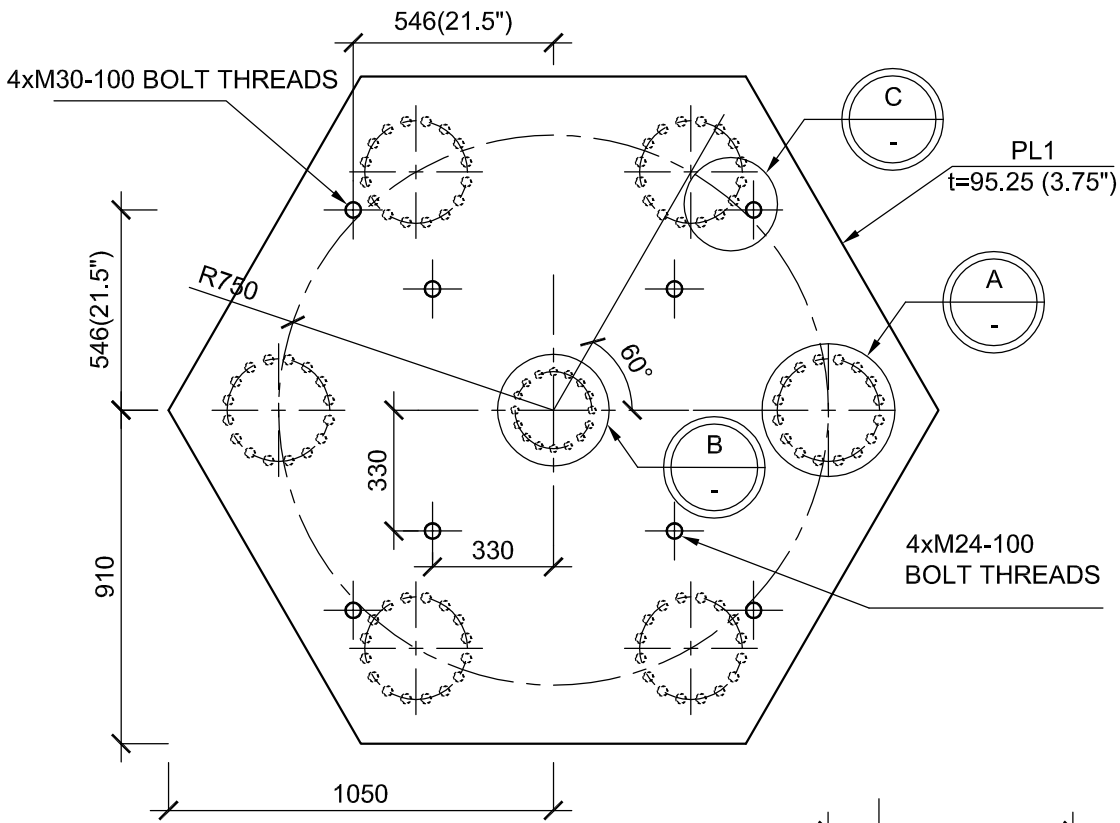
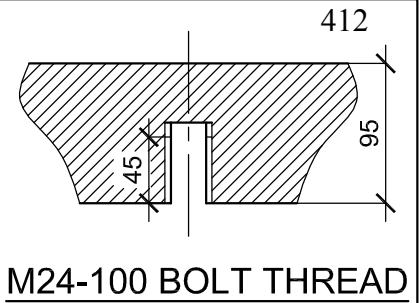
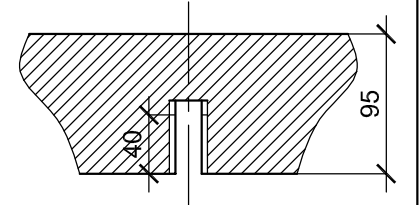


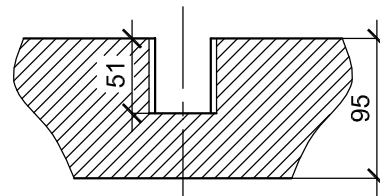
**PLATE PL1 - N, S, W COLUMNS (3 UNITS)**  
SCALE: 1/20



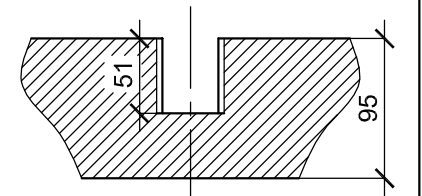
**M24-100 BOLT THREAD**  
SCALE: 1/5



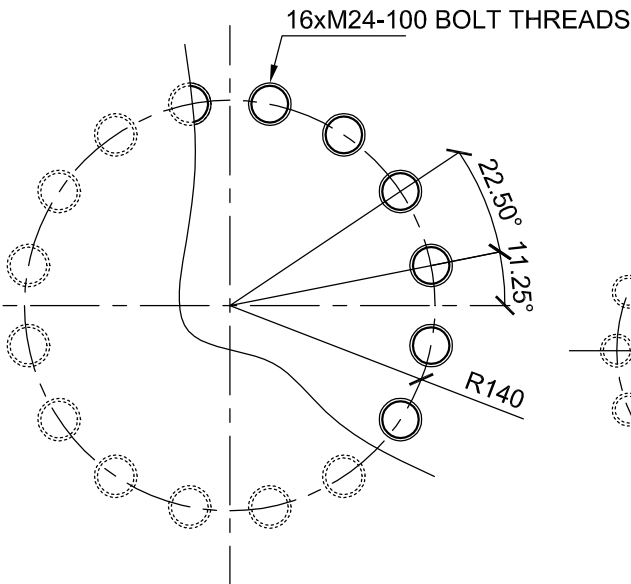
**M18-80 BOLT THREAD**  
SCALE: 1/5



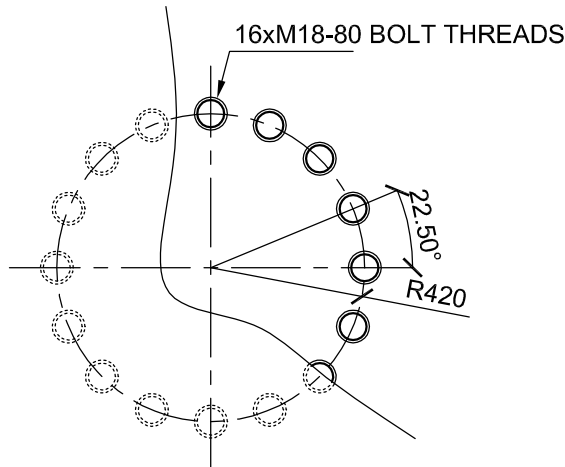
**M24-100 BOLT THREAD**  
SCALE: 1/5



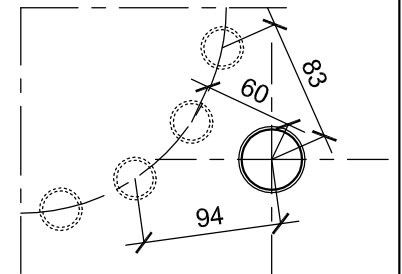
**M30-100 BOLT THREAD**  
SCALE: 1/5



**DETAIL A**  
SCALE: 1/5



**DETAIL B**  
SCALE: 1/5



**DETAIL C**  
SCALE: 1/5



UNIVERSITY OF NEVADA, RENO  
1664 N. Virginia St, Reno, NV 89557

EXPERIMENTAL EVALUATION OF  
AN INNOVATIVE ISOLATION SYSTEM  
FOR A LIGHTWEIGHT STEEL MOMENT FRAME BUILDING

CONNECTING PLATE PL2 -  
NORTH, SOUTH, WEST COLUMNS

Drawing: B-005  
Scale: As Shown  
Drawn by: N. D. Dao  
Checked by:  
Date: 28 Apr 2011



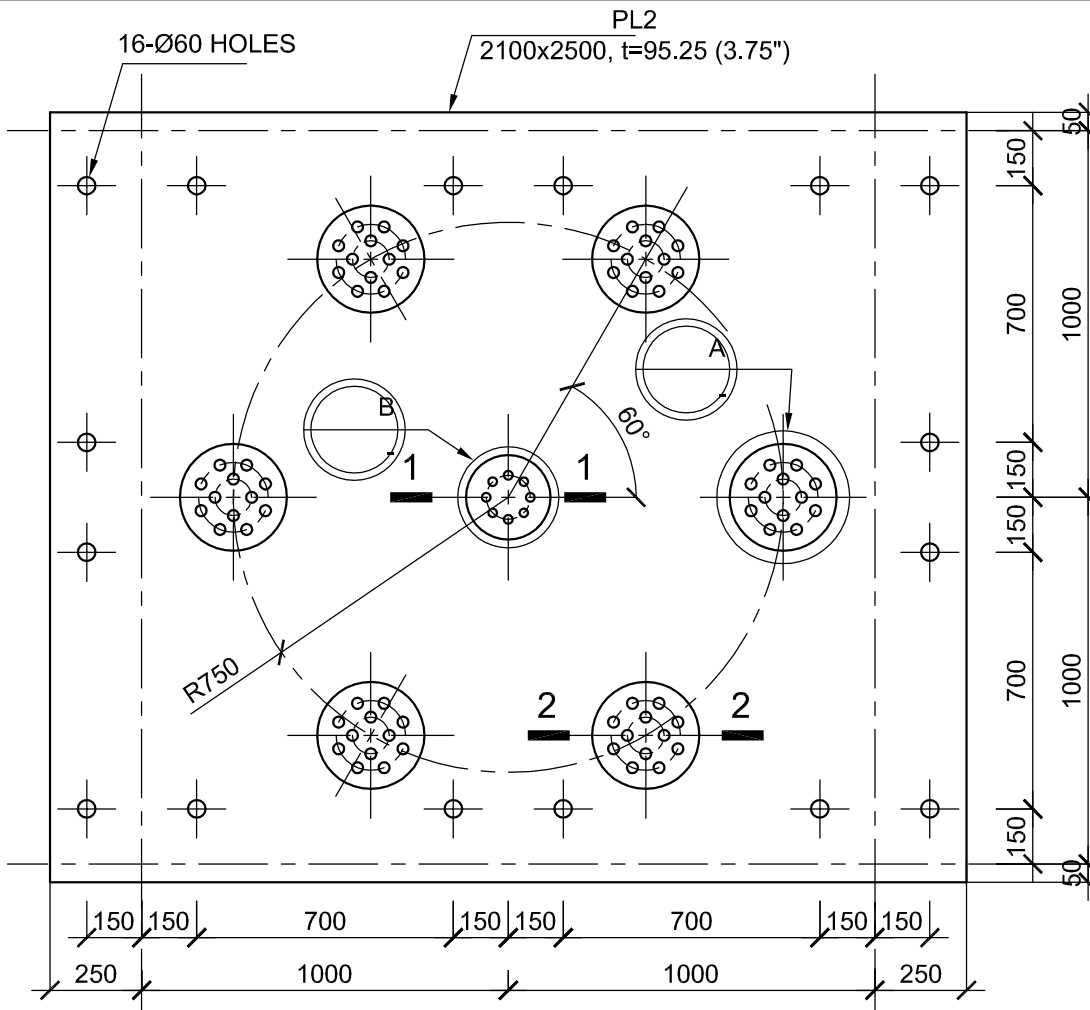
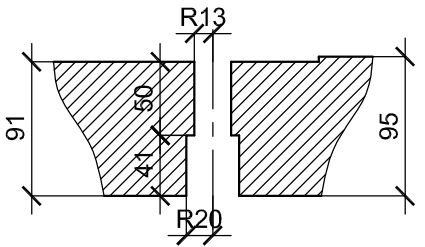


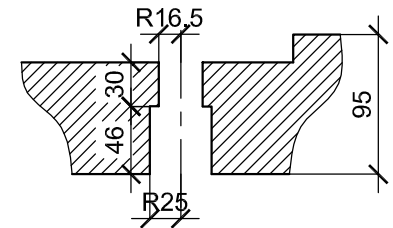
**PLATE PL2, N, S, W COLUMNS (3 UNITS)**

SCALE: 1/20



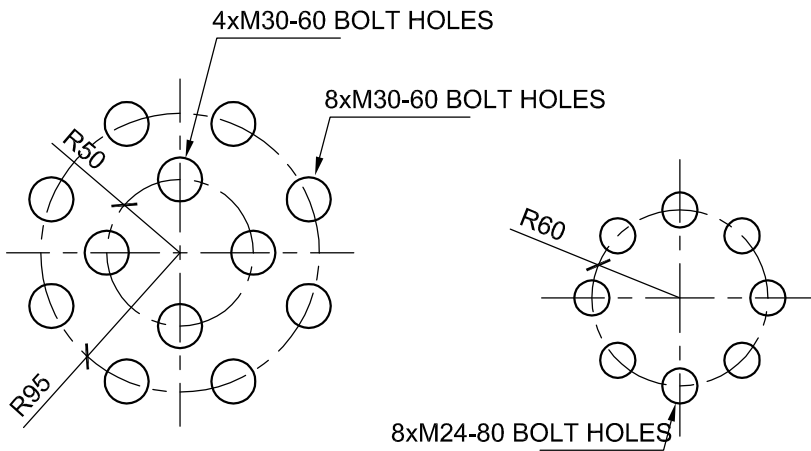
**M24-80 BOLT HOLE**

SCALE: 1/5



**M30-60 BOLT HOLE**

SCALE: 1/5

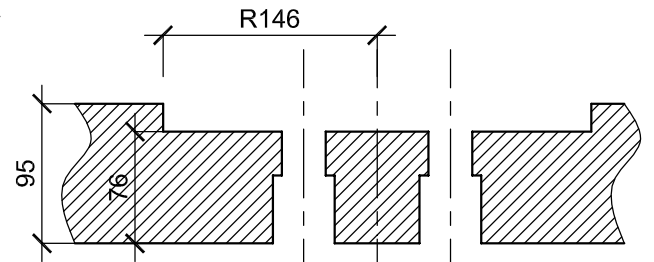


**DETAIL A**

SCALE: 1/5

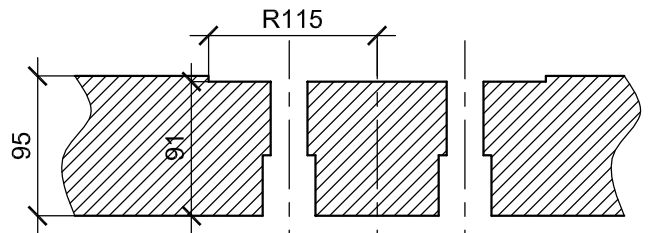
**DETAIL B**

SCALE: 1/5



**SECTION 2-2**

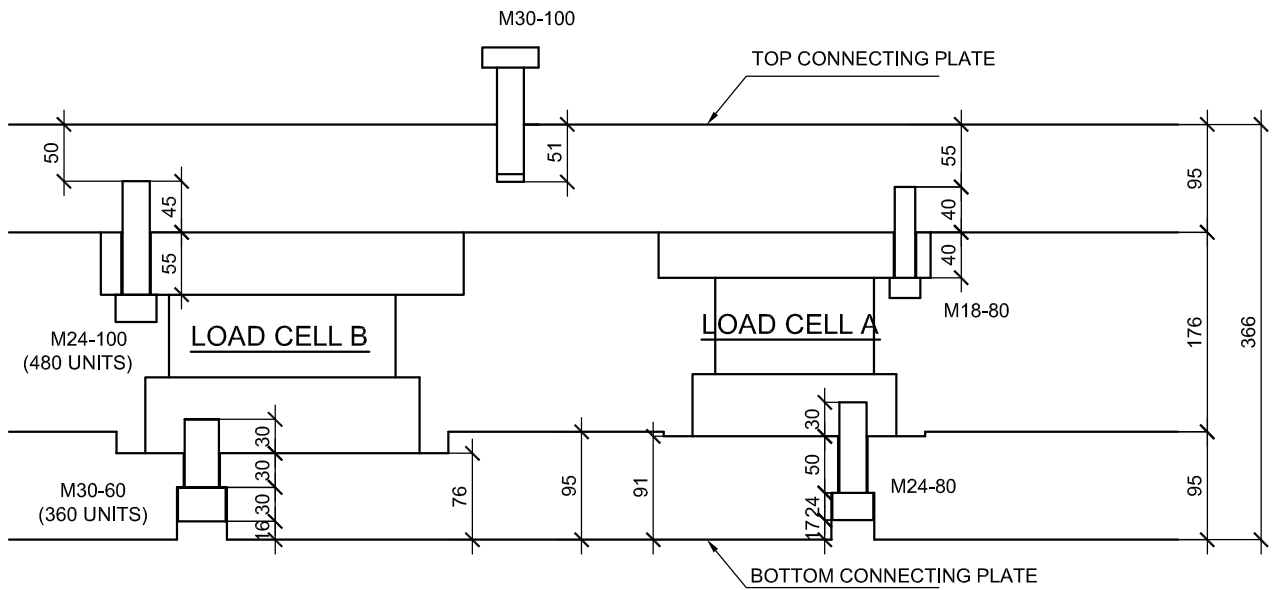
SCALE: 1/5



**SECTION 1-1**

SCALE: 1/5





UNIVERSITY OF NEVADA, RENO  
1664 N. Virginia St, Reno, NV 89557

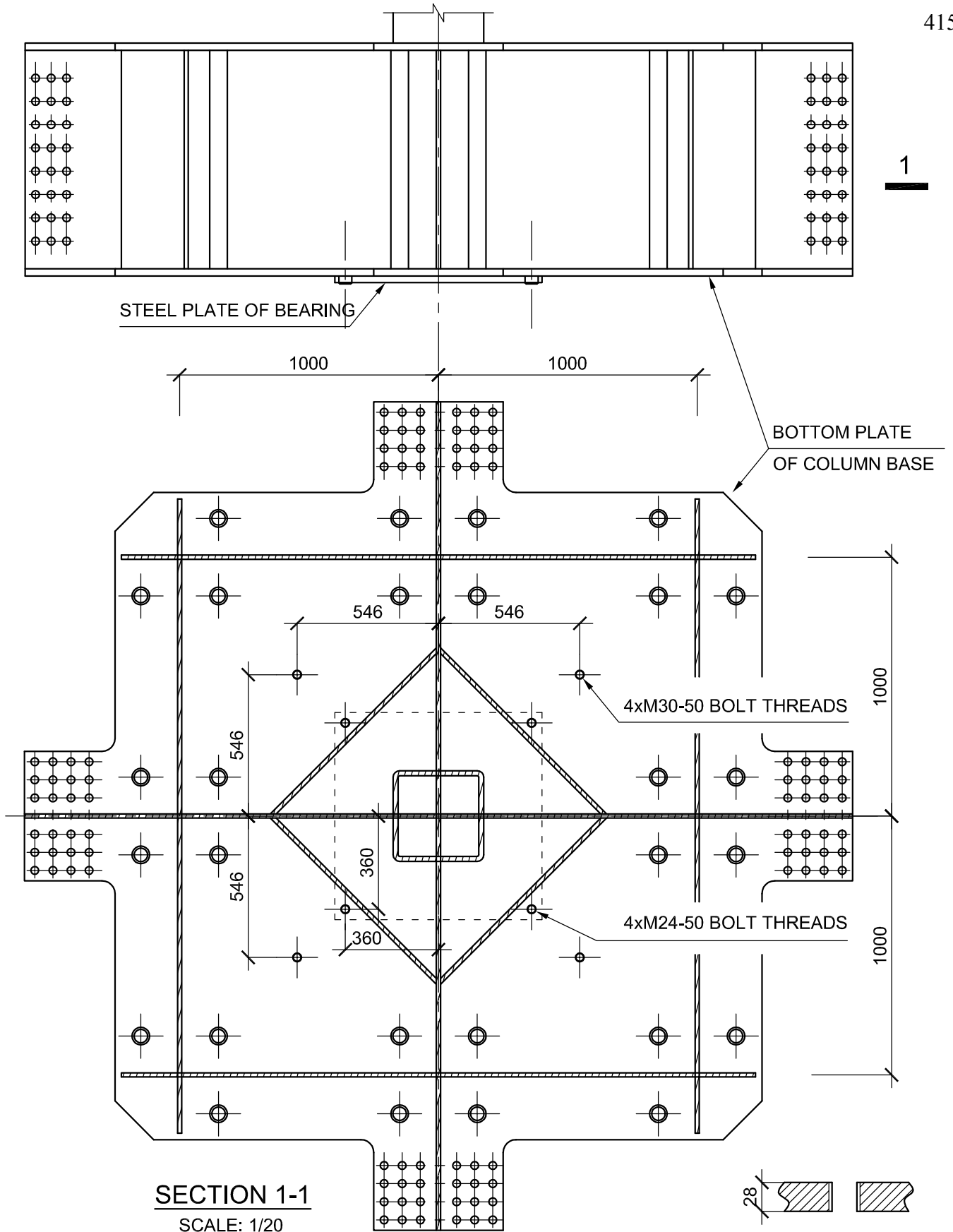
EXPERIMENTAL EVALUATION OF  
AN INNOVATIVE ISOLATION SYSTEM  
FOR A LIGHTWEIGHT STEEL MOMENT FRAME BUILDING

ELEVATION OF LOAD CELL CONNECTING

Drawing: B-007  
Scale: As Shown  
Drawn by: N. D. Dao  
Checked by:  
Date: 28 Apr 2011

1

1



## APPENDIX D

### Drawings for Structural Instrumentation Plan

Building Isolated with Hybrid Lead-Rubber Isolation System

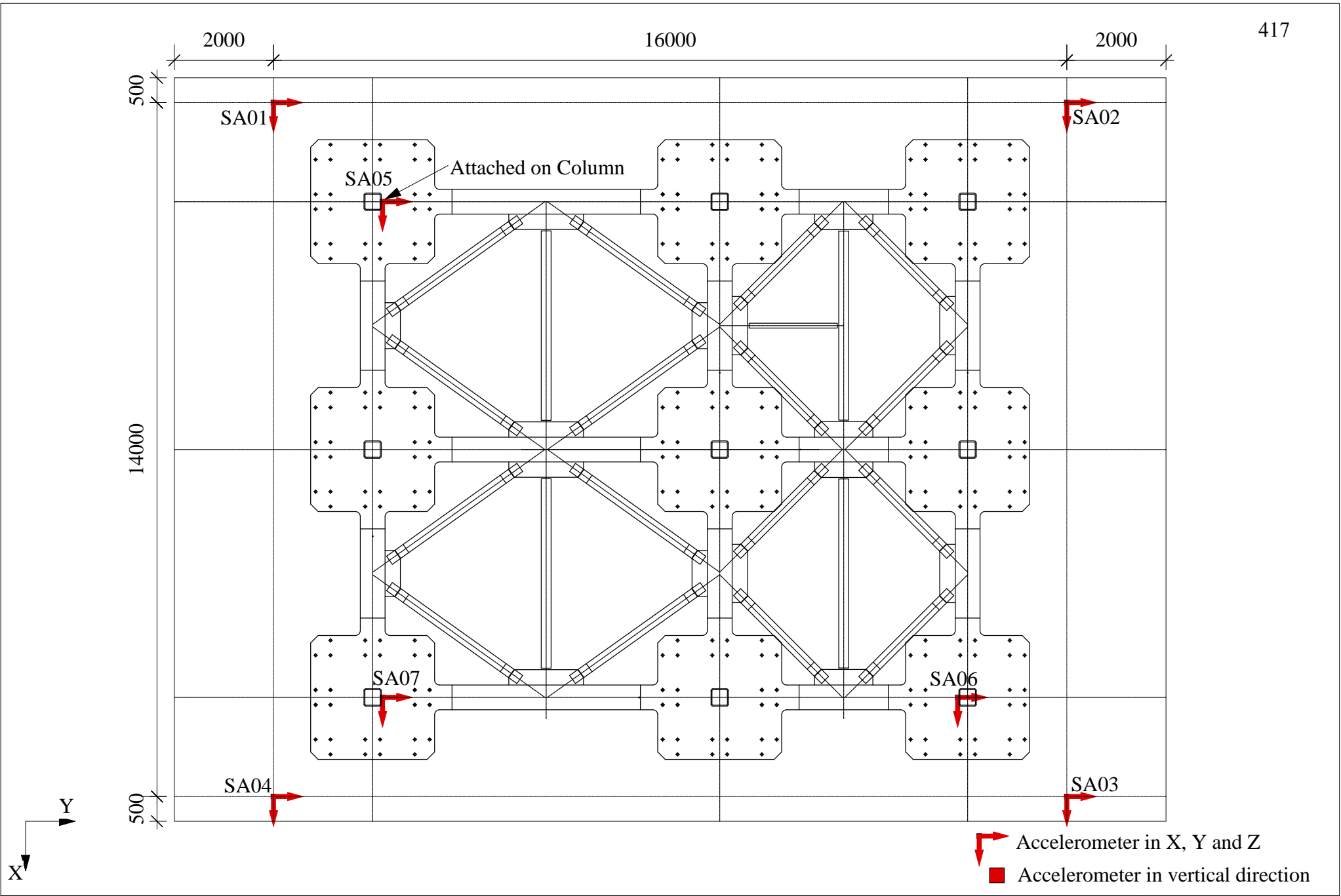
Developed by Hyogo Earthquake Engineering Research Center for NEES/E-Defense  
Collaborative

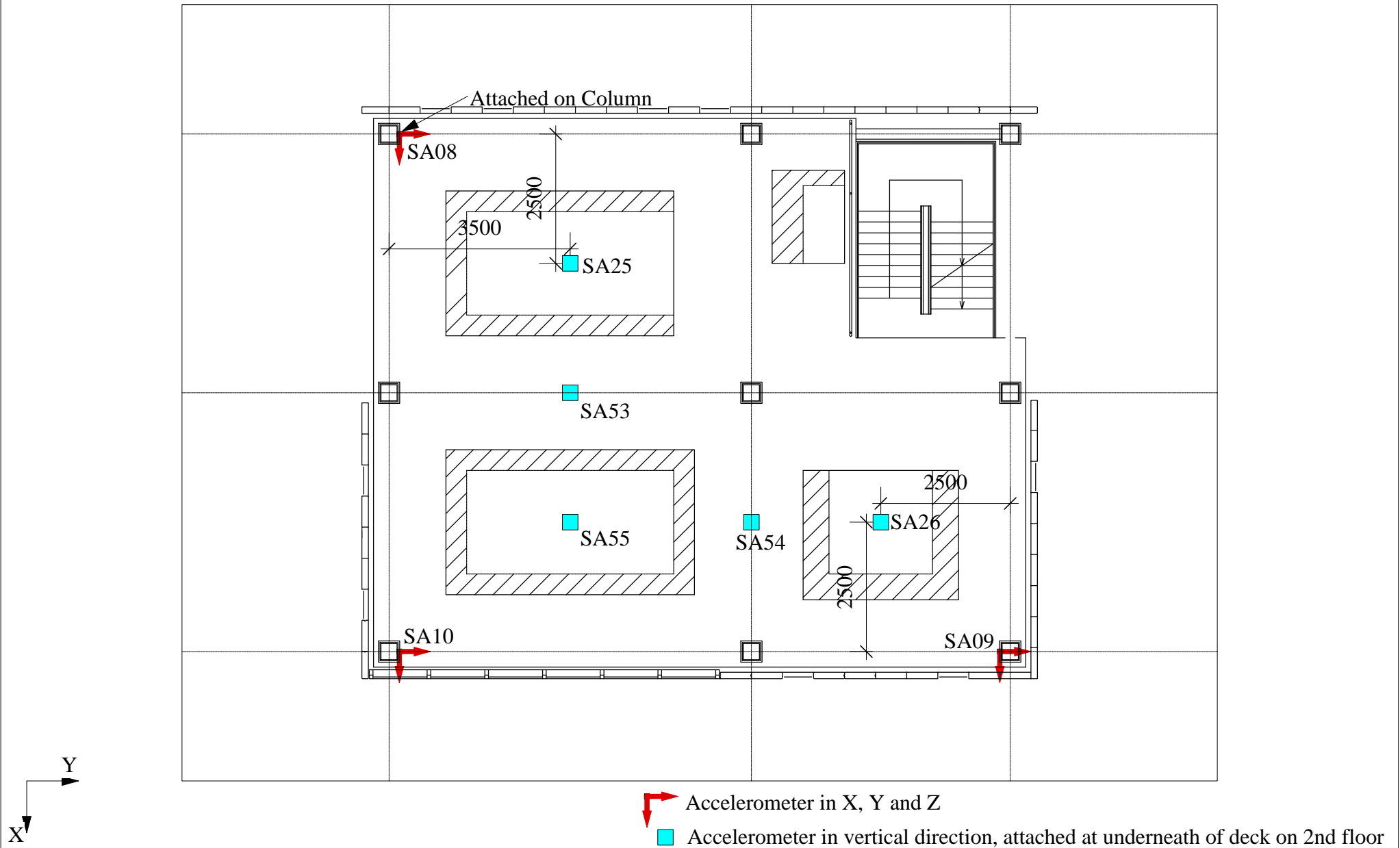
Test Program on Innovative Isolation Systems, 2011-2012

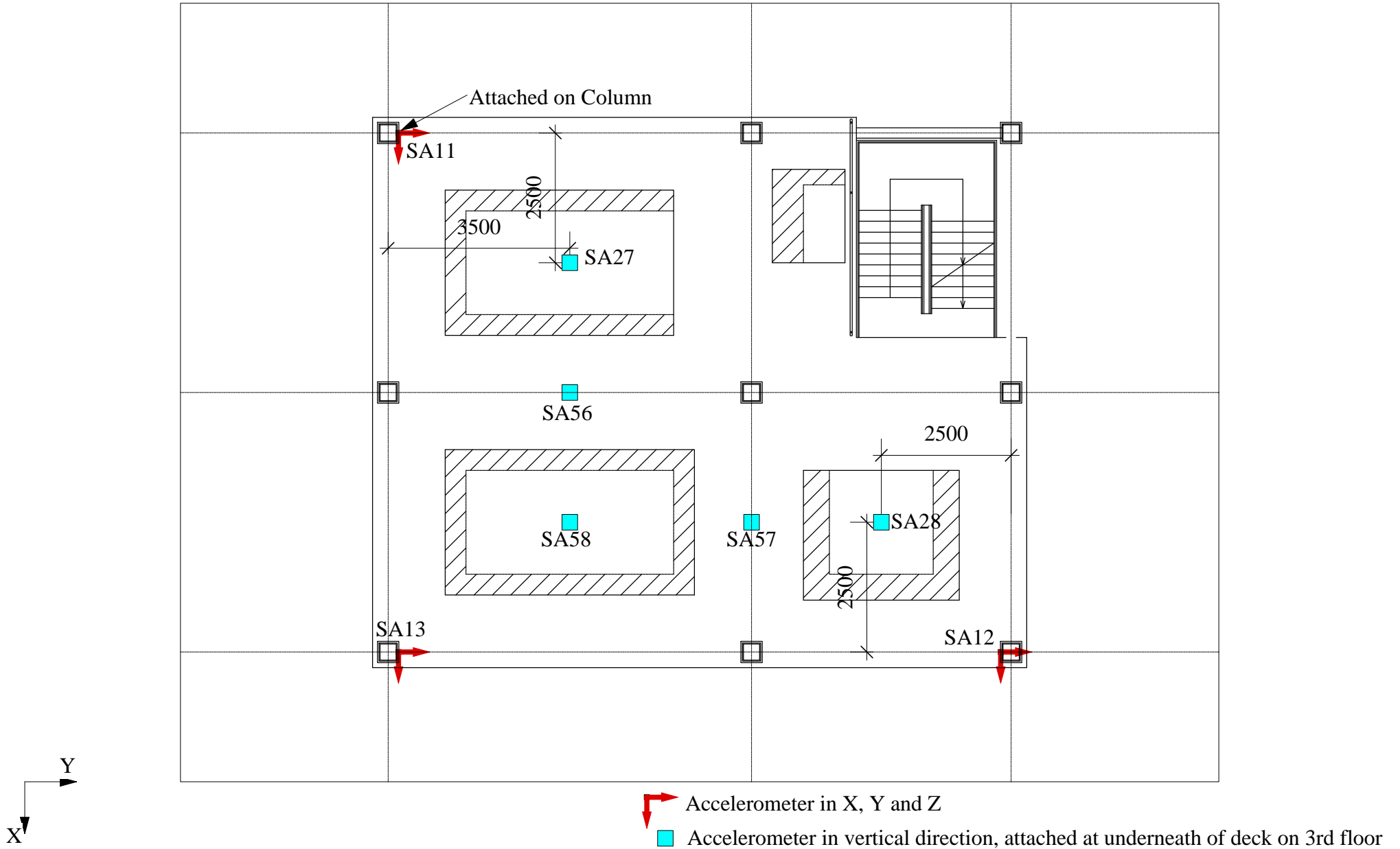
Lead Contributor: Tomohiro Sasaki

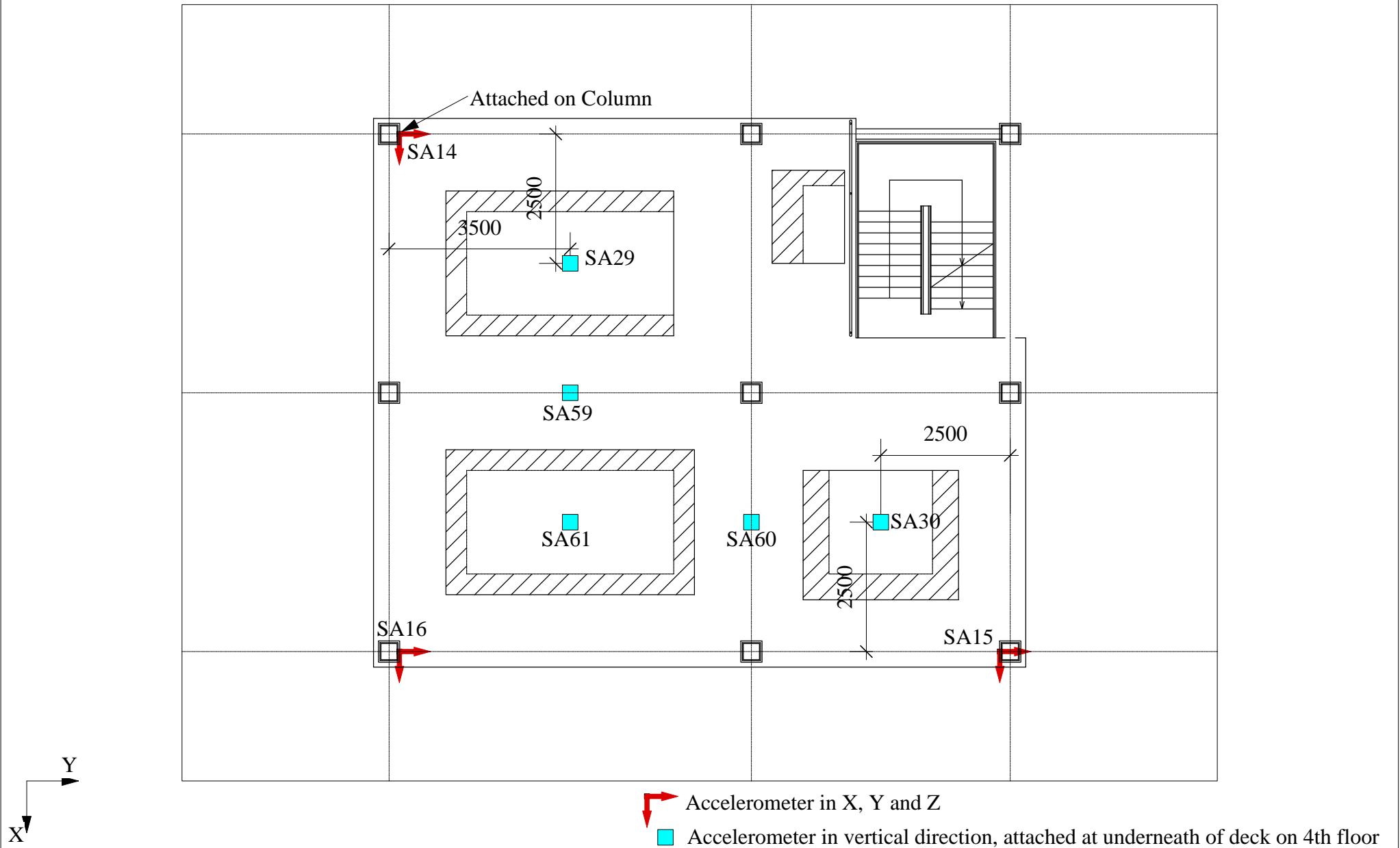
#### Instrumentation Drawings

Sheet 1	Accelerometer (Table & 1F)
Sheet 2	Accelerometer (2F)
Sheet 3	Accelerometer (3F)
Sheet 4	Accelerometer (4F)
Sheet 5	Accelerometer (5F)
Sheet 6	Accelerometer (RF)
Sheet 7	Accelerometers for Hexagon-shaped Steel Plates
Sheet 8	Displacement Transducers for Bearings
Sheet 9	Displacement Transducers (1F)
Sheet 10	Displacement Transducers (2F)
Sheet 11	Displacement Transducers (3F)
Sheet 12	Displacement Transducers (4F)
Sheet 13	Displacement Transducers (5F)
Sheet 14	Load cells for Bearings (LRB/CLB)
Sheet 15	Strain Gages on Column Faces (1F)
Sheet 16	Strain Gages on Column Faces (2F)
Sheet 17	Strain Gages on Column Faces (3F)
Sheet 18	Strain Gages on Column Faces (4F)

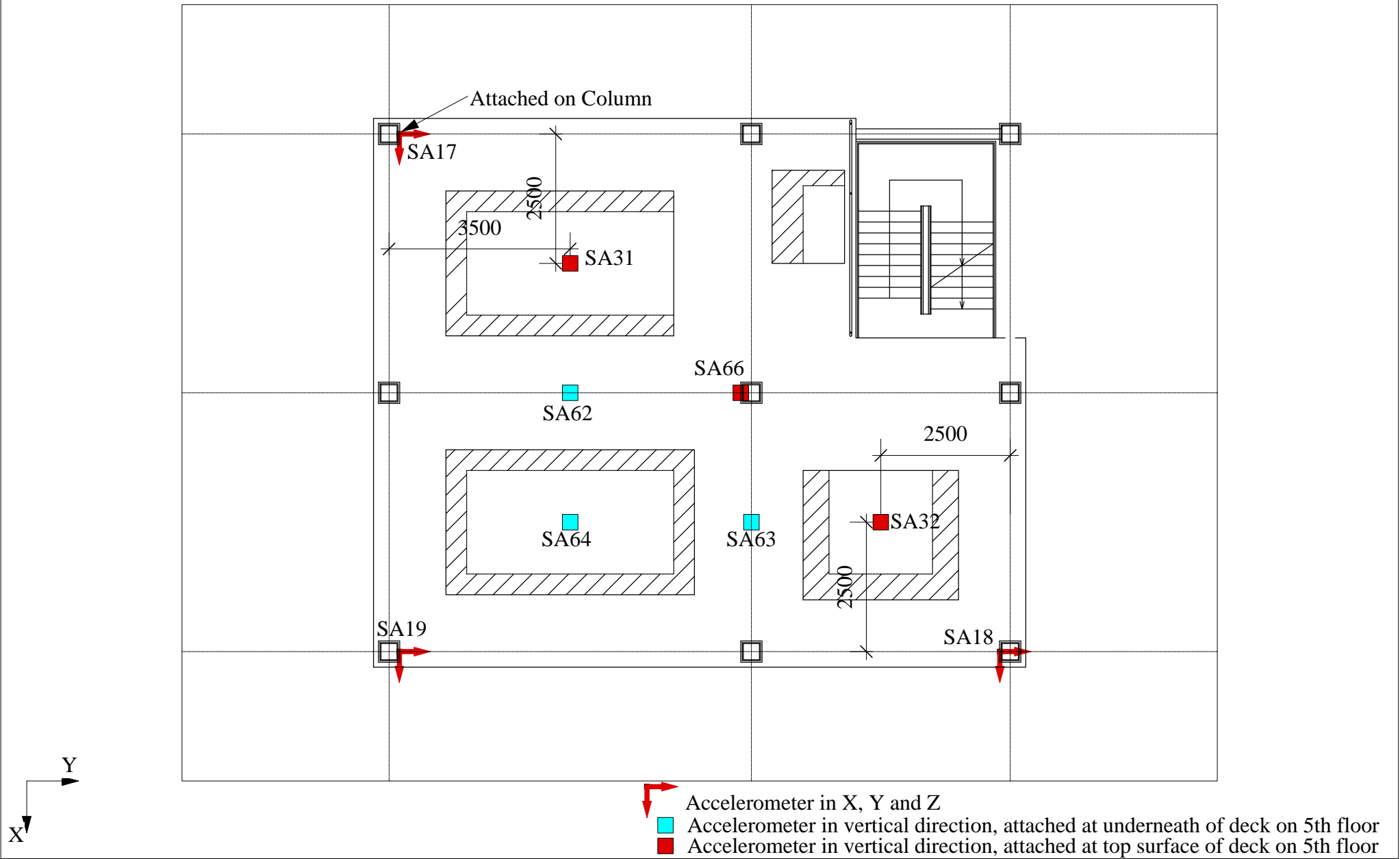


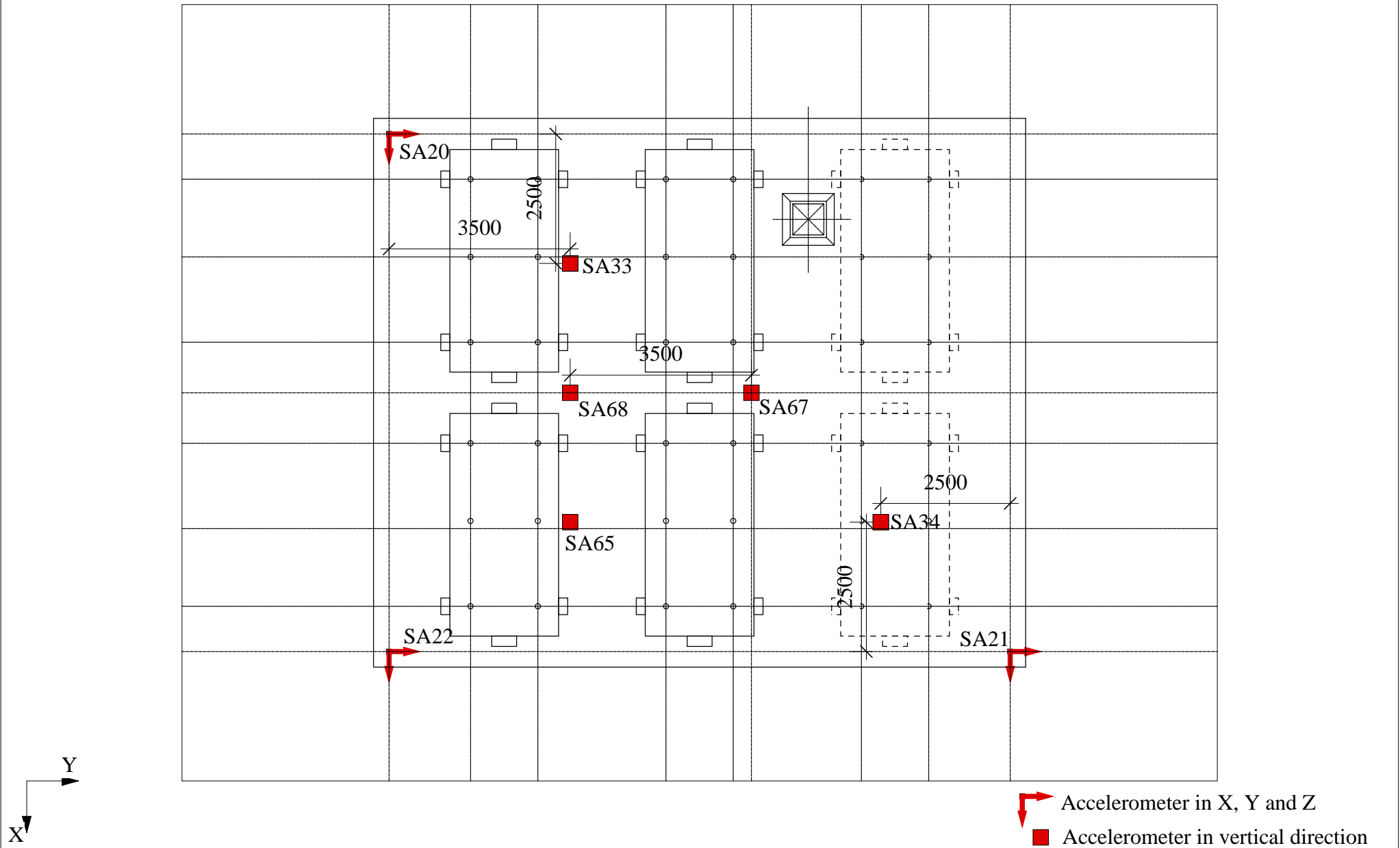


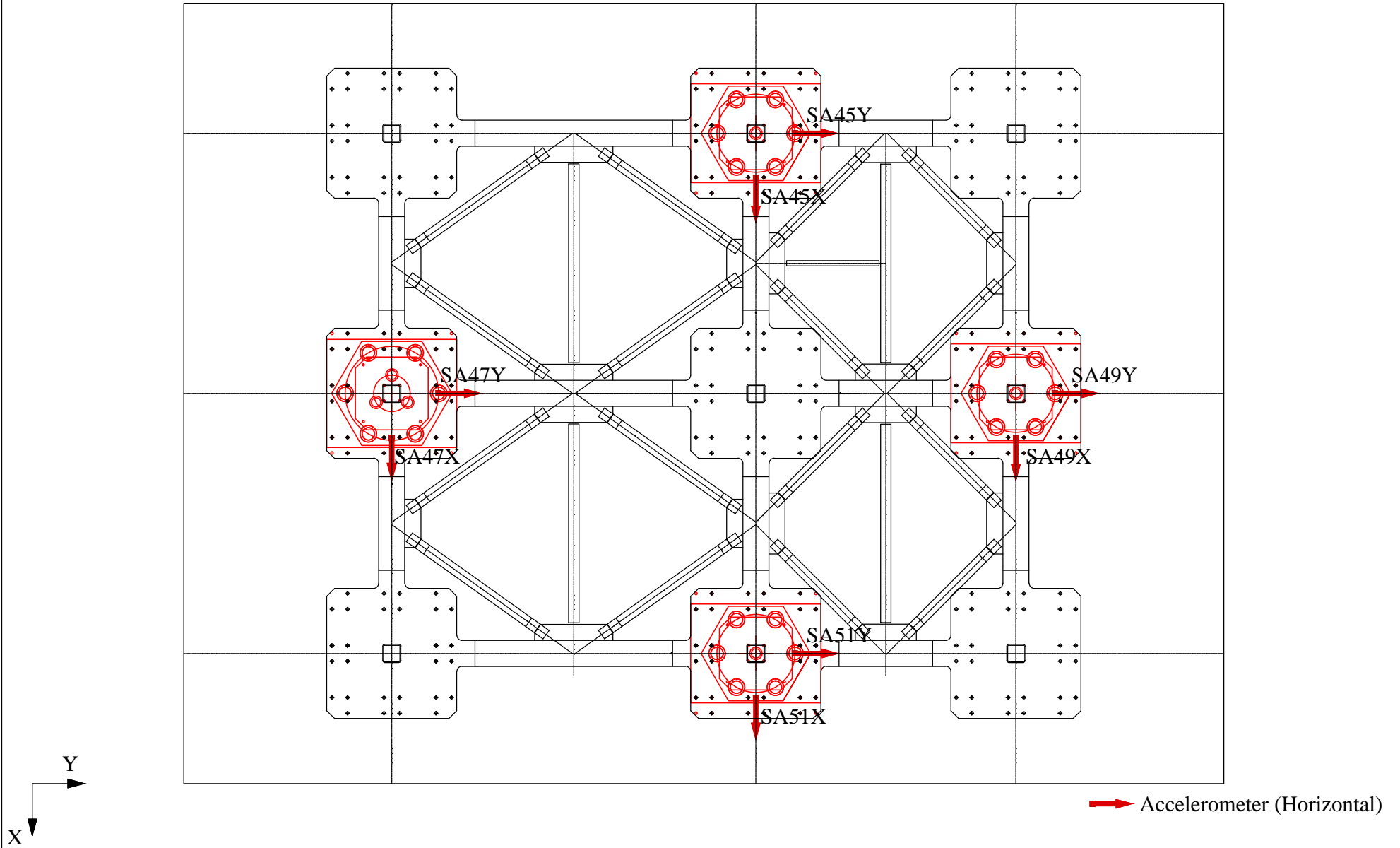


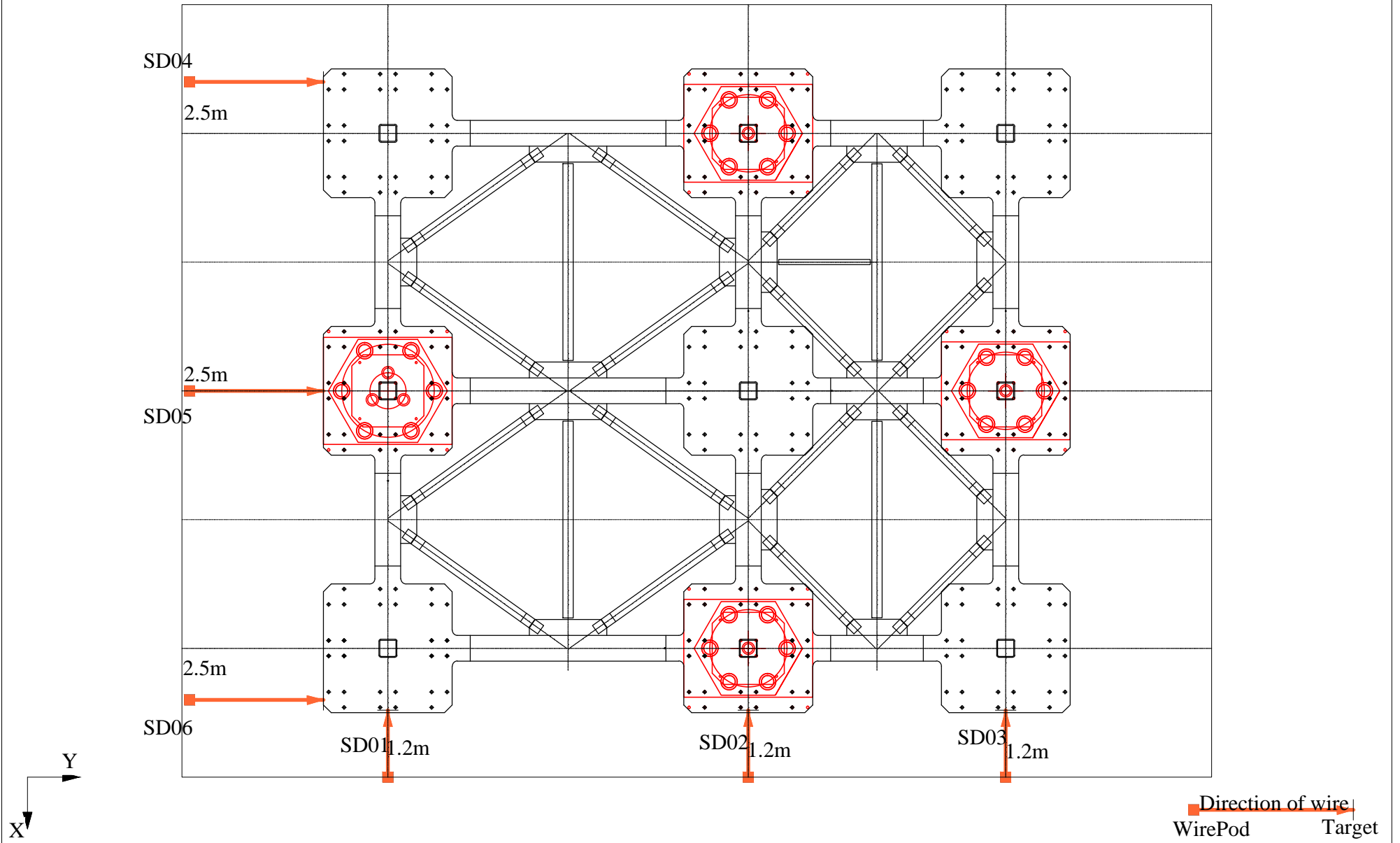


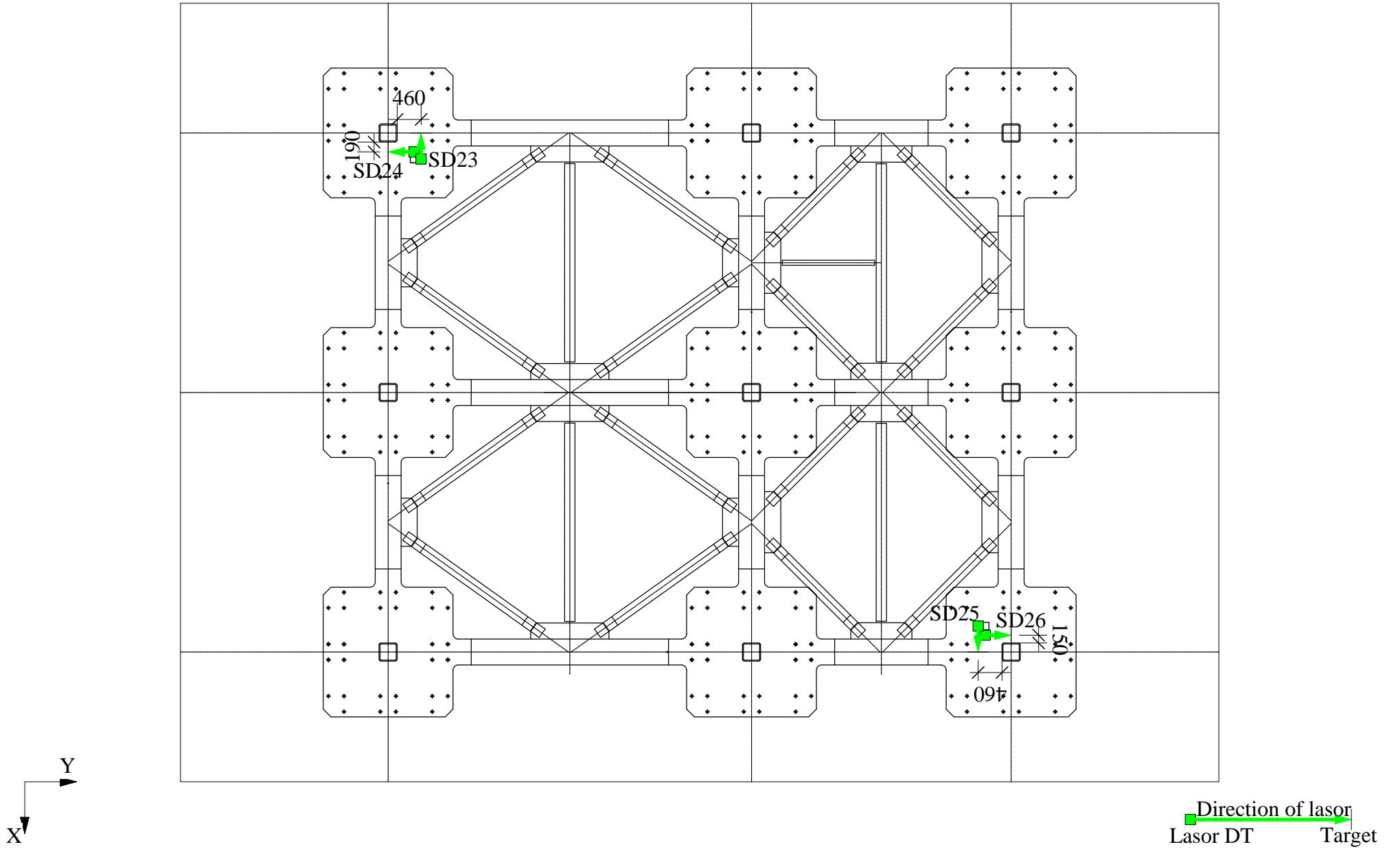


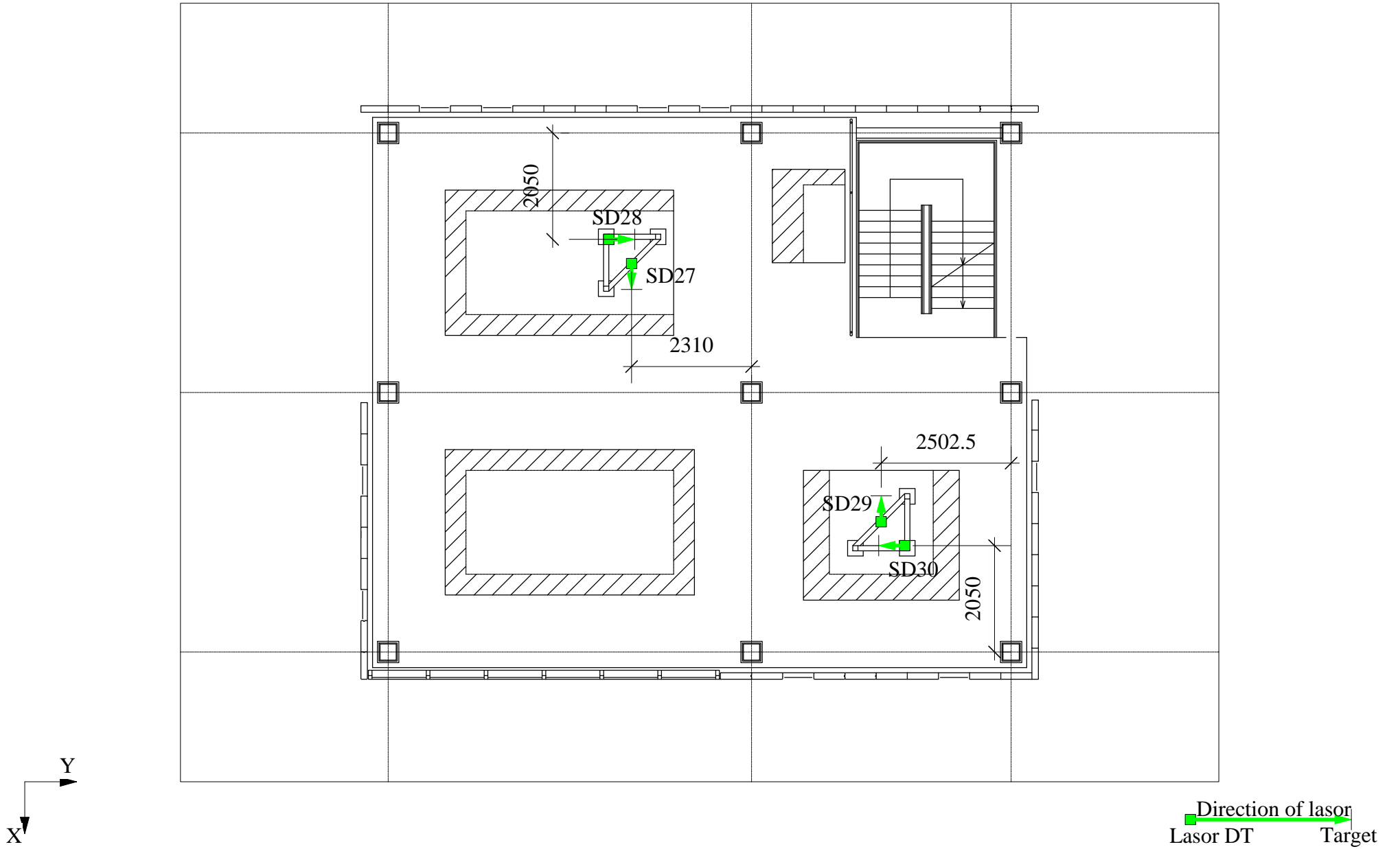


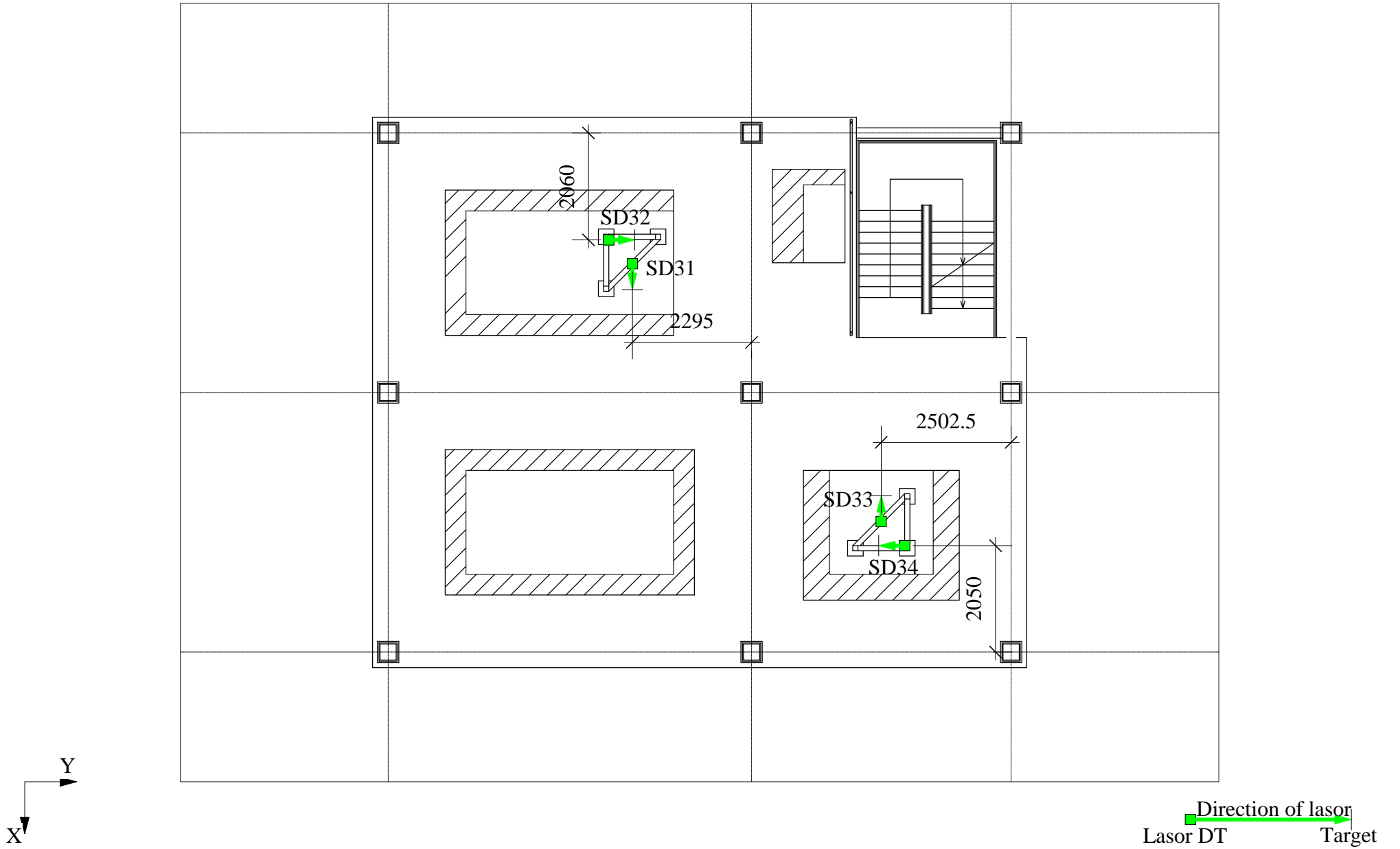


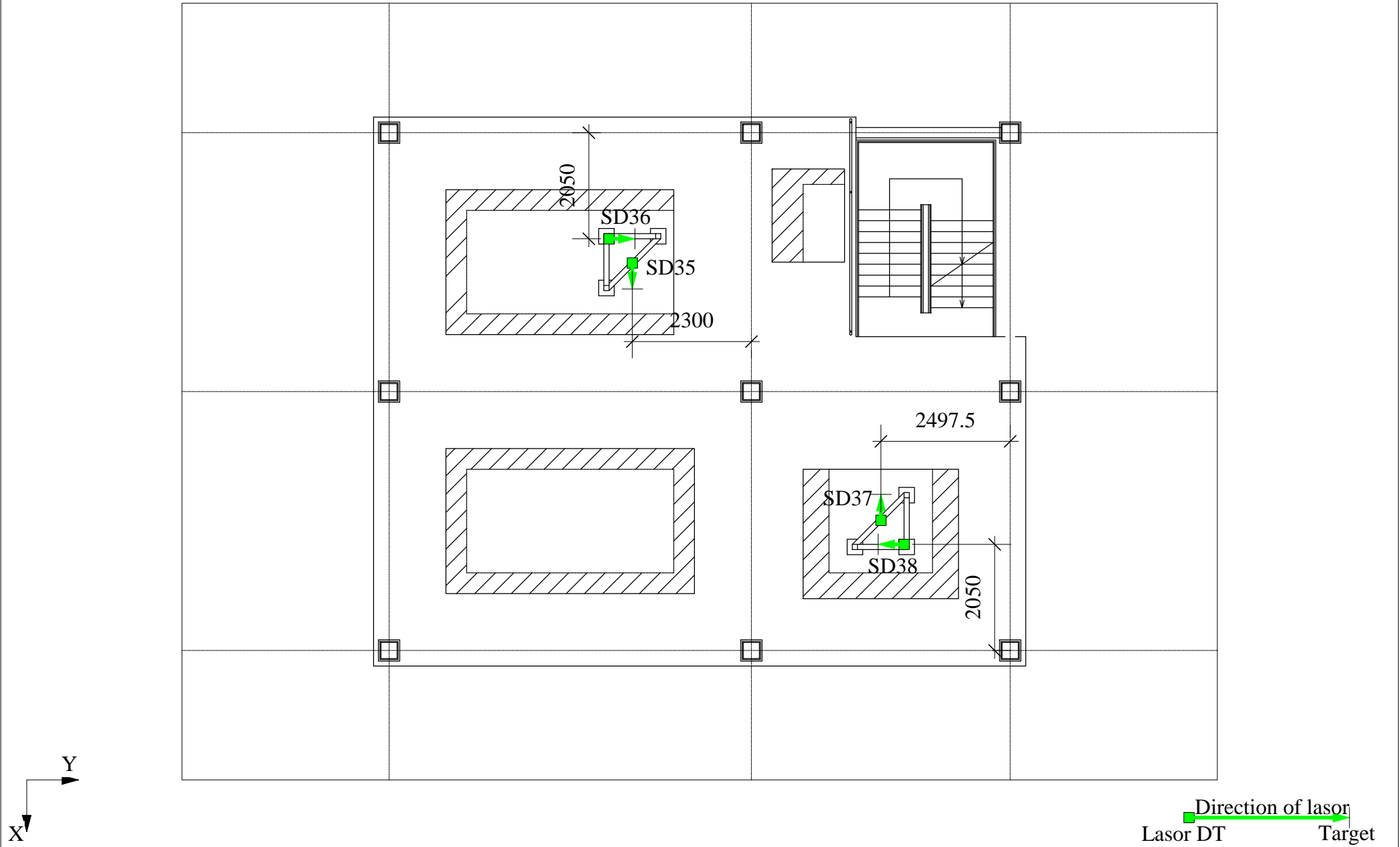




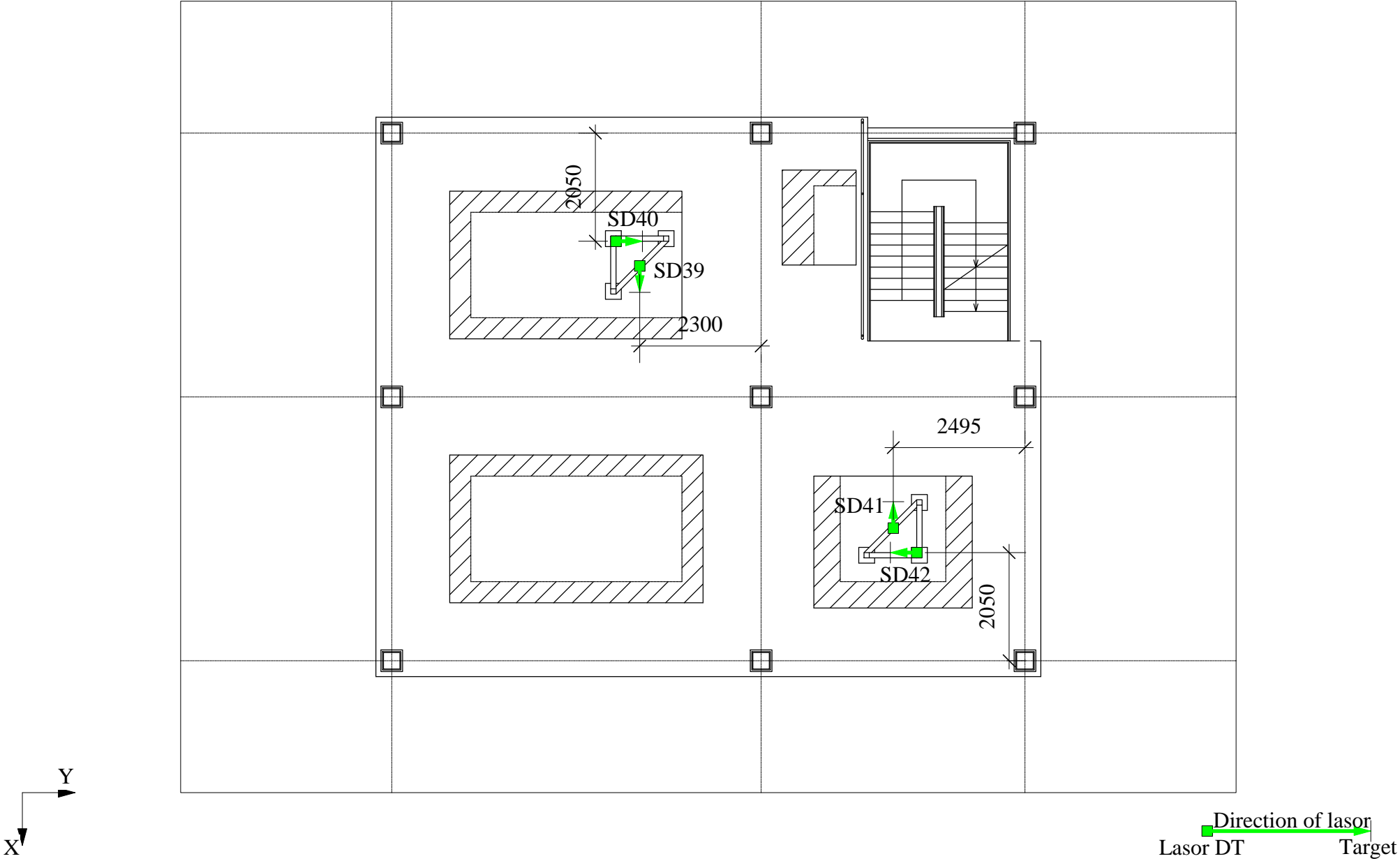


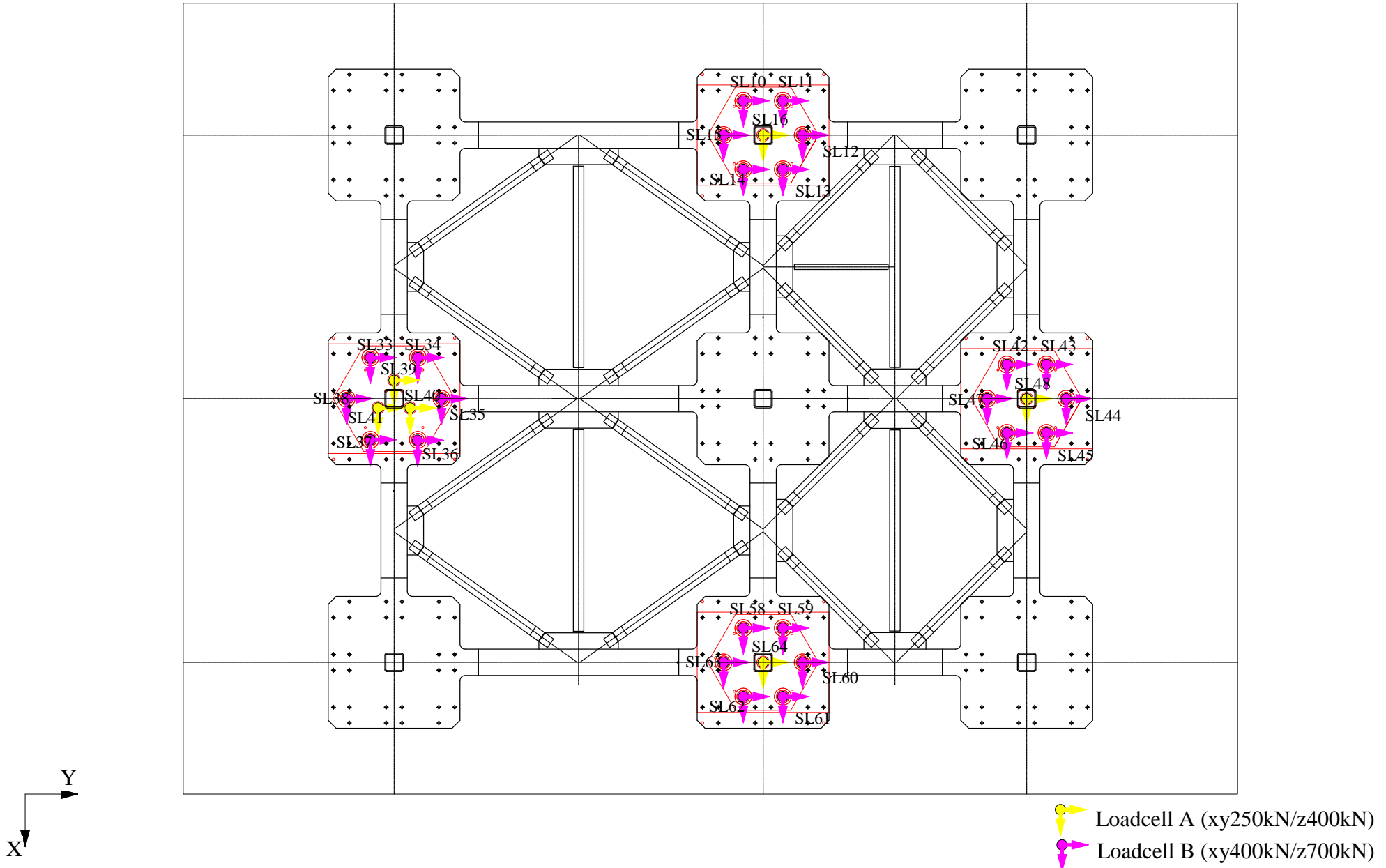


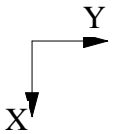
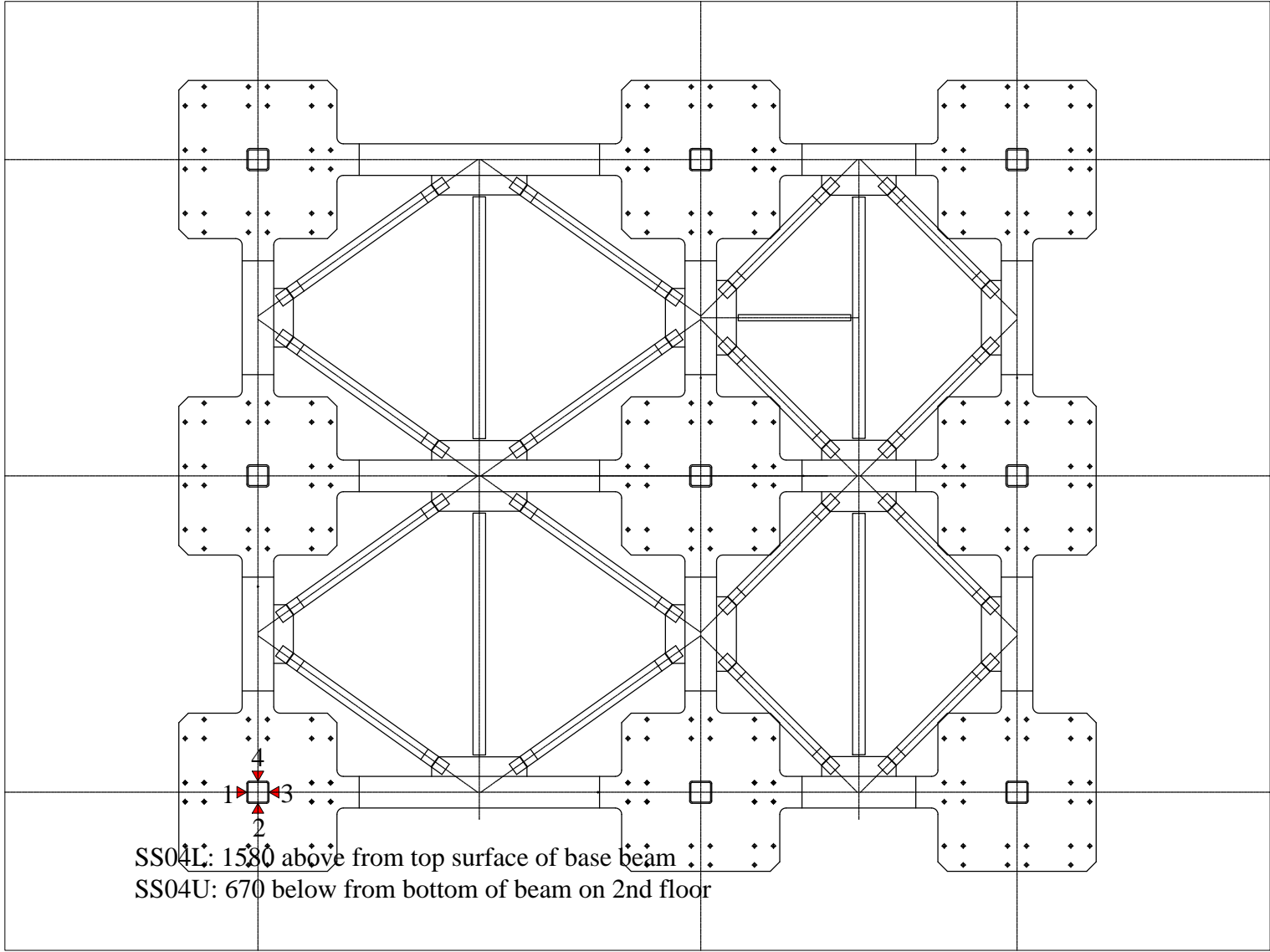




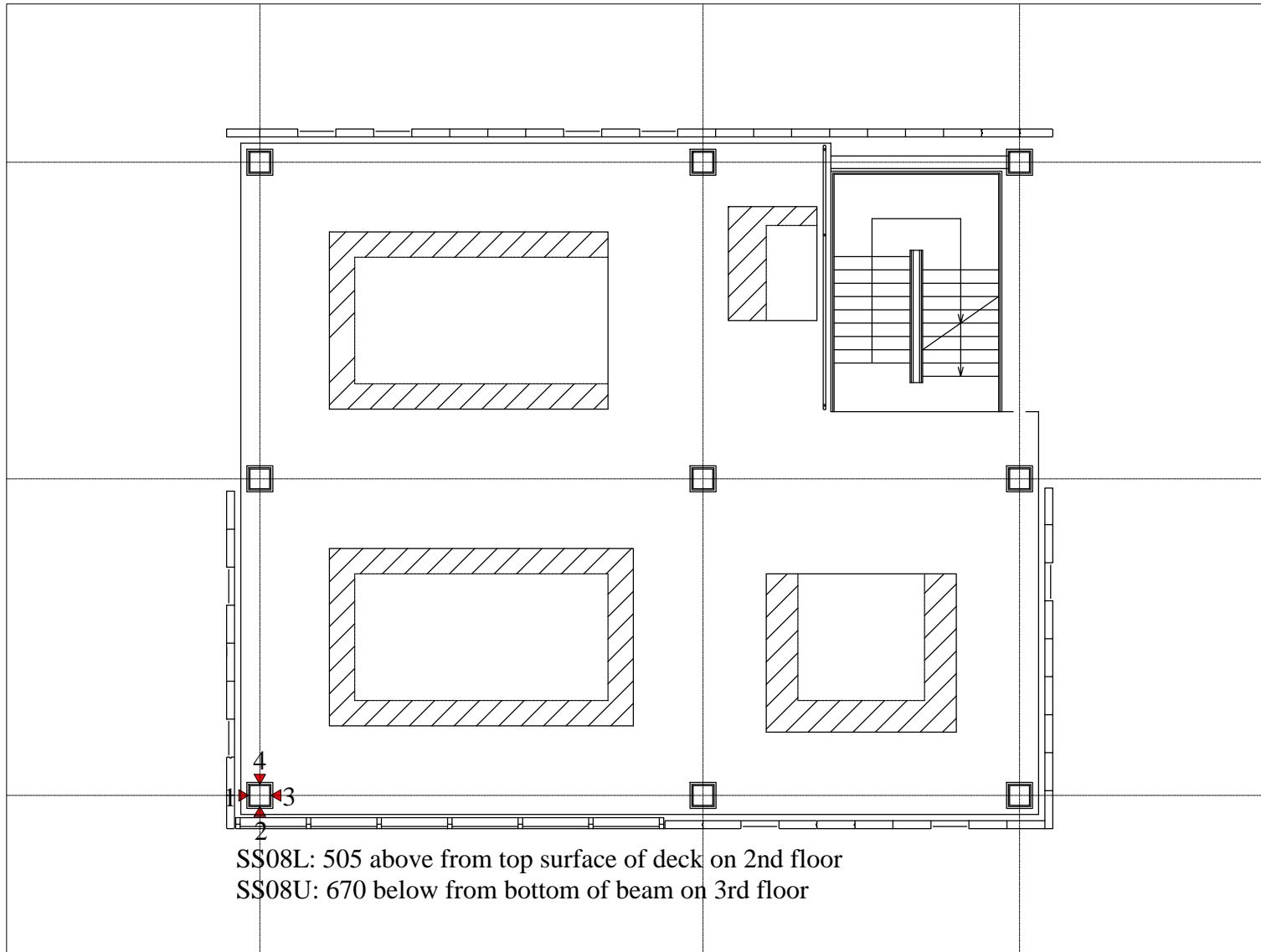




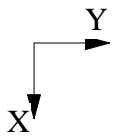




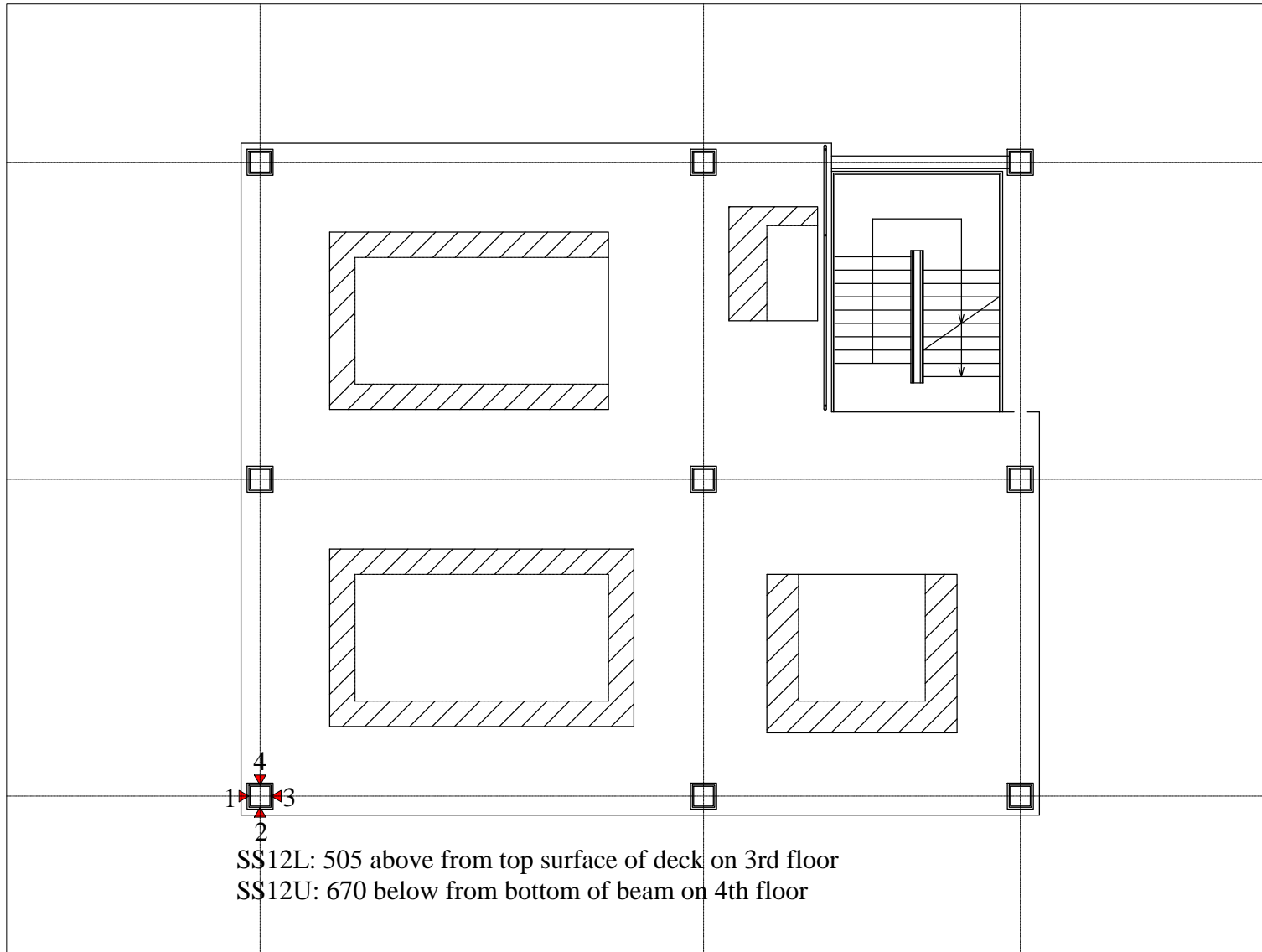
• Strain gauge



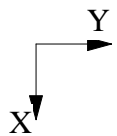
SS08L: 505 above from top surface of deck on 2nd floor  
 SS08U: 670 below from bottom of beam on 3rd floor



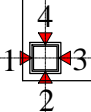
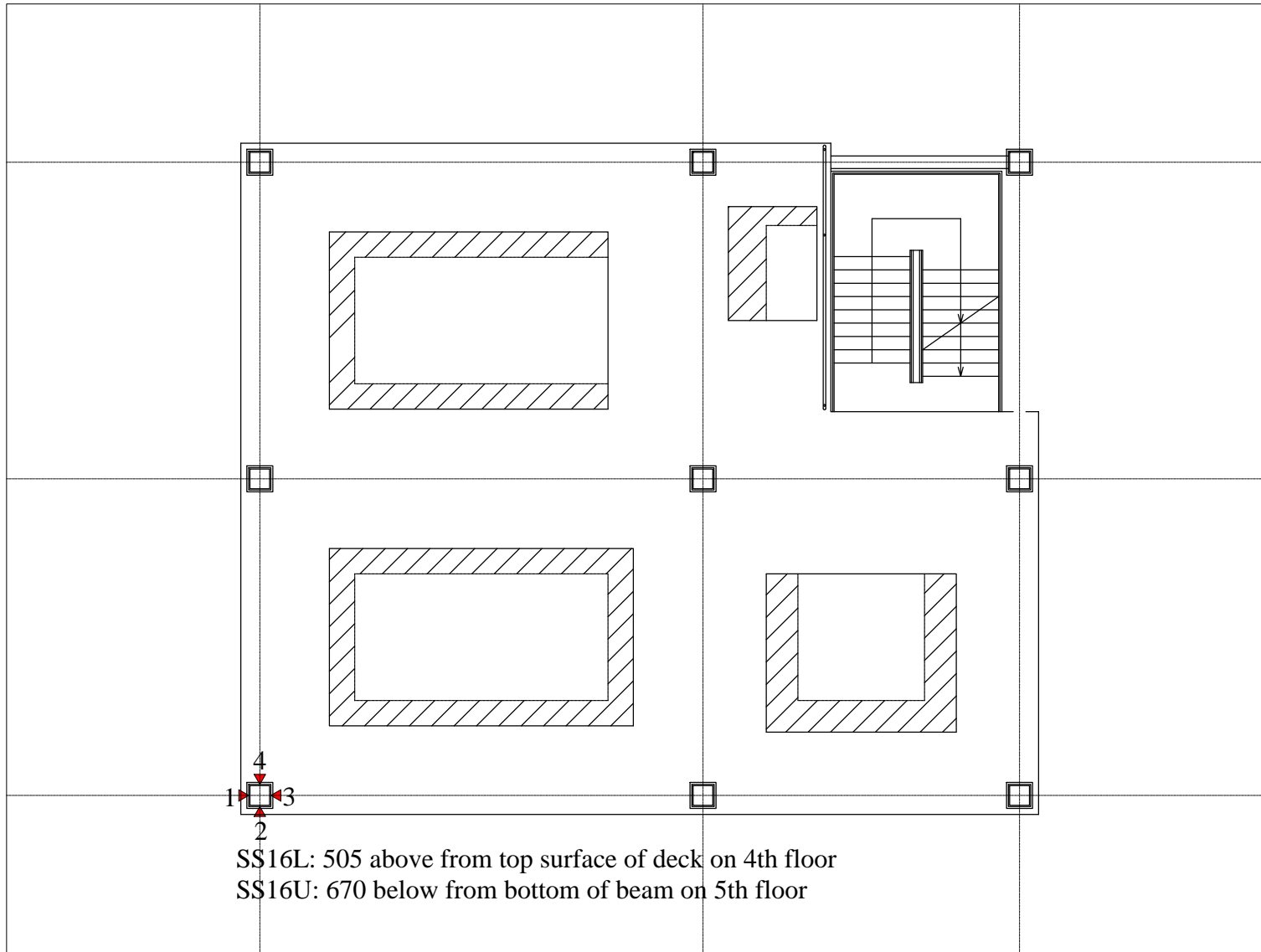
• Strain gauge



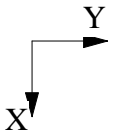
1 2 3 4  
 SS12L: 505 above from top surface of deck on 3rd floor  
 SS12U: 670 below from bottom of beam on 4th floor



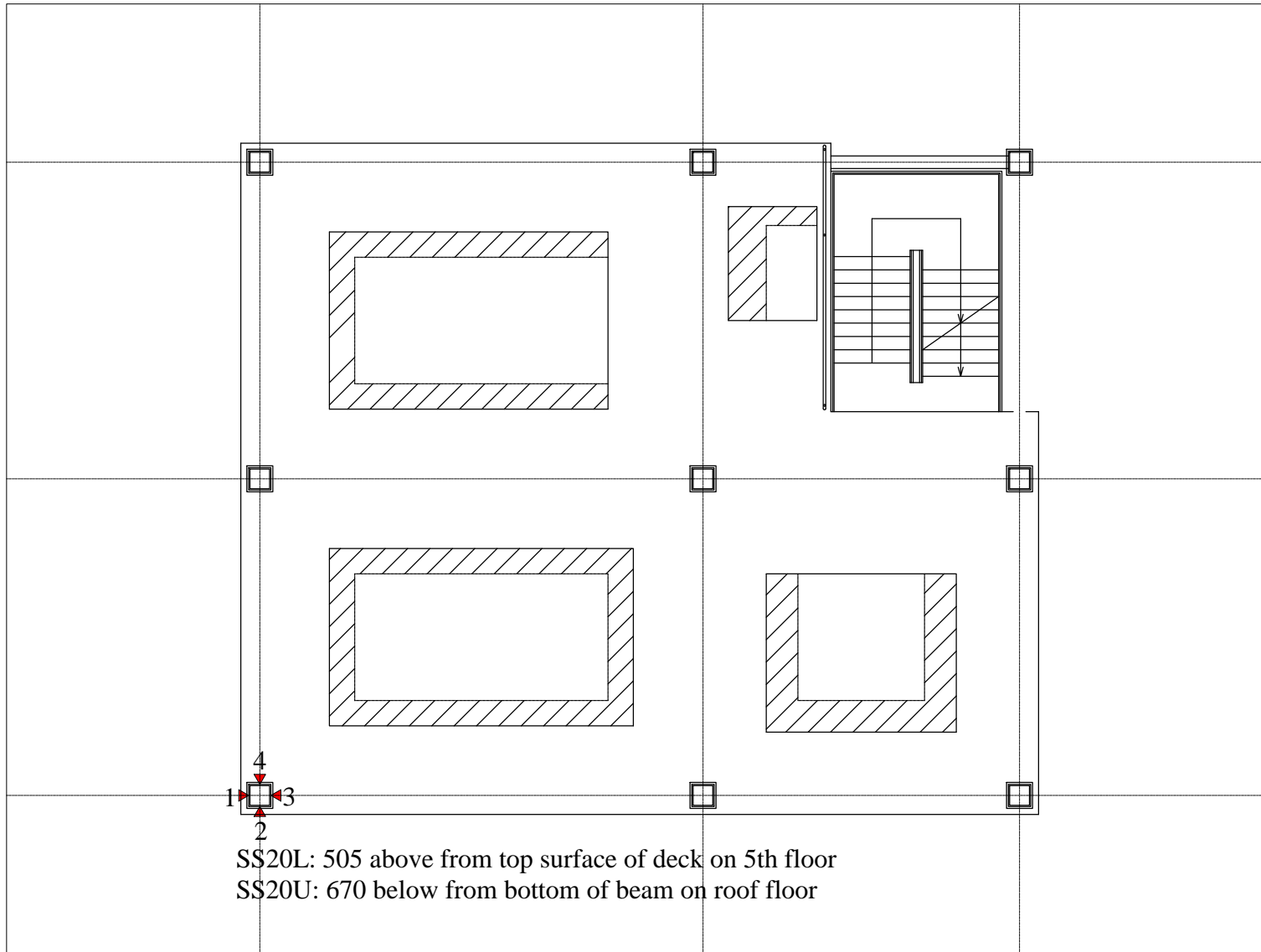
• Strain gauge



SS16L: 505 above from top surface of deck on 4th floor  
SS16U: 670 below from bottom of beam on 5th floor

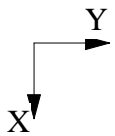


• Strain gauge



1  
2  
3  
4

SS20L: 505 above from top surface of deck on 5th floor  
 SS20U: 670 below from bottom of beam on roof floor



• Strain gauge

## **APPENDIX E**

### **Isolator Test Report for Lead-Rubber Bearings**

Building Isolated with Hybrid Lead-Rubber Isolation System

Contributed by Dynamic Isolation Systems, Inc.

Developed for NEES/E-Defense Collaborative Test Program on  
Innovative Isolation Systems, 2011-2012



## ISOLATOR TEST REPORT

**PROJECT NAME:** NRC

**DATE ISSUED:** JULY 11, 2011

**REPORT NUMBER:** 152-10

---

**PREPARED BY:** DIS INC.

## Introduction

This report has been prepared for Isolator Types A and B for the NRC project. Included in this report are the isolator testing plans, testing results, drawings, an overview of the testing facility, and the test rig calibration certificates.

The testing was performed on July 7, 2011 at DIS' test facility in McCarran, NV.

**Table 1 - Tested Bearing Serial Numbers**

<b>Bearing Type</b>	<b>Serial Number</b>
A	16439
	16443
B	16450
	16458

## Table of Contents

LIST OF TABLES .....	ii
LIST OF FIGURES.....	ii
<b>TEST MATRIX TABLE .....</b>	<b>1</b>
TEST MATRIX .....	1
COMPRESSION SHEAR TESTS.....	1
<b>MEASUREMENT &amp; CALCULATION PROCEDURES.....</b>	<b>4</b>
COMPRESSION SHEAR TESTS.....	4
<b>TEST RESULTS AND HYSTERESIS LOOPS.....</b>	<b>5</b>
DISCUSSION OF TEST RESULTS .....	5
SUMMARY OF TEST RESULTS .....	6
HYSTERESIS LOOPS .....	7
<b>TEST APPARATUS .....</b>	<b>16</b>
OVERVIEW OF TEST FACILITY .....	16
TEST RIG CALIBRATION .....	17

## List of Tables

Table 1 - Tested Bearing Serial Numbers.....	i
Table 2 - Isolator Type A - Test A Results .....	6
Table 3 - Isolator Type A - Test B Results .....	6
Table 4 - Isolator Type A - Test C Results.....	6
Table 5 - Isolator Type A - Test D Results .....	6

## List of Figures

Figure 1 - Combined Compression and Shear Test Matrix.....	2
Figure 2 - Isolator Type A Drawing .....	3
Figure 3 - Graphical Display of Isolator Shear Properties.....	4
Figure 4 - DIS Big Rig Photo.....	16
Figure 5 - DIS Big Rig Drawing.....	16

## **Test Matrix Table**

### **Test Matrix**

The test procedure is determined by a compilation of test information called "Test Matrix". The contents of the test matrix, such as the order of testing and number of tests, are determined by the designer (or the parties involved in the project). The test matrices for this project are presented in this section.

### **Compression Shear Tests**

Each test is described by one row of information in the test matrix table. Each test performed bears a test ID, shown in the first column of the test matrix table.

The testing parameters are:

- a) Compression load on the bearing to be maintained during the test.
- b) Displacement deformation to be imposed on the isolator.
- c) Number of fully-reversed-cycles of testing.
- d) The acceptance criteria for the test, if any.

One cycle of shear deformation consists of movement from the zero position to the maximum specified displacement in the positive direction ( $D_{max}$ ), then to the maximum specified displacement in the negative direction ( $D_{min}$ ), and back to the zero position. This movement is applied in a smooth continuous way, similar to a constant velocity saw-tooth shape.

**Combined Compression and Shear Test**


**Isolator Type A**

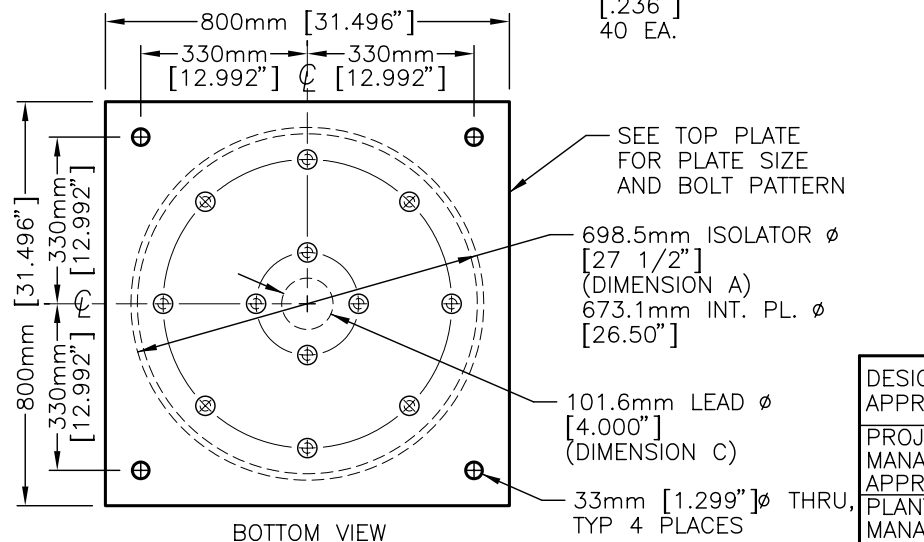
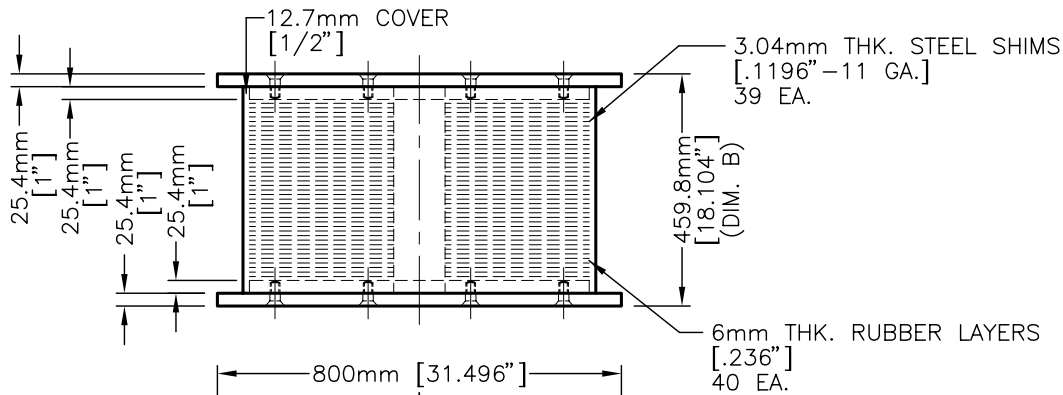
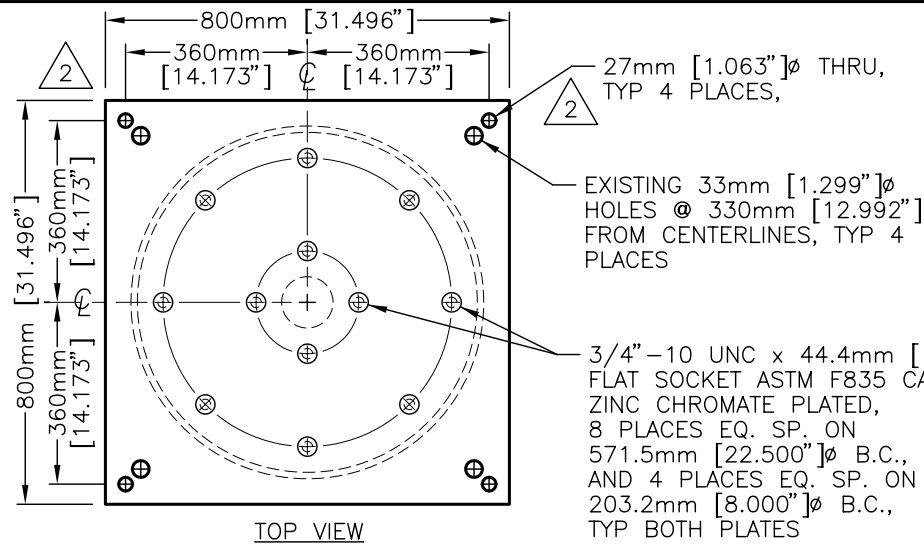
Test ID	Test Order	C. Stress (N/mm <sup>2</sup> )	Load (kN)	Number of Cycles	Shear Strain (%)	Displ. (mm)	Notes
A	1	1.7	600	3	125	300	Note 1
B	2	2.8	1000	3	208	500	Note 1
C	3	0.3	100	0.5	271	650	Note 1
D	4	1.7	600	3	125	300	Note 1

Revision Status			
Approval	Rev	Date	Description
KF	0	06/29/11	Issued for Approval

**Notes:**

1. Wait 15 minutes between tests

Customer Approval		 <b>DYNAMIC ISOLATION SYSTEMS</b>  <b>NRC</b>  <b>Production Isolators</b>  <b>Combined Compression &amp; Shear</b>  <b>Test Matrix No. 152-100-01</b>
Des. Eng. Approval		
Proj. Mng. Approval		
Test Sup. Approval		



REVISION STATUS			
APPR	REV	DATE	DESCRIPTION
AK	A	5/6/11	ISSUED FOR INFORMATION
AK	B	6/7/11	GEN. REV.-REISSUED FOR INFORMATION
TN	0	6/10/11	REV. DWG. #-ISSUED FOR APPROVAL
MG	1	6/10/11	ISSUED FOR FABRICATION
AK	2	6/24/11	REV. EXT. ENDPL-REISSUED FOR APPROVAL

NOTES:

- MATERIALS:  
ALL STEEL PL's ASTM A36.  
ALL STEEL SHIMS ASTM A1011 GR. 36.  
INTERNAL RUBBER IS DIS TYPE T.  
EXTERNAL RUBBER IS DIS TYPE E100S.
- DIMENSIONS ARE IN UNITS NOTED.  
DIMENSIONS IN BRACKETS ARE EQUIVALENTS FOR REFERENCE ONLY.
- DO NOT SCALE THIS DRAWING.
- FINISH: TO BE DETERMINED.

ISOLATOR DIMENSION TABLE			
		TYPE A ISOLATOR	
		C698.5/459.8/101.6	
QUANTITY		4+0	
		TARGET	TOL./ALLOWABLE
A	Isolator Diameter	698.5mm $\pm$ 2mm	$\pm$ 4mm
B	Overall Isolator Ht.	459.8mm $\pm$ 4mm	$\pm$ 6.35mm
C	Lead Core Diameter	101.6mm	$\pm$ 2mm
D	Parallelity	1/300	1/200
Estimated Weight		1,864 lb./847 kg	
Measurements are taken at 20°C.			

GENERAL TOLERANCES:

- ENDPLATE OVERALL DIMENSIONS:  $\pm$  3.18mm.
- BOLT HOLE LOCATIONS:  $\pm$  0.8mm.
- PLATE THICKNESS:  $\pm$  1.6mm.
- PLATE FLATNESS:  $\pm$  3.18mm.

THIS DRAWING IS THE PROPERTY OF DYNAMIC ISOLATION SYSTEMS, INC. INFORMATION AND KNOW-HOW HEREON ARE CONFIDENTIAL AND MAY NOT BE USED, REPRODUCED OR REVEALED TO OTHERS EXCEPT IN ACCORDANCE WITH THE CONTRACT OR OTHER WRITTEN PERMISSION OF DYNAMIC ISOLATION SYSTEMS, INC. ANY REPRODUCTIONS IN WHOLE OR IN PART SHALL INCLUDE THIS NOTATION.

DESIGNER APPROVAL	AK
PROJECT MANAGER APPROVAL	-
PLANT MANAGER APPROVAL	MG



**DYNAMIC ISOLATION SYSTEMS**

DIS SEISMIC ISOLATORS	
NRC Project at EDefense	
Type A Isolator	
<b>DWG. NO. 152-100</b>	SHEET: 1 of 1 ORIG: 5/6/11

## Measurement & Calculation Procedures

### Compression Shear Tests

Testing begins when the axial load is applied to the isolators. Maintaining the axial load, the isolators are sheared to the specified displacement for the appropriate number of cycles. Using the recorded shear force and displacements from the test, shear force-displacement plots (hysteresis loops) are generated. Since two isolators of the same type are tested simultaneously, the total measured shear force has been multiplied by one half during processing to produce hysteresis loops for a single isolator.

The essential properties of an isolator can be extracted from a hysteresis loop. Figure 2 shows an example of a hysteresis loop generated after a compression shear test and some of the isolator properties that are obtained from it. Three properties are measured directly from the recorded data, the maximum isolator displacement ( $D_{max}$ ), the maximum force required to displace the isolator ( $F_{max}$ ), and the area of the hysteresis loop which gives the total energy dissipated per cycle (EDC). The effective stiffness of the isolator ( $K_{eff}$ ) is equal to  $F_{max}/D_{max}$ . There is no engineering judgment or estimation involved in the determination of  $F_{max}$ ,  $D_{max}$ ,  $K_{eff}$ , or EDC.  $F_{max}$  and  $D_{max}$  are self-evident and EDC is determined by numerical integration of the recorded force-displacement data file.

The hysteresis loop has the following properties in addition to the measured properties listed above. These are the hysteretic force at zero displacement ( $Q_d$ ), the yielded stiffness of the isolator ( $K_2$ ), and the unloading stiffness of the isolator ( $K_1$ ). A bi-linear loop is fitted to the actual hysteresis loop such that the fitted loop has identical measured properties ( $K_{eff}$  and EDC) as the actual hysteresis loop.

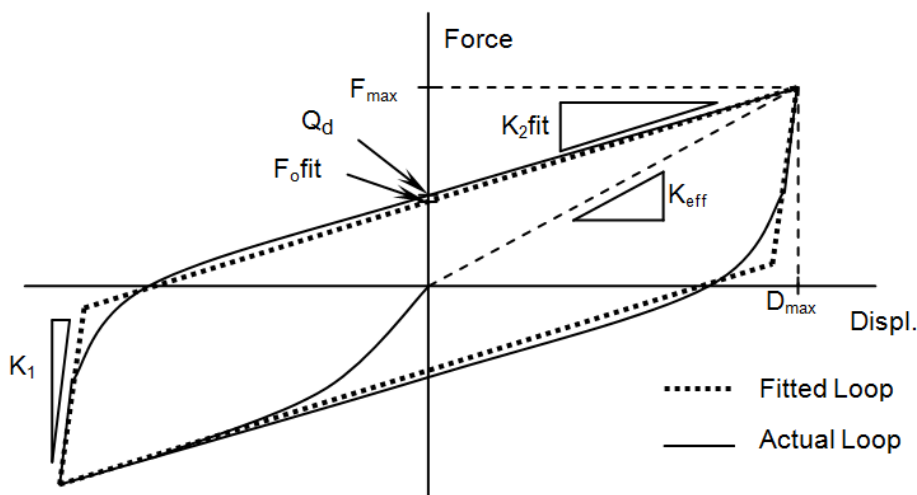


Figure 2 - Graphical Display of Isolator Shear Properties

## Test Results and Hysteresis Loops

### Discussion of Test Results

The compression shear and compression stiffness test results are summarized in Table 2 and **Error! Reference source not found.** as well the corresponding hysteresis loops. The hysteresis loops exhibit positive incremental stiffness and the isolators remained stable during testing.



**Summary of Test Results**
**Table 2 - Isolator Type A - Test A Results**

Serial Numbers	Axial Load	$D_{max}$	$K_d$	$Q_d$	$F_0$	$K_{eff}$
	(kN)	(mm)	(kN/cm)	(kN)	(kN)	(kN/cm)
16439	600	300	6.3	41.4	64.8	8.4
16443	600	300	6.3	41.4	64.8	8.4
16450	600	300	6.2	39.2	64.5	8.3
16458	600	300	6.2	39.2	64.5	8.3
<b>Average</b>	<b>600</b>	<b>300</b>	<b>6.3</b>	<b>40.3</b>	<b>64.7</b>	<b>8.4</b>

**Table 3 - Isolator Type A - Test B Results**

Serial Numbers	Axial Load	$D_{max}$	$K_d$	$Q_d$	$F_0$	$K_{eff}$
	(kN)	(mm)	(kN/cm)	(kN)	(kN)	(kN/cm)
16439	1000	500	5.1	45.9	75.7	6.6
16443	1000	500	5.1	45.9	75.7	6.6
16450	1000	500	5.0	43.6	75.5	6.5
16458	1000	500	5.0	43.6	75.5	6.5
<b>Average</b>	<b>1000</b>	<b>500</b>	<b>5.1</b>	<b>44.8</b>	<b>75.6</b>	<b>6.6</b>

**Table 4 - Isolator Type A - Test C Results**

Serial Numbers	Axial Load	$D_{max}$	$K_d$	$Q_d$	$F_0$	$K_{eff}$
	(kN)	(mm)	(kN/cm)	(kN)	(kN)	(kN/cm)
16439	100	650	5.5	56.2	85.1	6.8
16443	100	650	5.5	56.2	85.1	6.8
16450	100	650	5.4	53.1	86.1	6.8
16458	100	650	5.4	53.1	86.1	6.8
<b>Average</b>	<b>100</b>	<b>650</b>	<b>5.5</b>	<b>54.7</b>	<b>85.6</b>	<b>6.8</b>

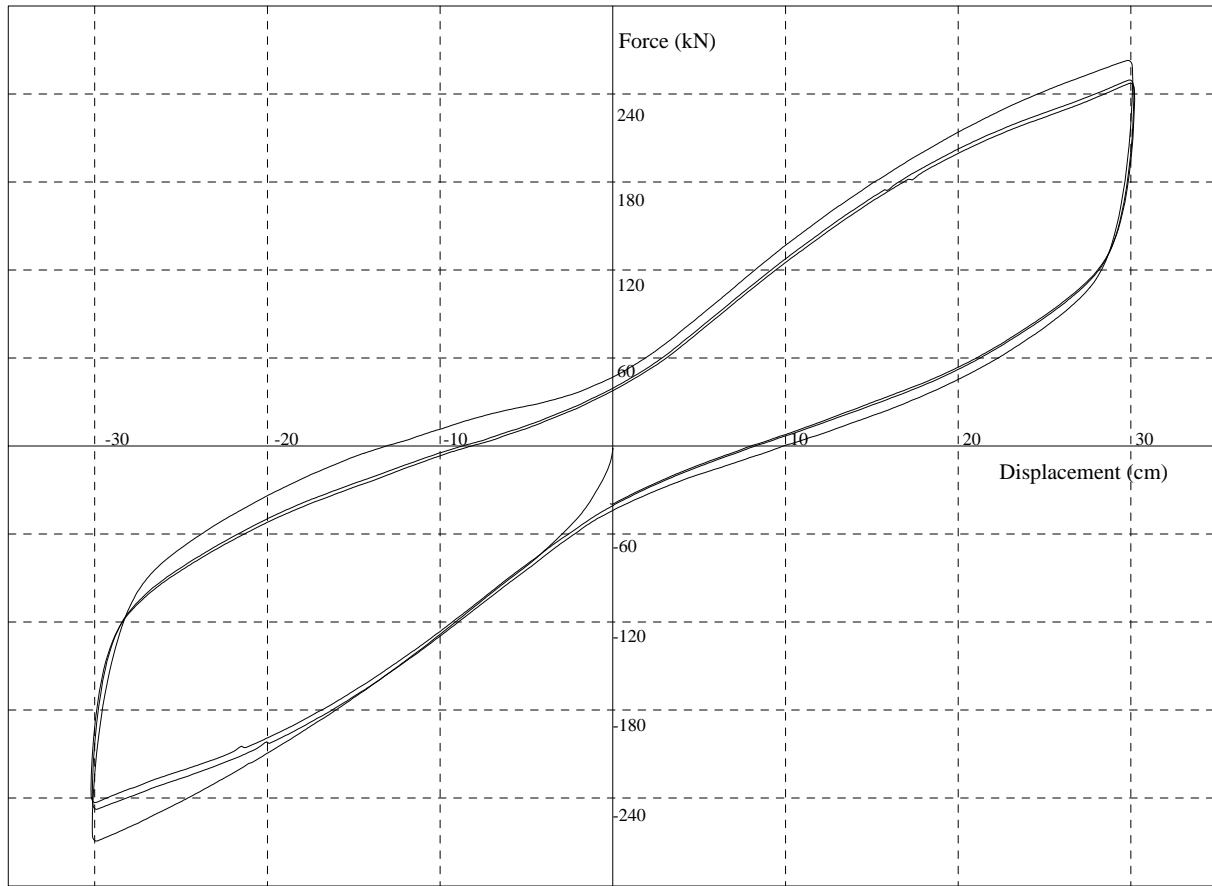
**Table 5 - Isolator Type A - Test D Results**

Serial Numbers	Axial Load	$D_{max}$	$K_d$	$Q_d$	$F_0$	$K_{eff}$
	(kN)	(mm)	(kN/cm)	(kN)	(kN)	(kN/cm)
16439	600	300	5.8	41.7	63.4	7.9
16443	600	300	5.8	41.7	63.4	7.9
16450	600	300	5.8	40.1	62.8	7.9
16458	600	300	5.8	40.1	62.8	7.9
<b>Average</b>	<b>600</b>	<b>300</b>	<b>5.8</b>	<b>40.9</b>	<b>63.1</b>	<b>7.9</b>



## **Hysteresis Loops**

---

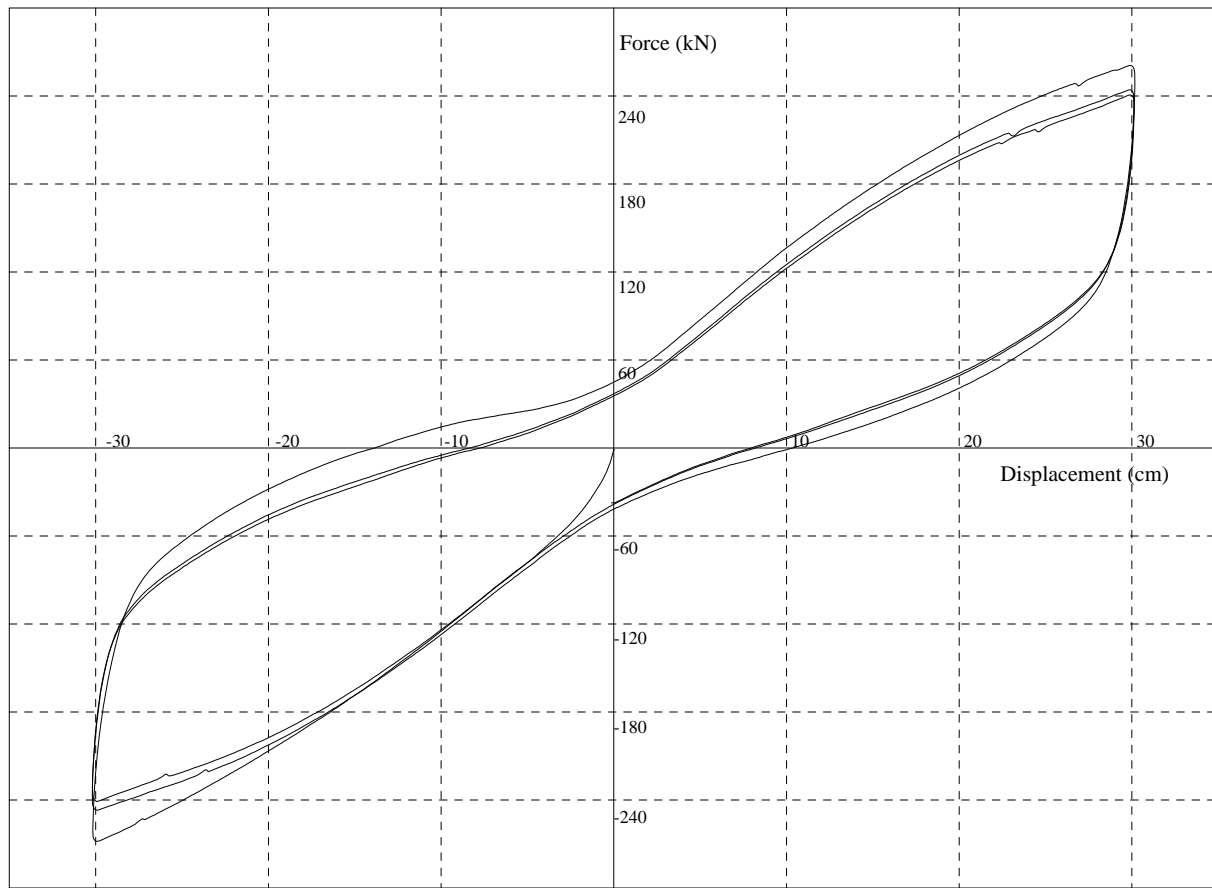


Job: 152 (NRC) Test Name : 25838-001.dat

Class: Production Type: A Isolators 16439 & 16443 Tested: 7/7/2011 5:55:42 PM

Test Type: Production Test Matrix ID: A (Stress: 1.7N/mm<sup>2</sup>, Strain: 125%)

<u>Cycle</u>	<u>Dmax(cm)</u>	<u>Fmax(kN)</u>	<u>Keff(kN/cm)</u>	<u>Qd(kN)</u>	<u>EDC(kN.cm)</u>	<u>K2fit(kN/cm)</u>	<u>Fofit(kN)</u>	<u>V(cm/min)</u>
1	30.12	266.15	8.84	45.46	8454.7	6.47	71.24	136.09
2	30.15	248.61	8.24	40.03	7486.1	6.16	62.90	140.41
3	30.21	245.26	8.12	38.61	7206.2	6.12	60.40	140.41
<b>AVERAGE</b>	<b>30.16</b>	<b>253.34</b>	<b>8.40</b>	<b>41.4</b>	<b>7715.7</b>	<b>6.25</b>	<b>64.84</b>	<b>139.0</b>

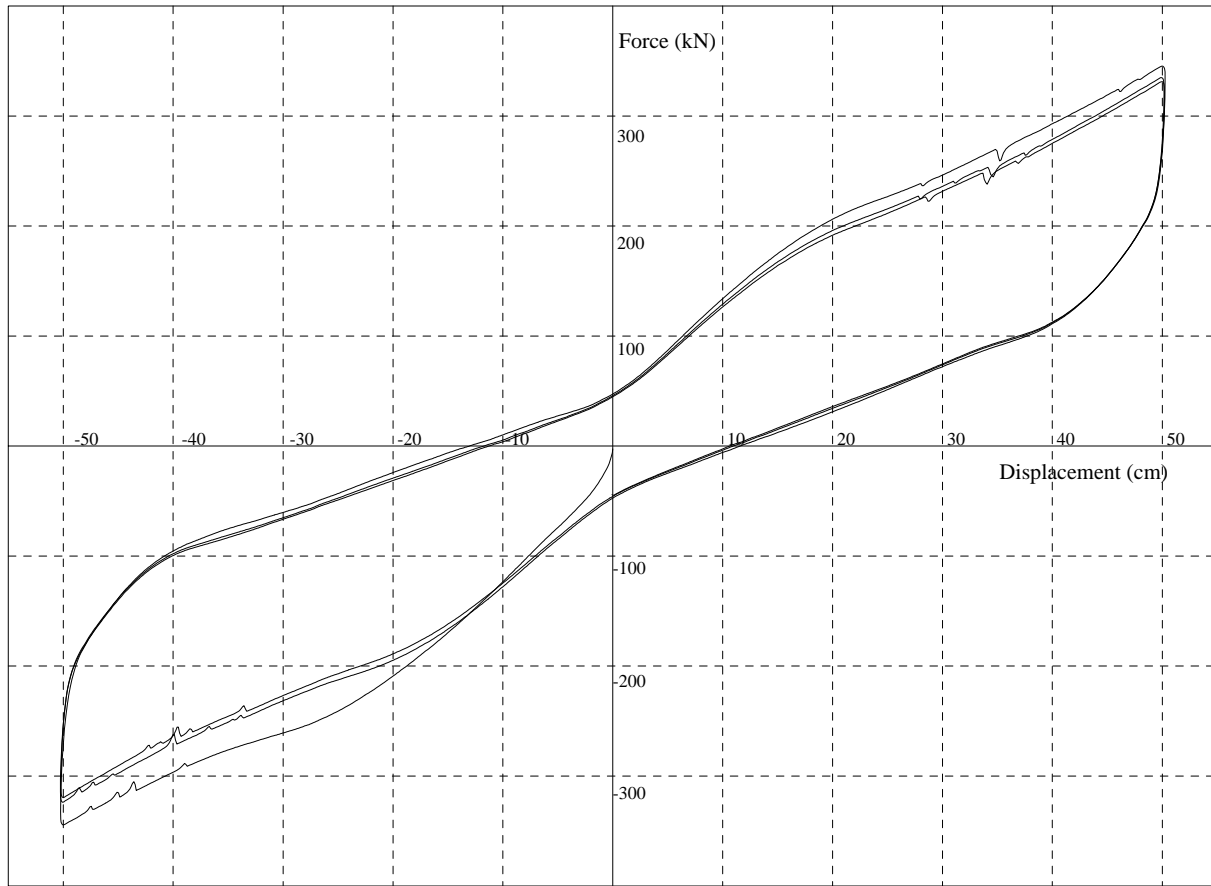


Job: 152 (NRC) Test Name : 25834-001.dat

Class: Production Type: A Isolators 16450 & 16458 Tested: 7/7/2011 2:28:21 PM

Test Type: Production Test Matrix ID: A (Stress: 1.7N/mm<sup>2</sup>, Strain: 125%)

<u>Cycle</u>	<u>Dmax(cm)</u>	<u>Fmax(kN)</u>	<u>Keff(kN/cm)</u>	<u>Qd(kN)</u>	<u>EDC(kN.cm)</u>	<u>K2fit(kN/cm)</u>	<u>Fofit(kN)</u>	<u>V(cm/min)</u>
1	30.17	264.55	8.77	43.29	8505.8	6.40	71.49	136.33
2	30.16	245.63	8.14	37.70	7433.0	6.08	62.38	140.40
3	30.16	240.83	7.99	36.49	7108.8	6.01	59.63	140.46
<b>AVERAGE</b>	<b>30.16</b>	<b>250.33</b>	<b>8.30</b>	<b>39.2</b>	<b>7682.5</b>	<b>6.16</b>	<b>64.49</b>	<b>139.1</b>

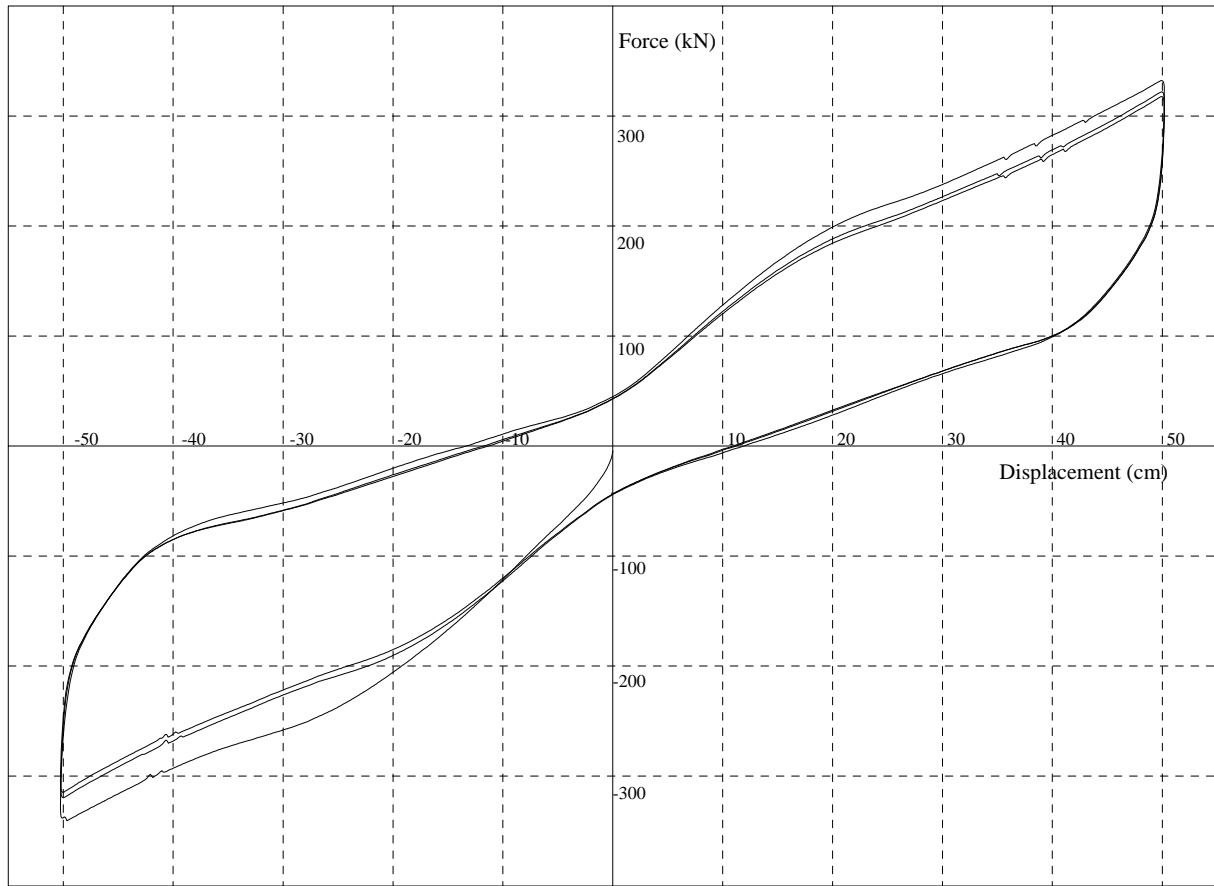


Job: 152 (NRC) Test Name : 25839-001.dat

Class: Production Type: A Isolators 16439 & 16443 Tested: 7/7/2011 6:27:49 PM

Test Type: Production Test Matrix ID: B (Stress: 2.8N/mm<sup>2</sup>, Strain: 208%)

<u>Cycle</u>	<u>Dmax(cm)</u>	<u>Fmax(kN)</u>	<u>Keff(kN/cm)</u>	<u>Qd(kN)</u>	<u>EDC(kN.cm)</u>	<u>K2fit(kN/cm)</u>	<u>Fofit(kN)</u>	<u>V(cm/min)</u>
1	50.25	344.95	6.86	47.36	16181.4	5.25	81.19	138.12
2	50.21	329.41	6.56	45.74	14809.4	5.08	74.31	140.96
3	50.21	325.42	6.48	44.73	14284.9	5.05	71.65	140.94
<b>AVERAGE</b>	<b>50.23</b>	<b>333.26</b>	<b>6.64</b>	<b>45.9</b>	<b>15091.9</b>	<b>5.13</b>	<b>75.72</b>	<b>140.0</b>

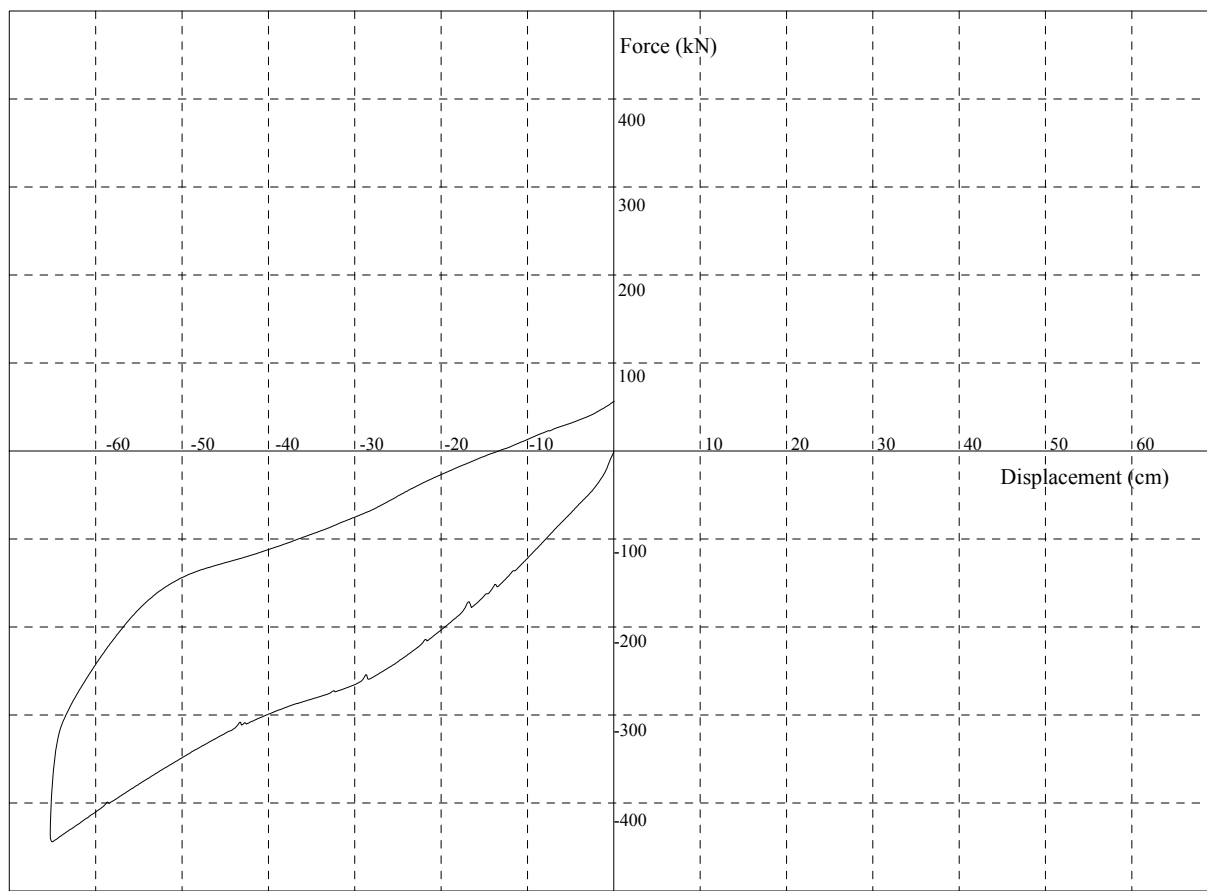


Job: 152 (NRC) Test Name : 25835-001.dat

Class: Production Type: A Isolators 16450 & 16458 Tested: 7/7/2011 2:54:06 PM

Test Type: Production Test Matrix ID: B (Stress: 2.8N/mm<sup>2</sup>, Strain: 208%)

<u>Cycle</u>	<u>Dmax(cm)</u>	<u>Fmax(kN)</u>	<u>Keff(kN/cm)</u>	<u>Qd(kN)</u>	<u>EDC(kN.cm)</u>	<u>K2fit(kN/cm)</u>	<u>Fofit(kN)</u>	<u>V(cm/min)</u>
1	50.22	336.42	6.70	44.52	16198.4	5.08	81.26	138.25
2	50.20	320.95	6.39	43.31	14690.8	4.93	73.67	141.01
3	50.21	316.35	6.30	42.97	14278.0	4.88	71.57	141.03
<b>AVERAGE</b>	<b>50.21</b>	<b>324.57</b>	<b>6.46</b>	<b>43.6</b>	<b>15055.7</b>	<b>4.96</b>	<b>75.50</b>	<b>140.1</b>

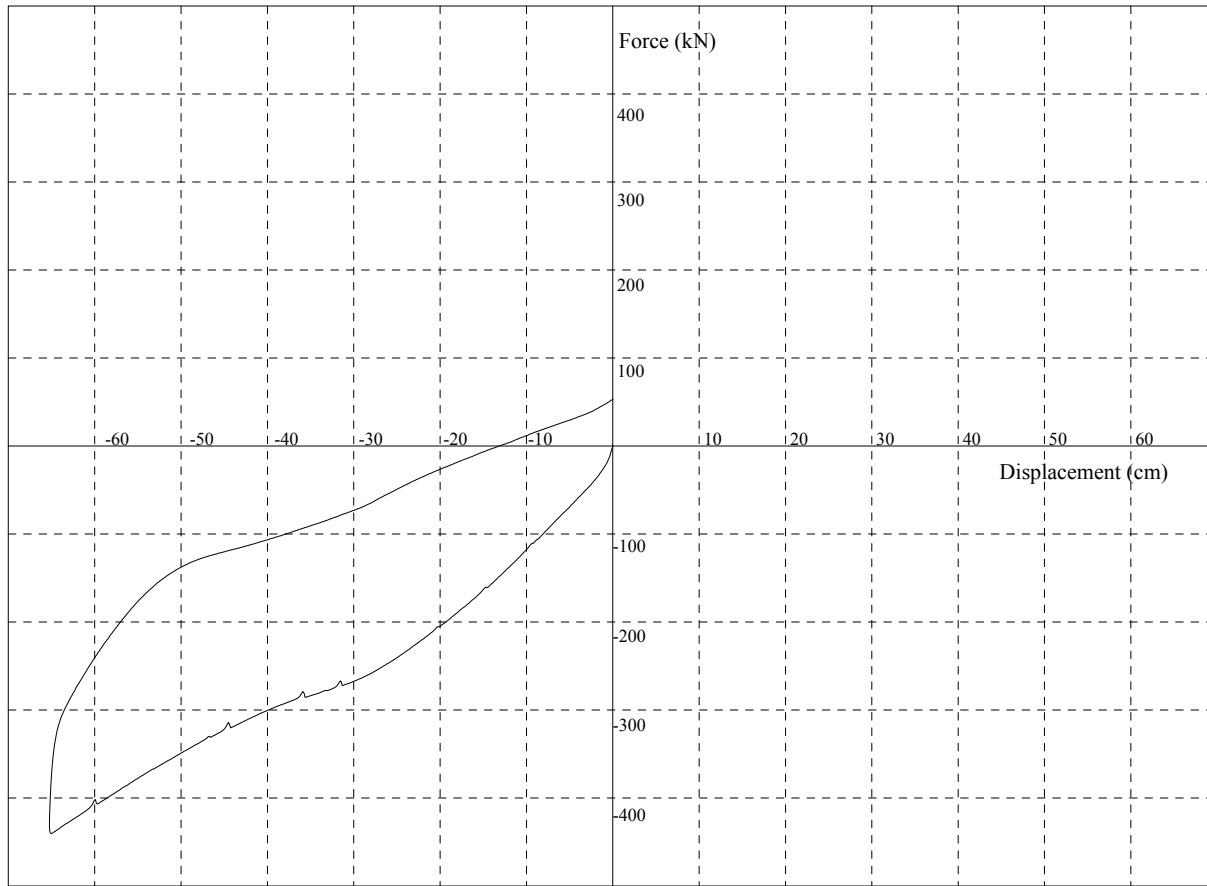


Job: 152 (NRC) Test Name : 25840-001a.dat

Class: Production Type: D6 Isolators 16439 & 16443 Tested: 7/14/2011 8:43:12 AM

Test Type: Production Test Matrix ID: C (Stress:0.3N/mm<sup>2</sup>, Strain: 271%)

<u>H.Cyc</u>	<u>Dmax(cm)</u>	<u>Fmax(kN)</u>	<u>Keff(kN/cm)</u>	<u>Qd(kN)</u>	<u>EDC(kN.cm)</u>	<u>K2fit(kN/cm)</u>	<u>Fofit(kN)</u>	<u>V(cm/min)</u>
1	-65.26	-444.11	6.80	56.19	10926.7	5.50	85.06	-136.44



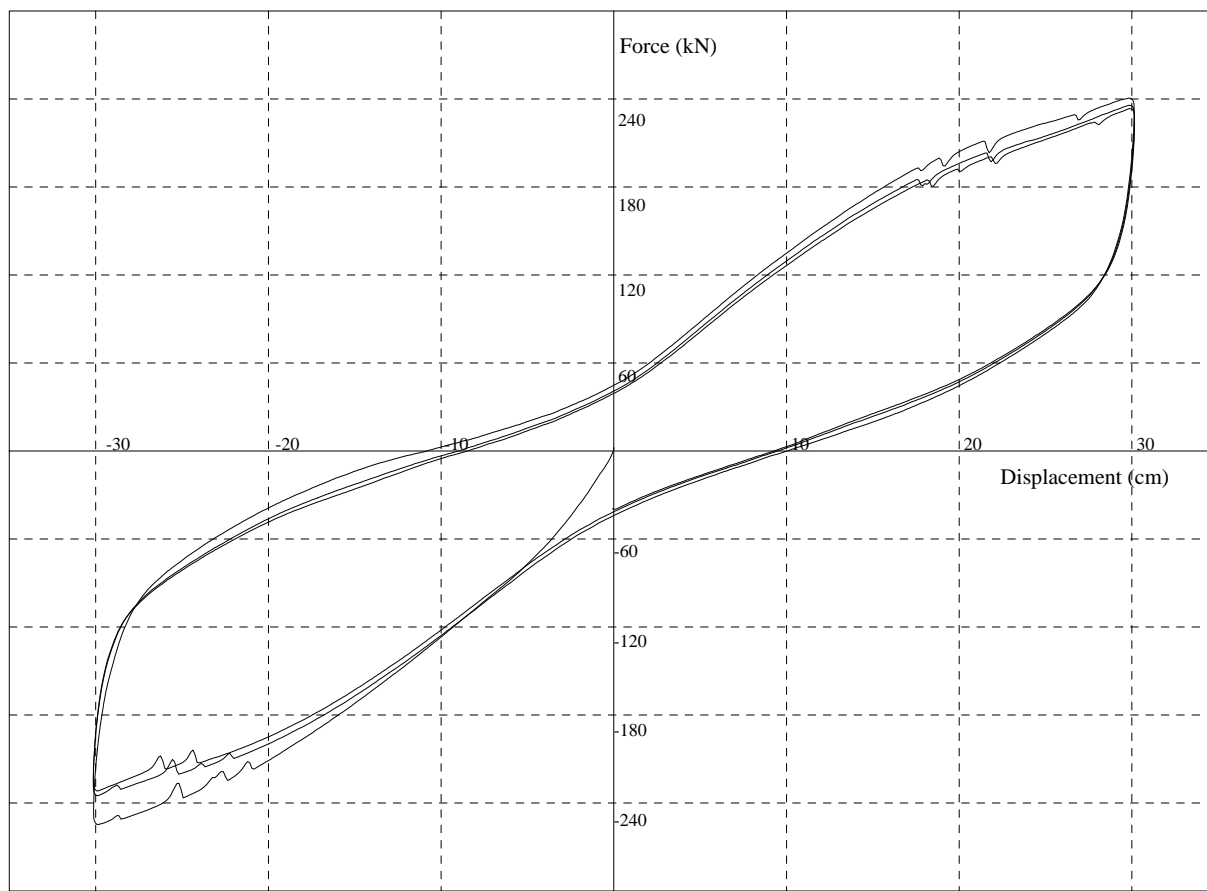
Job: 152 (NRC) Test Name : 25836-001a.dat

Class: Production Type: D6 Isolators 16450 & 16458 Tested: 7/14/2011 8:44:24 AM

Test Type: Production Test Matrix ID: C (Stress:0.3N/mm<sup>2</sup>, Strain: 271%)

<u>H.Cyc</u>	<u>Dmax(cm)</u>	<u>Fmax(kN)</u>	<u>Keff(kN/cm)</u>	<u>Qd(kN)</u>	<u>EDC(kN.cm)</u>	<u>K2fit(kN/cm)</u>	<u>Fofit(kN)</u>	<u>V(cm/min)</u>
1	-65.24	-440.48	6.75	53.11	11058.8	5.43	86.14	-136.15



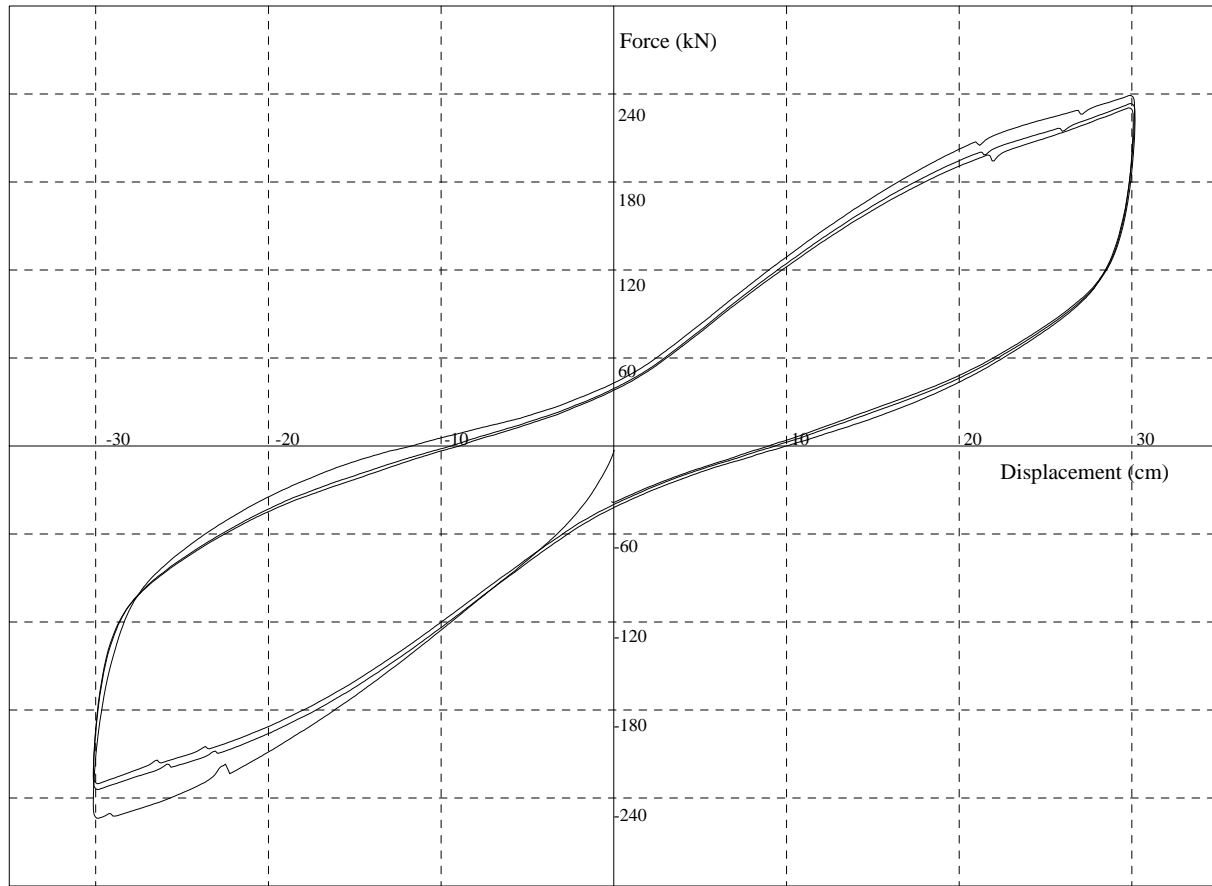


Job: 152 (NRC) Test Name : 25841-001.dat

Class: Production Type: A Isolators 16439 & 16443 Tested: 7/7/2011 7:16:44 PM

Test Type: Production Test Matrix ID: D (Stress: 1.7N/mm<sup>2</sup>, Strain: 125%)

<u>Cycle</u>	<u>Dmax(cm)</u>	<u>Fmax(kN)</u>	<u>Keff(kN/cm)</u>	<u>Qd(kN)</u>	<u>EDC(kN.cm)</u>	<u>K2fit(kN/cm)</u>	<u>Fofit(kN)</u>	<u>V(cm/min)</u>
1	30.13	247.63	8.22	44.42	7954.8	5.99	67.20	135.77
2	30.14	235.37	7.81	41.13	7439.2	5.73	62.74	140.41
3	30.14	232.66	7.72	39.48	7146.6	5.72	60.23	140.43
<b>AVERAGE</b>	<b>30.14</b>	<b>238.55</b>	<b>7.92</b>	<b>41.7</b>	<b>7513.6</b>	<b>5.81</b>	<b>63.39</b>	<b>138.9</b>



Job: 152 (NRC) Test Name : 25837-001.dat

Class: Production Type: A Isolators 16450 & 16458 Tested: 7/7/2011 3:38:45 PM

Test Type: Production Test Matrix ID: D (Stress: 1.7N/mm<sup>2</sup>, Strain: 125%)

<u>Cycle</u>	<u>Dmax(cm)</u>	<u>Fmax(kN)</u>	<u>Keff(kN/cm)</u>	<u>Qd(kN)</u>	<u>EDC(kN.cm)</u>	<u>K2fit(kN/cm)</u>	<u>Fofit(kN)</u>	<u>V(cm/min)</u>
1	30.15	246.41	8.17	42.47	7938.8	5.95	66.97	135.85
2	30.17	233.82	7.75	39.54	7350.9	5.70	61.89	140.58
3	30.10	230.44	7.65	38.24	7058.4	5.68	59.51	140.56
<b>AVERAGE</b>	<b>30.14</b>	<b>236.89</b>	<b>7.86</b>	<b>40.1</b>	<b>7449.3</b>	<b>5.78</b>	<b>62.79</b>	<b>139.0</b>

## Test Apparatus

### Overview of Test Facility

The DIS test facility is located at its manufacturing plant in McCarran, NV. The testing laboratory has approximately 4,000 square feet of available floor space and houses two combined compression and shear test rigs along with their support hardware and is serviced by a 10-ton overhead crane. The big test rig is illustrated in Figure 3 and Figure 4 below. As shown in the figures, two isolators are tested together in the hydraulically powered test rig. The isolators can be examined for both their shear and compression properties in the test rig.

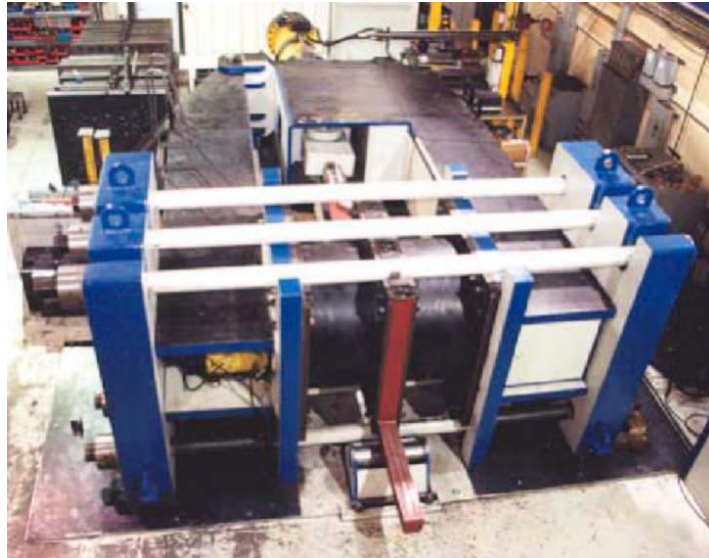


Figure 3 - DIS Big Rig Photo

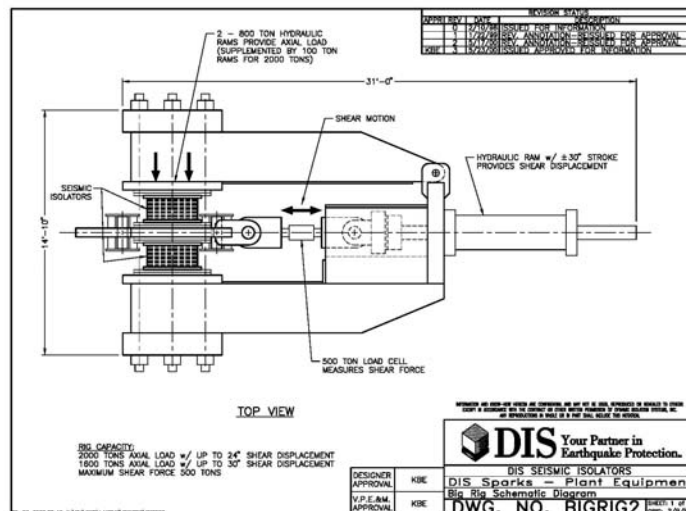


Figure 4 - DIS Big Rig Drawing



## **Test Rig Calibration**

---

## C E R T I F I C A T E   O F   V E R I F I C A T I O N

This is to Certify that the

Big Rig - Axial Mode                      3.2Mlb Nominal Capacity  
 Test Rig No. 3                              2 - Enerpac 800T Rams  
 APGroup Digital Gage Model: PG-10000    Serial: X3566

Located at

Dynamic Isolation Systems, Inc.  
 885 Denmark Drive  
 McCarran Nevada 89434

was calibrated on 25 March 2011 according to applicable procedures of ASTM Specification E4, and the fitted load table values determined to be within the required 1.0 % tolerance, or Gage resolution limits, of the true loads applied to the system over the following range(s):

MACHINE RANGE, LB	LOADING RANGE, LB Minimum - Maximum	Gage Reading...psi Minimum - Maximum
3,600,000	300,365 - 3,370,873	1,002 - 9,518

Systems used were verified according to ASTM Specification E 74 by the National Standards Testing Laboratory as indicated below:

INSTRUMENTS.... USED.....	CAPACITY. .....LB	SERIAL... .....NO	VERIFIED. .....DATE
E M E Load Cell	1,500,000	8512.03	17 Mar 11
E M E Load Cell	1,500,000	9709.05	21 Sep 10
E M E Load Cell	1,500,000	9709.06	21 Sep 11

RCN Enterprises, Inc.  
 371 Bowler Road  
 Waller Texas 77484

25 March 2011



## C E R T I F I C A T E   O F   V E R I F I C A T I O N

This is to Certify that the

Big Rig - Axial Mode                      4.8Mlb Nominal Capacity  
 Test Rig No 3            10 Enerpac Rams: 2-800T and 8-100T  
 APGroup Digital Gage Model: PG-10000 Serial: X3566

Located at

Dynamic Isolation Systems, Inc.  
 885 Denmark Drive  
 McCarran Nevada 89434

was calibrated on 25 March 2011 according to applicable procedures of ASTM Specification E4, and the fitted load table values determined to be within the required 1.0 % tolerance, or Gage resolution limits, of the true loads applied to the system over the following range(s):

MACHINE RANGE, LB	LOADING RANGE, LB Minimum - Maximum	Gage Reading...psi Minimum - Maximum
4,800,000	433,786 - 4,304,681	998 - 8,551

Systems used were verified according to ASTM Specification E 74 by the National Standards Testing Laboratory as indicated below:

INSTRUMENTS.... USED.....	CAPACITY. .....LB	SERIAL... .....NO	VERIFIED. .....DATE
E M E Load Cell	1,500,000	8512.03	17 Mar 11
E M E Load Cell	1,500,000	9709.05	21 Sep 10
E M E Load Cell	1,500,000	9709.06	21 Sep 11

RCN Enterprises, Inc.  
 371 Bowler Road  
 Waller Texas 77484

25 March 2011

## *Certificate of Verification*

This is to certify that the:

HSI Universal Load Cell – Capacity: 1.0Mlbs – Tension Loading  
 HSI Load Cell            Model: 3100-1000    Serial: 9951-001  
 National Instruments Data Acquisition System  
 LabView Software displaying Force on Load Cell

Located At:

Dynamic Isolation Systems  
 885 Denmark Drive  
 McCarran Nevada 89434

Was calibrated on 17 September 2009 according to the ASTM Standard E-4-10 and determined to indicate load within the specified 1.0 percent tolerance on the ranges listed below. This Certificate accompanies a Calibration Report which details the specific errors. The maximum error observed was 0.56 percent.

Machine Range, lb:	Loading Range, lb:
1,000,000	53,522 – 1,228,859

Ambient temperature recorded during this calibration: 66.0 F

Devices used were verified as noted below by National Standards Testing Laboratory or Morehouse Instrument Company according to ASTM Standard E-74-06.

Device:	Serial:	Class "A" Range, in Lbs:	Verified:
HSI Load Cell	3335-006	20,800 – 400,000	21 Jul 2009
HSI Load Cell	3335-006B	27,942.2 – 400,000	24 Aug 2010
EME Load Cell	9709.06	94,694.7 – 1,500,000	21 Sep 2010
EME Load Cell	9709.05	99,360.3 – 1,500,000	21 Sep 2010

RCN Enterprises, Inc.  
 371 Bowler Road  
 Waller, Texas 77484

25 March 2011

 Digitally  
 signed by  
 Roy Nash

## *Certificate of Verification*

This is to certify that the:

HSI Universal Load Cell – Capacity: 1.0Mlbs – Compression Loading  
 HSI Load Cell            Model: 3100-1000    Serial: 9951-001  
 National Instruments Data Acquisition System  
 LabView Software displaying Force on Load Cell

Located At:

Dynamic Isolation Systems  
 885 Denmark Drive  
 McCarran Nevada 89434

Was calibrated on 22 March 2011 according to ASTM Standard E-4-10 and determined to indicate load within the specified 1.0 percent tolerance on the ranges listed below. This Certificate accompanies a Calibration Report which details the specific errors. The maximum error observed was 0.61 percent.

Machine Range, lb:	Loading Range, lb:
1,000,000	40,019 – 1,200,891

Ambient temperature recorded during this calibration: 65.0 F

Devices used were verified as noted below by Morehouse Instrument Company according to ASTM Standard E-74-06.

Device:	Serial:	Class "A" Range, in Lbs:	Verified:
HSI Load Cell	3335-006B	27,942.2 – 400,000	24 Aug 2010
EME Load Cell	9709.05	94,694.7 – 1,500,000	21 Sep 2010

RCN Enterprises, Inc.  
 371 Bowler Road  
 Waller, Texas 77484

22 March 2011

 Digitally  
 signed by  
 Roy Nash



## APPENDIX F

### OpenSees Script for Multi-spring Bearing Model

Building Isolated with Hybrid Lead-Rubber Isolation System

Developed by Camila B. Coria

List of source codes:

**Main:** This is the main file to be executed by the user. The procedure to create the multi-spring bearing models (MS2 and MS4) are called from this file.

**PROCEDURE FOR MS2 BEARING MODEL:** Contains the procedure to create the MS2 bearing model.

**PROCEDURE FOR MS4 BEARING MODEL:** Contains the procedure to create the MS4 bearing model.

## MAIN FILE

```
#####
## MULTIPLE SPRING LEAD-RUBBER BEARING MODEL
## CREATED BY: CAMILA B. CORIA
## UNIVSERITY OF NEVADA, RENO
#####

# define UNITS -----
# units: SI (N, m, sec)
  set  m 1.;
  set  g 9.81;
  set  kN 1000.;
  set  cm 0.01;
  set  mm 0.001;
  set  MPa 1.e6;
  set  PI [expr 2*asin(1.0)];

# Model build -----
  wipe; # clear memory of all past model definitions
  model basic -ndm 3 -ndf 6 ; # Define the model builder, ndm=#dimension,
                                ndf=#dofs

# Define Isolator Properties -----
  set W [expr 583.*$kN]; #axial load on a single bearing
  set kv [expr 1000*$kN/$mm]; #adjusted vertical stiffness of the LRB
  set kd [expr 6.5*$kN/$cm]; #post-yield stiffness of LRB
  set Qd [expr 65.7*$kN]; #characteristic strength of LRB
  set uy [expr 1.128*$cm]; #yield displacement of LRB
  set fy [expr $Qd+$kd*$uy]; #yield force of LRB
  set k1 [expr 10.0*$kd]; #initial stiffness of LRB
  set b 0.1; #ratio of Kd/K1
  set G_rub [expr 0.414*$MPa]; #rubber shear modulus
  set Dout [expr 700.0*$mm]; #outside LRB diameter
  set Atot [expr $PI*$Dout*$Dout/4]; #LRB total area
  set NVS 2; #number of vertical springs in a given
              direction (excluding the center node)
              (must be even number)
  set ls [expr $Dout/$NVS]; #distance of edge vertical spring from
                              center vertical spring

# define GEOMETRY -----
  set XGrid "0. 5. 10.";
  set YGrid "0. 7. 12.";
```

```

set ZGrid      "0.    4.099  7.099  10.099  13.099  16.099";

# ##### BUILD MSS-LRB ISOLATOR
# #####
# Define distribution of vertical stiffness on vertical springs
# Note: top and bottom Vertical springs are in series. Each group of vertical springs need to have
# 2*Kv
      set ratio1      1.2;          #center node
      set ratio2      [expr (2. - $ratio1)/4]; #edge nodes

#To construct the MS2 bearing model:
      source isolatorMSS_MS2.tcl;
      IsolatorMSS_MS2 1 [lindex $XGrid 0] [lindex $YGrid 0] $ls      $Atot $fy
      $k1 $kd $Qd $b $kv $G_rub $ratio1 $ratio2;

#To construct the MS4 bearing model:
#Note: MS4 has double the number of edge vertical springs than MS2; therefore, ratio2 is
#divided by 2
      #source      isolatorMSS_MS4.tcl;
      #IsolatorMSS_MS4 1 [lindex $XGrid 0] [lindex $YGrid 0] $ls      $Atot $fy
      $k1 $kd $Qd $b $kv $G_rub $ratio1 [expr $ratio2/2];

# set up directory name
      set outDir "MS2_Pushover";
      set dataDir $outDir/;
      file mkdir $dataDir;
      puts "$outDir";

# Perform gravity analysis
      pattern Plain 1 Linear {
        load 902400 0.0 0.0 [expr -1.*$W] 0.0 0.0 0.0
      }

      puts "Gravity analysis starts..."
      set numSteps 50;
      system ProfileSPD;
      constraints Transformation;
      numberer RCM;
      test NormDispIncr 1.0e-10 10;
      algorithm Newton ;
      integrator LoadControl [expr 1.0/$numSteps]
      analysis Static
      analyze $numSteps;
      puts "End of Gravity Analysis"

      loadConst -time 0.0;

# Define Recorders

```

```

#x-direction
recorder Node -file $dataDir/NodeDisp8_X.out -time -node 912821
          902800 912811 -dof 1 2 3 4 5 6 disp;
recorder Node -file $dataDir/NodeDisp5_X.out -time -node 912521
          902500 912511 -dof 1 2 3 4 5 6 disp;
recorder Node -file $dataDir/NodeDisp4_X.out -time -node 912421
          902400 912411 -dof 1 2 3 4 5 6 disp;
recorder Node -file $dataDir/NodeDisp7_X.out -time -node 912721
          912711 912724 912713 -dof 1 2 3 4 5 6 disp;
recorder Node -file $dataDir/BaseReactMVS_X.out -time -node 912921
          902900 912911 -dof 1 2 3 4 5 6 reaction;
#y-direction (main)
recorder Node -file $dataDir/NodeDisp8_Y.out -time -node 902821
          902800 902811 -dof 1 2 3 4 5 6 disp;
recorder Node -file $dataDir/NodeDisp5_Y.out -time -node 902521
          902500 902511 -dof 1 2 3 4 5 6 disp;
recorder Node -file $dataDir/NodeDisp4_Y.out -time -node 902421
          902400 902411 -dof 1 2 3 4 5 6 disp;
recorder Node -file $dataDir/NodeDisp7_Y.out -time -node 902721
          902711 902724 902713 -dof 1 2 3 4 5 6 disp;
recorder Node -file $dataDir/BaseReactMVS_Y.out -time -node 902921
          902900 902911 -dof 1 2 3 4 5 6 reaction;

recorder Element -file $dataDir/BeamForce_X.out -time -ele 9121420
          9121401 9121520 9121501 9121820 9121801 force;
recorder Element -file $dataDir/VertSpringF98_X.out -time -ele 9129821
          9029800 9129811 force;
recorder Element -file $dataDir/VertSpringF54_X.out -time -ele 9125421
          9025400 9125411 force;
recorder Element -file $dataDir/VertBeamForce_X.out -time -ele 9122751
          9122872 9122752 9122871 force;
recorder Element -file $dataDir/ShearSpringB_X.out -time -ele 9124721
          9124743 force;
recorder Element -file $dataDir/ShearSpringT_X.out -time -ele 9123721
          9123743 force;

recorder Element -file $dataDir/BeamForce_Y.out -time -ele 9021420
          9021401 9021520 9021501 9021820 9021801 force;
recorder Element -file $dataDir/VertSpringF98_Y.out -time -ele 9029821
          9029800 9029811 force;
recorder Element -file $dataDir/VertSpringF54_Y.out -time -ele 9025421
          9025400 9025411 force;
recorder Element -file $dataDir/VertBeamForce_Y.out -time -ele 9022751
          9022872 9022752 9022871 force;
recorder Element -file $dataDir/ShearSpringB_Y.out -time -ele 9024721
          9024743 force;
recorder Element -file $dataDir/ShearSpringT_Y.out -time -ele 9023721
          9023743 force;

```

```

recorder      Element -file $dataDir/BeamForce_45x.out      -time -ele
9221420 9221401 9221520 9221501 9221820 9221801 force;
recorder      Element -file $dataDir/VertSpringF98_45x.out -time -ele 9229821
9029800 9229811      force;
recorder      Element -file $dataDir/VertSpringF54_45x.out -time -ele 9225421
9025400 9225411      force;
recorder      Element -file $dataDir/VertBeamForce_45x.out      -time -ele
9222751 9222872 9222752 9222871      force;
recorder      Element -file $dataDir/ShearSpringB_45x.out -time -ele 9224721
9224743      force;
recorder      Element -file $dataDir/ShearSpringT_45x.out -time -ele 9223721
9223743      force;

recorder      Element -file $dataDir/BeamForce_135x.out -time -ele 9321420
9321401 9321520 9321501 9321820 9321801      force;
recorder      Element -file $dataDir/VertSpringF98_135x.out -time -ele 9329821
9029800 9329811      force;
recorder      Element -file $dataDir/VertSpringF54_135x.out -time -ele 9325421
9025400 9325411      force;
recorder      Element -file $dataDir/VertBeamForce_135x.out -time -ele
9322751 9322872 9322752 9322871      force;
recorder      Element -file $dataDir/ShearSpringB_135x.out -time -ele 9324721
9324743      force;
recorder      Element -file $dataDir/ShearSpringT_135x.out -time -ele 9323721
9323743      force;

recorder      Node -file $dataDir/L4Reaction.out      -time -node 912421
912411 902421 902400 902411 922421 922411 932421 932411
-dof 1 2 3 reaction;
recorder      Node -file $dataDir/L8Reaction.out      -time -node 912821
912811 902821 902800 902811 922821 922811 932821 932811
-dof 1 2 3 reaction;
recorder      Node -file $dataDir/L9Reaction.out      -time -node 912921
912911 902921 902900 902911 922921 922911 932921 932911
-dof 1 2 3 reaction;
recorder      Node -file $dataDir/L9VertReaction.out -time -node 912921
912911 902921 902900 902911 922921 922911 932921 932911
-dof 3 reaction;
recorder      Element -file $dataDir/ForceLead.out      -time -ele 9025049
forces;

```

```
#####
```

```
# Static Pushover Analysis
set ctrlNode 902400;
```

```

set ctrlDOF 2;
set Dmax [expr 350.*$mm];
set Dincr [expr 0.2*$mm];

pattern Plain 2 Linear {
    load 902400          0.0 1.0 0.0 0.0 0.0 0.0
}

# pushover: Displacement Controlled Static Analysis
constraints Plain;
numberer RCM;
system BandGeneral;
test EnergyIncr 1.0e-5 600;
algorithm Newton;
integrator DisplacementControl $ctrlNode $ctrlDOF -$Dincr;
analysis Static
analyze [expr int(300.*$mm/$Dincr)];
integrator DisplacementControl $ctrlNode $ctrlDOF [expr $Dincr];
analysis Static
analyze [expr int(600.*$mm/$Dincr)];
integrator DisplacementControl $ctrlNode $ctrlDOF -$Dincr;
analysis Static
analyze [expr int(320.*$mm/$Dincr)];

puts "Done with Pushover Analysis"
#####

wipe all;

```

## PROCEDURE FOR MS2 BEARING MODEL

```
#####
## MULTI-SPRING LEAD-RUBBER BEARING MODEL
## CREATED BY: CAMILA B. CORIA
## UNIVERSITY OF NEVADA, RENO
#####

proc IsolatorMSS_MS2      {iIso XGrid YGrid ls Atot fy k1 kd Qd b kv G_rub ratio1
ratio2 } {

# Node ID includes 6 digits:
#   1st digit is for isolator node = 9
#   2nd digit = 0 for y-direction (main), 1 for x-direction
#   2nd digit indicates isolator ID
#   3rd digit indicates the vertical height of the nodes (layer), (4=top layer connected to
building, 5=bottom of 1st layer of vertical spring, 7 = shear spring layer, 8=top of bottom
vertical springs, 9=bottom layer of vertical springs (fixed)
#   4th digit horizontal distance from center line (2 = -$ls , 1 = $ls, 0 = at the center )
#   5th digit indicates number of vertical spring away from center in both directions (0 =
center, 1 = one node away from center in x-dir)
#   ex: 901921 = isolator node 9, 0 in y-direction, 1 = Isolator ID, 9=bottom layer of bottom
vert. springs (fixed), 2 = -$ls from center node, 1= one node from center node in the
horizontal direction.

# Create isolator nodes for multispring model
#y-direction (main)
node [expr 900000 + $iIso*1000 + 400] [expr $XGrid] [expr $YGrid + 0.0 ] [expr 0.0 +
0.46]; #Height of LRB = 460 mm
node [expr 900000 + $iIso*1000 + 421] [expr $XGrid] [expr $YGrid + -$ls ] [expr 0.0 +
0.46];
node [expr 900000 + $iIso*1000 + 411] [expr $XGrid] [expr $YGrid + $ls ] [expr 0.0 +
0.46];
node [expr 900000 + $iIso*1000 + 500] [expr $XGrid] [expr $YGrid + 0.0 ] [expr 0.0 +
0.46];
node [expr 900000 + $iIso*1000 + 521] [expr $XGrid] [expr $YGrid + -$ls ] [expr 0.0 +
0.46];
node [expr 900000 + $iIso*1000 + 511] [expr $XGrid] [expr $YGrid + $ls ] [expr 0.0 +
0.46];
node [expr 900000 + $iIso*1000 + 721] [expr $XGrid] [expr $YGrid + -$ls ] [expr 0.0 +
0.23];
node [expr 900000 + $iIso*1000 + 711] [expr $XGrid] [expr $YGrid + $ls ] [expr 0.0 +
0.23];
node [expr 900000 + $iIso*1000 + 724] [expr $XGrid] [expr $YGrid + -$ls ] [expr 0.0 +
0.23]; #2nd layer of shear
node [expr 900000 + $iIso*1000 + 713] [expr $XGrid] [expr $YGrid + $ls ] [expr 0.0 +
0.23]; #2nd layer of shear
node [expr 900000 + $iIso*1000 + 800] [expr $XGrid] [expr $YGrid + 0.0 ] [expr 0.0 +
0.0];
```

```

node [expr 900000 + $iIso*1000 + 821] [expr $XGrid] [expr $YGrid + -$ls ] [expr 0.0 +
0.0];
node [expr 900000 + $iIso*1000 + 811] [expr $XGrid] [expr $YGrid + $ls ] [expr 0.0 +
0.0];
node [expr 900000 + $iIso*1000 + 900] [expr $XGrid] [expr $YGrid + 0.0 ] [expr 0.0 +
0.0];
node [expr 900000 + $iIso*1000 + 921] [expr $XGrid] [expr $YGrid + -$ls ] [expr 0.0 +
0.0];
node [expr 900000 + $iIso*1000 + 911] [expr $XGrid] [expr $YGrid + $ls ] [expr 0.0 +
0.0];
# x-direction
node [expr 910000 + $iIso*1000 + 421] [expr $XGrid + -$ls ] [expr $YGrid] [expr 0.0 +
0.46];
node [expr 910000 + $iIso*1000 + 411] [expr $XGrid + $ls ] [expr $YGrid] [expr 0.0 +
0.46];
node [expr 910000 + $iIso*1000 + 521] [expr $XGrid + -$ls ] [expr $YGrid] [expr 0.0 +
0.46];
node [expr 910000 + $iIso*1000 + 511] [expr $XGrid + $ls ] [expr $YGrid] [expr 0.0 +
0.46];
node [expr 910000 + $iIso*1000 + 721] [expr $XGrid + -$ls ] [expr $YGrid] [expr 0.0 +
0.23];
node [expr 910000 + $iIso*1000 + 711] [expr $XGrid + $ls ] [expr $YGrid] [expr 0.0 +
0.23];
node [expr 910000 + $iIso*1000 + 724] [expr $XGrid + -$ls ] [expr $YGrid] [expr 0.0 +
0.23]; #2nd layer of shear
node [expr 910000 + $iIso*1000 + 713] [expr $XGrid + $ls ] [expr $YGrid] [expr 0.0 +
0.23]; #2nd layer of shear
node [expr 910000 + $iIso*1000 + 821] [expr $XGrid + -$ls ] [expr $YGrid] [expr 0.0 +
0.0];
node [expr 910000 + $iIso*1000 + 811] [expr $XGrid + $ls ] [expr $YGrid] [expr 0.0 +
0.0];
node [expr 910000 + $iIso*1000 + 921] [expr $XGrid + -$ls ] [expr $YGrid] [expr 0.0 +
0.0];
node [expr 910000 + $iIso*1000 + 911] [expr $XGrid + $ls ] [expr $YGrid] [expr 0.0 +
0.0];

```

```
# node constraints
```

```
#y-direction (main)
```

```
fix [expr 900000 + $iIso*1000 + 900] 1 1 1 1 1 1
```

```
fix [expr 900000 + $iIso*1000 + 921] 1 1 1 1 1 1
```

```
fix [expr 900000 + $iIso*1000 + 911] 1 1 1 1 1 1
```

```
#x-direction
```

```
fix [expr 910000 + $iIso*1000 + 921] 1 1 1 1 1 1
```

```
fix [expr 910000 + $iIso*1000 + 911] 1 1 1 1 1 1
```

```
# constraint to provide stability in a single bearing model.
```

```
fix [expr 900000 + $iIso*1000 + 400] 0 0 0 1 1 1;
```

```
#Imposed constraints to minimize number of elements
```



```
fix [expr 900000 + $iIso*1000 + 800] 1 1 0 0 0 1;
equalDOF [expr 900000 + $iIso*1000 + 400] [expr 900000 + $iIso*1000 + 500] 1 2 6 ;
```

```
# define geometric transformations
```

```
set TransBeamX [expr 10 + $iIso];
set TransBeamY [expr 20 + $iIso];
set TransCol [expr 30 + $iIso];
set TransCorotY [expr 40 + $iIso];
set TransCorotX [expr 50 + $iIso];
set MatVertSpringTagCenter [expr 60 + $iIso];
set MatVertSpringTag [expr 70 + $iIso];
set ShearRubberTag [expr 80 + $iIso];
set ShearLeadTag [expr 90 + $iIso];
```

```
geomTransf Linear $TransBeamX 0. -1. 0.;
geomTransf Linear $TransBeamY 1. 0. 0.;
geomTransf Linear $TransCol 0. 1. 0.;
geomTransf Corotational $TransCorotY 1. 0. 0.;
geomTransf Corotational $TransCorotX 0. -1. 0.;
```

```
# define horizontal and vertical material properties
```

```
#material for truss element (rubber)
```

```
uniaxialMaterial Elastic $ShearRubberTag [expr $kd/2]
```

```
#material for plastic spring (lead plug)
```

```
section Bidirectional $ShearLeadTag [expr $k1-$kd] $Qd 0. 0.;
```

```
#material for vertical springs (center and edge springs have different stiffness)
```

```
uniaxialMaterial Elastic $MatVertSpringTagCenter [expr $ratio1*$kv] ;
```

```
uniaxialMaterial Elastic $MatVertSpringTag [expr $ratio2*$kv] ;
```

```
# create horizontal and vertical beams to connect the nodes from multi spring isolator model
```

```
# element tag:
```

```
# 1st digit = element for multiple spring node 9
```

```
# 2nd digit = 0 for y-direction (main), 1 for x
```

```
# 3rd digit = isolator ID
```

```
# 4th digit = 1= horizontal stiff beam, 2= vertical stiff beams, 3=shear beam (truss), 4= shear beam
```

```
(rigid)
```

```
# 5th digit = vertical level of multi-spring
```

```
# 6th and 7th digits = node location from center line, (20 = connects the left node with the center
```

```
node, 01 = connects center node with the one on the right)
```

```
# example: 9111820
```

```
#horizontal stiff beam
```

```

set A 1.e15;
set Iz 1.e15;
set E 1.;
set G 1.e15;
set J 1.;
set Iy 1.e15;

```

```
#y-direction (main)
```

```

element elasticBeamColumn [expr 9001000 + $Iso*10000 + 820] [expr 900000 +
$Iso*1000 + 821] [expr 900000 + $Iso*1000 + 800] $A $E $G $J $Iy
$Iz $TransBeamY

```

```

element elasticBeamColumn [expr 9001000 + $Iso*10000 + 801] [expr 900000 +
$Iso*1000 + 800] [expr 900000 + $Iso*1000 + 811] $A $E $G $J $Iy
$Iz $TransBeamY

```

```

element elasticBeamColumn [expr 9001000 + $Iso*10000 + 520] [expr 900000 +
$Iso*1000 + 521] [expr 900000 + $Iso*1000 + 500] $A $E $G $J $Iy
$Iz $TransBeamY

```

```

element elasticBeamColumn [expr 9001000 + $Iso*10000 + 501] [expr 900000 +
$Iso*1000 + 500] [expr 900000 + $Iso*1000 + 511] $A $E $G $J $Iy
$Iz $TransBeamY

```

```

element elasticBeamColumn [expr 9001000 + $Iso*10000 + 420] [expr 900000 +
$Iso*1000 + 421] [expr 900000 + $Iso*1000 + 400] $A $E $G $J $Iy
$Iz $TransBeamY

```

```

element elasticBeamColumn [expr 9001000 + $Iso*10000 + 401] [expr 900000 +
$Iso*1000 + 400] [expr 900000 + $Iso*1000 + 411] $A $E $G $J $Iy
$Iz $TransBeamY

```

```
#x-direction
```

```

element elasticBeamColumn [expr 9101000 + $Iso*10000 + 820] [expr 910000 +
$Iso*1000 + 821] [expr 900000 + $Iso*1000 + 800] $A $E $G $J $Iy
$Iz $TransBeamX

```

```

element elasticBeamColumn [expr 9101000 + $Iso*10000 + 801] [expr 900000 +
$Iso*1000 + 800] [expr 910000 + $Iso*1000 + 811] $A $E $G $J $Iy
$Iz $TransBeamX

```

```

element elasticBeamColumn [expr 9101000 + $Iso*10000 + 520] [expr 910000 +
$Iso*1000 + 521] [expr 900000 + $Iso*1000 + 500] $A $E $G $J $Iy
$Iz $TransBeamX

```

```

element elasticBeamColumn [expr 9101000 + $Iso*10000 + 501] [expr 900000 +
$Iso*1000 + 500] [expr 910000 + $Iso*1000 + 511] $A $E $G $J $Iy
$Iz $TransBeamX

```

```

element elasticBeamColumn [expr 9101000 + $Iso*10000 + 420] [expr 910000 +
$Iso*1000 + 421] [expr 900000 + $Iso*1000 + 400] $A $E $G $J $Iy
$Iz $TransBeamX

```

```

element elasticBeamColumn [expr 9101000 + $Iso*10000 + 401] [expr 900000 +
$Iso*1000 + 400] [expr 910000 + $Iso*1000 + 411] $A $E $G $J $Iy
$Iz $TransBeamX

```

```

#vertical stiff beam
#y-direction (main)

```

element elasticBeamColumn [expr 9002000 + \$iIso\*10000 + 872] [expr 900000 + \$iIso\*1000 + 821] [expr 900000 + \$iIso\*1000 + 721] \$A \$E \$G \$J \$Iy \$Iz \$TransCol

element elasticBeamColumn [expr 9002000 + \$iIso\*10000 + 751] [expr 900000 + \$iIso\*1000 + 711] [expr 900000 + \$iIso\*1000 + 511] \$A \$E \$G \$J \$Iy \$Iz \$TransCol

element elasticBeamColumn [expr 9002000 + \$iIso\*10000 + 871] [expr 900000 + \$iIso\*1000 + 811] [expr 900000 + \$iIso\*1000 + 713] \$A \$E \$G \$J \$Iy \$Iz \$TransCol

element elasticBeamColumn [expr 9002000 + \$iIso\*10000 + 752] [expr 900000 + \$iIso\*1000 + 724] [expr 900000 + \$iIso\*1000 + 521] \$A \$E \$G \$J \$Iy \$Iz \$TransCol

#x-direction

element elasticBeamColumn [expr 9102000 + \$iIso\*10000 + 872] [expr 910000 + \$iIso\*1000 + 821] [expr 910000 + \$iIso\*1000 + 721] \$A \$E \$G \$J \$Iy \$Iz \$TransCol

element elasticBeamColumn [expr 9102000 + \$iIso\*10000 + 751] [expr 910000 + \$iIso\*1000 + 711] [expr 910000 + \$iIso\*1000 + 511] \$A \$E \$G \$J \$Iy \$Iz \$TransCol

element elasticBeamColumn [expr 9102000 + \$iIso\*10000 + 871] [expr 910000 + \$iIso\*1000 + 811] [expr 910000 + \$iIso\*1000 + 713] \$A \$E \$G \$J \$Iy \$Iz \$TransCol

element elasticBeamColumn [expr 9102000 + \$iIso\*10000 + 752] [expr 910000 + \$iIso\*1000 + 724] [expr 910000 + \$iIso\*1000 + 521] \$A \$E \$G \$J \$Iy \$Iz \$TransCol

#shear element

#y-direction(main)

element corotTruss [expr 9003000 + \$iIso\*10000 + 721] [expr 900000 + \$iIso\*1000 + 721] [expr 900000 + \$iIso\*1000 + 711] [expr 1.0\*2\*\$ls] \$ShearRubberTag;

element elasticBeamColumn [expr 9004000 + \$iIso\*10000 + 721] [expr 900000 + \$iIso\*1000 + 721] [expr 900000 + \$iIso\*1000 + 711] 1.e-7 1. 1. 1. 1.e-10 1.e8 \$TransCorotY

element corotTruss [expr 9003000 + \$iIso\*10000 + 743] [expr 900000 + \$iIso\*1000 + 724] [expr 900000 + \$iIso\*1000 + 713] [expr 1.0\*2\*\$ls] \$ShearRubberTag;

element elasticBeamColumn [expr 9004000 + \$iIso\*10000 + 743] [expr 900000 + \$iIso\*1000 + 724] [expr 900000 + \$iIso\*1000 + 713] 1.e-7 1. 1. 1. 1.e-10 1.e8 \$TransCorotY

#x-direction

element corotTruss [expr 9103000 + \$iIso\*10000 + 721] [expr 910000 + \$iIso\*1000 + 721] [expr 910000 + \$iIso\*1000 + 711] [expr 1.0\*2\*\$ls] \$ShearRubberTag;

element elasticBeamColumn [expr 9104000 + \$iIso\*10000 + 721] [expr 910000 + \$iIso\*1000 + 721] [expr 910000 + \$iIso\*1000 + 711] 1.e-7 1. 1. 1. 1.e-10 1.e8 \$TransCorotX

element corotTruss [expr 9103000 + \$iIso\*10000 + 743] [expr 910000 + \$iIso\*1000 + 724] [expr 910000 + \$iIso\*1000 + 713] [expr 1.0\*2\*\$ls] \$ShearRubberTag;

```

element elasticBeamColumn [expr 9104000 + $iIso*10000 + 743] [expr 910000 +
$iIso*1000 + 724] [expr 910000 + $iIso*1000 + 713] 1.e-7 1. 1. 1. 1.e-10
1.e8 $TransCorotX

# Lead plug
element zeroLengthSection [expr 9005000 + $iIso*10000 + 49] [expr 900000 +
$iIso*1000 + 900] [expr 900000 + $iIso*1000 + 400] $ShearLeadTag

# create vertical springs for multi spring isolator model
# element tag:
# 1st digit = element for multiple spring node 9
# 2nd digit = 0: y-direction (main), 1: x-direction
# 3rd digit = isolator ID
# 4th and 5th digits = connecting levels (eg.: 54 = connects level 5 (bott of top vertical
springs) with
level 4 (top of top vertical springs)
# 6th digit horizontal distance from center line (2 = -$ls , 1 = $ls, 0 = at the center )
# 7th digit indicates number of vertical spring away from center in both directions (0 = center,
1 = one node away from center in x-dir)
# examples: 9119800

#y-direction (main)
element zeroLength [expr 9000000 + $iIso*10000 + 9800] [expr 900000 + $iIso*1000 +
900] [expr 900000 + $iIso*1000 + 800] -mat $MatVertSpringTagCenter -dir 3 ;#center
element zeroLength [expr 9000000 + $iIso*10000 + 9811] [expr 900000 + $iIso*1000 +
911] [expr 900000 + $iIso*1000 + 811] -mat $MatVertSpringTag -dir 3 ;
element zeroLength [expr 9000000 + $iIso*10000 + 9821] [expr 900000 + $iIso*1000 +
921] [expr 900000 + $iIso*1000 + 821] -mat $MatVertSpringTag -dir 3 ;
element zeroLength [expr 9000000 + $iIso*10000 + 5400] [expr 900000 + $iIso*1000 +
500] [expr 900000 + $iIso*1000 + 400] -mat $MatVertSpringTagCenter -dir 3 ;#center
element zeroLength [expr 9000000 + $iIso*10000 + 5411] [expr 900000 + $iIso*1000 +
511] [expr 900000 + $iIso*1000 + 411] -mat $MatVertSpringTag -dir 3 ;
element zeroLength [expr 9000000 + $iIso*10000 + 5421] [expr 900000 + $iIso*1000 +
521] [expr 900000 + $iIso*1000 + 421] -mat $MatVertSpringTag -dir 3 ;
#x-direction
element zeroLength [expr 9100000 + $iIso*10000 + 9811] [expr 910000 + $iIso*1000 +
911] [expr 910000 + $iIso*1000 + 811] -mat $MatVertSpringTag -dir 3 ;
element zeroLength [expr 9100000 + $iIso*10000 + 9821] [expr 910000 + $iIso*1000 +
921] [expr 910000 + $iIso*1000 + 821] -mat $MatVertSpringTag -dir 3 ;
element zeroLength [expr 9100000 + $iIso*10000 + 5411] [expr 910000 + $iIso*1000 +
511] [expr 910000 + $iIso*1000 + 411] -mat $MatVertSpringTag -dir 3 ;
element zeroLength [expr 9100000 + $iIso*10000 + 5421] [expr 910000 + $iIso*1000 +
521] [expr 910000 + $iIso*1000 + 421] -mat $MatVertSpringTag -dir 3 ;
}

```

### PROCEDURE FOR MS4 BEARING MODEL

```
#####
## MULTI-SPRING LEAD-RUBBER BEARING MODEL
## CREATED BY: CAMILA B. CORIA
## UNIVERSITY OF NEVADA, RENO
#####

proc   IsolatorMSS_MS4      {iIso XGrid YGrid ls Atot fy k1 kd Qd b kv G_rub ratio1
ratio2 } {

# Node ID includes 6 digits:
#   1st digit is for isolator node = 9
#   2nd digit = 0 for y-direction (main), 1 for x-direction
#   2nd digit indicates isolator ID
#   3rd digit indicates the vertical height of the nodes (layer), (4=top layer connected to
building, 5=bottom of 1st layer of vertical spring, 7 = shear spring layer, 8=top of bottom
vertical springs, 9=bottom layer of vertical springs (fixed)
#   4th digit horizontal distance from center line (2 = -$ls , 1 = $ls, 0 = at the center)
#   5th digit indicates number of vertical spring away from center in both directions (0 =
center, 1 = one node away from center in x-dir)
#   ex: 901921 = isolator node 9, 0 in y-direction, 1 = Isolator ID, 9=bottom layer of bottom
vert. springs (fixed), 2 = -$ls from center node, 1= one node from center node in the
horizontal direction.

# Create isolator nodes for multispring model
#y-direction (main)
node [expr 900000 + $iIso*1000 + 400] [expr $XGrid] [expr $YGrid + 0.0 ] [expr 0.0 +
0.46]; #Height of LRB = 460 mm
node [expr 900000 + $iIso*1000 + 421] [expr $XGrid] [expr $YGrid + -$ls ] [expr 0.0 +
0.46];
node [expr 900000 + $iIso*1000 + 411] [expr $XGrid] [expr $YGrid + $ls ] [expr 0.0 +
0.46];
node [expr 900000 + $iIso*1000 + 500] [expr $XGrid] [expr $YGrid + 0.0 ] [expr 0.0 +
0.46];
node [expr 900000 + $iIso*1000 + 521] [expr $XGrid] [expr $YGrid + -$ls ] [expr 0.0 +
0.46];
node [expr 900000 + $iIso*1000 + 511] [expr $XGrid] [expr $YGrid + $ls ] [expr 0.0 +
0.46];
node [expr 900000 + $iIso*1000 + 721] [expr $XGrid] [expr $YGrid + -$ls ] [expr 0.0 +
0.23];
node [expr 900000 + $iIso*1000 + 711] [expr $XGrid] [expr $YGrid + $ls ] [expr 0.0 +
0.23];
node [expr 900000 + $iIso*1000 + 724] [expr $XGrid] [expr $YGrid + -$ls ] [expr 0.0 +
0.23]; #2nd layer of shear
node [expr 900000 + $iIso*1000 + 713] [expr $XGrid] [expr $YGrid + $ls ] [expr 0.0 +
0.23]; #2nd layer of shear
node [expr 900000 + $iIso*1000 + 800] [expr $XGrid] [expr $YGrid + 0.0 ] [expr 0.0 +
0.0];
```

```

node [expr 900000 + $iIso*1000 + 821] [expr $XGrid] [expr $YGrid + -$ls ] [expr 0.0 +
0.0];
node [expr 900000 + $iIso*1000 + 811] [expr $XGrid] [expr $YGrid + $ls ] [expr 0.0 +
0.0];
node [expr 900000 + $iIso*1000 + 900] [expr $XGrid] [expr $YGrid + 0.0 ] [expr 0.0 +
0.0];
node [expr 900000 + $iIso*1000 + 921] [expr $XGrid] [expr $YGrid + -$ls ] [expr 0.0 +
0.0];
node [expr 900000 + $iIso*1000 + 911] [expr $XGrid] [expr $YGrid + $ls ] [expr 0.0 +
0.0];
# x-direction
node [expr 910000 + $iIso*1000 + 421] [expr $XGrid + -$ls ] [expr $YGrid] [expr 0.0 +
0.46];
node [expr 910000 + $iIso*1000 + 411] [expr $XGrid + $ls ] [expr $YGrid] [expr 0.0 +
0.46];
node [expr 910000 + $iIso*1000 + 521] [expr $XGrid + -$ls ] [expr $YGrid] [expr 0.0 +
0.46];
node [expr 910000 + $iIso*1000 + 511] [expr $XGrid + $ls ] [expr $YGrid] [expr 0.0 +
0.46];
node [expr 910000 + $iIso*1000 + 721] [expr $XGrid + -$ls ] [expr $YGrid] [expr 0.0 +
0.23];
node [expr 910000 + $iIso*1000 + 711] [expr $XGrid + $ls ] [expr $YGrid] [expr 0.0 +
0.23];
node [expr 910000 + $iIso*1000 + 724] [expr $XGrid + -$ls ] [expr $YGrid] [expr 0.0 +
0.23]; #2nd layer of shear
node [expr 910000 + $iIso*1000 + 713] [expr $XGrid + $ls ] [expr $YGrid] [expr 0.0 +
0.23]; #2nd layer of shear
node [expr 910000 + $iIso*1000 + 821] [expr $XGrid + -$ls ] [expr $YGrid] [expr 0.0 +
0.0];
node [expr 910000 + $iIso*1000 + 811] [expr $XGrid + $ls ] [expr $YGrid] [expr 0.0 +
0.0];
node [expr 910000 + $iIso*1000 + 921] [expr $XGrid + -$ls ] [expr $YGrid] [expr 0.0 +
0.0];
node [expr 910000 + $iIso*1000 + 911] [expr $XGrid + $ls ] [expr $YGrid] [expr 0.0 +
0.0];
# 45degree from x-axis(Quadrant I and III)
node [expr 920000 + $iIso*1000 + 421] [expr $XGrid + -$ls/pow(2.,0.5) ] [expr $YGrid
+ -$ls/pow(2.,0.5) ] [expr 0.0 + 0.46];
node [expr 920000 + $iIso*1000 + 411] [expr $XGrid + $ls /pow(2.,0.5) ] [expr $YGrid
+ $ls /pow(2.,0.5) ] [expr 0.0 + 0.46];
node [expr 920000 + $iIso*1000 + 521] [expr $XGrid + -$ls/pow(2.,0.5) ] [expr $YGrid
+ -$ls/pow(2.,0.5) ] [expr 0.0 + 0.46];
node [expr 920000 + $iIso*1000 + 511] [expr $XGrid + $ls /pow(2.,0.5) ] [expr $YGrid
+ $ls /pow(2.,0.5) ] [expr 0.0 + 0.46];
node [expr 920000 + $iIso*1000 + 721] [expr $XGrid + -$ls/pow(2.,0.5) ] [expr $YGrid
+ -$ls/pow(2.,0.5) ] [expr 0.0 + 0.23];
node [expr 920000 + $iIso*1000 + 711] [expr $XGrid + $ls /pow(2.,0.5) ] [expr $YGrid
+ $ls /pow(2.,0.5) ] [expr 0.0 + 0.23];

```

```

node [expr 920000 + $iIso*1000 + 724] [expr $XGrid + -$ls/pow(2.,0.5) ] [expr $YGrid
+ -$ls/pow(2.,0.5) ] [expr 0.0 + 0.23]; #2nd layer of shear
node [expr 920000 + $iIso*1000 + 713] [expr $XGrid + $ls /pow(2.,0.5) ] [expr $YGrid
+ $ls /pow(2.,0.5) ] [expr 0.0 + 0.23]; #2nd layer of shear
node [expr 920000 + $iIso*1000 + 821] [expr $XGrid + -$ls/pow(2.,0.5) ] [expr $YGrid
+ -$ls/pow(2.,0.5) ] [expr 0.0 + 0.0];
node [expr 920000 + $iIso*1000 + 811] [expr $XGrid + $ls /pow(2.,0.5) ] [expr $YGrid
+ $ls /pow(2.,0.5) ] [expr 0.0 + 0.0];
node [expr 920000 + $iIso*1000 + 921] [expr $XGrid + -$ls/pow(2.,0.5) ] [expr
$YGrid + -$ls/pow(2.,0.5) ] [expr 0.0 + 0.0];
node [expr 920000 + $iIso*1000 + 911] [expr $XGrid + $ls /pow(2.,0.5) ] [expr $YGrid
+ $ls /pow(2.,0.5) ] [expr 0.0 + 0.0];

```

```
# -45degree from x-axis(Quadrant II and IV)
```

```

node [expr 930000 + $iIso*1000 + 421] [expr $XGrid + -$ls/pow(2.,0.5) ] [expr $YGrid
+ $ls/pow(2.,0.5) ] [expr 0.0 + 0.46];
node [expr 930000 + $iIso*1000 + 411] [expr $XGrid + $ls /pow(2.,0.5) ] [expr $YGrid
+ -$ls/pow(2.,0.5) ] [expr 0.0 + 0.46];
node [expr 930000 + $iIso*1000 + 521] [expr $XGrid + -$ls/pow(2.,0.5) ] [expr $YGrid
+ $ls/pow(2.,0.5) ] [expr 0.0 + 0.46];
node [expr 930000 + $iIso*1000 + 511] [expr $XGrid + $ls /pow(2.,0.5) ] [expr $YGrid
+ -$ls/pow(2.,0.5) ] [expr 0.0 + 0.46];
node [expr 930000 + $iIso*1000 + 721] [expr $XGrid + -$ls/pow(2.,0.5) ] [expr $YGrid
+ $ls/pow(2.,0.5) ] [expr 0.0 + 0.23];
node [expr 930000 + $iIso*1000 + 711] [expr $XGrid + $ls /pow(2.,0.5) ] [expr $YGrid
+ -$ls/pow(2.,0.5) ] [expr 0.0 + 0.23];
node [expr 930000 + $iIso*1000 + 724] [expr $XGrid + -$ls/pow(2.,0.5) ] [expr $YGrid
+ $ls/pow(2.,0.5) ] [expr 0.0 + 0.23]; #2nd layer of shear
node [expr 930000 + $iIso*1000 + 713] [expr $XGrid + $ls /pow(2.,0.5) ] [expr $YGrid
+ -$ls/pow(2.,0.5) ] [expr 0.0 + 0.23]; #2nd layer of shear
node [expr 930000 + $iIso*1000 + 821] [expr $XGrid + -$ls/pow(2.,0.5) ] [expr $YGrid
+ $ls/pow(2.,0.5) ] [expr 0.0 + 0.0];
node [expr 930000 + $iIso*1000 + 811] [expr $XGrid + $ls /pow(2.,0.5) ] [expr $YGrid
+ -$ls/pow(2.,0.5) ] [expr 0.0 + 0.0];
node [expr 930000 + $iIso*1000 + 921] [expr $XGrid + -$ls/pow(2.,0.5) ] [expr $YGrid
+ $ls/pow(2.,0.5) ] [expr 0.0 + 0.0];
node [expr 930000 + $iIso*1000 + 911] [expr $XGrid + $ls /pow(2.,0.5) ] [expr $YGrid
+ -$ls/pow(2.,0.5) ] [expr 0.0 + 0.0];

```

```
# node constraints
```

```
#y-direction (main)
```

```
fix [expr 900000 + $iIso*1000 + 900] 1 1 1 1 1 1
```

```
fix [expr 900000 + $iIso*1000 + 921] 1 1 1 1 1 1
```

```
fix [expr 900000 + $iIso*1000 + 911] 1 1 1 1 1 1
```

```
#x-direction
```

```
fix [expr 910000 + $iIso*1000 + 921] 1 1 1 1 1 1
```

```
fix [expr 910000 + $iIso*1000 + 911] 1 1 1 1 1 1
```

```
#45-direction
```

```
fix [expr 920000 + $iIso*1000 + 921] 1 1 1 1 1 1
```

```

fix [expr 920000 + $iIso*1000 + 911] 1 1 1 1 1 1
fix [expr 930000 + $iIso*1000 + 921] 1 1 1 1 1 1
fix [expr 930000 + $iIso*1000 + 911] 1 1 1 1 1 1

# constraint to provide stability in a single bearing model.
fix [expr 900000 + $iIso*1000 + 400] 0 0 0 1 1 1

#Imposed constraints to minimize number of elements
fix [expr 900000 + $iIso*1000 + 800] 1 1 0 0 0 1; #1 0 0 1 0 1
equalDOF [expr 900000 + $iIso*1000 + 400] [expr 900000 + $iIso*1000 + 500] 1 2 6
;#1246

# define geometric transformations
set TransBeamX [expr 10 + $iIso];
set TransBeamY [expr 20 + $iIso];
set TransCol [expr 30 + $iIso];
set TransCorotY [expr 40 + $iIso];
set TransCorotX [expr 50 + $iIso];
set TransBeam45x [expr 60 + $iIso];
set TransBeam135x [expr 70 + $iIso];
set TransCorot45x [expr 80 + $iIso];
set TransCorot135x [expr 90 + $iIso];
set ShearRubberTag [expr 100 + $iIso];
set ShearLeadTag [expr 110 + $iIso];
set MatVertSpringTagCenter [expr 120 + $iIso];
set MatVertSpringTag [expr 130 + $iIso];

geomTransf Linear $TransBeamX 0. -1. 0.;
geomTransf Linear $TransBeamY 1. 0. 0.;
geomTransf Linear $TransCol 0. 1. 0.;
geomTransf Corotational $TransCorotY 1. 0. 0.;
geomTransf Corotational $TransCorotX 0. -1. 0.;

# element orientated 45 degrees from x-axis
geomTransf Linear $TransBeam45x [expr 1./pow(2.,0.5)] [expr -
1./pow(2.,0.5)] 0.;
geomTransf Linear $TransBeam135x [expr -1./pow(2.,0.5)] [expr -
1./pow(2.,0.5)] 0.;
geomTransf Corotational $TransCorot45x [expr 1./pow(2.,0.5)] [expr -
1./pow(2.,0.5)] 0.;
geomTransf Corotational $TransCorot135x [expr -1./pow(2.,0.5)] [expr -
1./pow(2.,0.5)] 0.;

# define horizontal and vertical material properties
#material for truss element (rubber)
uniaxialMaterial Elastic $ShearRubberTag [expr $kd/2]
#material for plastic spring (lead plug)
section Bidirectional $ShearLeadTag [expr $k1-$kd] $Qd 0. 0.;

```



```

#material for vertical springs (center and edge springs have different stiffness)
    uniaxialMaterial Elastic $MatVertSpringTagCenter      [expr $ratio1*$kv] ;
    uniaxialMaterial Elastic $MatVertSpringTag           [expr $ratio2*$kv] ;

# create horizontal and vertical beams to connect the nodes from multi spring isolator model
# element tag:
# 1st digit = element for multiple spring node 9
# 2nd digit = 0 for y-direction (main), 1 for x
# 3rd digit = isolator ID
# 4th digit = 1= horizontal stiff beam, 2= vertical stiff beams, 3=shear beam (truss), 4= shear
beam
    (rigid)
# 5th digit = vertical level of multi-spring
# 6th and 7th digits = node location from center line, (20 = connects the left node with the
center
    node, 01 = connects center node with the one on the right)
# example: 9111820

    set A 1.e15;
    set Iz 1.e15;
    set E 1.;
    set G 1.e15;
    set J 1.;
    set Iy 1.e15;

#y-direction (main)
    element elasticBeamColumn [expr 9001000 + $iIso*10000 + 820] [expr 900000 +
    $iIso*1000 + 821] [expr 900000 + $iIso*1000 + 800] $A $E $G $J $Iy
    $Iz $TransBeamY
    element elasticBeamColumn [expr 9001000 + $iIso*10000 + 801] [expr 900000 +
    $iIso*1000 + 800] [expr 900000 + $iIso*1000 + 811] $A $E $G $J $Iy
    $Iz $TransBeamY
    element elasticBeamColumn [expr 9001000 + $iIso*10000 + 520] [expr 900000 +
    $iIso*1000 + 521] [expr 900000 + $iIso*1000 + 500] $A $E $G $J $Iy
    $Iz $TransBeamY
    element elasticBeamColumn [expr 9001000 + $iIso*10000 + 501] [expr 900000 +
    $iIso*1000 + 500] [expr 900000 + $iIso*1000 + 511] $A $E $G $J $Iy
    $Iz $TransBeamY
    element elasticBeamColumn [expr 9001000 + $iIso*10000 + 420] [expr 900000 +
    $iIso*1000 + 421] [expr 900000 + $iIso*1000 + 400] $A $E $G $J $Iy
    $Iz $TransBeamY
    element elasticBeamColumn [expr 9001000 + $iIso*10000 + 401] [expr 900000 +
    $iIso*1000 + 400] [expr 900000 + $iIso*1000 + 411] $A $E $G $J $Iy
    $Iz $TransBeamY
#x-direction

```

element elasticBeamColumn [expr 9101000 + \$Iso\*10000 + 820] [expr 910000 + \$Iso\*1000 + 821] [expr 900000 + \$Iso\*1000 + 800] \$A \$E \$G \$J \$Iy \$Iz \$TransBeamX  
 element elasticBeamColumn [expr 9101000 + \$Iso\*10000 + 801] [expr 900000 + \$Iso\*1000 + 800] [expr 910000 + \$Iso\*1000 + 811] \$A \$E \$G \$J \$Iy \$Iz \$TransBeamX  
 element elasticBeamColumn [expr 9101000 + \$Iso\*10000 + 520] [expr 910000 + \$Iso\*1000 + 521] [expr 900000 + \$Iso\*1000 + 500] \$A \$E \$G \$J \$Iy \$Iz \$TransBeamX  
 element elasticBeamColumn [expr 9101000 + \$Iso\*10000 + 501] [expr 900000 + \$Iso\*1000 + 500] [expr 910000 + \$Iso\*1000 + 511] \$A \$E \$G \$J \$Iy \$Iz \$TransBeamX  
 element elasticBeamColumn [expr 9101000 + \$Iso\*10000 + 420] [expr 910000 + \$Iso\*1000 + 421] [expr 900000 + \$Iso\*1000 + 400] \$A \$E \$G \$J \$Iy \$Iz \$TransBeamX  
 element elasticBeamColumn [expr 9101000 + \$Iso\*10000 + 401] [expr 900000 + \$Iso\*1000 + 400] [expr 910000 + \$Iso\*1000 + 411] \$A \$E \$G \$J \$Iy \$Iz \$TransBeamX  
 #45degree-direction  
 element elasticBeamColumn [expr 9201000 + \$Iso\*10000 + 820] [expr 920000 + \$Iso\*1000 + 821] [expr 900000 + \$Iso\*1000 + 800] \$A \$E \$G \$J \$Iy \$Iz \$TransBeam45x  
 element elasticBeamColumn [expr 9201000 + \$Iso\*10000 + 801] [expr 900000 + \$Iso\*1000 + 800] [expr 920000 + \$Iso\*1000 + 811] \$A \$E \$G \$J \$Iy \$Iz \$TransBeam45x  
 element elasticBeamColumn [expr 9201000 + \$Iso\*10000 + 520] [expr 920000 + \$Iso\*1000 + 521] [expr 900000 + \$Iso\*1000 + 500] \$A \$E \$G \$J \$Iy \$Iz \$TransBeam45x  
 element elasticBeamColumn [expr 9201000 + \$Iso\*10000 + 501] [expr 900000 + \$Iso\*1000 + 500] [expr 920000 + \$Iso\*1000 + 511] \$A \$E \$G \$J \$Iy \$Iz \$TransBeam45x  
 element elasticBeamColumn [expr 9201000 + \$Iso\*10000 + 420] [expr 920000 + \$Iso\*1000 + 421] [expr 900000 + \$Iso\*1000 + 400] \$A \$E \$G \$J \$Iy \$Iz \$TransBeam45x  
 element elasticBeamColumn [expr 9201000 + \$Iso\*10000 + 401] [expr 900000 + \$Iso\*1000 + 400] [expr 920000 + \$Iso\*1000 + 411] \$A \$E \$G \$J \$Iy \$Iz \$TransBeam45x  
  
 element elasticBeamColumn [expr 9301000 + \$Iso\*10000 + 820] [expr 930000 + \$Iso\*1000 + 821] [expr 900000 + \$Iso\*1000 + 800] \$A \$E \$G \$J \$Iy \$Iz \$TransBeam135x  
 element elasticBeamColumn [expr 9301000 + \$Iso\*10000 + 801] [expr 900000 + \$Iso\*1000 + 800] [expr 930000 + \$Iso\*1000 + 811] \$A \$E \$G \$J \$Iy \$Iz \$TransBeam135x  
 element elasticBeamColumn [expr 9301000 + \$Iso\*10000 + 520] [expr 930000 + \$Iso\*1000 + 521] [expr 900000 + \$Iso\*1000 + 500] \$A \$E \$G \$J \$Iy \$Iz \$TransBeam135x

element elasticBeamColumn [expr 9301000 + \$Iso\*10000 + 501] [expr 900000 + \$Iso\*1000 + 500] [expr 930000 + \$Iso\*1000 + 511] \$A \$E \$G \$J \$Iy  
\$Iz \$TransBeam135x

element elasticBeamColumn [expr 9301000 + \$Iso\*10000 + 420] [expr 930000 + \$Iso\*1000 + 421] [expr 900000 + \$Iso\*1000 + 400] \$A \$E \$G \$J \$Iy  
\$Iz \$TransBeam135x

element elasticBeamColumn [expr 9301000 + \$Iso\*10000 + 401] [expr 900000 + \$Iso\*1000 + 400] [expr 930000 + \$Iso\*1000 + 411] \$A \$E \$G \$J \$Iy  
\$Iz \$TransBeam135x

#vertical stiff beam

#y-direction (main)

element elasticBeamColumn [expr 9002000 + \$Iso\*10000 + 872] [expr 900000 + \$Iso\*1000 + 821] [expr 900000 + \$Iso\*1000 + 721] \$A \$E \$G \$J \$Iy  
\$Iz \$TransCol

element elasticBeamColumn [expr 9002000 + \$Iso\*10000 + 751] [expr 900000 + \$Iso\*1000 + 711] [expr 900000 + \$Iso\*1000 + 511] \$A \$E \$G \$J \$Iy  
\$Iz \$TransCol

element elasticBeamColumn [expr 9002000 + \$Iso\*10000 + 871] [expr 900000 + \$Iso\*1000 + 811] [expr 900000 + \$Iso\*1000 + 713] \$A \$E \$G \$J \$Iy  
\$Iz \$TransCol

element elasticBeamColumn [expr 9002000 + \$Iso\*10000 + 752] [expr 900000 + \$Iso\*1000 + 724] [expr 900000 + \$Iso\*1000 + 521] \$A \$E \$G \$J \$Iy  
\$Iz \$TransCol

#x-direction

element elasticBeamColumn [expr 9102000 + \$Iso\*10000 + 872] [expr 910000 + \$Iso\*1000 + 821] [expr 910000 + \$Iso\*1000 + 721] \$A \$E \$G \$J \$Iy  
\$Iz \$TransCol

element elasticBeamColumn [expr 9102000 + \$Iso\*10000 + 751] [expr 910000 + \$Iso\*1000 + 711] [expr 910000 + \$Iso\*1000 + 511] \$A \$E \$G \$J \$Iy  
\$Iz \$TransCol

element elasticBeamColumn [expr 9102000 + \$Iso\*10000 + 871] [expr 910000 + \$Iso\*1000 + 811] [expr 910000 + \$Iso\*1000 + 713] \$A \$E \$G \$J \$Iy  
\$Iz \$TransCol

element elasticBeamColumn [expr 9102000 + \$Iso\*10000 + 752] [expr 910000 + \$Iso\*1000 + 724] [expr 910000 + \$Iso\*1000 + 521] \$A \$E \$G \$J \$Iy  
\$Iz \$TransCol

#45degree-direction

element elasticBeamColumn [expr 9202000 + \$Iso\*10000 + 872] [expr 920000 + \$Iso\*1000 + 821] [expr 920000 + \$Iso\*1000 + 721] \$A \$E \$G \$J \$Iy  
\$Iz \$TransCol

element elasticBeamColumn [expr 9202000 + \$Iso\*10000 + 751] [expr 920000 + \$Iso\*1000 + 711] [expr 920000 + \$Iso\*1000 + 511] \$A \$E \$G \$J \$Iy  
\$Iz \$TransCol

```

element elasticBeamColumn [expr 9202000 + $Iso*10000 + 871] [expr 920000 +
$Iso*1000 + 811] [expr 920000 + $Iso*1000 + 713] $A $E $G $J $Iy
$Iz $TransCol

```

```

element elasticBeamColumn [expr 9202000 + $Iso*10000 + 752] [expr 920000 +
$Iso*1000 + 724] [expr 920000 + $Iso*1000 + 521] $A $E $G $J $Iy
$Iz $TransCol

```

```

element elasticBeamColumn [expr 9302000 + $Iso*10000 + 872] [expr 930000 +
$Iso*1000 + 821] [expr 930000 + $Iso*1000 + 721] $A $E $G $J $Iy
$Iz $TransCol

```

```

element elasticBeamColumn [expr 9302000 + $Iso*10000 + 751] [expr 930000 +
$Iso*1000 + 711] [expr 930000 + $Iso*1000 + 511] $A $E $G $J $Iy
$Iz $TransCol

```

```

element elasticBeamColumn [expr 9302000 + $Iso*10000 + 871] [expr 930000 +
$Iso*1000 + 811] [expr 930000 + $Iso*1000 + 713] $A $E $G $J $Iy
$Iz $TransCol

```

```

element elasticBeamColumn [expr 9302000 + $Iso*10000 + 752] [expr 930000 +
$Iso*1000 + 724] [expr 930000 + $Iso*1000 + 521] $A $E $G $J $Iy
$Iz $TransCol

```

```

#shear element

```

```

set Atruss [expr 1.0*2*$Is/2];

```

```

#y-direction(main)

```

```

element corotTruss [expr 9003000 + $Iso*10000 + 721] [expr 900000 + $Iso*1000 +
721] [expr 900000 + $Iso*1000 + 711] $Atruss $ShearRubberTag;

```

```

element elasticBeamColumn [expr 9004000 + $Iso*10000 + 721] [expr 900000 +
$Iso*1000 + 721] [expr 900000 + $Iso*1000 + 711] 1.e-7 1. 1. 1.e10 1.e-
10 1.e8 $TransCorotY

```

```

element corotTruss [expr 9003000 + $Iso*10000 + 743] [expr 900000 + $Iso*1000 +
724] [expr 900000 + $Iso*1000 + 713] $Atruss $ShearRubberTag;

```

```

element elasticBeamColumn [expr 9004000 + $Iso*10000 + 743] [expr 900000 +
$Iso*1000 + 724] [expr 900000 + $Iso*1000 + 713] 1.e-7 1. 1. 1.e10 1.e-
10 1.e8 $TransCorotY

```

```

#x-direction

```

```

element corotTruss [expr 9103000 + $Iso*10000 + 721] [expr 910000 + $Iso*1000 +
721] [expr 910000 + $Iso*1000 + 711] $Atruss $ShearRubberTag;

```

```

element elasticBeamColumn [expr 9104000 + $Iso*10000 + 721] [expr 910000 +
$Iso*1000 + 721] [expr 910000 + $Iso*1000 + 711] 1.e-7 1. 1. 1.e10 1.e-
10 1.e8 $TransCorotX

```

```

element corotTruss [expr 9103000 + $Iso*10000 + 743] [expr 910000 + $Iso*1000 +
724] [expr 910000 + $Iso*1000 + 713] $Atruss $ShearRubberTag;

```

```

element elasticBeamColumn [expr 9104000 + $Iso*10000 + 743] [expr 910000 +
$Iso*1000 + 724] [expr 910000 + $Iso*1000 + 713] 1.e-7 1. 1. 1.e10 1.e-
10 1.e8 $TransCorotX

```

```

#45degree-direction

```

```

element corotTruss [expr 9203000 + $iIso*10000 + 721] [expr 920000 + $iIso*1000 +
721] [expr 920000 + $iIso*1000 + 711] $Atruss $ShearRubberTag;
element elasticBeamColumn [expr 9204000 + $iIso*10000 + 721] [expr 920000 +
$iIso*1000 + 721] [expr 920000 + $iIso*1000 + 711] 1.e-7 1. 1. 1.e10 1.e-
10 1.e8 $TransCorot45x
element corotTruss [expr 9203000 + $iIso*10000 + 743] [expr 920000 + $iIso*1000 +
724] [expr 920000 + $iIso*1000 + 713] $Atruss $ShearRubberTag;
element elasticBeamColumn [expr 9204000 + $iIso*10000 + 743] [expr 920000 +
$iIso*1000 + 724] [expr 920000 + $iIso*1000 + 713] 1.e-7 1. 1. 1.e10 1.e-
10 1.e8 $TransCorot45x

element corotTruss [expr 9303000 + $iIso*10000 + 721] [expr 930000 + $iIso*1000 +
721] [expr 930000 + $iIso*1000 + 711] $Atruss $ShearRubberTag;
element elasticBeamColumn [expr 9304000 + $iIso*10000 + 721] [expr 930000 +
$iIso*1000 + 721] [expr 930000 + $iIso*1000 + 711] 1.e-7 1. 1. 1.e10 1.e-
10 1.e8 $TransCorot135x
element corotTruss [expr 9303000 + $iIso*10000 + 743] [expr 930000 + $iIso*1000 +
724] [expr 930000 + $iIso*1000 + 713] $Atruss $ShearRubberTag;
element elasticBeamColumn [expr 9304000 + $iIso*10000 + 743] [expr 930000 +
$iIso*1000 + 724] [expr 930000 + $iIso*1000 + 713] 1.e-7 1. 1. 1.e10 1.e-
10 1.e8 $TransCorot135x

# Lead plug
element zeroLengthSection [expr 9005000 + $iIso*10000 + 49] [expr 900000 +
$iIso*1000 + 900] [expr 900000 + $iIso*1000 + 400] $ShearLeadTag

# create vertical springs for multi spring isolator model
# element tag:
# 1st digit = element for multiple spring node 9
# 2nd digit = 0: y-direction (main), 1: x-direction, 2 and 3: 45degree direction
# 3rd digit = isolator ID
# 4th and 5th digits = connecting levels (eg.: 54 = connects level 5 (bott of top vertical
springs) with level 4 (top of top vertical springs)
# 6th digit horizontal distance from center line (2 = -$ls , 1 = $ls, 0 = at the center )
# 7th digit indicates number of vertical spring away from center in both directions (0 = center,
1 = one node away from center in x-dir)
# examples: 9119800

#y-direction (main)
element zeroLength [expr 9000000 + $iIso*10000 + 9800] [expr 900000 + $iIso*1000 +
900] [expr 900000 + $iIso*1000 + 800] -mat $MatVertSpringTagCenter -dir 3 ;
#center
element zeroLength [expr 9000000 + $iIso*10000 + 9811] [expr 900000 + $iIso*1000 +
911] [expr 900000 + $iIso*1000 + 811] -mat $MatVertSpringTag -dir 3 ;
element zeroLength [expr 9000000 + $iIso*10000 + 9821] [expr 900000 + $iIso*1000 +
921] [expr 900000 + $iIso*1000 + 821] -mat $MatVertSpringTag -dir 3 ;
element zeroLength [expr 9000000 + $iIso*10000 + 5400] [expr 900000 + $iIso*1000 +
500] [expr 900000 + $iIso*1000 + 400] -mat $MatVertSpringTagCenter -dir 3
;#center

```

```

element zeroLength [expr 900000 + $iIso*1000 + 5411] [expr 900000 + $iIso*1000 +
511] [expr 900000 + $iIso*1000 + 411] -mat $MatVertSpringTag -dir 3 ;
element zeroLength [expr 900000 + $iIso*1000 + 5421] [expr 900000 + $iIso*1000 +
521] [expr 900000 + $iIso*1000 + 421] -mat $MatVertSpringTag -dir 3 ;
#x-direction
element zeroLength [expr 9100000 + $iIso*10000 + 9811] [expr 910000 + $iIso*1000 +
911] [expr 910000 + $iIso*1000 + 811] -mat $MatVertSpringTag -dir 3 ;
element zeroLength [expr 9100000 + $iIso*10000 + 9821] [expr 910000 + $iIso*1000 +
921] [expr 910000 + $iIso*1000 + 821] -mat $MatVertSpringTag -dir 3 ;
element zeroLength [expr 9100000 + $iIso*10000 + 5411] [expr 910000 + $iIso*1000 +
511] [expr 910000 + $iIso*1000 + 411] -mat $MatVertSpringTag -dir 3 ;
element zeroLength [expr 9100000 + $iIso*10000 + 5421] [expr 910000 + $iIso*1000 +
521] [expr 910000 + $iIso*1000 + 421] -mat $MatVertSpringTag -dir 3 ;
#45-direction
element zeroLength [expr 9200000 + $iIso*10000 + 9811] [expr 920000 + $iIso*1000 +
911] [expr 920000 + $iIso*1000 + 811] -mat $MatVertSpringTag -dir 3 ;
element zeroLength [expr 9200000 + $iIso*10000 + 9821] [expr 920000 + $iIso*1000 +
921] [expr 920000 + $iIso*1000 + 821] -mat $MatVertSpringTag -dir 3 ;
element zeroLength [expr 9200000 + $iIso*10000 + 5411] [expr 920000 + $iIso*1000 +
511] [expr 920000 + $iIso*1000 + 411] -mat $MatVertSpringTag -dir 3 ;
element zeroLength [expr 9200000 + $iIso*10000 + 5421] [expr 920000 + $iIso*1000 +
521] [expr 920000 + $iIso*1000 + 421] -mat $MatVertSpringTag -dir 3 ;

element zeroLength [expr 9300000 + $iIso*10000 + 9811] [expr 930000 + $iIso*1000 +
911] [expr 930000 + $iIso*1000 + 811] -mat $MatVertSpringTag -dir 3 ;
element zeroLength [expr 9300000 + $iIso*10000 + 9821] [expr 930000 + $iIso*1000 +
921] [expr 930000 + $iIso*1000 + 821] -mat $MatVertSpringTag -dir 3 ;
element zeroLength [expr 9300000 + $iIso*10000 + 5411] [expr 930000 + $iIso*1000 +
511] [expr 930000 + $iIso*1000 + 411] -mat $MatVertSpringTag -dir 3 ;
element zeroLength [expr 9300000 + $iIso*10000 + 5421] [expr 930000 + $iIso*1000 +
521] [expr 930000 + $iIso*1000 + 421] -mat $MatVertSpringTag -dir 3 ;

}

```